THE UNIVERSITY of EDINBURGH

Edinburgh Research Explorer

Individual Dynamical Masses of Ultracool Dwarfs

Citation for published version:
Dupuy, TJ & Liu, MC 2017, 'Individual Dynamical Masses of Ultracool Dwarfs', *The Astrophysical Journal Supplement Series*, vol. 231, no. 2, 15. https://doi.org/10.3847/1538-4365/aa5e4c

Digital Object Identifier (DOI):
10.3847/1538-4365/aa5e4c

Link:
Link to publication record in Edinburgh Research Explorer

Document Version:
Peer reviewed version

Published In:
The Astrophysical Journal Supplement Series

General rights
Copyright for the publications made accessible via the Edinburgh Research Explorer is retained by the author(s) and / or other copyright owners and it is a condition of accessing these publications that users recognise and abide by the legal requirements associated with these rights.

Take down policy
The University of Edinburgh has made every reasonable effort to ensure that Edinburgh Research Explorer content complies with UK legislation. If you believe that the public display of this file breaches copyright please contact openaccess@ed.ac.uk providing details, and we will remove access to the work immediately and investigate your claim.

OPEN ACCESS

Download date: 31. Jul. 2020

arXiv:1703.05775v2 [astro-ph.SR] 1 Jun 2017

Individual Dynamical Masses of Ultracool Dwarfs*†‡

Trent J. Dupuy[1] and Michael C. Liu[2]

ABSTRACT

We present the full results of our decade-long astrometric monitoring programs targeting 31 ultracool binaries with component spectral types M7–T5. Joint analysis of resolved imaging from Keck Observatory and *Hubble Space Telescope* and unresolved astrometry from CFHT/WIRCam yields parallactic distances for all systems, robust orbit determinations for 23 systems, and photocenter orbits for 19 systems. As a result, we measure 38 precise individual masses spanning 30–115 $M_{\rm Jup}$. We determine a model-independent substellar boundary that is ≈70 $M_{\rm Jup}$ in mass (≈L4 in spectral type), and we validate Baraffe et al. (2015) evolutionary model predictions for the lithium-depletion boundary (60 $M_{\rm Jup}$ at field ages). Assuming each binary is coeval, we test models of the substellar mass–luminosity relation and that find in the L/T transition, only the Saumon & Marley (2008) "hybrid" models accounting for cloud clearing match our data. We derive a precise, mass-calibrated spectral type–effective temperature relation covering 1100–2800 K. Our masses enable a novel direct determination of the age distribution of field brown dwarfs spanning L4–T5 and 30–70 $M_{\rm Jup}$. We determine a median age of 1.3 Gyr, and our population synthesis modeling indicates our sample is consistent with a constant star formation history modulated by dynamical heating in the Galactic disk. We discover two triple-brown-dwarf systems, the first with directly measured masses and eccentricities. We examine the eccentricity distribution, carefully considering biases and completeness, and find that low-eccentricity orbits are significantly more common among ultracool binaries than solar-type binaries, possibly indicating the early influence of long-lived dissipative gas disks. Overall, this work represents a major advance in the empirical view of very low-mass stars and brown dwarfs.

---

*Data presented herein were obtained at the W.M. Keck Observatory, which is operated as a scientific partnership among the California Institute of Technology, the University of California, and the National Aeronautics and Space Administration. The Observatory was made possible by the generous financial support of the W.M. Keck Foundation.

†Based on data obtained with WIRCam, a joint project of CFHT, Taiwan, Korea, Canada, France, at the Canada-France-Hawaii Telescope, which is operated by the National Research Council of Canada, the Institute National des Sciences de l'Univers of the Centre National de la Recherche Scientifique of France, and the University of Hawaii.

‡Based on observations made with the NASA/ESA *Hubble Space Telescope*, obtained at the Space Telescope Science Institute, which is operated by the Association of Universities for Research in Astronomy, Inc., under NASA contract NAS 5-26555. These observations are associated with programs GO-11593, GO-12317, and GO-12661.

[1]The University of Texas at Austin, Department of Astronomy, 2515 Speedway C1400, Austin, TX 78712, USA

[2]Institute for Astronomy, University of Hawai'i, 2680 Woodlawn Drive, Honolulu, HI 96822, USA

Subject headings: astrometry — binaries: close — brown dwarfs — stars: evolution, fundamental parameters — parallaxes

1. Introduction

Mass is the most important property governing the destiny of self-gravitating gaseous objects in hydrostatic equilibrium. Mass determines whether an object becomes a star, generating sufficient energy through nuclear fusion of hydrogen to stabilize itself against gravitational collapse, or a brown dwarf, which primarily supports itself by degeneracy pressure. The dichotomy in the way these two classes of objects satisfy hydrostatic equilibrium results in drastically different evolutionary outcomes. Sufficiently massive objects maintain a relatively stable luminosity and temperature, becoming stars on the main sequence for millions to trillions of years. Meanwhile, objects of substellar mass steadily and drastically decrease in luminosity and temperature. One key observational consequence is that the coldest gaseous objects can be confidently identified as brown dwarfs (e.g., Oppenheimer et al. 1995). However, the masses of most ultracool dwarfs are indeterminate because observables like luminosity and temperature are degenerate between mass and age, such that the mass could be lower or higher if the object is younger or older, respectively.

The evolution of brown dwarfs and the substellar boundary itself are largely understood based on theoretical work over the last two decades (e.g., Saumon et al. 1994; Baraffe et al. 1995; Burrows et al. 1997; Chabrier & Baraffe 1997; Lodders 1999; Chabrier et al. 2000; Burrows et al. 2001; Baraffe et al. 2003; Saumon & Marley 2008; MacDonald & Mullan 2009; Baraffe et al. 2015). Broadly speaking, the interior physics of evolutionary models over this time has remained the same, while the treatment of the surface boundary conditions has advanced greatly due to improved molecular line lists, chemistry, and cloud modeling (see a recent review by Marley & Robinson 2015). Clouds in particular have long thought to be the key to explaining major variations in the emergent flux of brown dwarfs, especially in the change from L to T spectral types (the L/T transition). Understanding clouds in theoretical modeling is imperative given that they can exert great influence on the atmosphere's opacity, but the physical processes governing cloud formation, particle size distribution, and sedimentation are all effectively free parameters that can only be constrained loosely by observations. Over the past decade, model atmospheres have been largely developed with guidance from observations of colors, absolute magnitudes, and spectra, so they can reproduce the observed surface properties of ultracool dwarfs reasonably well. However, as atmospheres are a key input to evolutionary models, there arises an entirely different question of whether predictions of fundamental properties (luminosity, radius, etc.) are improved by the adoption of the latest cloud prescriptions and molecular opacities.

Direct mass measurements are central to tests of evolutionary models. Previous work on ultracool dwarfs (spectral types $\geq$M7) has focused on *total* dynamical masses that can be readily determined from *relative* astrometric orbits because the narrow field-of-view afforded by adaptive optics (AO) imaging rarely contains any reference stars that could be used for absolute astrometry. To date there are total dynamical masses for more than a dozen ultracool binaries (e.g., Lane et al. 2001; Leinert et al. 2001; Bouy et al. 2004; Liu et al. 2008; Dupuy et al. 2009a,b,c, 2010, 2014; Cardoso et al. 2009; Konopacky et al. 2010). In a few special cases, individual masses have been determined: for two single companions to main-sequence stars (Ireland et al. 2008; Crepp et al. 2012); for the companion AB Dor C by assuming a mass for AB Dor A (Close et al. 2005; Guirado et al. 2006); and for three ultracool binary systems where mass ratios are measured using radial velocities or absolute astrometry (Zapatero Osorio et al. 2004; Simon et al. 2006; Seifahrt et al. 2008; Konopacky et al. 2010; Köhler et al. 2012; Dupuy et al. 2016). However, most of the objects in this small sample in the literature are likely to be stars and not brown dwarfs. For additional context, our individual mass measurements for the L6.5+T1.5 binary SDSS J1052+4422AB marked the first individual masses for any field L or T dwarfs (Dupuy et al. 2015b). This stands in stark contrast to the situation for individual dynamical masses of earlier-type M dwarfs, where dozens of measurements over the years have now reached very high precision (e.g., Henry & McCarthy 1993; Delfosse et al. 2000; Benedict et al. 2016). Thus, even though significant progress has been made on ultracool dwarfs using mostly total dynamical masses, the individual masses needed for the strongest tests of models have been lacking.

We present here orbit and mass determinations for a large sample of ultracool binaries with component spectral types of M7–T5. Results here are based on a uniform (re-)analysis of Keck AO imaging and masking data from the past 10 years, as well as *HST* imaging from the past 20 years, and nearly a decade of absolute astrometric monitoring at the Canada-France-Hawaii Telescope (CFHT). The combined data set not only provides total dynamical masses from the relative orbits and CFHT parallaxes but also yields precise mass ratios from measurements of photocenter motion in our CFHT data. We report observations for our entire sample of 31 binaries, from which we determine robust orbits for 23 systems and individual masses for 19 systems (two of which turn out to be previously unknown triple systems). We critically examine some of the basic predictions of evolutionary models, such as the mass limits for hydrogen and lithium fusion, and we establish empirical relations between parameters such as mass, luminosity, effective temperature, absolute magnitude, and spectral type. We use the brown dwarfs in our sample as clocks (age-dated from models using mass and luminosity) to directly determine the age distribution of the field population. Finally, we re-visit the eccentricity distribution of ultracool dwarfs (initially discussed in Dupuy & Liu 2011) and the potential implications for the earliest stages of evolution.

2. Sample Selection for Keck & CFHT Orbit Monitoring

The orbit sample presented here was drawn from the very low-mass visual binaries ($M_{\rm tot} \lesssim 0.2\,M_{\odot}$; using published mass estimates) known to us in early 2008. In addition to the total mass criterion, we also excluded binaries with integrated light spectral types of M6 or earlier and published distance estimates $\gtrsim$40 pc. For the work presented here we also only consider binaries with types earlier than T6. As the starting point for defining this sample we used the summary table of Burgasser et al. (2007)[1] to which we added other binaries from the literature and from our own proprietary Keck LGS AO data in hand at the time. From this whole sample of binaries, we selected only those with estimated periods that suggested $\gtrsim$30% of their orbit could be complete by 2010. We computed these initial period estimates using the estimated total mass from the literature and a range of semimajor axes corresponding to the projected separation at discovery (e.g., Torres 1999; Dupuy & Liu 2011), where we adopted the 1σ minimum period for our estimates.

In Table 1 we list all 33 binaries in our Keck+CFHT astrometric monitoring sample, along with three other binaries that have published orbit and parallax measurements. We began obtaining resolved Keck AO astrometry in 2007–2008, and we combined our new astrometry with available data in the literature or public archives (e.g., *HST* and Gemini) to refine our orbital period estimates and thereby our prioritizaton for Keck observations. As described in Dupuy et al. (2011), we performed a Monte Carlo analysis of this multi-epoch data that provided period estimates based on actual orbital motion, not simply projected separations. We subsequently deprioritized Keck observations of the systems with longer expected periods, focusing our observational efforts on the shorter-period systems. We did occasionally obtain Keck astrometry for the systems with the longest expected periods in our sample.

For most of the binaries in our sample, we began integrated-light astrometric monitoring with CFHT in the second half of 2007 or in 2008 and continued collecting data until parallaxes were determined. We did not include in our CFHT program the three binaries with *Hipparcos* parallaxes (Gl 417BC, HD 130948BC, Gl 569Bab), but we did include other systems with published parallaxes at the time (11 binaries) in order to improve the distance accuracy. Indeed, for seven of these binaries we reduce the uncertainty by a factor of 1.9–6.7. Most of these initial parallax determinations were reported in Dupuy & Liu (2012). We have continued monitoring this sample with CFHT up to the present in order to place constraints on photocenter motion and thereby the binary mass ratios.

Our orbit sample selection is essentially based on spectral type and projected separation, but for some purposes, like studies of the eccentricity distribution (e.g., Dupuy & Liu 2011), it is important to consider whether our target selection and prioritization has introduced biases in our sample beyond those intrinsic to the population of ultracool binaries known in late 2007 and early 2008. Although our sample was initially defined in terms of the probability that a given binary would yield an orbit determination by 2010, we can retroactively determine over what range of observable

[1]We note the following significant updates to Table 1 of Burgasser et al. (2007): 2MASS J0652307+471034AB is listed as a 2.0 AU binary (Reid et al., in prep.), but Reid et al. (2006b), Konopacky et al. (2010), and Keck LGS AO observations of our own confirm that it is single; SDSS J233558.51−001304.1AB is much more distant (160 ± 30 pc) and thus wider (9.0 ± 1.7 AU) than previously estimated given that its spectral type is M7 (West et al. 2008) not early- to mid-L.

properties our sample is complete. To the best of our knowledge, our initial sample included all observable binaries known at the time with integrated-light spectral types of M6.5–T5.5,[2] projected separations ≤6 AU at discovery, and distances $\lesssim$40 pc (based on the spectrophotometric distance estimate in the absence of a parallax).[3] 2MASSI J1426316+155701AB is the only binary meeting these criteria for which we never ultimately obtained any CFHT or Keck LGS AO data because we de-prioritized it based on archival and published astrometry (Bouy et al. 2008) that showed its projected separation had increased from 4.1 AU at discovery to 6.9 AU projected separation by 2006 June. Although we have attempted to resolve 2MASSI J0856479+223518AB on multiple occasions with Keck LGS AO, we have never been successful, so this binary does not appear in any of the following discussion.

Practical observational considerations imposed some limitations on our sample that should not correspond to any physically meaningful selection biases. The largest subset of targets meeting the above criteria but excluded from our sample are those not accessible to Keck AO because they are too far south: GJ 1001BC (L5; Golimowski et al. 2004), DENIS J035726.9−441730AB (L0; Bouy et al. 2003; Gizis et al. 2003), SCR J1845−6357AB (M8.5; Biller et al. 2006), ϵ Ind Bab (T2.5; McCaughrean et al. 2004), and 2MASS J22551861−5713056AB (L6; Reid et al. 2008a). Another practical limitation is that not all ultracool binaries have a nearby star bright enough for tip-tilt correction as needed for LGS AO imaging at Keck ($R \lesssim 18.5$ mag within ≈65″). This excluded DENIS J100428.3−114648AB (M8), 2MASSW J1239272+551537AB (L5), and 2MASS J14304358+2915405AB (L2). This tip-tilt star limitation also excluded three of the most promising T dwarf binaries, SDSS J0423−0414AB (T0), SDSS J0926+5847AB (T4.5), and 2MASS J0518−2828AB (T1p), so we conducted *HST* monitoring of these binaries instead.

Some of our sample binaries already have published orbital monitoring results, either from our own work (Liu et al. 2008; Dupuy et al. 2009a,b,c, 2010; Dupuy & Liu 2011; Dupuy et al. 2014, 2015b) or from others (Lane et al. 2001; Zapatero Osorio et al. 2004; Simon et al. 2006; Konopacky et al. 2010). In the following, we perform a complete, uniform analysis of all data on these systems, even in cases where we have previously published results. 2MASS J0746+2000AB had a published orbit (Bouy et al. 2004) before we began our observing program, and Konopacky et al. (2010) provided significant additional astrometry and a refined orbit. We only obtained Keck

[2]Our spectral type cuts excluded the late type binaries 2MASSW J1225543−273947AB (T6) and 2MASS J15530228+1532369AB (T7). At earlier types, we excluded LSPM J1314+1320AB based on an estimated spectral type of M6 from Law et al. (2006), but note that it has since been updated to M7 (Lépine et al. 2009; Dupuy et al. 2016). Other notable systems near the boundary of our spectral type cutoff and thus not included here are L 726-8AB a.k.a. Gl 69AB (M5.5+M6; Geyer et al. 1988, Kirkpatrick et al. 1991), L 789-6ABC a.k.a. Gl 866ABC (M5+M5.5:+M6.5:; Henry et al. 1994, Delfosse et al. 2000), and GJ 1245ABC (M5.5+M5.5+M6.5:; Kirkpatrick et al. 2012; Benedict et al. 2016).

[3]By focusing on nearby systems, the only binaries with projected separations ≤6 AU that we excluded were 2MASS J16000548+1708328AB (61 pc; Bouy et al. 2003) and binaries in Taurus and Upper Scorpius (Kraus et al. 2005, 2006). The most distant binary in our sample is LP 415-20AB at 39.7 ± 1.1 pc, and its original estimated distance was actually 30 ± 5 pc (Siegler et al. 2003).

astrometry for 2MASS J0746+2000AB at one epoch, but we have been monitoring its absolute astrometry from CFHT since 2008. Therefore, we have re-analyzed published *HST* and Keck data of 2MASS J0746+2000AB from public archives in order to include it in our sample of joint Keck+CFHT orbital analysis. LHS 1070BC is the only other binary that would have been in our sample if it did not have a previously published orbit (Leinert et al. 2001; Seifahrt et al. 2008; Köhler et al. 2012). Since the published orbit of LHS 1070BC is not based on Keck astrometry, and we did not observe it as part of our CFHT astrometry program, we simply use the orbit parameters quoted in the literature and perform no orbital analysis of our own. We also include the recently published orbit for LSPM J1314+1320AB (Dupuy et al. 2016), which is based on the same orbital analysis presented here. The ϵ Ind Bab system is too far south to observe from Maunakea, but it also has a published orbit determination from Cardoso et al. (2009), so we include the published parameters in our discussion as well.

3. Observations

3.1. Relative Astrometry from High-Angular Resolution Observations

3.1.1. Keck/NIRC2 AO Imaging & Masking

We present here new Keck/NIRC2 AO imaging and non-redundant aperture masking observations, both in natural guide star and laser guide star modes, in addition to a re-analysis of our own previously published data and publicly available archival data for our sample binaries. Our approach for reducing NIRC2 imaging and obtaining the binary parameters separation, position angle (PA), and flux ratio is well established in our previous work (Liu et al. 2006, 2008; Dupuy et al. 2009a,b,c, 2010, 2015a). Briefly, we apply standard calibrations (dark subtraction, flat fielding) and then fit an analytic, three-component Gaussian model to each point source in the images. In cases where the binary components are spatially well separated, we perform PSF-fitting using StarFinder (Diolaiti et al. 2000). In other cases where a third, unsaturated star is in the field (e.g, Gl 569A and Gl 569Bab), we use the third single star as an empirical PSF to fit the binary. Analysis of our NIRC2 masking data was performed using a pipeline similar to previous papers (e.g., Ireland et al. 2008; Ireland & Kraus 2008) and is described in detail in Section 2.2 of Dupuy et al. (2009c). For NIRC2 narrow camera images obtained before 2015 April 13 UT, we use the astrometric solution of Yelda et al. (2010) to correct our measured (x, y) image coordinates for nonlinear optical distortion, using their derived pixel scale of $9.952 \pm 0.002\,\mathrm{mas\,pixel}^{-1}$ and $+0\overset{\circ}{.}252 \pm 0\overset{\circ}{.}0.009$ correction for the orientation given in the NIRC2 image headers. For narrow camera imaging obtained after 2015 April 13 UT, we use an updated distortion solution from Service et al. (2016) that accounts for the first ever realignment of the AO system. The post-realignment pixel scale and orientation are $9.971 \pm 0.004\,\mathrm{mas\,pixel}^{-1}$ and $+0\overset{\circ}{.}262 \pm 0\overset{\circ}{.}0.020$, respectively. For NIRC2 wide camera images, which represent a very small subset of our observations, we used the distortion solution of Fu et al. (2012, priv. comm.)[4] that assumes a pixel scale of 39.686 mas pixel^{-1} and the Yelda et al. PA offset of $+0\overset{\circ}{.}252$.

We have made some small improvements to our astrometric analysis compared to our previous work, as described in Dupuy et al. (2016). For data obtained in vertical angle mode, where the sky rotation of the images relative to the detector axes is constantly changing, we corrected the rotator angles reported in the header to correspond to the midpoint instead of the start of the exposure. We also apply corrections for differential aberration and atmospheric refraction. The refraction correction requires knowledge of the air temperature, pressure, and humidity on Maunakea during our observations, for which we used the weather data archived by CFHT.[5] We generally adopt errors that are the rms of measurements from individual dithers at a given epoch. In some cases where we have previously published astrometry we instead use estimates of errors from Monte Carlo simulations of fitting artificial binaries.

Table 2 gives our measured astrometry and flux ratios for all Keck AO data used in our orbital analysis. In total there are 339 distinct measurements (unique bandpass and epoch for a given target), where 302 of these are direct imaging and 37 are non-redundant aperture masking. The median Keck separation error is 0.6 mas with 90% of measurements having errors between 0.06–1.9 mas. The median PA error is $0\overset{\circ}{.}3$ with 90% of measurement errors between $0\overset{\circ}{.}02$ and $1\overset{\circ}{.}3$. (We caution that there are possible systematic effects, e.g., uncertainty in the distortion solution and tip-tilt jitter, that are difficult to quantify and may impact the few measurements with astrometric errors well below 0.1 mas. The fact that none of these data points show up as outliers in our orbit fitting analysis described later could be due to the fact that not all phases of all orbits are overconstrained by numerous degrees of freedom.) Eight of the imaging measurements are from six unpublished archival data sets. For HD 130948BC we used data sets from 2005 Feb 25 UT (PI Prato) and 2011 Mar 25 UT (PI Bowler). For Gl 569Bab we used data sets from 2003 Apr 15 UT (PI Simon), 2004 Aug 10 UT (PI Kulkarni), and 2011 Mar 25 UT (PI Bowler). For LSPM J1735+2634AB we used a JHK data set from 2007 Aug 1 UT (PI N. Law). Fourteen other measurements are from our re-analysis of ten previously published data sets in the archive: LP 349-25, 2MASS J0920+3517AB, 2MASS J0746+2000AB, HD 130948BC, 2MASS J1847+5522AB, and 2MASS J2206−2047AB (PI Ghez; Konopacky et al. 2010) and SDSS J2052−1609AB (PI C. Gelino; Bardalez Gagliuffi et al. 2015).

[4] `http://astro.physics.uiowa.edu/~fu/idl/nirc2wide/`

[5] `http://mkwc.ifa.hawaii.edu/archive/wx/cfht/`

3.1.2. HST/ACS-WFC Monitoring

In addition to our Keck AO monitoring, we also obtained data for three T dwarf binaries lacking suitable LGS tip-tilt stars over a 3-year *HST* program[6] using the Advanced Camera for Surveys (ACS) Wide Field Camera (WFC). ACS-WFC has a pixel scale of ≈50 mas, and we used the $F814W$ bandpass for all of our observations to optimize between S/N and angular resolution. SDSS J0423−0414AB (T0) and SDSS J0926+5847AB (T4.5) were both resolved in all of our images. 2MASS J0518−2828AB (T1p) was not resolved in any of our six observations spanning 2009 Dec 11 UT to 2012 Oct 27 UT. Based on simulations we performed for our observation proposal, we expected to readily resolve 2MASS J0518−2828AB if it was at a similar separation as its discovery (51 mas; Burgasser et al. 2006b). Given that the flux ratio of 2MASS J0518−2828AB in the $F814W$ band is unknown (and difficult to extrapolate from the available infrared data), and a larger flux ratio of ≈2 mag could make it quite difficult to clearly resolve, we conservatively estimate an upper limit of <50 mas on the putative companion's separation during our observations.

For the resolved binaries, we performed PSF fitting of our ACS-WFC images in a similar manner to our previous work on data from other *HST* cameras (e.g., Liu et al. 2008; Dupuy et al. 2009a,b). We used TinyTim (Krist et al. 2011) to generate a PSF model for each pipeline reduced (`flt`) FITS image that we downloaded from the *HST* archive. The only inputs to this model are the target's position on the detector and a template spectrum of comparable spectral type to the target. For the latter, we used optical-to-infrared spectra from Geballe et al. (2002), adopting the integrated-light spectrum of SDSS J0423−0414AB[7] for each of its components and the spectrum of 2MASS J0559−1404[8] for the components of SDSS J0926+5847AB. To test the impact of assuming the same spectrum for each component, we also tried L5 and T5 templates for both components of SDSS J0423−0414AB and found the astrometry changed by <0.6 mas ($<1\sigma$). We use the same PSF model for both components and shift, scale, and add them to each other to create a model binary image. We used the `amoeba` function in IDL, based the routine from Press et al. (1992), to find the best-fit parameters for the binary model: position and flux of the primary (x_0, y_0, f_0) and the binary separation, PA, and flux ratio. We used the information contained in the FITS files to correct our fitted (x, y) positions on the detector to sky coordinates. This accounts for detector defects from the `D2IMARR` FITS extension, a polynomial distortion correction contained in FITS header keywords, and non-polynomial distortion corrections from the `WCSDVARR` FITS extension (Kozhurina-Platais et al. 2015). We then applied the `CD` matrix in the FITS header and a tangent projection to convert the corrected x and y values to RA and Dec.

Table 3 reports the mean and rms of our best-fit binary parameters derived from the individual dithered ACS-WFC images for SDSS J0926+5847AB. While the first five observations show the

---

[6]Programs GO-11593, GO-12317, and GO-12661 (PI Dupuy).

[7]`http://staff.gemini.edu/~sleggett/spectra/T0_SDSS0423-04.txt`

[8]`http://staff.gemini.edu/~sleggett/spectra/T4.5_2MASS0559-14.txt`

binary moving outward and then inward slightly (67 mas to 73 mas to 63 mas), at the final epoch it had moved in significantly and was only marginally resolved. Over the first five epochs we measured flux ratios consistent with being constant at $\Delta F814W = 0.560 \pm 0.024$ mag. We therefore fixed the flux ratio to be 0.56 mag in our fitting of the final imaging observations, giving a separation of 33 ± 5 mas and a very uncertain PA of $283 \pm 30°$. We note that there is nominally an ambiguity in this measured PA, typical for marginally resolved binaries, such that it could be $103 \pm 30°$ instead. However, $283 \pm 30°$ is in better agreement with the orbit fit, so we adopt this value.

At separations of 104–151 mas, SDSS J0423−0414AB was much wider in our ACS-WFC imaging than SDSS J0926+5847AB. We found that using the rms of our SDSS J0423−0414AB measurements as the uncertainties produced a somewhat high χ^2 for the final orbit fit, implying that the rms does not fully capture all systematic errors for this well resolved binary. We therefore examined the rms about the orbit fit of our ACS-WFC data and used this as the common uncertainty in separation (0.6 mas) and PA (0.7°) for all epochs of SDSS J0423−0414AB imaging. The $F814W$ flux ratio we measured across multiple epochs shows some variation within the rms errors, but it would be consistent with being constant if there are 0.05 mag systematic errors in our measured SDSS J0423−0414AB flux ratios.

3.1.3. Other Published & Archival HST Imaging

Many of our sample binaries have *HST* imaging data in the public archive. These are often the observations that discovered the binaries initially, providing the first epoch of astrometry that we use in our orbit fits. As in our previous work, we have re-analyzed the available archival data using our own TinyTim PSF-fitting routine as described in Section 3.1.2. These data come from the WFPC2 Planetary Camera (WFPC2-PC1), ACS High Resolution Channel (ACS-HRC), and NICMOS Camera 1 (NICMOS-NIC1). For all three of these cameras, numerous images of single ultracool dwarfs are also available in the archive from various imaging surveys. We collected these images to make a library of observed single PSFs for each relevant camera and filter combination and used them to perform Monte Carlo simulations of our PSF fitting. For a given binary observation, we replicated the binary properties as closely as possible to the actual fractional pixel separation in x and y by co-adding two different library PSFs centered at different subpixel locations, and scaling the two PSFs to match the flux ratio and S/N of the actual binary data. We ran 100 simulations for each observation, applied the mean systematic offset as a correction to our measurement, and used the rms as the error.

Table 3 gives the resulting binary parameters from our analysis of archival WFPC2-PC1, ACS-HRC, and NICMOS-NIC1 imaging. WFPC2-PC1 data come from programs GO-6345 (PI Kirkpatrick), GO-8146 (PI Reid), GO-8581 (PI Reid), GO-8563 (PI Kirkpatrick), GO-8720 (PI Brandner), GO-9157 (PI Martín), GO-9345 (PI Martín), and GO-9968 (PI Martín). ACS-HRC data come from programs GO-9451 (PI Brandner) and GO-10559 (PI Bouy). NICMOS-NIC1 data come from programs GO-7952 (PI Martín), GO-9833 (PI Burgasser), GO-9843 (PI Gizis), GO-10143 (PI Reid), and GO-11136 (PI Liu).

3.2. Absolute Astrometry from CFHT/WIRCam

We obtained high-precision unresolved astrometry of our sample to determine parallaxes, proper motions, and to constrain the photocenter motion due to the binary orbits. We present here an updated analysis of our data from the Hawaii Infrared Parallax Program that uses the CFHT facility infrared camera WIRCam (Puget et al. 2004). Our observing strategy and custom astrometry pipeline are described in detail in Dupuy & Liu (2012). Briefly, for a given target we obtain data sets on multiple nights each season, with each data set typically comprising 20–30 dithered frames in J band, or in a narrow K-band filter ($K_{\rm H2}$) if the target would saturate in J. Queue observing constraints at CFHT are used to require good seeing and that all J-band observations occur near transit, i.e., at similar airmass, to guard against systematic astrometric errors due to differential chromatic refraction (DCR). We measure Gaussian-windowed centroids by running `sextractor v2.19.5` (Bertin & Arnouts 1996) on the detrended images provided by CFHT. We cross-match detections at a given epoch, using our custom distortion solution and simple linear transformations, and adopt the standard error on the mean as the astrometric measurement error for any given star at each epoch. We then solve for the linear transformations between epochs, iteratively solving for and masking high proper motion and/or parallax sources. We finally cross-match to an astrometric reference catalog (2MASS or SDSS-DR9) to provide absolute calibration of the linear terms and then solve for the proper motion and parallax of every star in the field.

Unlike our previous work, we do not use a stand-alone analysis of our CFHT data to compute the parallax and proper motion of our target binaries. This approach was used by Dupuy & Liu (2012), where we then applied evolutionary model-based corrections to account for the expected orbital motion in the CFHT photocenter. As we have continued monitoring our sample binaries from 2007 or 2008 up to the present, we now have data spanning a much longer fraction of many of our targets' orbital periods. It therefore becomes even more important to freely fit for photocenter motion (as described in Section 4), without imposing assumptions about mass–magnitude relations from evolutionary models or potentially unresolved multiplicity. Indeed, the fact that we are now in a position to detect significant photocenter motion allows us to place strong empirical constraints on the relationship between mass and magnitude, as we have recently demonstrated with SDSS J1052+4422AB (Dupuy et al. 2015b), and possibly detect higher-order multiplicity. We have also made some small changes to improve the performance of our pipeline compared to Dupuy & Liu (2012), such as using the mean instead of the median measured position of a given source at each epoch. In addition, when computing the correction from relative to absolute parallax and proper motion using the Besançon model of the Galaxy (Robin et al. 2003), we now exclude model stars with proper motions larger than the cutoff value we use in our iterative solution of the epoch-to-epoch linear terms.

Table 4 gives all of the absolute astrometry from CFHT for the sample of binaries for which we have orbit-monitoring data from Keck and *HST*. Many of these CFHT observations were originally published in Dupuy & Liu (2012), but the data presented here are nonetheless distinct from what was published previously since we no longer attempt to remove any photocenter motion from the reported absolute astrometry.

4. Joint Orbit & Parallax Analysis

We performed a Markov Chain Monte Carlo (MCMC) analysis to simultaneously fit a relative orbital solution and an absolute astrometric solution to our resolved (Keck, *HST*, etc.) and unresolved (CFHT) astrometry, respectively. This joint fitting approach was originally motivated by binaries that show significant photocenter motion in our CFHT data. However, this approach also has the advantage of appropriately marginalizing over the uncertainty in CFHT photocenter motion when determining parallaxes and proper motions. Fitting for photocenter motion, even if it ends up being consistent with zero, also allows us to constrain mass ratios given that we have independently measured flux ratios. For example, most binaries in our sample have flux ratios near unity, so if their mass ratios are not near unity due to unresolved triple components, then they would display photocenter motion commensurate with the amount of unresolved mass present.

Our joint orbit and parallax MCMC analysis method is similar to our previous work on SDSS J1052+4422AB (Dupuy et al. 2015b). Six orbital parameters are shared in common between the resolved and absolute astrometric solutions: period (P), eccentricity (e), inclination (i), PA of the ascending node (Ω), argument of periastron (ω), and mean longitude at the reference epoch ($\lambda_{\rm ref}$).[9] The reference epoch ($t_{\rm ref}$) is defined to be 2010 January 1 00:00 UT (2455197.5 JD) and is related to the time of periastron passage $T_0 = t_{\rm ref} - P\frac{\lambda_{\rm ref}-\omega}{360^\circ}$. For the resolved orbit we fit for the total semimajor axis ($a = a_1 + a_2$, where a_1 and a_2 are the semimajor axes of the primary and secondary components about the system barycenter). For the unresolved orbit we fit for a photocenter semimajor axis $a_{\rm phot}$. For the absolute astrometry we also fit for the usual five parameters of parallax (π), position in RA (α) and Dec (δ) at a reference epoch, which we choose to be the same as $t_{\rm ref}$ above, and proper motion in RA ($\mu_{\alpha^*} \equiv \mu_\alpha \cos\delta$) and Dec ($\mu_\delta$). For a circular orbit the parameter ω has no physical meaning. Therefore, in order to allow our MCMC to robustly explore parameter space for nearly circular orbits we chose to step in $\omega+\Omega$ and $\omega-\Omega$. Our priors are uniform in e, ω, Ω, $\lambda_{\rm ref}$, and the ratio of $a_{\rm phot}/a$. We adopt log-flat priors in P and a by multiplying likelihoods by $1/P$ and $1/a$. We allow for inclinations to be randomly distributed in space by multiplying likelihoods by $\sin(i)$. Our prior on parallax assumes a uniform density in space volume, and thus we multiply our likelihood by $1/\pi^2$.

---

[9]Here, in the absence of radial velocity information, there is a 180° ambiguity in Ω, and consequently ω and $\lambda_{\rm ref}$, such that one of Ω or $\Omega+180^\circ$ is actually the ascending node while the other is the descending node. Therefore, we follow the standard convention that $0^\circ \le \Omega \le 180^\circ$. If future radial velocities show that $\Omega+180^\circ$ is actually the ascending node then 180° should be added to our reported values of Ω, ω, and $\lambda_{\rm ref}$.

To determine the starting point of our chains, we made an initial estimate of the best-fit parameters. For the relative orbit parameters, we performed a grid search over the parameters P, e, and T_0. Once these three parameters are specified, then the eccentric anomaly can be computed and the best-fit orbit can be directly analytically determined, as described in detail by Lucy (2014). We searched across 10^4 randomly drawn values between $0 \leq e < 1$, $0 \leq T_0/P < 1$, and $\log(P)$ initially from 10^3 to 10^6 days. At subsequent iterations we refined the range of P to center on the best-fit orbital period from the previous trials. After three iterations, we passed the single set of orbit parameters with the lowest χ^2 to our custom least-squares minimization routine for orbit fitting (Dupuy et al. 2010), which is based on the MPFIT package in IDL (Markwardt 2009), in order to optimize our starting position for the MCMC. For the parallax parameters, including the photocenter orbit size $a_{\rm phot}$, we used the same method as described in Section 2.4.1 of Dupuy & Liu (2012) to find the best-fit values. Briefly, we used our best-fit orbit parameters, the binary flux ratio for the CFHT bandpass (either J or K band), and an estimated mass ratio from Cond evolutionary models (Baraffe et al. 2003). Combining the flux ratio and mass ratio gives the scale factor by which to multiply a in order to derive $a_{\rm phot}$. We then subtract the estimated photocenter orbit offsets from the CFHT astrometry and find the best-fit parallax, proper motion, and RA and Dec.

We used the Python implementation of the Goodman & Weare (2010) affine-invariant ensemble sampler `emcee v2.1.0` (Foreman-Mackey et al. 2013) to perform our MCMC analysis. We initialized 10^3 walkers with our best-fit parameters after adding a small amount of Gaussian noise having standard deviations of $P \times 10^{-4}$ in P; $a \times 10^{-4}$ in a; 10^{-4} in e; 10^{-4} radians in i, $\omega - \Omega$, $\omega + \Omega$, and $\lambda_{\rm ref}$; 10^{-6} degrees in RA and Dec; 10^{-8} degrees yr^{-1} in RA and Dec proper motion; $\pi \times 10^{-3}$ in π; and 10^{-3} in $a_{\rm phot}/a$. We allowed our 10^3 walkers to run for 10^5 steps, saving results every 500 steps. After removing the first 50% of the chains as burn-in, our final chains possess a total of 1.0×10^5 values for each parameter.

Our CFHT astrometry gives a measurement of the parallax and proper motion relative to the grid of reference stars. In order to determine distances and absolute proper motions, we estimate the parallax and proper motion of our reference grids using the Besançon model of the Galaxy (Robin et al. 2003)[10] in a similar fashion to our previous work (Dupuy & Liu 2012; Dupuy et al. 2015b). The only change we have adopted here is to exclude Besançon model stars with large proper motions and parallaxes. This accounts for the fact that our astrometric pipeline always excludes such stars from our reference grid, using cuts of 10 mas in parallax and 30 mas yr^{-1} in proper motion. Therefore, our relative-to-absolute corrections reported here are slightly smaller in amplitude than our past work. For example, in Dupuy et al. (2015b) we derived corrections of $\Delta\pi = 1.7 \pm 0.3$ mas, $\Delta\mu_{\alpha^*} = -6 \pm 3$ mas yr^{-1}, and $\Delta\mu_\delta = -7 \pm 3$ mas yr^{-1} for SDSS J1052+4422AB, but here we derive $1.33^{+0.13}_{-0.16}$ mas, -3.0 ± 1.4 mas yr^{-1}, and -4.2 ± 1.2 mas yr^{-1}, respectively. This results in a $<0.5\sigma$ change in our absolute parallax for SDSS J1052+4422AB (38.4 ± 0.7 mas previously, 38.1 ± 0.6 mas

[10] `http://model.obs-besancon.fr/`

here).

Tables 5–35 present for each binary the median, best-fit, and 1σ and 2σ credible intervals for the 13 parameters in our joint orbit and parallax analysis. These tables also report various properties of interest that can be derived from our fitted parameters, such as T_0, distance (d), and semimajor axis in AU. We also report the total system mass for each binary, $M_{\rm tot}/M_{\rm Jup} = 1047.93 \times (a/{\rm AU})^3 (P/{\rm yr})^{-2}$, both with and without including the uncertainty in the parallax so that future improvements in distances for our sample binaries can be easily adapted into improved masses. Table 36 gives the χ^2 values of the best-fit solutions as well as the final mean acceptance fraction for each MCMC chain. Figure 1 shows all of the relative and absolute astrometry used in our joint orbit/parallax analysis for each binary along with the resulting astrometric solution, and Figure 2 shows the resulting posterior distributions from our MCMC analysis.

4.1. Assessing Reliability of Orbit Determinations

Although we have applied our MCMC analysis to all of our astrometric data, not all binaries will have orbit determinations sufficiently reliable for astrophysical use. The primary quality metric for assessing our orbit fits should be the precision with which they constrain the system mass, as very large mass uncertainties will be of little use for constraining models in the following analysis. In addition, if orbital parameters are poorly determined, then the resulting posteriors will be strongly influenced by our adopted priors. While we have attempted to choose priors that are as uninformed as possible, we should not rely on them to constrain physical parameters (P, a, e) that are not sufficiently constrained by our data. Finally, some of our orbit determinations indicate that our observations span only a small fraction of the full orbital period. Therefore, we also consider this as a possible indicator of whether our data has provided reliable constraints on orbital parameters.

Table 37 provides a summary of the orbit quality metrics that we use to assess the reliability of our orbit fits. The metrics $\delta \log M_{\rm tot}$ and δe are computed as the difference between the maximum and minimum credible interval (1σ) of the total mass at fixed distance and eccentricity, respectively, and the metric $\Delta t_{\rm obs}/P$ is the fraction of the orbital period (median of the posterior) covered by our resolved astrometry. We now consider our orbit fits, beginning with the apparently least reliable, and moving toward binaries with better reliability metrics until we finally determine which orbits to carry forward in our analysis.

SDSS J0926+5847AB has the worst mass precision ($\delta \log M_{\rm tot} = 0.38$ dex) and eccentricity constraint ($\delta e = 0.38$). Even though it has a good time baseline ($\Delta t_{\rm obs}/P = 0.68$), the actual coverage of the orbit on the sky is poor, partly due to the fact that is seen nearly edge on ($i = 91.7^{+0.6}_{-0.8}{}^{\circ}$). The next worse mass precisions are $\Delta \log M_{\rm tot} = 0.23$ dex for SDSS J2052−1609AB and 0.20 dex for 2MASS J1750+4424AB. The latter has the smallest time baseline of any binary here ($\Delta t_{\rm obs}/P = 0.04$) owing to its very long, quite uncertain orbital period (210^{+40}_{-60} yr), although it only has a modestly large $\delta e = 0.15$. SDSS J2052−1609AB has a better time baseline ($\Delta t_{\rm obs}/P = 0.19$) but a poorly constrained eccentricity ($\delta e = 0.21$). 2MASS J0850+1057AB has relatively poor mass precision ($\Delta \log M_{\rm tot} = 0.12$ dex) as well as a poorly constrained eccentricity ($\delta e = 0.11$) despite a marginally acceptable time baseline ($\Delta t_{\rm obs}/P = 0.31$). All of the above orbits we do not consider sufficiently reliable to be used in the following analysis. SDSS J1534+1615AB and SDSS J1021−0304AB nominally have much better mass precision than any of the above ($\delta \log M_{\rm tot} = 0.09$ dex and 0.06 dex, respectively). However, both have poor time baselines with $\Delta t_{\rm obs}/P = 0.17$ and 0.10, respectively, and poorly constrained eccentricities with $\delta e = 0.43$ and 0.14, respectively. (For reference, our input prior on eccentricity alone would correspond to $\delta e = 0.68$.) We therefore also chose not to use these orbits.

DENIS J1228−1557AB and 2MASS J1847+5522AB are both marginal cases. DENIS J1228−1557AB has a modestly large mass error ($\delta \log M_{\rm tot} = 0.12$ dex) but a better constrained eccentricity ($\delta e = 0.06$) and longer observational baseline ($\Delta t_{\rm obs}/P = 0.29$). On the other hand, 2MASS J1847+5522AB has good mass precision ($\delta \log M_{\rm tot} = 0.035$ dex) but a poorly constrained eccentricity ($\delta e = 0.14$) and an observational baseline of only $\Delta t_{\rm obs}/P = 0.22$. We conservatively choose to place our cut-offs in orbit quality metrics to exclude these two marginal cases. The next worse mass precision in our sample is LP 415-20AB ($\delta \log M_{\rm tot} = 0.06$ dex), but it appears to have a reliably determined orbit, with $\delta e = 0.023$ and most of the orbital period covered by observations ($\Delta t_{\rm obs}/P = 0.67$). The worst eccentricity constraint for any of the remaining binaries is for 2MASS J1728+3948AB ($\delta e = 0.028$), but it has much better mass precision ($\delta \log M_{\rm tot} = 0.0089$ dex) and better orbital coverage ($\Delta t_{\rm obs}/P = 0.34$) compared to our excluded orbits. LSPM J1735+2634AB has the worst orbital coverage of our remaining sample ($\Delta t_{\rm obs}/P = 0.29$), but its orbit is very well determined ($\delta \log M_{\rm tot} = 0.0017$ dex, $\delta e = 0.0075$) thanks to our observations serendipitously bracketing its periastron passage.

In summary, we do not use the orbit determinations for 2MASS J0850+1057AB, SDSS J0926+5847AB, DENIS J1228−1557AB, 2MASS J1750+4424AB, 2MASS J1847+5522AB, and SDSS J2052−1609AB in our following analysis. The basis for their exclusion is poor mass precision, poor observational coverage of the orbit, and/or poorly constrained eccentricity that could make our results overly dependent on our uniform eccentricity prior. The remaining sample comprises 23 binaries with orbit quality metrics ranging from $\delta \log M_{\rm tot} = 0.0017$–$0.06$ dex, $\delta e = 0.0007$–0.028, and $\Delta t_{\rm obs}/P = 0.29$–$5.01$.

4.2. Comparison to Published Orbits

Some of the binaries in our sample have published orbital parameter determinations, either from work of our own or others. By far, the largest overlap of our 31-binary sample is with 14 binaries from Konopacky et al. (2010), followed closely by our own work (13 binaries). In most of these overlapping cases, our new orbit determinations agree with and improve upon previously published work as expected given our longer time baseline and more numerous epochs. For example, compared to Konopacky et al. (2010) our orbital period uncertainties are much smaller, with a median difference in errors of a factor of 7. We now discuss the cases where our new results for astrophysical parameters (i.e., mass, period, and eccentricity but not viewing angles) differ significantly ($\gtrsim 2\sigma$) from published work.

Gl 569Bab has had a number of published orbit determinations, and despite being a very well studied system the reported semimajor axes of the orbit have varied significantly compared to the reported errors. As discussed in Section 3.1 of Dupuy et al. (2010), this is likely mostly due to astrometric calibration issues in data sets that used an early generation of cameras behind the Keck AO system (KCAM and SCAM; Lane et al. 2001) that we did not use here or in our previous work. Our analysis here uses some archival NIRC2 imaging not included in our previous work, which improves the coverage of this short period orbit ($P = 2.3707 \pm 0.0005$ yr), and results in a semimajor axis of 93.64 ± 0.14 mas. This sits in between values derived in our prior work ($95.6^{+1.1}_{-1.0}$ mas Dupuy et al. 2010) and values published by others that largely relied on KCAM and SCAM data: 91.8 ± 1.0 mas (Zapatero Osorio et al. 2004), 90.4 ± 0.7 mas (Simon et al. 2006), and 90.8 ± 0.8 mas (Konopacky et al. 2010). In spite of these different semimajor axes, the dynamical total mass ($138 \pm 7\,M_{\rm Jup}$ here) varies by $<1\sigma$ because the error is dominated by the *Hipparcos* parallax uncertainty ($\sigma_\pi/\pi = 0.016$) not our semimajor axis measurement ($\sigma_a/a = 0.0016$). The improved precision of of our new orbit fit is due to more measurements (19 from astrometrically well calibrated Keck/NIRC2 or *HST* imaging) that now span 11.87 yr (i.e., 5.006 orbital periods).

HD 130948BC has a very well determined orbit, so small differences in orbital parameters are more statistically significant. In our most recent previous analysis we found $e = 0.176 \pm 0.006$ (Dupuy & Liu 2011) compared to 0.1627 ± 0.0017 here, a 2.1σ difference. This difference is not astrophysically significant, and perhaps it is simply a statistical fluctuation due to the significant improvement in other orbital parameters (e.g., both a and P are improved by nearly a factor of 20 compared to our original orbit in Dupuy et al. 2009b). Both our current and past values are consistent at $<2\sigma$ with the eccentricity of 0.16 ± 0.01 from Konopacky et al. (2010).

Our orbit for LP 415-20AB agrees with our previous work but disagrees somewhat with the analysis of Konopacky et al. (2010). This is discussed in detail in Section 2 of Dupuy & Liu (2011) as likely being jointly due to the small number of degrees of freedom in the Konopacky et al. (2010) analysis (1 dof) and one of their measurements being a significant outlier with respect to the rest of the available data. Compared to their orbital parameters, our period of 14.82 ± 0.24 yr is longer (compared to 11.5 ± 1.2 yr), our semimajor axis of $96.5^{+1.1}_{-1.4}$ mas is smaller (compared to 108 ± 24 mas), and our eccentricity of $0.706^{+0.011}_{-0.012}$ is smaller (compared to 0.9 ± 0.1). Our inferred total dynamical mass is quite discrepant from that of Konopacky et al. (2010), given that their fitted distance of 21 ± 5 pc (derived by combining astrometry and radial velocities) is 2.7σ different from our parallactic distance of 38.6 ± 1.1 pc. This is likely due both to our different orbit determinations and the fact that their radial velocity measurement ($\Delta{\rm RV} = -0.7 \pm 1.4\,{\rm km\,s^{-1}}$) disagrees with the prediction from our relative orbit ($\Delta{\rm RV} = -2.96 \pm 0.16\,{\rm km\,s^{-1}}$). With 12 measurements spanning 9.97 yr, our new orbit fit has many more degrees of freedom (17 dof) for the relative orbit fit than previous work, making the resulting orbit parameters more robust and more precise by a factor of

5–17.

Our orbit for 2MASS J1534−2952AB agrees well with Konopacky et al. (2010) but disagrees with Liu et al. (2008). The cause of the discrepancy with Liu et al. (2008) is the choice of eccentricity prior. In that work we adopted a prior of $p(e) = e$, which deweights smaller eccentricities and rules out circular orbits entirely, whereas we adopt here a more conservative uniform prior $p(e) = 1$. Our eccentricity posterior here piles up at zero with a 2σ interval of $e = 0.000$–0.014, and a and P are both correlated with e in the sense that larger e corresponds to smaller a and P. According to Figure 6 of Liu et al. (2008), that posterior distribution of P as e approaches zero would agree with our orbital period of $P = 20.29 \pm 0.07$ yr. According to Figure 8 of Liu et al. (2008), our values of P and $a = 213.7 \pm 0.5$ mas agree well with that P–a posterior distribution in spite of the difference in eccentricity priors. However, both Liu et al. (2008) and Konopacky et al. (2010) used the parallax of 73.6 ± 1.2 mas from Tinney et al. (2003) to convert their angular semimajor axes into physical units and thereby compute dynamical masses. As we discuss in Appendix B.17, our parallax of 63.0 ± 1.1 mas leads to very different dynamical masses than in previous work.

2MASS J2206−2047AB also has an eccentricity posterior that piles up at zero, which differs from the results of our previous work on this system. In Dupuy et al. (2009a) we used a prior of $p(e) = e$ that suppressed low eccentricity orbit solutions and resulted in $e = 0.25 \pm 0.08$. Our new posterior has a 2σ interval of $e = 0.000$–0.027. As a result of this difference, Dupuy et al. (2009a) found very different values for semimajor axis and period ($a = 213^{+24}_{-18}$ mas, $P = 35^{+6}_{-5}$ yr) compared to our new analysis ($a = 167.7 \pm 0.5$ mas, $P = 23.96^{+0.23}_{-0.21}$ yr). However, thanks to the strong correlation between a and P, our new values follow the posterior distribution of Dupuy et al. (2009a) as shown in their Figure 6. Therefore, the resulting total dynamical mass was $184 \pm 4\,M_{\rm Jup}$ from Dupuy et al. (2009a) but is $188.3^{+2.9}_{-3.1}\,M_{\rm Jup}$ here (assuming a fixed distance of 28.0 pc for the purpose of this comparison). Therefore, the choice of eccentricity prior does not change the best-fit total mass, although it would have affected the uncertainty in the mass, where the uniform e prior used here is more conservative.

SDSS J2052−1609AB has a preliminary orbit determination from Bardalez Gagliuffi et al. (2015) based on combining their data with published astrometry from Stumpf et al. (2011) and 3 epochs of our data retrieved from the NIRC2 archive. Their posterior eccentricity distribution ($e = 0.014^{+0.023}_{-0.010}$) is significantly different from what we find in our analysis ($e = 0.20^{+0.09}_{-0.11}$, with a 2σ interval of 0.08–0.50). Their quoted uncertainties in other parameters are also generally much smaller than ours, e.g., they find $M_{\rm tot} = 86.2^{+3.9}_{-1.8}\,M_{\rm Jup}$ while we find $M_{\rm tot} = 69^{+14}_{-20}\,M_{\rm Jup}$, despite our analysis using more data over a longer time baseline. We also performed a cursory analysis of their astrometry using our MCMC fitter and were unable to reproduce their posterior distributions. Therefore, we speculate that the difference in our results is most likely due to differing MCMC analysis methods. They report that acceptance fractions for their single Metropolis-Hastings sampled chain were typically 0.5%–1%, whereas our analysis using the affine-invariant sampler of `emcee` had much higher acceptance fractions of 8.7% (Table 36). Their MCMC also included distance as an eighth parameter in addition to the seven orbit parameters that are constrained by the relative astrometry. Since distance is not constrained by the relative astrometry, it appears that its use as a parameter was intended to marginalize over the uncertainty in the Dupuy & Liu (2012) parallax. It is therefore curious that the posterior distribution on distance from Bardalez Gagliuffi et al. (2015) had smaller errors ($30.7^{+0.2}_{-0.4}$ pc) than the input parallactic distance of 29.5 ± 0.7 pc. Regardless, it is not clear how this would explain the small uncertainties on the orbital parameters or why their MCMC analysis apparently avoided the part of parameter space preferred by our `emcee` analysis. Our new orbit fit is based on 8 epochs, rather than 6 epochs, spanning 8.58 yr instead of 4.55 yr, in addition to the fact that our joint Keck+CFHT analysis properly marginalizes over the uncertainty in orbital photocenter motion when determining the parallax. Therefore, we conservatively choose to use our own orbit fitting results in the following analysis.

Kelu-1AB has an unrefereed orbit determination by Stumpf et al. (2008) based on 9 epochs of astrometry spanning 2.84 yr. Our orbit based on 13 epochs spanning 16.66 yr agrees at $\lesssim 1\sigma$ with their eccentricity ($e = 0.82 \pm 0.10$) but not their semimajor axis ($a = 339^{+129}_{-66}$ mas) or orbital period ($P = 38^{+8}_{-6}$ yr). We find $a = 227.9^{+0.9}_{-1.1}$ mas and $P = 24.98 \pm 0.19$ yr. Assuming a fixed distance of 20.8 pc for both orbits, we find a total mass of $M_{\rm tot} = 180.1 \pm 1.1\, M_{\rm Jup}$ compared to their $M_{\rm tot} = 244^{+156}_{-76}\, M_{\rm Jup}$ that agrees within 1σ because of their large uncertainties.

4.3. Comparison to Published Parallaxes

In Table 38 we provide a comparison of the parallaxes we measure here with other values in the literature, including our own past work (Dupuy & Liu 2012; Dupuy et al. 2015b). Our previously published parallaxes are not statistically independent of the values given here, but they were derived from somewhat different analysis methods. Namely, in Dupuy & Liu (2012) we did not marginalize over the uncertainty in the orbital parameters or mass ratio in the same way as we have done here, and we used a slightly different method for computing the correction from relative to absolute parallax. It is therefore not surprising that one of the largest discrepancies is for 2MASS J0920+3517AB (2.0σ different from our published parallax), because we previously assumed a model-based mass ratio estimated from the measured flux ratio, but as we discuss in Section 7 and Appendix B.7 this system is likely a hierarchical triple where the fainter component is actually much more massive than the brighter component. The only other $\gtrsim 2\sigma$ difference is for 2MASS J1728+3948AB, where our new data spans 9.1 yr (instead of 3.3 yr) and with somewhat better parallax phase coverage resulting in a parallax that is 6% (2.5σ) smaller, and we suggest this is likely a natural statistical variation given the new better constraints on proper motion in both RA and Dec (the parallax amplitude in Dec is almost as large as RA for this object).

Among other literature parallaxes, the largest discrepancy is for 2MASS J1534−2952AB (3.9σ). As we have previously discussed in Dupuy & Liu (2012), this is likely due to the uncertainty in the Tinney et al. (2003) value of 73.6 ± 1.2 mas being somewhat underestimated. Our value of 63.0 ± 1.1 mas significantly changes the inferred dynamical mass since $M_{\rm tot} \propto d^3$, resulting in a factor of 1.6 increase in mass. The next largest discrepancies are 1.3–1.9σ for LP 349-25AB, SDSS J0423−0414AB, 2MASS J0700+3157AB, and 2MASS J0746+2000AB and the remaining 19 comparisons agree within $\leq 0.6\sigma$. Two binaries have parallaxes in the literature more precise than our CFHT values. Kelu-1AB has a parallax of 53.6 ± 2.0 mas from Dahn et al. (2002) and 51.75 ± 1.16 mas from Weinberger et al. (2016) that are both more precise but likely less conservative than our value of 49.8 ± 2.2 mas because we marginalize over photocenter orbital motion. All of these values agree with each other at 0.8–1.3σ, but using the different parallaxes results in quite different dynamical masses, and we therefore exclude Kelu-1AB from our further mass analysis (see Appendix B.13 for a discussion). 2MASS J0746+2000AB has a remarkably precise parallax of 81.9 ± 0.3 mas from the USNO optical program (Dahn et al. 2002). An updated USNO analysis that accounts for the photocenter orbital motion of 2MASS J0746+2000AB (Harris et al. 2015) results in a parallax of 81.24 ± 0.25 mas (H. Harris 2015, private communication). Given the longer time baseline and higher precision of the USNO parallax, we use their value in our following analysis.

5. Empirically Determined Properties

5.1. Spectral Types & Magnitudes

Most binaries in our sample have spectral types derived through spectral decomposition from Dupuy & Liu (2012), using integrated-light NIR spectra and resolved NIR photometry. For most of these we simply adopt the same spectral types as in that work, but a few binaries were not in that sample or have updated resolved photometry that warrants new analysis. We use the same method described in Section 5.2 of Dupuy & Liu (2012). Briefly, we pair spectra from a template library and find the optimal scaling ratio for each pair that best matches the observed integrated-light spectrum. We compute synthetic photometry for these pairs and then cull all pairings that do not agree with the observed resolved photometry, $p(\chi^2) < 0.05$. We then examine the remaining pairs, ranked by how well they match the observed spectrum, and assign types and errors on types that best represent the results. A summary of all available magnitudes for our sample binaries, both integrated-light and resolved, is given in Table 39. We report magnitudes on both the 2MASS and MKO photometric systems if data exist in either system by using the empirical relations between photometric system conversion and absolute magnitude that we derived in Appendix A.1.

LP 415-20AB and 2MASS J1047+4026AB were not included in the Dupuy & Liu (2012) sample. LP 415-20AB has an integrated-light optical spectral type of M7.5 (Gizis et al. 2000b), but we find that primary templates as early as M5 and as late as M7 provide good matches to the infrared SpeX SXD spectrum and resolved photometry, while the best secondary templates range from M7.5–M8.5. Therefore, we adopt types of M6.0 $\pm$ 1.0 for LP 415-20A and M8.0 $\pm$ 0.5 for LP 415-20B. 2MASS J1047+4026AB has an integrated-light optical type of M8 (Gizis et al. 2000a), and we find types of M8.0 $\pm$ 0.5 and L0.0 $\pm$ 1.0 in our spectral decompostion. In this work we have added new flux ratios in $CH4_S$ and K bands for 2MASS J1404−3159AB that allow us to refine our analysis, and we find the same spectral types as we did in Dupuy & Liu (2012), L9 $\pm$ 1 and T5.0 ± 0.5. We have added a J-, H-, and K-band flux ratios for 2MASS J2140+1625AB resulting in the same primary type (M8.0 ± 0.5) but an updated secondary type of L0.5 ± 1.0 (was M9.5 ± 0.5). Finally, for DENIS J2252−1730AB we have new flux ratios in Y, J, H, $CH4_S$, and K bands. This allows us to improve the spectral types to L4.0 ± 1.0 (was L4.5 ± 1.5) and T3.5 ± 0.5 (was T3.5 ± 1.0).

5.2. Individual Masses

Our joint analysis of resolved relative astrometry and unresolved absolute astrometry provides direct measurements of the relative orbit, parallax, and photocenter orbit. The first two of these give the total system mass directly. When the flux ratio of the binary is known, then the photocenter orbit can also be used to directly measure the individual component masses. Our absolute astrometry from CFHT/WIRCam is all in either J or $K_{\rm H2}$ bands, and we have resolved J- and K-band photometry for all of our binaries. Therefore, we can derive individual masses for any binary with a sufficiently well constrained photocenter orbit semimajor axis ($a_{\rm phot}$). As noted above, we assume a uniform prior in the ratio of the photocenter semimajor axis to the true semimajor axis ($a_{\rm phot}/a$). If we define the ratio of the secondary-to-total mass as $\mu \equiv M_2/(M_1 + M_2)$ and the ratio of secondary to total flux as $\beta \equiv F_2/(F_1 + F_2)$, then $a_{\rm phot}/a = \mu - \beta$. An unbounded and uniform prior on $a_{\rm phot}/a$ and β, as we have assumed, can in principle allow for unphysical values of $\mu < 0$. This is simply a consequence of not using any information about the flux ratio in our astrometric analysis, motivated by the fact that improved flux ratios could easily be obtained in the future. Therefore, not all astrometric solutions result in meaningful constraints on the individual mass ratios, but in our sample of well-determined orbits only Kelu-1AB has an $a_{\rm phot}$ uncertainty sufficiently large to encompass a wide range of unphysical values.

In order to derive flux ratios, we used the values of ΔJ and ΔK reported in Table 39. We use the MKO J-band data directly, while for the narrow-band $K_{\rm H2}$ filter on WIRCam we must derive a correction to be applied to our broadband K measurements. As described in Appendix A.2, we derived third order polynomial relations between K-band absolute magnitude and both $K_{\rm MKO} - K_{\rm H2}$ color and $K_{\rm 2MASS} - K_{\rm H2}$ color. These relations have an rms scatter of 0.021 mag and 0.025 mag, respectively. When applying the offset from these relations we added these values of the rms scatter in quadrature to the flux ratio uncertainty in any case where our observed ΔK was more than 2× larger than the scatter. In other words, for binaries with flux ratios within $\lesssim$0.05 mag of unity we did not add this uncertainty in quadrature.

Table 40 summarizes all of the photocenter orbit sizes and flux ratios measured in our analysis, including systems for which the dynamical masses are not reliable. Table 41 gives the resulting individual masses we derive from our dynamical total masses and photocenter mass ratios (19 systems) or from other information (3 systems). Two of the three binaries in our relative orbit sample that do not have absolute astrometry from CFHT have stellar companions with *Hipparcos* distances (Gl 417BC and HD 130948BC). We provide the model-derived individual masses in Table 41 for reference, but we do not consider them as part of the following analysis of individual masses. The third binary with an orbit but no CFHT data is Gl 569Bab, and for this system we use the mass ratio of $M_1/M_2 = 1.4 \pm 0.3$ derived from a joint analysis of all available radial velocity data by Konopacky et al. (2010, see their Section 5.4.6). Gl 569Bab along with LHS 1070BC (Köhler et al. 2012) are the only two ultracool binary systems that previously had individual mass determinations in the literature not from our own work. Our sample of 38 objects with individual masses therefore increases the sample size by an order of magnitude.

Figure 3 shows the all our our individual masses, as well as those from the literature, as a function of spectral type. In the analysis that follows, we will use this information to discuss the substellar boundary. Here we simply note that in most cases our individual masses do not grossly deviate from rough astrophysical expectations, e.g., nearly equal flux systems have mass ratios near unity and vice versa. There are a few remarkable exceptions, such as the secondary 2MASS J0920+3517B (L9.0 ± 1.5) that has a mass of $116^{+7}_{-8}\,M_{\rm Jup}$, well in excess of the expected hydrogen fusion limit ($\approx$70 $M_{\rm Jup}$; Section 7.1).

Figure 4 shows our dynamical mass sample on the color–magnitude diagram (CMD) with data points colored by the measured masses. Overall, mass broadly decreases through the CMD sequence, although there is not a one-to-one correspondence between mass and CMD location, as expected for our sample that is drawn from the field population of ultracool dwarfs spanning a wide range of ages. The most clear illustration of this is that the lowest mass objects happen to be located roughly in the middle of the L/T transition, while the latest-type, bluest objects are somewhat more massive. This more likely reflects the distribution of ages in our sample rather than indicating that later type objects tend to be more massive. Figure 5 shows our measured absolute magnitudes as a function of spectral type, colored according to mass, in order to assess the reliability of both plotted quantities. Our sample is broadly consistent with the field sequence, indicating the accuracy of our spectral types, with the largest outlier being 2MASS J0920+3517B, which is consistent with our dynamical masses showing that this is an unresolved pair of brown dwarfs in a triple system.

To provide a simple summary of our results, Table 42 reports the mean mass in seven spectral type bins selected to contain 3–7 objects per bin, excluding unusual objects (unresolved binaries and the pre–main-sequence system LP 349-25AB). As expected, the mean mass broadly decreases with spectral type. We caution that this table is simply meant to provide a guide to the typical masses of objects in the field population and is not intended to be used for any quantitative astrophysical purpose. At earlier spectral types, Table 42 may be useful for providing model-independent mass estimates for very low-mass stars. Next, we briefly compare these results to previous work and defer discussion of the astrophysical interpretation of our individual masses to later sections.

5.2.1. Comparison to Literature Mass Ratios

Four of our 19 systems with individual masses have mass ratios derived from radial velocities by Konopacky et al. (2010). They quote mass ratios as M_1/M_2, rather than the standard $q \equiv M_2/M_1$, so for the purposes of comparison here we quote our measurements as $1/q$ as well. For 2MASS J0746+2000AB we find $1/q = 1.05 \pm 0.03$, which agrees within the large uncertainties of $4.0^{+0.1}_{-3.8}$ as found by Konopacky et al. (2010). They report a similar mass ratio for 2MASS J2140+1625AB with much smaller uncertainties ($4.0^{+0.0}_{-0.1}$), which disagrees at $\approx$8σ with our result ($1.65^{+0.19}_{-0.23}$). This seems to confirm the suggestion in Section 5.4.5 of Konopacky et al. (2010) that their mass ratio for this binary was likely more uncertain than the quoted errors implied. One of our most precise mass ratios is for LHS 2397aAB ($1/q = 1.42^{+0.05}_{-0.06}$), and it agrees well with the value of $1.5^{+7.1}_{-1.4}$ reported by Konopacky et al. (2010). Finally, we find $1/q = 1.06 \pm 0.03$ for LP 349-25AB, which disagrees with the value of 0.5 ± 0.3 found by Konopacky et al. (2010). As discussed in Section 4.2 of Dupuy et al. (2010), a mass ratio that agrees with our value can be accommodated by the radial velocities of Konopacky et al. (2010), suggesting that their quoted errors may be underestimated.

The only other directly measured mass ratio in the literature for a system in our sample is from Harris et al. (2015) for 2MASS J0746+2000AB. Their USNO astrometry gives a value of $q = 0.925$, which agrees well with our value of $0.952^{+0.026}_{-0.027}$.

5.3. Bolometric Luminosities

We have derived luminosities for all objects in our sample using our resolved photometry along with the empirical relations between luminosity and absolute magnitude that are described in Appendix A.3. This is somewhat different from our past work where we relied on bolometric correction–spectral type relations to derive individual luminosities. Our new approach obviates the need to reference spectral types, as it links absolute magnitude directly to luminosity. Given that J- and H-band absolute magnitudes get brighter and plateau across the L/T transition, respectively, only K-band absolute magnitudes are suitable for the entire range of luminosity of our sample. The luminosity scatter about the K-band polynomial relation is somewhat higher across the L/T transition (0.07 dex; $M_K > 13.0$ mag) than at brighter magnitudes (0.04 dex). Interestingly, if we only consider the late-M and earlier L dwarfs with $M_H < 13.3$ mag, the scatter in luminosity about the H-band relation is significantly lower (0.023 dex). It is not obvious why this should be the case from an astrophysical perspective, but we nonetheless use this to our advantage. For binaries where both components have $M_H < 13.3$ mag, we use the H-band relation with luminosity, and for the remainder we use the K-band relation. In all cases we used whichever photometry was more precise between 2MASS and MKO. We report the resulting component luminosities in Table 41, and Figure 6 shows our derived luminosities as a function of our individual masses.

As a check on our method, we compare our results to published work using integrated-light spectra and photometry to derive luminosities. For objects in common with Golimowski et al. (2004), Dieterich et al. (2014), and Filippazzo et al. (2015), all of whom use somewhat different methods and generations of models for deriving luminosities, we find that our total luminosities agree well within the errors after accounting for the different distances assumed in each work. For example, summing our luminosities for the components of 2MASS J0746+2000AB we find $\log(L_{\rm bol}/L_{\odot}) = -3.375 \pm 0.020$ dex, which agrees well with published values of -3.41 ± 0.02 dex (Golimowski et al. 2004), -3.413 ± 0.009 dex (Dieterich et al. 2014), and -3.391 ± 0.003 dex (Filippazzo et al. 2015). Other objects in common include Kelu-1, LHS 2397a, SDSS J0423−0414, and 2MASS J1728+3948.

6. Evolutionary Model-Derived Properties

Directly measured masses and luminosities are just two of the many physical properties that are of interest in characterizing our sample of very low-mass stellar and brown dwarf binaries. In principle, all physical properties of both stars and brown dwarfs can be predicted from just a few fundamental parameters: mass, age, and composition. (Other properties such as the entropy of formation, initial angular momentum, and magnetic fields may also be important as initial conditions.) Our dynamical mass sample consists of binaries that may be conservatively presumed to be coeval to within a few Myr and to be composed of the same material. It is therefore an ideal sample for pairing with evolutionary models, since the three most fundamental parameters are all constrained at some level.

We consider two families of evolutionary models here, the Lyon group's models and the Saumon & Marley (2008) models (Figure 7 shows all model grids used here). The most recent grid from the Lyon group comes from Baraffe et al. (2015), hereinafter BHAC, and extends over masses of 0.01–1.4 $M_{\odot}$. The published BHAC grid samples masses in the range 0.02–0.1 $M_{\odot}$ in increments of 0.01 $M_{\odot}$ (with two extra models at 0.072 $M_{\odot}$ and 0.075 $M_{\odot}$) and only tracks evolution down to $T_{\rm eff}$ = 1500 K. We have obtained BHAC model tracks that extend down to 1300 K (only for fundamental properties, not absolute magnitudes), as well as more finely gridded tracks over the mass range 0.05–0.07 $M_{\odot}$ in 0.001 $M_{\odot}$ increments. This enhanced BHAC evolutionary model grid was kindly provided by I. Baraffe (2016, private communication) so that we could more accurately sample the hydrogen-fusion and lithium-fusion mass limits. Many of our sample binary components have luminosities too low to be covered by the BHAC grid, and when this is the case we use the Lyon Cond models instead (Baraffe et al. 2003). We do not consider Lyon Dusty models (Chabrier & Baraffe 2000) as these have been supplanted by BHAC models over the luminosity range for which they would be appropriate (namely late-M and L dwarfs). The second family of models we consider are from Saumon & Marley (2008), hereinafter SM08, which conversely to BHAC only cover cooler temperatures ($T_{\rm eff} \lesssim 2400$ K; $\log(L_{\rm bol}/L_{\odot}) \lesssim -3.3$ dex) and thus many of our more luminous objects are not covered by the SM08 grid. These hard limits on the model grids means that we cannot always report model-derived properties for a given component because we do not extrapolate beyond the range of any model grid.

In order to perform tests of models, we first use the observed properties of mass and luminosity to infer other properties from evolutionary models. For our entire sample we have individual luminosities and precise total masses. In most cases (19 of 22 systems) we also have individual masses, but the precision of our mass ratios causes most of these individual masses to be less precise than the total mass. Therefore we take a two-pronged approach to inferring physical properties from models, either using the more precise total mass alone or the full individual mass information.

The total-mass analysis we use here is distinct from methods that we have used in our previous work (e.g., Liu et al. 2008; Dupuy et al. 2009b) as well as other approaches in the brown dwarf literature (see Section 4.5 of Dupuy et al. 2010 for a discussion of different methods). Our past Monte Carlo methods relied on a two-step interpolation, first using the individual luminosities to compute a model-predicted total mass as a function of age, and then applying our observational constraint on the total mass to determine the age distribution. Such a method is susceptible to numerical problems where more than one mass corresponds to a given luminosity either at a given age (e.g., due to deuterium burning) or over a range of ages (e.g., even very low-mass stars become slightly more luminous at old ages than they were on the zero age main sequence). More importantly, measurement errors can cause Monte Carlo samples to fall in regions of parameter space not covered by models, e.g., a luminosity that scatters low so that models predict a star of that mass would never be that faint, which causes a simple interpolation approach to fail. Such interpolation problems can also occur in the case of individual-mass analysis methods applied to stars, even though they have worked well for brown dwarfs and young stars in our previous studies (Dupuy et al. 2015b; Dupuy et al. 2016).

Therefore, we have developed a new approach for deriving physical properties from models that is based on the statistical technique of rejection sampling. This approach works well when the number of parameters of interest is small, and in the individual-mass analysis we only need to find the probability distribution for one unknown parameter—age—because age combined with mass allows all other properties to be directly interpolated from models. Our approach begins with a uniform distribution of Monte Carlo drawn ages spanning the minimum to maximum age of a given model grid, and through rejection sampling we end up with a distribution of ages that match the observed luminosities at the measured masses. For the case of individual masses this is conceptually straightforward, but when using only the total mass we must simultaneously try both random ages and component masses (i.e., essentially allowing for one more unknown parameter, mass ratio). In both cases, we use the final individual mass and age samples remaining at the end of the rejection sampling to derive other properties from models ($L_{\rm bol}$, radius, $T_{\rm eff}$, etc.). We now describe each case in more detail.

In our individual-mass analysis, we begin with 10^6 Monte Carlo trials of age that are randomly paired with masses from our MCMC results. The input distribution of ages defines the prior on age, and we choose uniformly distributed values, i.e., a flat prior. Each mass and age uniquely corresponds to a luminosity from models, which we determine from bilinear interpolation of a uniform 2-d grid of mass and age constructed using Delaunay triangulation as implemented in the `trigrid` function in IDL. We compute a χ^2 for each sample given our measured median $L_{\rm bol}$ and its uncertainty. We account for the fact that our luminosity and mass measurements are correlated (due to the common parallax) by fitting a line to $\log(L_{\rm bol})$ as a function of $\log(M)$. At each Monte Carlo-drawn mass, the effective luminosity ($L'_{\rm bol}$) is given by the coefficients of this linear fit. The observational error in luminosity at fixed mass ($\sigma_{L'_{\rm bol}}$) is given by the rms scatter about the fit, which is equal to or smaller than the actual $L_{\rm bol}$ error depending on the degree of covariance. Thus, we compute $\chi^2 = (L_{\rm bol,model} - L'_{\rm bol})^2/\sigma^2_{L'_{\rm bol}}$ and a corresponding probability of $p = e^{-(\chi^2 - \min(\chi^2))/2}$, normalized by the Monte Carlo sample with the lowest χ^2. We then draw random, uniformly distributed variates u, and we rejected samples where $p < u$. In order to efficiently sample the most relevant ages, we iterated this process gradually narrowing the trial age distribution based on the results of the previous iteration. We found that after three iterations the number of successful Monte Carlo trials stabilized. After determining our final age distribution, we then determined other properties ($T_{\rm eff}$, lithium depletion, etc.) from 2-d grids constructed with `trigrid` in the same way as for luminosity.

In our total-mass analysis we have two unknown parameters, age and mass ratio. Therefore, we not only draw random, uniformly distributed ages as above, but also uniformly distributed values of $\log(M_1)$ for one component. The mass of the other component can then be computed from the total mass in that Monte Carlo sample, $M_2 = M_{\rm tot} - M_1$. We initially sample all ages covered by the model tracks and masses for M_1 ranging from the lowest mass model to the maximum total mass in the MCMC chain. We interpolate the luminosity from models for each component mass and age pair and compute a total χ^2 by comparing the interpolated luminosities for both components to our measurements. As in our individual-mass analysis, we account for correlation between our measured total mass and component luminosities by fitting lines to $\log(L_{\rm bol,1})$ and $\log(L_{\rm bol,2})$ as a function of $\log(M_{\rm tot})$. We reject Monte Carlo samples based on the probabilities computed from the sum of the components' χ^2 and then iteratively narrow the range of age and component mass searched, again finding three iterations sufficient in all cases. We use the final remaining samples of age and component masses to interpolate other properties ($T_{\rm eff}$, etc.) from the 2-d model grids.

Tables 43–67 show the results of our analyses using total mass and individual luminosities as well as, when possible, individual masses and luminosities. Our rejection sampling analysis naturally produces output distributions of individual luminosities and masses in all cases. Conceptually, this is because any inputs to the rejection sampling (even measured quantities) can be thought of as priors on those properties, so the output distributions may be somewhat different (narrower or slightly shifted). The final output properties will always be fully consistent with model predictions. For example, in the case of a star on the main sequence, combining our measured luminosity and age prior typically results in a much narrower range of masses according to models because only certain masses are predicted to correspond to the input luminosity. In most cases, the median mass and luminosity output by the rejection sampling analysis agrees within $\lesssim$1.5σ of the input values, as expected, but exceptional cases are discussed in the following sections. Figure 8 shows our input measurements compared to model tracks and the resulting age distributions from both individual-mass and total-mass analyses.

Our new approach to deriving properties from models via rejection sampling gives essentially identical results as our past approach for cases where a given mass and luminosity measurement lie well within the bounds of model isochrones, i.e., for brown dwarfs and young stars. The main advantage to rejection sampling is that it properly handles stars on the main-sequence and that it explicitly specifies a prior on age. For example, in our past work on LHS 1901AB we quoted median and $\pm1\sigma$ values from our age posterior from Lyon models of $0.28^{+9.72}_{-0.08}$ Gyr (Dupuy et al. 2010). This low median age was a consequence of directly interpolating our measured luminosity that is slightly higher than, but still well within the 1σ errors of, the model-predicted main-sequence luminosity for objects of that mass. Using our new method we report a more sensible result of $5.2^{+1.9}_{-4.7}$ Gyr, thanks to both allowing measured luminosities to scatter above and below the main sequence value and imposing an explicit age prior. In addition, in our new approach we always interpolate directly from model grids in mass and age, which circumvents issues related to the fact that luminosity can be double-valued at a given mass as a function of age.

Finally, we note that the models used in our analysis all assume solar metallicity. Different assumptions about metallicity would impact opacities and likely also influence cloud formation and evolution, both of which would change how luminosity evolves with time. In our work on Gl 417BC (Dupuy et al. 2014), we discussed this impact of changing opacities on cooling, inferring from the cloudless SM08 models that a change of ±0.3 dex in metallicity changes luminosity by no more than ±0.05 dex (super-solar models are more luminous at a given mass and age). Thus, if our sample is on average significantly offset from solar metallicity for some reason, this would result in only a slight systematic shift in our results. For reference, Santos et al. (2008) report a mean and rms metallicity of -0.10 ± 0.24 dex for stars in the solar neighborhood. Even for such relatively large metallicity differences as ±0.3 dex, the corresponding difference in luminosity is comparable to our typical luminosity uncertainties, so we do not expect metallicity to strongly affect our conclusions.

7. Discussion

Our large sample of dynamical masses enables a broad array of empirical tests of substellar evolution, many of which have not been possible before without precise individual masses. We now discuss a number of key topics, both in testing model predictions and establishing empirical relations. In the following analysis we will mostly deal with our results as whole, but a detailed discussion of each individual system is provided in Appendix B. When discussing our results below, we generally do not explicitly exclude anomalous objects (e.g., the unresolved components of triple systems discussed in Section 7.4) every time they might be relevant.

7.1. Empirical Test of the Substellar Boundary

Our work represents the first sample of individual masses for spectrally classified L and T dwarfs. This allows us to examine the maximum mass of the latest-type objects, which is the mass of the boundary between stars and brown dwarfs. Figure 6 shows our 38 individual mass and luminosity measurements along with all other published model-independent masses, including the spectrally unclassified objects Gl 802B ($80 \pm 14\,M_{\rm Jup}$; Ireland et al. 2008) and HR 7672B ($68.7^{+2.4}_{-3.1}\,M_{\rm Jup}$; Crepp et al. 2012), as well as the M8.5+M9 binary Gl 569Bab ($80^{+9}_{-8}\,M_{\rm Jup}$ and $58^{+7}_{-9}\,M_{\rm Jup}$; Konopacky et al. 2010), the M9.5+L0 binary LHS 1070BC ($81 \pm 5\,M_{\rm Jup}$ and $74 \pm 4\,M_{\rm Jup}$; Köhler et al. 2012), and the M7+M7 binary LSPM J1314+1320AB ($92.8 \pm 0.6\,M_{\rm Jup}$ and $91.7 \pm 1.0\,M_{\rm Jup}$; Dupuy et al. 2016). None of the components violate the most basic predictions of models within the observational uncertainties, except for systems suspected to be higher-order multiples based on our analysis independent of models. No objects have a lower luminosity than expected given their mass and the finite age of the Universe.

Figure 3 shows our individual masses as a function of spectral type. The lack of objects at high mass and late spectral type is empirical evidence for a mass limit to hydrogen fusion. Moreover, examining the maximum mass of the latest-type objects (or equivalently the lowest luminosity objects in Figure 6) allows us to constrain the upper limit on the mass of the substellar boundary, and correspondingly a lower limit of the mass of main sequence stars. In fact, our dynamical mass sample is (somewhat unfortunately) ideal for this test because we are biased toward high masses. The main observational limitation in measuring masses to date has been achieving the time baseline needed for robust orbit determinations of binaries with typical periods of 20–30 yr. The highest mass late-L or T dwarfs in our sample are 2MASS J1728+3948B (L7.0±1.0; $67 \pm 5\,M_{\rm Jup}$; $\log(L_{\rm bol}/L_\odot) = -4.49 \pm 0.04$ dex) and 2MASS J1404−3159A (L9.0 ± 1.0; $65 \pm 6\,M_{\rm Jup}$; $\log(L_{\rm bol}/L_\odot) = -4.52 \pm 0.05$ dex). The next most massive late-type object is 2MASS J2132+1341B (L8.5±1.5; $60 \pm 4\,M_{\rm Jup}$; $\log(L_{\rm bol}/L_\odot) = -4.50^{+0.05}_{-0.04}$ dex). Going to earlier types, there are three objects that have masses and spectral types that are consistent among each other within the errors: 2MASS J0920+3517A (L5.5 ± 1.0; $71 \pm 5\,M_{\rm Jup}$; $\log(L_{\rm bol}/L_\odot) = -4.28 \pm 0.03$ dex), 2MASS J1728+3948A (L5.0 ± 1.0; $73 \pm 7\,M_{\rm Jup}$; $\log(L_{\rm bol}/L_\odot) = -4.29^{+0.04}_{-0.05}$ dex), and 2MASS J2132+1341A (L4.5 ± 1.5; $68 \pm 4\,M_{\rm Jup}$; $\log(L_{\rm bol}/L_\odot) = -4.22 \pm 0.05$ dex). Despite the fact that we are more sensitive to massive systems, even our most massive late-type objects are only consistent with having masses as high as $71\,M_{\rm Jup}$ within 1σ, and even at spectral types as early as L4 the most massive objects are consistent with $70\,M_{\rm Jup}$. Therefore, we estimate an empirical substellar boundary of $\approx 70\,M_{\rm Jup}$.

The theoretical mass limit of hydrogen fusion quoted in the literature varies widely. One review by Burrows et al. (2001) places the minimum mass for H fusion between 0.070–0.075 $M_\odot$ (73–79 $M_{\rm Jup}$) for solar metallicity and at $0.092\,M_\odot$ ($96\,M_{\rm Jup}$) for zero metallicity. More recent models from Burrows et al. (2011) also show a range of 0.070–0.075 $M_\odot$ for the H-fusion mass assuming different helium fractions (their Figure 6). A review by Chabrier & Baraffe (2000) gives the minimum mass of H fusion as $0.070\,M_\odot$ ($73\,M_{\rm Jup}$) when cloud opacity is included and $0.072\,M_\odot$ ($75\,M_{\rm Jup}$) for cloudless atmospheres. If the H-fusion mass limit is indeed as high as $\approx 75\,M_{\rm Jup}$, then it is surprising that we have not uncovered objects with masses closer to this limit in our sample. Figure 7 shows more recent tracks from BHAC that includes a $0.072\,M_{\odot}$ ($75\,M_{\rm Jup}$) track that stabilizes in luminosity after ≈2 Gyr and thus we would consider a star. Some of the next lower mass tracks appear more star-like in that sense, but by $0.067\,M_{\odot}$ ($70\,M_{\rm Jup}$) the luminosity appears to be on course to monotonically decrease for the age of the Universe. Finally, SM08 quote a minimum mass of $0.070\,M_{\odot}$ ($73\,M_{\rm Jup}$) from their cloudy models, because that track ultimately reaches 1550 K where clouds are very significant in the atmosphere. Thus, the lack of any $\gtrsim$70 $M_{\rm Jup}$ brown dwarfs in our sample is consistent with the lower range of predictions in the literature for the minimum mass of H fusion (70–73 $M_{\rm Jup}$).

If we adopt our empirical substellar boundary of ≈70 $M_{\rm Jup}$, we can then determine the latest spectral type of objects above this boundary (i.e., objects that may be stars at the very bottom of the main sequence). The most precise stellar mass in our sample is for 2MASS J0746+2000B (L1.5 $\pm$ 0.5; $78.4 \pm 1.4\,M_{\rm Jup}$; $\log(L_{\rm bol}/L_{\odot}) = -3.777^{+0.028}_{-0.027}$ dex), but this is likely well above the H-fusion limit. Going to later spectral types we find 2MASS J0700+3157A (L3.0±1.0; $68.0\pm2.6\,M_{\rm Jup}$; $\log(L_{\rm bol}/L_{\odot}) = -3.95\pm0.04$ dex) and 2MASS J1017+1308B (L3.0±1.0; $75\pm7\,M_{\rm Jup}$; $\log(L_{\rm bol}/L_{\odot}) = -3.84 \pm 0.04$ dex). After this is the cluster of ≈L4–L6 objects with masses consistent with 70 $M_{\rm Jup}$ mentioned above. We therefore conclude that the end of the main sequence occurs within the range of spectral types of L3–L5 and luminosities of $10^{-4.3}$ to $10^{-3.9}$ dex, independent of model assumptions. Objects with spectral types later than this, or luminosities lower than this, are brown dwarfs, while objects with earlier types or higher luminosities could either be stars or brown dwarfs. Our result is consistent with early work on the first samples of L dwarfs that showed the substellar boundary was likely within this spectral type range (e.g., Kirkpatrick et al. 1999). A larger sample and more precise component spectral types would enable us to refine the location of this empirically defined substellar boundary.

Finally, we discuss our results in the context of the work of Dieterich et al. (2014) on the substellar boundary. Their approach uses the minimum radius (determined via luminosity and a temperature derived from model atmospheres) on the Hertzsprung-Russell diagram. The physical motivation is that the transition to degeneracy-dominated interiors marks the beginning of the substellar regime, as degeneracy pressure is what prevents objects below a critical mass from reaching sufficiently high core temperatures to generate a significant amount of energy by fusing hydrogen. To perform their test, they start at the late-M dwarfs and examine progressively cooler objects that have progressively smaller radii, until the trend reverses and cooler objects no longer have significantly smaller radii. Dieterich et al. (2014) find that this occurs at a radius of $0.086 \pm 0.003\,R_{\odot}$ for the object 2MASS J0523−1403, which has a spectral type of L2.5 and $\log(L/L_{\odot}) = -3.9$ dex, and they conclude that this marks the end of the main sequence. Compared to the boundary derived here using mass, their result is somewhat earlier in type and more luminous than our result but broadly consistent within the uncertainties. Dieterich et al. (2014) discuss the fact that models predict a locus for their radius test at somewhat cooler temperatures and suggest that lowering the metal abundances adopted in current models could explain the discrepancy; however, they also note that such a change in the abundances would alter the mass limit of the boundary to higher masses. The fact that we find a rather low mass limit for the substellar boundary would therefore seem to indicate that abundances alone will not rectify the tensions between models and the results of Dieterich et al. (2014). We speculate that one possibility could be systematic errors in temperatures derived from model atmospheres akin to those identified in our previous work on late-M dwarfs (Dupuy et al. 2010), where model atmospheres gave higher temperatures than implied by evolutionary model radii and measured luminosities.

7.2. Lithium Fusion Mass Limit

Theoretical predictions of lithium depletion in ultracool dwarfs as a function of mass and age are thought to be one of the most reliable methods for age-dating young clusters (e.g., Chabrier et al. 1996; Bildsten et al. 1997; Binks & Jeffries 2014; Kraus et al. 2014). They have also long been used as a method of confirming ultracool dwarfs as substellar (e.g., Rebolo et al. 1992; Basri et al. 1996). The brown dwarfs in our sample span masses both above and below the predicted lithium depletion boundary, and many of them are in systems with published optical, integrated-light spectroscopy that constrains the presence or absence of lithium. One potential complication is that the Li I doublet at 6708 Å, which provides the most sensitive observational probe of lithium, is expected to disappear in cool objects where monatomic lithium becomes incorporated into LiCl and LiOH molecules or at cooler temperatures condenses into LiF and Li_2S (e.g., Lodders 1999). This chemical depletion at low temperatures has not previously been tested with objects of known mass. The latest-type object known to display Li I absorption is WISE J1049−5319B (T0; Faherty et al. 2014; Lodieu et al. 2015), implying that any of the L dwarfs in our sample might plausibly display Li I absorption if they are not depleted by Li fusion.

Figure 9 shows our individual masses as a function of age for the 13 systems with well constrained model-derived ages, i.e., systems containing at least one brown dwarf, as well as the pre–main-sequence binary LP 349-25AB. (The low-mass main-sequence binaries in our sample have unconstrained ages, and, as expected, none are known to display Li I absorption.) Only two of these 13 binaries have published lithium detections, SDSS J0423−0414AB (EW = 11 Å; Kirkpatrick et al. 2008) and Gl 417BC (EW = 11.5 Å; Kirkpatrick et al. 2001). Seven more systems have published spectra that exclude lithium absorption in integrated light: LP 349-25AB (<0.5 Å; Reiners & Basri 2009), 2MASS J0700+3157AB (<0.3 Å; Thorstensen & Kirkpatrick 2003), LHS 2397aAB (<0.5 Å; Reiners & Basri 2009), 2MASS J1728+3948AB (<4 Å; Kirkpatrick et al. 2000), 2MASS J2132+1341AB (Cruz et al. 2007), and DENIS J2252−1730AB (Reid et al. 2008b). (See Appendix B for a detailed discussion of all of these binaries and their lithium constraints.)

Also shown in Figure 9 are the lithium-depletion mass limits predicted by the BHAC models and by the Tucson models (Burrows et al. 1997). While we do not use the Tucson models in our other model analysis, mainly because in addition to their non-gray atmosphere models they used gray atmospheres at the higher temperatures (including some temperatures relevant for our sample) in order to cover the full range of evolution, we include them here because they are the only other available evolutionary tracks that report lithium depletion. As expected, lithium nondetections in the most massive objects, LHS 2397aA (M8, $93 \pm 4\,M_{\rm Jup}$) and the young (271^{+22}_{-29} Myr, BHAC) components of LP 349-25AB (M7+M8, $85 \pm 4\,M_{\rm Jup}$ and $80 \pm 3\,M_{\rm Jup}$), are all consistent with model-predicted lithium depletion. Likewise, the two systems with strong lithium detections comprise some of the lowest mass components in the sample ($\lesssim 50\,M_{\rm Jup}$), so they are consistent with both sets of models that predict they should be abundant in lithium.

The lowest mass objects with lithium not detected are the $59 \pm 5\,M_{\rm Jup}$ and $41 \pm 4\,M_{\rm Jup}$ components of DENIS J2252−1730AB (L4+T3.5; $1.10^{+0.15}_{-0.18}$ Gyr). Within the 1σ uncertainties the primary is consistent with being strongly depleted according to BHAC models, $\log({\rm Li/Li_{init}}) = -2.1^{+0.7}_{-1.5}$ dex (Cond), and the late-type secondary is likely too cool to possess monatomic lithium. In contrast, the Tucson models predict that DENIS J2252−1730A should have retained most of its lithium, $\log({\rm Li/Li_{init}}) = -0.04^{+0.04}_{-0.06}$ dex, and are only consistent with full depletion at 2.0σ. Five other objects in four systems with masses below $70\,M_{\rm Jup}$ (2MASS J2132+1341AB, 2MASS J0700+3157A, LHS 2397aB, 2MASS J1728+3948B) are all consistent at $\leq 1\sigma$ with full lithium depletion according to BHAC models. In contrast, Tucson models predict that all of these objects could possess a substantial fraction (up to 100%) of their initial lithium within the 1σ errors. This can be seen visually in Figure 9 as the cluster of lithium nondetections around 60–70 $M_{\rm Jup}$ and 2 Gyr that mostly lie above the BHAC 99.9% depletion curve but that lie entirely below the Tucson 99.9% depletion curve.

We have noted this tension between predictions of Lyon and Tucson models in our previous work on HD 130948BC (Dupuy et al. 2009b). Our large sample of individual masses below the substellar boundary suggests that the lithium is destroyed via fusion at lower masses than the Tucson models predict but at masses consistent with BHAC models. The fact that the Tucson models predict a higher mass limit for lithium fusion indicates that their central temperatures are lower, which can be understood as a consequence of their atmospheres being less opaque as discussed in detail in Section 3.2 of SM08. According to BHAC models, at field ages of $\gtrsim$1 Gyr the lithium depletion boundary is at a mass of 60 $M_{\rm Jup}$. Some of the most interesting systems for testing lithium depletion are the young (400–800 Myr) binaries Gl 569Bab, HD 130948BC, and Gl 417BC that span masses of ≈50–70 $M_{\rm Jup}$ but that do not yet have directly measured individual masses and/or optical spectra. Individual masses are attainable in the future with absolute astrometry, either relative to their stellar hosts (Gl 569Bab, HD 130948BC) or from wide-field *HST* imaging (Gl 417BC). In addition, resolved optical spectra from *HST*/STIS would benefit the entire sample, enabling stricter tests of models than is currently possible with integrated-light spectra.

7.3. Coevality Tests & the Mass–Luminosity Relation in the L/T Transition

In principle, every binary in our sample can be thought of as a "mini-cluster" of coeval, co-compositional objects that can be used to test model isochrones (e.g., Liu et al. 2010). The most straightforward approach is to frame this as a test of coevality. Given our directly measured individual masses and luminosities, we derive from models an age posterior distribution for each component (t_1 and t_2). We then examine the posterior distribution of the difference in ages, and the extent to which it is different from zero corresponds to a discrepancy in the mass–luminosity relation predicted by model isochrones. Because we use a Monte Carlo approach, covariances due to parameters in common between components (distance and total mass) are naturally accounted for in our analysis.

Figure 10 displays the median and 1σ intervals of the posterior distributions for $\Delta \log(t) \equiv \log t_2 - \log t_1$. To examine how this coevality criterion depends on the underlying physical properties, we plot these values as a function of the secondary component mass (i.e., component that is less luminous). At the highest masses, where the binaries are composed of two main-sequence stars that each have unconstrained age posteriors, the resulting coevality values are all $\Delta \log t \approx 0.0 \pm 0.5$ dex at 1σ. In other words, both stars are consistent with the full range of main sequence ages (a few hundred Myr, depending on mass, to 10 Gyr, the maximum age of models).

The more interesting coevality tests are for binaries composed of two brown dwarfs. All but two of these systems give consistent ages for the primary and secondary at $\lesssim 1\sigma$ across all models. The exceptions are two binaries spanning the L/T transition that have the lowest-mass secondaries of any objects in our sample. According to Lyon Cond models, SDSS J0423−0414AB and SDSS J1052+4422AB are 3.0σ and 1.5σ discrepant with coevality, respectively. In contrast, the SM08 models predict a shallower mass–luminosity relation in the L/T transition and thus yield coeval ages for both systems (consistent at 0.5σ and 0.2σ, respectively). The key difference between Lyon models (Cond and Dusty) and SM08 hybrid models is that SM08 prescribes an ad hoc change from a cloudy to a cloudless photosphere as temperature drops from 1400 K to 1200 K. This results in luminosity dropping less quickly during and immediately following the transition from cloudy to cloudless atmospheres.

We originally discussed this discrepancy between SM08 and Lyon models for SDSS J1052+4422AB in Dupuy et al. (2015b). The case of SDSS J0423−0414AB (L6.5±1.5 and T2.0±0.5) is very similar to SDSS J1052+4422AB (L6.5 ± 1.5 and T1.5 ± 1.0). The primary masses are the same within the errors ($51.6^{+2.3}_{-2.5}\,M_{\rm Jup}$ and $51 \pm 3\,M_{\rm Jup}$, respectively), but SDSS J0423−0414AB has a lower mass ratio (0.62 ± 0.04 compared to 0.78 ± 0.07) and luminosity ratio ($\Delta \log(L_{\rm bol}) = 0.31^{+0.09}_{-0.08}$ dex compared to 0.13 ± 0.08 dex). Thus, SDSS J0423−0414AB has even more leverage in our coevality test, and indeed it confirms our previous findings at even higher significance. The reason for the coevality test failure in both cases is that the secondary is more luminous (or equivalently the primary is less luminous) than predicted for their masses at a single age in Lyon models. According to the SM08 hybrid models, luminosity does not fade as quickly during and immediately following the transition from cloudy to cloud-free atmospheres. So according to SM08 models it is the secondary that is more luminous than expected (rather than a suppressed luminosity of the primary) because the secondary has already cooled through the L/T transition and lost its clouds.

A new physical explanation for the L/T transition has been proposed by Tremblin et al. (2016), where the primary driver is a thermo-chemical instability in the carbon chemistry (CO/CH_4). Our measurement of the mass–luminosity relation through the L/T transition will provide a key test of this new idea after it is implemented in evolutionary models in the future.

7.4. Discovery of Triple Systems

Our individual mass and luminosity measurements have revealed that some objects in our sample are likely triple systems where the higher order multiplicity is unresolved by current observations. The most extreme case is 2MASS J0920+3517AB (L5.5+L9), where the total mass of $187 \pm 11\,M_{\rm Jup}$ is high enough that it suggests the presence of an unresolved massive component. Our individual masses reveal that indeed the less luminous (by 0.06 ± 0.04 dex) component 2MASS J0920+3517B is much more massive ($116^{+7}_{-8}\,M_{\rm Jup}$) than the more luminous 2MASS J0920+3517A ($71 \pm 5\,M_{\rm Jup}$). In fact, the anomalous mass of 2MASS J0920+3517B would be obvious on its own, given that its spectral type is L9.0 $\pm$ 1.5, and that models cannot reproduce its luminosity at such a high mass (Figure 11). 2MASS J0920+3517B can plausibly be explained by a simplistic model in which it is composed of two equal-luminosity components with equal masses of $58^{+3}_{-4}\,M_{\rm Jup}$. The unresolved pair must be rather tight, as we have never observed an elongated PSF for the secondary relative to the primary, and the astrometric residuals about the resolved orbit fit have an rms of 0.5 mas for the better half (13 out of 25) of our measurements. This implies an inner orbit that is much smaller than the observed outer orbit ($a = 68.15 \pm 0.23$ mas, 2.11 ± 0.04 AU). We discuss this system in more detail in Appendix B.7.

Unlike 2MASS J0920+3517AB, the total mass of the L3+L6.5 binary 2MASS J0700+3157AB ($141^{+4}_{-5}\,M_{\rm Jup}$) is not unusually high. Indeed, our total-mass model analysis readily finds a self-consistent way to apportion the mass of the two components ($76.8^{+1.5}_{-1.3}\,M_{\rm Jup}$ and $66^{+4}_{-3}\,M_{\rm Jup}$, Cond) according to their quite different luminosities ($\Delta\log(L_{\rm bol}/L_\odot) = 0.50 \pm 0.06$ dex) at an age of $2.1^{+0.4}_{-0.6}$ Gyr. However, our directly measured masses are $68.0 \pm 2.6\,M_{\rm Jup}$ and $73.3^{+2.9}_{-3.0}\,M_{\rm Jup}$. The less luminous component is again the more massive one, implying that 2MASS J0700+3157B is in fact an unresolved binary. The model-derived ages for 2MASS J0700+3157A are $0.76^{+0.09}_{-0.14}$ Gyr (SM08) and $1.01^{+0.13}_{-0.19}$ Gyr (Cond). If we assume that 2MASS J0700+3157B is composed of equal-luminosity components with equal masses of $36.7^{+1.4}_{-1.5}\,M_{\rm Jup}$, their model-derived ages are somewhat inconsistent with the primary's ($1.15^{+0.11}_{-0.12}$ Gyr and $0.83^{+0.08}_{-0.09}$ Gyr, respectively), suggesting that this simplistic scenario is not likely. As with 2MASS J0920+3517AB, we have never observed evidence for PSF elongation of 2MASS J0700+3157B in our Keck LGS AO imaging, and the rms about the relative orbit fit is 0.22 mas for the better half (11 out of 22) of our measurements. Thus, the inner orbit in this system is likely very small relative to the outer orbit ($a = 377^{+5}_{-6}$ mas, 4.25 ± 0.08 AU). We discuss this system in more detail in Appendix B.4.

We have identified a third candidate triple system. The total mass of LP 415-20AB ($248^{+26}_{-29}\,M_{\rm Jup}$) is very high for such late spectral type components (M6+M8). Our individual masses show that this is because the primary is very massive ($156^{+17}_{-18}\,M_{\rm Jup}$), while the secondary's mass ($92^{+16}_{-18}\,M_{\rm Jup}$) is consistent with its luminosity according to BHAC models. Given the relatively large individual mass uncertainties, it is unclear whether the putative unresolved component of LP 415-20A is another low-mass star or if it is a brown dwarf. It is less likely, but still possible, that the apparent discrepancy here is due to the rather large observational uncertainties. An improved parallax for this system, which is also notable as a possible member of the Hyades, will help clarify the situation as we discuss in more detail in Appendix B.2.

2MASS J0700+3157 and 2MASS J0920+3517 bring the tally of high-order multiples composed entirely of likely brown dwarfs to five, and these are the first such triple systems with directly measured masses, semimajor axes, and eccentricities. The first triple brown dwarf identified was DENIS J020529.0−115925 (Bouy et al. 2005), where the primary (L5) is orbited by a L/T transition binary (L8+T0). Radigan et al. (2013) discovered the triple T dwarf system 2MASS J08381155+1511155, where the brightest component (T3) is orbited by two slightly fainter components (T3+T4.5). Stone et al. (2016) discovered that the primary in the young system VHS J125601.92−125723.9 (Gauza et al. 2015) is actually a binary; making this the only one of these hierarchical triples in which the inner pair contains the most massive components. (Note that the distance of VHS J1256−1257 is not secure, and the more massive inner pair could be composed of low-mass stars and not brown dwarfs.) The hierarchical mass ordering of the DENIS J0205−1159 and 2MASS J0838+1511 systems appear to be similar to 2MASS J0700+3157 and 2MASS J0920+3517, but the relative sizes of inner and outer orbits may be different. The inner and outer pairs of DENIS J0205−1159 have projected separations of 1.3 AU and 7 AU, respectively, and 2MASS J0838+1511 has projected separations of 2.5 AU and 27 AU. If the inner pairs of 2MASS J0700+3157 and 2MASS J0920+3517 were only a factor of 7–10× smaller than orbit, then we would have either resolved them directly or possibly seen perturbations in our relative astrometry. Thus, it is likely that the semimajor axis ratios of 2MASS J0700+3157 and 2MASS J0920+3517 are much smaller than for DENIS J0205−1159 and 2MASS J0838+1511. Finally, we note that the eccentricity of the outer orbit is very low for 2MASS J0700+3157 ($0.017^{+0.005}_{-0.007}$) and is also rather low for 2MASS J0920+3517 ($0.180^{+0.006}_{-0.007}$). This would seem to rule out a violent dynamical origin for these triple systems.

7.5. Effective Temperature Relations

Without directly measured radii for field brown dwarfs of known spectral type, all previous work on spectral type–$T_{\rm eff}$ relations has relied on assumptions about age combined with model radii (e.g., Golimowski et al. 2004; Vrba et al. 2004; Stephens et al. 2009; Filippazzo et al. 2015). Our sample of visual binaries with directly measured luminosities and precise model-derived ages and radii allows us to examine spectral type–$T_{\rm eff}$ relations without uncertainties in radius due to the unknown ages or masses. We consider the effective temperatures derived from BHAC and Cond models as a single "Lyon" relation, using BHAC results when available. We used results from our individual-mass analysis when possible, relying on our total-mass analysis for the three systems without astrometric mass ratios (Gl 417BC, Gl 569Bab, and HD 130948BC). We excluded the three likely unresolved binaries LP 415-20A, 2MASS J0700+3157B, and 2MASS J0920+3517B. LHS 2397aB is also excluded because it lacks a spectral type determination. This results in a sample of 40 objects with Lyon temperatures and 22 objects with SM08 temperatures. (SM08 results are only for the coolest objects; our highest SM08 model-derived $T_{\rm eff}$ is 2090 ± 50 K for 2MASS J1017+1308A.)

Figure 12 shows our model-derived effective temperatures as a function of spectral type. We calculated second-order polynomial fits of $T_{\rm eff}$ as a function of spectral type, weighting by the quadrature average of the $+1\sigma$ and -1σ uncertainties in $T_{\rm eff}$. The coefficients of these fits are given in Table 68. The Lyon fit covers spectral types of M7–T5 and $T_{\rm eff} \approx$ 1100–2800 K, and the residuals have an rms scatter of 90 K. The SM08 fit covers spectral types of L1.5–T5 and $T_{\rm eff} \approx$ 1100–2100 K, and the residuals have an rms scatter of 80 K. The two fits agree reasonably well in the overlapping spectral type range, with the main difference being that the SM08 fit gives ≈100 K cooler temperatures for L4–L7 dwarfs. This seems to be a reflection of the fact that the SM08 model-derived temperatures for these objects are indeed systematically lower, due to SM08 radii being ≈10% larger than Cond radii at these temperatures, and not simply a quirk of the polynomial fit. This is expected from the fact that SM08 models have clouds while Cond models do not (e.g., see discussion of cloudy versus clear models by Burrows et al. 2011). There are no significant outliers in the SM08 fit, and in the Lyon fit only Gl 569Bb appears be be $\gtrsim 1.5\sigma$ discrepant. It has a model-derived temperature that is 310 K cooler than expected given its M9 spectral type and more consistent with L0.5–L1 types. Gl 569Ba is also slightly discrepant for its M8.5 spectral type (140 K cooler than the fit). Therefore, Gl 569Bb may appear discrepant because the system as whole is a slight outlier in $T_{\rm eff}$ due to the shared distance uncertainty in addition to the spectral type of Gl 569Bb perhaps being slightly underestimated.

Figure 12 also shows literature polynomial relations from Golimowski et al. (2004) and Filippazzo et al. (2015). Our mass-calibrated relation broadly agrees with this past work, except for the temperature of the L/T transition from Golimowski et al. (2004) which is systematically high, likely due to the presence of unrecognized binaries in that early work (e.g., Burgasser et al. 2005; Liu et al. 2006). The relation of Filippazzo et al. (2015) is systematically lower than our Lyon relation by ≈90 K, which appears to be due to the fact that they used SM08 model radii. Our SM08 relation agrees very well with Filippazzo et al. (2015), except at the extreme late-type end where we find a 150 K warmer $T_{\rm eff}$ for spectral type T5. This seems to be due to their polynomial not capturing the near-plateau in temperatures through the L/T transition that in our data extends to at least a type of T5. While our sample does not span exactly the same range in spectral type, the scatter about our polynomial relation (90 K for M7–T5) is somewhat smaller than previous relations spanning M6–T8 (124 K for Golimowski et al. 2004; 113 K for Filippazzo et al. (2015)).

Interestingly, all six T dwarfs in our sample, ranging from T1.5–T5, have effective temperatures that are consistent with each other within the uncertainties, i.e., $p(\chi^2) \approx 0.5$. The weighted average and rms of the model-derived temperatures is 1200 ± 60 K for Lyon and 1190 ± 60 K for SM08. The batch of objects at slightly earlier types are five L6.5–L8.5 dwarfs that also have internally consistent temperatures of 1475 ± 30 K (Lyon) and 1400 ± 25 K (SM08). In comparison, the only object in our sample without a spectral type determination is LHS 2397aB, which has model-derived temperatures of 1520 ± 40 K (Lyon) and 1440 ± 40 K (SM08), consistent with the warmer L6.5–L8.5 dwarfs. This is the first significant sample of objects with individually measured masses spanning the L/T transition. Their model-derived radii combined with our luminosities imply that the spectral type range of L6.5–T5 corresponds to a temperature range of only 200–300 K, with Lyon models favoring the slightly larger temperature range. The narrower $T_{\rm eff}$ range derived from the SM08 models is likely due to the fact that $L_{\rm bol}$ does not drop as steeply through the L/T transition, as discussed in the previous subsection.

Figure 13 shows our sample on the CMD with the data points colored according to their model-derived temperatures. As expected, temperature correlates strongly with the location along the CMD sequence, consistent with temperature being a primary driver of the spectral energy distributions of ultracool dwarfs. Of course, our derived $T_{\rm eff}$ is directly correlated with the plotted absolute magnitudes that are also used to derive $L_{\rm bol}$. However, in the L/T transition, objects have similar absolute magnitudes and yet they span a relatively wide range of temperatures ($\approx$1500 K to $\approx$1100 K), with objects bluer in $J - K$ having systematically cooler model-derived temperatures.

7.6. Age Distribution

The age distribution of the field population provides information about the star formation history of the galaxy and is a key component in studies of substellar mass function in the solar neighborhood (e.g., Burningham et al. 2010; Kirkpatrick et al. 2012). Without directly measured fundamental properties, the age distribution of ultracool dwarfs has previously only been constrained in a statistical sense from kinematic or population synthesis studies (e.g., Burgasser 2004; Allen et al. 2005; Zapatero Osorio et al. 2007; Faherty et al. 2009). However, precise age information is potentially available for brown dwarfs because, unlike stars, they are continuously changing their most easily observable properties, namely luminosity and temperature. The most precise age-dating method within current capabilities is to combine mass and luminosity, two properties that can be measured very accurately as we have shown here and in our past work, and infer an age from evolutionary models (for a review of various brown dwarf age-dating techniques see Burgasser 2009). Note that, as in all stellar astrophysics, age determinations for brown dwarfs are model dependent, so the accuracy of the derived ages will depend on how well evolutionary models predict substellar luminosity evolution. As we have found in our past work, this is not yet a solved problem, with potential issues at the factor of $\approx$2 level (e.g., Dupuy et al. 2009b, 2014, 2015b). However, given that our derived ages span nearly two orders of magnitude ($\sim$250 Myr to $\sim$10 Gyr), such inaccuracies should not have significant influence on the broad trends in our sample.

Figure 14 shows the distribution of system ages for the 10 binaries in our sample with at least one substellar component and thereby a well-determined age. When possible we use SM08 model-derived ages from our total-mass analysis; we only use our individual-mass analysis for the special cases of 2MASS J0700+3157AB, where the secondary is an unresolved binary, and LHS 2397aAB, where the primary is main-sequence star. We also tested ages derived from Cond models and found that they tended to give slightly (≈10%) older ages. We exclude two systems from our analysis here because their presence in our sample is not independent of their age. HD 130948BC and Gl 569Bab were both discovered in targeted surveys of young stars, and so it would not be correct to include them in this sample of field objects that have different observational selection effects with respect to age. Unlike these two companion systems, Gl 417BC was originally identified on its own in 2MASS and was only later associated with the young star Gl 417 by Kirkpatrick et al. (2001). Likewise, the pre–main-sequence binary LP 349-25AB is not included here because it only has a precise age determination by virtue of its youth.

The median age of our sample of field brown dwarfs is 1.3 Gyr (2.3 Gyr mean), and the age interval containing 90% of the joint posterior distribution of all 10 systems is 0.4–4.2 Gyr. This age distribution is broadly consistent with or somewhat younger than previous statistical age distributions. From a kinematic analysis of 21 L and T dwarfs, Zapatero Osorio et al. (2007) found a statistical age of $1.2^{+1.1}_{-0.7}$ Gyr, in good agreement with our age distribution. (Their sample includes just one of our age-dated systems, 2MASS J1728+3948AB.) In contrast, Faherty et al. (2009) found an older statistical age range from a kinematic analysis of proper motions for a much larger sample of 184 L0–T8 dwarfs, ranging from 3–8 Gyr for the whole sample or 2–4 Gyr excluding high tangential velocity ($>$100 km s^{-1}) objects. (None of our systems have such high tangential velocities.) The Faherty et al. (2009) results are thus systematically older than but marginally consistent with our age distribution.

Allen et al. (2005) found that brown dwarfs with spectral types ranging from L5 to early-T are expected to have a mean age of 3 Gyr, given a uniform prior on age from 0–10 Gyr and a nominal mass function of $\Psi(m) \propto m^{-0.8}$. The fact that we find a younger mean age could imply that the solar neighborhood comprises objects with a slightly younger age distribution. To investigate this possible discrepancy we performed a population synthesis simulation using a power-law mass function that is consistent with recent work ($\Psi(m) \propto m^{0.5}$; Kirkpatrick et al. 2012; Burningham et al. 2013) for a range in mass of 30–70 $M_{\rm Jup}$, i.e., the lowest to highest masses covered by our age-dated sample. Rather than assume a constant input age distribution, we adopted the Besançon model for the solar neighborhood that assumes a constant star formation rate and accounts for Galactic dynamics in a self-consistent way (Robin et al. 2003).[11] Because the Sun lies near the Galactic midplane, dynamical heating skews the age distribution toward younger ages as older stars are preferentially scattered away from the midplane over time. In our simulation we assume that

[11]To be clear about the terminology we are using, "star formation rate" refers to the number of stars and brown dwarfs that were formed in the Galactic disk as a function of time. "Age distribution" refers to the local, present day number of stars and brown dwarfs as a function of age.

ages are distributed uniformly among each of the Besançon model age bins, where each bin contains a fraction of the total population as follows: 20.0% for 0.15–1 Gyr, 16.1% for 1–2 Gyr, 11.9% for 2–3 Gyr, 16.6% for 3–5 Gyr, 12.9% for 5–7 Gyr, and 14.4% for 7–10 Gyr. We drew random ages according to this distribution, restricting our population synthesis simulation to 0.3–10 Gyr in order to accurately represent our observed sample.

After assigning masses and ages to each simulated object, we interpolated $T_{\rm eff}$ from the SM08 models, keeping only simulated objects that fall within the temperature range of our sample (1100–2100 K). As a check, the fractional breakdown in spectral types between ≤L6, L6.5–L8.5, and L9–T5 dwarfs was 0.22/0.36/0.42, very similar to the actual breakdown of objects in our age-dated sample (0.28/0.33/0.39). Also note that by performing our simulation with the same evolutionary models used to derive ages for our sample, the two age distributions are self-consistent by construction. In other words, the simulation output is directly comparable to our age distribution, even if the models were to have large systematic uncertainties in the absolute ages.

The age distribution resulting from our simple population synthesis simulation is shown in Figure 14. It has a median of 1.7 Gyr, a mean of 2.3 Gyr, and the interval 0.3–5.0 Gyr contains 90% of the distribution. The general shape of the distribution is quite similar to our observations, piling up at younger ages and tailing off at older ages. We checked if the input mass function might change this results, but using $\alpha = 0$ or -1 instead of -0.5 only changed the final median age by ≈5%. The simulation predicts that we would have found ≈1 old system (>5 Gyr) in our sample of 10 binaries, and the fact that none of our sample is definitively that old is the main cause of the slight discrepancy between the population synthesis and our observations. Overall however, our age distribution is remarkably consistent with our input assumption of a constant star formation rate.

The simulated population accounts for the main selection effects in our sample, namely a limited spectral type range and the fact that we can only age-date brown dwarfs and not stars (i.e., objects with mass $\lesssim$70 $M_{\rm Jup}$). The spectral type selection should bias our sample against old ages, and indeed the simulation indicates that we are the most complete at young ages. There is one remaining selection effect that is difficult to quantify, the fact that the youngest binaries at a given spectral type will have the lowest masses, and lower system masses correspond to longer orbital periods for a given semimajor axis range. Our dynamical mass sample relies on robust orbit determinations and thus suffers incompleteness at long periods (and thereby low masses and young ages) because there has been insufficient time to constrain the longest period orbits. (See Section 7.8 for a detailed discussion of this selection effect.) The fact that our sample is biased in this way against young ages, and yet we still find an age distribution skewed slightly younger than our simulation suggests that this selection effect has only a marginal influence.

Overall, our population synthesis simulation demonstrates that our observed age distribution is consistent with a constant star formation rate in the Galactic disk. We find that the age distribution of M7–T5 dwarfs in the solar neighborhood is somewhat younger than in previous work, but we determine that this can be explained by accounting for dynamical heating in the disk that boosts the scale height of older stars, removing them from the local volume. As a test, we performed a second simulation with uniform age input (i.e., constant star formation rate without dynamical heating) and this skewed the output median age older by almost a factor of two. In the future it will be possible to extend to older ages this empirical determination of the age distribution in the solar neighborhood with dynamical mass measurements for even cooler brown dwarfs (e.g., Dupuy et al. 2015a).

7.7. Eccentricity Distribution

We have previously examined the eccentricities of ultracool binaries and the implications for formation models in Dupuy & Liu (2011). The sample we used previously included eleven visual binaries, four spectroscopic binaries, and one eclipsing binary, and we had to contend with potential selection effects in this sample due to discovery bias (eccentric visual binaries are easier to discover with poor angular resolution), our own bias in selecting which binaries to monitor, and whether eccentricity might make some binaries more difficult to yield orbit determinations. Our new sample is not only much larger (ten new orbits), but we are also in a better position to address issues regarding observer and orbit-fitting biases. This is because we present here our entire monitoring sample with orbit fits for all binaries. The only selection is therefore based on the quality of the resulting fits, and this allows us to robustly quantify the completeness of our sample.

As described in detail in Section 2, our input sample of 31 binaries is, to the best of our knowledge, complete for binaries with projected separations at discovery of $\leq$6 AU, given our other non-orbit related selection criteria (spectral types M6.5–T5.5, $d \leq 40$ pc, observable from Maunakea with Keck LGS AO). Figure 15 shows all orbit fitting results for our sample, including binaries with marginally or poorly determined orbits, as well as visual binary orbits from the literature. As expected, the binaries with the widest separations at discovery have turned out to have longer orbital periods. Because we are hampered by the available observational time baseline for longer period binaries, many of these do not have well determined orbits. Only one binary with $P > 30$ yr has a well determined orbit (2MASS J1728+3948AB); all the rest are marginal or poor. The only binary at $P < 30$ yr that does not have a well determined orbit is SDSS J0926+5847AB ($e = 0.00$–0.58 at 2σ). This is a pathological case where the orbit is very close to being viewed edge on, and the phase coverage from our 3-year *HST* program does not allow us to uniquely determine the orbit. It is likely that if SDSS J0926+5847AB were observable with Keck LGS AO, then we would have better phase coverage over a longer time baseline that would enable an orbit fit. Therefore, we conclude that for periods <30 yr, our sample of orbit determinations is effectively complete, including 22 binaries from our sample and 3 binaries from the literature.

A complete sample can still be biased, with the key effect here being "discovery bias," which is explored in detail in Section 3.1.1 of Dupuy & Liu (2011). Briefly, every imaging survey has an inner working angle (IWA) inside of which binary companions are not detectable. Given a binary with semimajor axis a, the projected separation will sometimes be inside of this limit, depending on the inclination, eccentricity, and epoch of observation. When IWA $\ll a$, the probability of detecting any binary approaches unity. When IWA $> a$, circular binaries are completely undetectable while more eccentric binaries are more favorable to detect because the apoastron distance is $a \times (1 + e)$ (see Figure 1 of Dupuy & Liu 2011). By excluding binaries discovered very near the IWA of a survey we can minimize the impact of this discovery bias. Figure 16 shows the ratio of IWA/a for binaries in our sample. The highest IWA/a ratios are 1.58 and 1.24 for 2MASS J1047+4026AB and LP 415-20AB, respectively, and indeed both of these binaries are quite eccentric (0.7485 ± 0.0013 and $0.706^{+0.011}_{-0.012}$). The next highest are IWA/$a = 0.88$ for 2MASS J0920+3517AB ($e = 0.180^{+0.006}_{-0.007}$) and IWA/$a = 0.69$ for LP 349-25AB ($e = 0.0468^{+0.0019}_{-0.0018}$). Based on the simulations of Dupuy & Liu (2011), we adopt a cutoff of IWA/$a < 0.75$ to mitigate discovery bias in our sample, and this includes 2MASS J1047+4026AB, LP 415-20AB, and the more marginal case of 2MASS J0920+3517AB. Eccentricities for our entire sample, along with the three other published visual binary orbits, are shown in Figure 17 as a function of semimajor axis.

After making the cuts described above, the final complete, de-biased sample comprises 22 ultracool visual binaries. In addition, we examine published orbits for various unresolved binaries: three astrometric orbits (Sahlmann et al. 2015a,b; Koren et al. 2016), three spectroscopic orbits (Basri & Martín 1999; Joergens et al. 2010; Burgasser et al. 2016), and one double-lined eclipsing orbit for a very young brown dwarf binary in Orion (Stassun et al. 2006). Figure 18 shows all of these results, spanning more than three orders of magnitude in period. The unresolved binaries all have modest eccentricities (0.2–0.6), whereas our sample has a number of very eccentric (>0.7) and nearly circular (0.0–0.1) systems. The lack of low eccentricities (<0.2) in the seven unresolved binaries is the most striking, as nearly half (10 of 22) of the visual binaries have $e < 0.2$. More short-period binaries are needed to determine the significance of this apparent difference, given the current small sample with short periods.

Figure 19 shows the eccentricity distribution of our de-biased visual binary sample. The abundance of low eccentricity orbits is the most clear result, reinforcing the conclusion of Dupuy & Liu (2011) that very-low mass binaries are very inconsistent with the high eccentricity orbits found in simulations from Stamatellos & Whitworth (2009) but consistent with the more modest eccentricities predicted from the simulations of Bate (2009). In fact, our larger sample here is less consistent with the Bate (2009) results that do not predict as many nearly circular orbits. For both sets of simulations, it is possible that the influence of gas over timescales longer than the simulated durations would damp eccentricities further and bring the simulations into better agreement with our observations.

Compared to the extensive orbital information available for solar-type binaries spanning $\approx$6 orders of magnitude in period (e.g., Duquennoy & Mayor 1991; Raghavan et al. 2010), our visual binary sample covers a relatively narrow range of periods ($\lesssim$1 order of magnitude). However, one striking feature of the recent large Raghavan et al. (2010) compilation of solar-type multiple systems (127 eccentricities) from is that for a wide range of periods ($\sim 10^2$–10^6 d), there are no binary orbits with $e < 0.1$ and only three orbits in triple or quadruple systems with $e < 0.1$. In contrast, our de-biased visual binary sample has 5 out of 22 orbits with $e < 0.1$. Two of these are orbits in triple systems, where one is an "inner" orbit (i.e., the orbit of the tighter pair in the hierarchical triple; HD 130948BC) and one is an "outer" outer (2MASS J0700+3157AB). The other three are all seem to be binaries with no other companions (LP 349-25AB, 2MASS J1534−2952AB, and 2MASS J2206−2047AB). This discrepancy between the very low-mass and and solar-type orbits samples was first noted in Dupuy & Liu (2011), and it is even stronger now after roughly doubling the sample size of visual binaries. For example, the Fisher exact test comparing the number of binaries above and below $e = 0.1$ in our sample to Raghavan et al. (2010) gives a p-value of 0.0019, implying the two samples are inconsistent at 3.1σ. This difference in low-e orbits could be due to differences in initial conditions (i.e., binary formation is different at very low masses) and/or early evolution (i.e., different physical processes at work after formation). In the latter case, if dissipative gas disks are longer lived for very low-mass objects than solar type stars, this could potentially result in a higher fraction of nearly circular orbits even if the initial conditions are the same for both samples.

7.8. The Lowest Mass Brown Dwarfs in the Sample?

As described in Section 4.1, we have excluded some binaries from our analysis because of their uncertain orbits. This is largely due to poor orbital coverage given their apparently long orbital periods relative to our observational time baseline. Since our sample was selected to have the smallest semimajor axes possible, some of these binaries are likely to be the lowest mass systems in our sample. Indeed, if we take our orbit determinations at face value, then 2MASS J0850+1057AB, SDSS J1021−0304AB, SDSS J1534+1615AB, and SDSS J2052−1609AB all have lower total masses than the lowest mass object used in our analysis (SDSS J0423−0414AB, $M_{\rm tot} = 83 \pm 3\,M_{\rm Jup}$).

2MASS J0850+1057AB (L6.5+L8.5) has a total mass of only $54 \pm 8\,M_{\rm Jup}$, and thus perhaps component masses of 20–30 $M_{\rm Jup}$. Given the component luminosities, this would correspond to an age of 150–400 Myr according to both Lyon and SM08 models. The 2MASS J0850+1057 system has previously been suggested to be young based on having an M dwarf companion (NLTT 20346; $4\farcm13$ or 8000 AU away) with a young X-ray activity age (Faherty et al. 2011) and based on 2MASS J0850+1057A being bright at J-band for its spectral type (Burgasser et al. 2011). However, the physical association of NLTT 20346 to the 2MASS J0850+1057 system is questionable (see Section 6.4 of Dupuy & Liu 2012), and the discovery and characterization of young late-L dwarfs indicates that they tend to be fainter at J-band, not brighter (Faherty et al. 2012; Liu et al. 2013a; Liu et al. 2016). Our improved proper motion measurement for the 2MASS J0850+1057 system is consistent with our previous findings, discrepant by 45 mas yr^{-1} (6.3σ) with the Faherty et al. (2011) proper motion for NLTT 20346, implying that the wide pair is not likely to be physically associated. Burgasser et al. (2011) also suggested that 2MASS J0850+1057A could be an unresolved binary based on its unusually bright J- and K-band absolute magnitudes given its spectral type of

L7, making this a triple system of ultracool dwarfs. Our distance (31.8 ± 0.6 pc instead of 38 ± 6 pc) and spectral type of L6.5 $\pm$ 1.0 give absolute magnitudes comparable to other L5–L7 dwarfs (see Table 15 of Dupuy & Liu 2012), reducing the reason to suspect 2MASS J0850+1057A is an unresolved binary. Moreover, if our low total mass is accurate, then the component masses (if a triple system) would be 10–15 $M_{\rm Jup}$, making the system even younger. This seems unlikely given that the integrated-light spectrum lacks spectral similarities to other comparably young late-L dwarfs (e.g., Liu et al. 2013b; Gizis et al. 2015).

SDSS J1021−0304AB (T0+T5, $M_{\rm tot} = 52^{+6}_{-7}\,M_{\rm Jup}$) and SDSS J1534+1615AB (T0+T5.5, $M_{\rm tot} = 46^{+6}_{-7}\,M_{\rm Jup}$) have the most precise masses of any of the systems with poorly determined orbits. For plausible mass ratios the implied component masses of these binaries would be 20–30 $M_{\rm Jup}$. With orbital period posteriors of 86^{+13}_{-17} yr and 58^{+39}_{-24} yr, respectively, it is unlikely that we will achieve significant improvement in their orbit determinations in the near future. SDSS J2052−1609AB (L8.5+T1.5, $M_{\rm tot} = 69^{+14}_{-20}\,M_{\rm Jup}$) has a very uncertain total mass but the best chance of yielding a robust orbit in the near term, as its derived period is 44^{+10}_{-14} yr and our observations already cover 20% of this.

8. Conclusions

We present astrometric monitoring of a well-defined sample of 31 ultracool dwarf visual binaries (component spectral types M7–T5) from our ground- and space-based observing programs spanning nearly a decade in time baseline. We determine robust orbits using resolved astrometry by combining our Keck laser guide star adaptive optics imaging and aperture masking interferometry observations, *HST* imaging, and other published archival data. Our unresolved infrared imaging from CFHT/WIRCam allows us to measure precise parallactic distances and constrain the photocenter orbital motion of our binaries. We perform a simultaneous MCMC analysis of both resolved and unresolved astrometry in order to accurately determine posterior distributions of all 13 astrometric parameters. By careful consideration of our posteriors, we propose orbit quality metrics that separate robustly determined orbits (23 systems) from marginal and poorly determined orbits that typically have long orbital periods ($\gtrsim$50 yr) and thus lack sufficient observational time baseline. Our combined orbit and parallax results directly yield dynamical total masses (median precision 5%, as good as 1.1%), and combining our measured infrared flux ratios with the photocenter orbit constraints enables determination of individual masses for 19 systems (median precision 7%, as good as 1.7%).

We perform empirical tests of evolutionary models based solely on the observed properties of our sample. Also, we critically examine the fundamental properties of objects from the bottom of the main sequence through the L/T transition by deriving precise ages, radii, etc. from the models. For this analysis, we develop new relations for deriving bolometric luminosity from H- and K-band absolute magnitudes, as well as a method for inferring parameters from models given our mass and luminosity constraints. Unlike our past work that used simple interpolation of models, our new approach is based on the Monte Carlo technique of rejection sampling and allows for explicit definitions of age priors as well as proper treatment of cases where an object of a given mass might have the same luminosity at multiple times during its evolution (e.g., a star on the main sequence or a deuterium-burning brown dwarf). We summarize our findings as follows.

1. We perform a novel empirical test of the mass limit for hydrogen fusion in stars by examining the maximum mass of the coolest objects in our sample. Among all late-L and T dwarfs, we find no objects more massive than 70 $M_{\rm Jup}$, implying a substellar boundary that is lower in mass than found in some previous work (75 $M_{\rm Jup}$ has often been quoted) but reasonably consistent with the latest BHAC evolutionary tracks. Among objects more massive than 70 $M_{\rm Jup}$ the latest spectral types are L3–L5, implying that any object with a later spectral type than this is likely to be a brown dwarf independent of any model assumptions.

2. We examine the mass limit for lithium fusion in brown dwarfs. Our sample has 13 systems with at least one substellar component, and two of these have integrated-light Li I absorption reported in the literature while seven have published nondetections of lithium. After considering the potential for chemical depletion of monatomic lithium into molecular form (e.g., LiCl, LiOH), the observations are fully consistent with predictions of lithium depletion from Lyon evolutionary models (Baraffe et al. 2015). In contrast, Tucson models (Burrows et al. 1997) predict that lithium should be present at detectable levels in some of our more massive binary components (60–65 $M_{\rm Jup}$), but this is inconsistent with numerous Li I nondetections. The most massive objects in systems with lithium detected (SDSS J0423−0414A and Gl 417B) have masses of ≈52 $M_{\rm Jup}$, consistent with (in fact, much lower than) the BHAC model-predicted lithium depletion boundary of 60 $M_{\rm Jup}$ at ages $\gtrsim$1 Gyr.

3. We perform coevality tests, deriving ages for each binary component independently and checking for consistency to test evolutionary model isochrones. All binaries are consistent with predictions from the various models we tested, except for two binaries spanning the L/T transition that have the lowest mass secondary components in our sample (SDSS J0423−0414AB and SDSS J1052+4422AB). For these two systems, our observations show a smaller difference in luminosity between the binary components given their difference in mass than predicted by Lyon models (3.0σ and 1.5σ, respectively). However, both binaries are consistent with SM08 hybrid models that assume a gradual loss of cloud opacity as objects cool from 1400 K to 1200 K, which has the side effect of making the mass–luminosity relation shallower through the L/T transition. This reinforces the results of Dupuy et al. (2015b).

4. We discover two new brown dwarf triple systems, where the inner pairs are identified via direct mass measurements but not spatially resolved. 2MASS J0700+3157B and 2MASS J0920+3517B are each the fainter component of a visual binary but are significantly more massive than the brighter component, implying that they are each unresolved, roughly equal-mass binaries. A third system LP 415-20AB has an unusually massive primary (156^{+17}_{-18} $M_{\rm Jup}$) given its M6 spectral type, making this a third candidate triple in our sample. 2MASS J0700+3157 and

2MASS J0920+3517 are only the fourth and fifth known triple brown dwarf systems known, and they are the only such systems with directly measured masses, semimajor axes, and eccentricities, information that could be used to understand their origins.

5. We construct a spectral type–effective temperature relation for ultracool dwarfs that is based on model radii free of assumptions about mass or age. We fit a second order polynomial to temperatures derived from Lyon models (a sample that spans M7–T5 and 1100–2800 K) as well as SM08 models (valid over a narrower range of L1.5–T5 and 1100–2100 K). The scatter about the fit is 90 K for Lyon models and 80 K for SM08 models. Examining individual subsets of objects, we find that all six T1.5–T5 dwarfs have consistent temperatures within their uncertainties (weighted average and rms of 1190 ± 60 K using SM08 models), and the five L6.5–L8.5 dwarfs likewise have internally consistent temperatures (1400 ± 25 K using SM08 models).

6. The 10 systems in our sample with precisely determined ages (and provenances free of explicit age bias) allow us to directly measure the age distribution of brown dwarfs in the solar neighborhood for the first time. The median age of our sample is 1.3 Gyr, and the mean is 2.3 Gyr. Compared to previous statistical age constraints on the field population, our age distribution is either consistent (Zapatero Osorio et al. 2007) or systematically younger (Faherty et al. 2009), and it is also younger than previous modeling of the solar neighborhood (e.g., Allen et al. 2005). We performed a population synthesis simulation designed to mimic our sample in mass and spectral type range, using an input constant star formation history. We find good agreement with our observations only after accounting for dynamical heating in the Galactic disk, which preferentially removes older stars from the solar neighborhood. Thus, our sample is consistent with a constant star formation rate in the Galactic disk, at least over the relatively young ages that we probe ($\lesssim$4 Gyr).

7. We have revisited the eccentricity distribution of very low-mass binaries. In general, our results reinforce the conclusions of Dupuy & Liu (2011), now with a larger sample and more robustly quantified completeness. Perhaps the most striking feature of our visual binaries is the preponderance of low-eccentricity orbits. Out of 22 orbits in our de-biased sample, ten have $e < 0.2$ and five have $e < 0.1$. This is stark contrast to solar-type binaries and possibly also the relatively small sample of seven short-period, unresolved ultracool binaries with spectroscopic or astrometric orbits. We speculate that low-eccentricity orbits could reflect more extensive tidal damping during the early evolution of ultracool binaries if their gas disks are longer lived than more massive stars.

Our individual masses provide a direct window into substellar astrophysics, empirically quantifying the mass limits for hydrogen (and lithium) fusion. The unique ability of binaries to serve as "mini-clusters" has provided the strongest tests of the mass–luminosity relation in the poorly understood L/T transition. Indeed, recent theoretical work by Tremblin et al. (2016) has called into question the primacy of clouds in driving changes in the most readily observable properties (colors, magnitudes, and spectral types) across the L/T transition. Our results highlight how the modeling of surface properties can have a significant influence on the bulk evolution of brown dwarfs, as the only available models that match our mass–luminosity relation data are those that treat the L/T transition as a change in cloud properties. Evolutionary models adopting the alternative hypothesis that the L/T transition is driven by a CO/CH_4 thermo-chemical instability are needed to test this idea against our observations.

Our sample lays the groundwork for future tests of models using objects of known mass. For example, objects from our sample will have a significant advantage for testing model atmospheres as they provide a joint constraint on $T_{\rm eff}$ and $\log(g)$ (via radius) given the directly measured masses and luminosities. To enable such tests, resolved spectroscopy of our binaries will need to be obtained, and this is within reach of existing and future high angular resolution facilities. Moreover, resolved optical spectroscopy will be key in strengthening our tests of lithium depletion, as our current tests rely on integrated-light spectroscopy alone. In the farther future, dynamical masses for late-T and Y dwarf binaries (e.g., Liu et al. 2011; Dupuy et al. 2015a) will open the door to new tests of models. Such measurements will reveal both the older analogs of the $\gtrsim$30 $M_{\rm Jup}$ brown dwarfs in our current sample, as well as pushing to much lower masses, perhaps even to the mass range shared by directly imaged planets (5–15 $M_{\rm Jup}$).

We are deeply grateful to Michael Ireland, especially for his early contributions to this project that included training the author on analysis of masking data from NIRC2, as well as very helpful comments on this manuscript. We also are very thankful to Andrew Mann for assistance in validating our methods for determining bolometric luminosities. This work would not have been possible without the excellent, long running support of CFHT staff past and present, including Loïc Albert, Todd Burdullis, Pascal Fouqué, Nadine Manset, Karun Thanjavur, Kanoa Withington, and all service observers who have executed our program over the last nine years. It is a pleasure to thank the Keck Observatory staff for assistance with the Keck LGS AO observing, including Joel Aycock, Randy Campbell, Al Conrad, Scott Dahm, Greg Doppmann, Heather Hershley, Marc Kassis, Jim Lyke, Jason McIlroy, Carolyn Jordan, Gary Punawai, Julie Riviera, Luca Rizzi, Terry Stickel, Hien Tran, and Cynthia Wilburn. We thank Isabelle Baraffe, Didier Saumon, and Mark Marley for providing expanded model grids and helpful discussions about substellar evolution; and the anonymous referee for a thoughtful and timely review. T.J.D. is indebted to many people for providing useful discussions over the course of this project, including Katelyn Allers, Josh Carter, Rio Jennings, Adam Kraus, and Aaron Rizzuto. This work was supported by multiple NASA Keck PI Data Awards, administered by the NASA Exoplanet Science Institute. Support for our long-term *HST* program (GO-11593, GO-12317, and GO-12661) was provided by NASA through a grant from the Space Telescope Science Institute, which is operated by the Association of Universities for Research in Astronomy, Inc., under NASA contract NAS 5-26555. T.J.D. also acknowledges support from NASA Exoplanet Research Program grant NNX15AD23G. M.C.L. acknowledges support from NSF grants AST09-09222 and AST15-18339. Our research has employed NASA's Astrophysical Data System; Posse East; the SIMBAD database operated at CDS, Strasbourg, France; the 2MASS data products; and the SpeX Prism Spectral Libraries, maintained by Adam Burgasser at `http://www.browndwarfs.org/spexprism`. Finally, the authors wish to recognize and acknowledge the very significant cultural role and reverence that the summit of Maunakea has always had within the indigenous Hawaiian community. We are most fortunate to have the opportunity to conduct observations from this mountain.

Facilities: HST (WFC3) Keck:II (LGS AO, NIRC2) CFHT (WIRCam) IRTF (SpeX)

REFERENCES

Allard, F., Hauschildt, P. H., Alexander, D. R., Tamanai, A., & Schweitzer, A. 2001, ApJ, 556, 357

Allen, P. R., Koerner, D. W., Reid, I. N., & Trilling, D. E. 2005, ApJ, 625, 385

Allers, K. N., & Liu, M. C. 2013, ApJ, 772, 79

Baraffe, I., Chabrier, G., Allard, F., & Hauschildt, P. H. 1995, ApJ, 446, L35

Baraffe, I., Chabrier, G., Barman, T. S., Allard, F., & Hauschildt, P. H. 2003, A&A, 402, 701

Baraffe, I., Homeier, D., Allard, F., & Chabrier, G. 2015, A&A, 577, A42

Bardalez Gagliuffi, D. C., Gelino, C. R., & Burgasser, A. J. 2015, AJ, 150, 163

Basri, G., Marcy, G. W., & Graham, J. R. 1996, ApJ, 458, 600

Basri, G., & Martín, E. L. 1999, AJ, 118, 2460

Bate, M. R. 2009, MNRAS, 392, 590

Benedict, G. F., Henry, T. J., Franz, O. G., et al. 2016, AJ, 152, 141

Berger, E., Rutledge, R. E., Phan-Bao, N., et al. 2009, ApJ, 695, 310

Bertin, E., & Arnouts, S. 1996, A&AS, 117, 393

Bildsten, L., Brown, E. F., Matzner, C. D., & Ushomirsky, G. 1997, ApJ, 482, 442

Biller, B. A., Kasper, M., Close, L. M., Brandner, W., & Kellner, S. 2006, ApJ, 641, L141

Binks, A. S., & Jeffries, R. D. 2014, MNRAS, 438, L11

Bouy, H., Brandner, W., Martín, E. L., et al. 2003, AJ, 126, 1526

Bouy, H., Martín, E. L., Brandner, W., & Bouvier, J. 2005, AJ, 129, 511

Bouy, H., Duchêne, G., Köhler, R., et al. 2004, A&A, 423, 341

Bouy, H., Martín, E. L., Brandner, W., et al. 2008, A&A, 481, 757

Brandt, T. D., & Huang, C. X. 2015, ApJ, 807, 58

Bryja, C., Jones, T. J., Humphreys, R. M., et al. 1992, ApJ, 388, L23

Burgasser, A. J. 2004, ApJS, 155, 191

Burgasser, A. J. 2009, in IAU Symposium, Vol. 258, The Ages of Stars, ed. E. E. Mamajek, D. R. Soderblom, & R. F. G. Wyse, 317–326

Burgasser, A. J., Bardalez-Gagliuffi, D. C., & Gizis, J. E. 2011, AJ, 141, 70

Burgasser, A. J., Blake, C. H., Gelino, C. R., Sahlmann, J., & Bardalez Gagliuffi, D. 2016, ApJ, 827, 25

Burgasser, A. J., Geballe, T. R., Leggett, S. K., Kirkpatrick, J. D., & Golimowski, D. A. 2006a, ApJ, 637, 1067

Burgasser, A. J., Kirkpatrick, J. D., Cruz, K. L., et al. 2006b, ApJS, 166, 585

Burgasser, A. J., Kirkpatrick, J. D., Liebert, J., & Burrows, A. 2003a, ApJ, 594, 510

Burgasser, A. J., Kirkpatrick, J. D., Reid, I. N., et al. 2003b, ApJ, 586, 512

Burgasser, A. J., Reid, I. N., Leggett, S. K., et al. 2005, ApJ, 634, L177

Burgasser, A. J., Reid, I. N., Siegler, N., et al. 2007, in Protostars and Planets V, ed. B. Reipurth, D. Jewitt, & K. Keil, 427–441

Burningham, B., Pinfield, D. J., Lucas, P. W., et al. 2010, MNRAS, 406, 1885

Burningham, B., Cardoso, C. V., Smith, L., et al. 2013, MNRAS, 433, 457

Burrows, A., Heng, K., & Nampaisarn, T. 2011, ApJ, 736, 47

Burrows, A., Hubbard, W. B., Lunine, J. I., & Liebert, J. 2001, Reviews of Modern Physics, 73, 719

Burrows, A., Marley, M., Hubbard, W. B., et al. 1997, ApJ, 491, 856

Cardoso, C. V., McCaughrean, M. J., King, R. R., et al. 2009, in American Institute of Physics Conference Series, Vol. 1094, American Institute of Physics Conference Series, ed. E. Stempels, 509–512

Chabrier, G., & Baraffe, I. 1997, A&A, 327, 1039

—. 2000, ARA&A, 38, 337

Chabrier, G., Baraffe, I., Allard, F., & Hauschildt, P. 2000, ApJ, 542, 464

Chabrier, G., Baraffe, I., & Plez, B. 1996, ApJ, 459, L91

Chiu, K., Fan, X., Leggett, S. K., et al. 2006, AJ, 131, 2722

Close, L. M., Potter, D., Brandner, W., et al. 2002a, ApJ, 566, 1095

Close, L. M., Siegler, N., Freed, M., & Biller, B. 2003, ApJ, 587, 407

Close, L. M., Siegler, N., Potter, D., Brandner, W., & Liebert, J. 2002b, ApJ, 567, L53

Close, L. M., Lenzen, R., Guirado, J. C., et al. 2005, Nature, 433, 286

Costa, E., Méndez, R. A., Jao, W.-C., et al. 2006, AJ, 132, 1234

Crepp, J. R., Johnson, J. A., Fischer, D. A., et al. 2012, ApJ, 751, 97

Cruz, K. L., Reid, I. N., Liebert, J., Kirkpatrick, J. D., & Lowrance, P. J. 2003, AJ, 126, 2421

Cruz, K. L., Reid, I. N., Kirkpatrick, J. D., et al. 2007, AJ, 133, 439

Cutri, R. M., Skrutskie, M. F., van Dyk, S., et al. 2003, 2MASS All Sky Catalog of point sources. (The IRSA 2MASS All-Sky Point Source Catalog, NASA/IPAC Infrared Science Archive. http://irsa.ipac.caltech.edu/applications/Gator/)

Dahn, C. C., Harris, H. C., Vrba, F. J., et al. 2002, AJ, 124, 1170

de Bruijne, J. H. J., Hoogerwerf, R., & de Zeeuw, P. T. 2001, A&A, 367, 111

Delfosse, X., Forveille, T., Ségransan, D., et al. 2000, A&A, 364, 217

Dieterich, S. B., Henry, T. J., Jao, W.-C., et al. 2014, AJ, 147, 94

Diolaiti, E., Bendinelli, O., Bonaccini, D., et al. 2000, A&AS, 147, 335

Dupuy, T. J., Forbrich, J., Rizzuto, A., et al. 2016, ApJ, 827, 23

Dupuy, T. J., Kratter, K. M., Kraus, A. L., et al. 2016, ApJ, 817, 80

Dupuy, T. J., & Liu, M. C. 2011, ApJ, 733, 122

—. 2012, ApJS, 201, 19

Dupuy, T. J., Liu, M. C., & Bowler, B. P. 2009a, ApJ, 706, 328

Dupuy, T. J., Liu, M. C., Bowler, B. P., et al. 2010, ApJ, 721, 1725

Dupuy, T. J., Liu, M. C., & Ireland, M. J. 2009b, ApJ, 692, 729

—. 2009c, ApJ, 699, 168

—. 2011, Research, Science and Technology of Brown Dwarfs and Exoplanets: Proceedings of an International Conference held in Shangai on Occasion of a Total Eclipse of the Sun, Shangai, China, Edited by E.L. Martin; J. Ge; W. Lin; EPJ Web of Conferences, Volume 16, id.04004, 160, 4004

—. 2014, ApJ, 790, 133

Dupuy, T. J., Liu, M. C., & Leggett, S. K. 2015a, ApJ, 803, 102

Dupuy, T. J., Liu, M. C., Leggett, S. K., et al. 2015b, ApJ, 805, 56

Duquennoy, A., & Mayor, M. 1991, A&A, 248, 485

Faherty, J. K., Beletsky, Y., Burgasser, A. J., et al. 2014, ApJ, 790, 90

Faherty, J. K., Burgasser, A. J., Bochanski, J. J., et al. 2011, AJ, 141, 71

Faherty, J. K., Burgasser, A. J., Cruz, K. L., et al. 2009, AJ, 137, 1

Faherty, J. K., Burgasser, A. J., Walter, F. M., et al. 2012, ApJ, 752, 56

Filippazzo, J. C., Rice, E. L., Faherty, J., et al. 2015, ApJ, 810, 158

Forbrich, J., Dupuy, T. J., Reid, M. J., et al. 2016, ApJ, 827, 22

Foreman-Mackey, D., Hogg, D. W., Lang, D., & Goodman, J. 2013, PASP, 125, 306

Forveille, T., Beuzit, J., Delorme, P., et al. 2005, A&A, 435, L5

Freed, M., Close, L. M., & Siegler, N. 2003, ApJ, 584, 453

Gatewood, G., & Coban, L. 2009, AJ, 137, 402

Gauza, B., Béjar, V. J. S., Pérez-Garrido, A., et al. 2015, ApJ, 804, 96

Geballe, T. R., Knapp, G. R., Leggett, S. K., et al. 2002, ApJ, 564, 466

Geyer, D. W., Harrington, R. S., & Worley, C. E. 1988, AJ, 95, 1841

Gizis, J. E., Allers, K. N., Liu, M. C., et al. 2015, ApJ, 799, 203

Gizis, J. E., Monet, D. G., Reid, I. N., Kirkpatrick, J. D., & Burgasser, A. J. 2000a, MNRAS, 311, 385

Gizis, J. E., Monet, D. G., Reid, I. N., et al. 2000b, AJ, 120, 1085

Gizis, J. E., & Reid, I. N. 2006, AJ, 131, 638

Gizis, J. E., Reid, I. N., Knapp, G. R., et al. 2003, AJ, 125, 3302

Golimowski, D. A., Leggett, S. K., Marley, M. S., et al. 2004, AJ, 127, 3516

Golimowski, D. A., Henry, T. J., Krist, J. E., et al. 2004, AJ, 128, 1733

Goodman, J., & Weare, J. 2010, Commun. Appl. Math. Comput. Sci., 5, 65

Guirado, J. C., Martí-Vidal, I., Marcaide, J. M., et al. 2006, A&A, 446, 733

Harding, L. K., Hallinan, G., Boyle, R. P., et al. 2013, ApJ, 779, 101

Harris, H. C., Dahn, C. C., & Dupuy, T. J. 2015, in Cambridge Workshop on Cool Stars, Stellar Systems, and the Sun, Vol. 18, 18th Cambridge Workshop on Cool Stars, Stellar Systems, and the Sun, ed. G. T. van Belle & H. C. Harris, 413–418

Henry, T. J., & Kirkpatrick, J. D. 1990, ApJ, 354, L29

Henry, T. J., Kirkpatrick, J. D., & Simons, D. A. 1994, AJ, 108, 1437

Henry, T. J., & McCarthy, Jr., D. W. 1993, AJ, 106, 773

Ireland, M. J., Kraus, A., Martinache, F., Lloyd, J. P., & Tuthill, P. G. 2008, ApJ, 678, 463

Ireland, M. J., & Kraus, A. L. 2008, ApJ, 678, L59

Joergens, V., Müller, A., & Reffert, S. 2010, A&A, 521, A24

Kendall, T. R., Delfosse, X., Martín, E. L., & Forveille, T. 2004, A&A, 416, L17

King, R. R., McCaughrean, M. J., Homeier, D., et al. 2010, A&A, 510, A99

Kirkpatrick, J. D., Dahn, C. C., Monet, D. G., et al. 2001, AJ, 121, 3235

Kirkpatrick, J. D., Henry, T. J., & McCarthy, Jr., D. W. 1991, ApJS, 77, 417

Kirkpatrick, J. D., Henry, T. J., & Simons, D. A. 1995, AJ, 109, 797

Kirkpatrick, J. D., Reid, I. N., Liebert, J., et al. 1999, ApJ, 519, 802

—. 2000, AJ, 120, 447

Kirkpatrick, J. D., Cruz, K. L., Barman, T. S., et al. 2008, ApJ, 689, 1295

Kirkpatrick, J. D., Gelino, C. R., Cushing, M. C., et al. 2012, ApJ, 753, 156

Knapp, G. R., Leggett, S. K., Fan, X., et al. 2004, AJ, 127, 3553

Köhler, R., Ratzka, T., & Leinert, C. 2012, A&A, 541, A29

Konopacky, Q. M., Ghez, A. M., Barman, T. S., et al. 2010, ApJ, 711, 1087

Konopacky, Q. M., Ghez, A. M., Fabrycky, D. C., et al. 2012, ApJ, 750, 79

Koren, S. C., Blake, C. H., Dahn, C. C., & Harris, H. C. 2016, AJ, 151, 57

Kozhurina-Platais, V., Borncamp, D., Anderson, J., Grogin, N., & Hack, M. 2015, ACS/WFC Revised Geometric Distortion for DrizzlePac, Tech. rep., Space Telescope Science Institute

Kraus, A. L., Shkolnik, E. L., Allers, K. N., & Liu, M. C. 2014, AJ, 147, 146

Kraus, A. L., White, R. J., & Hillenbrand, L. A. 2005, ApJ, 633, 452

—. 2006, ApJ, 649, 306

Krist, J. E., Hook, R. N., & Stoehr, F. 2011, in Society of Photo-Optical Instrumentation Engineers (SPIE) Conference Series, Vol. 8127, Society of Photo-Optical Instrumentation Engineers (SPIE) Conference Series, 0

Lane, B. F., Zapatero Osorio, M. R., Britton, M. C., Martín, E. L., & Kulkarni, S. R. 2001, ApJ, 560, 390

Law, N. M., Hodgkin, S. T., & Mackay, C. D. 2006, MNRAS, 368, 1917

Leggett, S. K., Geballe, T. R., Fan, X., et al. 2000, ApJ, 536, L35

Leggett, S. K., Golimowski, D. A., Fan, X., et al. 2002, ApJ, 564, 452

Leinert, C., Allard, F., Richichi, A., & Hauschildt, P. H. 2000, A&A, 353, 691

Leinert, C., Jahreiß, H., Woitas, J., et al. 2001, A&A, 367, 183

Leinert, C., Weitzel, N., Richichi, A., Eckart, A., & Tacconi-Garman, L. E. 1994, A&A, 291, L47

Lépine, S., Thorstensen, J. R., Shara, M. M., & Rich, R. M. 2009, AJ, 137, 4109

Lindegren, L., Lammers, U., Bastian, U., et al. 2016, A&A, 595, A4

Liu, M. C., Dupuy, T. J., & Allers, K. N. 2013a, Astronomische Nachrichten, 334, 85

Liu, M. C., Dupuy, T. J., & Allers, K. N. 2016, ApJ, 833, 96

Liu, M. C., Dupuy, T. J., & Ireland, M. J. 2008, ApJ, 689, 436

Liu, M. C., Dupuy, T. J., & Leggett, S. K. 2010, ApJ, 722, 311

Liu, M. C., & Leggett, S. K. 2005, ApJ, 634, 616

Liu, M. C., Leggett, S. K., Golimowski, D. A., et al. 2006, ApJ, 647, 1393

Liu, M. C., Delorme, P., Dupuy, T. J., et al. 2011, ApJ, 740, 108

Liu, M. C., Magnier, E. A., Deacon, N. R., et al. 2013b, ApJ, 777, L20

Lodders, K. 1999, ApJ, 519, 793

Lodieu, N., Zapatero Osorio, M. R., Rebolo, R., et al. 2015, A&A, 581, A73

Looper, D. L., Gelino, C. R., Burgasser, A. J., & Kirkpatrick, J. D. 2008, ApJ, 685, 1183

Looper, D. L., Kirkpatrick, J. D., & Burgasser, A. J. 2007, AJ, 134, 1162

Lucy, L. B. 2014, A&A, 563, A126

MacDonald, J., & Mullan, D. J. 2009, ApJ, 700, 387

Markwardt, C. B. 2009, in Astronomical Society of the Pacific Conference Series, ed. D. A. Bohlender, D. Durand, & P. Dowler, Vol. 411, 251

Marley, M. S., & Robinson, T. D. 2015, ARA&A, 53, 279

Marocco, F., Andrei, A. H., Smart, R. L., et al. 2013, AJ, 146, 161

Martín, E. L., Brandner, W., & Basri, G. 1999, Science, 283, 1718

Martín, E. L., Brandner, W., Bouy, H., et al. 2006, A&A, 456, 253

Martín, E. L., Koresko, C. D., Kulkarni, S. R., Lane, B. F., & Wizinowich, P. L. 2000, ApJ, 529, L37

McCaughrean, M. J., Close, L. M., Scholz, R.-D., et al. 2004, A&A, 413, 1029

Monet, D. G., Dahn, C. C., Vrba, F. J., et al. 1992, AJ, 103, 638

Montagnier, G., Ségransan, D., Beuzit, J., et al. 2006, A&A, 460, L19

Oppenheimer, B. R., Kulkarni, S. R., Matthews, K., & Nakajima, T. 1995, Science, 270, 1478

Osten, R. A., Phan-Bao, N., Hawley, S. L., Reid, I. N., & Ojha, R. 2009, ApJ, 700, 1750

Pavlenko, Y., Zapatero Osorio, M. R., & Rebolo, R. 2000, A&A, 355, 245

Phan-Bao, N., Forveille, T., Martín, E. L., & Delfosse, X. 2006, ApJ, 645, L153

Phan-Bao, N., Martín, E. L., Reylé, C., Forveille, T., & Lim, J. 2005, A&A, 439, L19

Phan-Bao, N., Osten, R. A., Lim, J., Martín, E. L., & Ho, P. T. P. 2007, ApJ, 658, 553

Potter, D., Martín, E. L., Cushing, M. C., et al. 2002, ApJ, 567, L133

Press, W. H., Teukolsky, S. A., Vetterling, W. T., & Flannery, B. P. 1992, Numerical Recipes in C: The Art of Scientific Computing (Cambridge: Cambridge University Press, 2nd ed.)

Puget, P., Stadler, E., Doyon, R., et al. 2004, in Society of Photo-Optical Instrumentation Engineers (SPIE) Conference Series, ed. A. F. M. Moorwood & M. Iye, Vol. 5492, 978

Radigan, J., Jayawardhana, R., Lafrenière, D., et al. 2013, ApJ, 778, 36

Raghavan, D., McAlister, H. A., Henry, T. J., et al. 2010, ApJS, 190, 1

Rajpurohit, A. S., Reylé, C., Schultheis, M., et al. 2012, A&A, 545, A85

Rebolo, R., Martin, E. L., & Magazzu, A. 1992, ApJ, 389, L83

Reid, I. N., Cruz, K. L., Burgasser, A. J., & Liu, M. C. 2008a, AJ, 135, 580

Reid, I. N., Cruz, K. L., Kirkpatrick, J. D., et al. 2008b, AJ, 136, 1290

Reid, I. N., Gizis, J. E., Kirkpatrick, J. D., & Koerner, D. W. 2001, AJ, 121, 489

Reid, I. N., Lewitus, E., Allen, P. R., Cruz, K. L., & Burgasser, A. J. 2006a, AJ, 132, 891

Reid, I. N., Lewitus, E., Burgasser, A. J., & Cruz, K. L. 2006b, ApJ, 639, 1114

Reiners, A., & Basri, G. 2009, ApJ, 705, 1416

Robin, A. C., Reylé, C., Derrière, S., & Picaud, S. 2003, A&A, 409, 523

Sahlmann, J., Lazorenko, P. F., Ségransan, D., et al. 2015a, A&A, 577, A15

Sahlmann, J., Burgasser, A. J., Martín, E. L., et al. 2015b, A&A, 579, A61

Santos, N. C., Melo, C., James, D. J., et al. 2008, A&A, 480, 889

Saumon, D., Bergeron, P., Lunine, J. I., Hubbard, W. B., & Burrows, A. 1994, ApJ, 424, 333

Saumon, D., & Marley, M. S. 2008, ApJ, 689, 1327

Schmidt, S. J., Cruz, K. L., Bongiorno, B. J., Liebert, J., & Reid, I. N. 2007, AJ, 133, 2258

Scholz, R.-D., McCaughrean, M. J., Lodieu, N., & Kuhlbrodt, B. 2003, A&A, 398, L29

Seifahrt, A., Röll, T., Neuhäuser, R., et al. 2008, A&A, 484, 429

Service, M., Lu, J. R., Campbell, R., et al. 2016, PASP, 128, 095004

Siegler, N., Close, L. M., Burgasser, A. J., et al. 2007, AJ, 133, 2320

Siegler, N., Close, L. M., Cruz, K. L., Martín, E. L., & Reid, I. N. 2005, ApJ, 621, 1023

Siegler, N., Close, L. M., Mamajek, E. E., & Freed, M. 2003, ApJ, 598, 1265

Simon, M., Bender, C., & Prato, L. 2006, ApJ, 644, 1183

Stamatellos, D., & Whitworth, A. P. 2009, MNRAS, 392, 413

Stassun, K. G., Mathieu, R. D., & Valenti, J. A. 2006, Nature, 440, 311

Stephens, D. C., Leggett, S. K., Cushing, M. C., et al. 2009, ApJ, 702, 154

Stone, J. M., Skemer, A. J., Kratter, K. M., et al. 2016, ApJ, 818, L12

Stumpf, M. B., Brandner, W., & Henning, T. 2005, in Protostars and Planets V Posters, 8571

Stumpf, M. B., Brandner, W., Henning, T., et al. 2008, arxiv/0811.0556, arXiv:0811.0556

Stumpf, M. B., Geißler, K., Bouy, H., et al. 2011, A&A, 525, A123

Thorstensen, J. R., & Kirkpatrick, J. D. 2003, PASP, 115, 1207

Tinney, C. G., Burgasser, A. J., & Kirkpatrick, J. D. 2003, AJ, 126, 975

Torres, G. 1999, PASP, 111, 169

Tremblin, P., Amundsen, D. S., Chabrier, G., et al. 2016, ApJ, 817, L19

Vrba, F. J., Henden, A. A., Luginbuhl, C. B., et al. 2004, AJ, 127, 2948

Weinberger, A. J., Boss, A. P., Keiser, S. A., et al. 2016, AJ, 152, 24

West, A. A., Hawley, S. L., Bochanski, J. J., et al. 2008, AJ, 135, 785

Wilson, J. C., Miller, N. A., Gizis, J. E., et al. 2003, in IAU Symposium, Vol. 211, Brown Dwarfs, ed. E. Martín, 197

Yelda, S., Lu, J. R., Ghez, A. M., et al. 2010, ApJ, 725, 331

Zapatero Osorio, M. R., Lane, B. F., Pavlenko, Y., et al. 2004, ApJ, 615, 958

Zapatero Osorio, M. R., Martín, E. L., Béjar, V. J. S., et al. 2007, ApJ, 666, 1205

This preprint was prepared with the AAS LaTeX macros v5.2.

A. Empirical Relations with Absolute Magnitude

While there are many useful empirical relations in the literature based on spectral type, many tight binary components do not have directly measured spectra. However, we do have accurate near-infrared absolute magnitudes for all of our binaries from parallactic distances and resolved photometry. We will soon have many more late-M and L dwarfs with distances from *Gaia* that will not immediately have spectra available. Therefore, we have derived empirical relations of various useful quantities with respect to absolute magnitude using the existing sample of ultracool dwarfs with parallaxes. Because J- and H-band absolute magnitudes do not change monotonically through the L/T transition (e.g., Dupuy & Liu 2012), we primarily derive these relations using K-band absolute magnitudes on the 2MASS and MKO photometric systems. We also examined some relations as a function of H-band absolute magnitude for $M_H < 13.3$ mag objects for which the relations have lower scatter in luminosity and spectral type and color changes monotonically.

A.1. 2MASS-to-MKO Photometric Conversion

In order to report complete photometry across both MKO and 2MASS photometric systems for our sample binaries, we compute photometric system conversions based solely on K-band absolute magnitude. We used our compilation of ultracool dwarf parallaxes available online,[12] selecting only single objects with a published spectrum, a parallax error of <15%, and a "null" object flag, meaning that there is nothing unusual about the object. We use synthesized 2MASS/MKO photometric conversions from Dupuy & Liu (2012) for each of the 46 objects in each of J, H, and K bands. For J and H bands, we found that a third-order polynomial provided a good fit to the data. The K-band conversion undergoes a steep jump between $M_K \approx 13$–14 mag that cannot be well approximated by a single polynomial. Therefore, we computed a three-part piecewise linear fit to the K-band conversion as a function of M_K. In addition to these relations as a function of M_K, we also computed an H-band conversion as a function of M_H. The polynomial coefficients are given in Table 68 and the fits are displayed in Figure 20. The typical rms about the fits ranges from 0.003 mag for H-band to 0.015 mag for J band.

A.2. Broadband K to Narrowband CFHT/WIRCam $K_{\rm H2}$ Conversion

Determining mass ratios from photocenter motion requires knowing the flux ratios in the imaging bandpass. Our absolute astrometry for the brightest targets observed with CFHT/WIRCam was obtained in a narrow K-band filter, $K_{\rm H2}$, centered on 2.122 μm with a bandwidth of 0.032 μm. We do not have resolved photometry for these binaries in this specialized filter, so we must synthesize it from our broadband K photometry in order to determine the flux ratios of our binaries in

[12] http://www.as.utexas.edu/~tdupuy/plx

our CFHT imaging.

We used the same sample of objects selected from our online parallax compilation as described in the previous section. We used the filter curve provided by CFHT to synthesize $K_{\rm H2}$ photometry,[13] and we assume that the difference between this scan done in the lab and the transmission at colder operational temperatures is negligible for our purposes. We computed $K_{\rm H2} - K$ and $K_{\rm H2} - K_S$ colors for these objects and found a smooth relation for objects with $M_K < 13.1$ mag, corresponding roughly to spectral types <L9. (The smooth relations break down for later types as the $K_{\rm H2}$ filter samples part of the K-band flux peak of T dwarfs while their broadband K flux plummets.) We fit a second-order polynomial as a function of M_K for 25 objects. The coefficients are given in Table 68 and the fits are displayed in Figure 20. The rms about these fits were 0.025 mag for K and 0.021 mag for K_S.

A.3. Bolometric Luminosity

Determining the component luminosities using our resolved photometry is a critical part of our model tests. We have used the large sample of luminosities from Filippazzo et al. (2015) to derive polynomial relations between luminosity and absolute magnitude. We used only objects with parallactic distances, nominal ages $\gtrsim$0.5 Gyr, and normal properties (i.e., no subdwarfs, young objects, or objects dubbed peculiar in their spectral type). We supplemented the observed magnitudes reported by Filippazzo et al. (2015) by applying our 2MASS/MKO conversions from above. For any object with either a 2MASS or MKO measurement, we derived the complementary magnitude using the K-band absolute magnitude. For objects with both 2MASS and MKO measurements, we used the more precise magnitude to derive the complementary magnitude, supplanting the directly observed value. This results in a sample of 126 normal field objects with luminosities and K-band absolute magnitudes. (Since our 2MASS/MKO relations are only valid between $M_K = 9.1$–17.0 mag, there are a few objects with only 2MASS or MKO photometry that changes the input sample slightly between 2MASS and MKO.) A subset of 76 of these objects had magnitudes of $M_H < 13.3$ mag, which we used in our H-band relations.

We fit luminosity as a function of K-band absolute magnitude with a fifth-order polynomial, since there was clear structure in the residuals using only a third order polynomial. For the more limited H-band magnitude range, a third-order polynomial was sufficient. In K-band, it was visually apparent that the scatter at brighter magnitudes was less than at fainter magnitudes. The fact that the nominal errors on the magnitudes and luminosites are not significantly larger for the fainter objects implies that this increased scatter is due to either unquantified systematic errors in the luminosities of the lower luminosity objects or real astrophysical scatter in the relationship between K-band absolute magnitude and luminosity. Regardless, we quantify this effect by separately

[13] `http://www.cfht.hawaii.edu/Instruments/Filters/curves/cfh8304.dat`

computing the rms scatter at the bright end ($M_K \leq 13.0$ mag; rms of 0.04 dex for 90 objects) and faint end (rms of 0.07 dex for 36 objects). The coefficients for all relations are given in Table 68, and the fits and residuals are displayed in Figure 21.

B. Discussion of Individual Objects

B.1. LP 349-25AB (M7+M8)

In our previous work, we used a parallax of 75.8 ± 1.6 mas from Gatewood & Coban (2009) to compute luminosities and a total mass that gave a Lyon Dusty model-derived age of 127^{+21}_{-17} Myr (Dupuy et al. 2010). Our new more accurate parallax of 69.2 ± 0.9 mas from CFHT results in somewhat higher masses and luminosities but still the youngest model-derived age of any object in our sample, 271^{+22}_{-29} Myr (BHAC). We now have directly measured individual masses, and the ages derived from the component masses and luminosities are coeval within the uncertainties ($\Delta t = 50 \pm 50$ Myr). Our measured mass ratio ($q = 0.941^{+0.029}_{-0.030}$) is consistent within the uncertainties with the model-derived mass ratio from our total-mass analysis ($0.88^{+0.03}_{-0.04}$). Such a young age implies that LP 349-25AB is a pair of pre–main-sequence stars with masses of $85 \pm 4\,M_{\rm Jup}$ and $80 \pm 3\,M_{\rm Jup}$. At a distance of only $14.45^{+0.18}_{-0.19}$ pc, this is the nearest pre–main-sequence system containing very low-mass stars ($<0.1\,M_\odot$), with the next closest being LSPM J1314+1320AB (M7+M7; Dupuy et al. 2016) at 17.25 pc.

According to the BHAC tracks, a $0.075\,M_\odot$ object comparable to LP 349-25B requires ≈130 Myr to deplete 99.9% of its initial supply lithium, while $0.075\,M_\odot$ object comparable to LP 349-25B would need ≈110 Myr. Therefore, BHAC models predict both components are fully depleted in lithium, in agreement with the nondetection of Li I absorption (<0.5 Å) reported by Reiners & Basri (2009). LP 349-25AB therefore provides a critical test of the lithium depletion boundary in low-mass stars and brown dwarfs at young ages that is used to age-date young clusters at ∼20–200 Myr (e.g., Bildsten et al. 1997; Binks & Jeffries 2014; Kraus et al. 2014). It joins LSPM J1314+1320AB as the only other pre–main-sequence system where objects of known mass empirically constrain the model-predicted lithium depletion boundary (Dupuy et al. 2016). Like LSPM J1314+1320AB, LP 349-25AB is a luminous radio source (Phan-Bao et al. 2007; Osten et al. 2009), which makes it a rare benchmark for characterizing radio emission in ultracool dwarfs. High-precision VLBI astrometry may be possible for LP 349-25AB, like Forbrich et al. (2016) recently showed for LSPM J1314+1320AB, which would refine the individual mass precision and enable even stronger constraints on models.

LP 349-25AB has not previously been reported as having spectral signatures of low surface gravity. However, examination of our own integrated light SpeX SXD spectrum ($R \approx 1200$) indicates that it has a classification of M8 INT-G on the Allers & Liu (2013) system. Given the gap in known young associations between the ages of the AB Doradus (∼150 Myr) and Ursa Majoris (∼400 Myr) groups, LP 349-25AB (250–300 Myr) provides unique evidence that spectral signatures of low gravity in the infrared can persist to at least 250 Myr for late-M dwarfs. There is only one other system of ultracool dwarfs with spectral signatures of youth that have directly measured masses, LSPM J1314+1320AB ($92.8 \pm 0.6\,M_{\rm Jup}$ and $91.7 \pm 1.0\,M_{\rm Jup}$; Dupuy et al. 2016). Despite LSPM J1314+1320AB having more marginal signatures of low gravity, its components actually have lower model-derived surface gravities ($\log(g) \simeq 4.8$ dex) than the older and somewhat less massive LP 349-25AB (5.1 dex). This implies that while the current gravity classification system does indeed pick out young objects ($\lesssim$300 Myr), there is a limit to the granularity by which relative strengths of spectral features can be used to distinguish surface gravity and thus age.

B.2. LP 415-20AB (M6+M8)

LP 415-20AB has the largest total mass in our sample ($248^{+26}_{-29}\,M_{\rm Jup}$) and also the largest fractional uncertainty in its mass ($^{+10}_{-12}$%). Given the component spectral types of M6.0 ± 1.0 and M8.0 ± 0.5, and the integrated-light optical type of M7.5 found by Gizis et al. (2000b), a mass as large as $250\,M_{\rm Jup}$ would be quite puzzling. The implied component masses would be ≈120–130 $M_{\rm Jup}$, and objects that massive are not known at such late spectral types (e.g., L 726-8AB and L 789-6ABC are both M5.5 in integrated light; Delfosse et al. 2000). The size of our mass uncertainty suggests that LP 415-20AB could simply be a $\gtrsim 2\sigma$ outlier, but we also consider the possibility that it is an unresolved triple system. Our directly measured mass ratio of $0.59^{+0.10}_{-0.12}$ is rather far from unity despite a modest luminosity ratio of $\Delta \log(L_{\rm bol}/L_{\odot}) = 0.25^{+0.04}_{-0.03}$ dex. This is also consistent with higher order multiplicity, but the mass ratio uncertainty is too large to make a definitive statement.

In our total-mass analysis, rejection sampling eschewed masses at the high end of the input distribution, resulting in $M_{\rm tot} = 201^{+4}_{-3}\,M_{\rm Jup}$, 1.7σ lower than our measurement (Table 44). This is because the models do not allow the higher masses to correspond to the luminosity we measure for LP 415-20A (Figure 11). The individual-mass analysis confirms that this mass discrepancy is found to be due entirely to the primary. The mass of LP 415-20A after rejection sampling is $109.8^{+3.1}_{-2.9}\,M_{\rm Jup}$, 2.6σ lower than the input $156^{+17}_{-18}\,M_{\rm Jup}$, whereas the input and output secondary masses are essentially unchanged. Therefore, both sets of analyses suggest that if our unusually high mass is due to an unresolved component of LP 415-20A, its mass is expected to be $\approx 50\,M_{\rm Jup}$ (assuming that the unresolved component contributes negligibly to the luminosity).

As a test, we also performed our analysis for a hypothetical scenario where LP 415-20A is an equal-mass, equal-flux binary with each component having $M = 78^{+8}_{-9}\,M_{\rm Jup}$ and $\log(L_{\rm bol}/L_{\odot}) = -3.32 \pm 0.03$ dex. This scenario is the simplest to implement because we do not need to invoke a mass–luminosity relation to apportion flux between the hypothetical components. We found reasonable agreement with models, though the resulting LP 415-20A component masses after rejection sampling preferred a somewhat higher mass of $92.3^{+2.2}_{-1.6}\,M_{\rm Jup}$ (Table 45). This is consistent with the idea that if LP 415-20A is an unresolved binary, its components are somewhat unequal in mass. However, we reiterate that this discrepancy could also simply be a statistical outlier, e.g., due to the somewhat uncertain parallax ($\sigma_\pi/\pi = 3\%$) that dominates the mass uncertainty. As one of the brighter targets in our sample, LP 415-20AB should be well detected by *Gaia*, which would resolve the current mass discrepancy.

In all cases above, the masses and luminosities of the components of LP 415-20 are consistent with being coeval stars, most likely on the main sequence but also consistent with ages of a few hundred Myr (the BHAC model-derived age for LP 415-20B is $5.0^{+1.9}_{-4.7}$ Gyr). Thus, from our model-derived age distribution alone we do not rule out the possibility that LP 415-20 could be a member of the Hyades (750 ± 150 Myr; Brandt & Huang 2015), as was originally noted by Bryja et al. (1992). We can however use the kinematic information, both from our own astrometry and the literature, to reassess its potential membership. We have projected the space velocity of the Hyades, $(U, V, W) = (42.3, -19.1, -1.5)\,\mathrm{km\,s^{-1}}$ (de Bruijne et al. 2001), into proper motion and radial velocity using our RA, Dec, and parallax of LP 415-20. We simulate the $0.3\,\mathrm{km\,s^{-1}}$ velocity dispersion of the Hyades and our parallax uncertainty in a Monte Carlo fashion, finding $\mu_{\alpha^*} = 132.2 \pm 4.4\,\mathrm{mas\,yr^{-1}}$, $\mu_\delta = -42.8 \pm 2.1\,\mathrm{mas\,yr^{-1}}$, and $v_{\mathrm{rad}} = 38.8 \pm 0.3\,\mathrm{km\,s^{-1}}$. In comparison, our measured absolute proper motion is $126.1\pm0.7\,\mathrm{mas\,yr^{-1}}$ and $-38.2\pm0.8\,\mathrm{mas\,yr^{-1}}$, which is only $8.5\pm3.4\,\mathrm{mas\,yr^{-1}}$ ($1.6\pm 0.5\,\mathrm{km\,s^{-1}}$) away from the predicted proper motion assuming Hyades kinematics. Thus, under these assumptions, the motion of LP 415-20AB appears fairly inconsistent (2.5σ) with membership. The mean radial velocity of the two components from Konopacky et al. (2010) is $40.8 \pm 1.4\,\mathrm{km\,s^{-1}}$, only $2.0 \pm 1.4\,\mathrm{km\,s^{-1}}$ different from the predicted Hyades value. The full 3-d distance in UVW between the proper motion and RV measurements and the predicted Hyades values is $2.7 \pm 1.1\,\mathrm{km\,s^{-1}}$, indicating that it is only a marginal candidate for membership in the Hyades. However, if the velocity dispersion of the Hyades were larger than currently thought, e.g., $1\,\mathrm{km\,s^{-1}}$ as is seen for other young clusters, then LP 415-20AB would be a stronger candidate member.

B.3. SDSS J0423−0414AB (L6.5+T2)

SDSS J0423−0414AB has the lowest total mass in our sample ($83 \pm 3\,M_{\mathrm{Jup}}$), and it also has a well determined mass ratio from our CFHT data (0.62 ± 0.04), yielding individual masses of $51.6^{+2.3}_{-2.5}\,M_{\mathrm{Jup}}$ and $31.8^{+1.5}_{-1.6}\,M_{\mathrm{Jup}}$. Our total-mass analysis gives an SM08 model-derived mass ratio of $0.65^{+0.05}_{-0.06}$, in good agreement with our measurement, and a system age of $0.81^{+0.07}_{-0.09}$ Gyr. In contrast, Lyon Cond models give a mass ratio of 0.80 ± 0.05 (2.8σ discrepant with our measurement) but a very similar age ($0.80^{+0.07}_{-0.08}$ Gyr). Our measured mass ratio of 0.62 ± 0.04 is much lower than previous estimates, e.g., 0.8–1.0 from Burgasser et al. (2005) and 0.80 ± 0.03 from Liu et al. (2010).

The case of SDSS J0423−0414AB is similar to SDSS J1052+4422AB (L6.5 $\pm$ 1.5+T1.5 $\pm$ 1.0, SM08 age of $1.04^{+0.14}_{-0.15}$ Gyr), with a nearly identical primary mass but with mass and luminosity ratios further from unity. Like we find for SDSS J0423−0414AB, Dupuy et al. (2015b) found a similar discrepancy between the measured and the Lyon model-derived mass ratios for SDSS J1052+4422AB but agreement with SM08 models. Using the individual mass and luminosity of each component independently, in both cases the Lyon models predict a younger age for the secondary as compared to the primary, $\Delta t = -0.44 \pm 0.15$ Gyr for SDSS J0423−0414AB and $-0.35^{+0.25}_{-0.22}$ Gyr for SDSS J1052+4422AB. This is caused by the secondary being more luminous than expected according to Lyon models, resulting in a younger model-derived age. In contrast, SM08 models give a higher luminosity for the secondary because they predict that luminosity does not fade as quickly during and immediately following the transition from cloudy to cloud-free atmospheres, which they prescribe ad hoc to occur as temperature drops from 1400 K to 1200 K. The components of SDSS J0423−0414AB have SM08 model-derived temperatures straddling this transition, 1430^{+30}_{-40} K and 1200 ± 40 K.

Both components of SDSS J0423−0414AB have masses so low that they should never significantly deplete their initial supply of lithium ($\lesssim 55\,M_{\rm Jup}$; Chabrier & Baraffe 2000). However, the monatomic lithium that is readily probed by the Li I doublet at 6708 Å can be removed from the atmosphere chemically. Models from Lodders (1999) indicate that monatomic lithium ceases to be the dominant lithium-bearing species below $T_{\rm eff} \approx 1500$ K at pressures near the photosphere (∼1 bar). Detailed spectral synthesis modeling shows that Li I absorption can in fact persist to much lower temperatures (e.g., Pavlenko et al. 2000; Allard et al. 2001), and indeed it has been detected in objects as cool as WISE J1049−5319B (T0; Faherty et al. 2014; Lodieu et al. 2015). Kirkpatrick et al. (2008) reported strong Li I absorption (EW = 11 Å) in the integrated-light spectrum of SDSS J0423−0414AB. This is consistent with our Lyon Cond model analysis that predicts SDSS J0423−0414A should still possess all or most of its initial lithium, $\log({\rm Li/Li_{init}}) = -0.04^{+0.04}_{-0.20}$ dex, along with the previous detection of lithium in even cooler objects than SDSS J0423−0414A.

B.4. 2MASS J0700+3157AB (L3+L6.5)

Our measured mass ratio of $q = 1.08 \pm 0.05$ indicates that 2MASS J0700+3157B is in fact slightly more massive than 2MASS J0700+3157A, despite the fact that it is 0.50 ± 0.06 dex less luminous. Combined with our total mass of $141^{+4}_{-5}\,M_{\rm Jup}$, we find individual masses for 2MASS J0700+3157A and 2MASS J0700+3157B of $68.0 \pm 2.6\,M_{\rm Jup}$ and $73.0^{+2.9}_{-3.0}\,M_{\rm Jup}$, respectively. These masses and luminosities result in very different SM08 model-derived ages, $0.76^{+0.09}_{-0.14}$ Gyr for 2MASS J0700+3157A and $7.8^{+2.8}_{-5.2}$ Gyr for 2MASS J0700+3157B, or in other words, a difference of $\Delta \log t = 1.00^{+0.29}_{-0.20}$ dex.

The most natural explanation is that 2MASS J0700+3157B is an unresolved binary itself composed of two brown dwarfs. We performed a simple test, dividing the mass and luminosity of 2MASS J0700+3157B in two ($36.7 \pm 1.5\,M_{\rm Jup}$, -4.75 ± 0.04 dex) and repeating our model analysis. In this hypothetical scenario, we found model-derived ages that agreed better between 2MASS J0700+3157A and 2MASS J0700+3157B ($\Delta \log t = 0.18^{+0.09}_{-0.07}$ dex for SM08, $-0.09^{+0.09}_{-0.08}$ dex for Cond).

Interestingly, the total mass of 2MASS J0700+3157AB is not high enough to betray its unresolved higher-order multiplicity without additional mass-ratio information. When we performed our total-mass analysis, evolutionary models are able to self-consistently apportion the total mass between the two components at their appropriate luminosities at a single coeval age ($1.9^{+0.6}_{-0.7}$ Gyr for SM08, $2.1^{+0.4}_{-0.6}$ Gyr for Cond). But the model-derived mass ratio, e.g., $0.86^{0.04}_{-0.03}$ from Cond, is 3.4σ lower than we measure. This case highlights the important role directly measured mass ratios play in the substellar regime, where a given mass does not correspond to a particular luminosity or spectral type unlike for main-sequence stars.

Thorstensen & Kirkpatrick (2003) reported a lack of Li I absorption in the integrated-light spectrum of 2MASS J0700+3157AB (EW < 0.3 Å). This is consistent with the prediction from Lyon models that the $68.0\pm2.6\,M_{\rm Jup}$ primary should deplete 99.9% of its lithium within ≈200 Myr. Given the unknown nature of the unresolved secondary's individual components, it is not clear whether or not they should cause lithium absorption to the integrated-light spectrum. When present, lithium is routinely detected at EW ∼ 10 Å in late-L dwarfs, so it seems plausible that if one of the unresolved components of 2MASS J0700+3157B were lithium-bearing it would have been detectable even when diluted by up to a factor of ∼20 in flux given typical detection limits of EW ∼ 0.5 Å. The lack of a Li I detection therefore hints at two possible scenarios for the unresolved components. (1) A lithium-depleted higher mass object is paired with a lower mass object that either has lithium but is too diluted in flux or has lithium in molecular form only (LiCl, LiOH) because it is very cool. (2) 2MASS J0700+3157B is composed of two cool, chemically depleted objects. In the equal-flux, equal-mass scenario, the absolute magnitudes of the components would be $M_J = 15.06 \pm 0.04$ mag and $M_K = 13.44 \pm 0.04$ mag (MKO), roughly consistent with the faint end of field objects with spectral type L7–T0 (see Table 15 of Dupuy & Liu 2012). This is the same range of spectral type over which lithium becomes undetectable in field objects, with later-type objects being more likely to be chemically depleted in lithium. Later-type objects would also display some methane absorption, and this could be detectable in the spectrum of 2MASS J0700+3157B even if it were somewhat diluted by an earlier type component. No evidence of methane is seen in the integrated light spectrum of 2MASS J0700+3157 (see Figure 13 of Dupuy & Liu 2012), so resolved spectroscopy with AO or spectroastrometry will be needed to further examine the possible presence of an unresolved methane-bearing component.

2MASS J0700+3157 was originally discovered by Thorstensen & Kirkpatrick (2003) as an unresolved single L3.5 dwarf displaying parallax and proper motion during the course of an astrometry program targeting cataclysmic variables. Therefore, unlike most other known ultracool dwarfs, the discovery of 2MASS J0700+3157 did not involve a traditional magnitude-selected sample, which would have been subject to Malmquist bias favoring the discovery of such high-order multiples. However, our own dynamical-mass sample is more complete for the most massive systems as they orbit faster at a given semimajor axis ($P \propto {M_{\rm tot}}^{-1/2}$), and our orbit determinations are mostly limited by having sufficient time baseline. Therefore, our dynamical-mass sample is slightly biased toward more massive systems. As example of the potential amplitude of such bias, the period we measure for 2MASS J0700+3157AB is 23.9 ± 0.5 yr, but if this system contained only $\frac{2}{3}$ of the mass the period would have been 29.3 yr.

B.5. LHS 1901AB (M7+M7)

In our previous work, we used a parallax of 77.8 ± 3.0 mas from Lépine et al. (2009) to compute a total mass of $203^{+26}_{-22}\,M_{\rm Jup}$ (Dupuy et al. 2010). Our new more accurate parallax from CFHT (76.4 ± 1.1 mas) and updated orbit determination results in a consistent but more precise mass of $213^{+9}_{-10}\,M_{\rm Jup}$. We also now have directly measured individual masses of $113 \pm 8\,M_{\rm Jup}$ and $99 \pm 7\,M_{\rm Jup}$, based on our mass ratio of $0.87^{+0.09}_{-0.11}$. In our total-mass analysis, the BHAC model-derived mass ratio is somewhat higher but consistent within the errors ($0.97^{+0.03}_{-0.04}$), as expected given that the luminosity ratio is near unity ($\Delta\log(L_{\rm bol}) = 0.04 \pm 0.03$ dex). Given our measured masses and luminosities, LHS 1901AB is consistent with being a main-sequence stellar binary, with a correspondingly unconstrained age (BHAC models only give a 3σ lower limit of >0.3 Gyr from our total mass analysis). As noted by Dupuy et al. (2010), this system is likely to be old given that it is lacking Hα emission, which is unusual for late-M dwarfs (e.g., West et al. 2008). Finally, we note that in our latest CFHT imaging from 2016 that we do not use here, LHS 1901AB has become blended with a background source that had previously been well separated, making these images unusable for absolute astrometry.

B.6. 2MASS J0746+2000AB (L0+L1.5)

The masses of 2MASS J0746+2000A ($82.4^{+1.4}_{-1.5}\,M_{\rm Jup}$) and 2MASS J0746+2000B ($78.4 \pm 1.4\,M_{\rm Jup}$) have the highest fractional precision (2%) of any individual masses in our sample. Given our determination of the substellar boundary of $\approx 70\,M_{\rm Jup}$, the masses indicate that this binary is pair of stars and that neither is a brown dwarf, in contrast to the analysis of Bouy et al. (2004) but in agreement with Gizis & Reid (2006). Our measured mass ratio of $0.952^{+0.026}_{-0.027}$ agrees well with the BHAC model-derived mass ratio from our total mass analysis ($0.957^{+0.012}_{-0.010}$), indicating that our masses and luminosities follow BHAC isochrones well. However, because the components of 2MASS J0746+2000AB are both main-sequence stars, the age is essentially unconstrained by models, which only give 3σ lower limits of >0.9 Gyr for 2MASS J0746+2000A and >1.0 Gyr for 2MASS J0746+2000B.

One of the components of 2MASS J0746+2000AB is a radio emitter with a rotation period of 2.0720 ± 0.0018 hr (Berger et al. 2009). In addition, Harding et al. (2013) report optical variability in integrated light with a period of 3.32 ± 0.15 hr. Unfortunately, it is not known which component corresponds to which period. Konopacky et al. (2012) report $v \sin i_\star = 19 \pm 2\,{\rm km\,s^{-1}}$ and $33 \pm 3\,{\rm km\,s^{-1}}$ for the primary and secondary components, respectively, suggesting that the secondary may be radio emitter. We consider this possibility (Case I) and the alternative (Case II) and compare the implied stellar radii from combining the rotation periods with projected rotational velocities to the radii predicted from evolutionary models. In Case I, we compute minimum radii of the primary and secondary of $R \sin i_\star = 0.50 \pm 0.06\,R_{\rm Jup}$ and $0.55 \pm 0.05\,R_{\rm Jup}$, respectively. In Case II we compute minimum radii of the primary and secondary of $R \sin i_\star = 0.32 \pm 0.03\,R_{\rm Jup}$ and

$0.89 \pm 0.09\,R_{\rm Jup}$, respectively.

BHAC models predict radii of $0.959^{+0.007}_{-0.008}\,R_{\rm Jup}$ and $0.914^{+0.007}_{-0.008}\,R_{\rm Jup}$ for the primary and secondary, respectively. Both possibilities that we consider are consistent with these model radii, i.e., no minimum radii are larger than these values, but they would correspond to very different projected alignments of the stellar spin axes. In Case I, inclinations of $i_\star = 32 \pm 4^\circ$ and $37 \pm 4^\circ$ for the primary and secondary, respectively, would be needed to match the model radii. This is consistent with co-alignment of stellar spin axes, as well as rough alignment with the orbital plane ($i = 138.56^{+0.20}_{-0.21}{}^\circ$ means that the spin axes would need to be $i_\star = 138.56^\circ$ or 41.44° to be aligned). In contrast, for Case II projected stellar inclinations of $i_\star = 19 \pm 2^\circ$ and $67 \pm 4^\circ$ for the primary and secondary, respectively, would be needed to match the model radii. This would rule out either of the stellar spin axes from being aligned with each other or with the orbital plane. We conclude that Case I is more likely because of the remarkable coincidence of the stellar spin axes and orbital inclination all being within $\pm 5^\circ$ of each other. However, we note that this is still only a probabilistic argument and that the stellar spin axis angles are only seen in projection, and we cannot rule out determine if they are aligned or misaligned out of the plane of the sky.

B.7. 2MASS J0920+3517AB (L5.5+L9)

The integrated-light spectral type of 2MASS J0920+3517AB is L6.5 in the optical (Kirkpatrick et al. 2000) and T0p in the infrared (Burgasser et al. 2006a). We determined component types of L5.5 ± 1.0 and L9.0 ± 1.5 from spectral deconvolution (Dupuy & Liu 2012). It is therefore surprising that we find a mass of $116^{+7}_{-8}\,M_{\rm Jup}$ for the fainter 2MASS J0920+3517B, much higher than the substellar boundary ($\approx 70\,M_{\rm Jup}$). Moreover, the total system mass $187 \pm 11\,M_{\rm Jup}$ suggests that there is more mass in this system than two brown dwarfs. The most plausible explanation is that 2MASS J0920+3517B is itself an unresolved binary.

Using only the primary mass ($71 \pm 5\,M_{\rm Jup}$) and luminosity, SM08 models give an essentially unconstrained age of 7^{+3}_{-5} Gyr and Cond models give a somewhat more tightly constrained age of $3.1^{+1.5}_{-1.7}$ Gyr. If we arbitrarily divide 2MASS J0920+3517B into two equal-mass ($58^{+3}_{-4}\,M_{\rm Jup}$), equal-luminosity components, then we find ages from SM08 ($2.3^{+0.3}_{-0.4}$ Gyr) and Cond ($1.99^{+0.25}_{-0.37}$ Gyr) that are in reasonable agreement with the primary. Therefore, the model-derived ages are consistent with the hypothesis that 2MASS J0920+3517B is an unresolved, nearly equal-mass binary.

The nondetection of Li I absorption in the integrated light spectrum (<0.5 Å; Kirkpatrick et al. 2000) is consistent with the fact that the primary mass ($71 \pm 5\,M_{\rm Jup}$) is well above the 55–60 $M_{\rm Jup}$ lithium depletion boundary at field ages (Section 7.2). In principle, a lithium-bearing component in 2MASS J0920+3517B could still be detectable even when diluted by the somewhat brighter 2MASS J0920+3517A ($\Delta F814W = 0.30 \pm 0.10$ mag). In our hypothetical equal-mass binary scenario for 2MASS J0920+3517B, our interpolation of Cond models predicts only modest lithium depletion of $\log({\rm Li}/{\rm Li}_{\rm init}) = -0.0215^{+0.0019}_{-0.0018}$ dex for the components. The case of 2MASS J0920+3517B is therefore quite similar to that of 2MASS J0700+3157B, which we discussed in detail above. We note that while the unresolved components of 2MASS J0920+3517B are likely both substellar, the primary 2MASS J0920+3517A could be a star or brown dwarf within the measurement uncertainties.

B.8. 2MASS J1017+1308AB (L1.5+L3)

2MASS J1017+1308AB (L1.5+L3) has one of the larger fractional uncertainties in total mass ($^{+9}_{-12}$%) in our sample, owing to a somewhat large parallax uncertainty (3.4%). Our directly measured mass ratio (0.92 ± 0.08) results in component masses of $81^{+10}_{-11}\,M_{\rm Jup}$ and $75 \pm 7\,M_{\rm Jup}$. Our measured mass ratio agrees well with the model-derived mass ratios from our total mass analysis ($0.987^{+0.017}_{-0.015}$ from BHAC, and SM08 gives essentially the same result). This means that our individual masses and luminosities agree with both model mass–luminosity relations, although this system does not offer a very strong test of models given the near-unity mass and luminosity ratios. Because the components of 2MASS J1017+1308AB are both likely main-sequence stars, the system age is essentially unconstrained by models, which only give 3σ lower limits of >0.6 Gyr (BHAC) and >0.5 Gyr (SM08) from our total-mass analysis.

B.9. 2MASS J1047+4026AB a.k.a. LP 213-68AB (M8+L0)

We measure a total mass of $178^{+11}_{-12}\,M_{\rm Jup}$ for 2MASS J1047+4026AB and individual masses of $97^{+6}_{-7}\,M_{\rm Jup}$ and $80 \pm 6\,M_{\rm Jup}$. Our measured mass ratio of 0.82 ± 0.06 agrees somewhat lower than but consistent within the uncertainties of the BHAC model-derived mass ratio from our total-mass analysis (0.947 ± 0.029), indicating that our masses and luminosities are consistent with BHAC isochrones. However, because the components of 2MASS J1047+4026AB are both main-sequence stars, the age is essentially unconstrained by models, which only give a 3σ lower limits of >0.5 Gyr from our total mass analysis.

The M8 dwarf 2MASSW J1047138+402649 (a.k.a. LP 213-68) is a proper motion companion to the M6.5 dwarf LP 213-67 (2MASSW J1047126+402643, 14$''$.4 away) as described by Gizis et al. (2000a) in their paper presenting the discovery of both objects as ultracool dwarfs. Close et al. (2003) reported the discovery of several binaries from their Gemini AO survey, but they report conflicting information regarding this source. Close et al. (2003) use the 2MASS name of the M6.5 dwarf LP 213-67 but refer to the object they observed as an M8 dwarf. We believe that they indeed observed the M8 dwarf LP 213-68, given that we have observed more than a full orbital period of this binary with Keck and the separation and PA reported by Close et al. (2003) agree very well with our orbit. If Close et al. (2003) observed LP 213-67, then it would have to be a binary that happened to have a separation and PA matching our ephemeris for LP 213-68 at the epoch of their observations, which would be a remarkable coincidence. Bouy et al. (2008) present Lick

AO observations with very clear details indicating that they observed LP 213-68 (despite referring to it by the 2MASS name of LP 213-67 in their tables), and their reported separation and PA (106 ± 14 mas and $319.3 \pm 1.0°$) agree reasonably well with our ephemeris for LP 213-68 at that epoch (109 ± 2 mas and $307.3 \pm 1.9°$). In contrast, Konopacky et al. (2010) report observations that do not appear to be consistent with our ephemeris of LP 213-68. They detected a binary at 32 ± 2 mas on 2006 Jun 21 UT but nothing outside of 47 mas on 2006 Nov 27 UT and 2007 Dec 2 UT. Our ephemeris predicts separations and PAs on those respective dates of: 87 ± 5 mas and $292 \pm 3°$; 101 ± 3 mas and $302 \pm 2°$, and 117.5 ± 1.0 mas and $316.6 \pm 1.6°$. It is possible that Konopacky et al. (2010) observed the M6.5 dwarf LP 213-67 instead of the M8 dwarf LP 213-68 because their tables use the 2MASS name and coordinates of LP 213-67. We conclude that this is the most likely explanation for their measurements. Interestingly, this implies that the M6.5 companion is also a binary, even tighter than LP 213-68, making this a hierarchical quadruple system. Unlike other known quadruples containing ultracool dwarfs (e.g., Gl 337, 2MASS J04414565+2301580) the LP 213-67/LP 213-68 system seems to be entirely composed of >M6 dwarfs.

B.10. SDSS J1052+4422AB (L6.5+T1.5)

The properties of SDSS J1052+4422AB are discussed in detail in Dupuy et al. (2015b). Our new homogeneous analysis here results in slightly revised properties for both mass and luminosity, but the key results are unchanged. Our measured mass ratio of 0.78 ± 0.07 is further from unity than expected given the near-unity luminosity ratio $\Delta \log(L_{\rm bol}) = 0.13 \pm 0.08$ dex. The mass ratio derived from SM08 models ($0.82^{+0.09}_{-0.11}$, 0.3σ different) provides a better match to our measurement than Cond models (0.91 ± 0.05, 1.5σ different). Or put in terms of age, our directly measured individual masses and luminosities yield ages that agree within the errors from SM08 models ($\Delta \log t = -0.02 \pm 0.12$ dex) but somewhat discrepant ages from Cond models ($\Delta \log t = -0.15 \pm 0.10$ dex).

B.11. Gl 417BC (L4.5+L6)

The properties of Gl 417BC and corresponding astrophysical interpretation are discussed in detail in Dupuy et al. (2014). Our new homogeneous analysis here results in slightly revised properties for both mass and luminosity, but the key results are unchanged.

Gl 417 is the only system in our sample for which a *Gaia* DR1 parallax is available from the Tycho-Gaia Astrometric Solution (Lindegren et al. 2016). Unfortunately, this parallax (43.86 ± 0.34 mas) is 3.1σ discrepant with the *Hipparcos* value (45.61 ± 0.44 mas) used in our previous work and the analysis presented here. If we adopt the *Gaia*-DR1 parallax, the total mass would be higher ($111.6^{+2.9}_{-3.1}\,M_{\rm Jup}$, compared to $99.2^{+3.0}_{-3.3}\,M_{\rm Jup}$), the component luminosities would be 0.03 dex higher, and the model-derived ages would be correspondingly older. Using the *Hipparcos* parallax, both BHAC and SM08 models give an age of 490^{+30}_{-40} Myr, but using the *Gaia*-DR1 parallax the BHAC and SM08 models would give ages of 620 ± 40 Myr and 600 ± 40 Myr, respectively. Such older ages are more consistent with the gyrochronology-derived age of 740^{+150}_{-120} Myr for the primary star Gl 417A and would consequently reduce the significance of the substellar "luminosity problem" for this system. The quality of *Gaia*-DR1 parallaxes have only just begun to be assessed by the community, and we defer judgment on the discrepancy for this system until the Tycho-Gaia Astrometric Solution errors are better understood.

B.12. LHS 2397aAB (M8+L dwarf)

We originally presented an analysis of this system based on the total mass alone in Dupuy et al. (2009c), but we noted that the photocenter orbit should be readily measurable given a long enough time baseline. Indeed, we detect the photocenter motion of LHS 2397aAB at the highest significance of any binary in our sample (37σ), allowing us to measure a mass ratio of $0.706^{+0.027}_{-0.028}$. Only the Cond models cover the mass and luminosity of both the primary and secondary, and they predict a mass ratio ($0.75^{+0.07}_{-0.04}$) that is in excellent agreement with our much more precise measurement. As expected, the primary is a star ($93 \pm 4\,M_{\rm Jup}$), and the secondary is consistent with being substellar ($66 \pm 4\,M_{\rm Jup}$). The Cond model-derived age of the secondary is $2.6^{+0.6}_{-1.0}$ Gyr, while the age of the primary is essentially unconstrained but consistent with the secondary. The SM08 models give a similar age for the secondary of $2.8^{+2.1}_{-1.5}$ Gyr.

Despite the fact that the components of LHS 2397aAB are different in luminosity by 1.14 ± 0.06 dex, further from unity than any other binary in our sample, the fact that the components are a star and a brown dwarf means that this system on its own does not actually provide a strong test of the mass–luminosity relation predicted by models. Such a wide range of ages are allowed for the primary given that it is on the main sequence that models are free to match the mass and luminosity of the secondary exactly by fine-tuning the age. Models predict that LHS 2397aB is strongly depleted in lithium, $\log({\rm Li}/{\rm Li}_{\rm init}) = -1.8^{+0.7}_{-0.6}$ dex, which is consistent with the nondetection (EW < 0.5 Å) in the integrated-light spectrum from Reiners & Basri (2009).

B.13. Kelu-1AB (L2+L4)

Kelu-1AB is the only one of our sample binaries with a CFHT parallax but without a measured mass ratio, owing to the relatively short time baseline (2.26 yr) of the available CFHT observations. Moreover, our parallax (48.0 ± 2.2 mas) disagrees somewhat with other comparably precise published values of 53.6 ± 2.0 mas (Dahn et al. 2002) and 51.75 ± 1.16 mas (Weinberger et al. 2016). Using our parallax, the total mass is $180^{+22}_{-26}\,M_{\rm Jup}$. In comparison, the Dahn et al. (2002) parallax gives $129^{+13}_{-16}\,M_{\rm Jup}$ and the Weinberger et al. (2016) parallax gives $144^{+9}_{-10}\,M_{\rm Jup}$. Given the lack of mass ratio information and that the published parallaxes, including our own, span such a wide range of possible masses, we exclude Kelu-1AB from our analysis. The fact that Li I absorption is detected in integrated light (EW = 1.7 Å; Kirkpatrick et al. 1999) implies that at least one component in the system should be $\lesssim 60\,M_{\rm Jup}$ according to BHAC models, which would potentially favor the lower system mass (larger parallax). Liu & Leggett (2005) noted that the components of Kelu-1AB might straddle the lithium fusion boundary, providing a uniquely constraining test of models. However, the current uncertainty in the dynamical mass is too large to distinguish whether the components of Kelu-1AB are both stars or brown dwarfs, let alone assess whether they are lithium bearing.

In unrefereed work, Stumpf et al. (2008) proposed that Kelu-1AB is a triple system. They computed a dynamical mass with large errors ($185^{+118}_{-58}\,M_{\rm Jup}$)[14] and found an H-band feature in their resolved spectrum of Kelu-1A that they claimed as evidence of an unresolved T-dwarf companion. This feature is strong enough that it should appear in the integrated-light spectrum of the whole system even after being diluted by Kelu-1B, but an inspection of the published unresolved spectrum of Kelu-1AB shows no such feature. We therefore conclude that there is no strong evidence that Kelu-1AB is actually a triple system.

B.14. 2MASS J1404−3159AB (L9+T5)

2MASS J1404−3159AB is a J-band flux-reversal binary (Looper et al. 2008), and using our photometry here we find component spectral types of L9.0 ± 1.0 and T5.0 ± 0.5 by spectral decomposition, making 2MASS J1404−3159B one of the latest-type objects in our sample. We have a well determined total mass ($120^{+11}_{-13}\,M_{\rm Jup}$) and mass ratio ($0.84 \pm 0.06$), resulting in individual masses of $65 \pm 6\,M_{\rm Jup}$ and $55^{+6}_{-7}\,M_{\rm Jup}$. In our total-mass analysis, both sets of models give mass ratios in good agreement with our measurement ($0.79^{+0.08}_{-0.11}$ from SM08 and $0.85^{+0.07}_{-0.06}$ from Cond). The model-derived ages are also consistent with SM08 giving $3.0^{+0.8}_{-1.3}$ Gyr and Cond giving $2.5^{+0.6}_{-0.9}$ Gyr.

The only other J-band flux-reversal binary in our final mass sample is SDSS J1052+4422AB, and its mass ratio of 0.78 ± 0.07 is similar to that of 2MASS J1404−3159AB. (Note that SDSS J1534+1615AB is a J-band flux-reversal binary in our input sample, but it does not have a secure orbit determination.) However, in that case there were discrepancies between models and observations due to the fact that Lyon models, either Cond here or Dusty in Dupuy et al. (2015b), predicted a much steeper drop in luminosity given the change in mass. The lack of such discrepancies for 2MASS J1404−3159AB is because despite having a similar mass ratio, its luminosity ratio is much further from unity, $\Delta\log(L_{\rm bol}) = 0.35 \pm 0.09$ dex compared to 0.13 ± 0.08 dex for SDSS J1052+4422AB. The SM08 model-derived temperature for 2MASS J1404−3159A (1400^{+40}_{-50} K) is comparable to that of SDSS J1052+4422A (1366^{+25}_{-29} K), while 2MASS J1404−3159B (1190 ± 50 K) is slightly cooler than SDSS J1052+4422B (1270 ± 40 K).

2MASS J1404−3159A is consistent with being massive enough that it would be depleted in

[14]We quote the mass implied by their given period and semimajor axis, because their own quoted mass seems to assume a conversion factor of $1000\,M_{\rm Jup}/M_{\odot}$, not the correct $1048\,M_{\rm Jup}/M_{\odot}$.

lithium, $\log(\mathrm{Li/Li_{init}} = -1.0^{+1.0}_{-0.5}$ dex, although within 1σ range includes the possibility that it has not depleted any lithium. In contrast, Cond models predict that 2MASS J1404−3159B retains almost all of its initial lithium, $\log(\mathrm{Li/Li_{init}} = -0.018^{+0.003}_{-0.006}$ dex. However, the T5 spectral type of 2MASS J1404−3159B suggests that no Li I will be observable in its spectrum because monatomic lithium will be chemically depleted into LiCl and/or LiOH. No optical spectroscopy is yet available to test these model predictions of lithium depletion, or lack thereof, for this system.

B.15. HD 130948BC (L4+L4)

The properties of HD 130948BC and corresponding astrophysical interpretation are discussed in detail in Dupuy et al. (2009b) and updated in Dupuy et al. (2014). Our new homogeneous analysis here results in slightly revised properties for both mass and luminosity, but the key results are unchanged. (HD 130948A does not appear in the *Gaia*-DR1 Tycho-Gaia Astrometric Solution catalog of parallaxes.)

B.16. Gl 569Bab (M8.5+M9)

In our previous work, we used Keck and *HST* data to measure the orbit of Gl 569Bab, finding a semimajor axis of $95.6^{+1.1}_{-1.0}$ mas (Dupuy et al. 2010) from which we computed a system mass of $147^{+9}_{-8}\,M_{\mathrm{Jup}}$. We discussed why this may be discrepant with other literature measurements, the smallest of which was 90.4 ± 0.7 mas from Simon et al. (2006). Our new measurement of 93.64 ± 0.14 mas, based on a much more extensive data set with better orbital phase coverage, is still inconsistent (4.1σ) with the Simon et al. (2006) value, and it is also 2.0σ smaller than our previously published value. This results in a somewhat smaller system mass of $138 \pm 7\,M_{\mathrm{Jup}}$, which is only 0.8σ different from our previously published value, because the error is dominated by the *Hipparcos* parallax ($\sigma_\pi/\pi = 0.016$) not our semimajor axis measurement ($\sigma_a/a = 0.0016$). (Gl 569A does not appear in the *Gaia*-DR1 Tycho-Gaia Astrometric Solution catalog of parallaxes.)

The BHAC model-derived age of Gl 569Bab is 440^{+50}_{-60} Myr, in good agreement with our past work (460^{+70}_{-110} Myr from Dusty models; Dupuy et al. 2010). The model-derived mass ratio is $q = 0.85 \pm 0.03$, or $1/q = 1.17 \pm 0.05$. This is in good agreement with the measured mass ratio of $1/q = 1.4 \pm 0.3$ based on a homogeneous analysis of radial velocities by Konopacky et al. (2010). The model-derived individual masses are $75 \pm 4\,M_{\mathrm{Jup}}$ and $64 \pm 4\,M_{\mathrm{Jup}}$. Using our total mass and the mass ratio from Konopacky et al. (2010) results in individual masses of $80^{+9}_{-8}\,M_{\mathrm{Jup}}$ and $58^{+7}_{-9}\,M_{\mathrm{Jup}}$. In both cases, given our empirical substellar boundary of $\approx 70\,M_{\mathrm{Jup}}$, Gl 569Bb is likely a brown dwarf and Gl 569Ba could be a brown dwarf or a star.

B.17. 2MASS J1534−2952AB (T4.5+T5)

In our previous work, Liu et al. (2008) used a parallax of 73.6 ± 1.2 mas from Tinney et al. (2003) and a different orbit analysis method to determine a total dynamical mass of $59 \pm 3\,M_{\rm Jup}$. Our CFHT parallax (first published in Dupuy & Liu 2012) is 63.0 ± 1.1 mas, putting this binary significantly farther away and thus making its semimajor axis and mass measurements larger. Liu et al. (2008) quoted a total mass of $58.3^{+2.0}_{-1.8}\,M_{\odot}$ at a fixed parallax of 73.6 mas. We can therefore readily compute how the total mass from that orbit analysis would have changed if we instead use our parallax, finding $92.9^{+3.2}_{-2.8}\,M_{\rm Jup}$ at a fixed parallax of 63.0 mas. The dynamical mass we derive here with more data and a different analysis method is $99.5^{+0.8}_{-0.6}\,M_{\rm Jup}$ at a fixed parallax of 63.0 mas, which is somewhat higher but consistent within 2σ. As discussed in Section 4.2, this is largely due to a difference in eccentricity prior for this nearly circular orbit. After incorporating the parallax uncertainty, our newly determined total mass is $99 \pm 5\,M_{\rm Jup}$.

In our total-mass analysis, SM08 models give an age of $3.0^{+0.4}_{-0.5}$ Gyr, which is somewhat older than the Cond age of $2.25^{+0.29}_{-0.32}$ Gyr. Models give consistent mass ratios of 0.96 ± 0.06 (SM08) and 0.95 ± 0.07 (Cond), which agree well with our measured mass ratio of $0.95^{+0.13}_{-0.16}$. Thus, properties derived from our total-mass analysis agree well with our individual-mass analysis, and the two components are coeval according to models. With individual masses of $51 \pm 5\,M_{\rm Jup}$ and $48 \pm 5\,M_{\rm Jup}$, both components are predicted by Cond models to have retained $\geq$95% (1σ) of their initial lithium. No Li I absorption is observed in the integrated light spectrum of 2MASS J1534−2952AB (Burgasser et al. 2003a), implying that monatomic lithium is likely chemically depleted into LiCl and/or LiOH as expected. The component temperatures derived from Cond models are 1170 ± 50 K and 1110^{+40}_{-50} K. This provides an empirical lower limit on the effective temperature at which lithium is chemically depleted for field brown dwarfs. Finally, we note that despite being the latest-type binary in our sample, the components of 2MASS J1534−2952AB are in fact similar in mass to some of the L and early-T dwarfs in our sample (e.g., SDSS J0423−0414A, SDSS J1052+4422A, Gl 417B, and Gl 417C).

B.18. 2MASS J1728+3948AB (L5+L7)

Combining our total mass ($140^{+7}_{-8}\,M_{\rm Jup}$) and mass ratio ($0.93^{+0.11}_{-0.13}$) gives individual masses of $73 \pm 7\,M_{\rm Jup}$ for 2MASS J1728+3948A (L5 $\pm$ 1) and $67 \pm 5\,M_{\rm Jup}$ for 2MASS J1728+3948B (L7 $\pm$ 1). In our total-mass analysis, models give mass ratios in good agreement with our measurement, and correspondingly the ages derived in our individual-mass analysis are consistent between primary and secondary. The total-mass analysis gives the tightest age constraints of $3.4^{+2.8}_{-2.1}$ Gyr (SM08) and $2.9^{+0.7}_{-1.1}$ Gyr (Cond). 2MASS J1728+3948A is predicted to be strongly depleted of lithium, with $\log({\rm Li/Li_{init}}) = -2.9^{+0.4}_{-0.7}$ dex, while within 1σ 2MASS J1728+3948B ranges from somewhat to severely depleted in lithium, $\log({\rm Li/Li_{init}}) = -1.5^{+0.7}_{-0.6}$ dex. Given these predictions it would be possible for the integrated-light spectrum to show weak lithium absorption due to

2MASS J1728+3948B. The lack of a strong Li I detection (EW < 4 Å) by Kirkpatrick et al. (2000) does not rule out such weak absorption, although it is also consistent with both components being fully depleted of lithium. In that case, this nondetection of lithium would be an indication that the secondary mass is on the higher side of our quoted 1σ intervals.

B.19. LSPM J1735+2634AB (M7.5+L0)

Combining our total mass ($187\pm7\,M_{\rm Jup}$) and mass ratio ($0.868^{+0.023}_{-0.025}$) gives individual masses of $100\pm4\,M_{\rm Jup}$ for LSPM J1735+2634A (M7.5) and $87\pm3\,M_{\rm Jup}$ for LSPM J1735+2634B (L0). Having one of the more precise mass ratios, and one that is further from unity than most, LSPM J1735+2634AB provides a good test of the model-predicted mass–luminosity relation. In our total-mass analysis, BHAC models predict a mass ratio of $0.913^{+0.019}_{-0.017}$, which is only marginally (1.6σ) higher than we measure. Because the components of LSPM J1735+2634AB are both likely main-sequence stars, the age is essentially unconstrained by models, which only give a 3σ lower limit of >0.6 Gyr from both total-mass and individual-mass analyses.

B.20. 2MASS J2132+1341AB (L4.5+L8.5)

Combining our total mass ($128^{+7}_{-8}\,M_{\rm Jup}$) and mass ratio ($0.88^{+0.04}_{-0.05}$) gives individual masses of $68\pm4\,M_{\rm Jup}$ for 2MASS J2132+1341A (L4.5±1.5) and $60\pm4\,M_{\rm Jup}$ for 2MASS J2132+1341B (L8.5± 1.5). In our total-mass analysis, models give mass ratios in good agreement with our measurement, and correspondingly the ages derived in our individual mass analysis are consistent between primary and secondary. The total-mass analysis gives the tightest age constraints of $1.44^{+0.26}_{-0.37}$ Gyr (SM08) and $1.71^{+0.28}_{-0.38}$ Gyr (Cond). 2MASS J2132+1341A is predicted to be severely depleted of lithium, while 2MASS J2132+1341B straddles the lithium-fusion boundary within the errors but is predicted to mostly be above it and thus not strongly depleted in lithium, $\log({\rm Li}/{\rm Li}_{\rm init}) = -1.1^{+1.1}_{-0.4}$. If Li I were present, then Cruz et al. (2007) would likely have detected it in their integrated-light spectrum of 2MASS J2132+1341, although they do not quote EW limits. Their lack of a detection is would be more consistent with the model predictions if 2MASS J2132+1341B is on the more massive end of our measurement uncertainties.

B.21. 2MASS J2140+1625AB (M8+L0.5)

Our measured mass ratio for 2MASS J2140+1625AB is quite low ($0.60^{+0.07}_{-0.08}$), such that it divides up our total mass ($183^{+14}_{-17}\,M_{\rm Jup}$) into a quite massive M8 primary ($114^{+10}_{-12}\,M_{\rm Jup}$) and a rather low-mass L0.5 secondary ($69^{+8}_{-9}\,M_{\rm Jup}$). This is strongly disfavored by models, mainly because the primary is much less luminous than expected for such a high mass. Our total-mass analysis using BHAC models predicts a mass ratio of $0.882^{+0.028}_{-0.024}$, 3.8σ discrepant with our measurement.

Interestingly, both our total-mass and individual-mass analyses end up with an essentially identical total mass as we measure. The individual-mass analysis demonstrates how this can be the case despite such a discrepant model-derived mass ratio: the primary mass after performing rejection sampling was 1.7σ lower than we input, and the secondary mass was 2.0σ higher than we input.

This apparent discrepancy could be jointly due to two smaller ($\approx1.5\sigma$) discrepancies in the measured mass ratio and parallax. 2MASS J2140+1625 has one of the less precise mass ratios in our sample and a 3% parallax uncertainty that leads to an atypically large total mass error ($^{+8}_{-9}$%). Therefore, higher-precision data would be useful in determining if 2MASS J2140+1625AB is truly an astrophysical outlier.

B.22. 2MASS J2206−2047AB (M8+M8)

In our previous work, we used a parallax of 37.5 ± 3.4 mas from Costa et al. (2006) to determine a dynamical total mass and model-derived properties (Dupuy et al. 2009a). Our CFHT parallax of 35.7 ± 1.2 mas was first presented in Dupuy & Liu (2012), and the updated analysis here gives 35.8 ± 1.0 mas, which allows for a more precise total mass than in Dupuy et al. (2009a) as well as individual masses from our photocenter analysis. Our total mass is $188^{+16}_{-17}\,M_{\rm Jup}$, consistent with our previous measurement of $160^{+50}_{-30}\,M_{\rm Jup}$ (Dupuy et al. 2009a). Our measured mass ratio of $0.84^{+0.09}_{-0.10}$, consistent with the BHAC model-derived value of $0.986^{+0.028}_{-0.029}$, gives component masses of $102^{+10}_{-11}\,M_{\rm Jup}$ and $86^{+8}_{-10}\,M_{\rm Jup}$. In both total-mass and individual-mass analyses, rejection sampling results in slightly higher secondary masses and lower primary masses in the output distributions ($96\,M_{\rm Jup}$ and $95\,M_{\rm Jup}$) but they are consistent with the inputs to within $\leq1\sigma$. The masses and luminosities of 2MASS J2206−2047AB are consistent with this being a pair of main-sequence stars, with BHAC models giving a 3σ lower limit on the age of >0.27 Gyr.

B.23. DENIS J2252−1730AB (L4+T3.5)

Combining our total mass ($101 \pm 7\,M_{\rm Jup}$) and mass ratio ($0.70^{+0.08}_{-0.09}$) gives individual masses of $59 \pm 5\,M_{\rm Jup}$ for DENIS J2252−1730A (L4.0 ± 1.0) and $41 \pm 4\,M_{\rm Jup}$ for DENIS J2252−1730B (T3.5 ± 0.5). Therefore, both components are unambiguously substellar. In our total-mass analysis, SM08 models prefer a somewhat lower mass ratio ($0.57^{+0.03}_{-0.05}$), consistent with our measurement within the uncertainties, while Cond models predict a somewhat higher mass ratio ($0.71^{+0.05}_{-0.04}$). Both sets of models give consistent ages, with the total mass analysis providing the tightest age constraints of $1.11^{+0.19}_{-0.22}$ Gyr (SM08) and $1.10^{+0.15}_{-0.18}$ Gyr (Cond). According to Cond models, DENIS J2252−1730B is predicted to have retained nearly all its lithium, while DENIS J2252−1730A straddles the lithium fusion boundary within the errors, $\log(\mathrm{Li}/\mathrm{Li}_{\rm init}) = -2.1^{+0.7}_{-1.5}$ dex. DENIS J2252−1730B is quite cool (1230^{+50}_{-60} K, Cond) and thus may not be expected to display Li I in absorption due to being chemically depleted. DENIS J2252−1730A on the other hand is an L2 dwarf that should be amenable to lithium-absorption measurement. Reid et al. (2008b) obtained an integrated-light optical spectrum for this relatively bright binary and did not report lithium absorption for this source. This suggests that DENIS J2252−1730A is indeed above the lithium-fusion limit and thus its true mass may be in the higher range of our quoted 1σ mass interval.

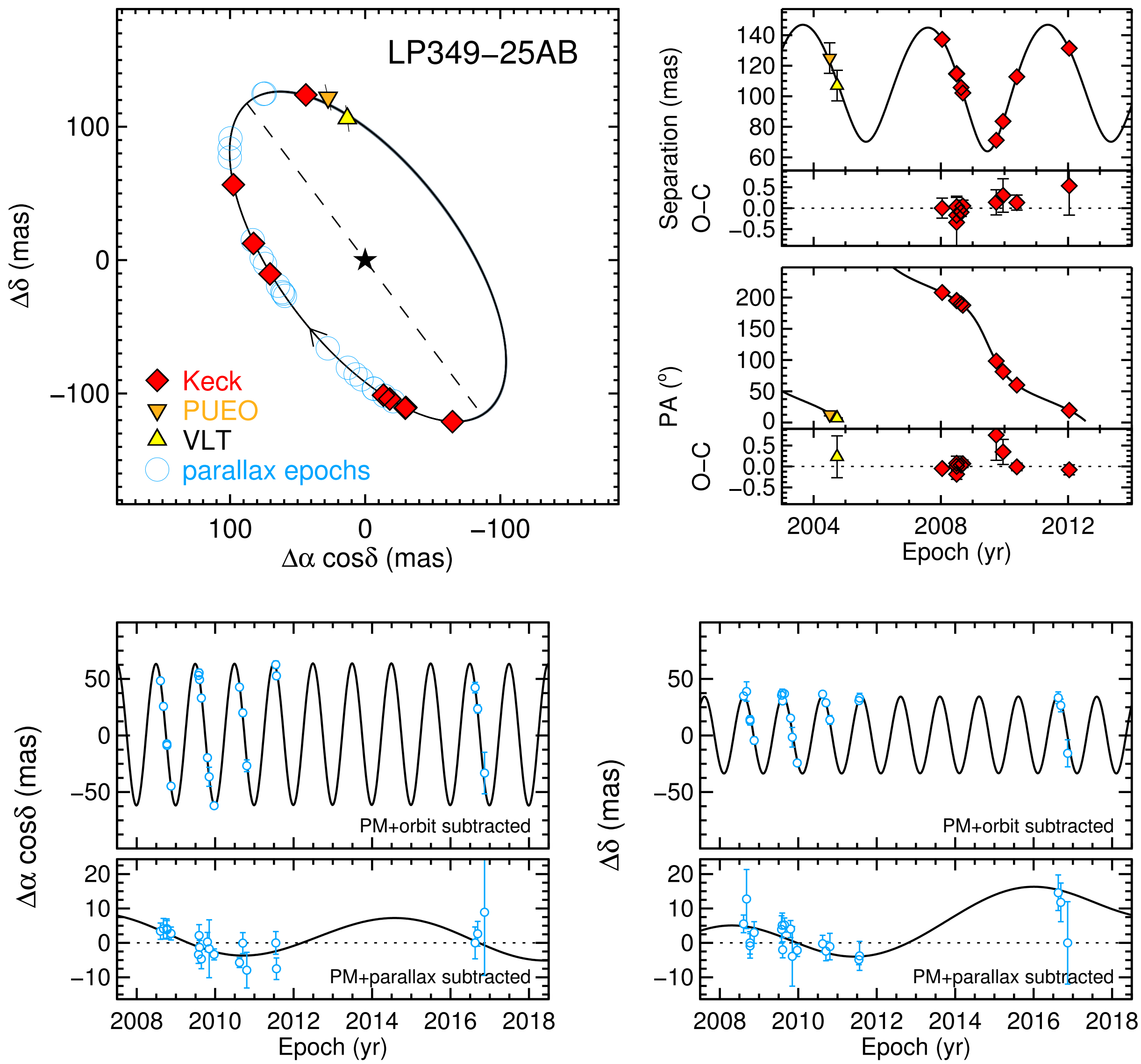

Fig. 1.— *Top left:* resolved relative astrometry (filled symbols) shown alongside the best-fit orbit (thick black line) and 100 randomly drawn orbits from our MCMC chain (thin gray lines). The plotting symbols typically are larger than the error bars. Open blue circles indicate the epochs at which we obtained unresolved CFHT/WIRCam astrometry. *Top right:* our relative astrometry shown as a function of time (top sub-panels) and after subtracting the best-fit orbit solution (bottom sub-panels). *Bottom:* CFHT/WIRCam astrometry from unresolved, seeing-limited imaging. Top panels show the data with the proper motion and photocenter orbital motion subtracted in order to display our best-fit parallax solution (thick black line). Bottom panels show the residuals and our best-fit astrometric solution (thick black line) after subtracting our best-fit parallax and linear motion as a function of time (including both true proper motion and linear orbital motion).

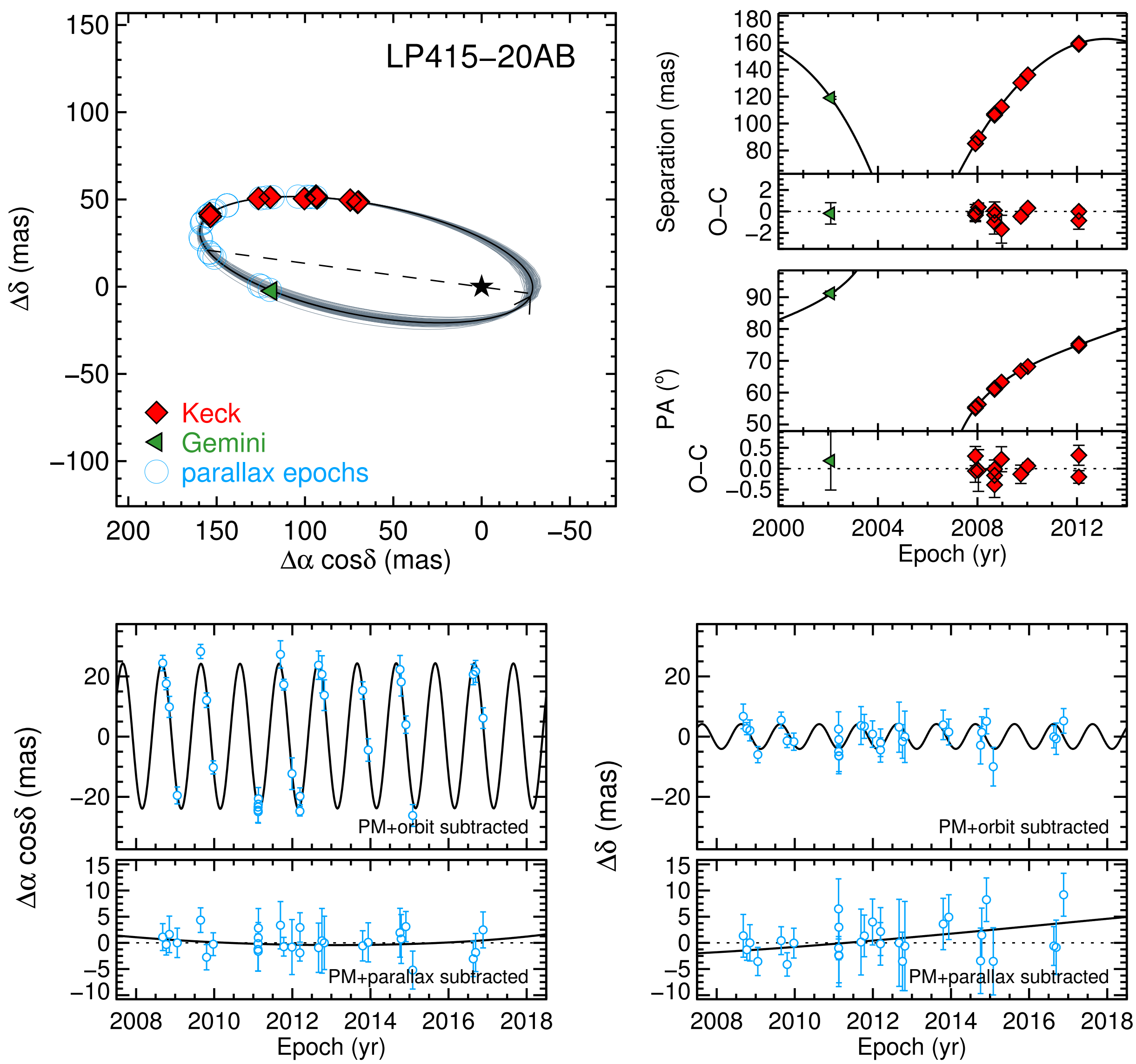

Fig. 1.— (Continued)

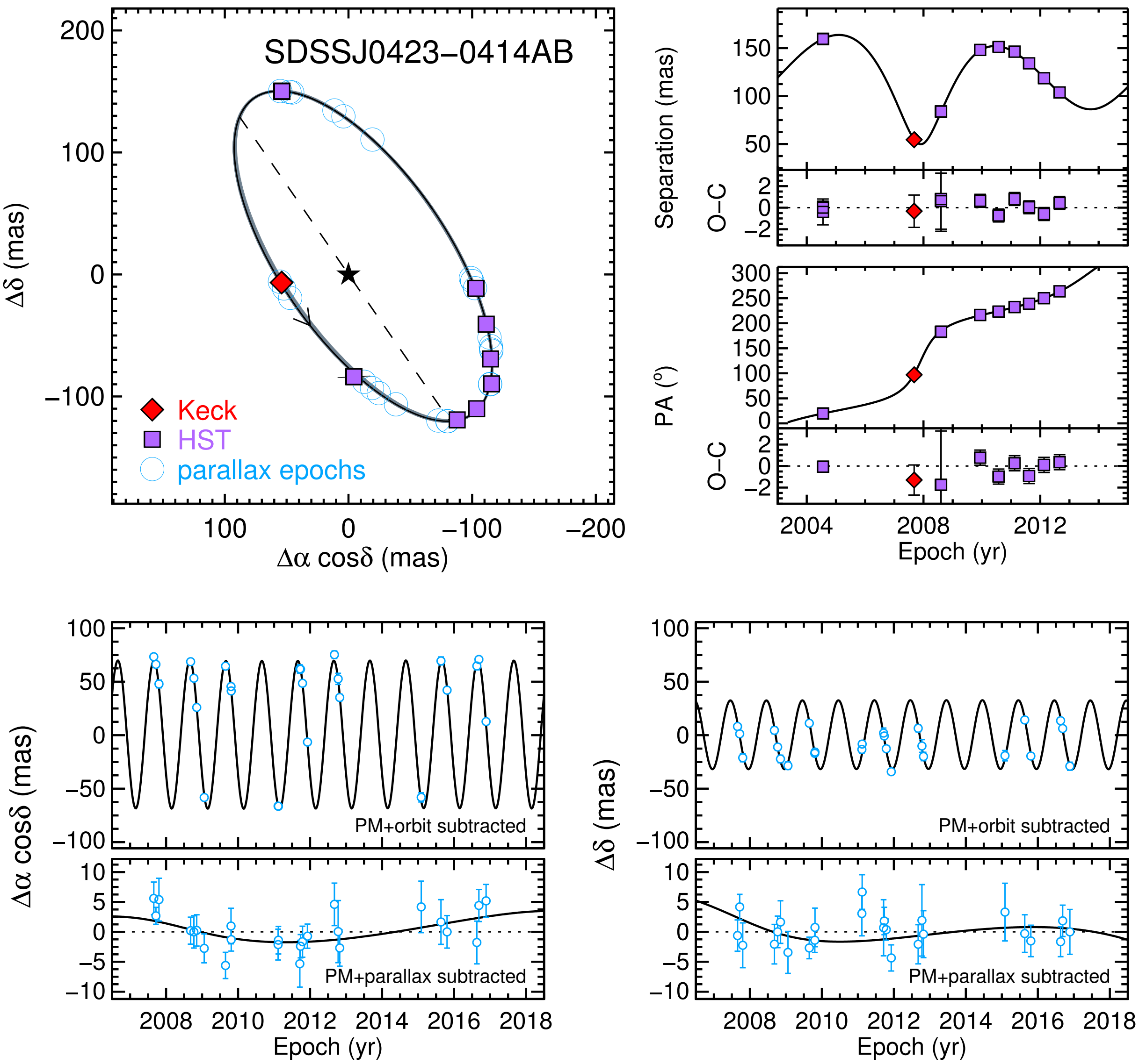

Fig. 1.— (Continued)

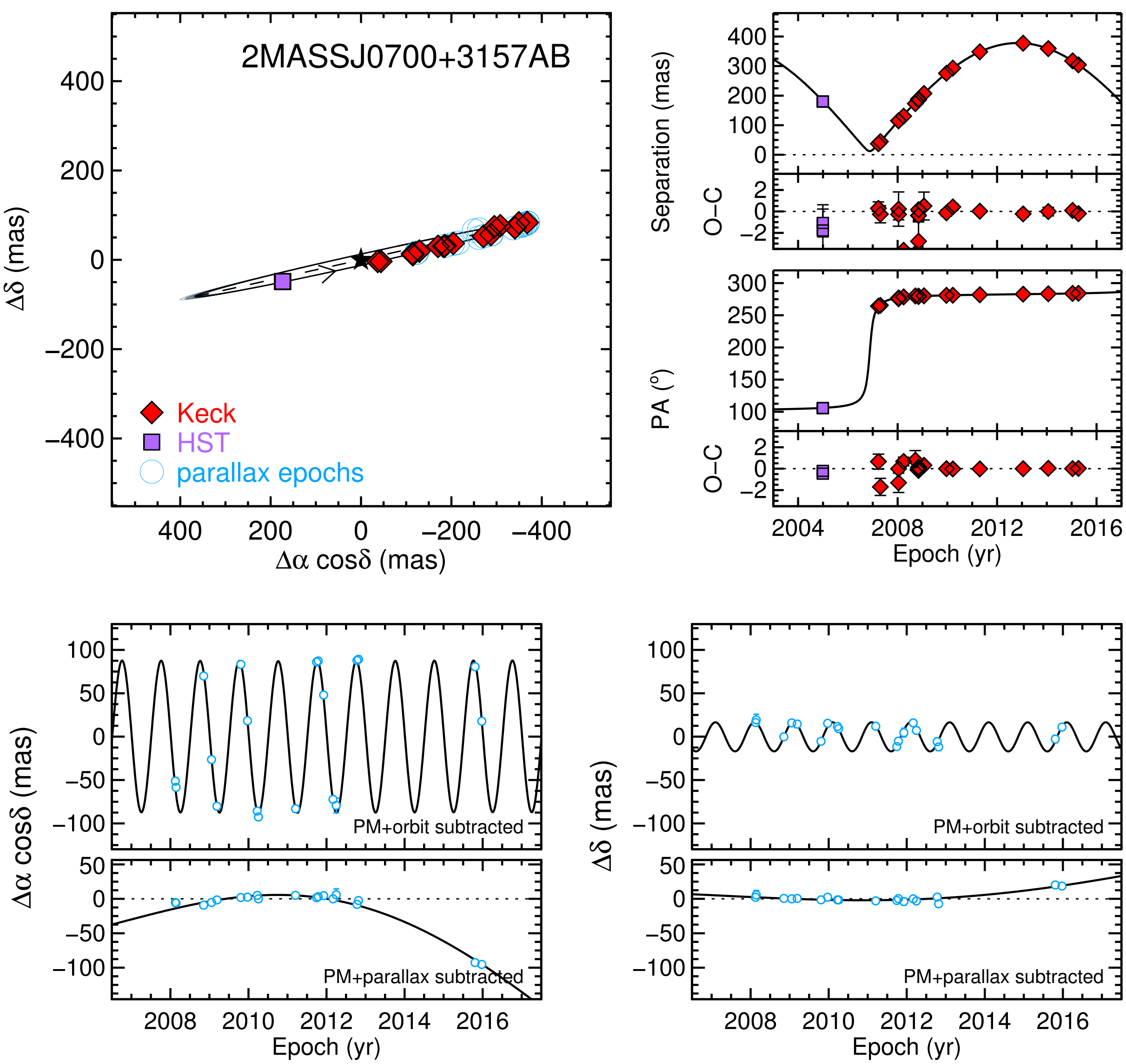

Fig. 1.— (Continued)

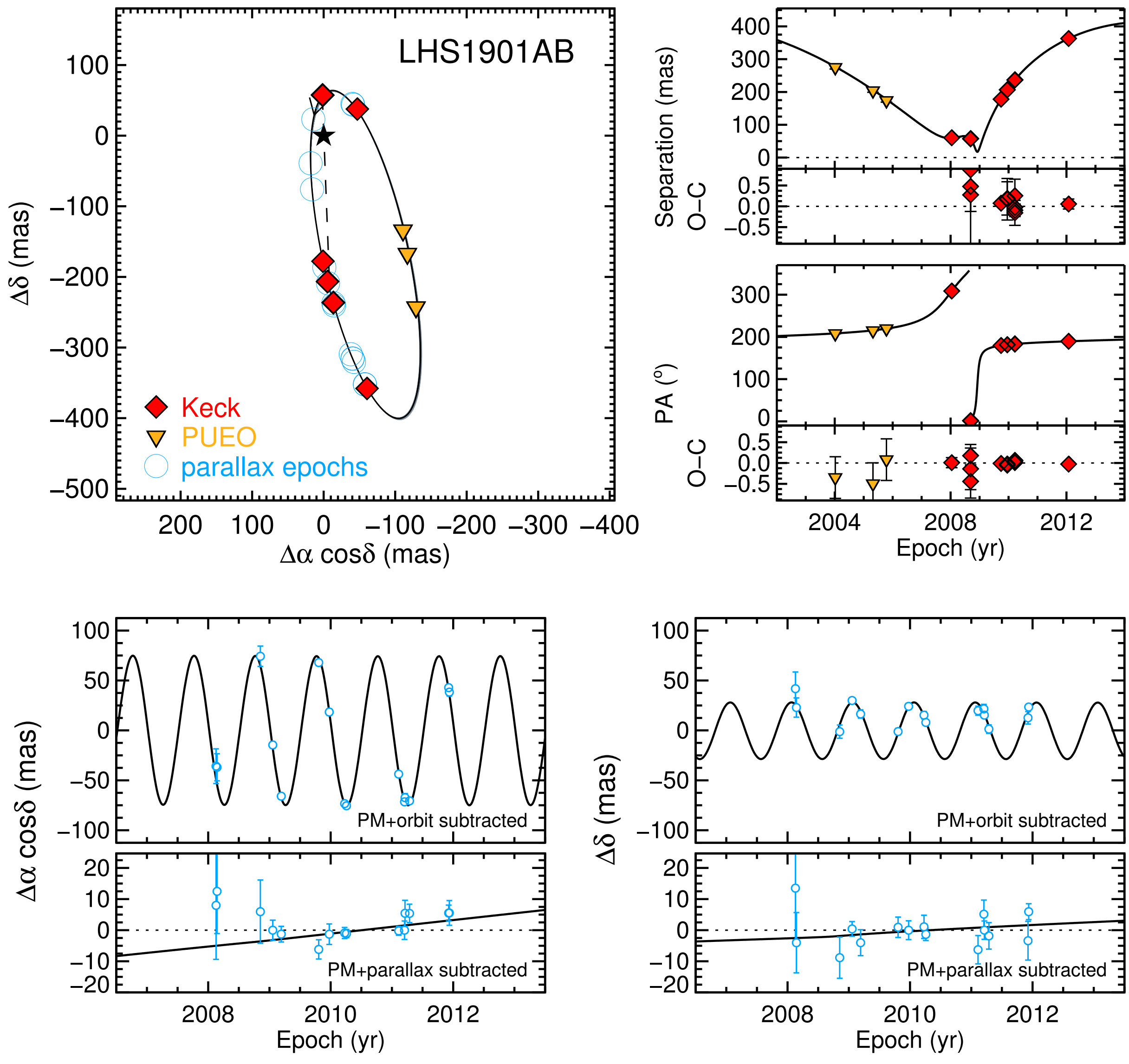

Fig. 1.— (Continued)

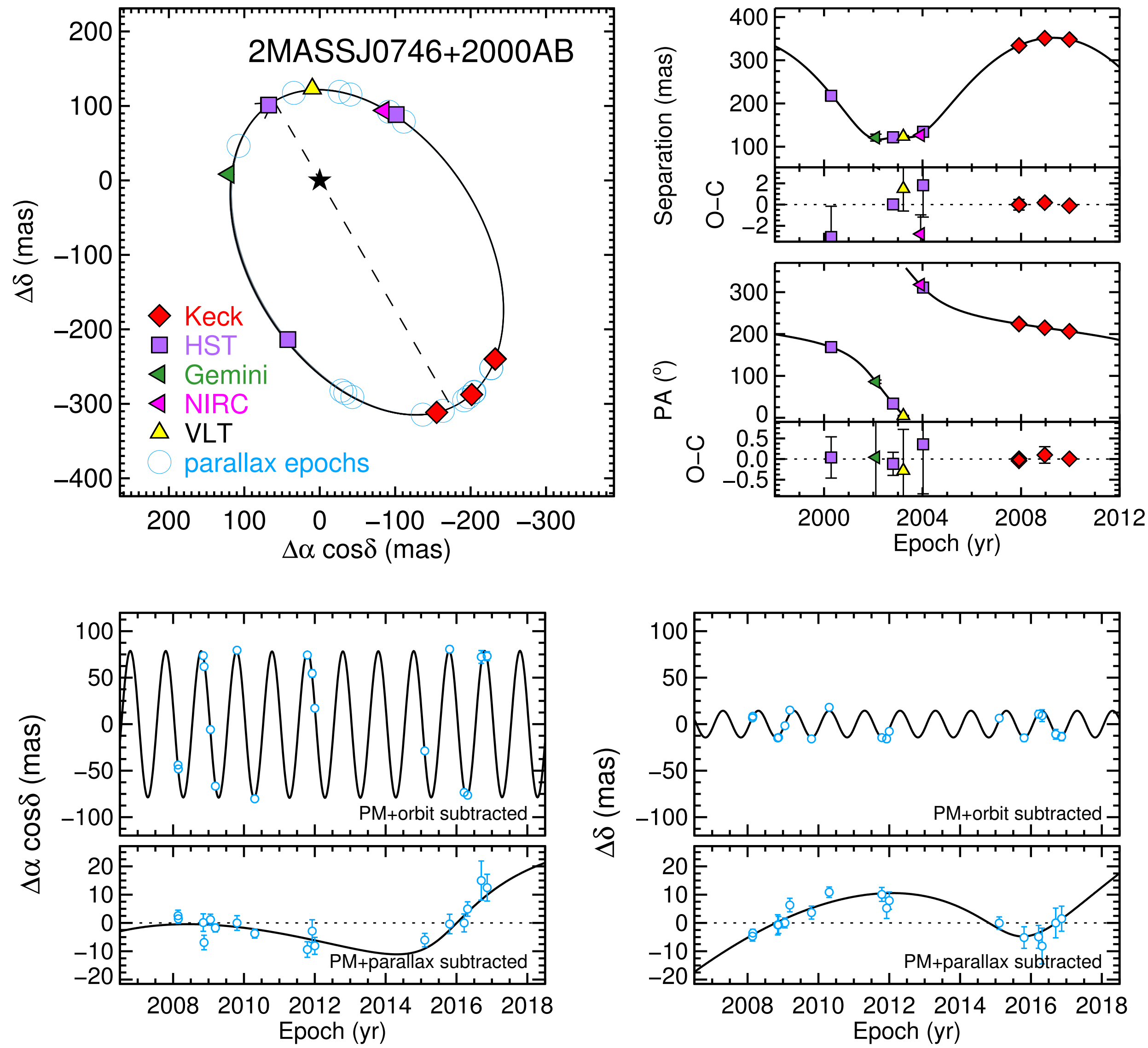

Fig. 1.— (Continued)

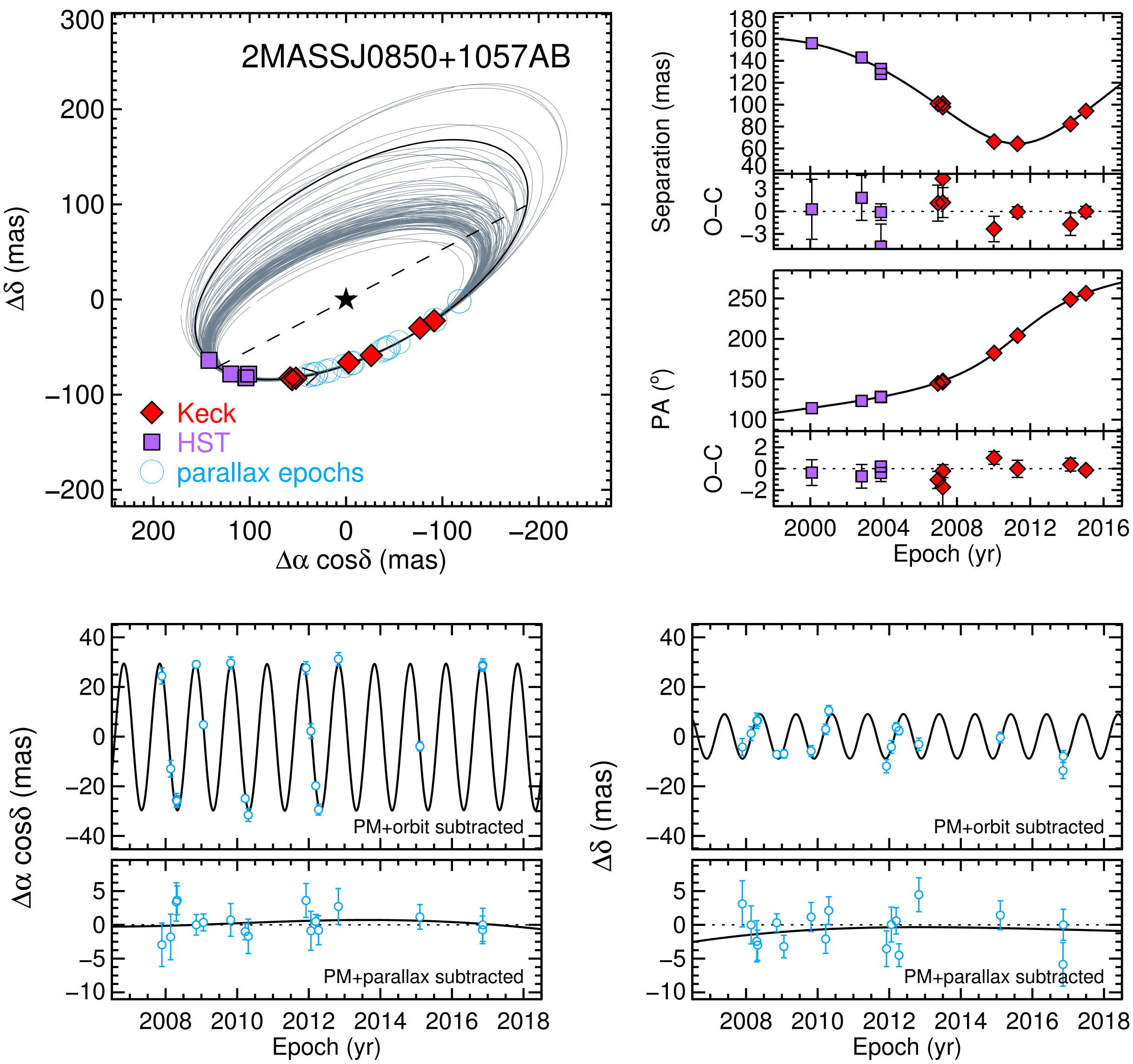

Fig. 1.— (Continued)

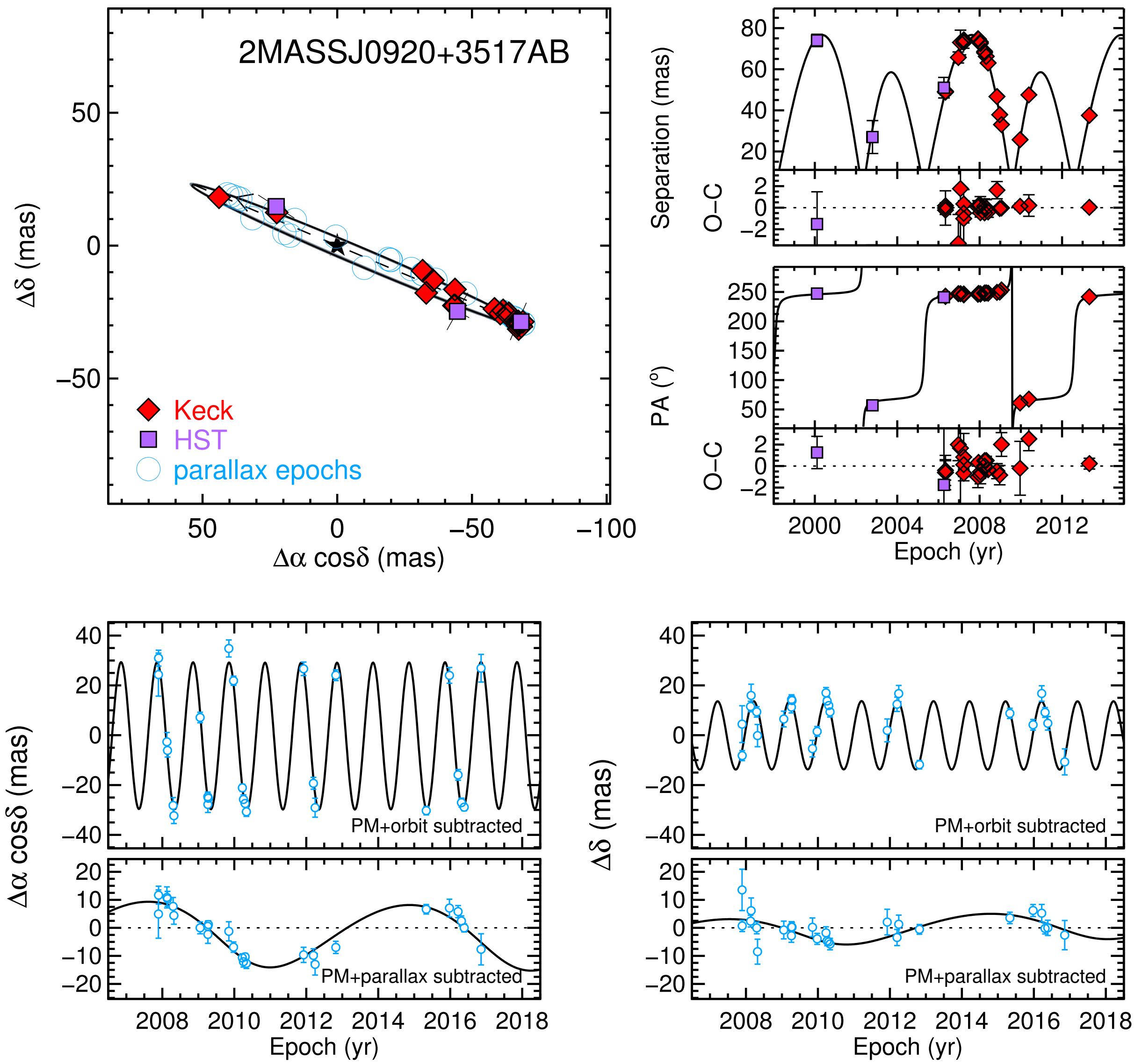

Fig. 1.— (Continued)

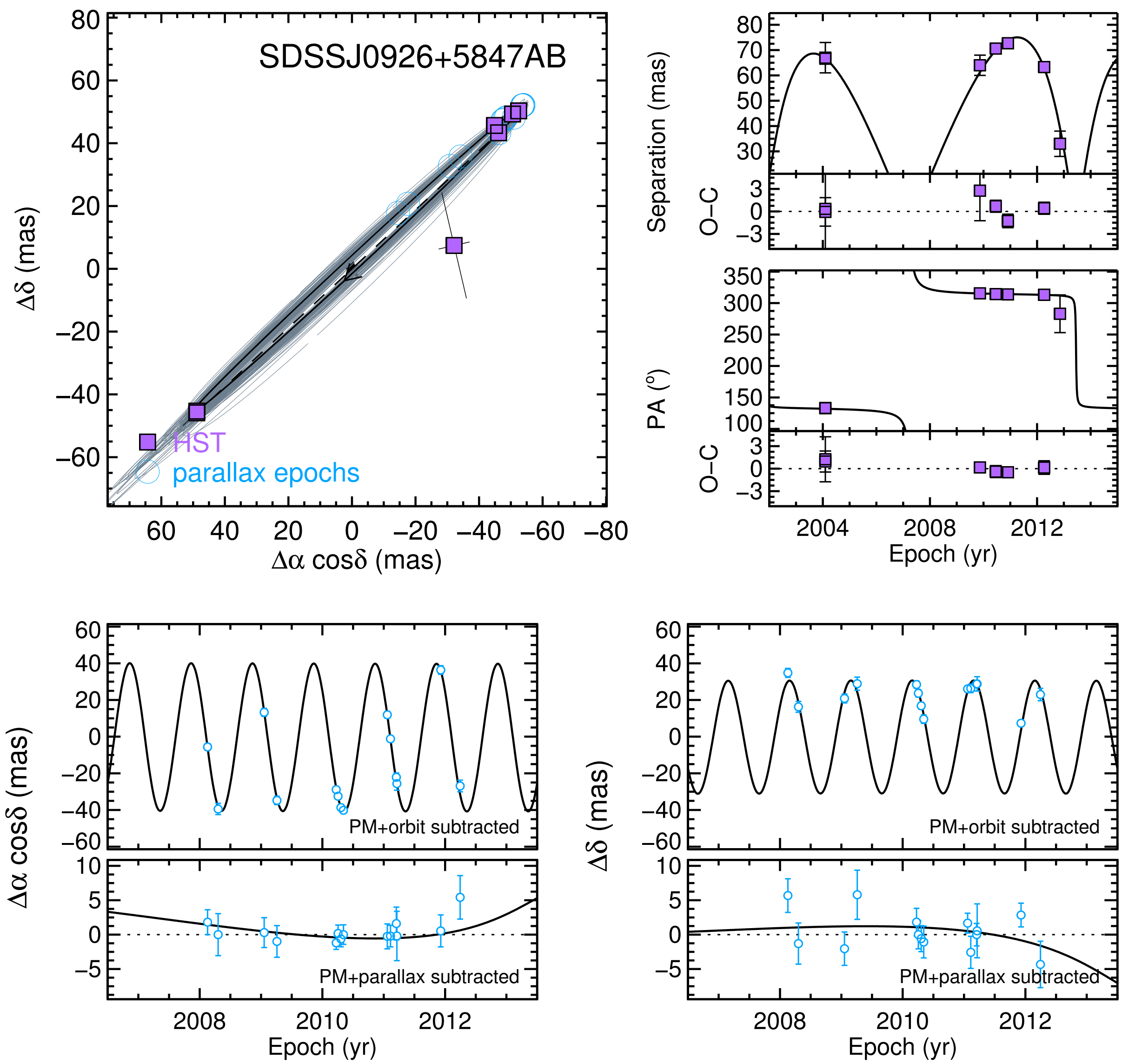

Fig. 1.— (Continued)

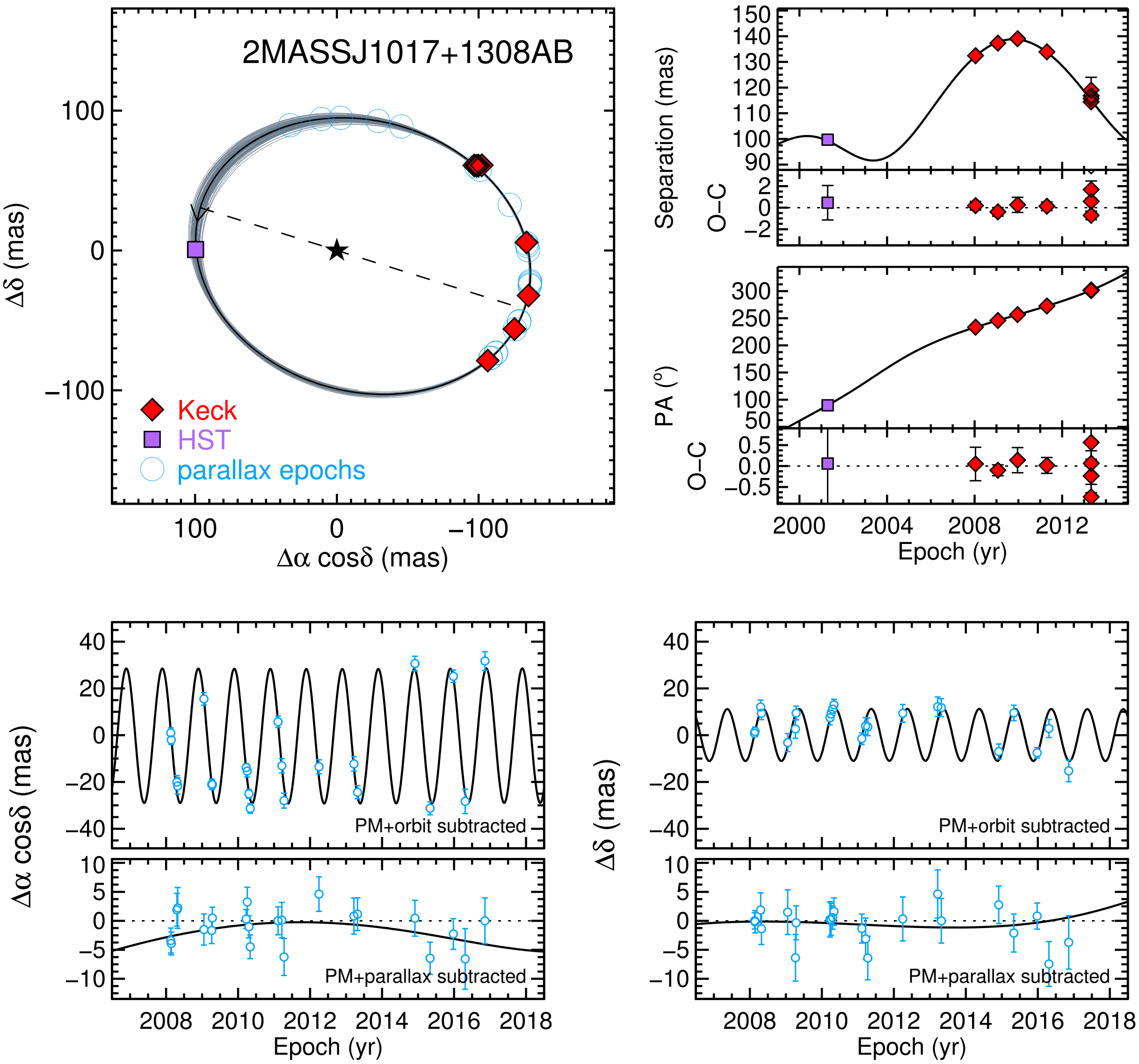

Fig. 1.— (Continued)

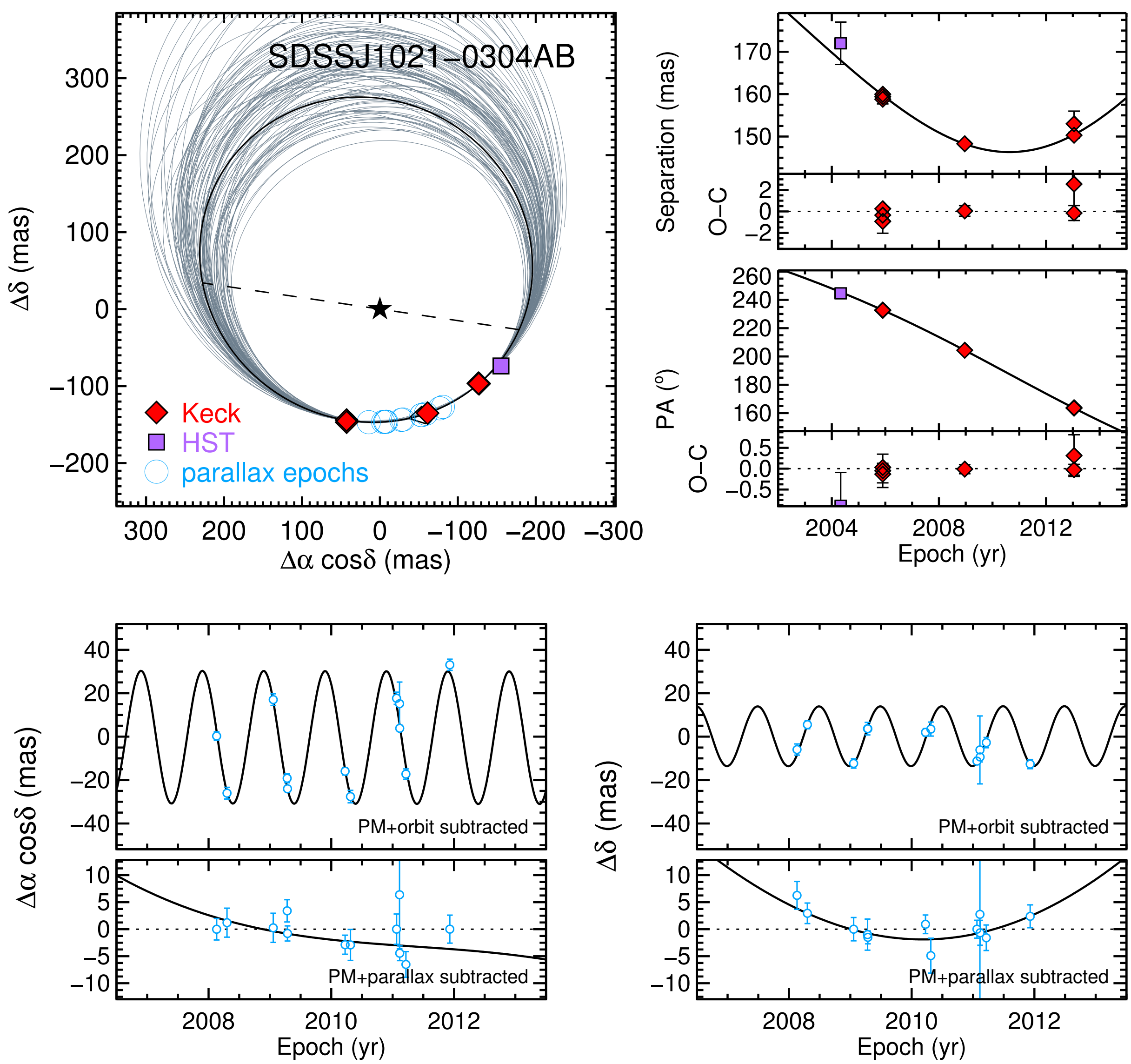

Fig. 1.— (Continued)

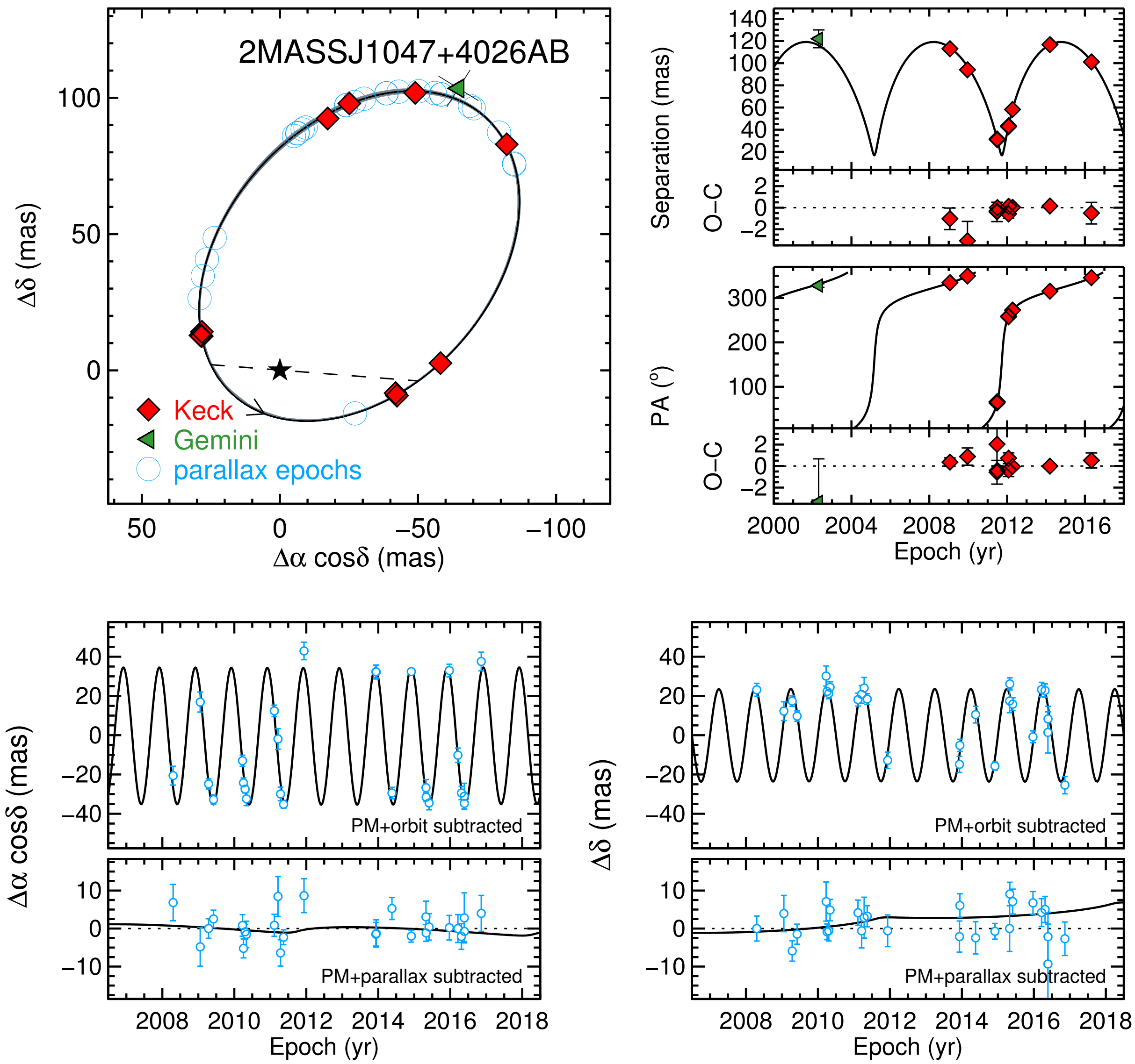

Fig. 1.— (Continued)

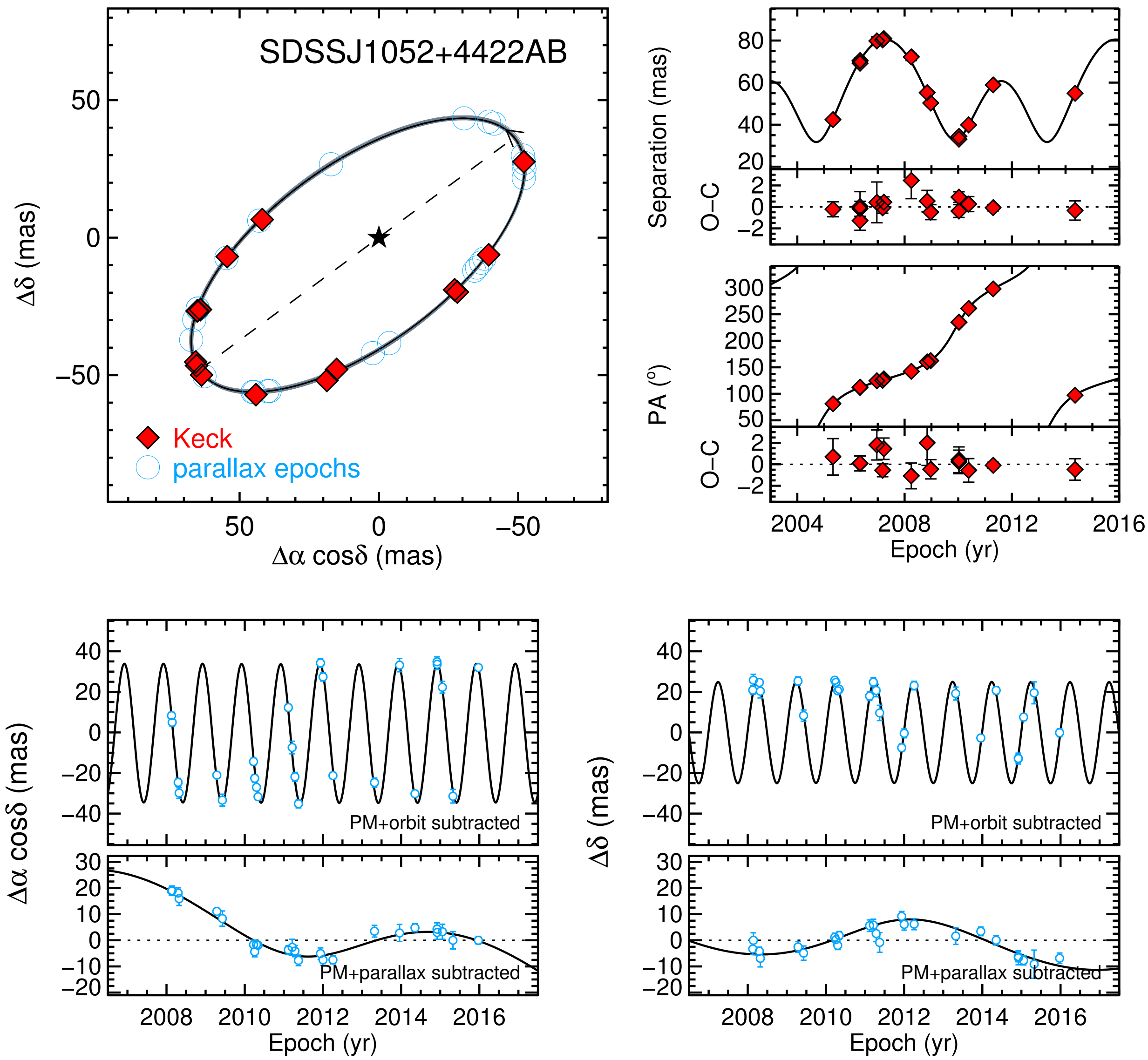

Fig. 1.— (Continued)

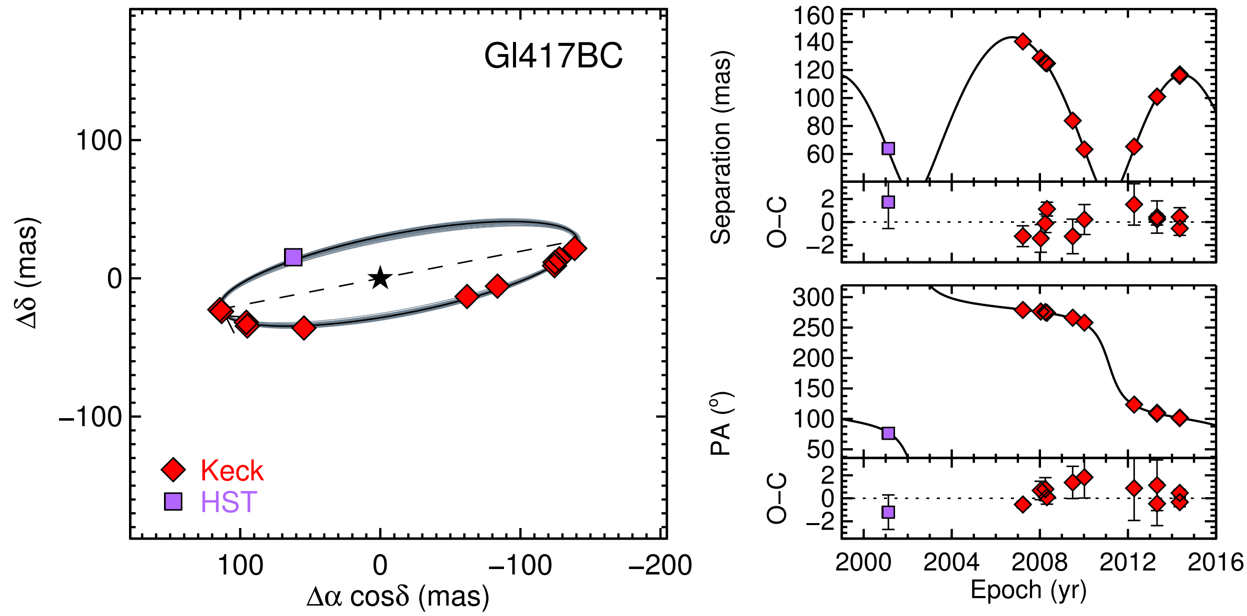

Fig. 1.— (Continued)

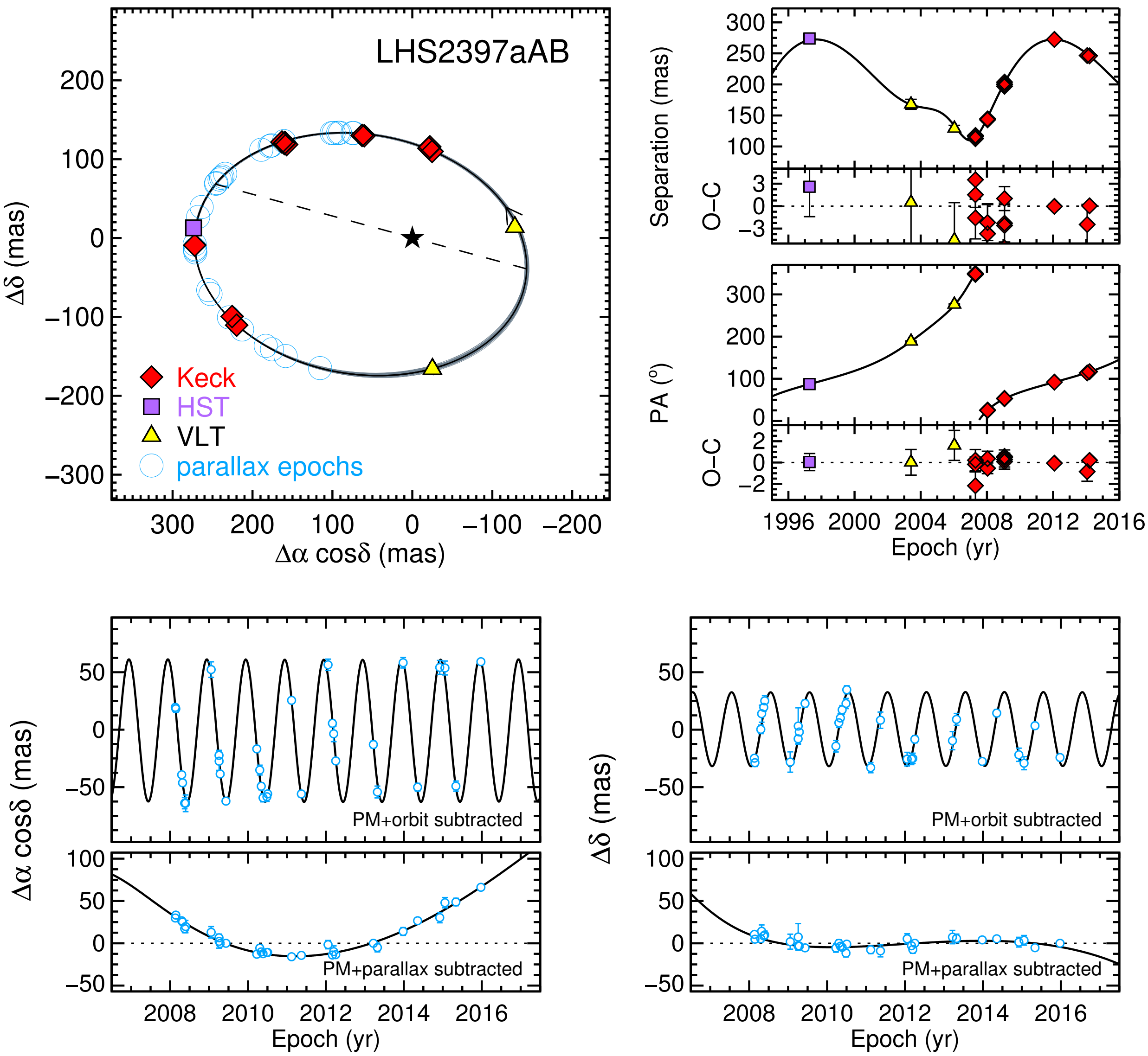

Fig. 1.— (Continued)

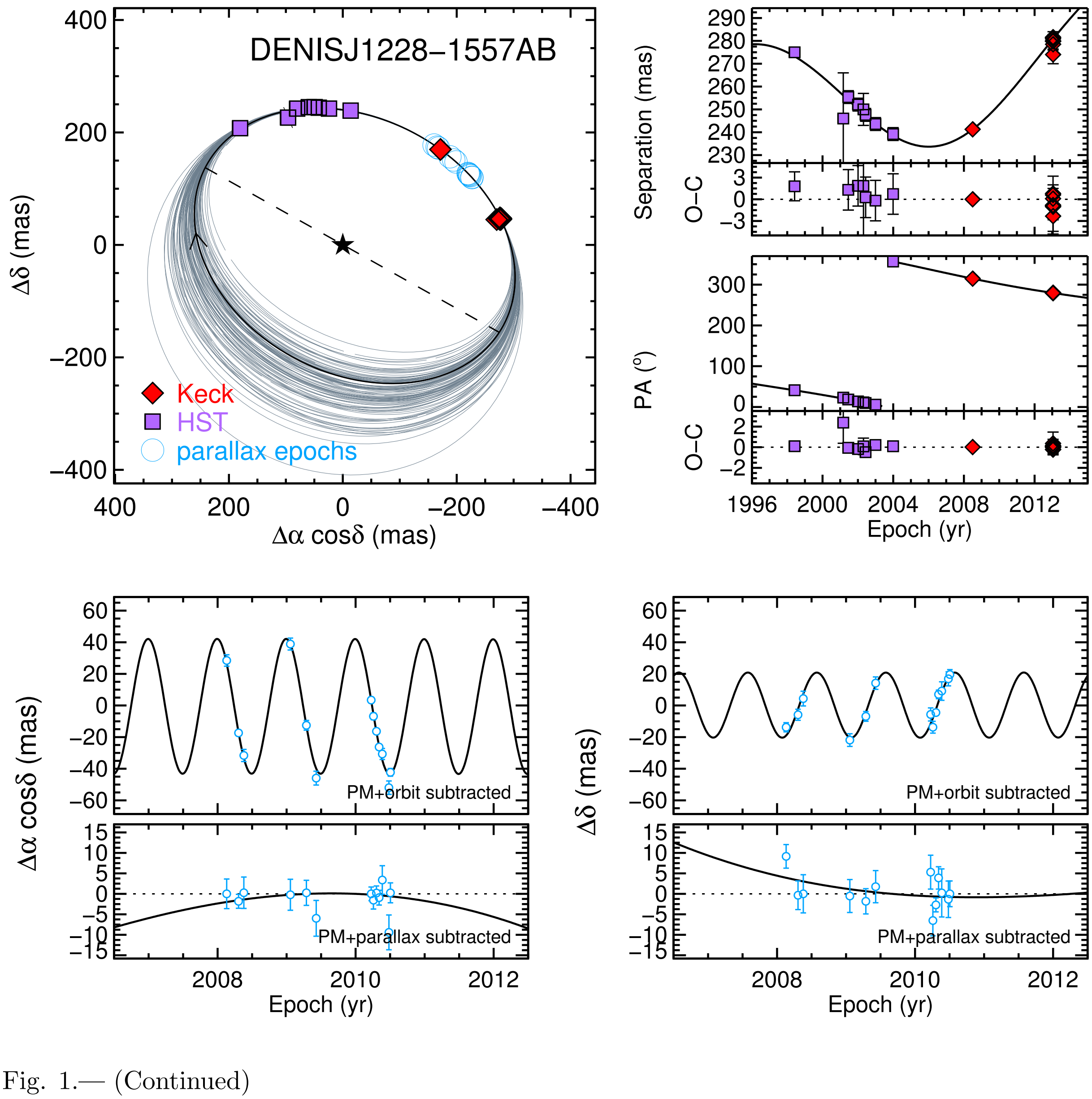

Fig. 1.— (Continued)

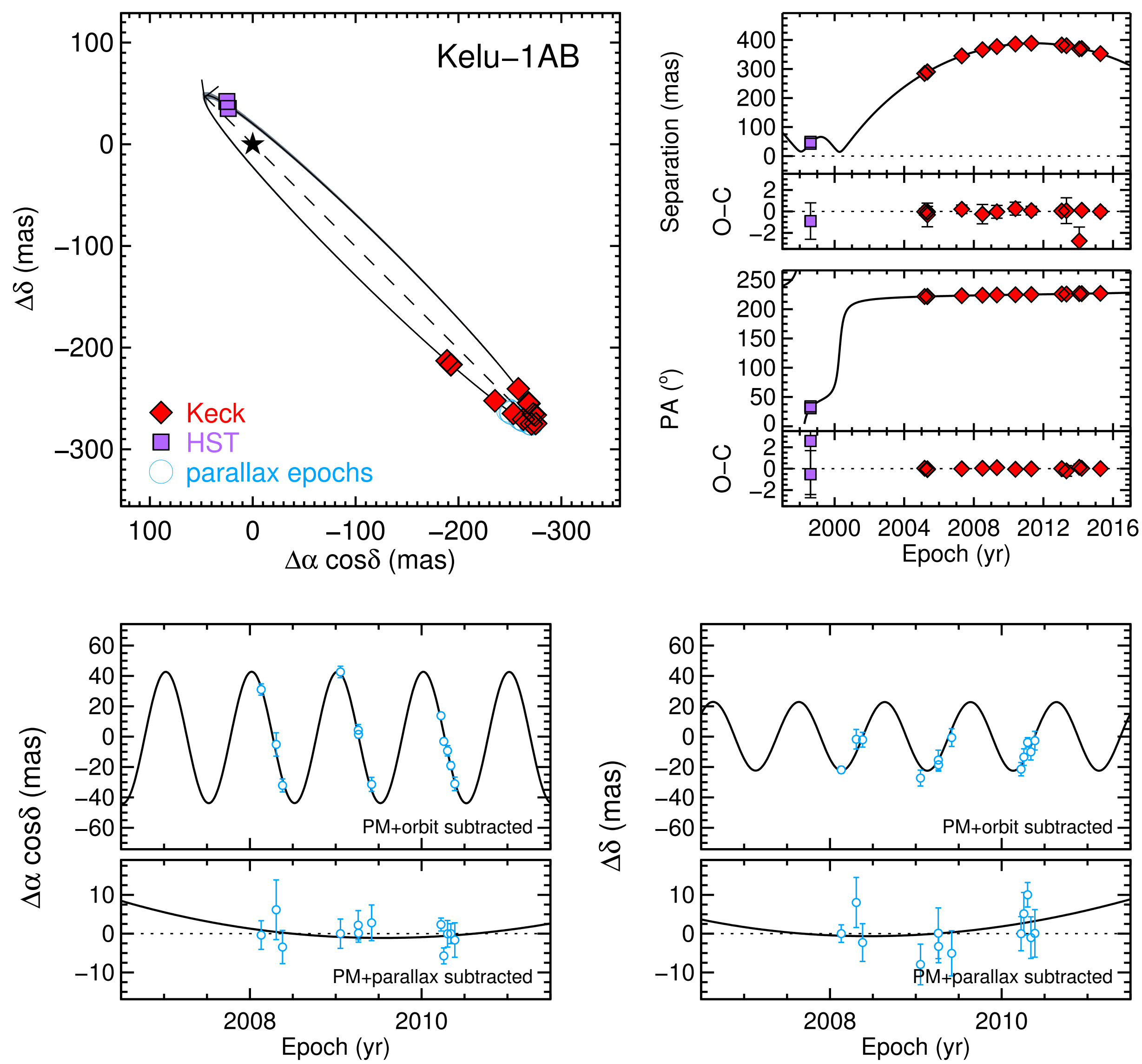

Fig. 1.— (Continued)

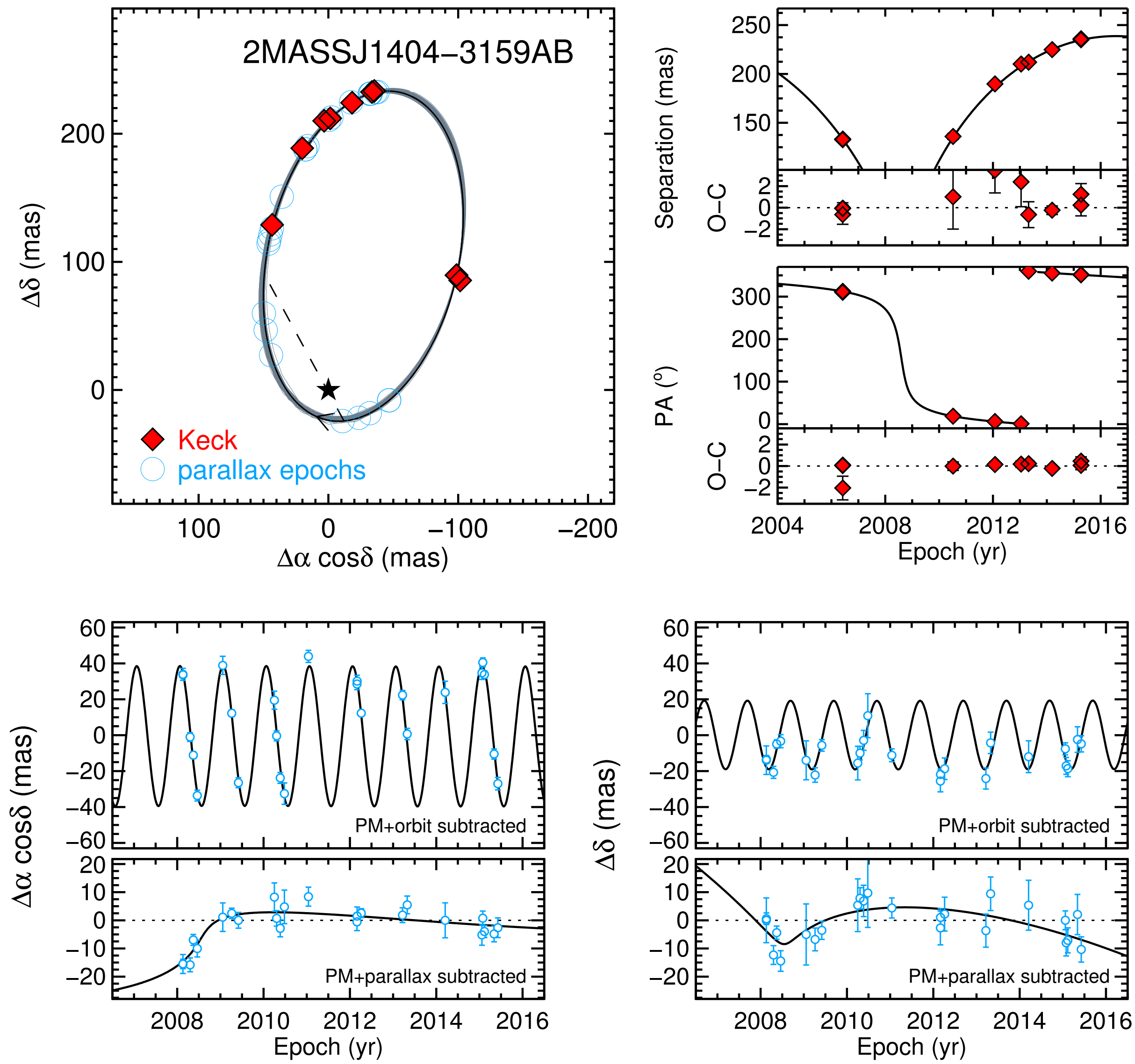

Fig. 1.— (Continued)

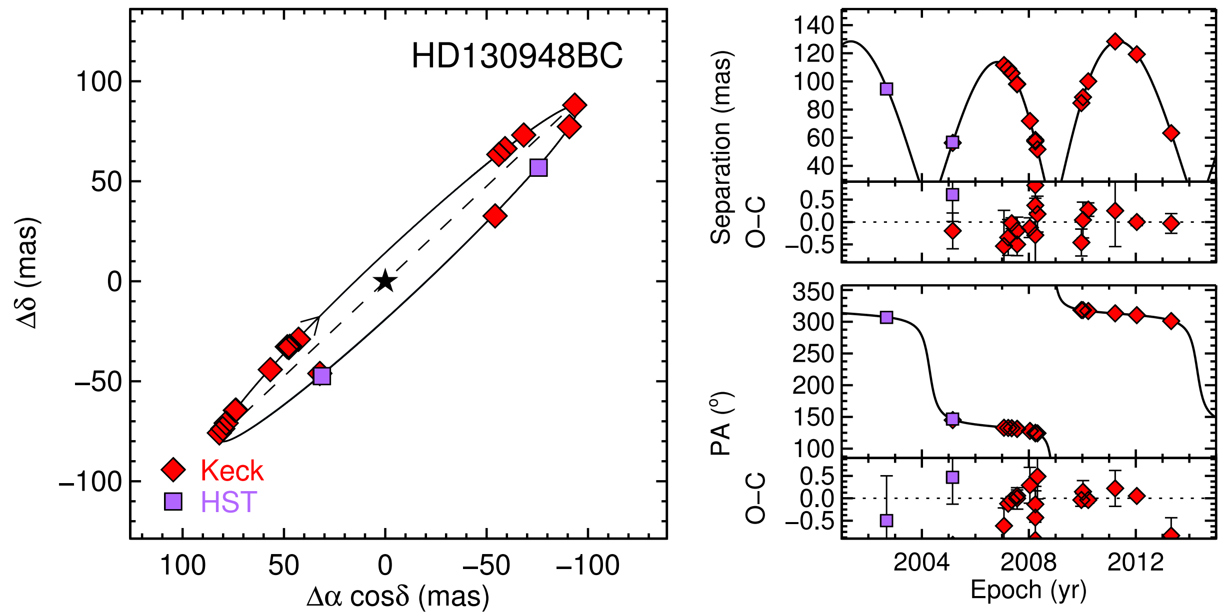

Fig. 1.— (Continued)

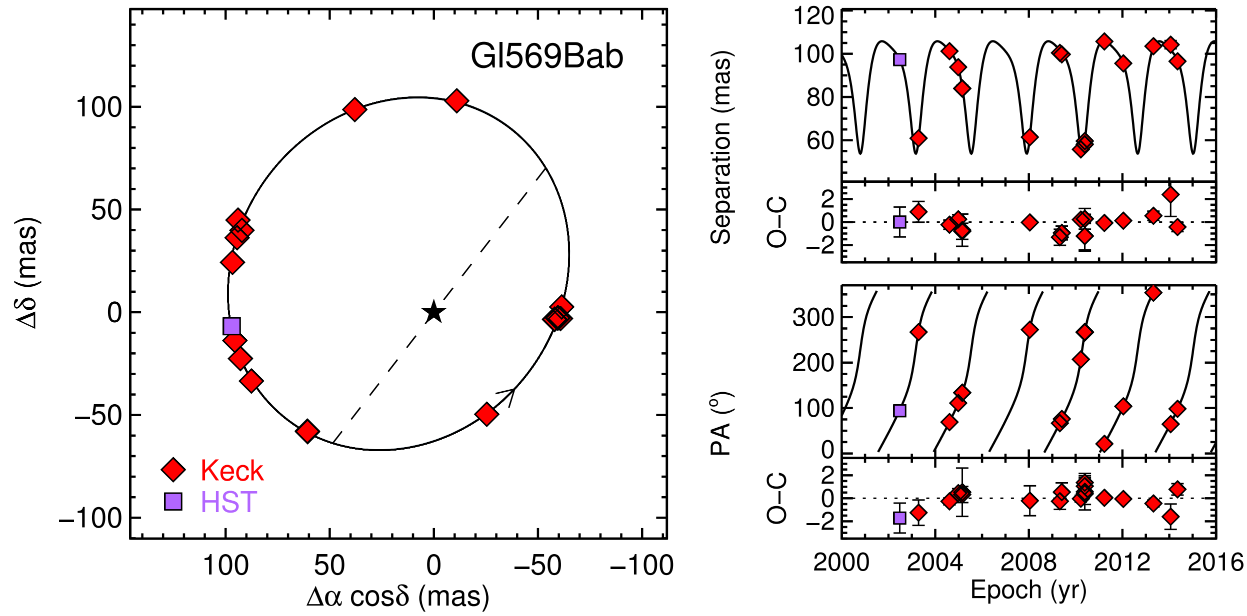

Fig. 1.— (Continued)

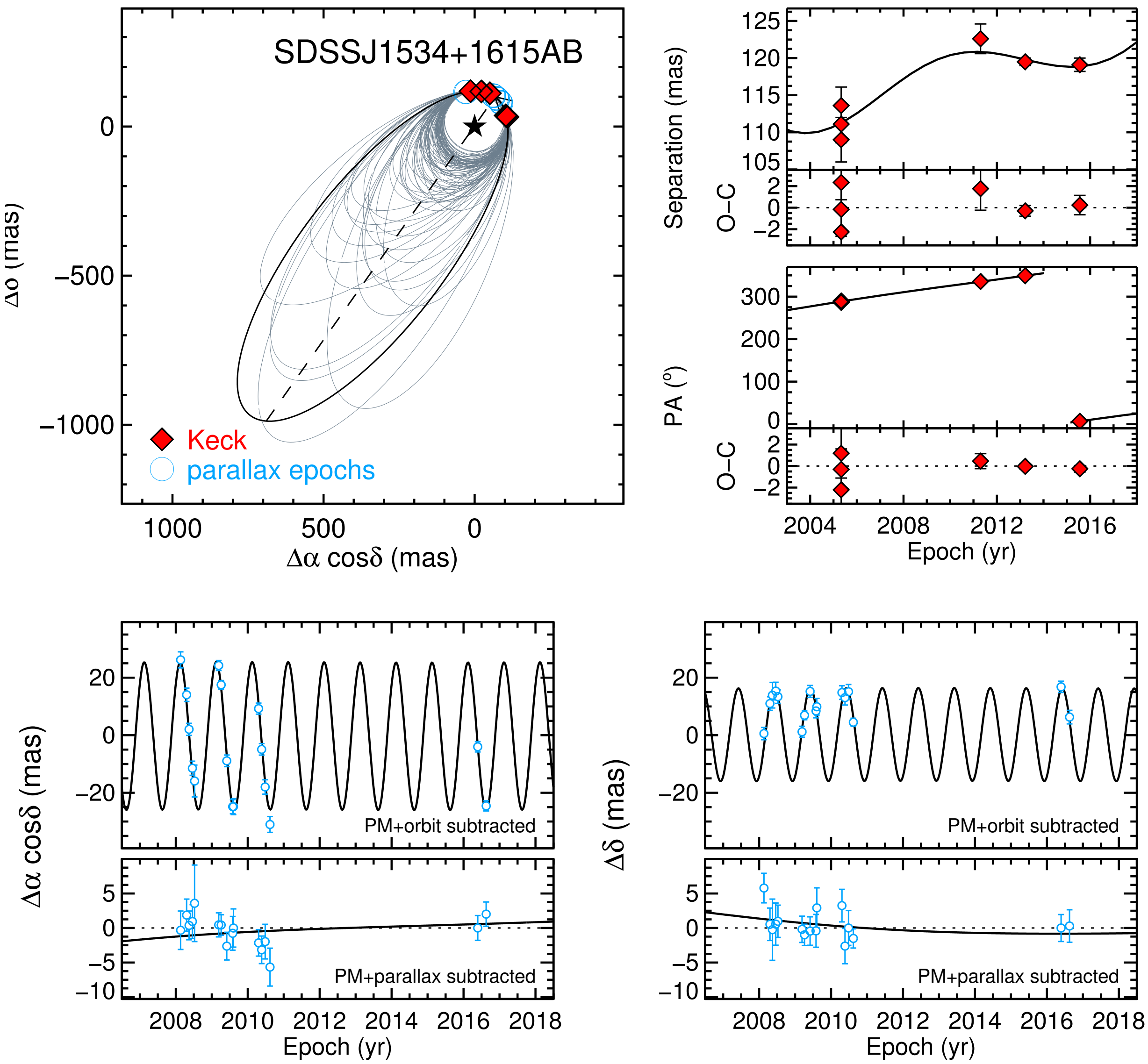

Fig. 1.— (Continued)

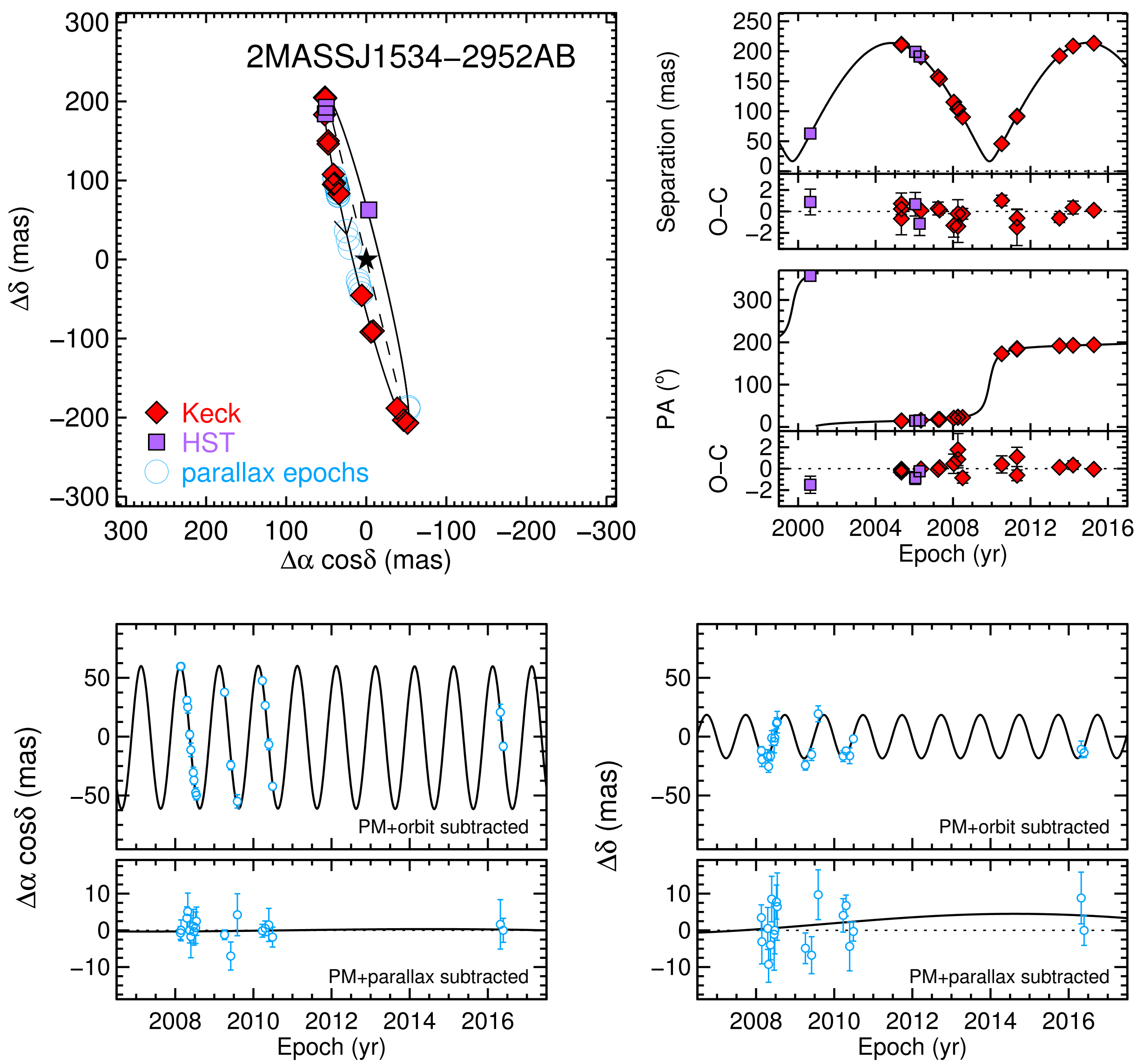

Fig. 1.— (Continued)

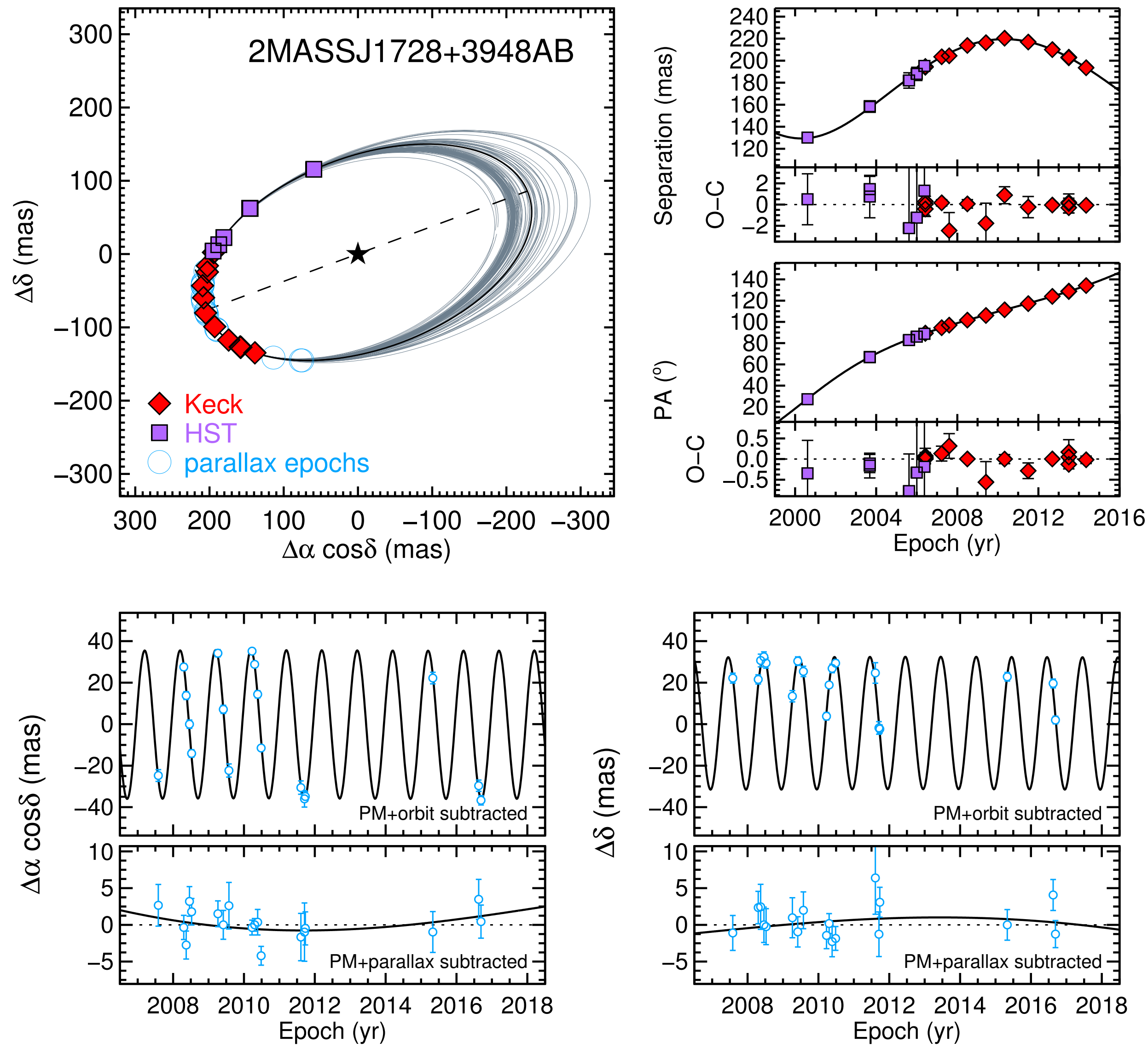

Fig. 1.— (Continued)

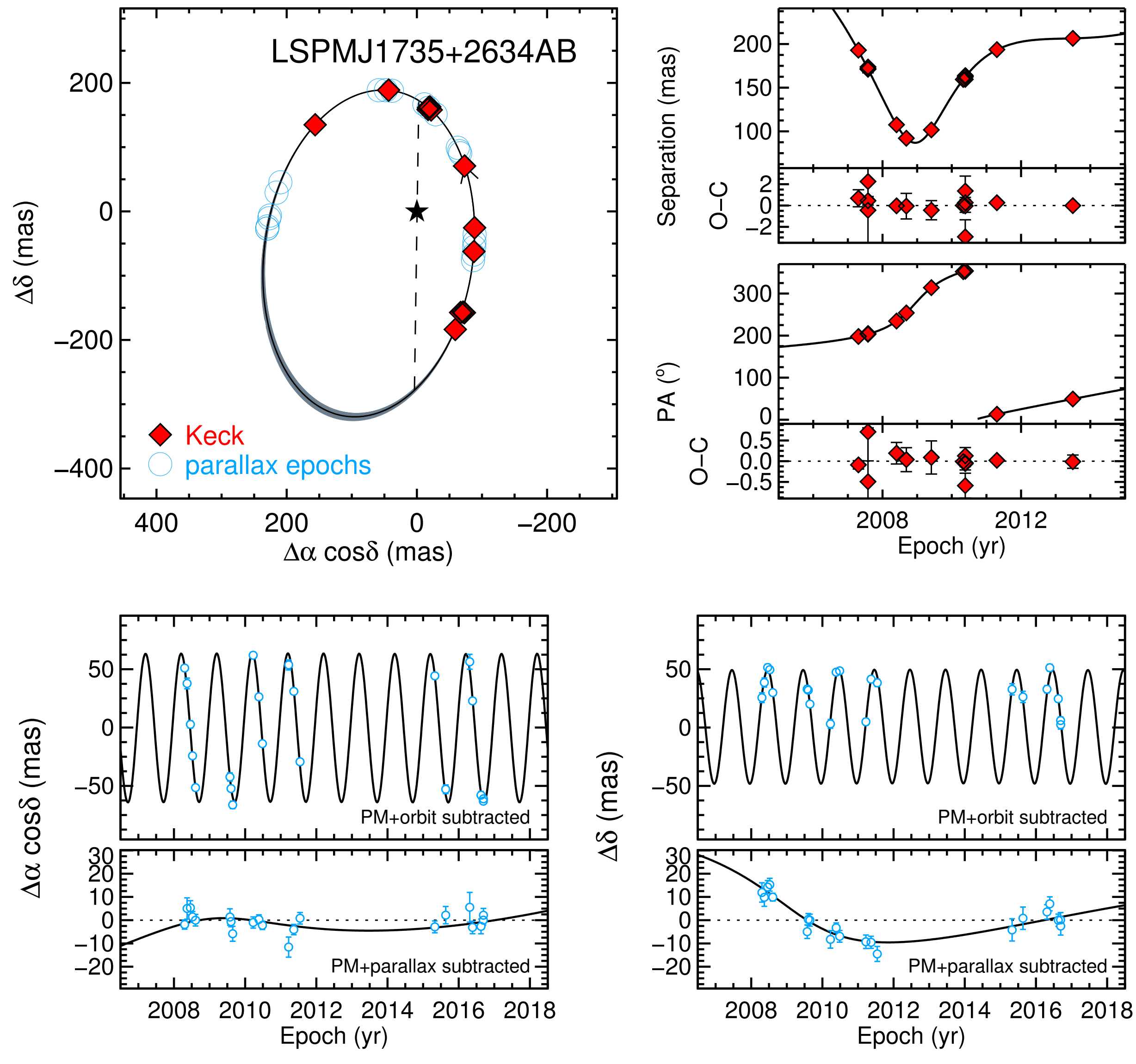

Fig. 1.— (Continued)

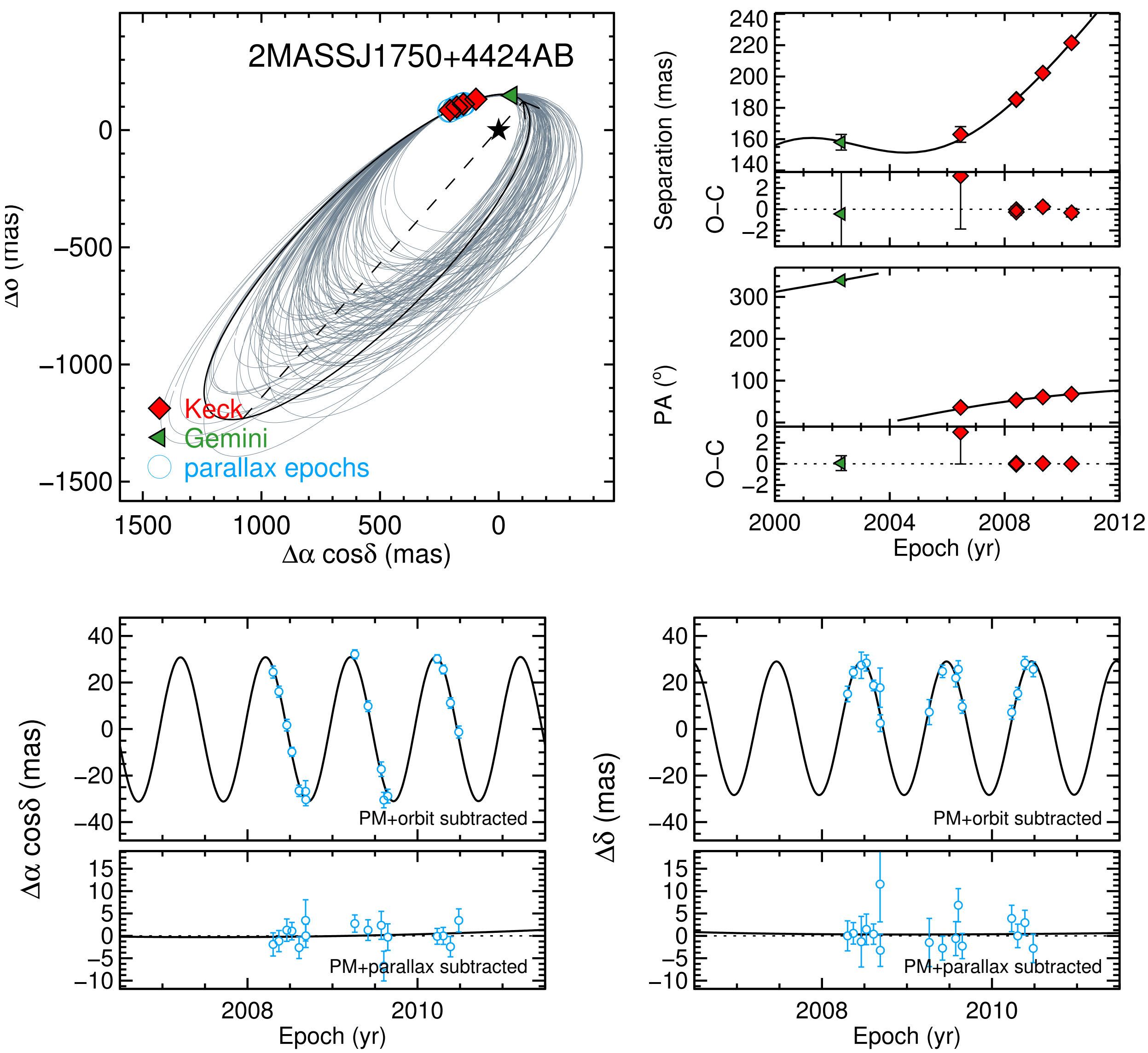

Fig. 1.— (Continued)

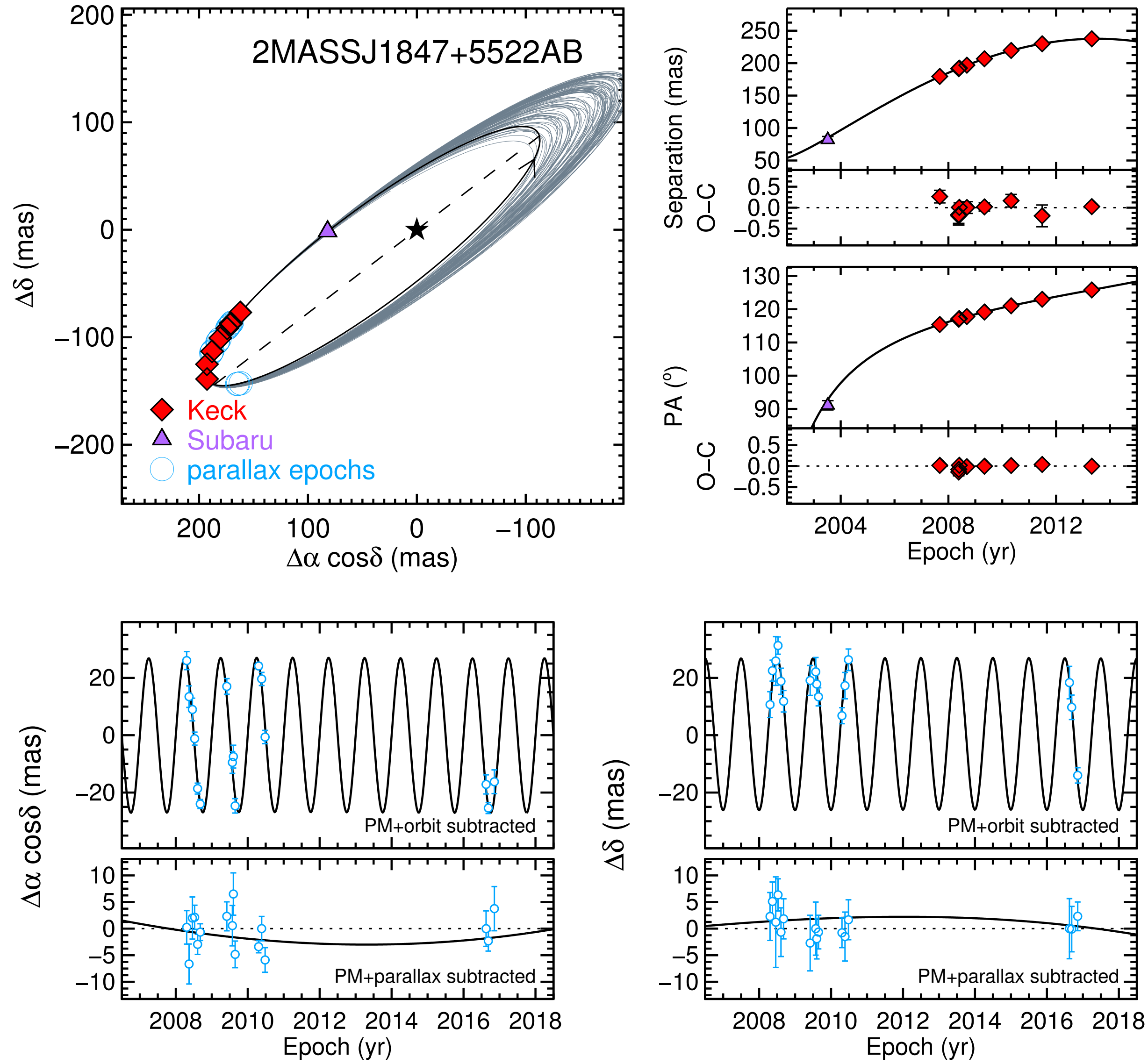

Fig. 1.— (Continued)

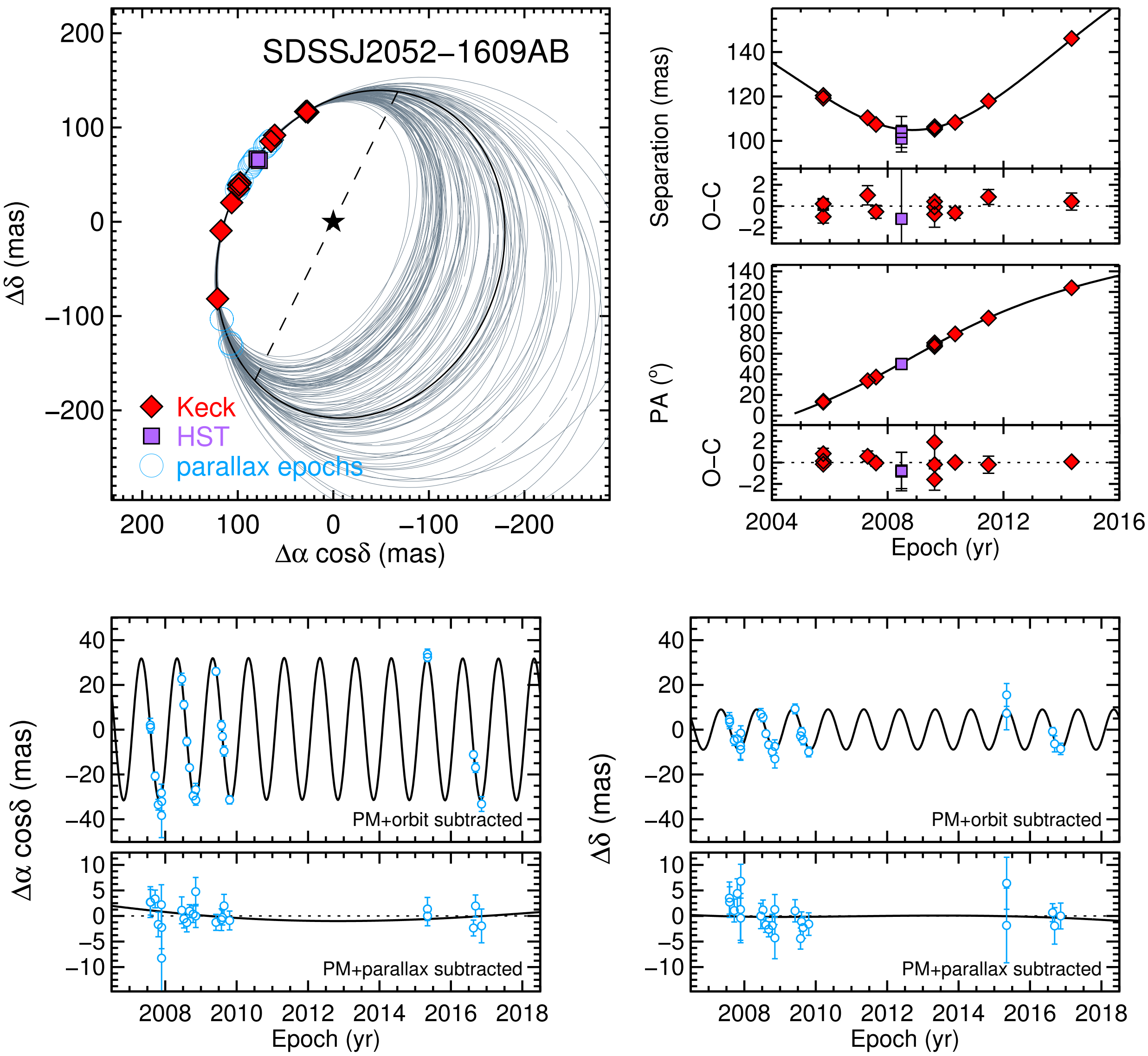

Fig. 1.— (Continued)

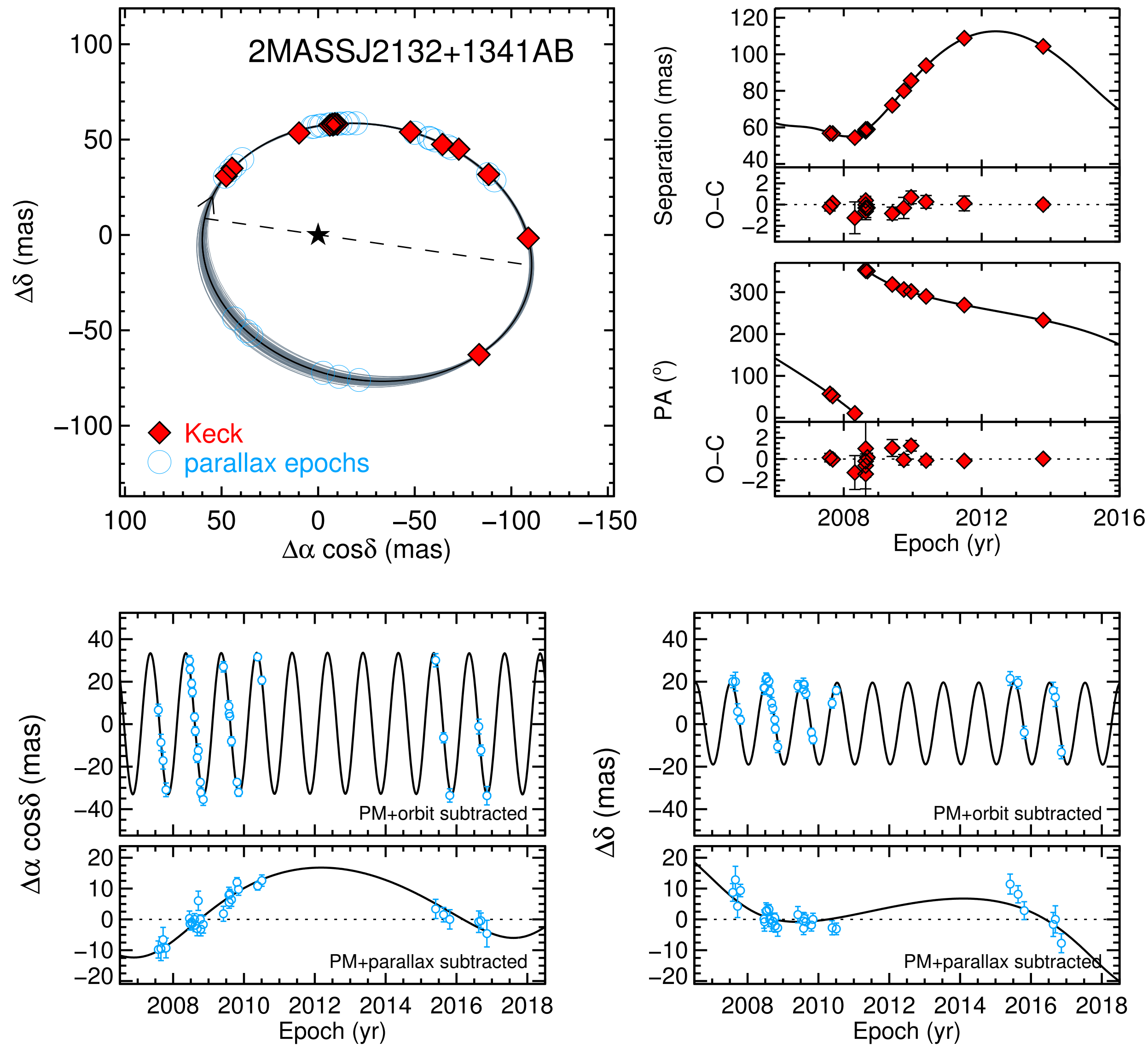

Fig. 1.— (Continued)

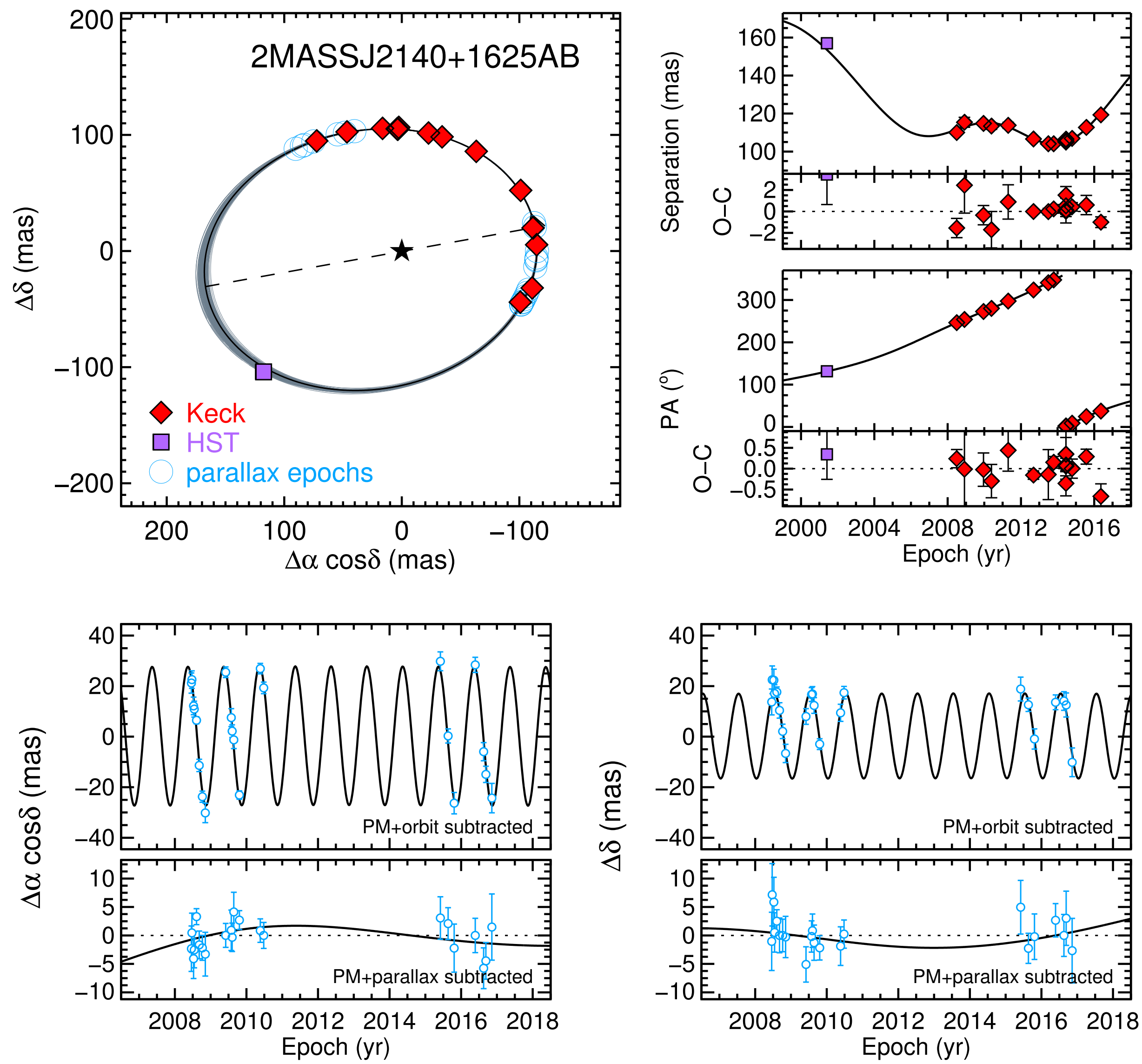

Fig. 1.— (Continued)

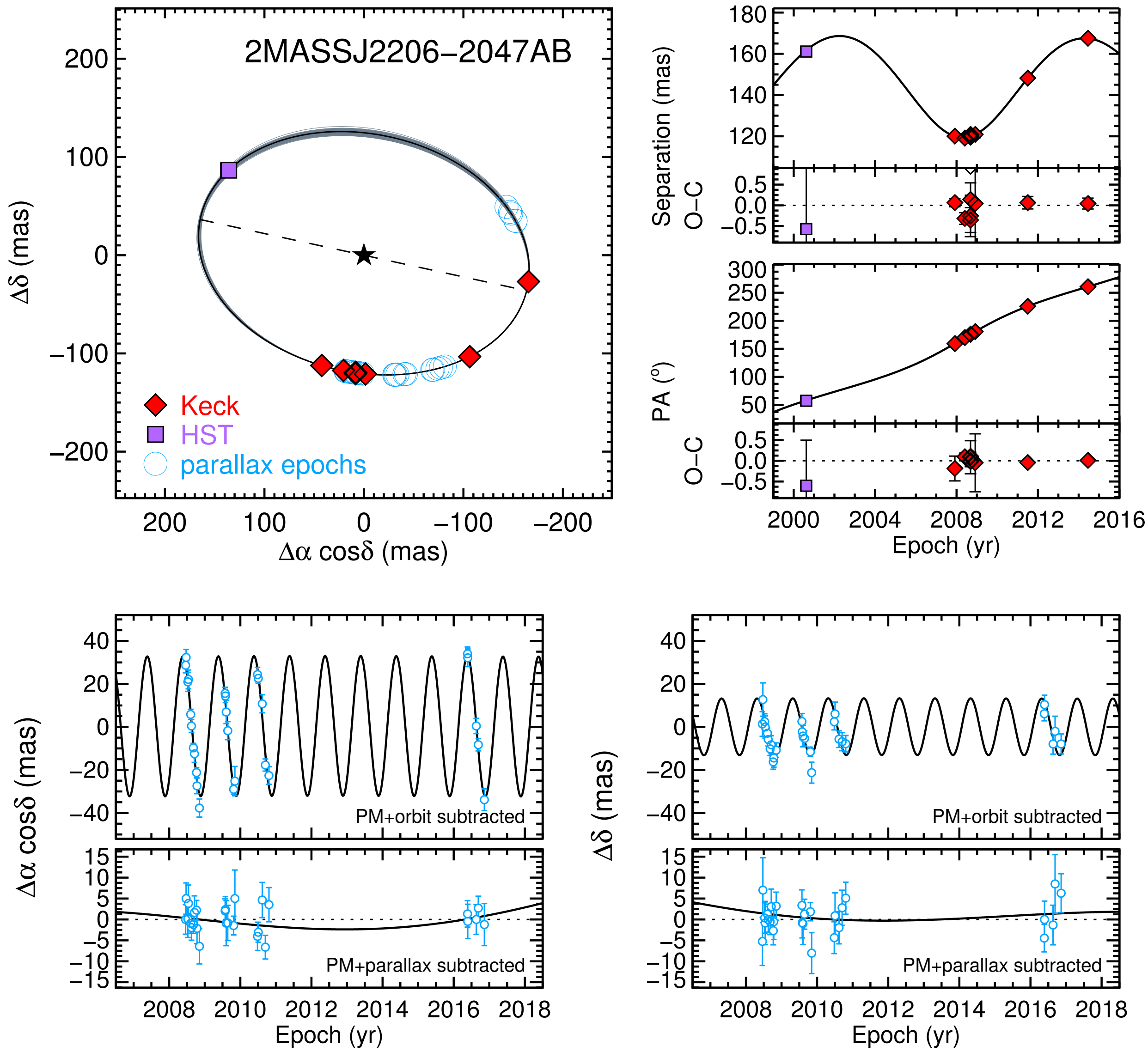

Fig. 1.— (Continued)

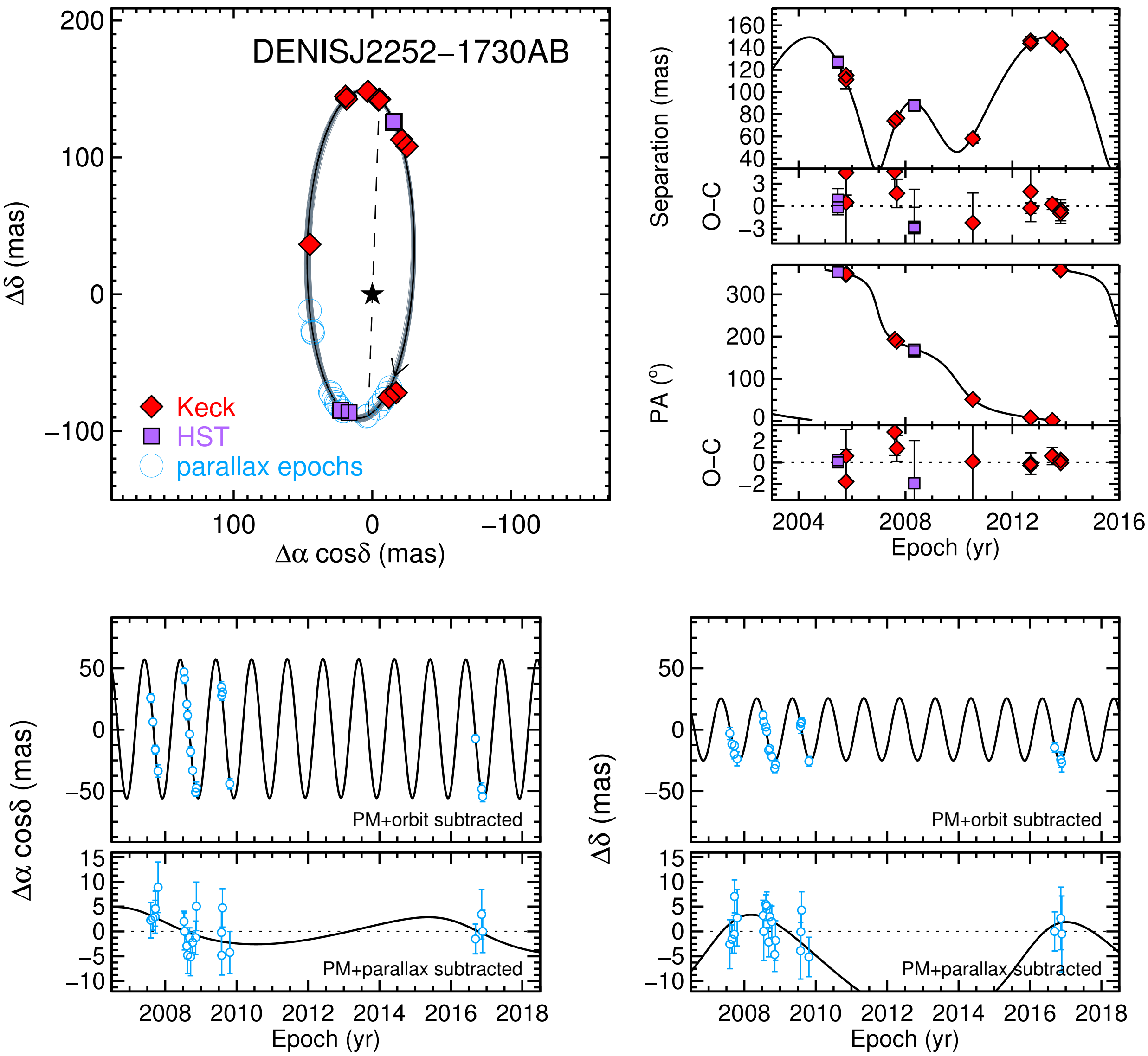

Fig. 1.— (Continued)

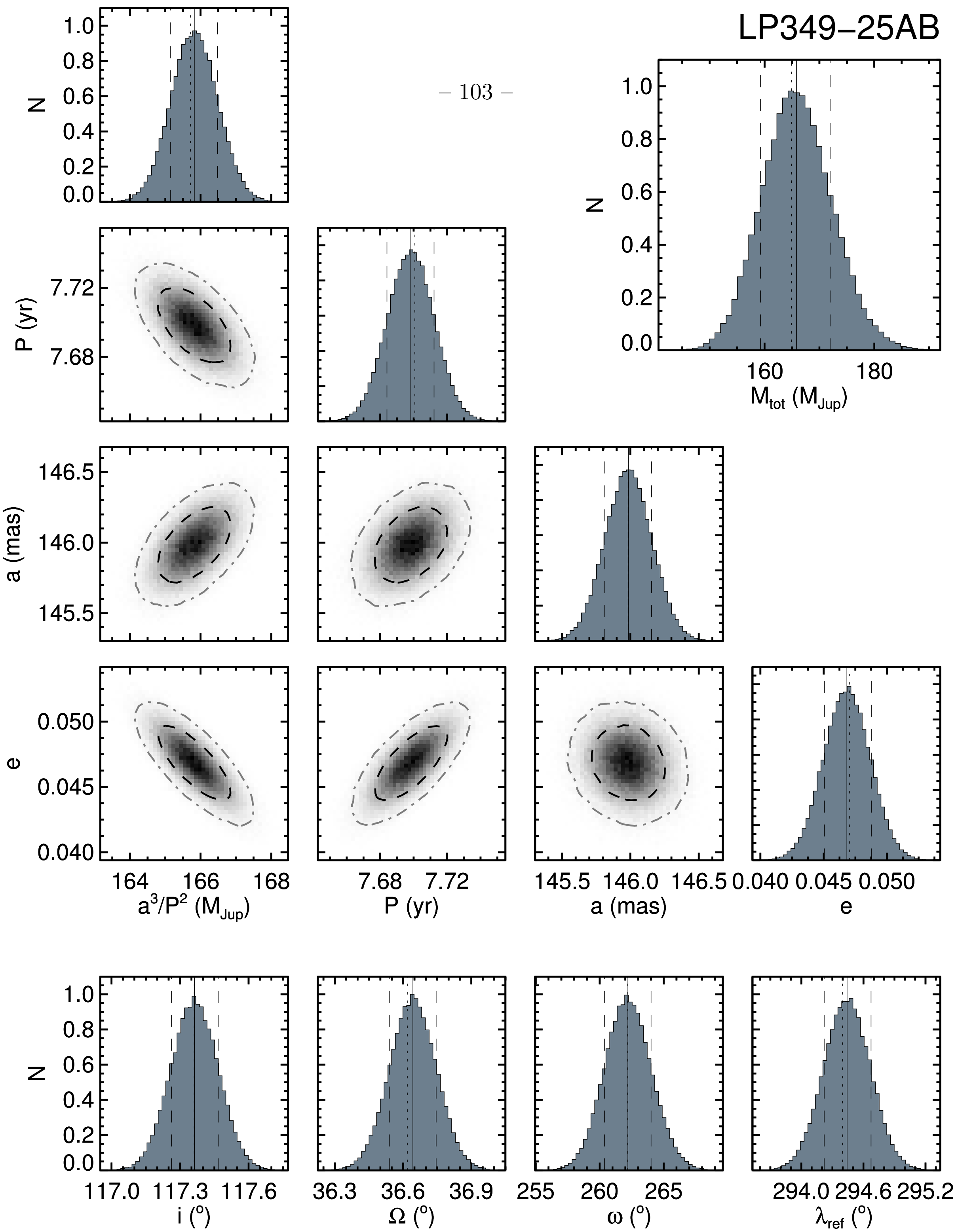

Fig. 2.— Posterior distributions of orbital parameters from our MCMC analysis. In histograms, solid lines show the medians, dotted lines show the best-fit values, and dashed lines show the 68.3% (1σ) credible intervals. In contour plots, regions containing 68.3% and 95.4% of the posterior are indicated by black dashed lines and gray dash-dotted lines, respectively. *Top right:* the final posterior in total system mass after including both the orbit and parallax uncertainties. *Middle triangle plot:* Histograms and correlations for the astrophysical parameters of mass, period, semimajor axis, and eccentricity. In the triangle plot neither mass nor semimajor axis includes the error in distance from the parallax, thus showing the uncertainties and correlations in parameters from the orbit fit alone. *Bottom:* Histograms of the various viewing angles that are part of the orbit fit.

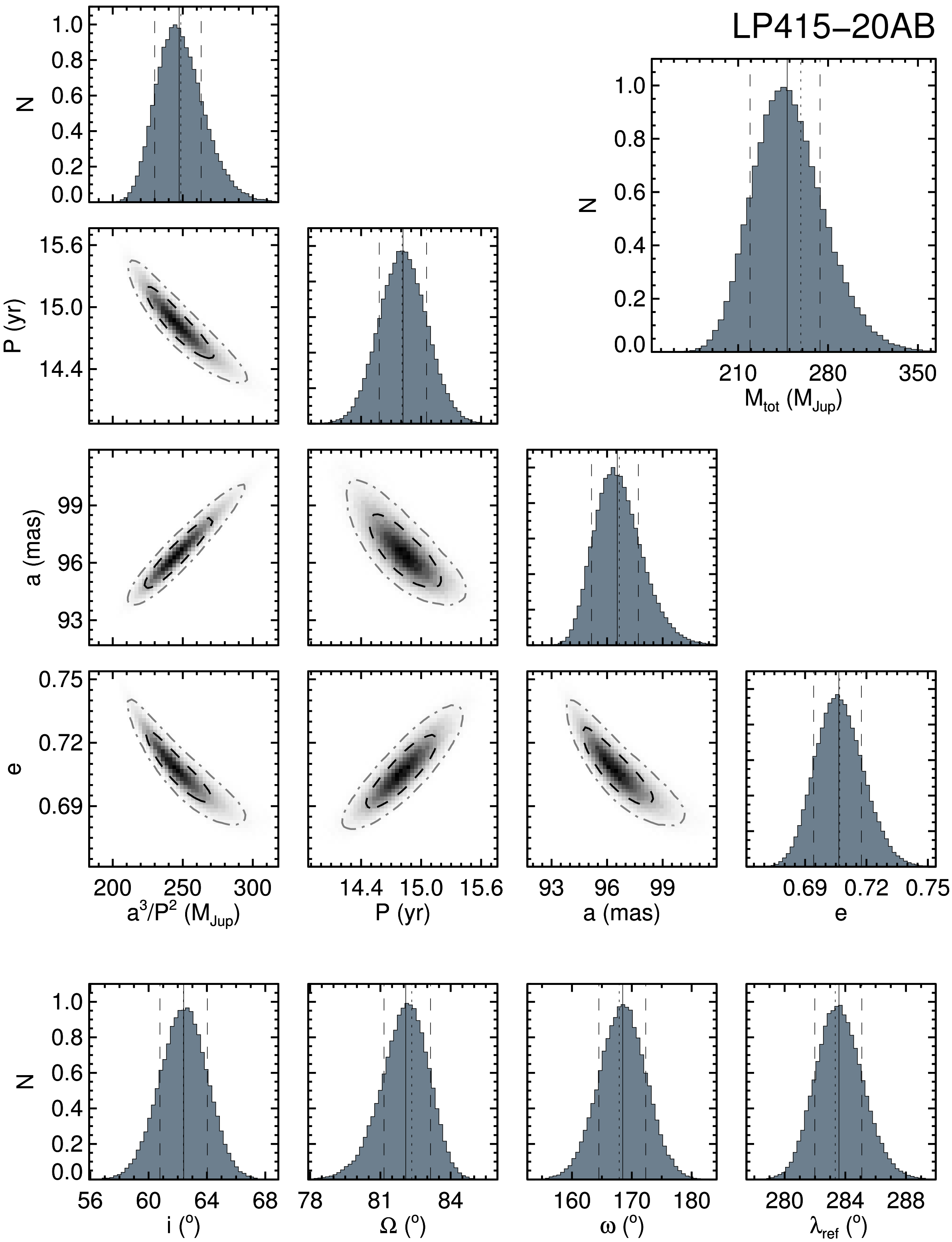

Fig. 2.— (Continued)

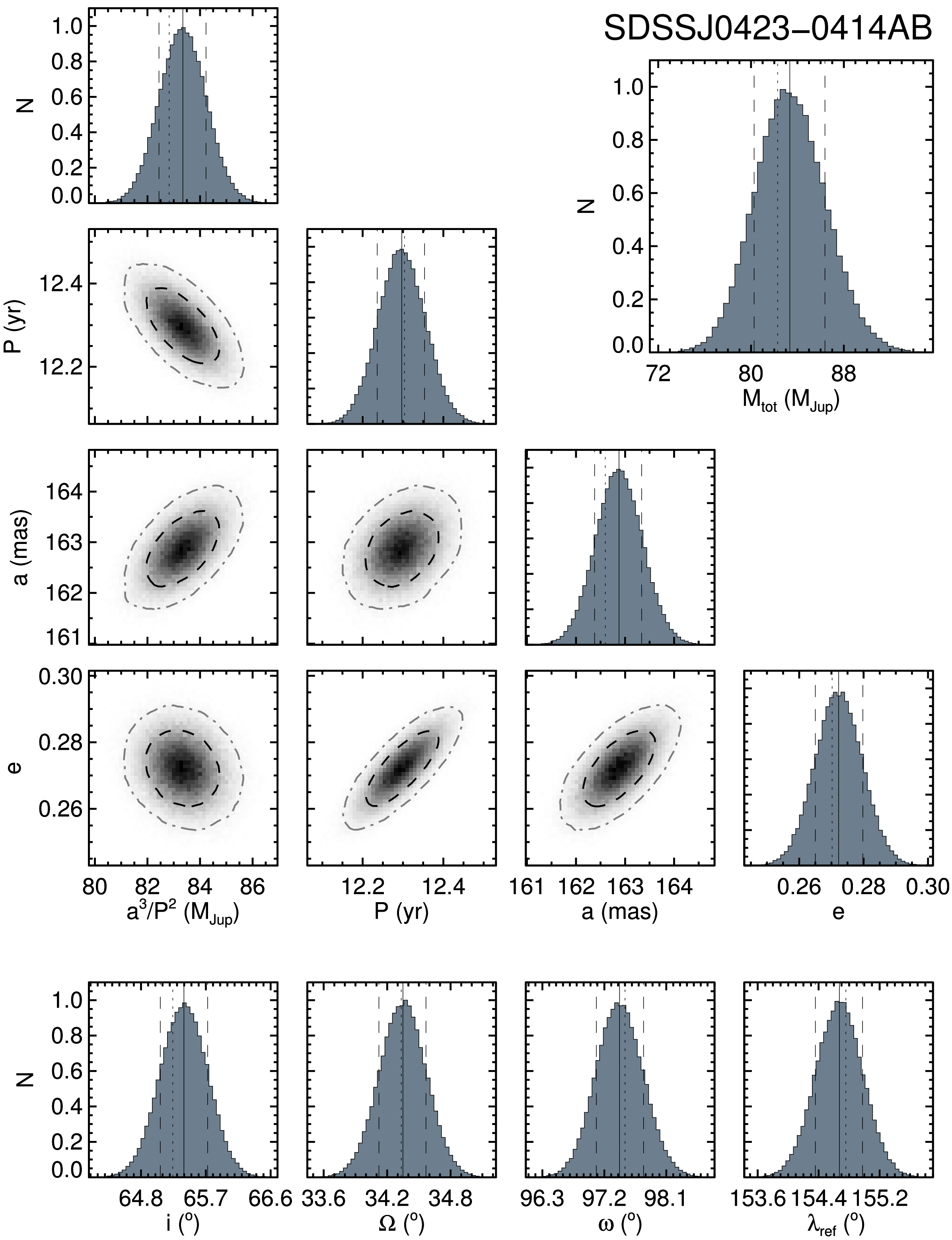

Fig. 2.— (Continued)

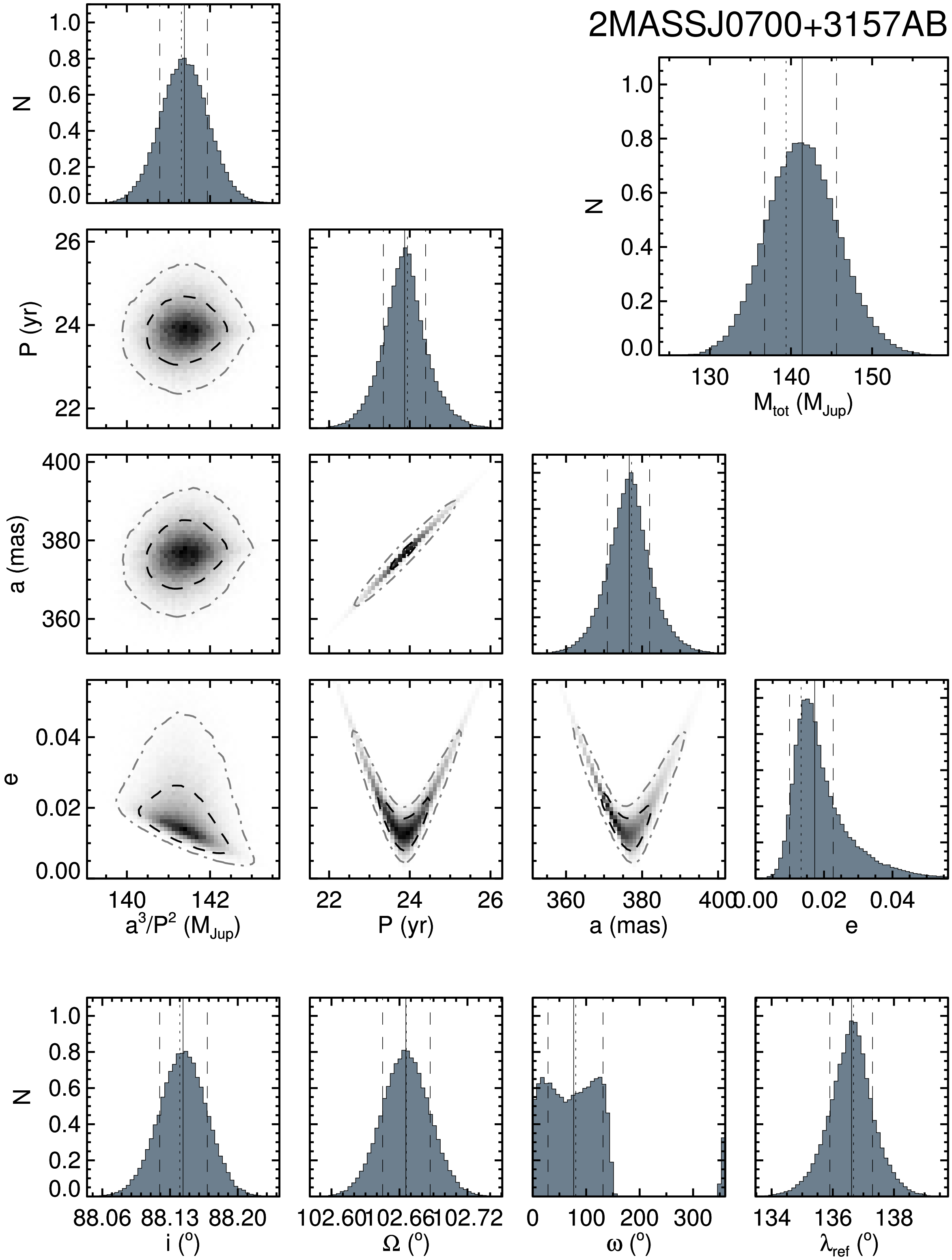

Fig. 2.— (Continued)

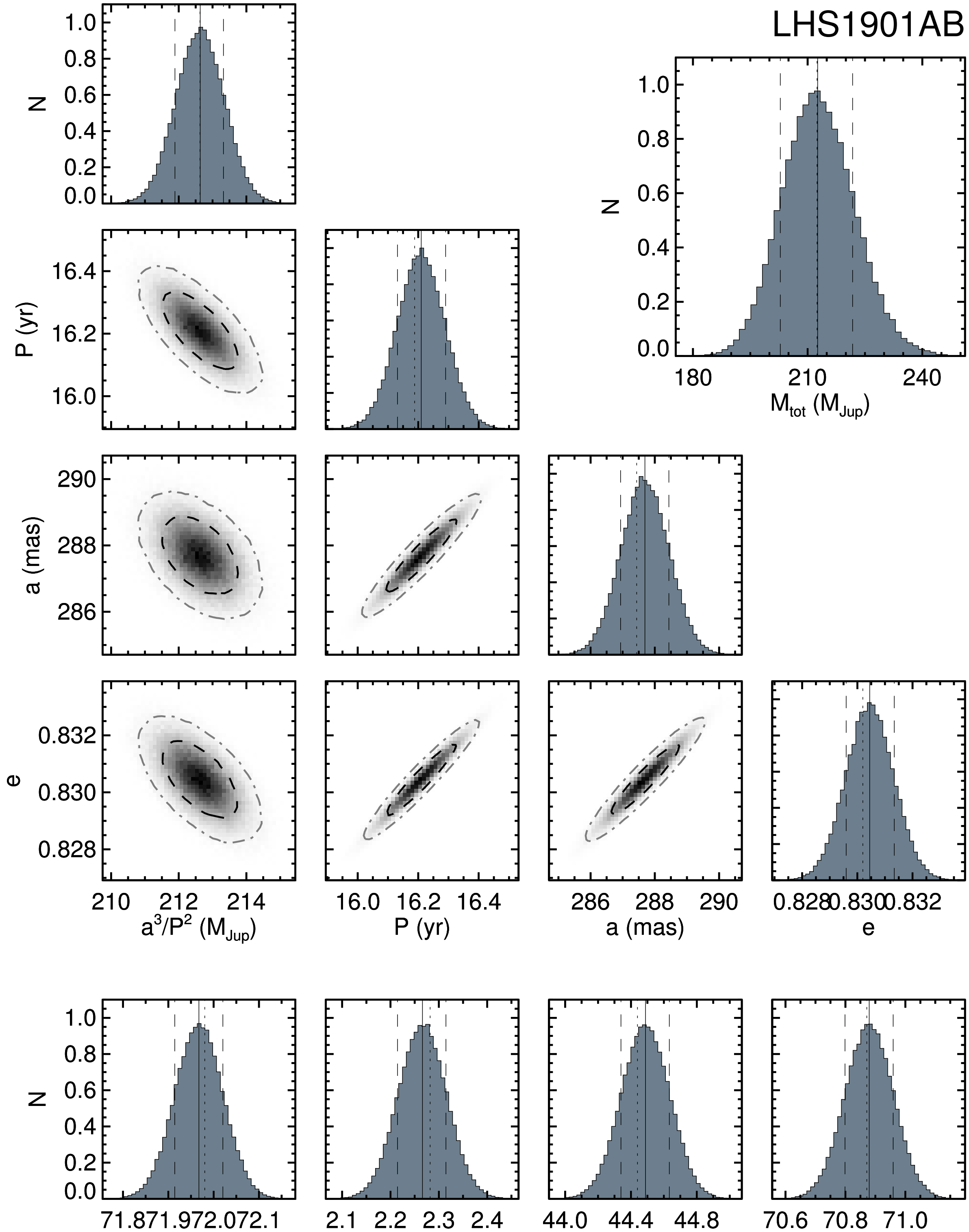

Fig. 2.— (Continued)

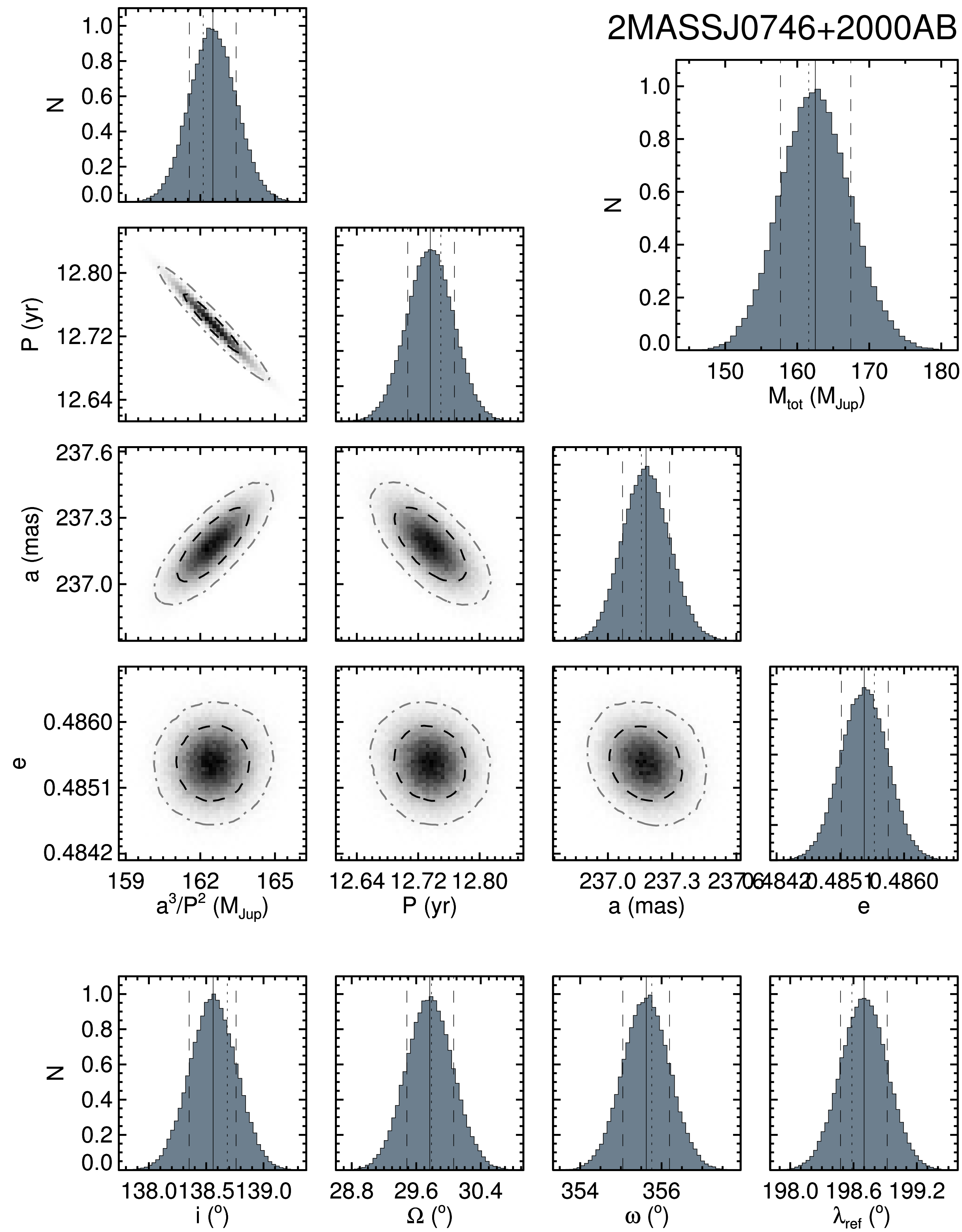

Fig. 2.— (Continued)

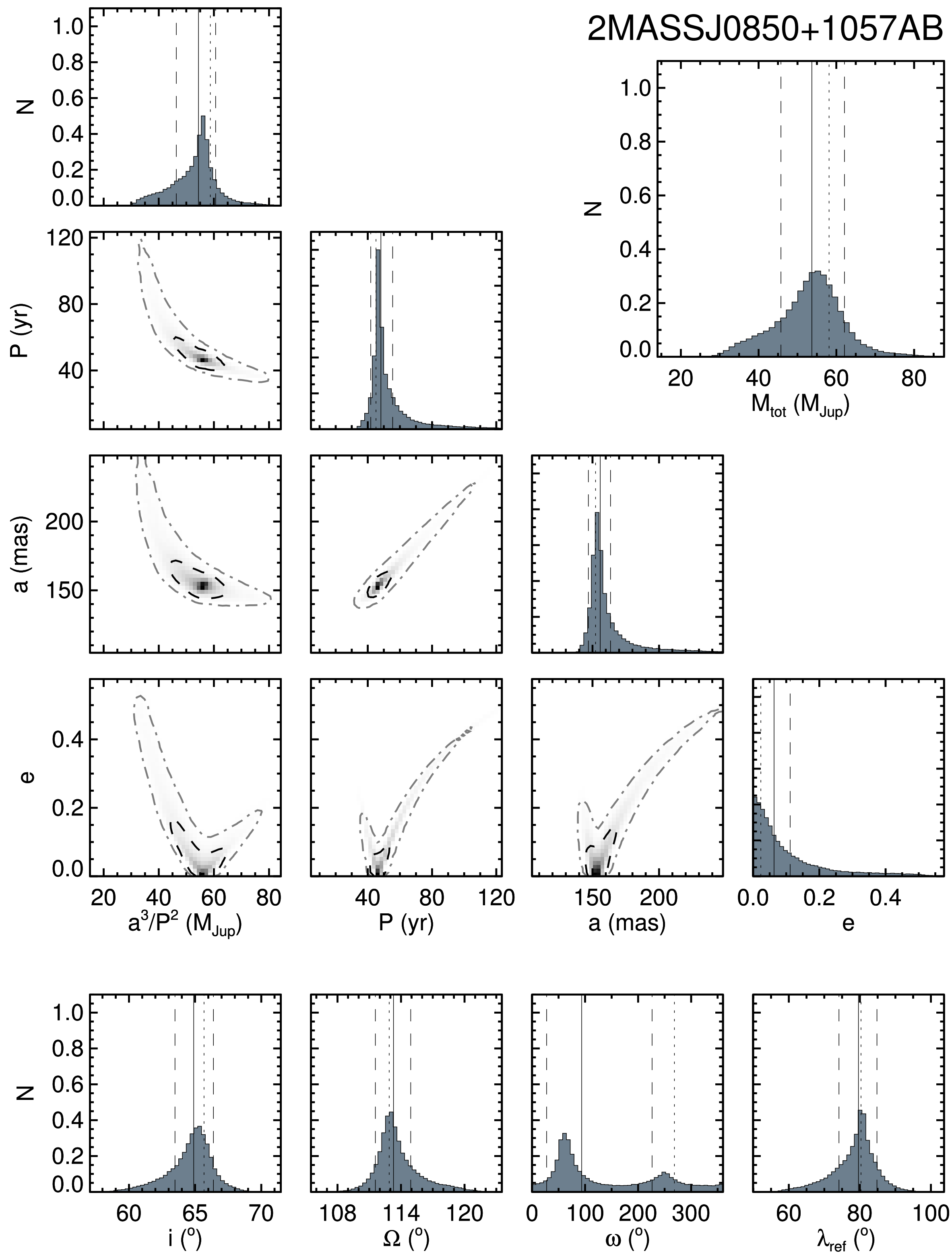

Fig. 2.— (Continued)

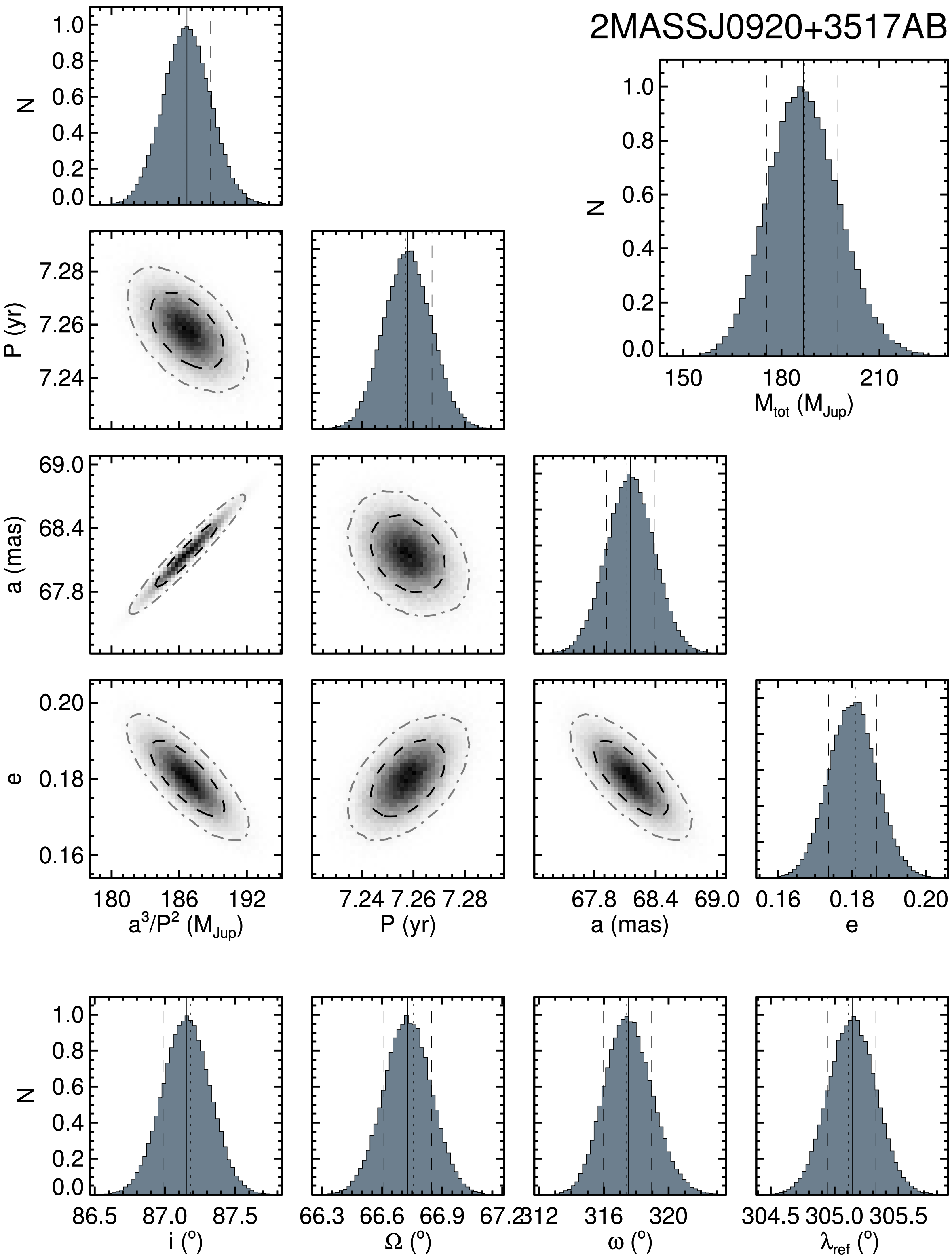

Fig. 2.— (Continued)

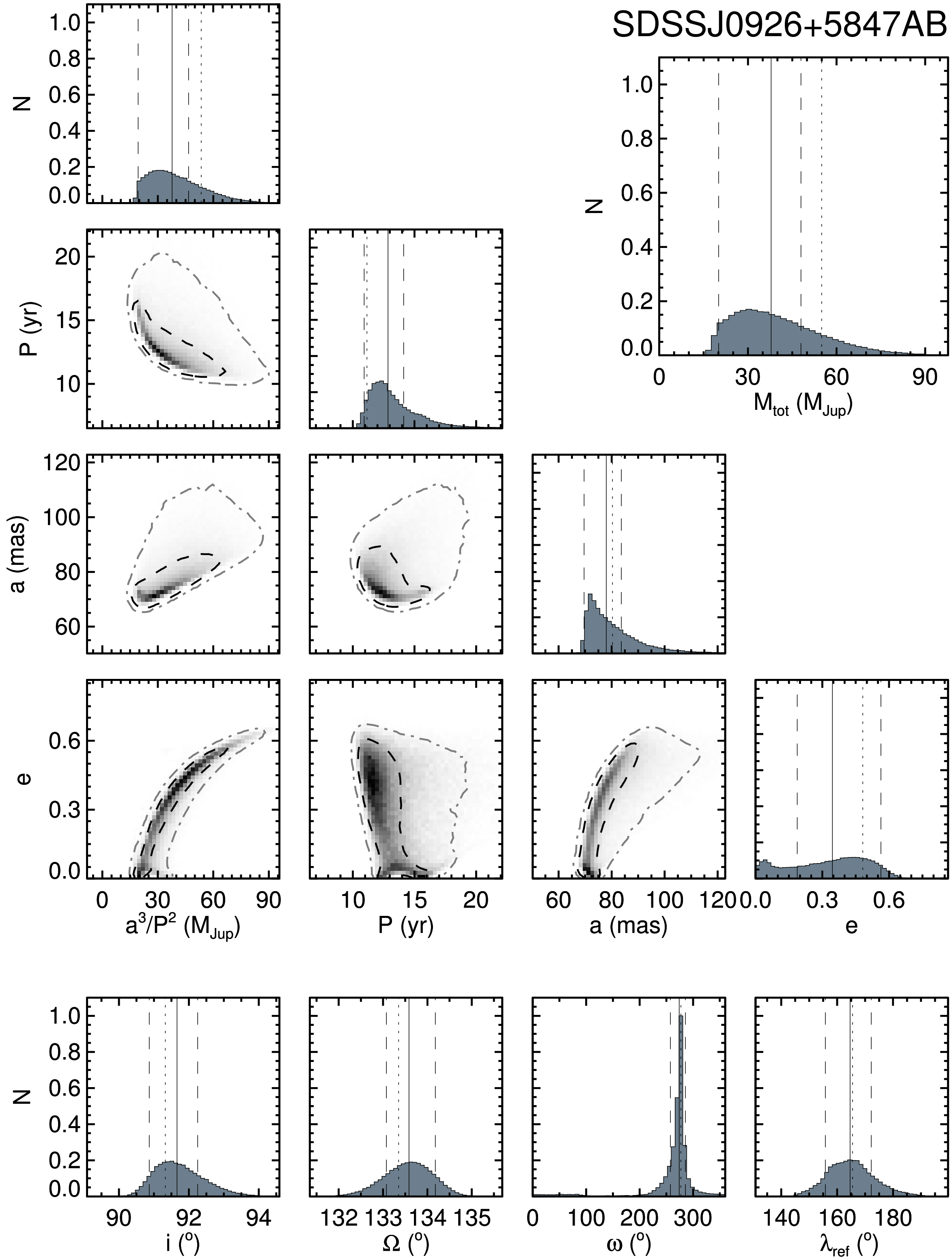

Fig. 2.— (Continued)

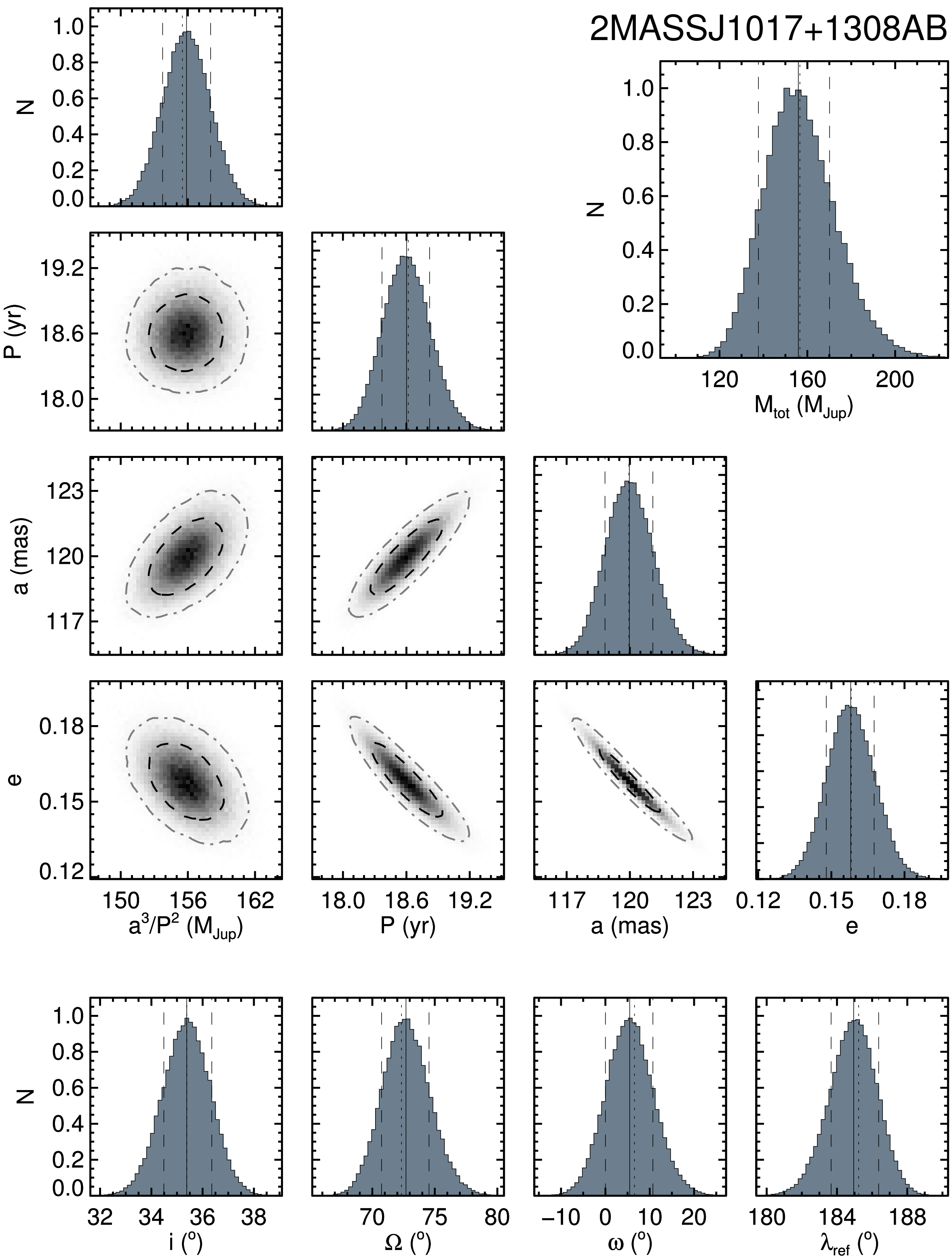

Fig. 2.— (Continued)

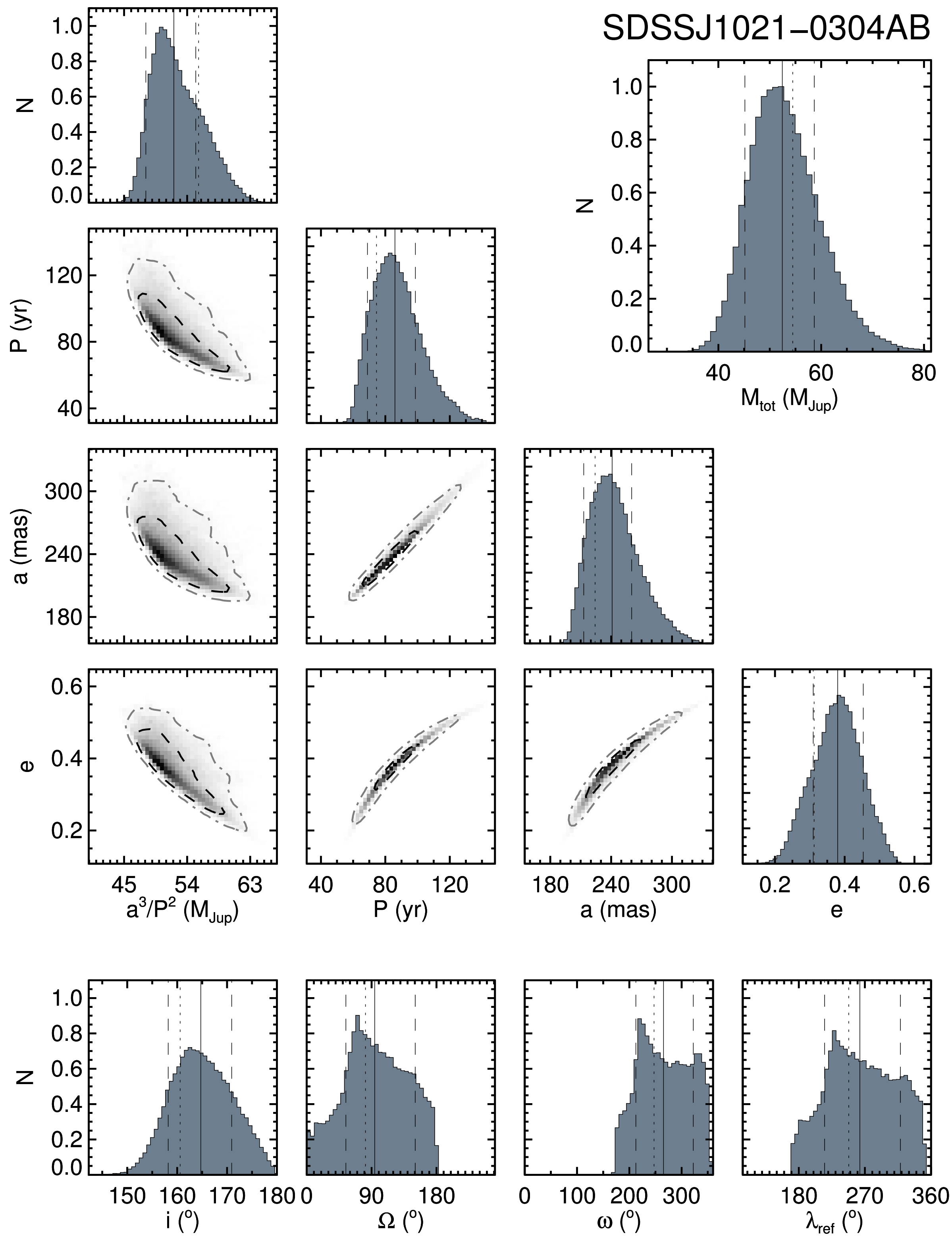

Fig. 2.— (Continued)

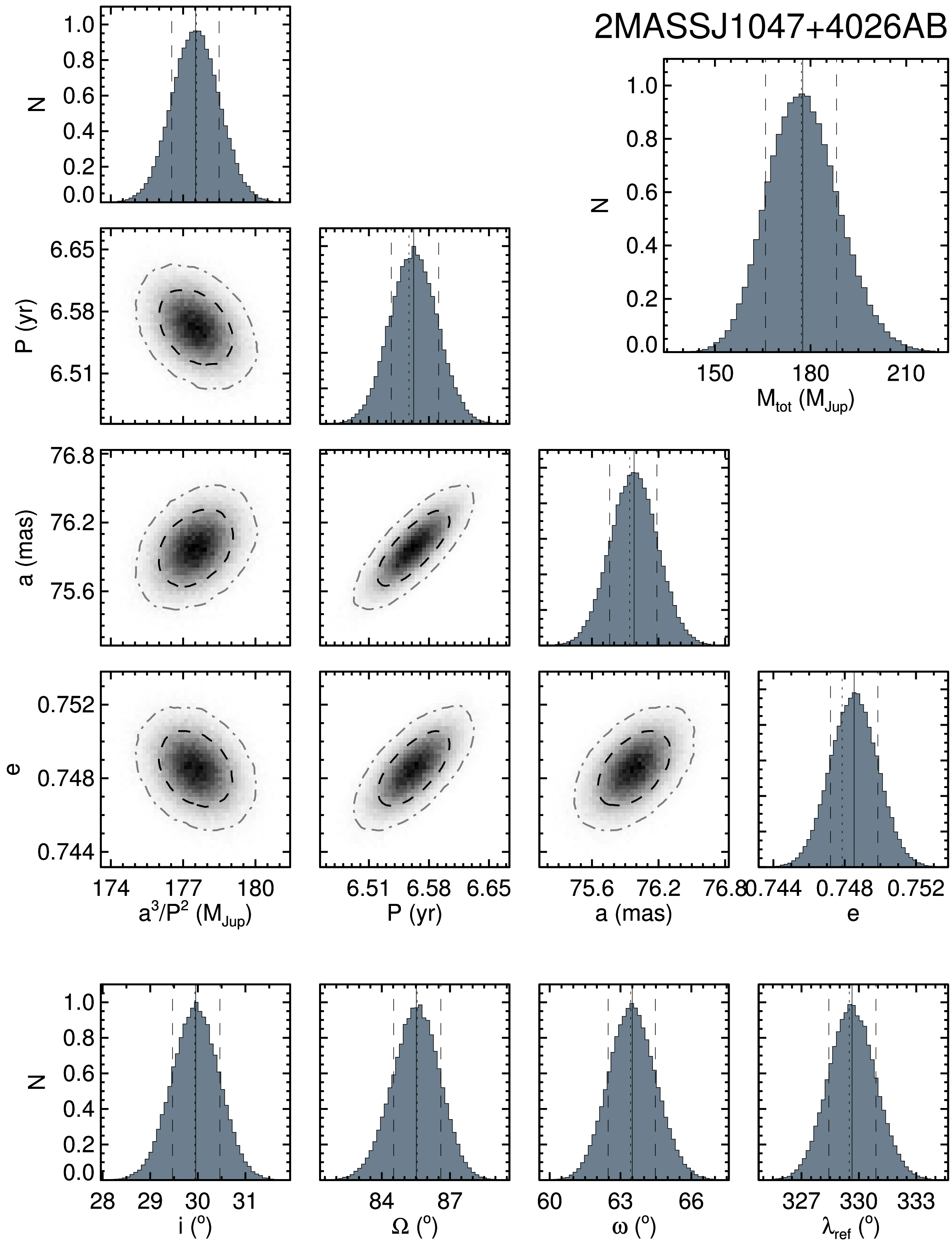

Fig. 2.— (Continued)

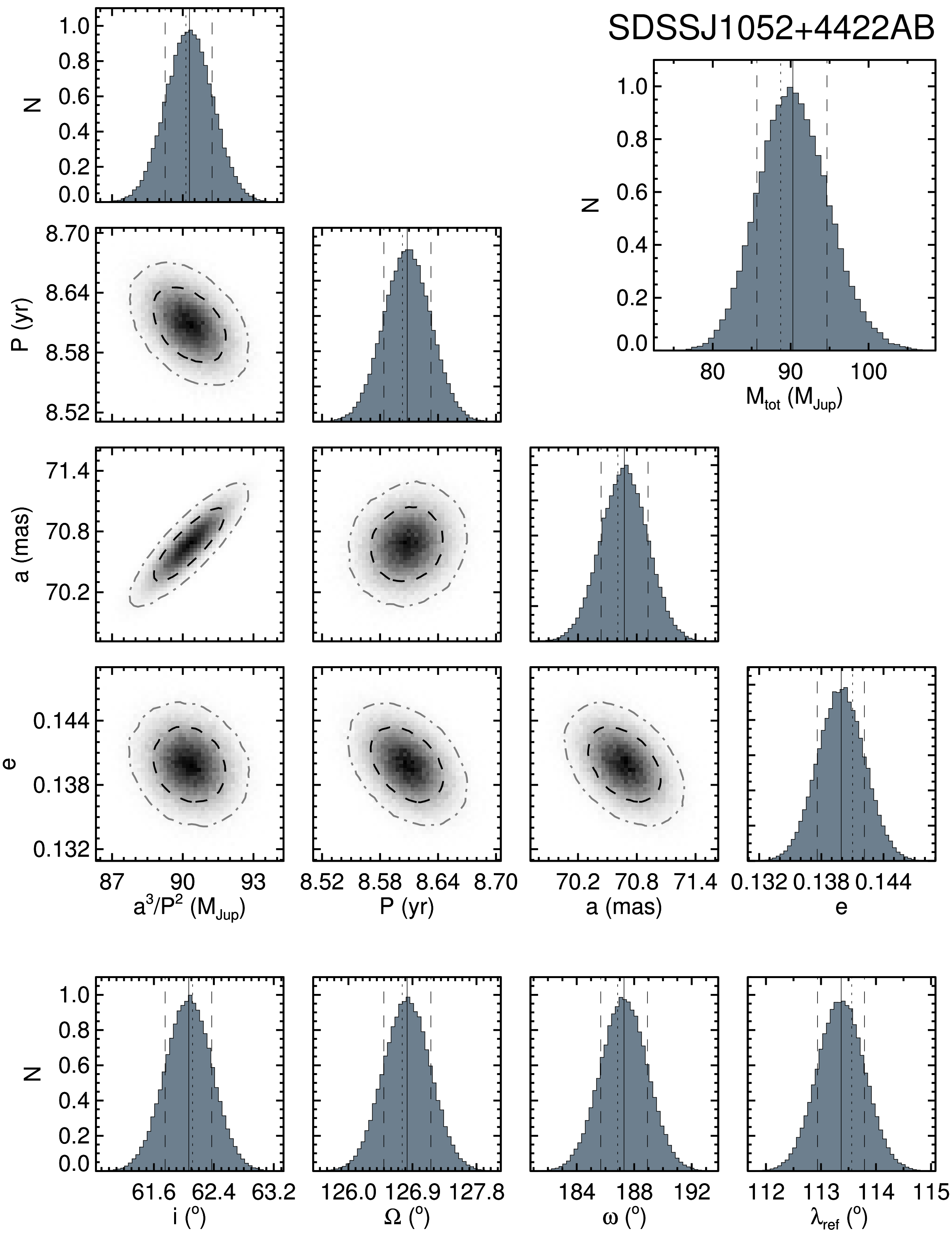

Fig. 2.— (Continued)

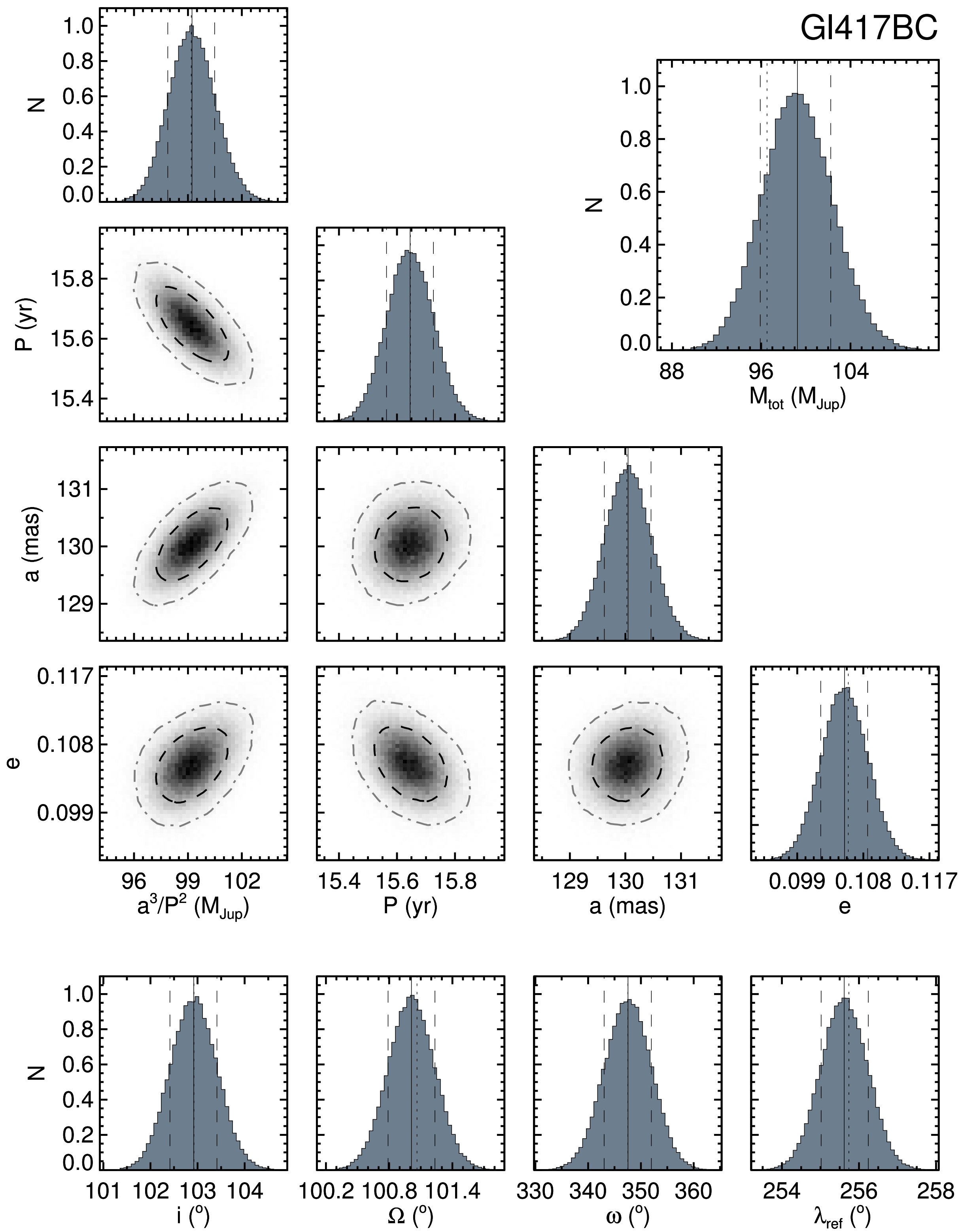

Fig. 2.— (Continued)

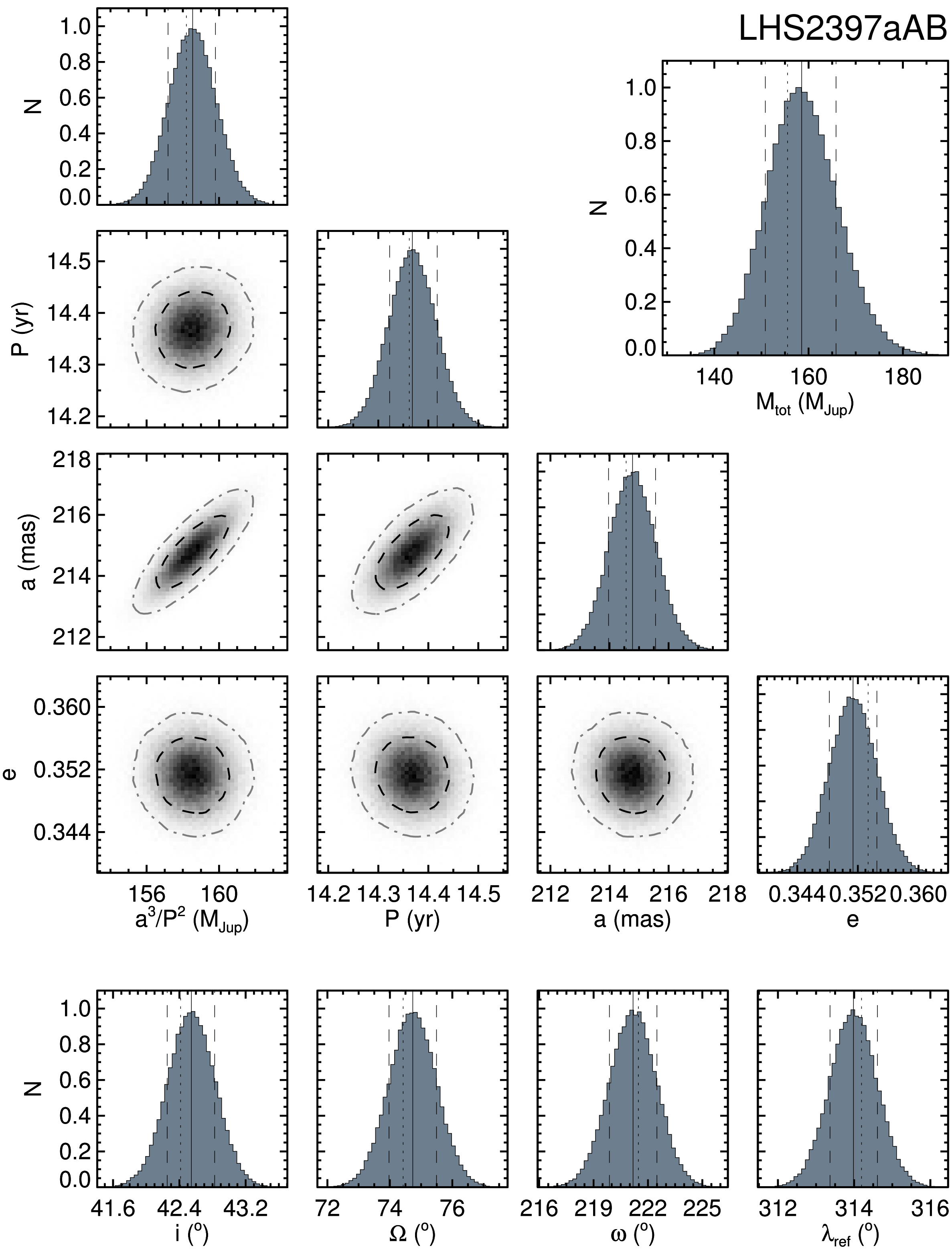

Fig. 2.— (Continued)

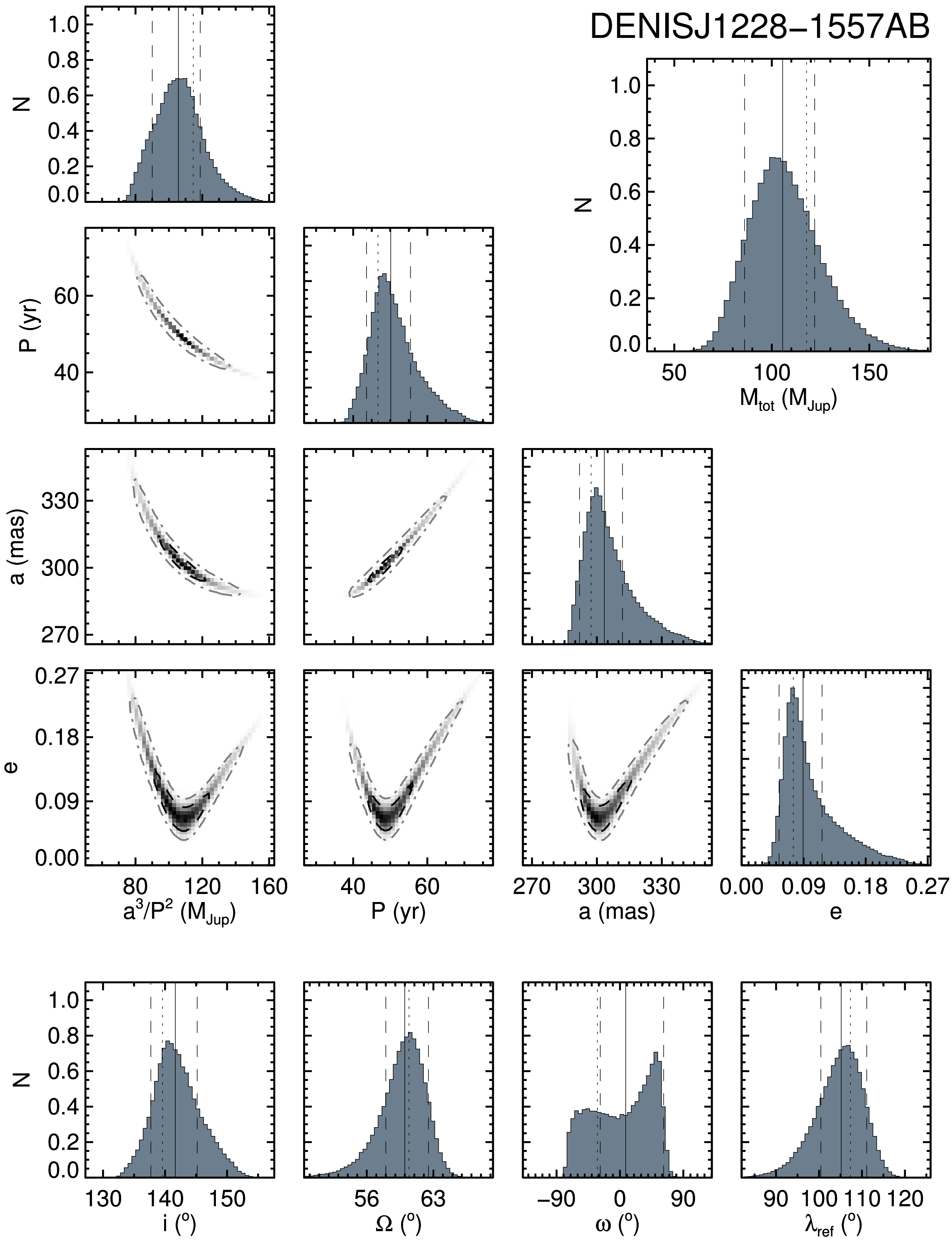

Fig. 2.— (Continued)

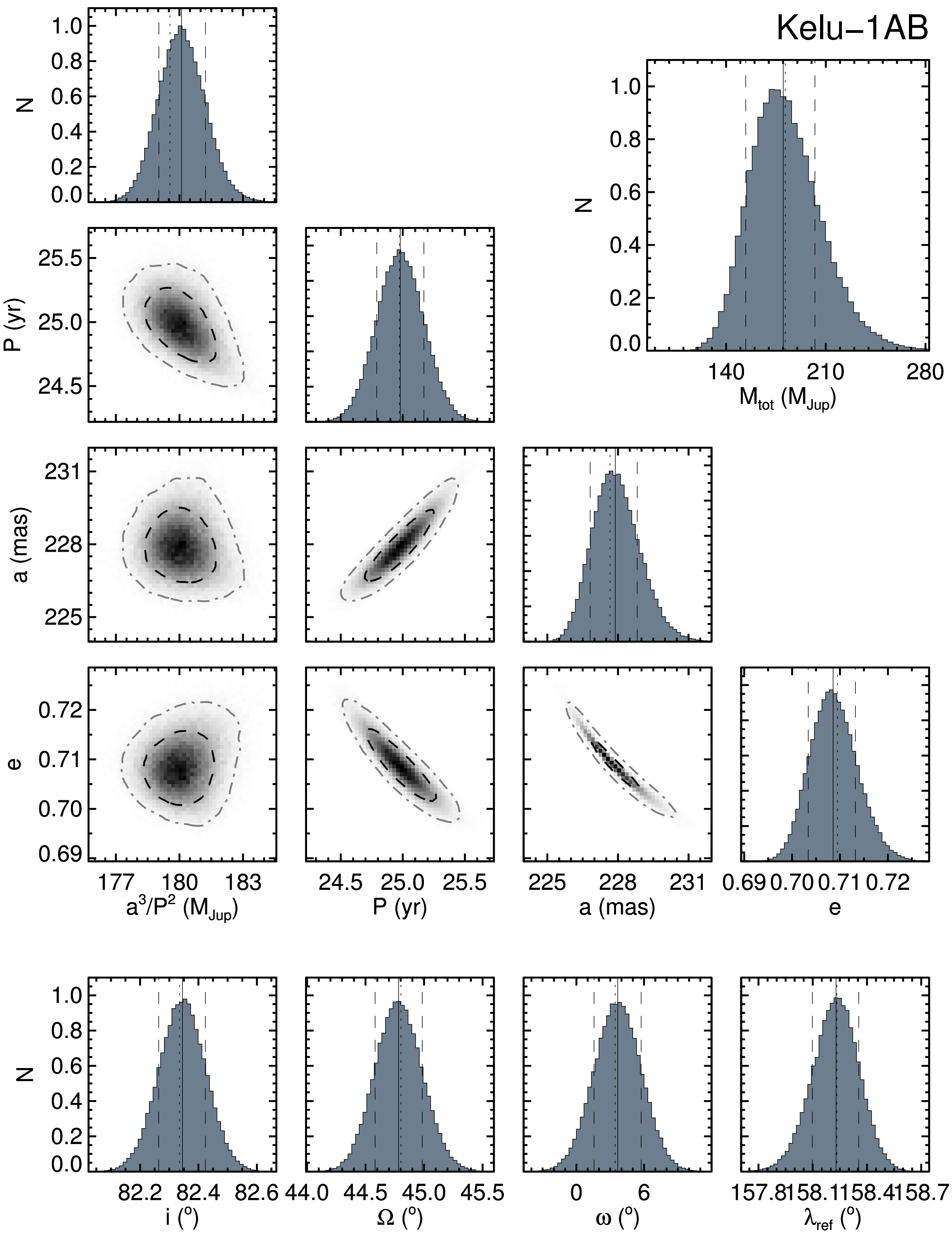

Fig. 2.— (Continued)

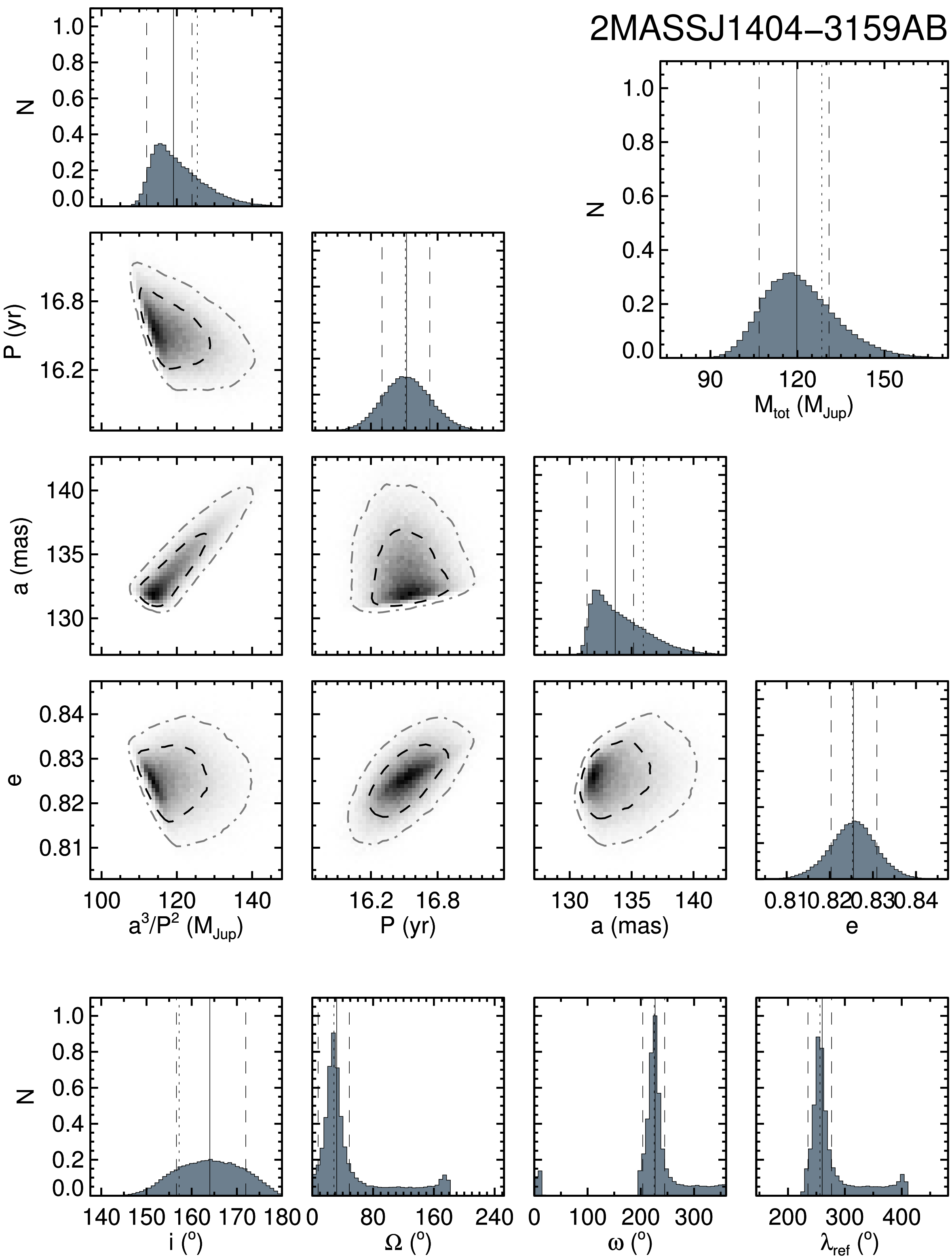

Fig. 2.— (Continued)

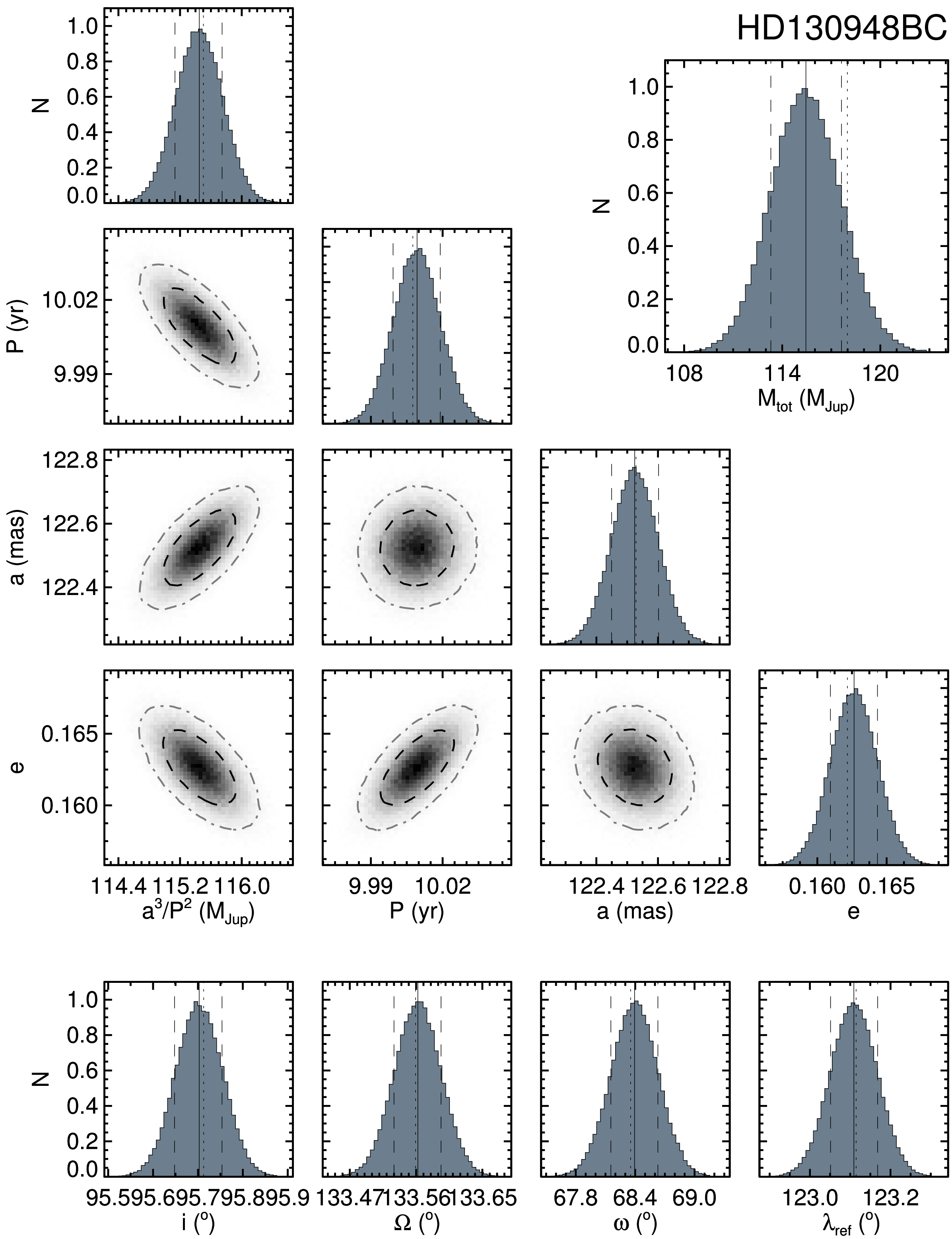

Fig. 2.— (Continued)

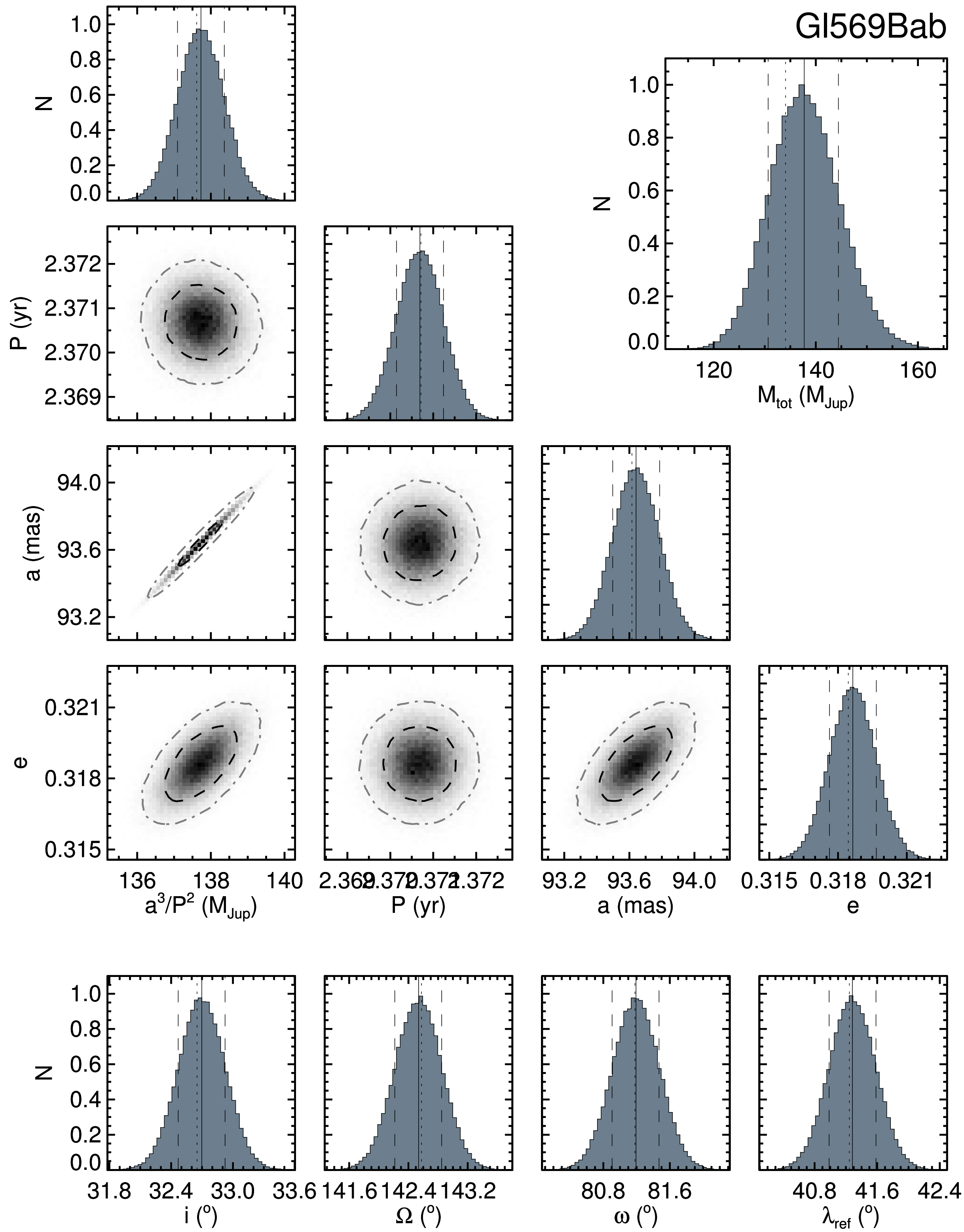

Fig. 2.— (Continued)

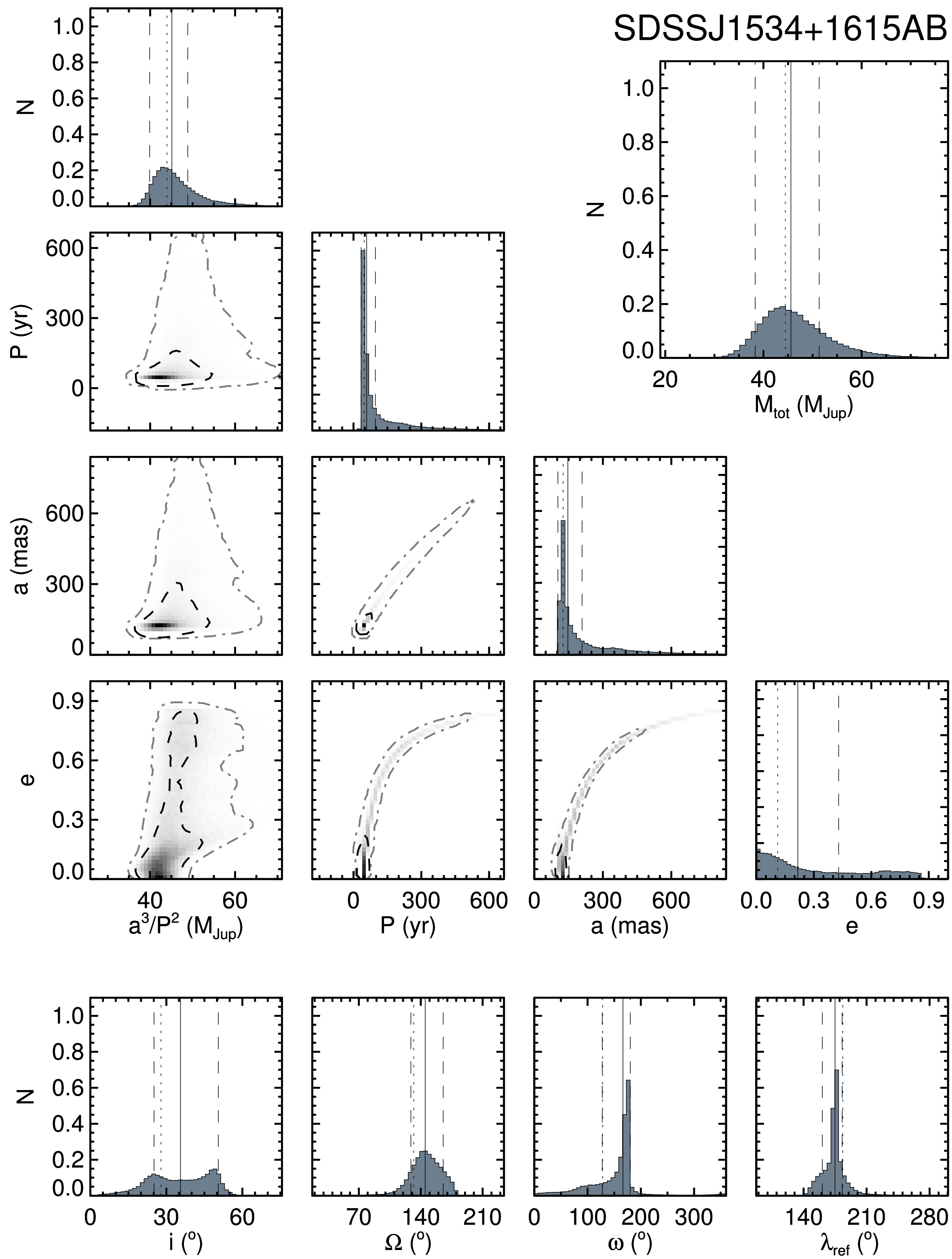

Fig. 2.— (Continued)

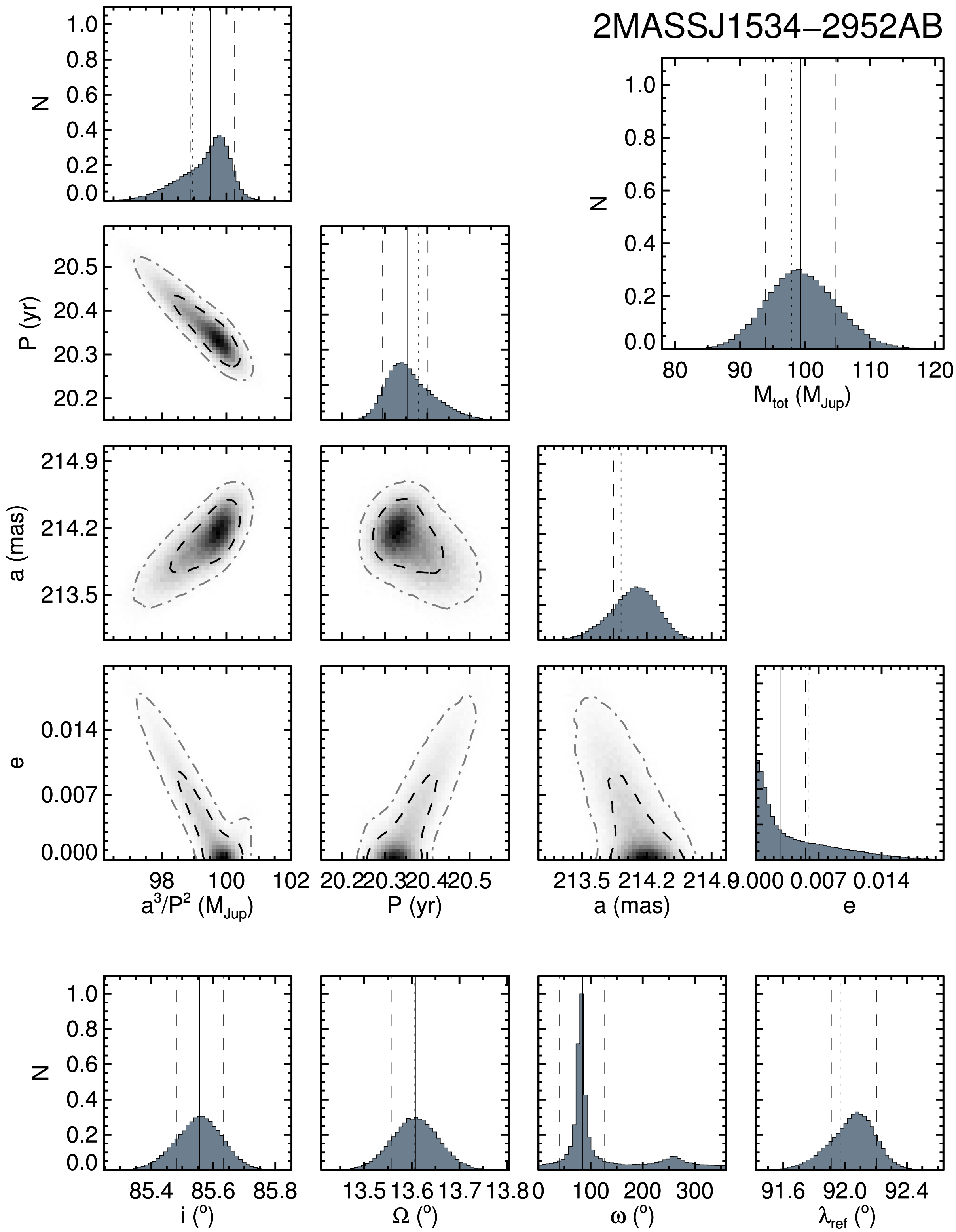

Fig. 2.— (Continued)

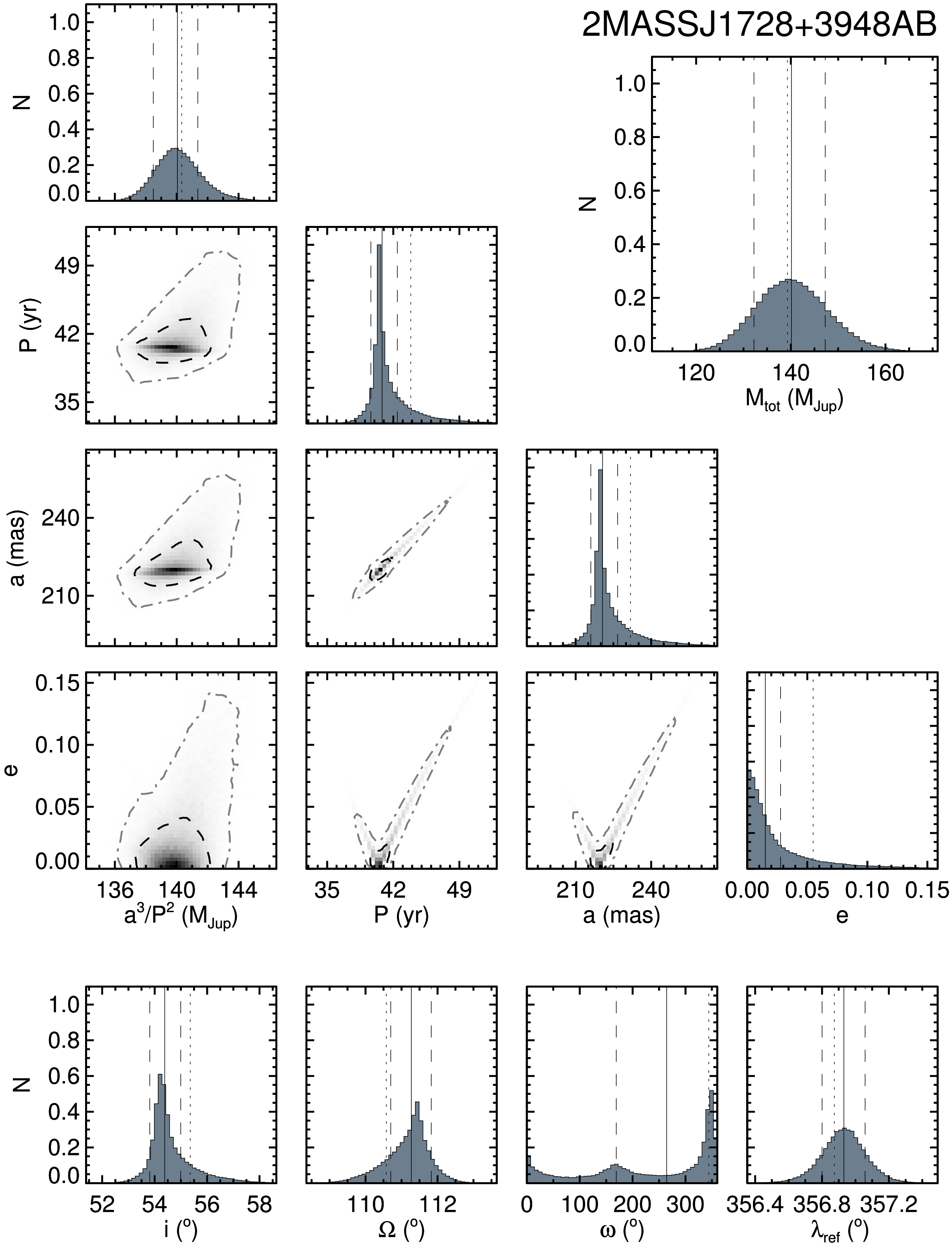

Fig. 2.— (Continued)

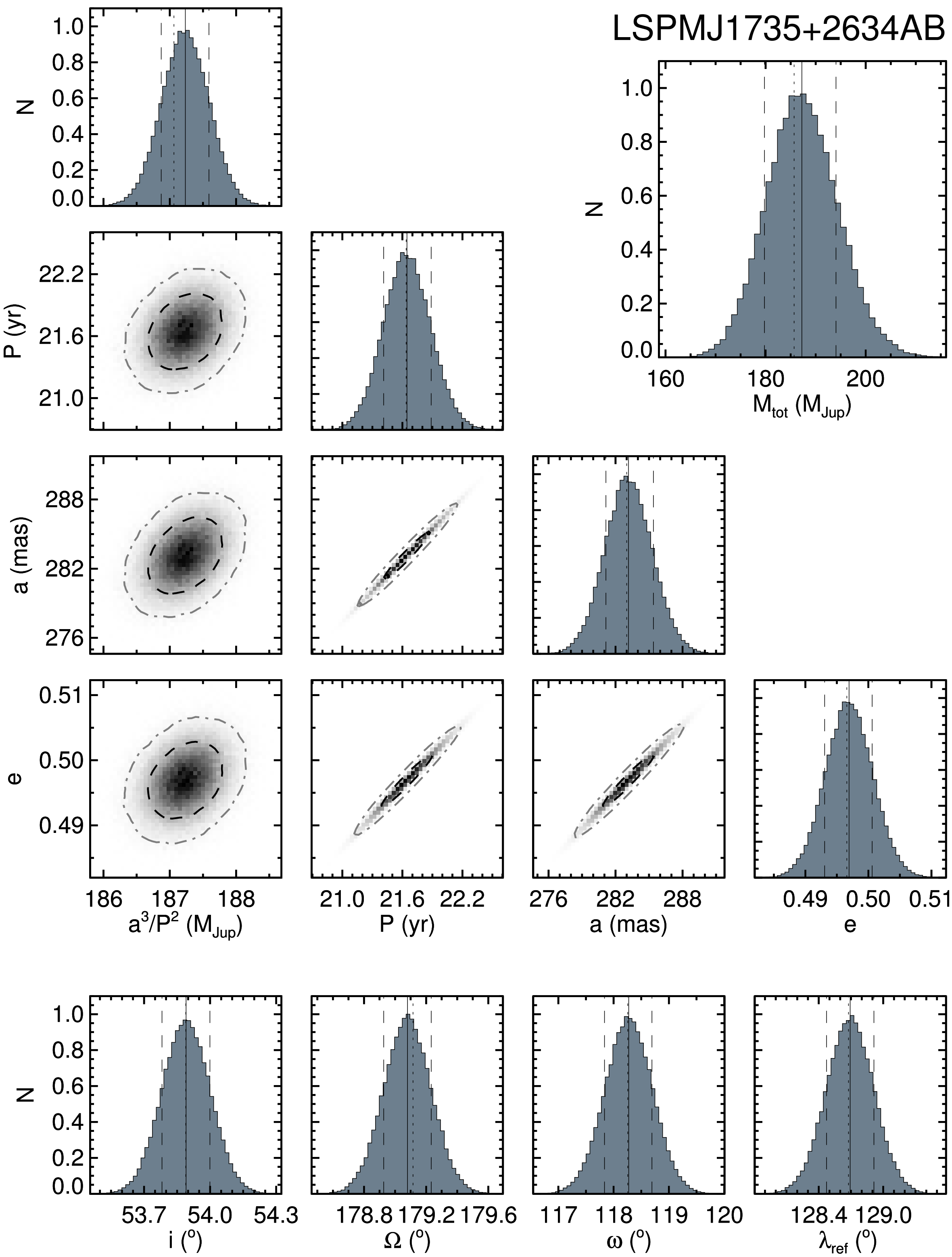

Fig. 2.— (Continued)

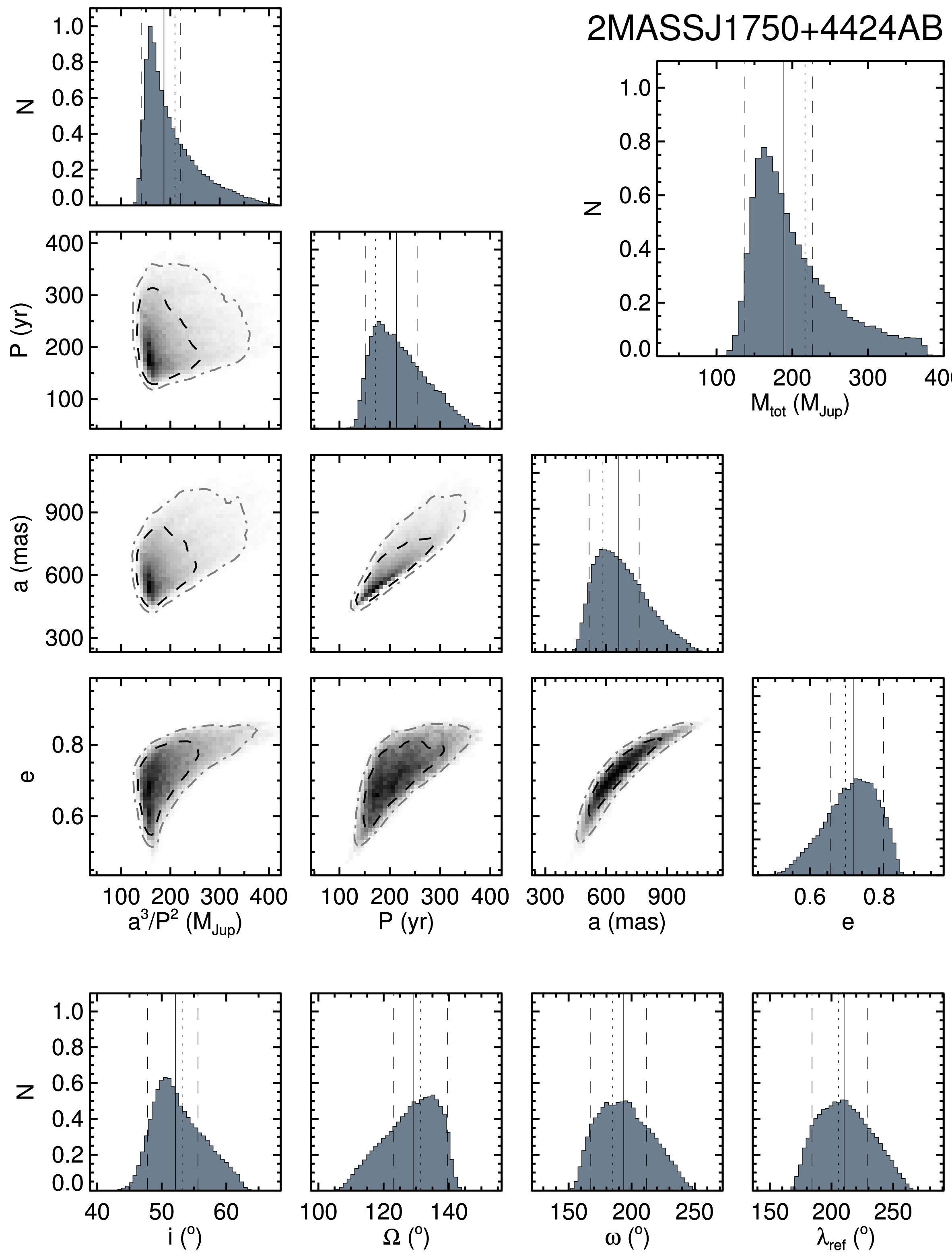

Fig. 2.— (Continued)

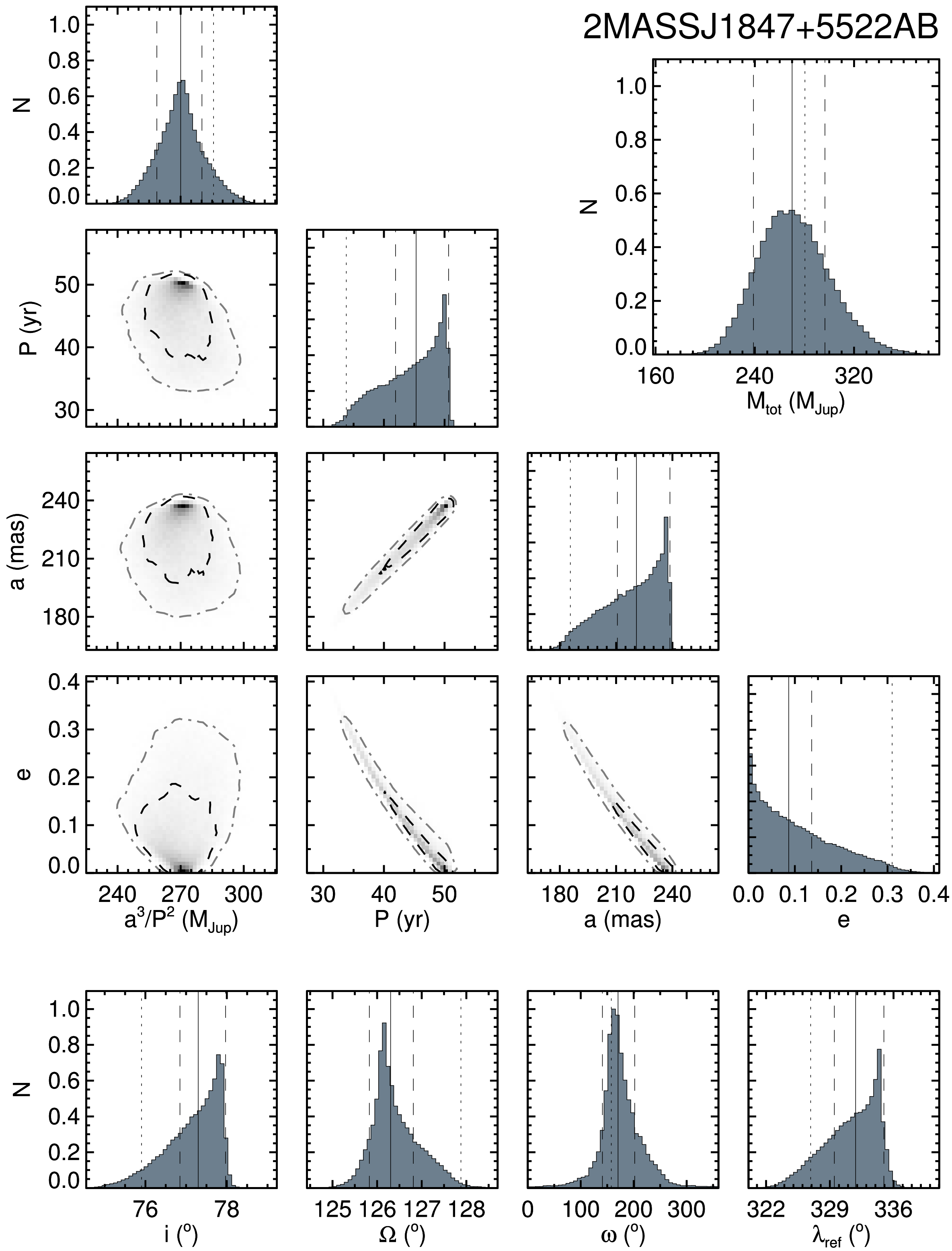

Fig. 2.— (Continued)

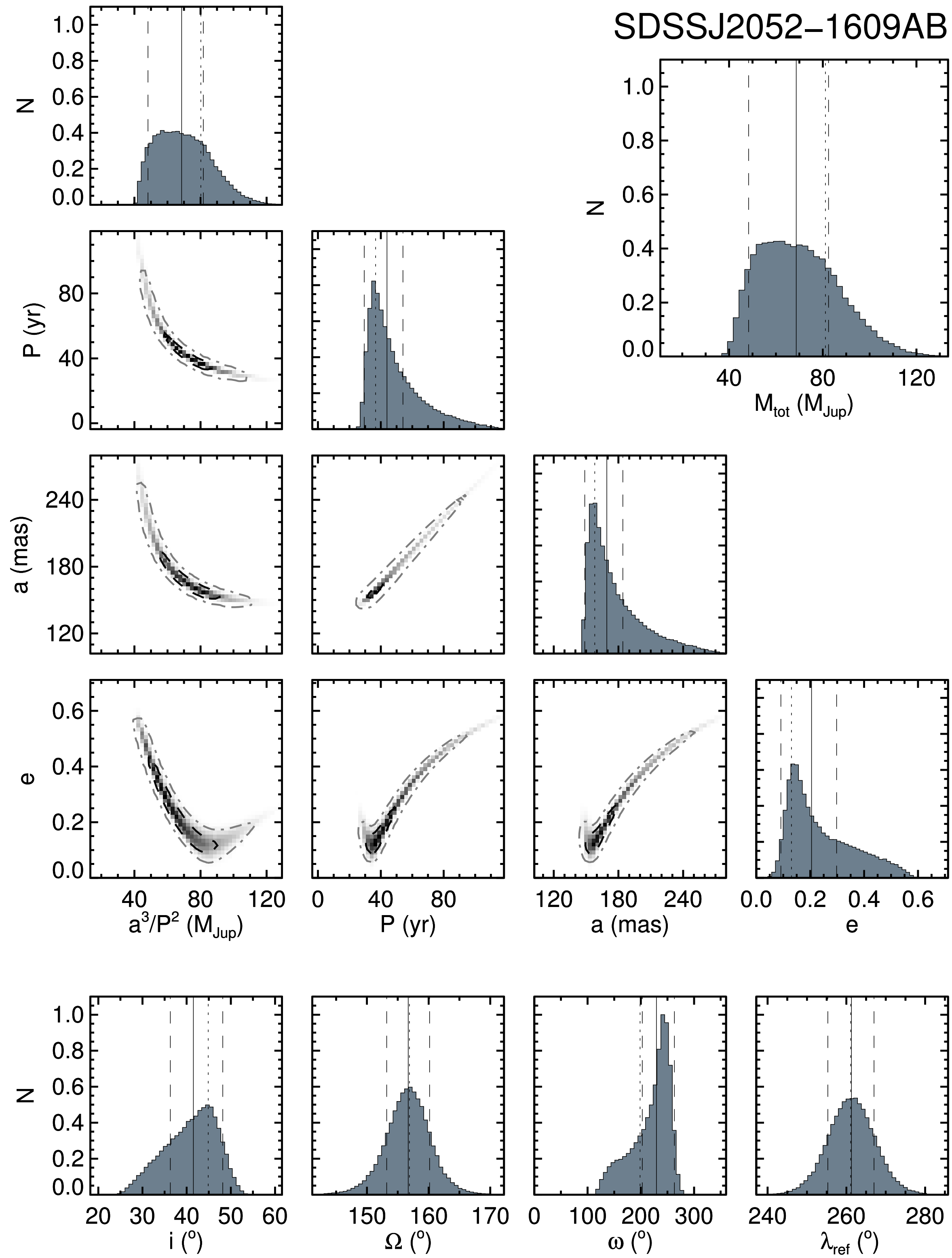

Fig. 2.— (Continued)

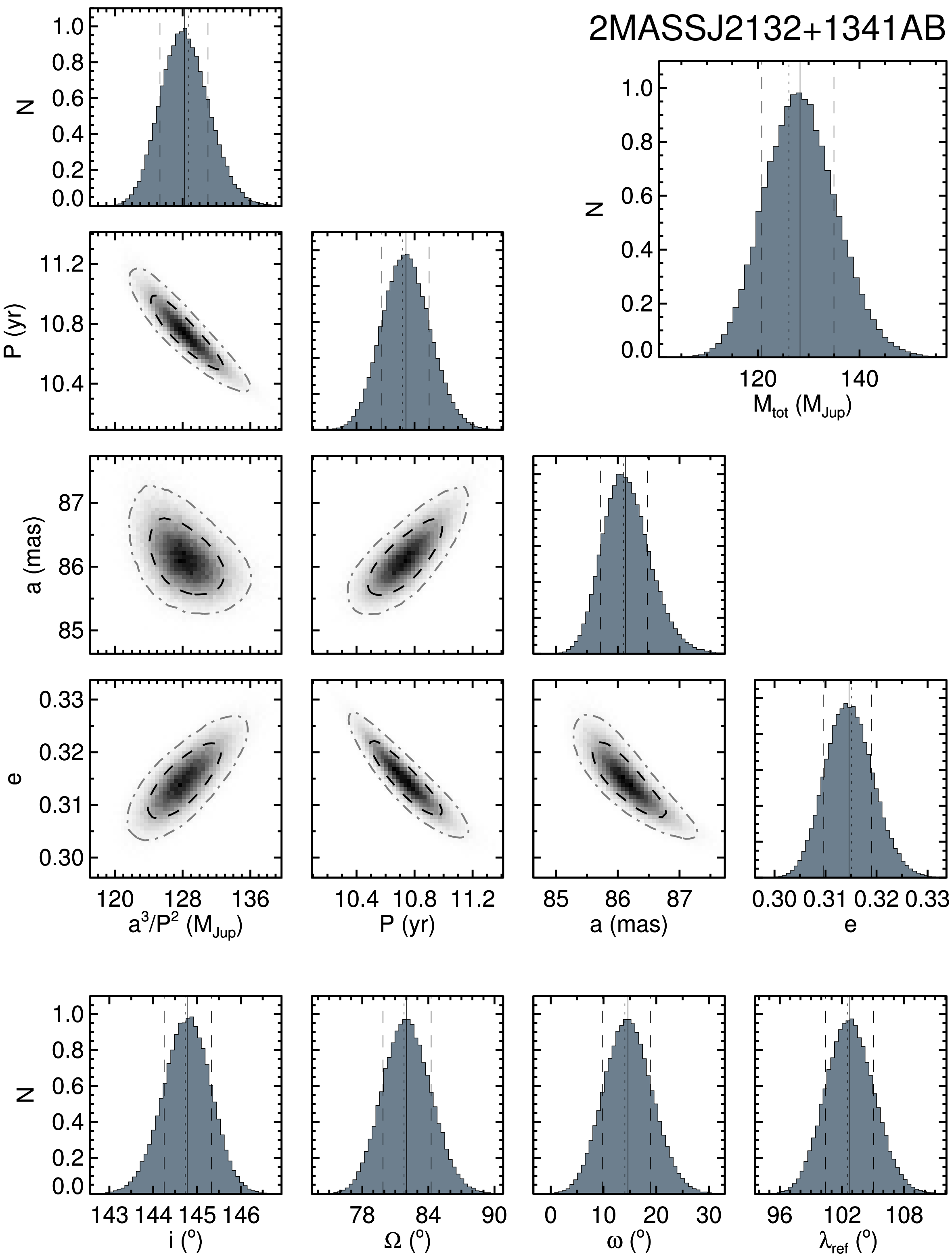

Fig. 2.— (Continued)

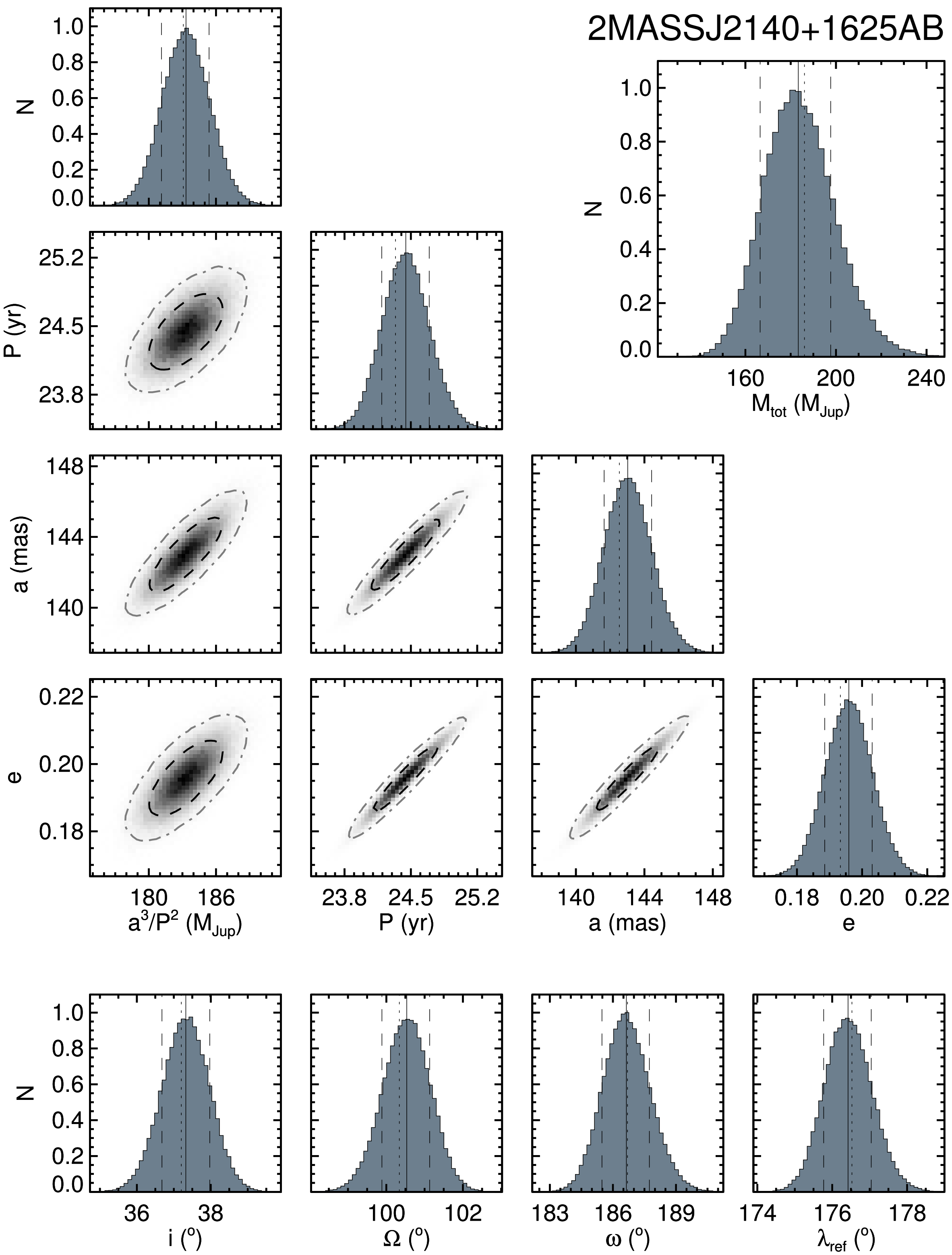

Fig. 2.— (Continued)

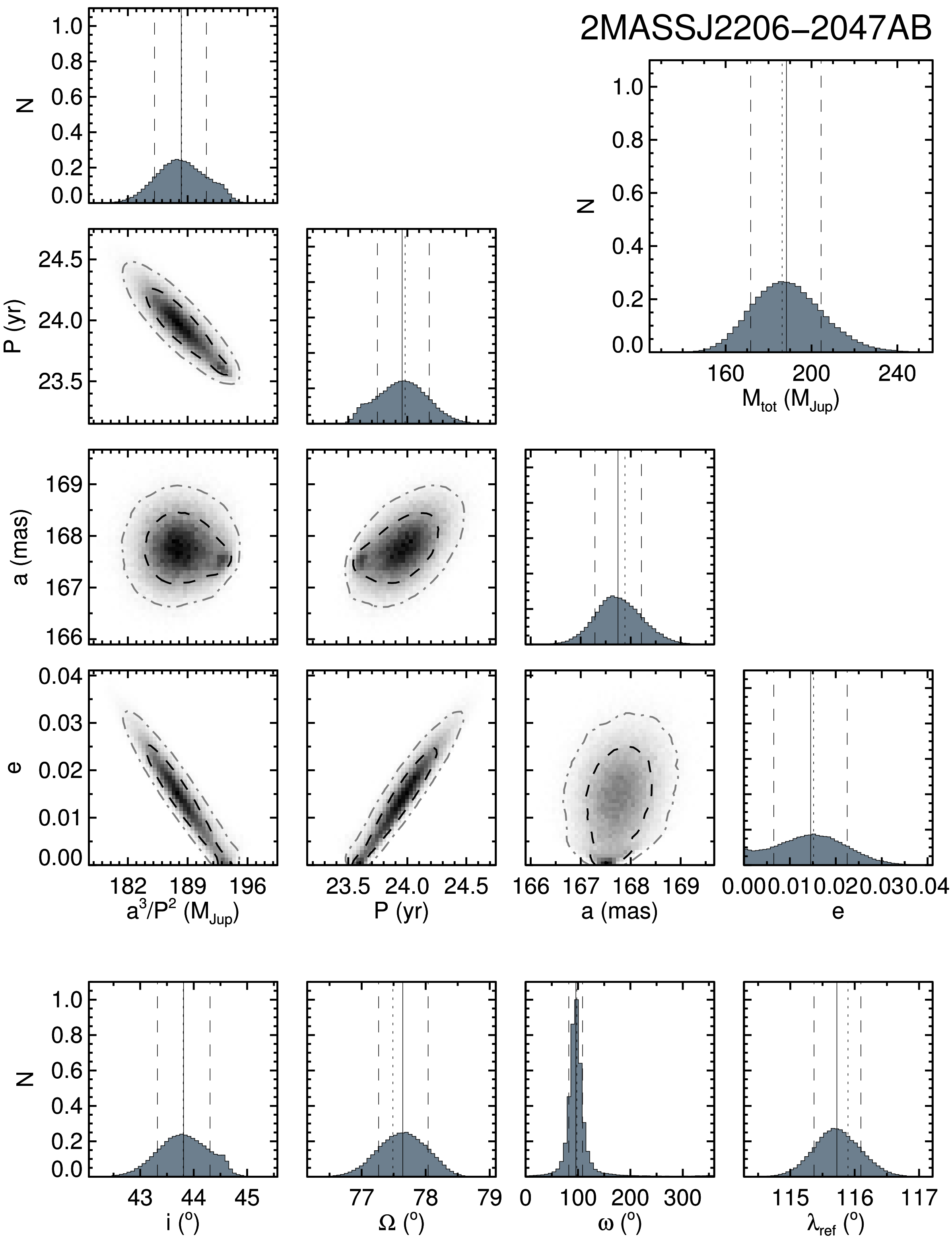

Fig. 2.— (Continued)

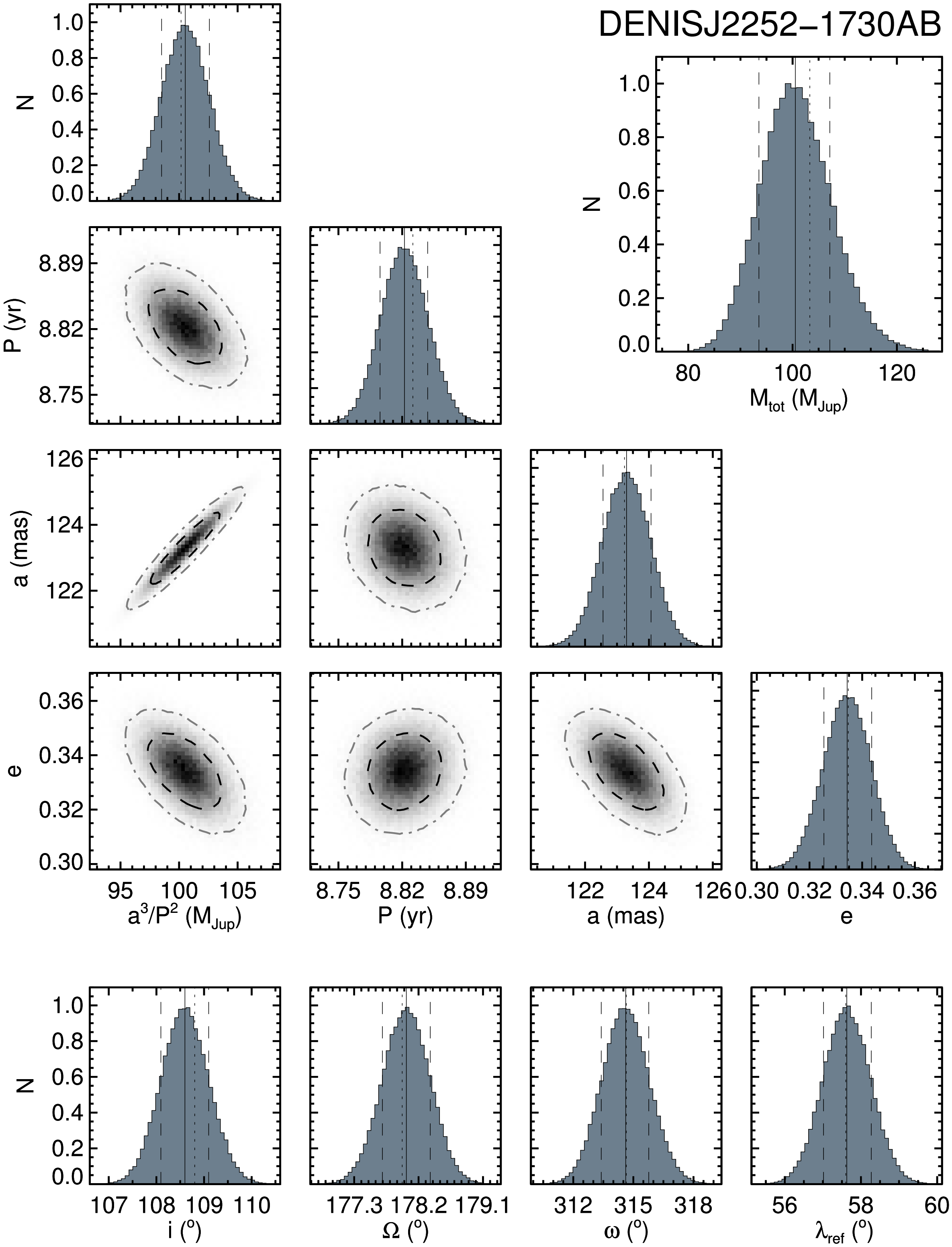

Fig. 2.— (Continued)

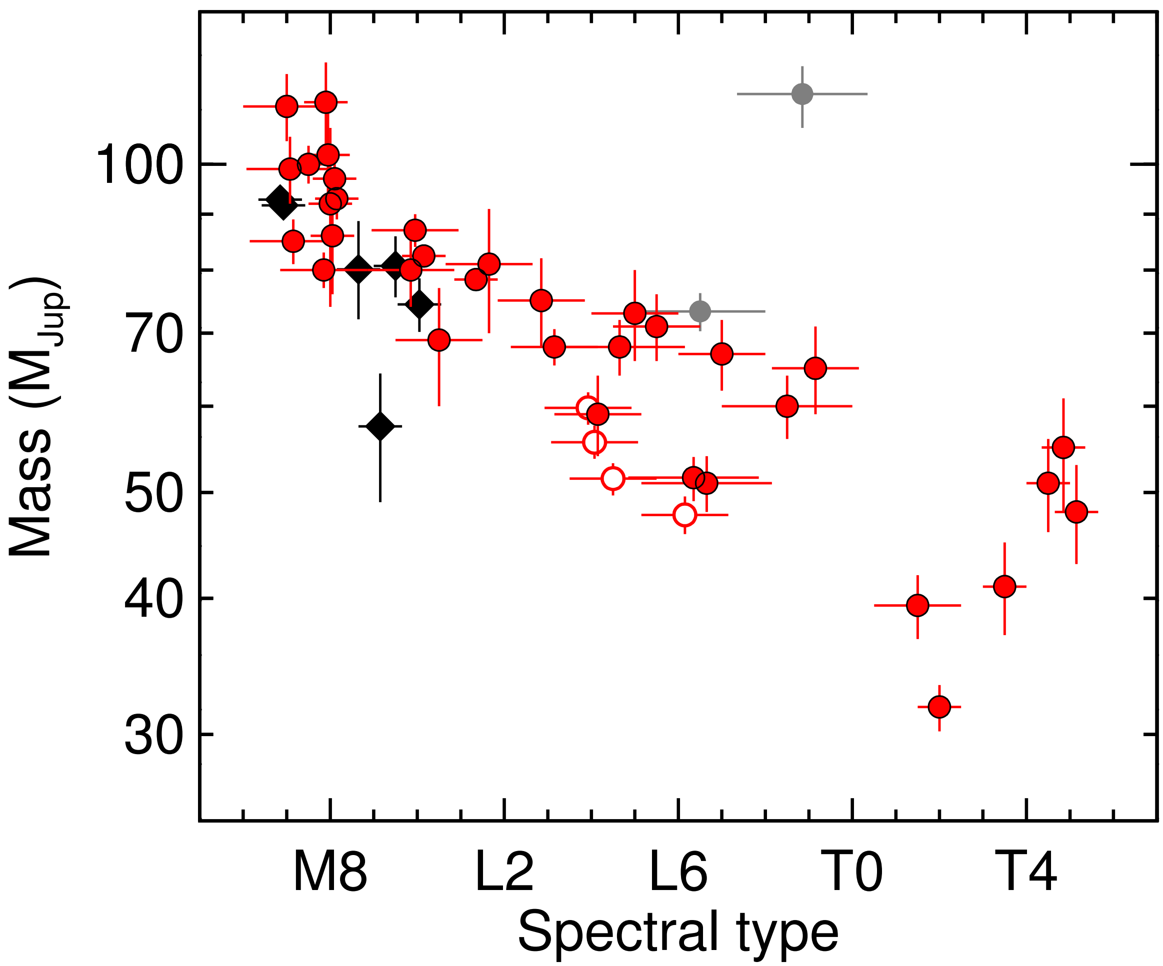

Fig. 3.— Mass as function of spectral type for objects with directly measured individual masses in our sample (filled red circles) and from the literature (filled black diamonds). Open red circles show objects from our sample with individual masses computed from our measured total mass and SM08 model-derived mass ratios. The likely unresolved multiple systems (gray circles) have high masses for their spectral type, as expected. Otherwise, no objects later than L4 have masses above 70 $M_{\rm Jup}$, implying that this is roughly the spectral type and mass corresponding to the hydrogen-fusion limit for the field population. The lowest mass object in our sample (SDSS J0423−0414B) is not the latest spectral type, illustrating that our field sample spans a range of ages. (For clarity of viewing many data points at the same spectral type, small offsets to the spectral type values have been added for plotting here.)

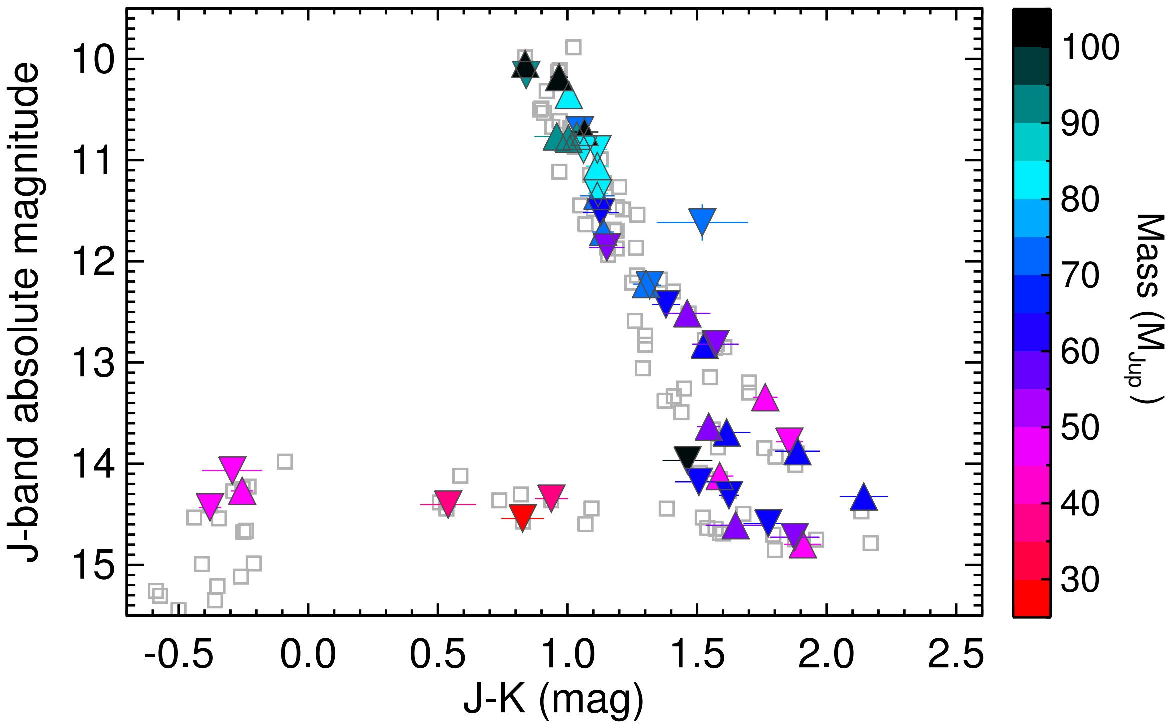

Fig. 4.— Color–magnitude diagram (CMD) showing our dynamical mass sample with symbols colored according to their directly measured individual masses. (The color bar is the same as used in all other plots with this color scheme.) Up-pointing triangles indicate primary components, down-pointing triangles indicate secondary components, and the field sequence is shown for reference as gray squares using the latest compilation of ultracool dwarf parallaxes at `http://www.as.utexas.edu/~tdupuy/plx`. (We plot only normal, single field objects that have S/N > 10 parallaxes and $J-K$ uncertainties <0.10 mag.) While mass generally decreases through the CMD sequence, there is not a one-to-one correspondence with mass and CMD location given that our sample is drawn from the field population of ultracool dwarfs spanning a range of ages. For example, the latest-type T dwarfs ($J-K = -0.5$ to 0.0 mag) happen to not be the least massive objects in our sample. By chance, the least massive objects are all located roughly in the middle of the L/T transition ($J-K = 0.5$–1.0 mag). The massive object in the bottom right part of the CMD (black down-pointing triangle near $M_J = 14$ mag) is 2MASS J0920+3517B, an unresolved pair of brown dwarfs in a triple system.

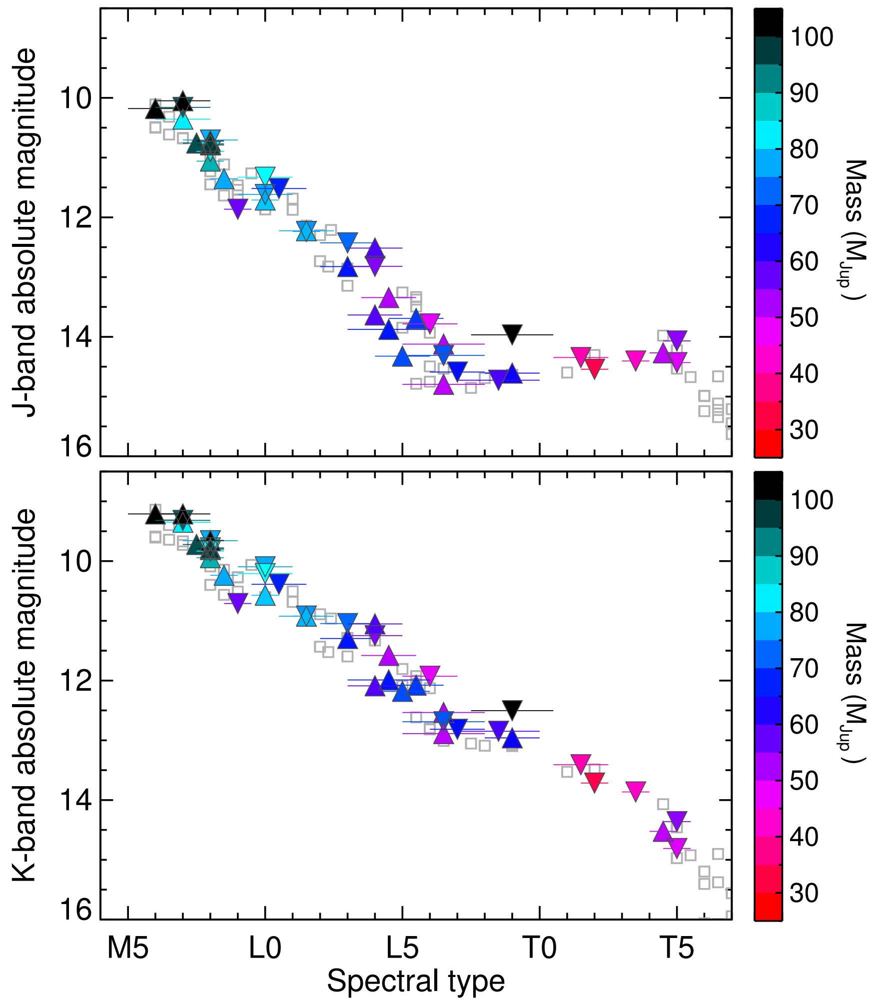

Fig. 5.— Absolute magnitude plotted as a function of spectral type for our dynamical mass sample with symbols colored according to their directly measured individual masses. (The color bar is the same as used in all other plots with this color scheme.) Up-pointing triangles indicate primary components, down-pointing triangles indicate secondary components, and the field sequence is shown for reference as gray squares using the latest compilation of ultracool dwarf parallaxes at `http://www.as.utexas.edu/~tdupuy/plx`. (We plot only normal, single field objects that have S/N > 10 parallaxes and $J-K$ uncertainties $<$0.10 mag.) Our sample is broadly consistent with the field sequence, indicating the accuracy of our spectral types that we derived by decomposing each binary's integrated-light spectrum using our resolved photometry and a library of spectral templates. The largest outlier is 2MASS J0920+3517B (L9.0 $\pm$ 1.5 sitting well above the L/T transition sequence on the J-band plot), which is consistent with our dynamical masses showing that this is an unresolved pair of brown dwarfs in a triple system. 2MASS J0700+3157B, the other such unresolved pair, is not an outlier on these plots because our derived spectral type (L6.5 $\pm$ 1.5) and absolute magnitudes happen to be consistent with the field sequence.

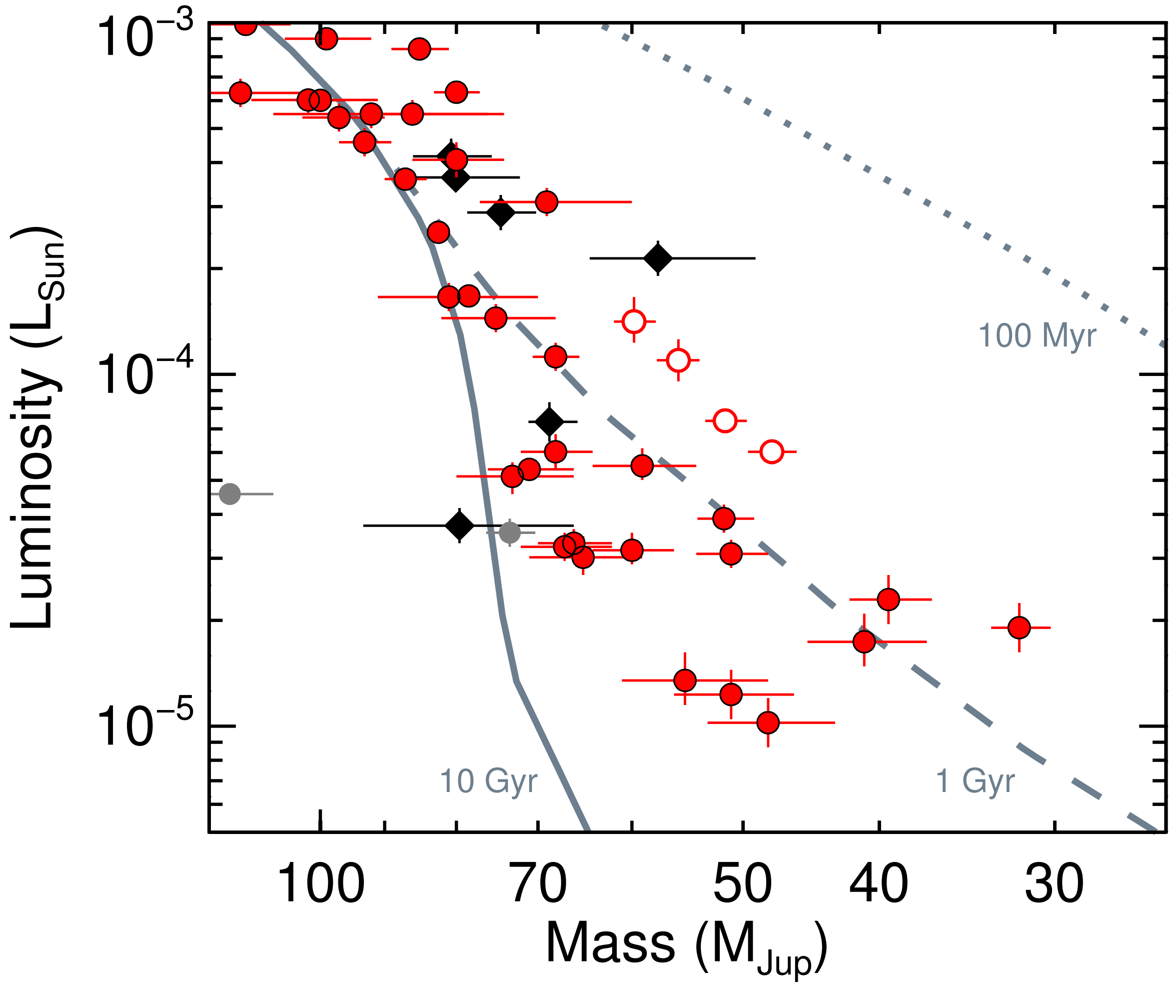

Fig. 6.— Luminosity as function of mass for objects with directly measured individual masses in our sample (filled red circles) and from the literature (filled black diamonds). Open red circles show objects from our sample with individual masses computed from our measured total mass and SM08 model-derived mass ratios. Filled gray circles indicate the likely unresolved multiples in our sample 2MASS J0920+3517B and 2MASS J0700+3157B. The other possible unresolved multiple LP 415-20A ($156^{+17}_{-18}\,M_{\rm Jup}$) does not appear on this plot because it is too massive. Cond model isochrones are shown for reference, indicating that most objects in our sample are consistent with having ages of ∼1–10 Gyr. For Gl 569Bab we use black diamonds to indicate that the literature mass ratio is used to compute individual masses, even though it is in our sample and we use our dynamical total mass here.

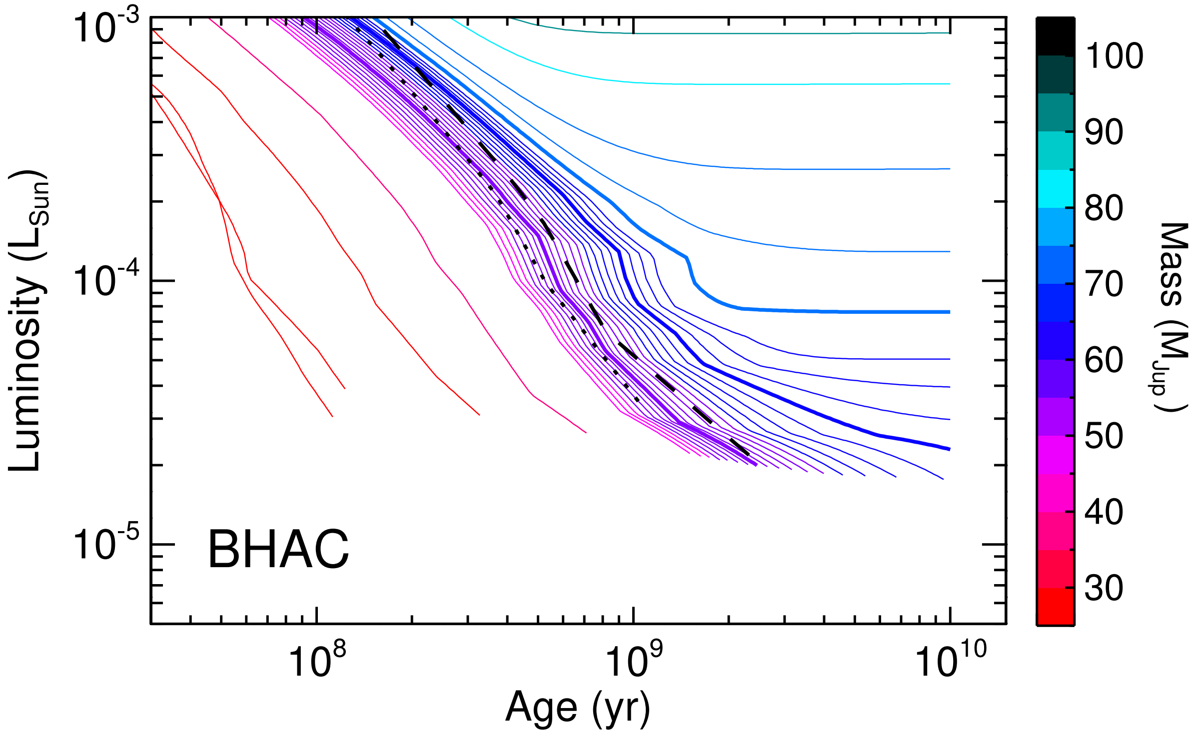

Fig. 7.— Evolutionary models used in our analysis. Each colored line shows the predicted luminosity as a function of age for an object of given mass. The 75 $M_{\rm Jup}$, 70 $M_{\rm Jup}$, and 60 $M_{\rm Jup}$ models are plotted with thicker lines as a visual aid. All model masses are integer multiples of 0.001 $M_{\odot}$ (1.048 $M_{\rm Jup}$), and only masses of 0.015–0.100 $M_{\odot}$ (15–105 $M_{\rm Jup}$) are plotted here. BHAC models are uniformly sampled at steps of 0.001 $M_{\odot}$ over the range 0.050–0.070 $M_{\odot}$ (52–73 $M_{\rm Jup}$) and at coarser steps at other masses. Dotted and dashed and lines indicate boundaries in lithium depletion of 50% and 99.9% depleted, respectively. BHAC models are only available down to $T_{\rm eff} \approx 1300$ K, while SM08 models are only available below ≈2400 K. (The color bar is the same as used in all other plots with this color scheme.)

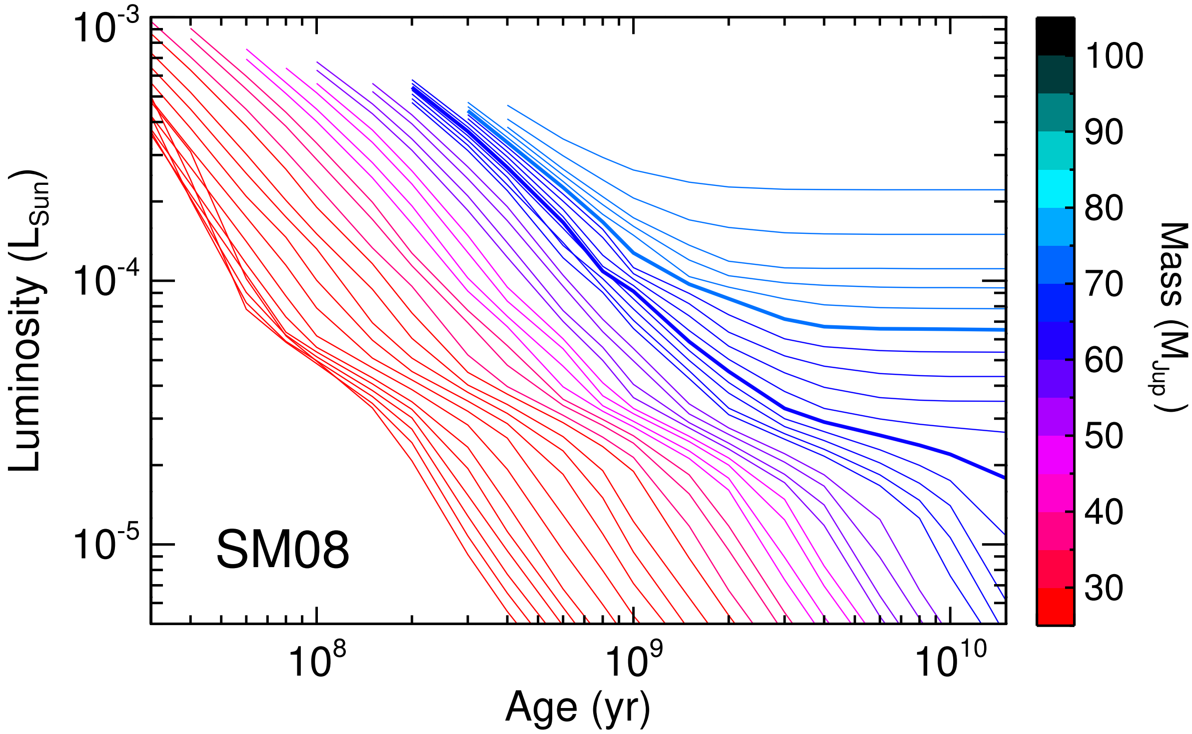

Fig. 7.— (Continued)

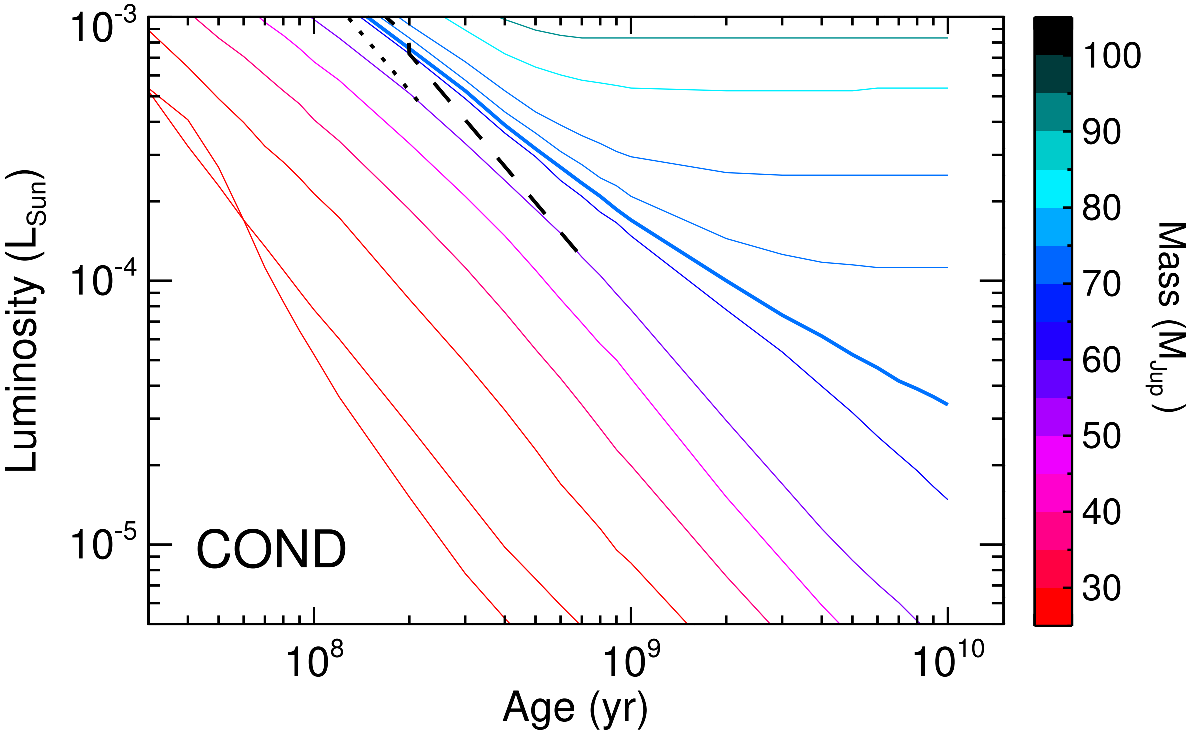

Fig. 7.— (Continued)

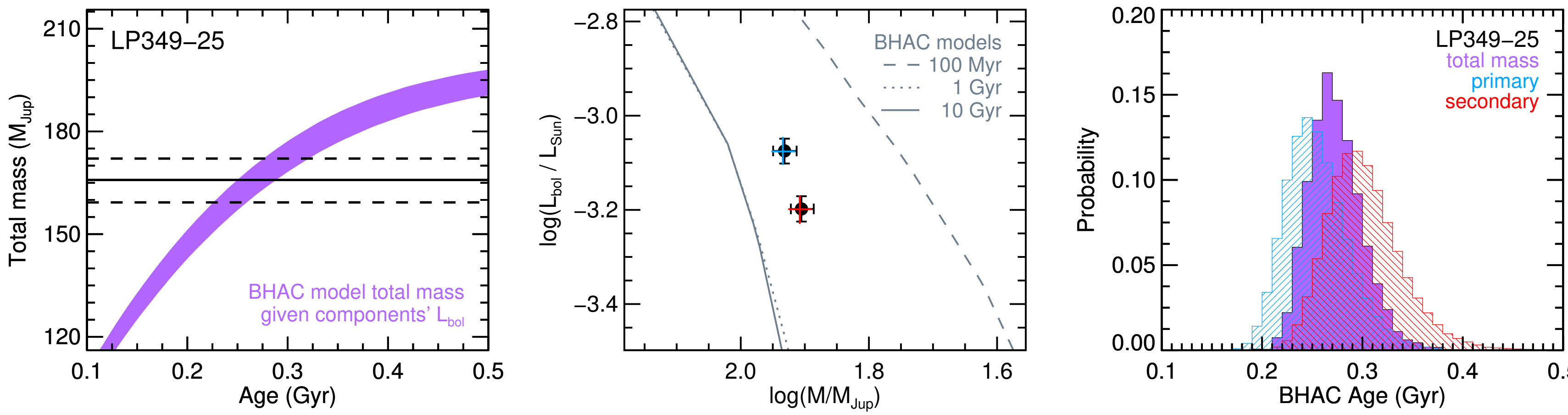

Fig. 8.— **Left panel:** Total mass derived from models using the component luminosities over a range of ages (purple), where the vertical extent of the shaded region corresponds to the 1σ uncertainties in the luminosities. Our measured total mass and 1σ confidence interval are shown by a solid line and dashed lines, respectively. (This panel is for display purposes only as our actual analysis is based on rejection sampling as described in Section 6.) **Middle panel:** Our directly measured individual masses and luminosities are plotted as black filled circles with 1σ error bars. Model isochrones are shown as gray lines. The 1σ interval in mass and luminosity after performing our rejection sampling analysis is shown by the colored error bars for the primary (blue) and secondary (red). When there are offsets between these colored points and the measurements, or differences in the error bars, it is caused by rejecting input Monte Carlo samples that do not agree with models and/or by imposing our uniform age prior. **Right panel:** Final age distribution derived from our rejection sampling analysis using the total mass and individual luminosities (solid purple), the primary mass and luminosity (blue hatched), and the secondary mass and luminosity (red hatched). Our uniform prior in age results in many stellar binaries having nearly flat age distributions over the range of main sequence ages covered by models, whereas brown dwarfs and pre–main-seuqence stars like LP 349-25AB have well constrained model-derived ages.

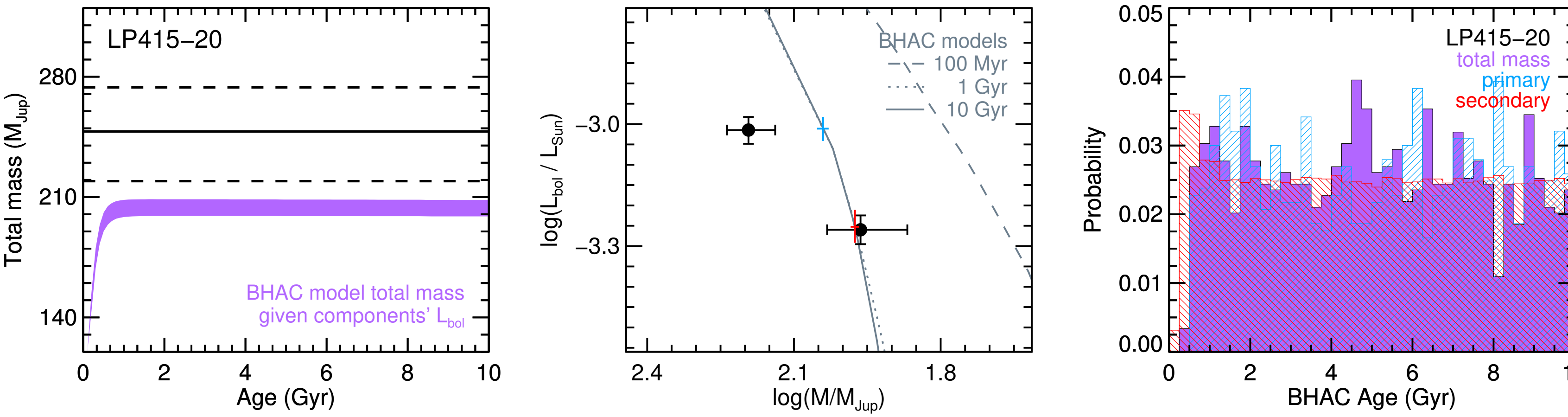

Fig. 8.— (Continued)

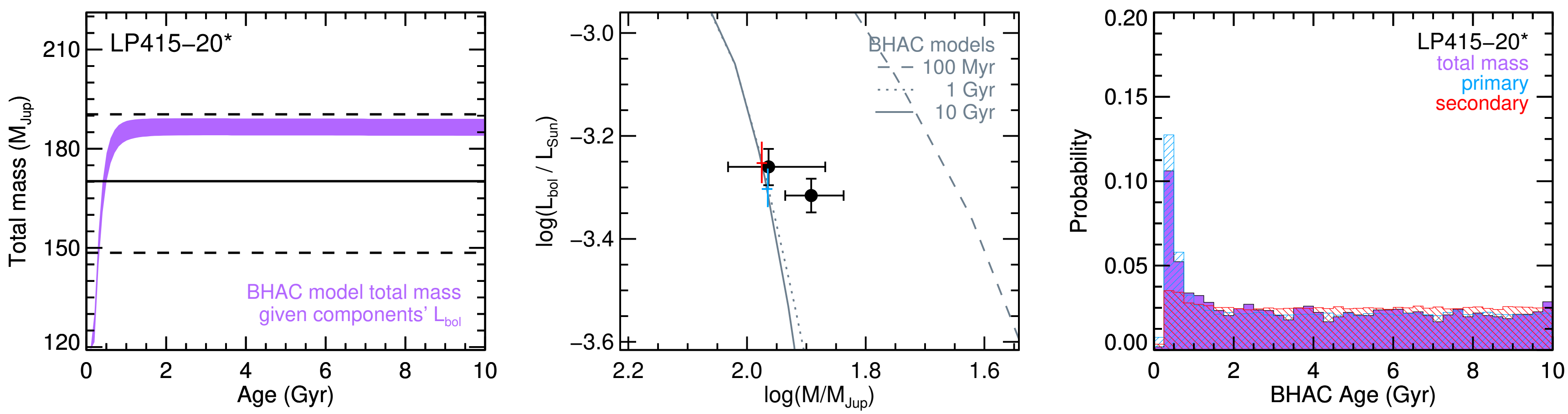

Fig. 8.— (Continued)

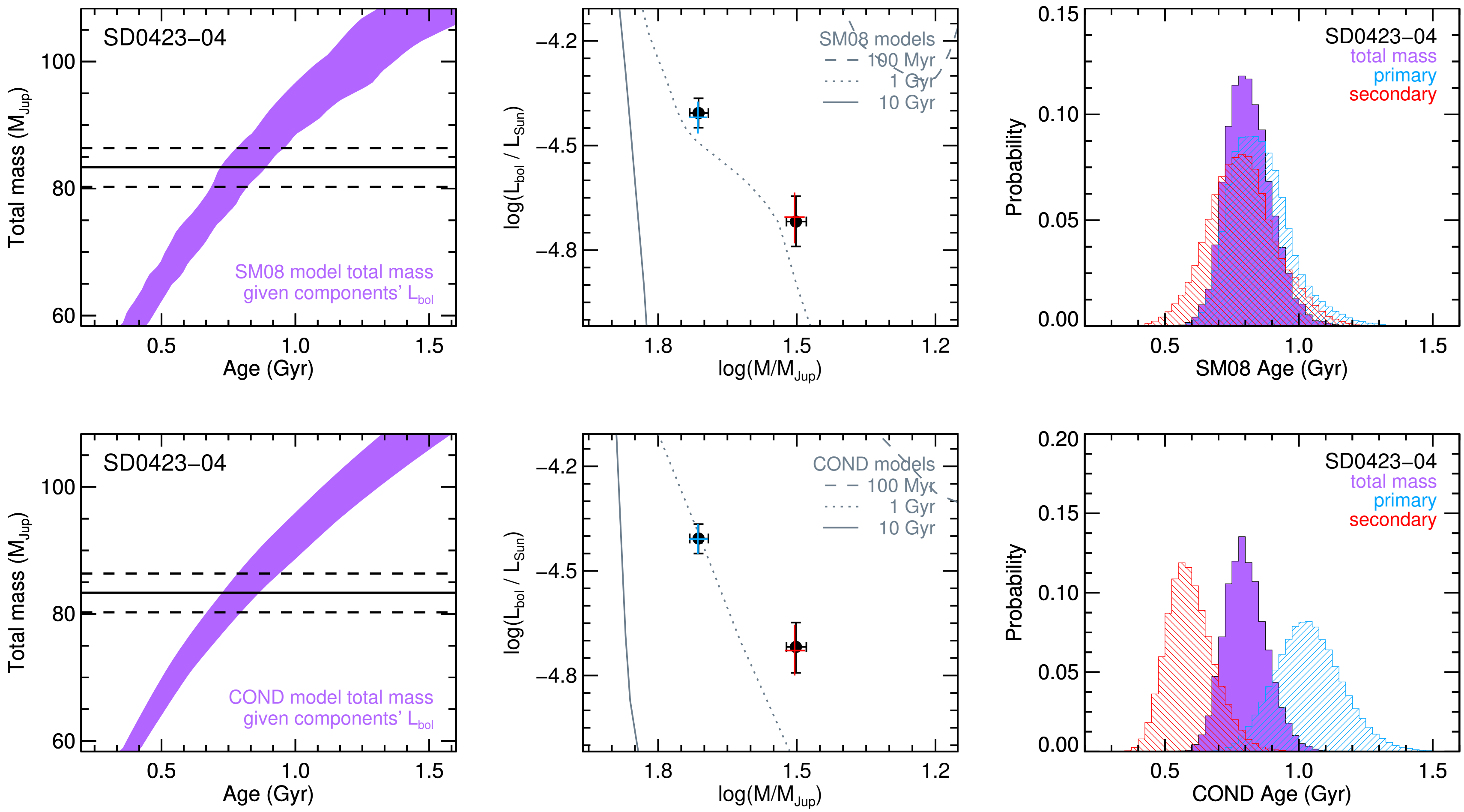

Fig. 8.— (Continued)

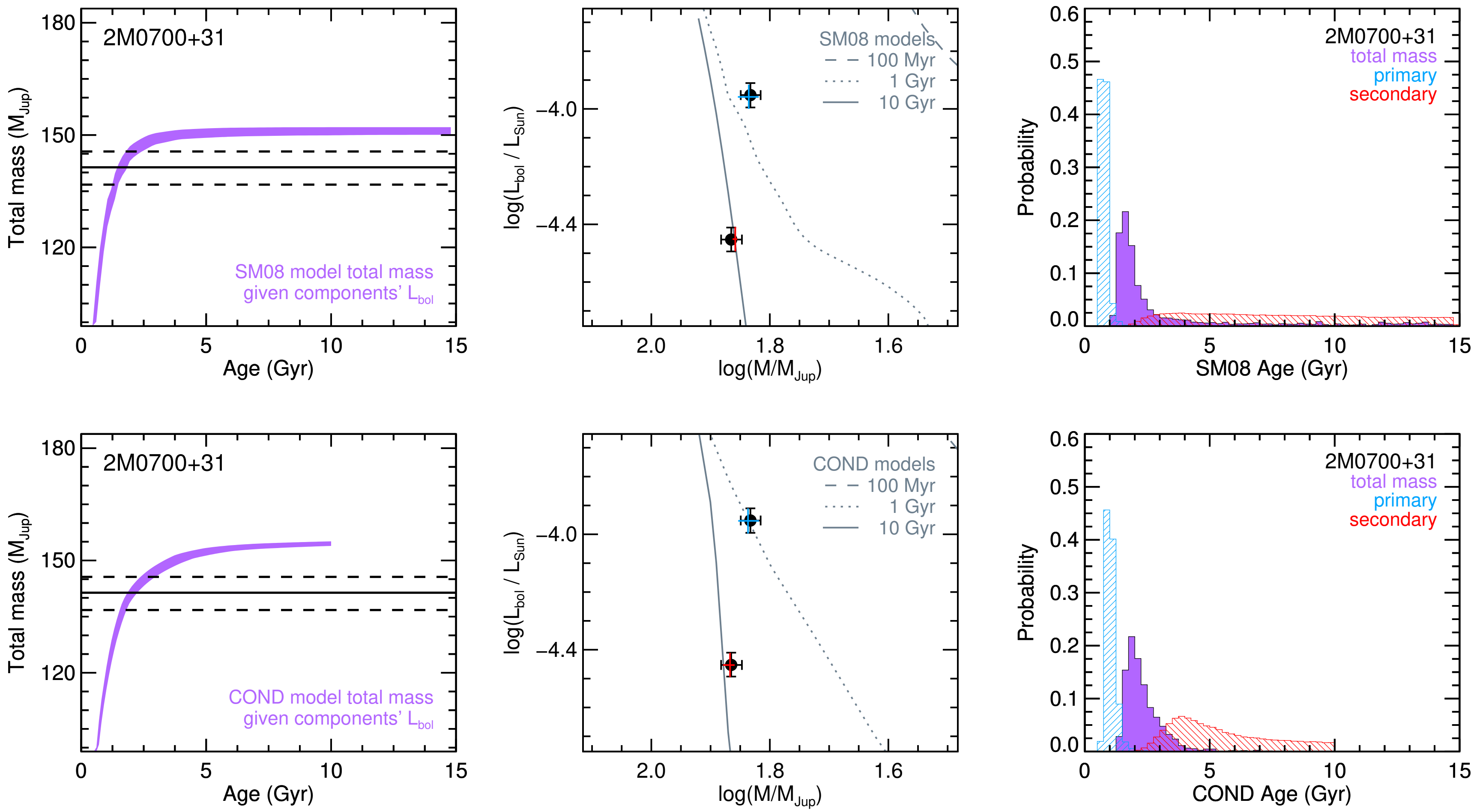

Fig. 8.— (Continued)

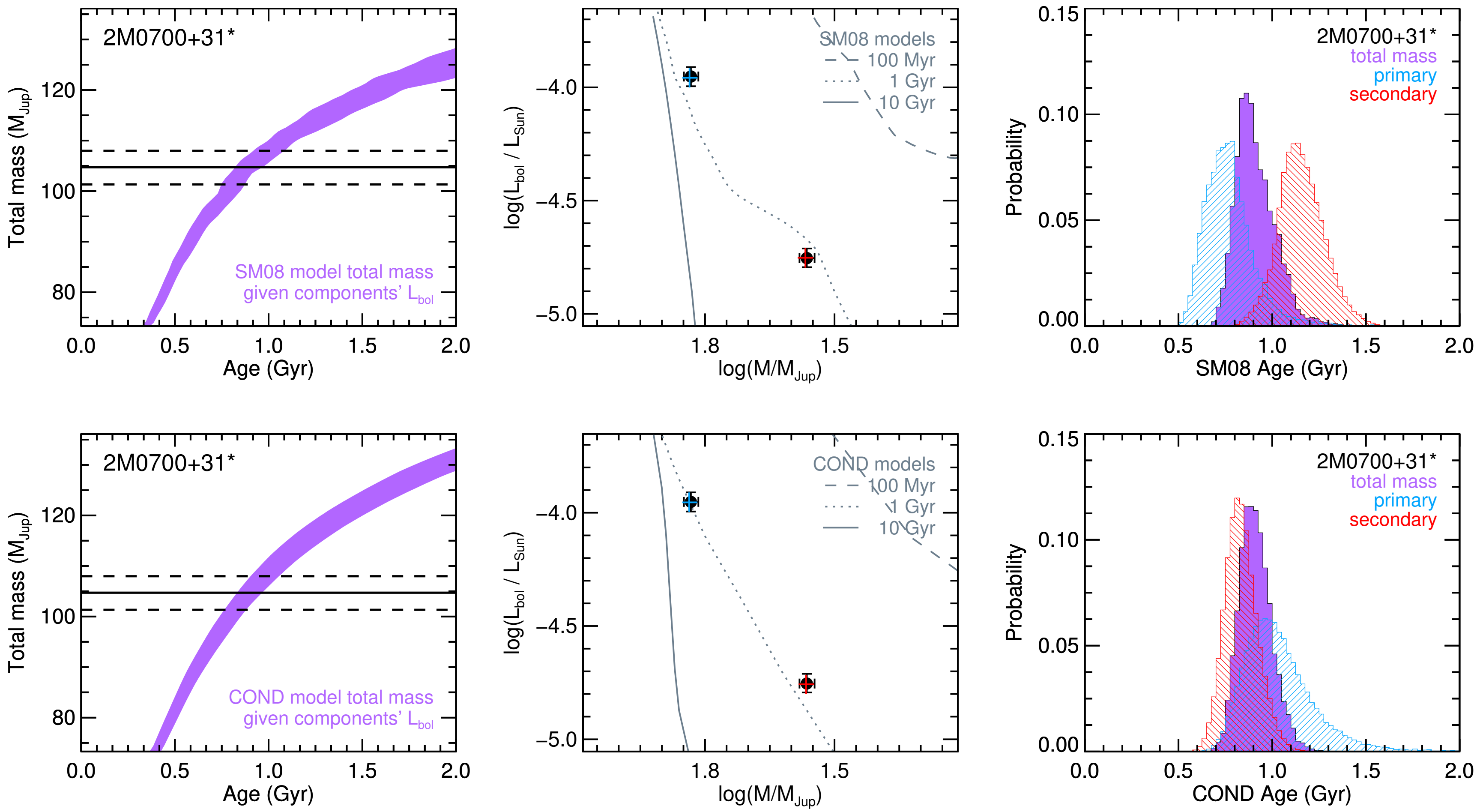

Fig. 8.— (Continued)

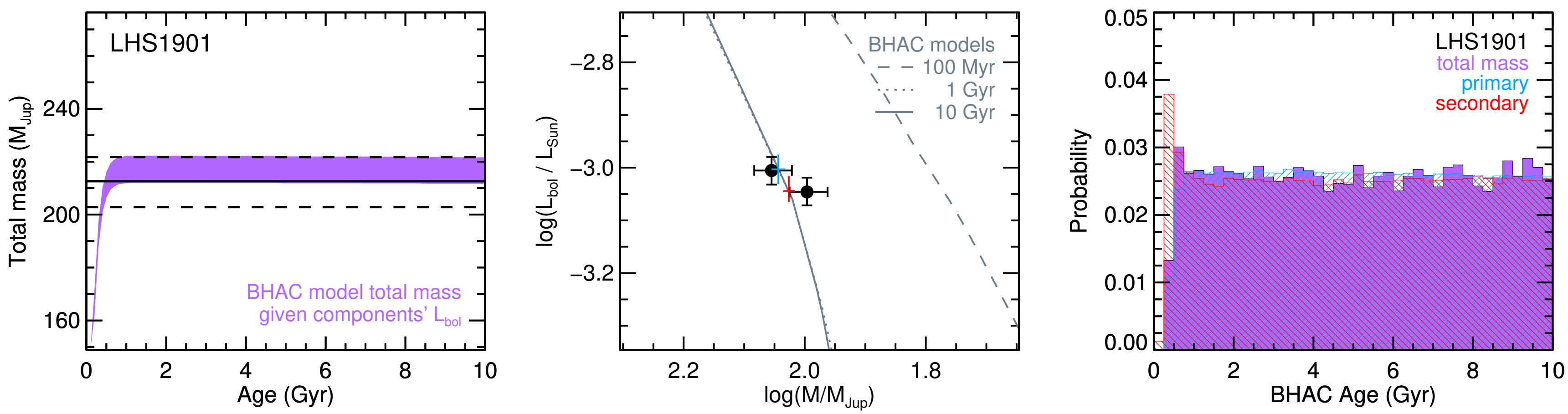

Fig. 8.— (Continued)

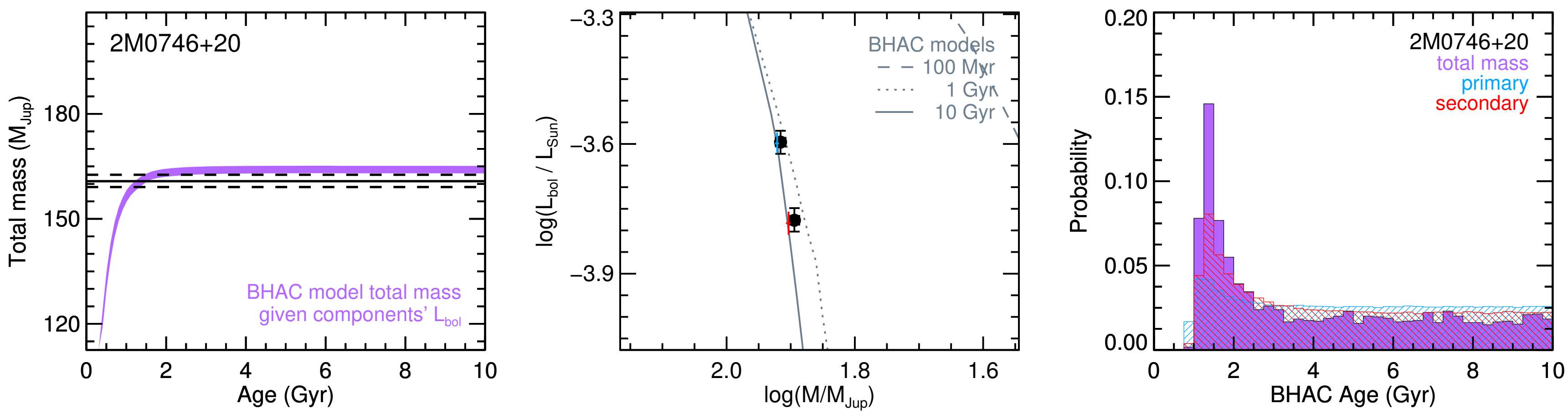

Fig. 8.— (Continued)

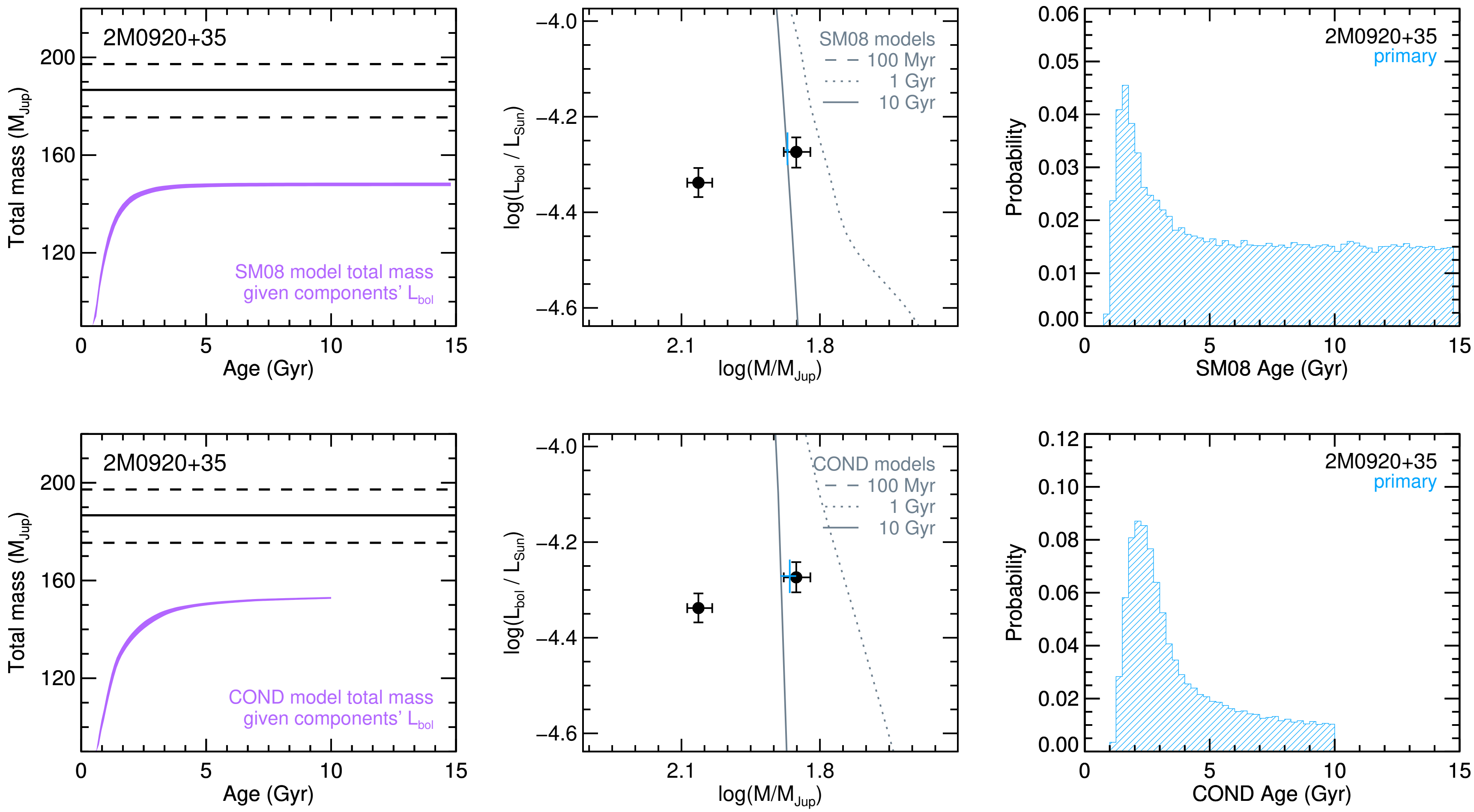

Fig. 8.— (Continued)

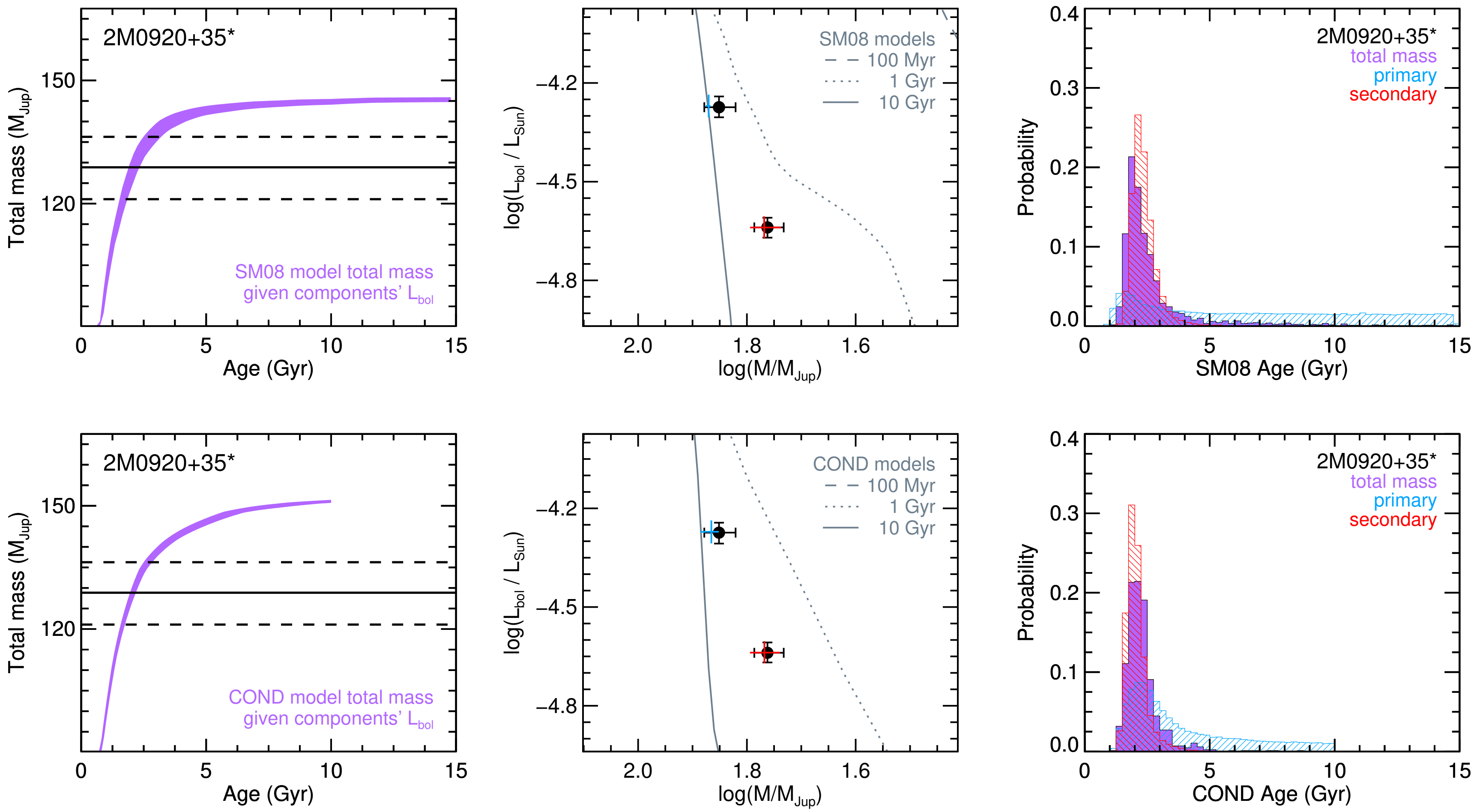

Fig. 8.— (Continued)

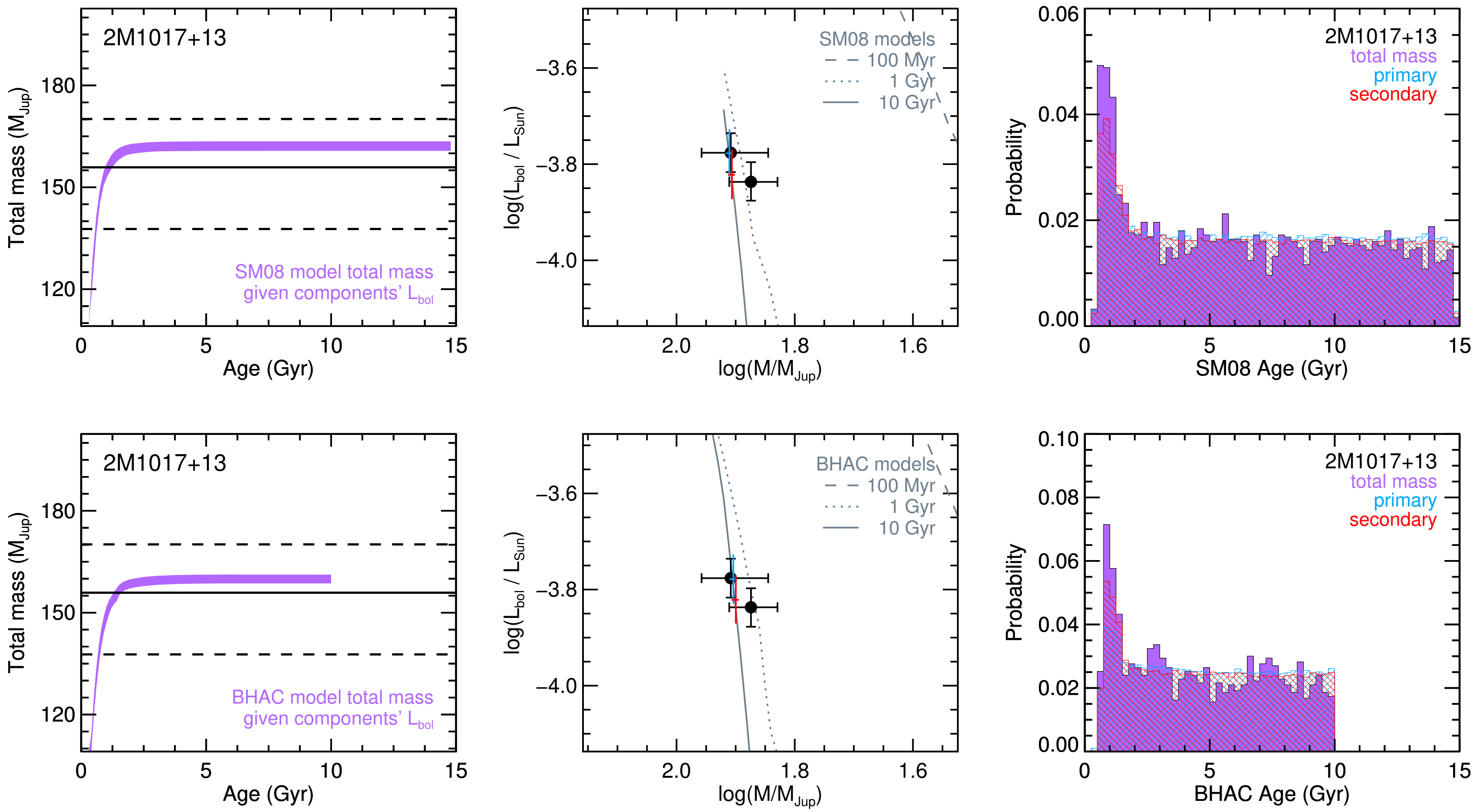

Fig. 8.— (Continued)

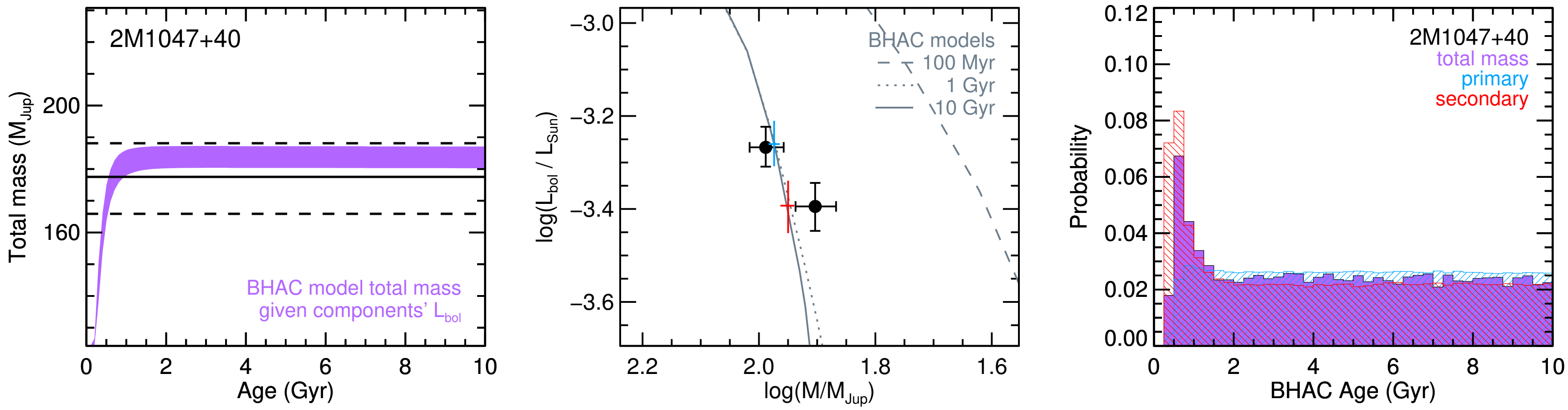

Fig. 8.— (Continued)

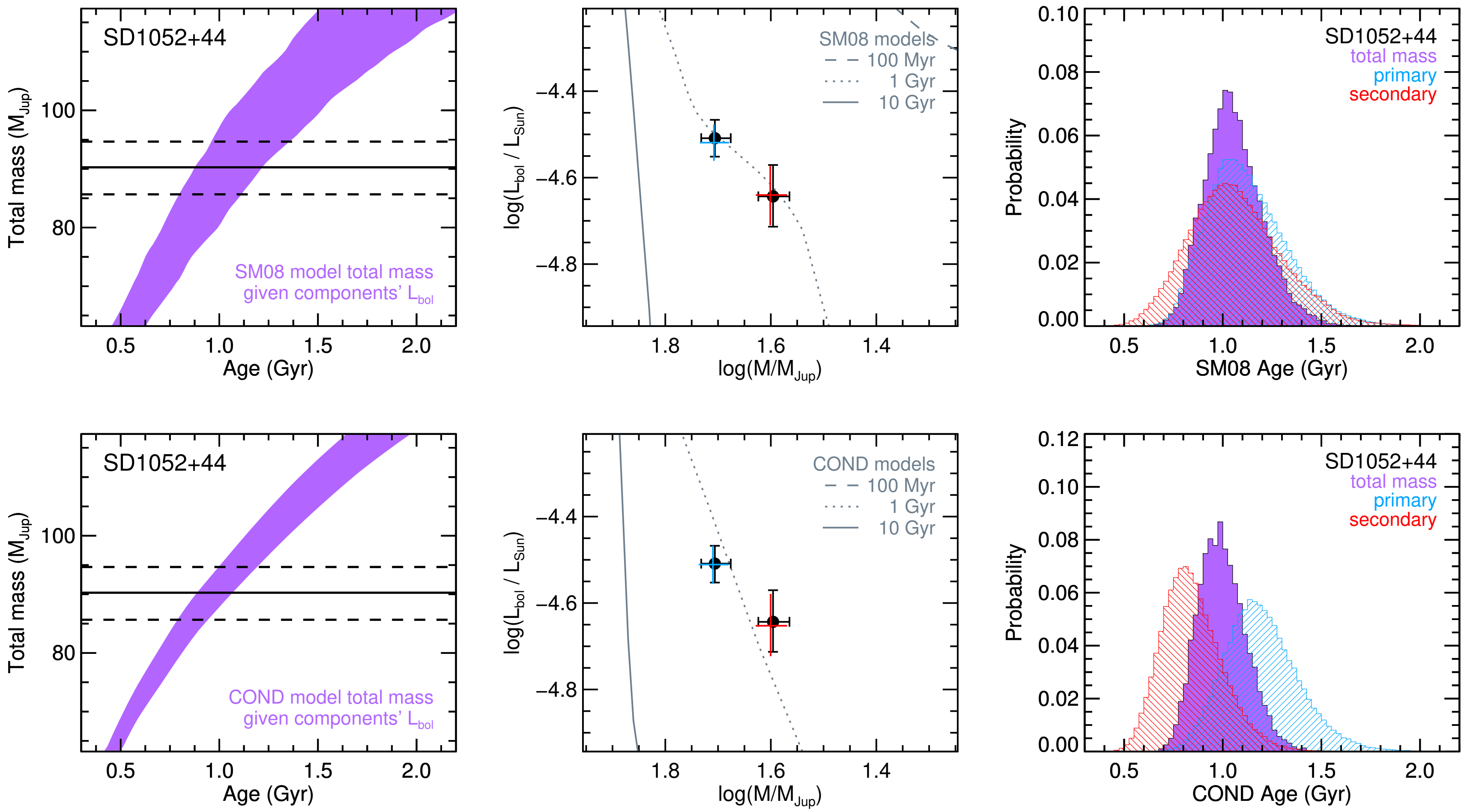

Fig. 8.— (Continued)

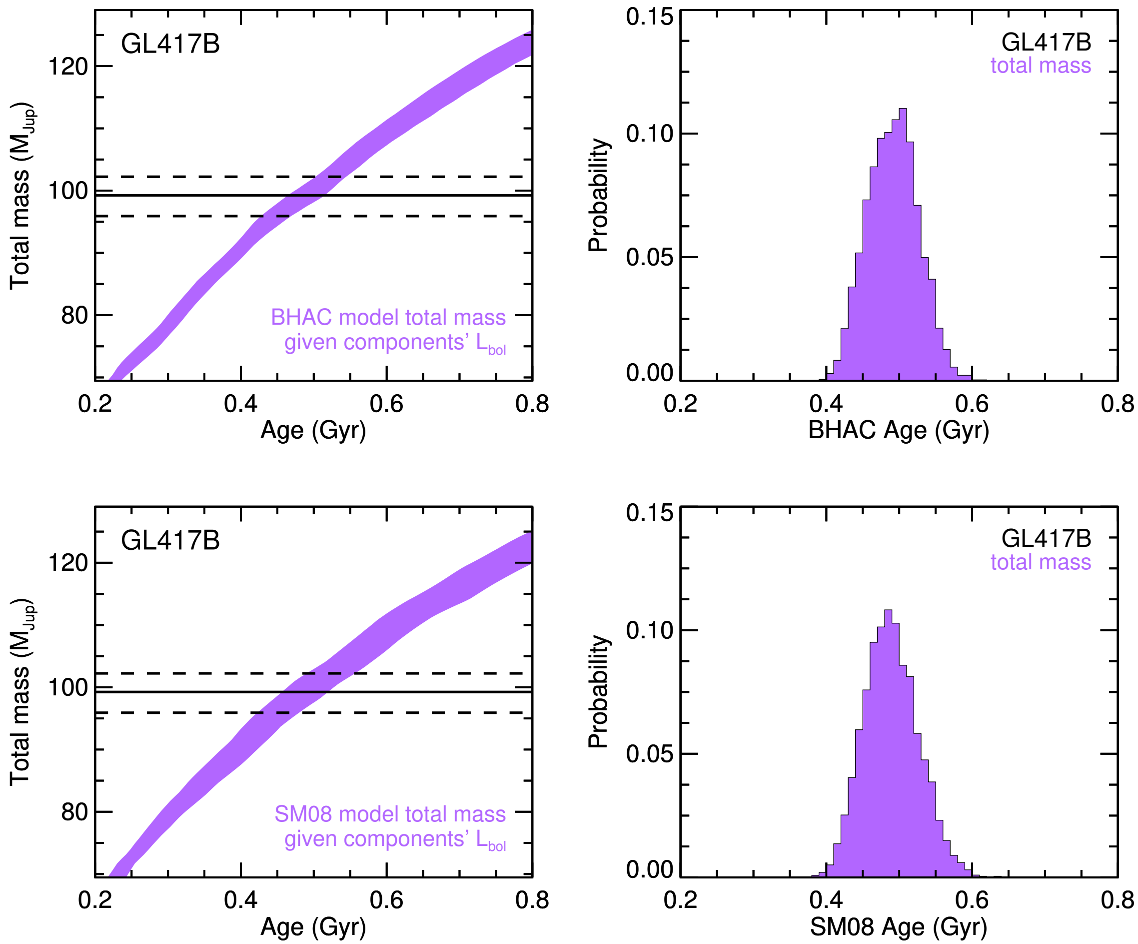

Fig. 8.— (Continued)

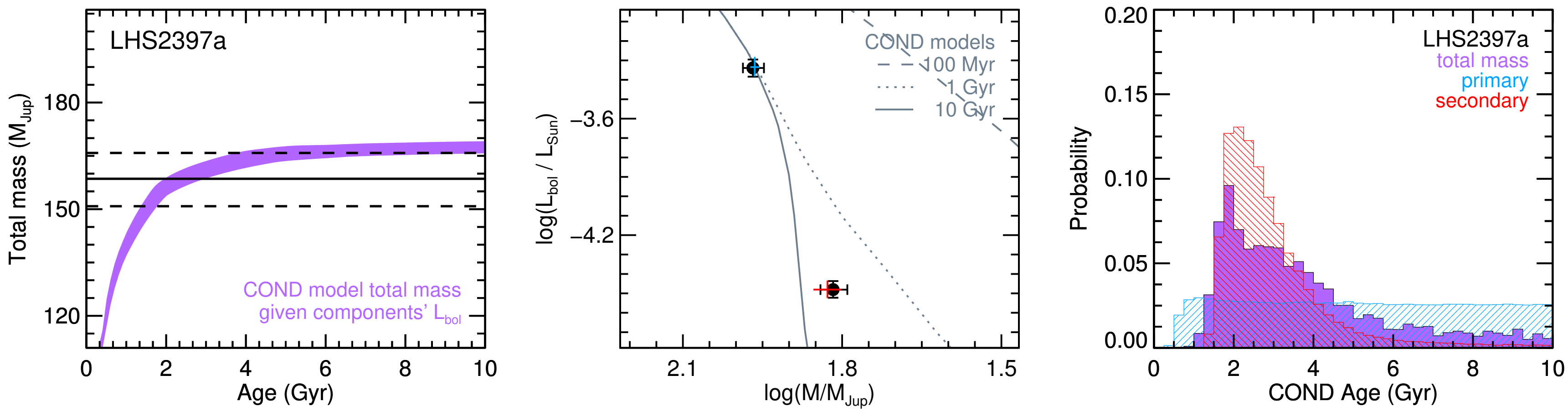

Fig. 8.— (Continued)

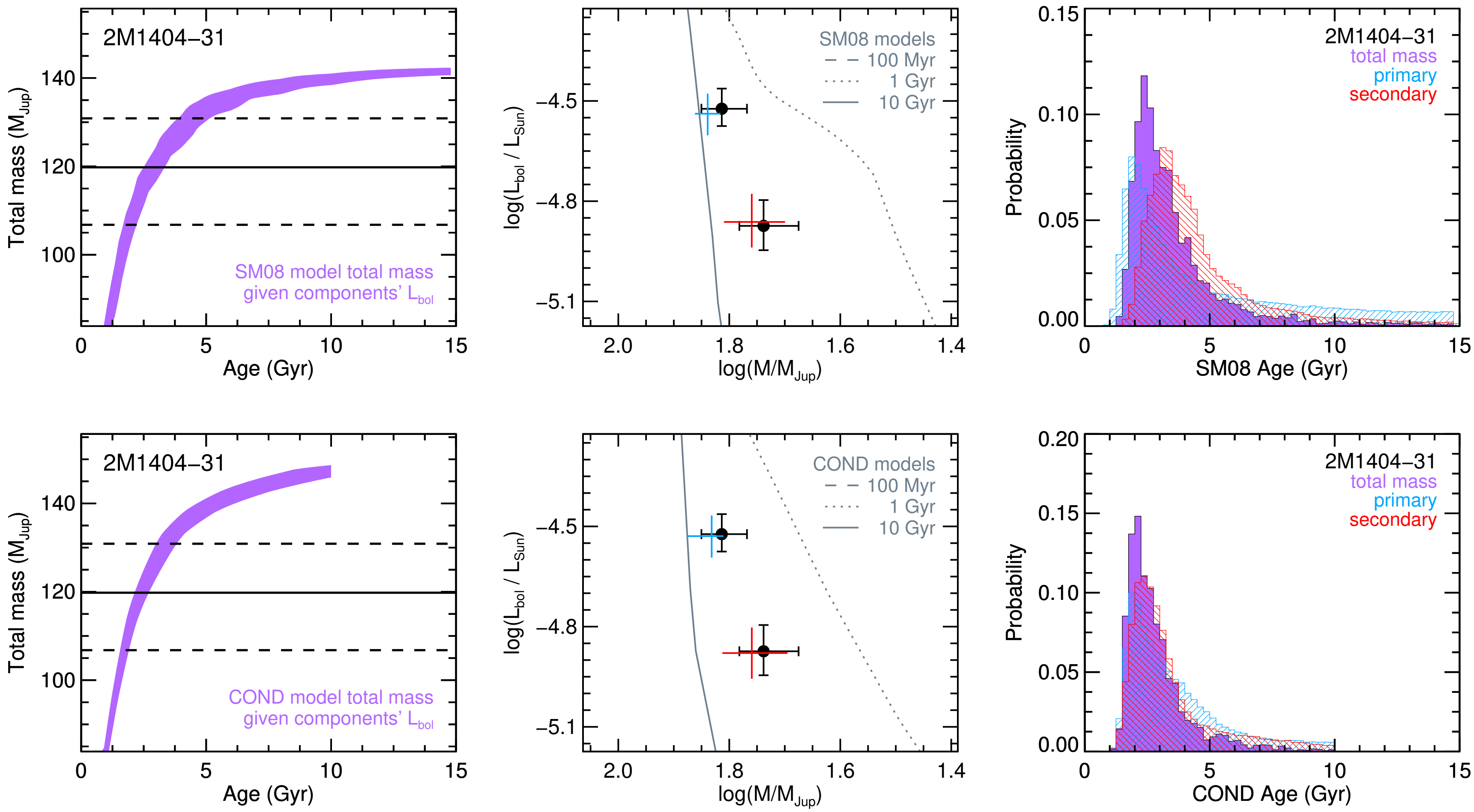

Fig. 8.— (Continued)

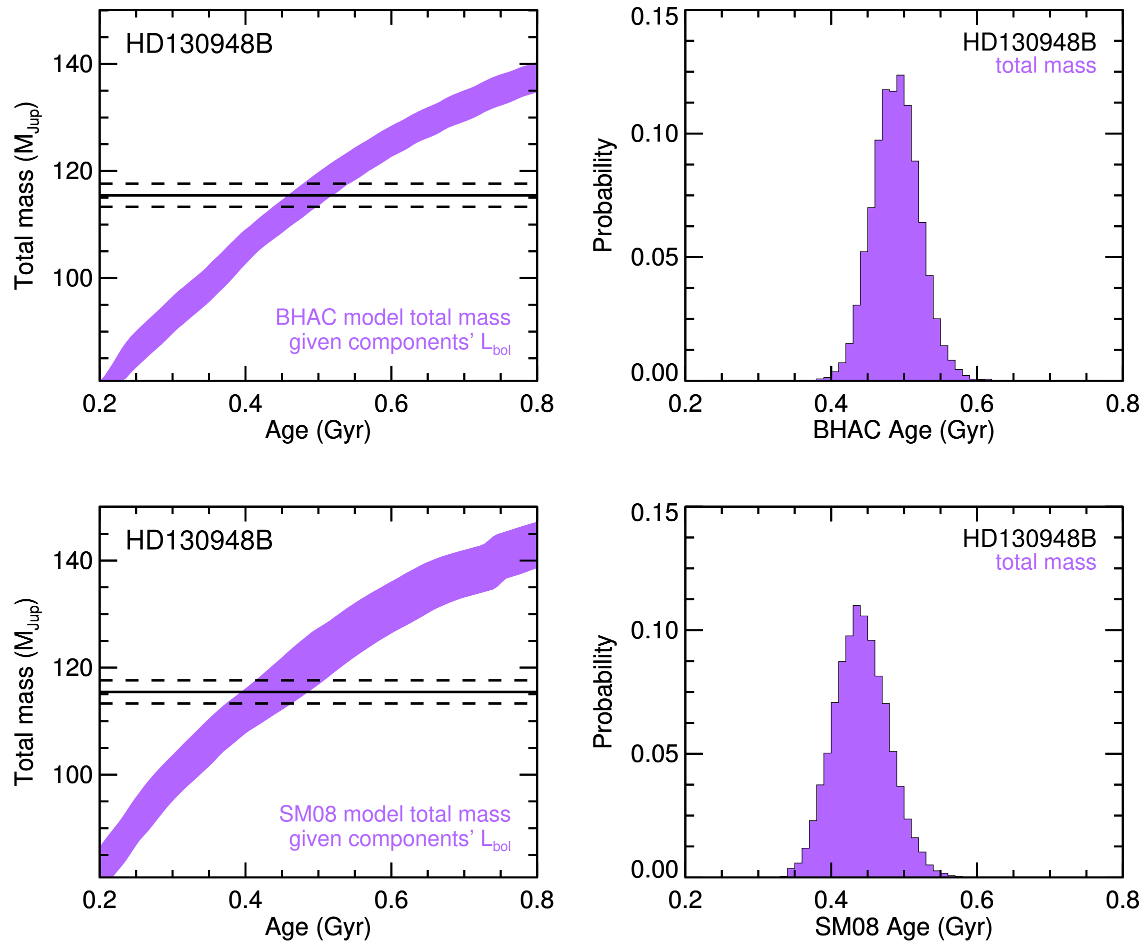

Fig. 8.— (Continued)

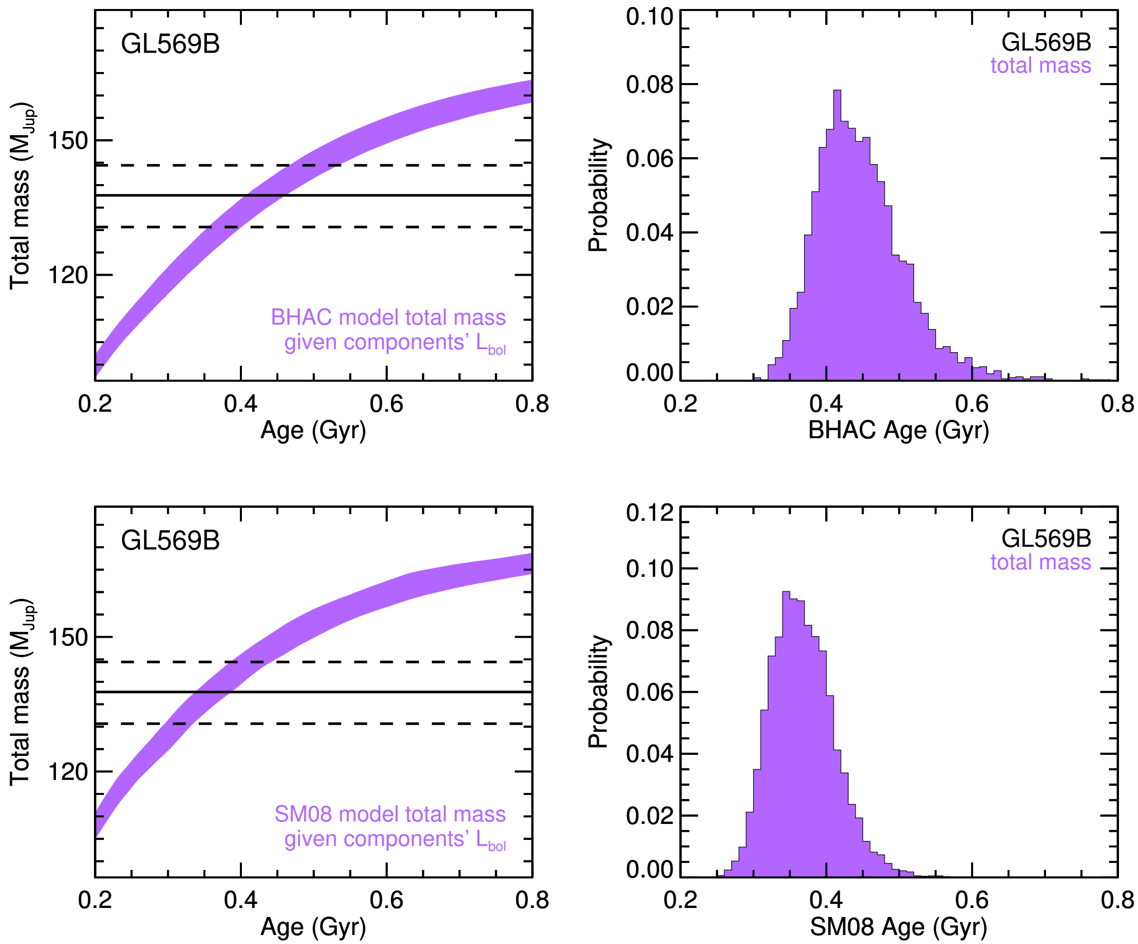

Fig. 8.— (Continued)

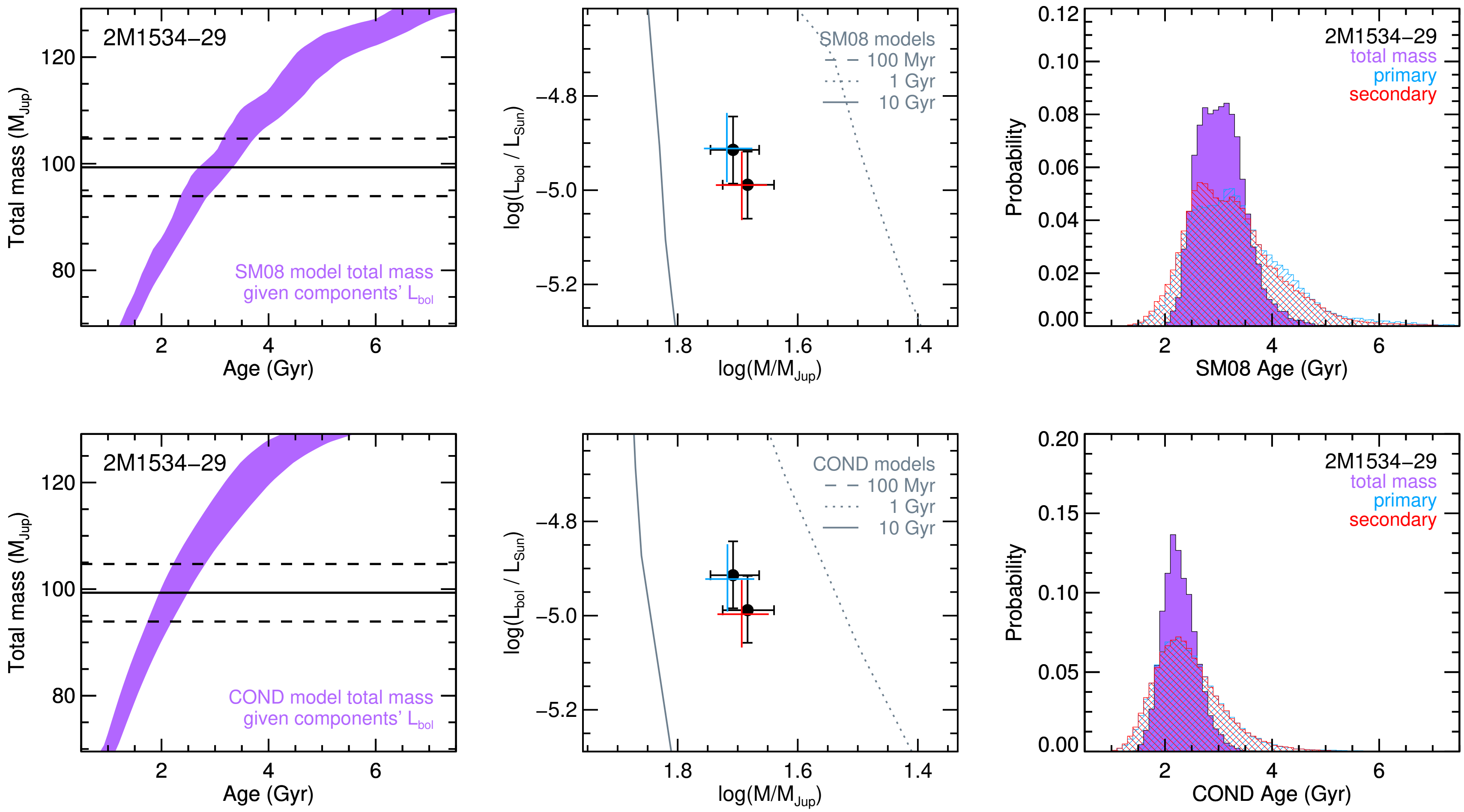

Fig. 8.— (Continued)

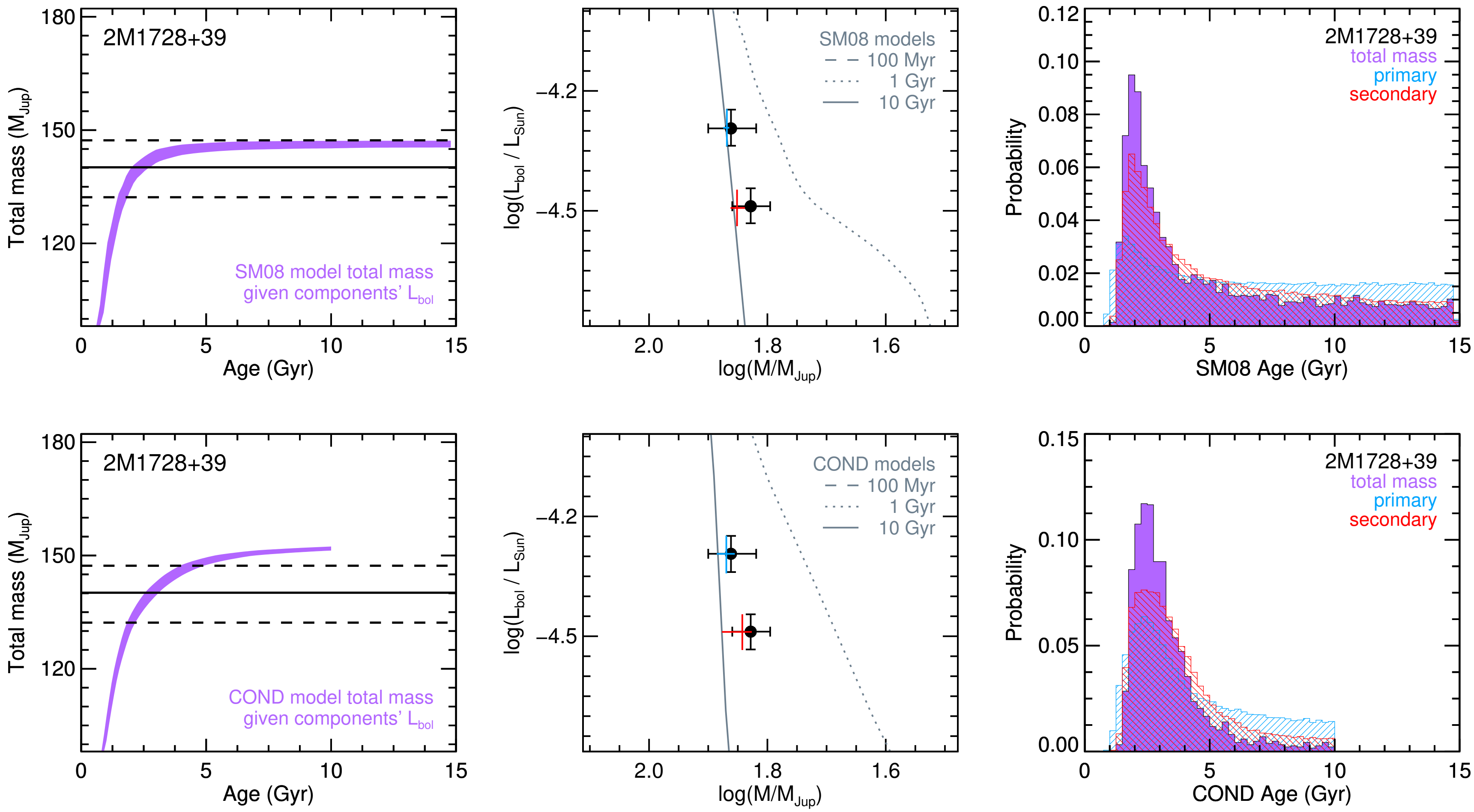

Fig. 8.— (Continued)

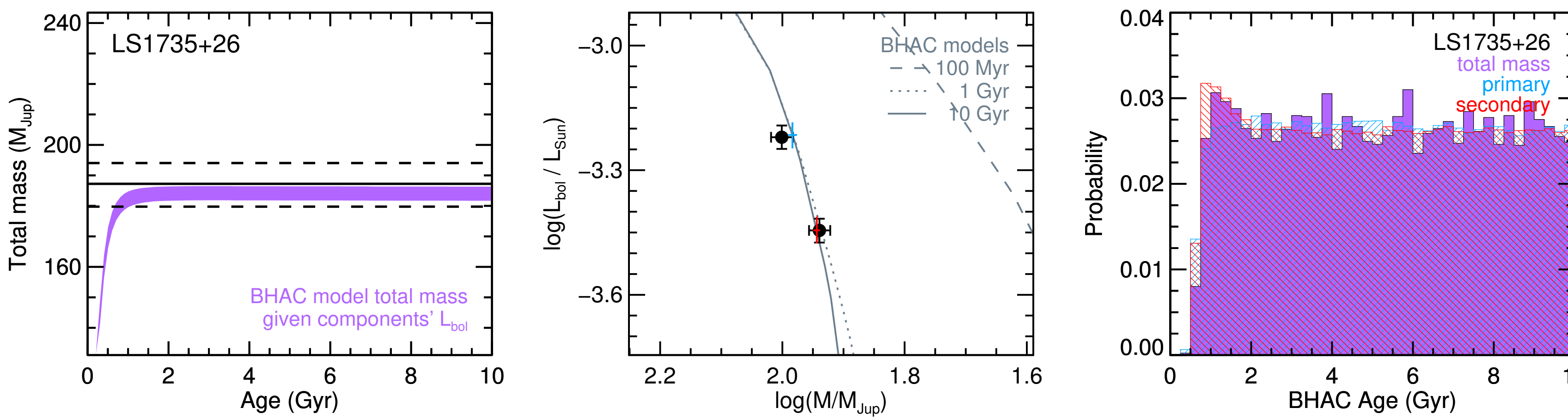

Fig. 8.— (Continued)

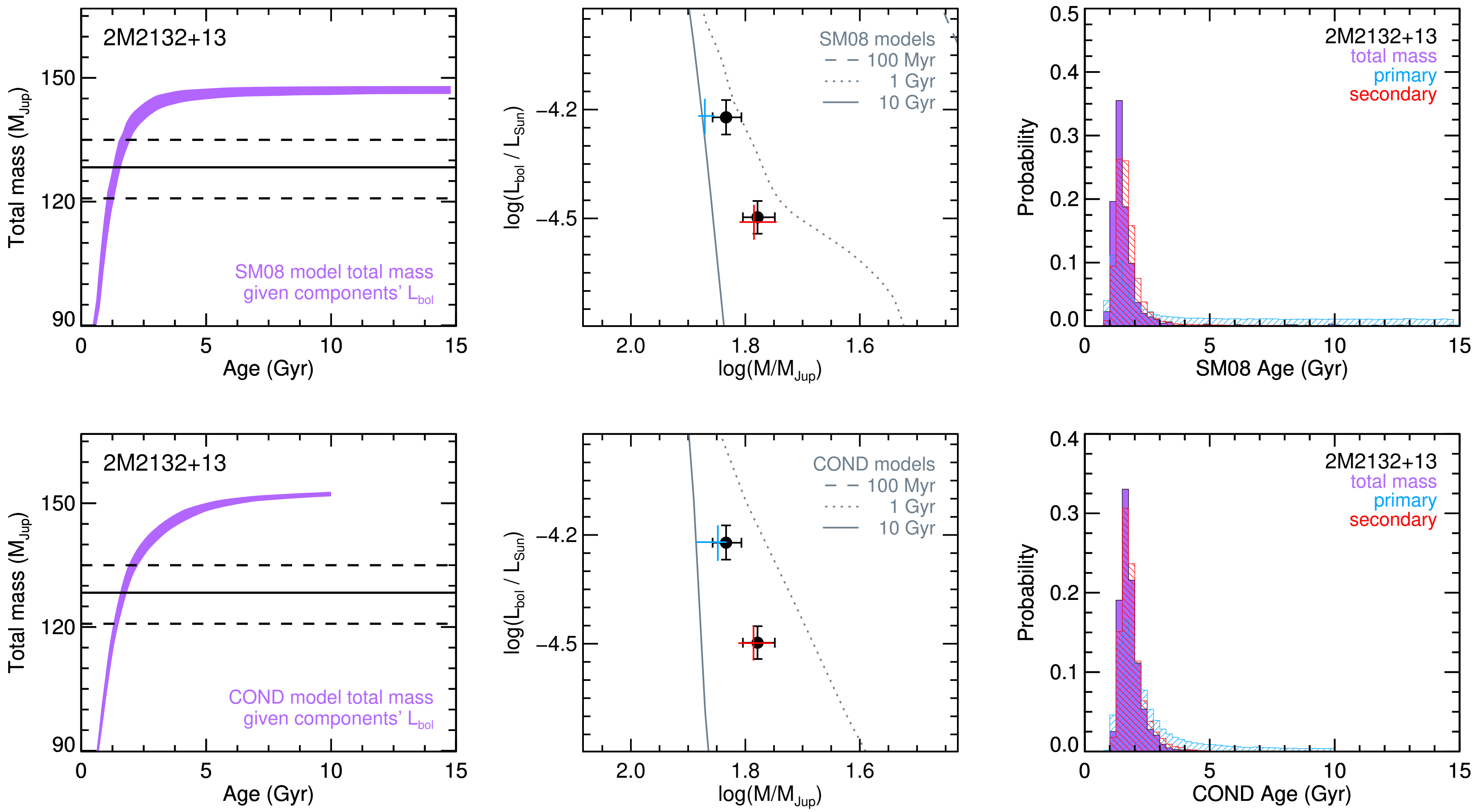

Fig. 8.— (Continued)

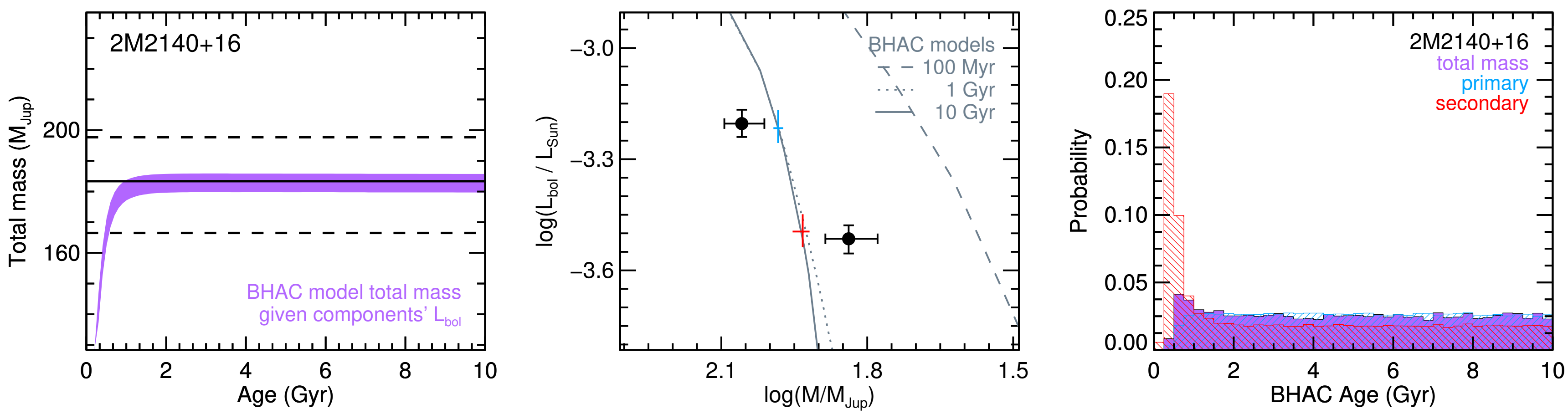

Fig. 8.— (Continued)

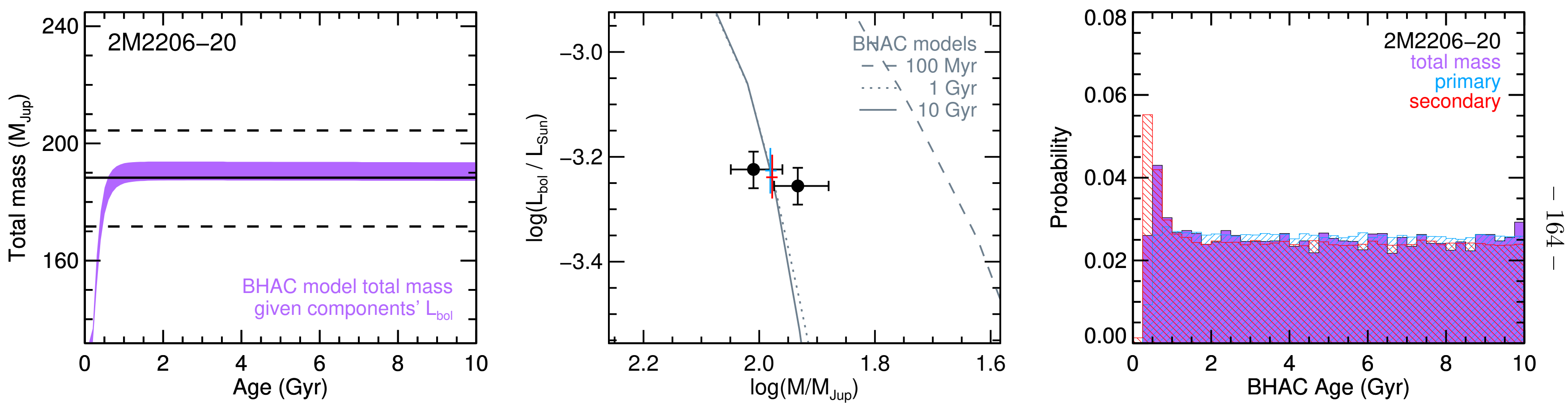

Fig. 8.— (Continued)

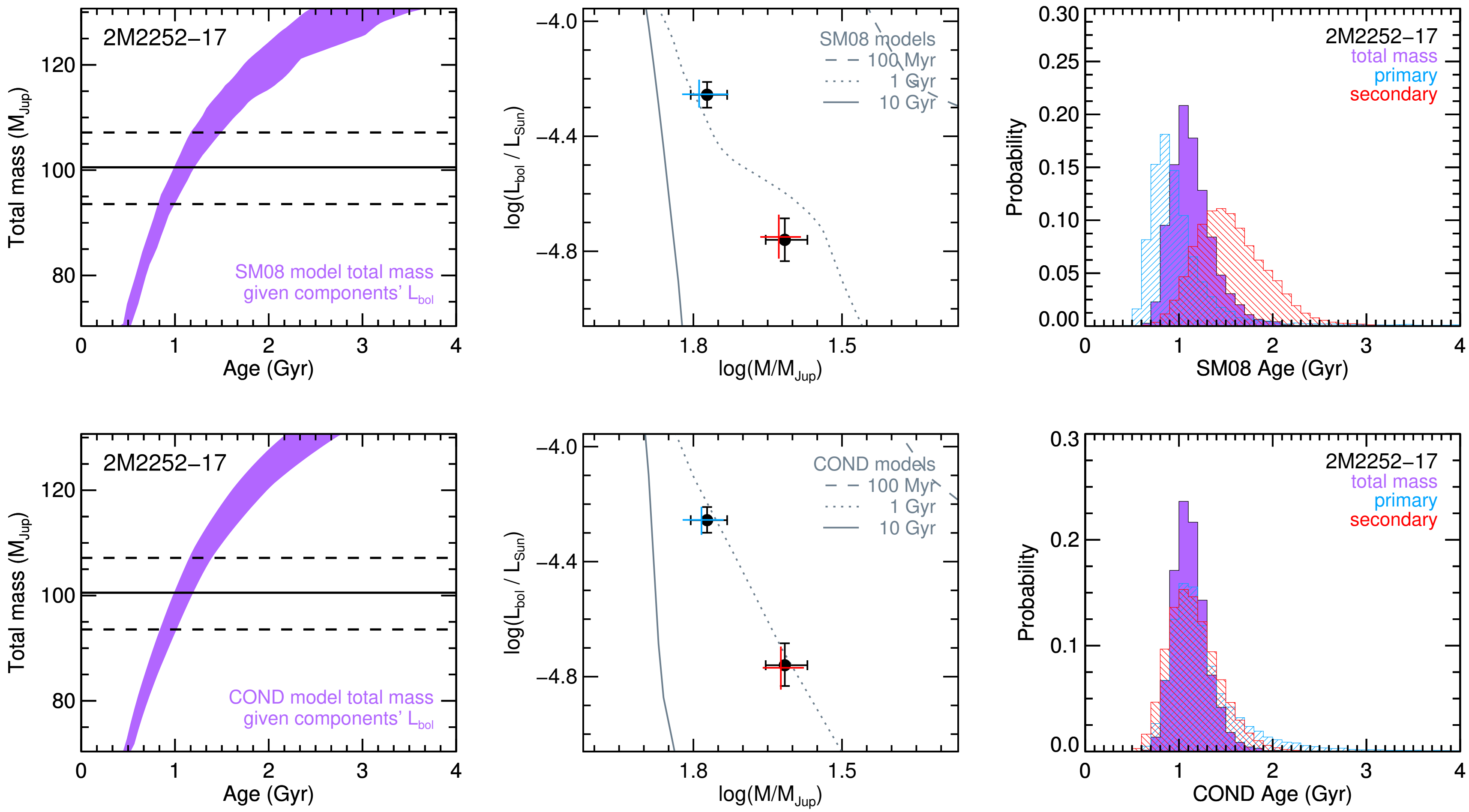

Fig. 8.— (Continued)

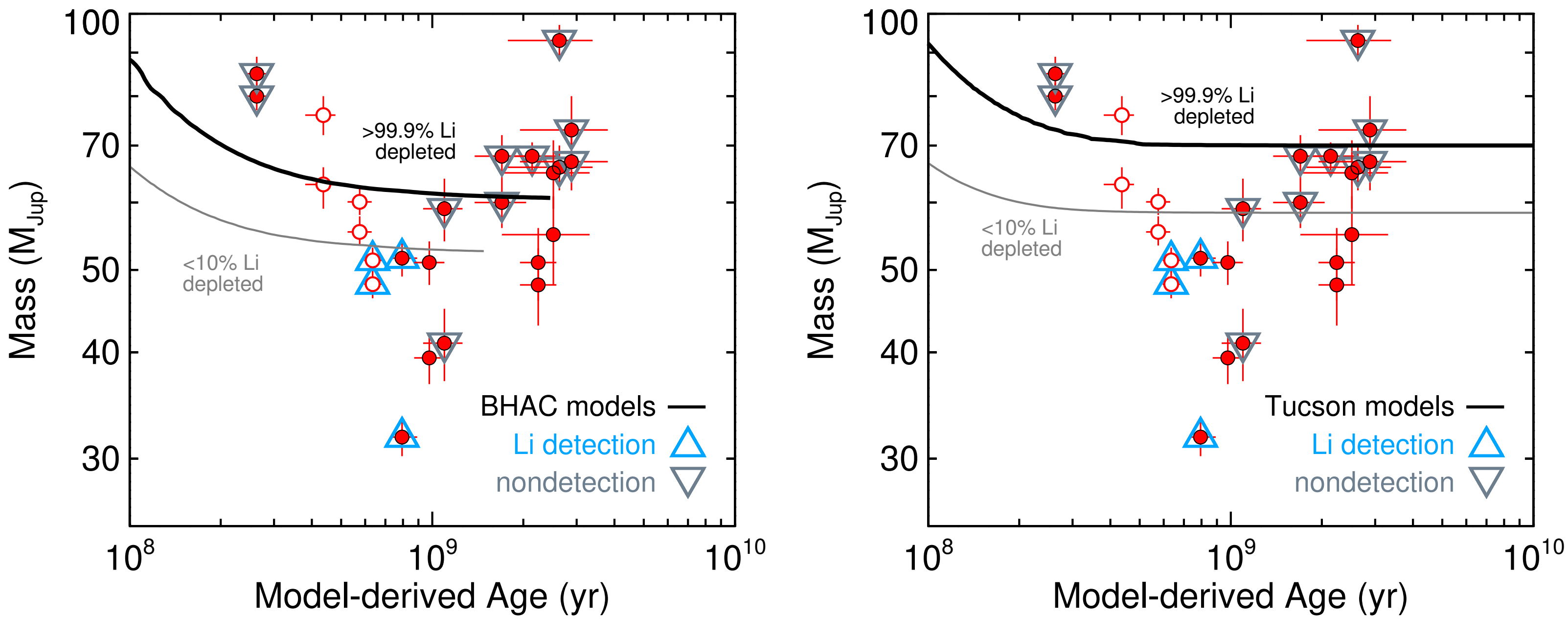

Fig. 9.— Individual masses plotted at their system ages for the 13 of our sample binaries that have well constrained ages according to evolutionary models. Open symbols indicate systems where we use model-derived mass ratios to compute individual masses, including Gl 569Bab. Up-pointing blue triangles indicate components of binaries where lithium is detected in integrated light, while down-pointing orange triangles indicate systems for which an optical spectrum is available and does not display lithium absorption. Model predicted mass limits for strong (>99.9%) and weak (<10%) lithium depletion are shown as thick black and thin gray lines, respectively. The models shown here are BHAC (Baraffe et al. 2015) and Tucson (Burrows et al. 1997). Lithium detections and nondetections seem to generally agree well with BHAC model-predicted lithium depletion, within the observational uncertainties on mass. The mass limit for lithium depletion is higher in Tucson models (70 $M_{\rm Jup}$ instead of 60 $M_{\rm Jup}$), making many nondetections of lithium seemingly discrepant with model predictions. (Note that we use Cond model ages for plotting here because they are the only models that cover the full range of luminosities in our sample, and they tend to agree very well with the results from SM08 and BHAC models. We use the ages from our total-mass analysis, except for LHS 2397aAB where we use the age from the individual-mass analysis of the secondary. For clarity, the unresolved multiples 2MASS J0920+3517B and 2MASS J0700+3157B are not shown. The two young systems that lack lithium information are Gl 569Bab and HD 130948BC.)

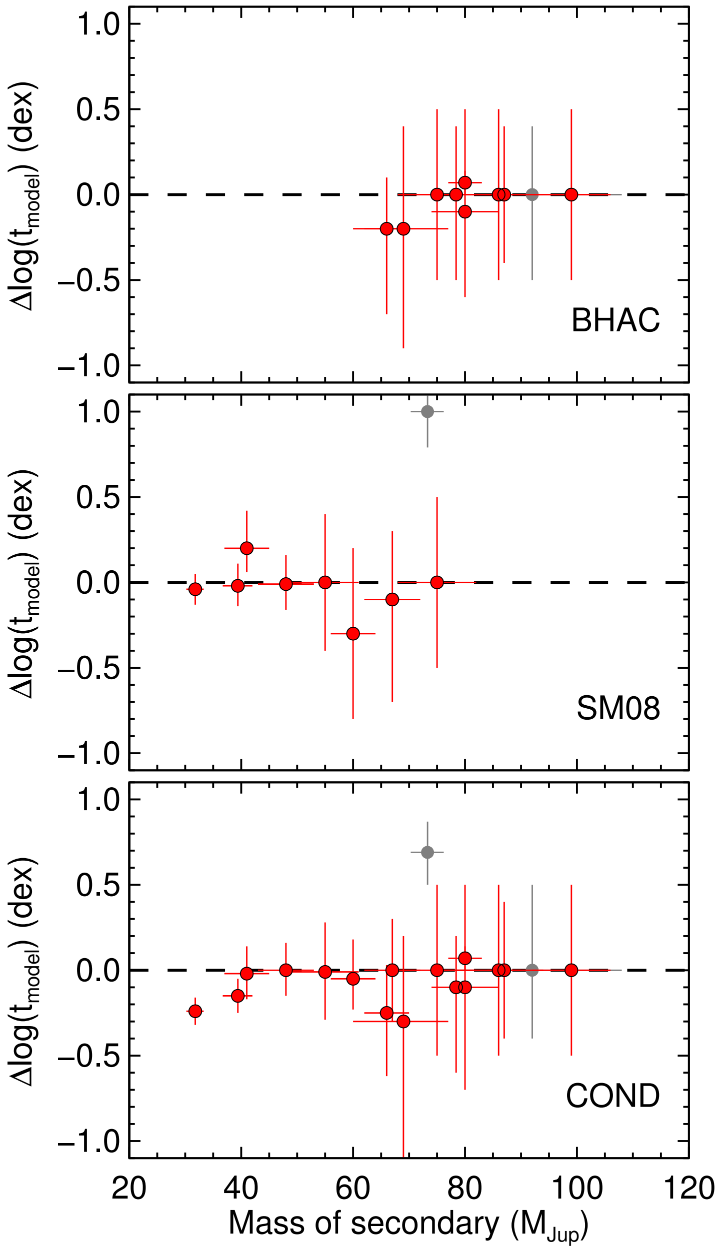

Fig. 10.— Coevality determinations plotted as a function of the mass of the secondary component. For each system with directly measured individual masses and luminosities, we derive the age of each component from models (t_1 and t_2). The data points here show the median and 1σ intervals in the posterior distribution of the logarithm of the difference in age, computed as $\log t_2 - \log t_1$. Gray symbols indicate two of the likely unresolved multiples LP 415-20 and 2MASS J0700+3157. Binaries composed of main-sequence stars (secondary masses $>70\,M_{\rm Jup}$ here) have essentially unconstrained ages and thus $\Delta \log t \approx 0.0 \pm 0.5$ dex (i.e., both stars consistent with any main sequence age at 1σ). Aside from the unresolved multiple 2MASS J0700+3157, all but two systems give consistent ages for the primary and secondary at $\lesssim 1\sigma$. These are two binaries spanning the L/T transition that have the lowest mass secondaries. SDSS J0423−0414AB and SDSS J1052+4422AB are 3.0σ and 1.5σ, respectively, discrepant with coevality in the Cond models. In contrast, the SM08 models that predict a shallower mass–luminosity relation in the L/T transition yield coeval ages for both systems.

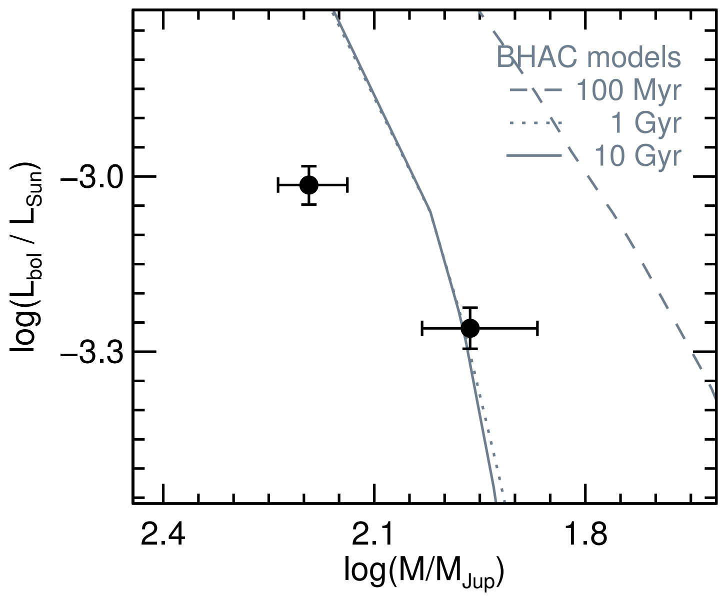

Fig. 11.— Individual mass and luminosity measurements shown alongside models. These are all likely triples given that the data points significantly deviate from coevality (i.e., falling on a single isochrone). In the cases of 2MASS J0700+3157AB and 2MASS J0920+3517AB, the less luminous secondary is actually more massive than the more luminous primary, implying that the secondaries are in fact unresolved binaries. In the case of LP 415-20AB, the primary is much less luminous than expected given its mass, implying that it is an unresolved pair of lower luminosity, lower mass objects.

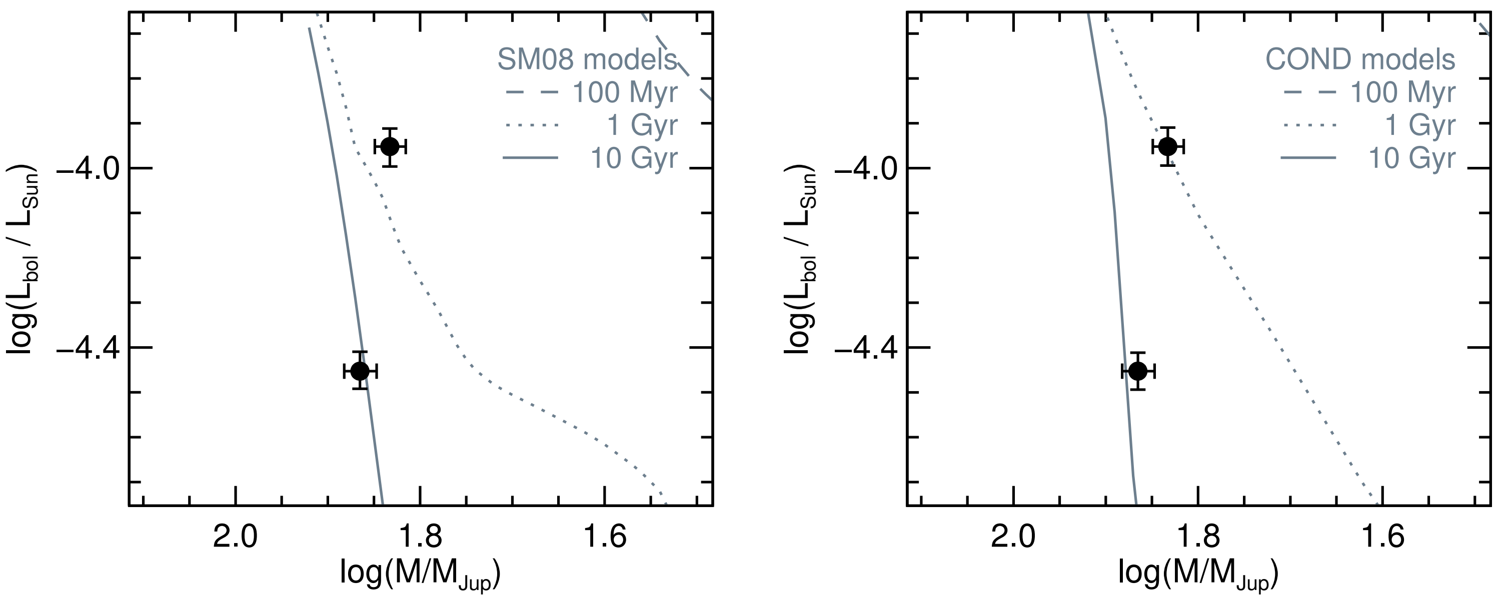

Fig. 11.— (Continued)

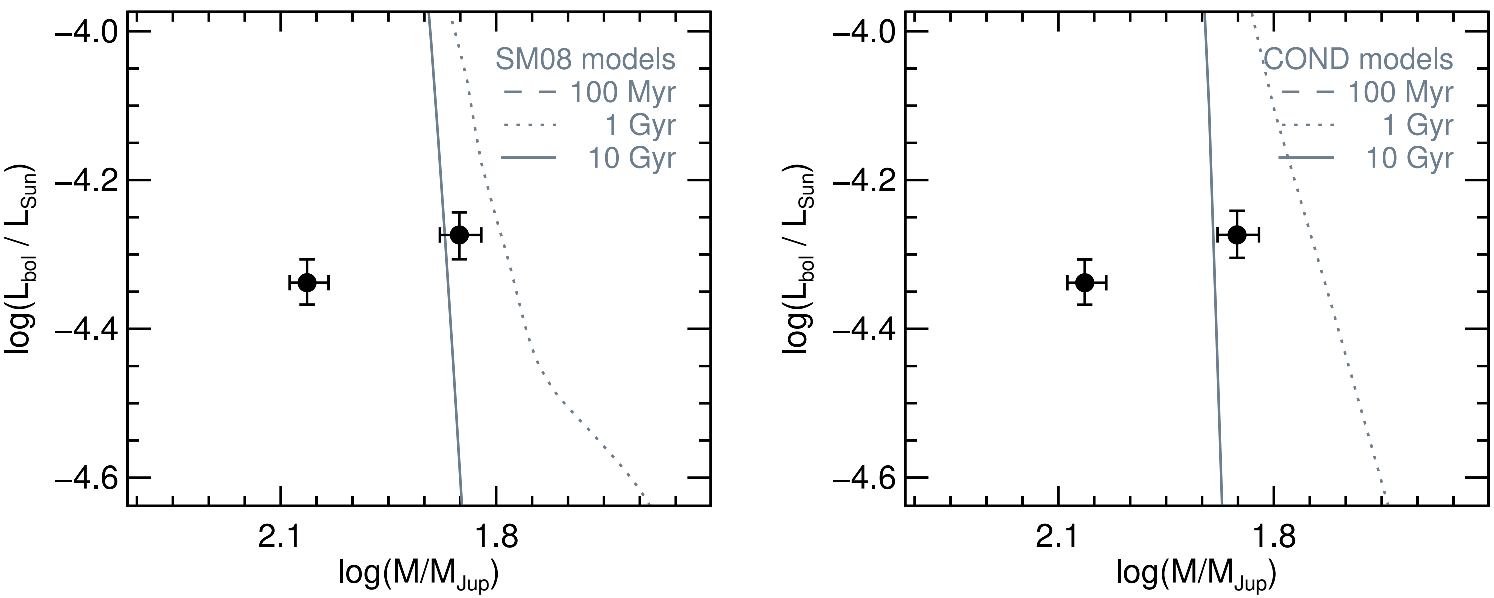

Fig. 11.— (Continued)

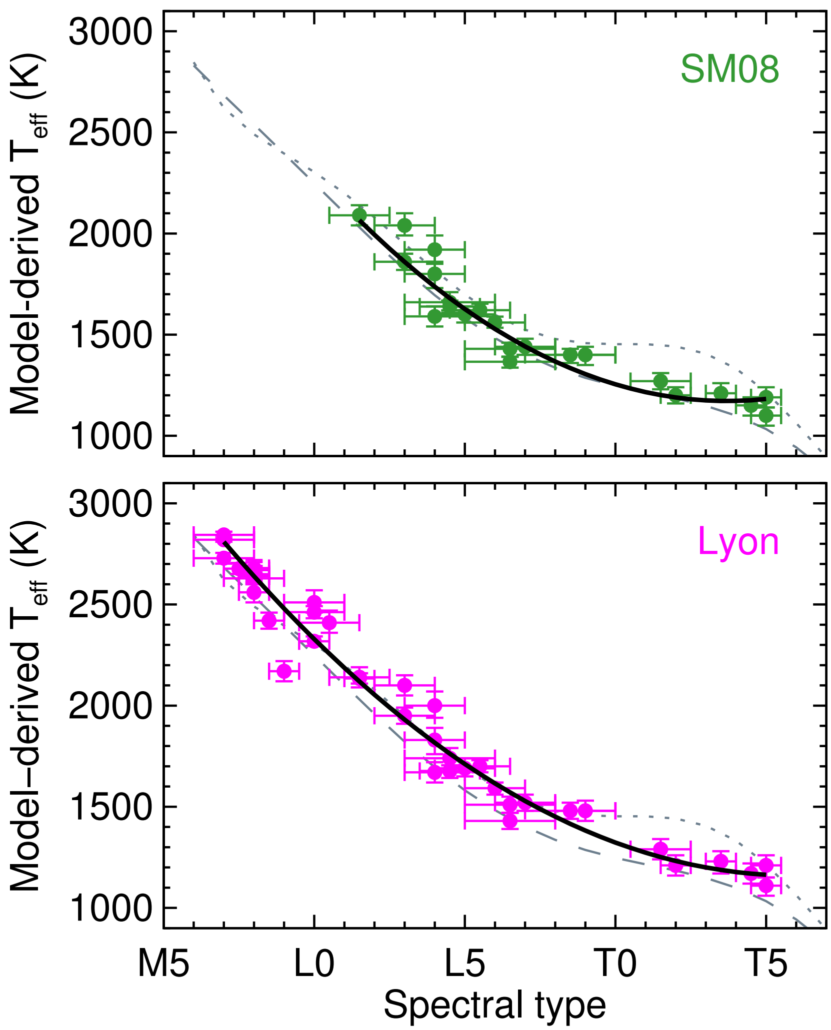

Fig. 12.— Effective temperatures derived from SM08 models (top) and from Lyon models (bottom; BHAC and Cond). Solid black lines show our second-order polynomials to the relations, having rms scatter about the fit of 90 K for the 40 objects with Lyon temperatures and 80 K for the 22 objects with SM08 temperatures. Gray lines indicate previous literature polynomial relations from Golimowski et al. (2004, dotted) and Filippazzo et al. (2015, dashed).

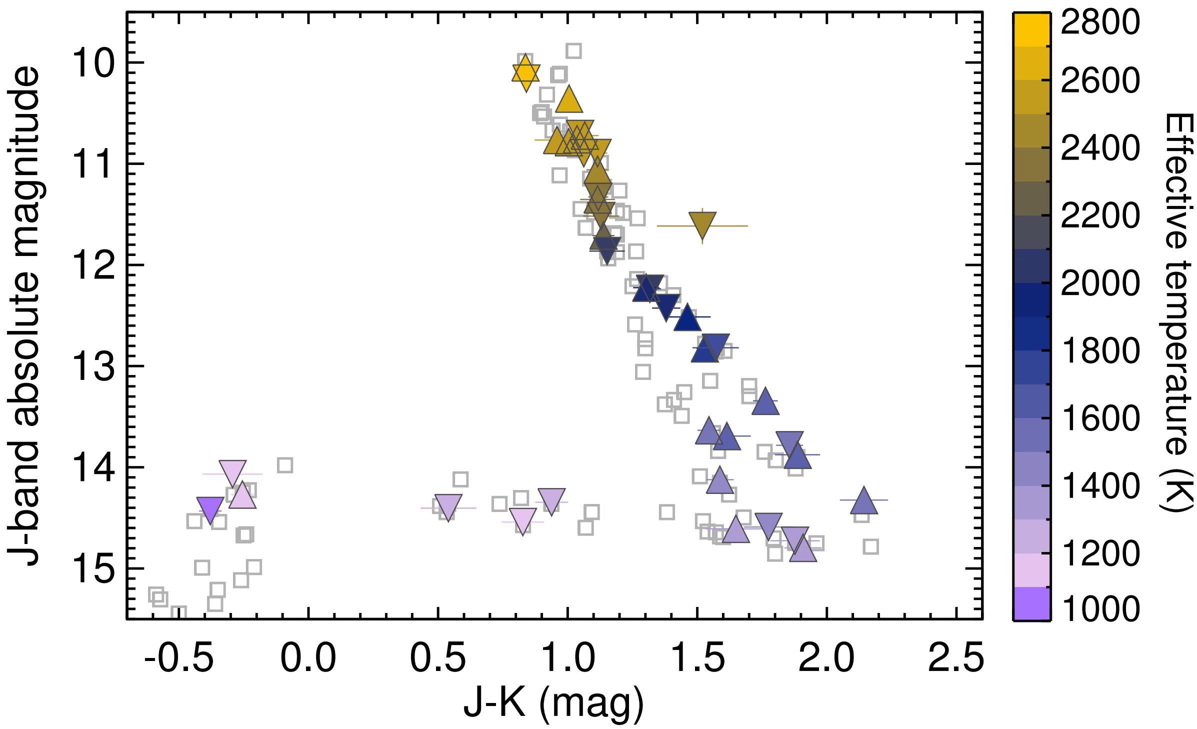

Fig. 13.— Color–magnitude diagram (CMD) showing our dynamical mass sample with symbols colored according to their Lyon model-derived effective temperatures (BHAC when possible, otherwise Cond). Up-pointing triangles indicate primary components, down-pointing triangles indicate secondary components, and the field sequence is shown for reference as gray squares using the latest compilation of ultracool dwarf parallaxes at `http://www.as.utexas.edu/~tdupuy/plx`. As expected, temperature correlates strongly with the location along the CMD sequence, consistent with temperature being a primary driver of the spectral energy distributions of ultracool dwarfs. Objects at the faintest magnitudes ($M_J = 14$–15 mag) span temperatures of ≈1500 K to ≈1100 K, where objects with bluer $J - K$ colors have cooler model-derived temperatures.

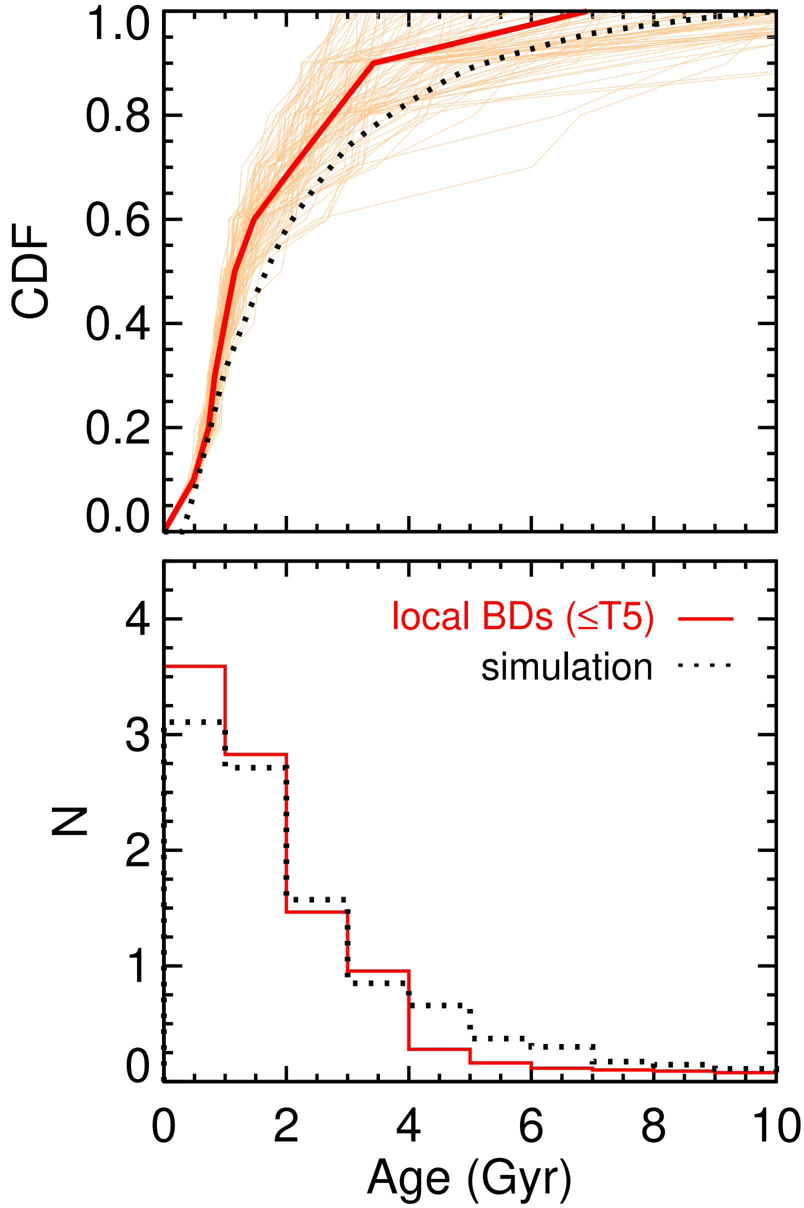

Fig. 14.— Bottom: age distribution for the systems with well determined ages (solid red line). The histogram is a mean of 10^4 posterior values for each system, resulting in noninteger values for each 1-Gyr-wide bin. The dotted line shows the age distribution of a synthesized population of brown dwarfs with masses of 30–70 $M_{\rm Jup}$ and assuming a constant star formation rate (but including the young-age skew due to dynamical heating that removes old objects from the Galactic midplane, according to the Besançon model of the solar neighborhood). Top: cumulative distribution functions computed for the median age of each system (thick red line) and for 100 randomly drawn posterior age values for each system (thin orange lines). The observed distribution is remarkably consistent with the simplistic synthesized population that assumes a constant star formation rate for the thin disk and a spectral type cut of T5, as is the case for our sample of brown dwarfs here.

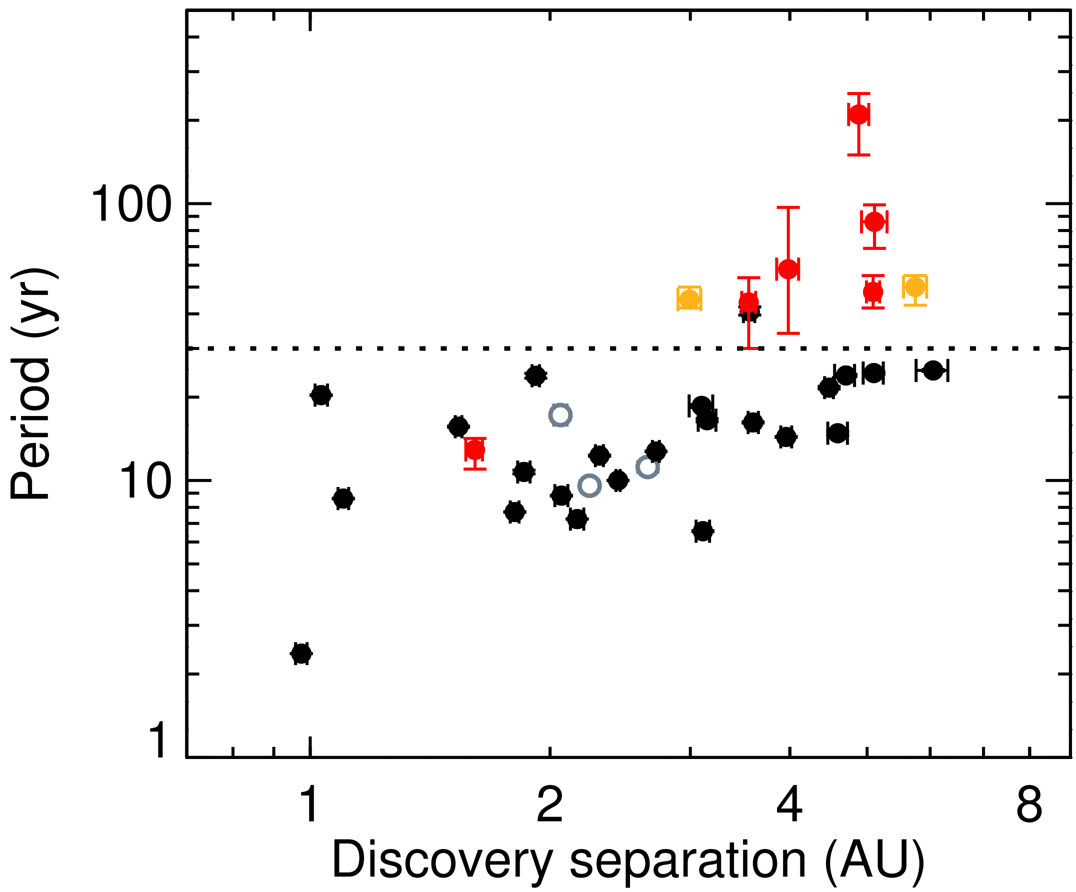

Fig. 15.— Orbital period of our sample binaries plotted as a function of projected separation at discovery. Symbols are colored according to the quality of the orbit determination: good (black), marginal (orange), and poor (red). Open gray symbols indicate results from the literature for LHS 1070BC, ϵ Ind Bab, and LSPM J1314+1320AB. The quality of our orbit determinations are almost entirely determined by having sufficient observational time coverage, so the longest-period orbits tend to be poorly determined. The only $P < 30$ yr binary with a poor orbit is 2MASS J0926+5847AB, which is seen nearly edge on and lacks the phase coverage from our 3-year *HST* program needed to robustly determine the orbit from such a challenging viewing angle. Therefore, we conclude that a cut of $P < 30$ yr (dotted line) yields an effectively complete sample of orbit determinations to be used in a statistical study of orbital eccentricities. Most orbits have error bars smaller than the plotting symbols.

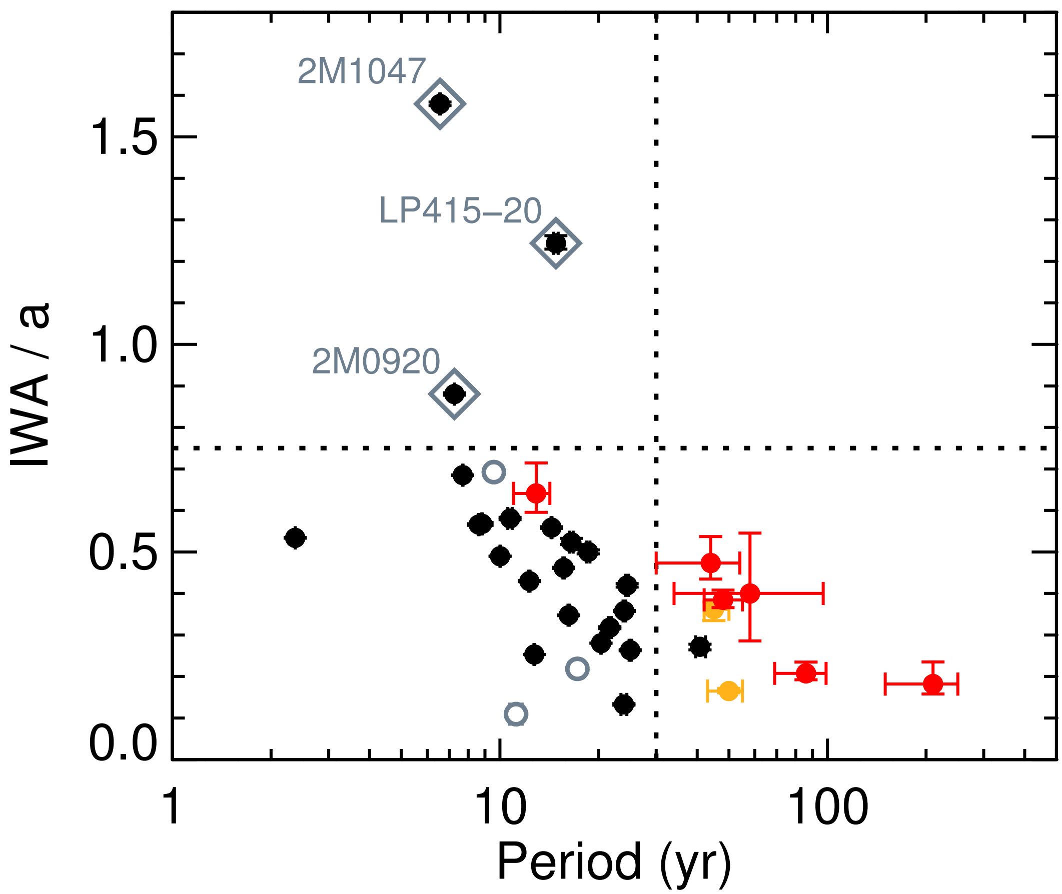

Fig. 16.— The ratio of the inner working angle (IWA) of the discovery data for each binary to its semimajor axis (a). For a given a, a survey with IWA $\ll a$ is sensitive to binaries of all eccentricities, while a survey with IWA $> a$ is strongly biased toward discovering eccentric binaries. According to simulations from Dupuy & Liu (2011), a cutoff of IWA/$a < 0.75$ will result in minimal bias in the resulting eccentricity distribution. Therefore, we exclude the binaries 2MASS J1047+4026AB, LP 415-20AB, and 2MASS J0920+3517AB (gray diamonds) from our statistical analysis. The first two of these have IWA/$a > 1$ and indeed turn out to have quite eccentric ($\geq$0.7) orbits. Most orbits have error bars smaller than the plotting symbols.

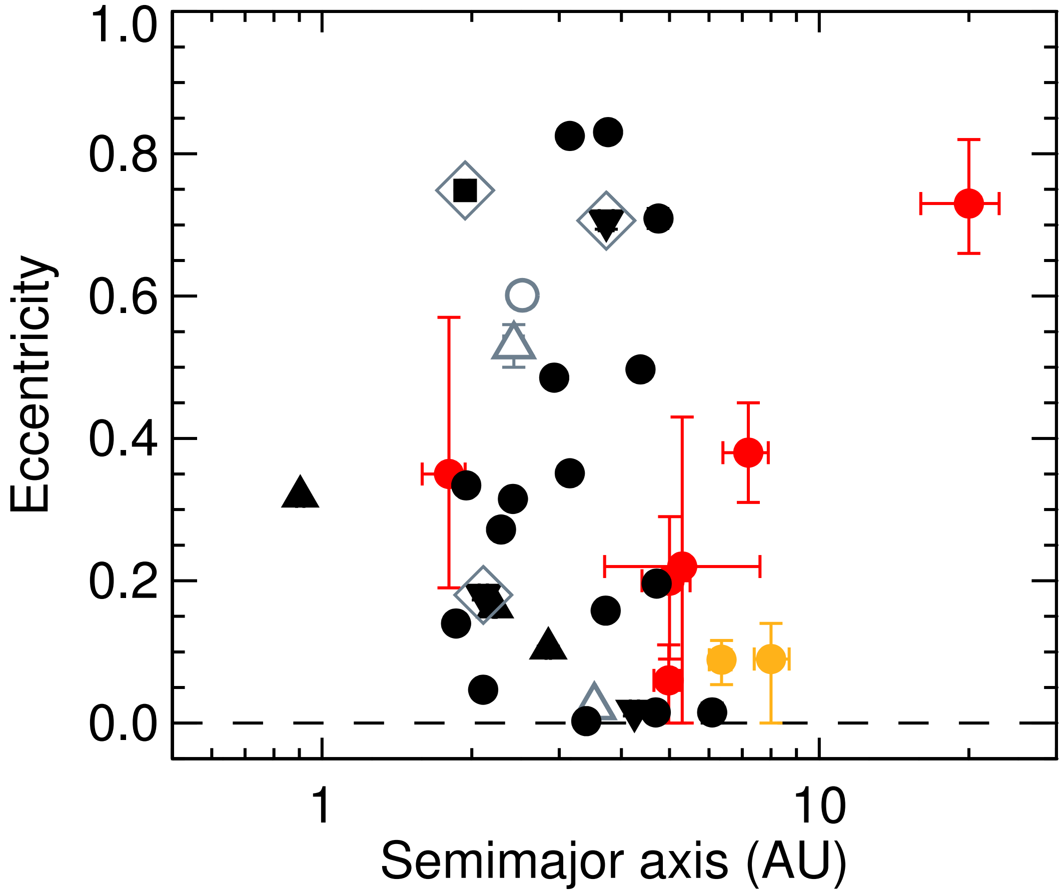

Fig. 17.— Eccentricity as a function of semimajor axis for all orbits in our sample. Symbol shapes indicate orbits that are simple binaries (circles), inner pairs of hierarchical triples (up-pointing triangles), outer pairs of hierarchical triples (down-pointing triangles), or an inner pair in a quadruple (square). Symbols are colored according to the quality of the orbit determination: good (black), marginal (orange), and poor (red). Open gray symbols indicate results from the literature for LHS 1070BC, ϵ Ind Bab, and LSPM J1314+1320AB. Objects expected to be impacted by discovery bias (IWA/a > 0.75) are enclosed by large gray diamonds. No significant trends in eccentricity with semimajor axis are apparent. Most orbits have error bars smaller than the plotting symbols.

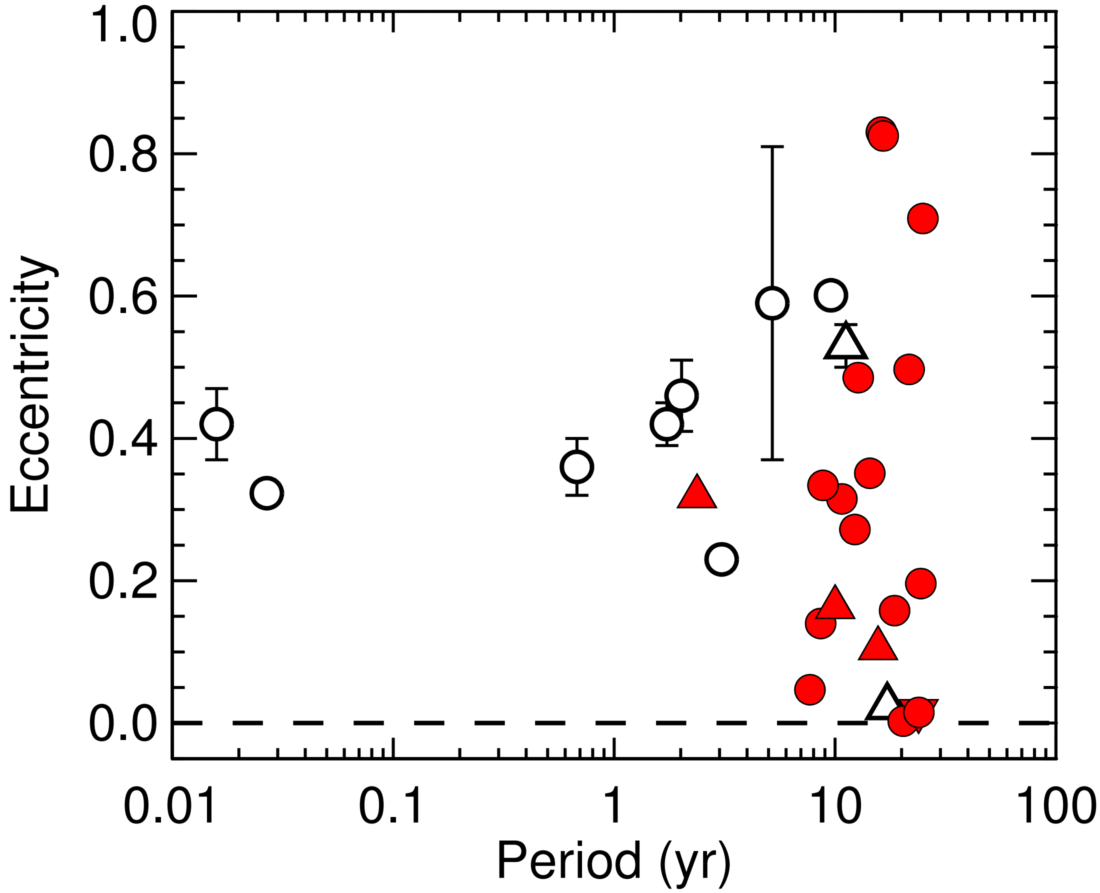

Fig. 18.— Eccentricity as a function of orbital period for binaries in our de-biased sample (filled red) and from the literature (open black). Symbol shapes indicates orbits that are simple binaries (circles), inner pairs of a hierarchical triples (up-pointing triangles), or outer pairs of hierarchical triples (down-pointing triangles). Our sample and some published orbits have error bars smaller than the plotting symbols. Literature results for spectroscopic, astrometric, and eclipsing binaries tend to have short periods and modest eccentricities (0.2–0.6). In contrast, visual binaries at longer periods have some very eccentric orbits ($\geq$0.7) and a substantial fraction of low-e orbits (10 of 22 have $e = 0.0$–0.2). Whether this is indicative of an actual difference in orbital properties will require a larger sample of short-period binaries.

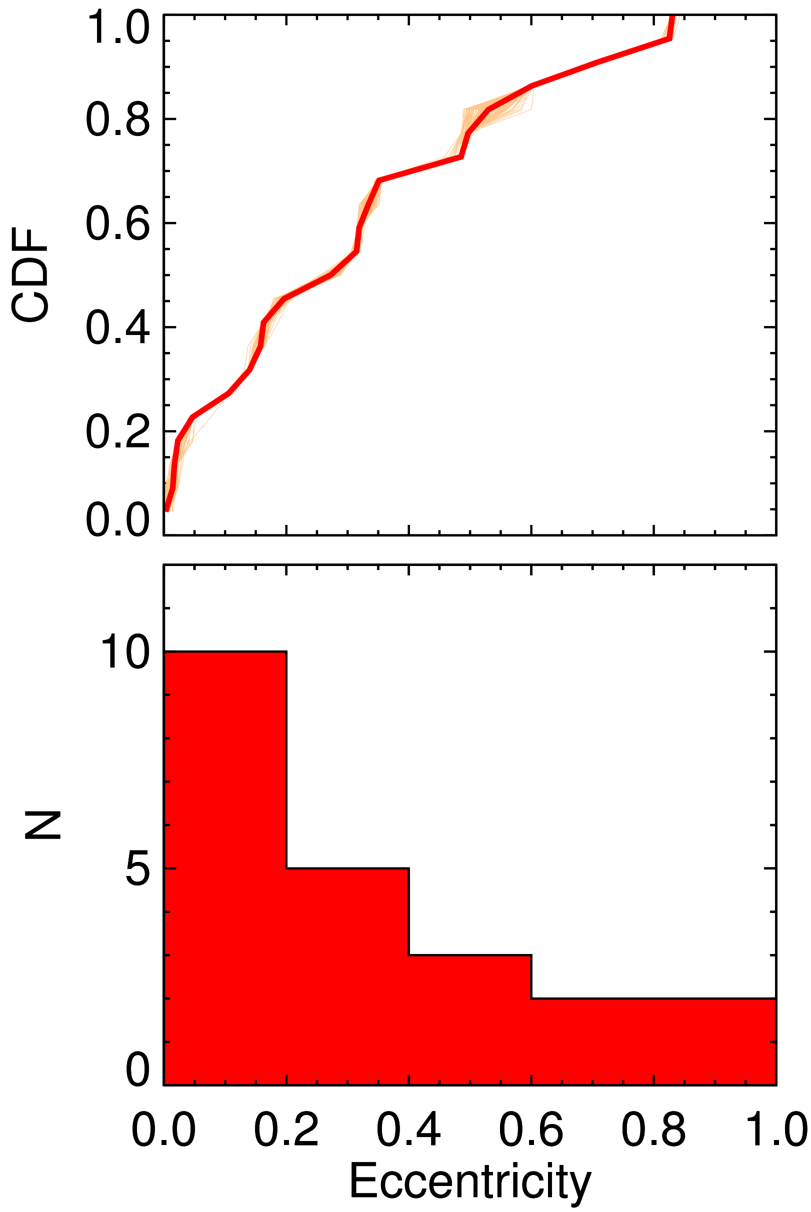

Fig. 19.— Bottom: eccentricity distribution of our de-biased visual binary sample ($P < 30\,\mathrm{yr}$). Top: cumulative distribution functions computed for the median eccentricity of each orbit (thick red line) and for 100 randomly drawn posterior values for each orbit (thin orange lines). Almost half of the orbits (10 of 22) have low eccentricities (0.0–0.2).

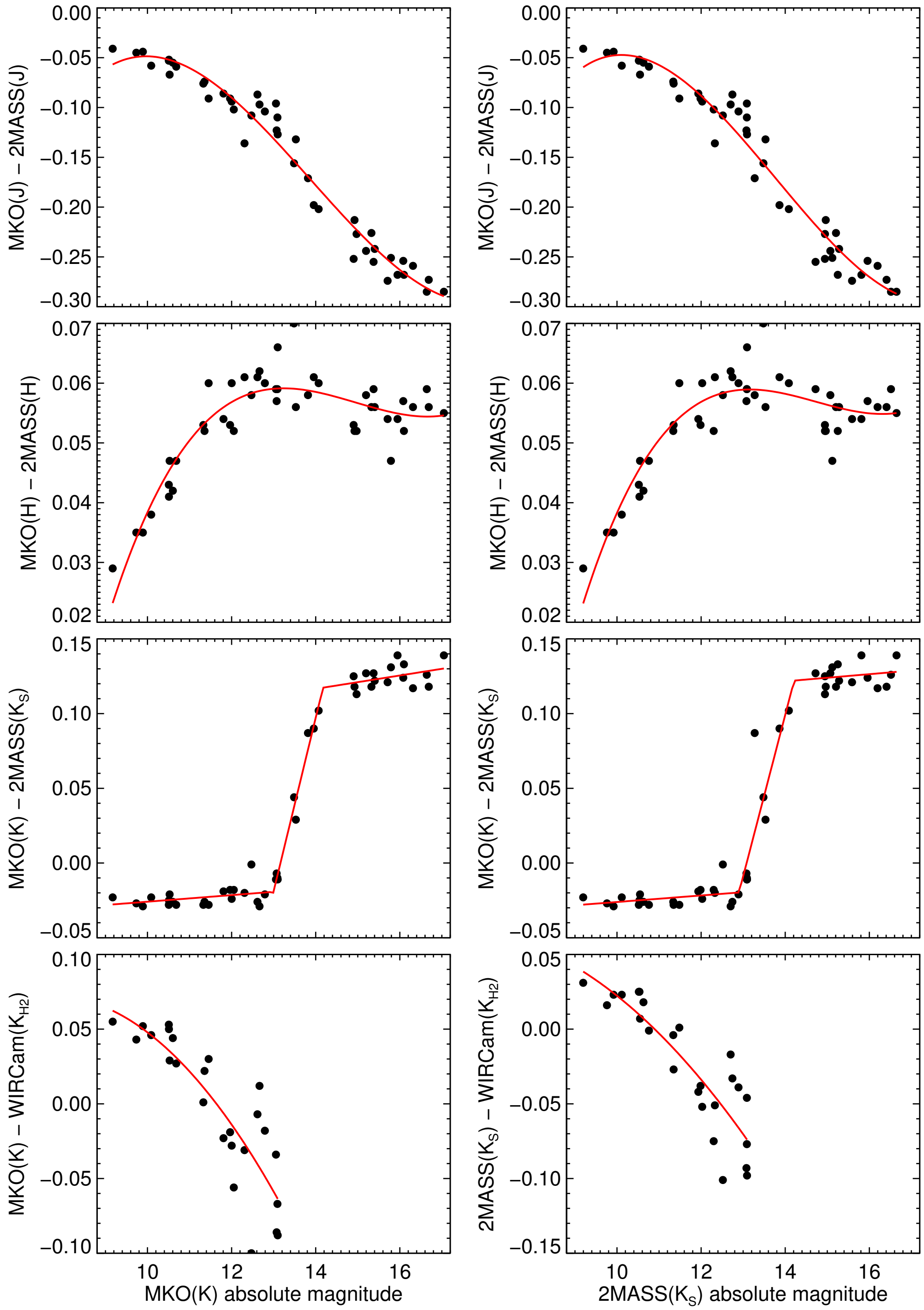

Fig. 20.— Polynomial relations between MKO-to-2MASS photometric conversions and absolute magnitude. K-band is a three-part piecewise linear fit, while others are single polynomial fits. The input data used to derive these fits (black points) are computed by synthetic photometry as described in Sections A.1 and A.2. We use these relations to derive JHK photometry on both 2MASS and MKO systems in cases where it is not measured directly.

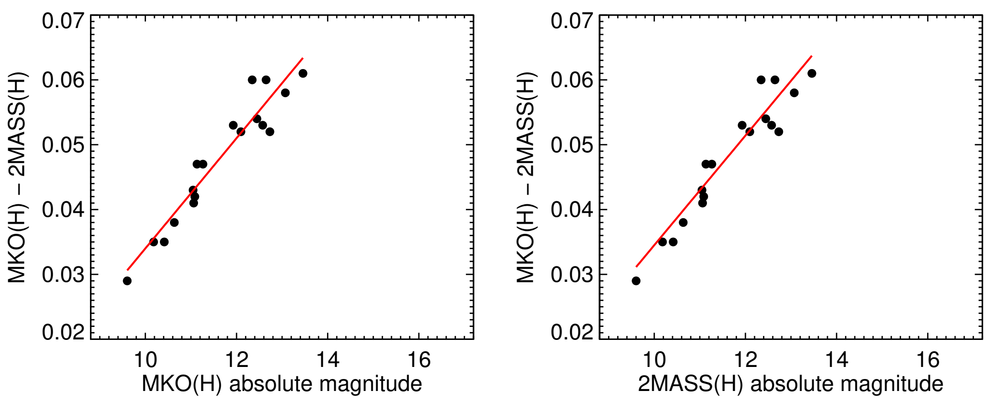

Fig. 20.— (Continued)

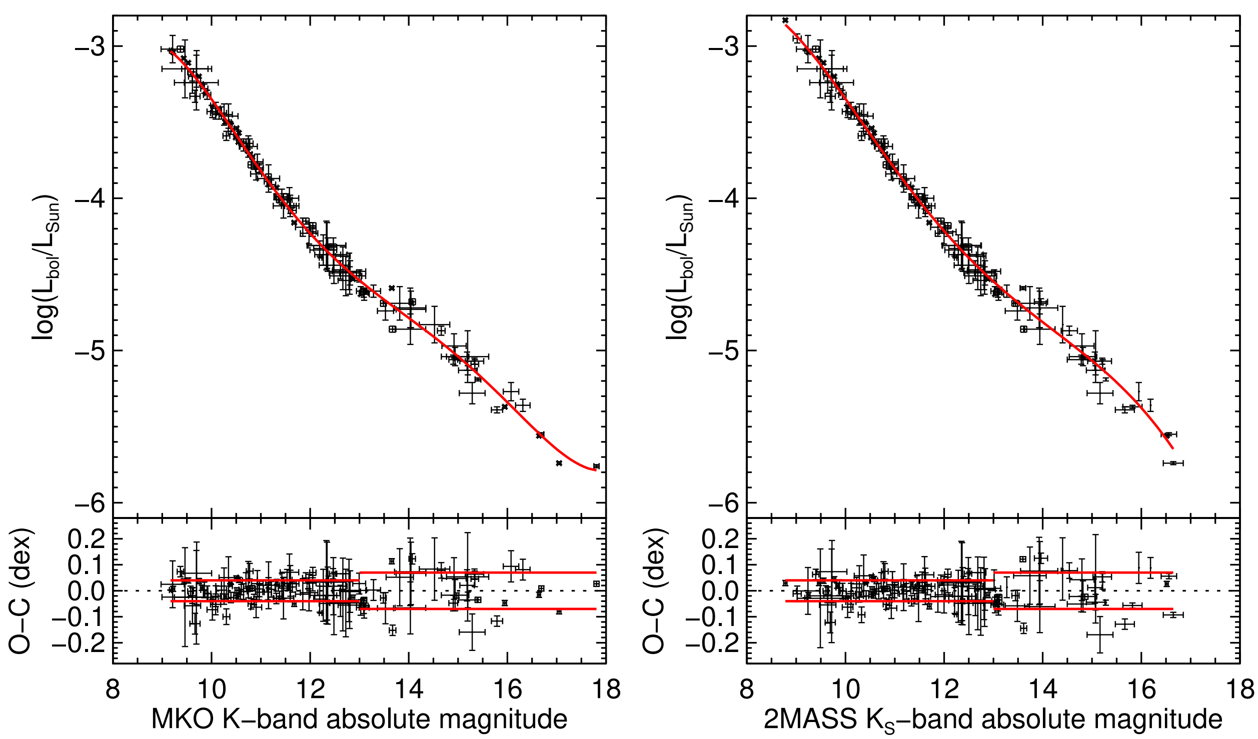

Fig. 21.— Polynomial relations between bolometric luminosity and absolute magnitude (red) derived from input data from Filippazzo et al. (2015) (black points) as described in Section A.3. Bottom panels show the residuals in the input data after subtracting the polynomials. We use these relations to derive the component luminosities for our sample binaries. When both components have $M_H < 13.3\,\mathrm{mag}$, we use the H-band relations, otherwise we use K-band relations.

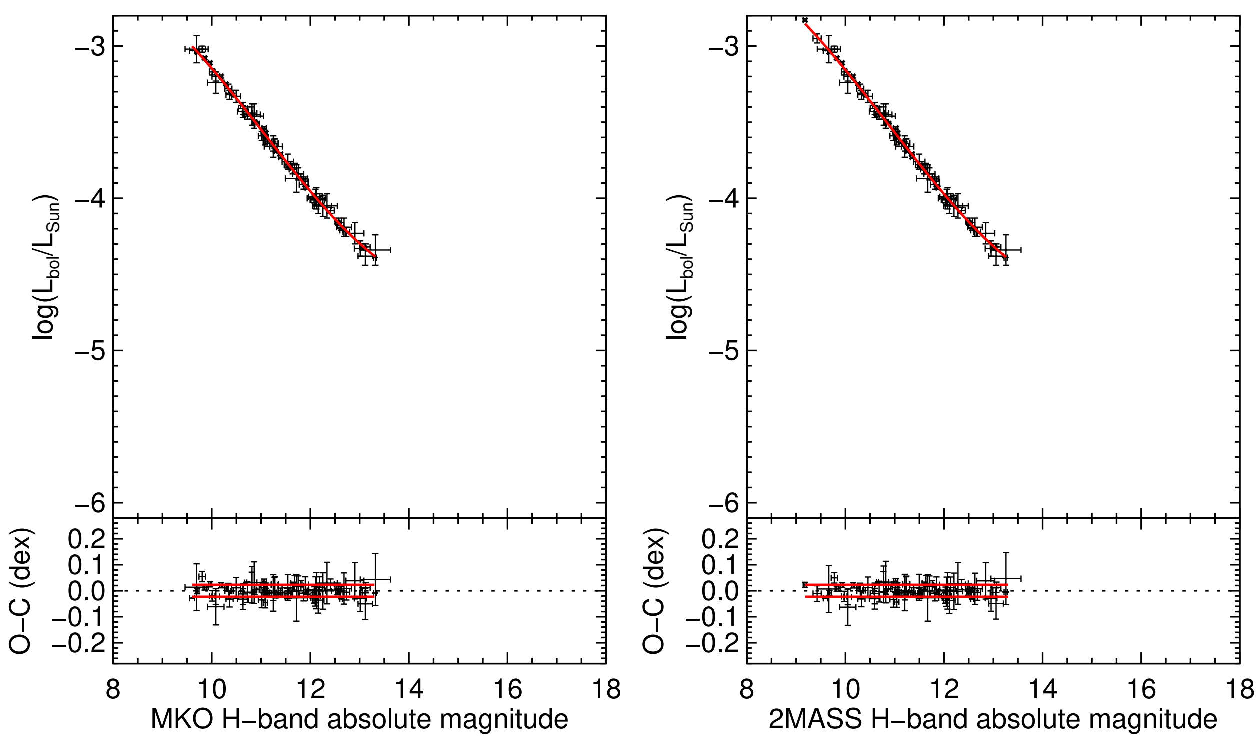

Fig. 21.— (Continued)

Table 1. Orbit Monitoring Sample

Name	Binary Discovery			Integrated-Light Spec. Type		Component Spec. Types	
	Sep.	Epoch (UT)	Ref.	optical/IR	Ref.	A+B	Ref.
LP 349-25AB	0.″125	2004-07-03	Forv05	M8/M8 INT-G	Gizi00, Dupu16b	M7:+M8:	Dupu12
LP 415-20AB	0.″119	2002-02-07	Sieg03	M7.5/ ···	Gizi00	M6:+M8	Dupu16b
SDSSp J042348.57−041403.5AB	0.″164	2004-07-22	Burg05	L7.5/T0	Cruz03, Burg06a	L6.5:+T2	Dupu12
2MASS J05185995−2828372AB	0.″051	2004-09-07	Burg06b	L7/T1p	Kirk08, Burg06a	L6:+T4	Dupu12
2MASS J07003664+3157266AB	0.″170	2004-12-29	Reid06a	L3.5/ ···	Thor03	L3:+L6.5:.	Dupu12
LHS 1901AB	0.″275	2004-01-08	Mont06	M7/M7	Lepi09, Dupu10	M7:+M7:	Dupu12
2MASSI J0746425+200032AB	0.″220	2000-04-25	Reid01	L0.5/L1	Kirk00, Knap04	L0+L1.5*	Bouy04
2MASSs J0850359+105716AB	0.″160	2000-02-01	Reid01	L6/ ···	Kirk99	L6.5:+L8.5:	Dupu12
2MASSI J0856479+223518AB	0.″098	2001-04-24	Bouy03	L3:/ ···	Cruz03	···	···
2MASSW J0920122+351742AB	0.″070	2000-02-09	Reid01	L6.5/T0p	Kirk00, Burg06a	L5.5:+L9:.	Dupu12
SDSS J092615.38+584720.9AB	0.″070	2004-02-05	Burg06b	··· /T4.5	Burg06a	T3.5:+T5:	Dupu12
2MASSI J1017075+130839AB	0.″100	2001-04-16	Gizi03	L2:/L1	Cruz03, Wils03	L1.5:+L3:	Dupu12
SDSS J102109.69−030420.1AB	0.″172	2004-05-02	Burg06b	T3.5/T3	Kirk08, Burg06a	T0:+T5	Dupu12
2MASSW J1047138+402649AB	0.″122	2002-04-25	Clos03	M8/ ···	Gizi00a	M8+L0:	Dupu16b
SDSS J105213.51+442255.7AB	0.″042	2005-05-01	Dupu15	··· /T0.5	Chiu06	L6.5:.+T1.5:	Dupu15
Gl 417BC	0.″070	2001-02-14	Bouy03	L4.5/ ···	Kirk00	L4.5:+L6:	Dupu12
LHS 2397aAB	0.″270	1997-04-12	Free03	M8/ ···	Kirk95	M8* + ···	Dupu09b
DENIS-P J1228.2−1547AB	0.″275	1998-06-02	Mart99	L5/L6 ± 2	Kirk99, Knap04	L5.5:+L5.5:	Dupu12
Kelu-1AB	0.″291	2005-05-01	Liu05	L2/ ···	Kirk99	L2:+L4:	Dupu12
2MASS J14044948−3159330AB	0.″134	2006-06-03	Loop08	T0/T2.5	Loop08, Loop07	L9:+T5	Dupu16b
HD 130948BC	0.″134	2001-02-24	Pott02	··· / ···	···	L4:+L4:	Goto02
Gl 569Bab	0.″101	1999-08-28	Mart00	M8.5/ ···	Henr90	M8.5+M9	Lane01
SDSS J153417.05+161546.1AB	0.″110	2005-05-01	Liu06	··· /T3.5	Chiu06	T0:+T5.5	Dupu12
2MASS J15344984−2952274AB	0.″065	2000-08-18	Burg03b	T6/T5.5	Burg03a, Burg06a	T4.5+T5	Dupu12
2MASSW J1728114+394859AB	0.″130	2000-08-12	Gizi03	L7/ ···	Kirk00	L5:+L7:	Dupu12
LSPM J1735+2634AB	0.″290	2005-06-05	Law06	M7.5/ ···	Schm07	M7.5+L0:	Dupu12
2MASSW J1750129+442404AB	0.″158	2002-04-25	Sieg03	M7.5/M8	Gizi00b, Dupu12	M6.5:+M8.5:	Dupu12
2MASSI J1847034+552243AB	0.″082	2003-07-10	Sieg05	M6.5/ ···	Cruz03	M6+M7	Dupu12
SDSS J205235.31−160929.8AB	0.″103	2008-06-24	Stum11	··· /T1:	Chiu06	L8.5:.+T1.5	Dupu12
2MASSI J2132114+134158AB	0.″066	2006-06-17	Sieg07	L6/ ···	Cruz07	L4.5:.+L8.5:.	Dupu12
2MASSW J2140293+162518AB	0.″155	2001-09-22	Clos02b	M8.5/ ···	Gizi00b	M8+L0.5:	Dupu16b
2MASSW J2206228−204705AB	0.″168	2001-09-22	Clos02b	M8/M8	Gizi00b, Dupu09a	M8+M8	Dupu09a
DENIS-P J225210.7−173013AB	0.″130	2005-06-21	Reid06b	··· /L7.5	Kend04	L4:+T3.5	Dupu16b
Other Ultracool Visual Binaries with Published Orbits and Parallaxes							
LHS 1070BC	0.″267	1993-07-29	Lein94	M8.5/ ···	Lein00	M9.5+L0*	Rajp12
LSPM J1314+1320AB	0.″130	2005-06-15	Law06	M7/M6 FLD-G	Lepi09, Dupu16a	···	···
ϵ Ind Bab	0.″732	2003-08-13	McCa04	··· /T2.5	Scho03	T1+T6	King10

References. — Bouy03 = Bouy et al. (2003); Bouy04 = Bouy et al. (2004); Burg03a = Burgasser et al. (2003a); Burg03b = Burgasser et al. (2003b); Burg05 = Burgasser et al. (2005); Burg06a = Burgasser et al. (2006a); Burg06b = Burgasser et al. (2006b); Chiu06 = Chiu et al. (2006); Clos02a = Close et al. (2002a); Clos02b = Close et al. (2002b); Clos03 = Close et al. (2003); Cruz03 = Cruz et al. (2003); Cruz07 = Cruz et al. (2007); Dupu09a = Dupuy et al. (2009a); Dupu09b = Dupuy et al. (2009c); Dupu10 = Dupuy et al. (2010); Dupu12 = Dupuy & Liu (2012); Dupu15 = Dupuy et al. (2015b); Dupu16a = Dupuy et al. (2016); Dupu16b = this work; Forv05 = Forveille et al. (2005); Free03 = Freed et al. (2003); Gizi00a = Gizis et al. (2000a); Gizi00b = Gizis et al. (2000b); Gizi03 = Gizis et al. (2003); Henr90 = Henry & Kirkpatrick (1990); Kend04 = Kendall et al. (2004); King10 = King et al. (2010); Kirk00 = Kirkpatrick et al. (2000); Kirk08 = Kirkpatrick et al. (2008); Kirk95 = Kirkpatrick et al. (1995); Kirk99 = Kirkpatrick et al. (1999); Knap04 = Knapp et al. (2004); Lane01 = Lane et al. (2001); Law06 = Law et al. (2006); Lein00 = Leinert et al. (2000); Lein94 = Leinert et al. (1994); Lepi09 = Lépine et al. (2009); Liu05 = Liu & Leggett (2005); Liu06 = Liu et al. (2006); Loop07 = Looper et al. (2007); Loop08 = Looper et al. (2008); Mart00 = Martín et al. (2000); Mart06 = Martín et al. (2006); Mart99 = Martín et al. (1999); McCa04 = McCaughrean et al. (2004); Mont06 = Montagnier et al. (2006); Phan05 = Phan-Bao et al. (2005); Phan06 = Phan-Bao et al. (2006); Pott02 = Potter et al. (2002); Rajp12 = Rajpurohit et al. (2012); Reid01 = Reid et al. (2001); Reid06a = Reid et al. (2006a); Reid06b = Reid et al. (2006b); Schm07 = Schmidt et al. (2007); Scho03 = Scholz et al. (2003); Sieg03 = Siegler et al. (2003); Sieg05 = Siegler et al. (2005); Sieg07 = Siegler et al. (2007); Stum05 = Stumpf et al. (2005); Stum11 = Stumpf et al. (2011); Thor03 = Thorstensen & Kirkpatrick (2003); Wils03 = Wilson et al. (2003).

*The component spectral types in these cases come from resolved optical spectroscopy. All other component types are based on near-IR spectra, either resolved or deconvolved from the integrated-light near-IR spectrum using near-IR resolved photometry. For LHS 2397aAB, the primary spectral type is assumed to be the same as the optical integrated-light type given the large contrast ratio in the optical.

Table 2. Relative astrometry from Keck/NIRC2 Adaptive Optics Imaging and Masking

Observation Date (UT)	(MJD)	Separation (mas)	PA (°)	Δm (mag)	Bandpass	$N_{\rm frames}$	Notes
			LP 349-25AB ($N_{\rm ep} = 8, \Delta t = 3.99\,{\rm yr}$)				
2008 Jan 16	54481.25	137.25 ± 0.24	208.07 ± 0.06	0.335 ± 0.016	K_S	10	I
2008 Jun 30	54647.55	114.88 ± 0.25	194.94 ± 0.12	0.285 ± 0.011	K_S	9	I
2008 Jun 30	54647.56	114.67 ± 0.23	195.13 ± 0.08	0.303 ± 0.004	H	7	I
2008 Jun 30	54647.56	114.5 ± 0.6	195.20 ± 0.17	0.345 ± 0.011	J	11	I
2008 Aug 20	54698.61	105.71 ± 0.10	189.90 ± 0.05	0.353 ± 0.010	K_S	12	I
2008 Sep 9	54718.58	102.17 ± 0.14	187.62 ± 0.09	0.243 ± 0.005	L'	12	I
2009 Sep 28	55102.56	71.20 ± 0.30	98.4 ± 0.6	0.230 ± 0.030	K_S	14	I
2009 Dec 15	55180.37	83.6 ± 0.4	81.40 ± 0.30	0.37 ± 0.06	K	14	I
2010 May 22	55338.62	112.76 ± 0.18	59.93 ± 0.09	0.397 ± 0.019	K	13	I*
2012 Jan 14	55940.25	131.4 ± 0.7	19.52 ± 0.12	0.258 ± 0.011	K	15	I
			LP 415-20AB ($N_{\rm ep} = 7, \Delta t = 4.16\,{\rm yr}$)				
2007 Dec 2	54436.38	85.0 ± 0.5	55.11 ± 0.27	0.71 ± 0.08	K'	6	I
2007 Dec 2	54436.40	85.2 ± 0.8	55.47 ± 0.23	0.71 ± 0.05	J	6	I
2008 Jan 15	54480.26	89.4 ± 0.4	56.3 ± 0.5	0.60 ± 0.07	K_S	10	I
2008 Sep 8	54717.56	107.2 ± 0.8	61.00 ± 0.30	0.596 ± 0.027	K_S	8	I
2008 Sep 8	54717.56	106.1 ± 1.1	61.38 ± 0.22	0.652 ± 0.011	H	6	I
2008 Sep 8	54717.56	106.8 ± 0.5	61.23 ± 0.24	0.716 ± 0.027	J	7	I
2008 Dec 18	54818.40	112.3 ± 1.3	63.30 ± 0.30	0.45 ± 0.06	K'	8	I
2009 Sep 28	55102.63	130.18 ± 0.28	66.81 ± 0.22	0.537 ± 0.017	K_S	9	I
2010 Jan 9	55205.34	136.08 ± 0.18	68.19 ± 0.08	0.571 ± 0.010	K_S	11	I
2012 Jan 28	55954.38	159.56 ± 0.27	74.79 ± 0.15	0.566 ± 0.009	K	12	I
2012 Jan 28	55954.39	158.7 ± 0.8	75.31 ± 0.24	0.481 ± 0.027	L'	6	I
			SDSS J0423−0414AB ($N_{\rm ep} = 1, \Delta t = 0.00\,{\rm yr}$)				
2007 Sep 6	54349.59	54.5 ± 1.5	97.0 ± 1.4	1.19 ± 0.08	K_S	18	M
			2MASS J0700+3157AB ($N_{\rm ep} = 14, \Delta t = 8.04\,{\rm yr}$)				
2007 Mar 25	54184.32	37.2 ± 0.6	264.3 ± 0.7	1.348 ± 0.029	K_S	12	M
2007 Apr 23	54213.29	44.2 ± 0.8	265.3 ± 0.8	1.40 ± 0.04	K_S	12	M
2008 Jan 15	54480.38	114.7 ± 0.5	276.91 ± 0.20	1.49 ± 0.04	K_S	12	M
2008 Jan 15	54480.39	115.2 ± 1.6	275.6 ± 0.9	1.45 ± 0.17	K_S	9	I
2008 Mar 29	54554.26	130.4 ± 2.5	278.5 ± 0.4	1.378 ± 0.027	K_S	9	I
2008 Sep 17	54726.63	173 ± 4	280.0 ± 0.9	1.26 ± 0.10	K_S	5	I
2008 Nov 3	54773.59	188.34 ± 0.23	279.62 ± 0.09	1.391 ± 0.011	K_S	9	I
2008 Nov 3	54773.60	187.8 ± 0.5	279.49 ± 0.23	1.487 ± 0.021	J	9	I
2008 Nov 3	54773.60	187.8 ± 0.4	279.46 ± 0.08	1.403 ± 0.017	H	8	I
2008 Nov 3	54773.61	185.4 ± 1.8	279.31 ± 0.17	0.926 ± 0.027	L'	9	I
2009 Jan 22	54853.46	207.3 ± 1.3	280.18 ± 0.19	1.45 ± 0.04	K_S	8	I

Table 2—Continued

Observation Date (UT)	(MJD)	Separation (mas)	PA (°)	Δm (mag)	Bandpass	$N_{\rm frames}$	Notes
2009 Dec 18	55183.56	275.60 ± 0.30	280.95 ± 0.06	1.389 ± 0.009	K_S	15	I
2010 Mar 22	55277.26	293.00 ± 0.30	281.15 ± 0.06	1.401 ± 0.020	K	8	I
2011 Apr 22	55673.26	348.16 ± 0.13	281.88 ± 0.030	1.404 ± 0.010	K	13	I
2013 Jan 17	56309.50	377.20 ± 0.30	282.79 ± 0.04	1.407 ± 0.016	K	38	I
2014 Jan 22	56679.36	358.8 ± 0.4	283.34 ± 0.06	1.397 ± 0.017	K	15	I
2015 Jan 14	57036.41	317.47 ± 0.12	283.90 ± 0.030	1.360 ± 0.012	K	27	I
2015 Apr 10	57122.32	304.05 ± 0.23	284.09 ± 0.06	1.394 ± 0.008	K	8	I
LHS 1901AB ($N_{\rm ep} = 7, \Delta t = 4.04\,{\rm yr}$)							
2008 Jan 15	54480.46	60.3 ± 1.5	308.72 ± 0.12	0.163 ± 0.015	K_S	9	I
2008 Sep 9	54718.62	57.2 ± 1.3	1.4 ± 0.5	0.270 ± 0.030	H	12	I
2008 Sep 9	54718.63	57.4 ± 0.6	1.1 ± 0.4	0.28 ± 0.04	J	9	I
2008 Sep 9	54718.63	57.8 ± 1.0	1.72 ± 0.27	0.150 ± 0.014	K_S	18	I
2009 Sep 28	55102.65	177.88 ± 0.06	179.68 ± 0.010	0.079 ± 0.008	K_S	5	I
2009 Dec 15	55180.43	206.5 ± 0.4	181.50 ± 0.04	0.098 ± 0.004	$K_{\rm cont}$	5	I
2009 Dec 16	55181.37	206.8 ± 0.5	181.49 ± 0.030	0.096 ± 0.004	K_S	12	I
2010 Mar 22	55277.25	236.59 ± 0.30	183.30 ± 0.030	0.088 ± 0.018	J	6	I
2010 Mar 22	55277.25	237.0 ± 0.4	183.29 ± 0.030	0.092 ± 0.004	L'	6	I
2010 Mar 22	55277.25	236.65 ± 0.15	183.25 ± 0.020	0.111 ± 0.008	H	7	I
2010 Mar 22	55277.25	236.72 ± 0.08	183.25 ± 0.010	0.105 ± 0.005	K	6	I
2012 Jan 28	55954.37	363.00 ± 0.12	189.62 ± 0.020	0.092 ± 0.009	K	9	I
2MASS J0746+2000AB ($N_{\rm ep} = 3, \Delta t = 2.05\,{\rm yr}$)							
2007 Dec 1	54435.62	334.13 ± 0.19	224.14 ± 0.020	0.360 ± 0.012	K'	7	I*
2007 Dec 1	54435.63	334.1 ± 0.5	224.09 ± 0.06	0.526 ± 0.010	J	7	I*
2008 Dec 18	54818.48	351.09 ± 0.29	215.00 ± 0.20	0.352 ± 0.013	K'	9	I*
2009 Dec 18	55183.50	347.97 ± 0.15	206.45 ± 0.020	0.345 ± 0.004	K	18	I
2MASS J0850+1057AB ($N_{\rm ep} = 6, \Delta t = 8.07\,{\rm yr}$)							
2006 Dec 19	54088.61	100.8 ± 2.4	144.9 ± 0.8	1.02 ± 0.05	K	4	I
2007 Mar 25	54184.27	97.8 ± 2.0	147.8 ± 0.6	1.06 ± 0.09	H	6	I
2007 Mar 25	54184.28	101.0 ± 2.6	146.3 ± 1.8	1.34 ± 0.13	J	5	I
2010 Jan 10	55206.60	66.2 ± 1.7	182.4 ± 0.6	0.84 ± 0.10	K_S	6	I
2011 Apr 22	55673.26	64.3 ± 0.7	204.0 ± 0.8	0.85 ± 0.04	K	13	M
2014 Mar 14	56730.37	82.3 ± 1.5	248.7 ± 0.6	0.80 ± 0.08	K	10	I
2015 Jan 14	57036.58	94.1 ± 0.7	256.30 ± 0.30	0.800 ± 0.030	K	19	I
2MASS J0920+3517AB ($N_{\rm ep} = 17, \Delta t = 6.99\,{\rm yr}$)							
2006 May 5	53860.26	49.0 ± 1.6	242.5 ± 1.6	0.323 ± 0.010	K_S	6	I
2006 May 5	53860.27	49.20 ± 0.29	242.7 ± 0.9	0.227 ± 0.025	H	6	I

Table 2—Continued

Observation Date (UT)	(MJD)	Separation (mas)	PA (°)	Δm (mag)	Bandpass	$N_{\rm frames}$	Notes
2006 May 5	53860.28	48.8 ± 0.4	242.5 ± 1.2	0.24 ± 0.07	J	6	I
2007 Jan 26	54126.54	73 ± 6	247 ± 6	0.42 ± 0.05	K	3	I
2007 Mar 25	54184.42	73.4 ± 0.9	245.8 ± 0.4	0.320 ± 0.014	K_S	4	I
2007 Mar 26	54185.29	74.30 ± 0.30	245.00 ± 0.30	0.277 ± 0.018	J	5	I
2007 Dec 2	54436.53	74.8 ± 0.6	246.0 ± 1.0	0.41 ± 0.07	K'	8	I*
2007 Dec 12	54446.65	74.60 ± 0.30	247.40 ± 0.30	0.31 ± 0.04	K_S	8	I
2008 Jan 14	54479.50	72.5 ± 0.4	246.7 ± 0.6	0.341 ± 0.029	K_S	9	I
2008 Jan 14	54479.52	73.2 ± 0.8	246.4 ± 0.8	0.203 ± 0.025	H	14	I
2008 Mar 29	54554.32	68.6 ± 0.7	248.2 ± 0.4	0.409 ± 0.010	K_S	7	I
2008 Mar 29	54554.33	68.0 ± 0.4	247.7 ± 0.6	0.27 ± 0.04	H	6	I
2008 Apr 27	54583.35	66.2 ± 0.8	248.4 ± 0.4	0.525 ± 0.028	K_S	11	I
2008 May 30	54616.27	63.0 ± 0.5	247.79 ± 0.27	0.41 ± 0.09	K'	7	I*
2008 Nov 3	54773.66	46.7 ± 0.8	249.3 ± 0.7	0.415 ± 0.015	K_S	7	I
2006 Dec 19	54088.68	65.7 ± 2.7	247.1 ± 1.5	0.45 ± 0.12	K	8	M
2007 Mar 25	54184.41	72.9 ± 2.7	246.5 ± 2.2	0.33 ± 0.07	K_S	8	M
2008 Dec 22	54822.57	37.85 ± 0.25	249.8 ± 0.9	0.339 ± 0.019	K'	8	M
2009 Jan 22	54853.59	33.04 ± 0.19	253.4 ± 1.1	0.12 ± 0.05	K_S	12	M
2009 Dec 18	55183.60	25.70 ± 0.30	61.0 ± 2.5	0.20 ± 0.07	K_S	12	M
2010 May 23	55339.25	47.5 ± 1.0	67.5 ± 1.1	0.54 ± 0.05	K	10	M
2013 Apr 30	56412.24	37.51 ± 0.26	241.7 ± 0.5	0.454 ± 0.015	K	9	M
2MASS J1017+1308AB ($N_{\rm ep} = 5, \Delta t = 5.28\,{\rm yr}$)							
2008 Jan 16	54481.65	132.4 ± 0.4	233.5 ± 0.4	0.134 ± 0.015	K_S	8	I
2009 Jan 23	54854.46	137.3 ± 0.4	245.84 ± 0.13	0.114 ± 0.012	K_S	8	I
2009 Dec 18	55183.54	139.0 ± 0.7	256.60 ± 0.30	0.087 ± 0.020	K_S	15	I
2011 Apr 21	55672.38	133.9 ± 0.4	272.48 ± 0.19	0.155 ± 0.010	K	11	I
2013 Apr 29	56411.32	119 ± 5	300.8 ± 2.4	0.14 ± 0.06	L'	6	I
2013 Apr 29	56411.32	115.7 ± 1.0	301.60 ± 0.30	0.15 ± 0.04	H	7	I
2013 Apr 29	56411.32	114.4 ± 0.4	302.1 ± 1.0	0.090 ± 0.024	K	8	I
2013 Apr 29	56411.32	116.8 ± 0.8	301.3 ± 0.4	0.201 ± 0.018	J	5	I
SDSS J1021−0304AB ($N_{\rm ep} = 3, \Delta t = 7.14\,{\rm yr}$)							
2005 Nov 26	53700.60	159.98 ± 0.15	232.7 ± 0.4	-0.104 ± 0.012	J	8	I
2005 Nov 26	53700.60	158.8 ± 1.1	232.62 ± 0.21	0.989 ± 0.018	K_S	5	I
2005 Nov 26	53700.61	159.38 ± 0.22	232.78 ± 0.10	0.745 ± 0.023	H	7	I
2008 Dec 18	54818.54	148.3 ± 0.5	204.36 ± 0.11	1.002 ± 0.014	K'	6	I
2013 Jan 17	56309.51	150.3 ± 0.7	163.46 ± 0.13	1.134 ± 0.022	K	7	I
2013 Jan 17	56309.52	153.0 ± 3.0	163.8 ± 0.5	0.518 ± 0.030	CH_4s	3	I
2MASS J1047+4026AB (a.k.a. LP 213-68) ($N_{\rm ep} = 8, \Delta t = 7.27\,{\rm yr}$)							

Table 2—Continued

Observation Date (UT)	(MJD)	Separation (mas)	PA (°)	Δm (mag)	Bandpass	$N_{\rm frames}$	Notes
2009 Jan 22	54853.62	113.0 ± 1.0	334.3 ± 0.4	0.265 ± 0.026	K_S	14	I
2009 Dec 18	55183.59	94.0 ± 1.8	349.4 ± 0.8	0.241 ± 0.029	K_S	17	I
2011 Jun 26	55738.27	31.5 ± 0.9	66.0 ± 2.0	0.23 ± 0.08	H	6	M
2011 Jun 26	55738.27	31.58 ± 0.27	63.4 ± 1.1	0.38 ± 0.09	K	8	M
2011 Jul 1	55743.26	30.95 ± 0.10	66.1 ± 0.4	0.311 ± 0.009	K	9	M
2012 Jan 28	55954.48	43.41 ± 0.22	257.6 ± 0.6	0.291 ± 0.010	K	11	M
2012 Jan 28	55954.48	42.7 ± 0.4	258.7 ± 0.5	0.39 ± 0.04	H	6	M
2012 Apr 12	56029.37	58.20 ± 0.13	272.59 ± 0.21	0.278 ± 0.012	K	13	M
2014 Mar 14	56730.47	116.72 ± 0.17	315.29 ± 0.20	0.345 ± 0.015	K	14	I
2016 May 2	57510.39	101.1 ± 1.0	345.6 ± 0.7	0.240 ± 0.030	K	3	I
SDSS J1052+4422AB ($N_{\rm ep} = 12, \Delta t = 9.02$ yr)							
2005 May 1	53491.39	42.4 ± 0.7	81.1 ± 1.7	0.510 ± 0.030	K'	5	I
2006 May 5	53860.36	70.3 ± 0.7	112.2 ± 0.7	0.49 ± 0.05	K_S	6	I
2006 May 5	53860.39	70.5 ± 1.4	112.2 ± 0.7	0.00 ± 0.13	H	6	I
2006 May 5	53860.41	69.2 ± 0.9	112.2 ± 0.7	-0.61 ± 0.11	J	6	I
2006 Dec 19	54088.65	79.8 ± 1.9	124.5 ± 1.4	0.49 ± 0.15	K	4	I
2007 Mar 8	54167.45	80.3 ± 0.5	125.4 ± 0.6	0.45 ± 0.06	K'	12	I
2007 Mar 25	54184.37	80.9 ± 0.5	128.1 ± 1.0	-0.36 ± 0.05	J	7	I
2008 Apr 1	54557.50	72.2 ± 1.7	142.3 ± 1.2	0.42 ± 0.07	K	8	I
2008 Nov 3	54773.65	55.2 ± 1.0	160.2 ± 2.1	-0.01 ± 0.07	H	9	I
2008 Dec 22	54822.59	50.3 ± 0.7	162.4 ± 0.9	0.510 ± 0.030	K'	6	M
2010 Jan 10	55206.50	34.4 ± 0.5	234.9 ± 1.1	0.140 ± 0.030	H	10	M
2010 Jan 10	55206.51	33.1 ± 0.6	235.1 ± 1.2	0.57 ± 0.05	K	10	M
2010 May 22	55338.32	39.9 ± 0.7	261.0 ± 1.1	0.56 ± 0.04	K	9	M
2011 Apr 21	55672.38	58.90 ± 0.30	297.91 ± 0.29	0.545 ± 0.016	K	11	M
2014 May 10	56787.36	54.9 ± 0.9	97.2 ± 1.0	0.51 ± 0.04	K	12	M
Gl 417BC ($N_{\rm ep} = 9, \Delta t = 7.12$ yr)							
2007 Mar 25	54184.51	140.4 ± 0.9	278.84 ± 0.28	0.319 ± 0.014	K	6	I
2008 Jan 15	54480.65	128.6 ± 1.2	276.3 ± 0.8	0.35 ± 0.04	K_S	6	I
2008 Apr 1	54557.49	125.2 ± 0.8	275.3 ± 1.0	0.407 ± 0.030	K_S	10	I
2008 Apr 27	54583.44	124.7 ± 0.6	274.2 ± 0.6	0.47 ± 0.04	K_S	7	I
2009 Jun 29	55011.28	83.8 ± 1.5	266.1 ± 1.4	0.47 ± 0.11	K_S	7	I
2010 Jan 9	55205.53	63.3 ± 1.3	258.0 ± 1.8	0.43 ± 0.08	K_S	46	I
2012 Apr 12	56029.38	65.3 ± 1.8	123.4 ± 2.8	0.34 ± 0.14	K	29	I
2013 Apr 28	56410.38	101.0 ± 1.4	110.0 ± 2.2	0.28 ± 0.13	K	9	I
2013 Apr 28	56410.38	100.8 ± 0.5	108.4 ± 1.9	0.26 ± 0.09	H	4	I
2014 May 9	56786.32	116.8 ± 0.8	101.2 ± 0.4	0.44 ± 0.04	J	10	I
2014 May 9	56786.34	115.8 ± 0.6	102.00 ± 0.30	0.40 ± 0.04	Y	6	I

Table 2—Continued

Observation Date (UT)	(MJD)	Separation (mas)	PA (°)	Δm (mag)	Bandpass	$N_{\rm frames}$	Notes
			LHS 2397aAB ($N_{\rm ep}=6, \Delta t = 6.89\,{\rm yr}$)				
2007 Apr 22	54212.32	117.7 ± 2.6	349.3 ± 0.7	2.93 ± 0.09	K_S	6	I
2007 Apr 22	54212.33	112.6 ± 2.8	347.3 ± 1.3	3.37 ± 0.24	CH_4s	9	M
2007 Apr 22	54212.42	115.7 ± 1.7	349.7 ± 1.0	2.78 ± 0.11	K_S	13	M
2008 Jan 15	54480.62	143 ± 4	24.9 ± 0.5	2.71 ± 0.10	K_S	5	I
2008 Jan 15	54480.62	144.5 ± 2.4	25.8 ± 0.7	2.98 ± 0.13	K_S	8	M
2009 Jan 23	54854.54	203.6 ± 1.6	53.29 ± 0.30	2.800 ± 0.030	K_S	9	I
2009 Jan 23	54854.55	200.3 ± 2.5	52.8 ± 0.5	2.94 ± 0.05	H	11	I
2009 Jan 23	54854.56	197 ± 4	53.0 ± 0.9	3.07 ± 0.09	J	7	I
2009 Jan 23	54854.57	200.0 ± 3.0	53.2 ± 0.4	1.92 ± 0.06	L'	12	I
2012 Jan 29	55955.57	272.4 ± 0.4	91.89 ± 0.06	2.76 ± 0.04	K	13	I
2014 Jan 22	56679.50	246.5 ± 2.7	113.8 ± 0.9	2.79 ± 0.06	K	62	I
2014 Mar 14	56730.50	246.00 ± 0.19	116.67 ± 0.13	2.724 ± 0.010	K	8	I
			DENIS J1228−1557AB ($N_{\rm ep}=3, \Delta t = 4.55\,{\rm yr}$)				
2008 Jun 30	54647.28	241.26 ± 0.25	314.70 ± 0.08	0.126 ± 0.013	K_S	6	I
2013 Jan 17	56309.56	281.6 ± 0.7	279.61 ± 0.12	0.113 ± 0.012	H	16	I
2013 Jan 17	56309.56	281.4 ± 1.4	279.3 ± 0.4	0.08 ± 0.04	J	14	I
2013 Jan 17	56309.56	280.89 ± 0.28	279.58 ± 0.08	0.123 ± 0.005	K	17	I
2013 Jan 17	56309.57	279.9 ± 1.5	279.7 ± 0.6	0.07 ± 0.04	L'	6	I
2013 Jan 17	56309.57	280 ± 4	279.9 ± 1.1	0.010 ± 0.030	Y	6	I
2013 Jan 18	56310.57	279.8 ± 1.8	279.30 ± 0.30	0.09 ± 0.04	K	17	I
2013 Jan 18	56310.58	278.5 ± 2.1	279.6 ± 0.4	0.110 ± 0.030	H	17	I
2013 Jan 18	56310.59	274 ± 4	279.48 ± 0.28	0.13 ± 0.04	J	10	I
			Kelu-1AB ($N_{\rm ep}=12, \Delta t = 10.10\,{\rm yr}$)				
2005 Mar 4	53433.51	284.60 ± 0.30	221.57 ± 0.04	0.421 ± 0.018	K'	11	I
2005 May 1	53491.37	290.05 ± 0.21	221.64 ± 0.030	0.409 ± 0.012	K'	6	I
2005 May 1	53491.38	289.8 ± 1.1	221.58 ± 0.22	0.70 ± 0.05	J	6	I
2005 May 1	53491.38	290.1 ± 0.5	221.66 ± 0.06	0.525 ± 0.007	H	6	I
2007 Apr 23	54213.47	345.1 ± 0.4	223.03 ± 0.04	0.420 ± 0.004	K	4	I
2008 Jun 30	54647.26	366.4 ± 0.9	223.73 ± 0.030	0.407 ± 0.011	K_S	6	I
2009 Apr 29	54950.40	377.3 ± 0.6	224.21 ± 0.11	0.457 ± 0.020	K	6	I
2010 May 23	55339.32	386.1 ± 0.6	224.57 ± 0.06	0.422 ± 0.012	K	21	I
2011 Apr 22	55673.40	388.7 ± 0.4	225.04 ± 0.020	0.407 ± 0.015	K	21	I
2013 Jan 17	56309.58	382.60 ± 0.26	225.88 ± 0.05	0.404 ± 0.013	K	8	I
2013 Apr 28	56410.45	380.3 ± 1.2	225.8 ± 0.5	0.454 ± 0.016	K	5	I
2014 Jan 22	56679.60	369.4 ± 1.3	226.50 ± 0.30	0.47 ± 0.05	K	15	I
2014 Mar 14	56730.50	370.43 ± 0.19	226.47 ± 0.030	0.403 ± 0.006	K	14	I

Table 2—Continued

Observation Date (UT)	(MJD)	Separation (mas)	PA (°)	Δm (mag)	Bandpass	$N_{\rm frames}$	Notes
2015 Apr 11	57123.44	352.80 ± 0.30	227.02 ± 0.030	0.431 ± 0.013	K	12	I
		2MASS J1404−3159AB ($N_{\rm ep} = 7, \Delta t = 8.85\,{\rm yr}$)					
2006 Jun 3	53889.29	133.3 ± 0.5	312.23 ± 0.17	1.206 ± 0.010	K_S	6	I
2006 Jun 3	53889.30	133.27 ± 0.18	312.18 ± 0.16	0.519 ± 0.019	H	5	I
2006 Jun 3	53889.31	132.7 ± 0.9	310.1 ± 1.1	-0.540 ± 0.030	J	7	I
2010 Jul 9	55386.26	136.0 ± 3.0	18.6 ± 0.4	1.440 ± 0.030	K	3	I
2012 Jan 28	55954.65	189.8 ± 2.1	6.10 ± 0.25	1.401 ± 0.008	K	11	I
2013 Jan 17	56309.66	210.1 ± 2.3	0.90 ± 0.30	0.61 ± 0.06	H	3	I
2013 Apr 29	56411.37	212.0 ± 1.2	359.62 ± 0.29	1.374 ± 0.024	K	6	I
2014 Mar 14	56730.51	224.9 ± 0.4	355.36 ± 0.15	0.310 ± 0.017	CH_4s	9	I
2015 Apr 10	57122.49	236.0 ± 1.0	351.4 ± 0.4	0.552 ± 0.012	H	8	I
2015 Apr 10	57122.49	235.0 ± 1.0	351.8 ± 0.4	1.410 ± 0.016	K	6	I
		HD 130948BC ($N_{\rm ep} = 14, \Delta t = 8.17\,{\rm yr}$)					
2005 Feb 25	53426.48	56.3 ± 0.4	145.0 ± 1.4	0.24 ± 0.05	H	10	I**
2007 Jan 26	54126.59	111.6 ± 0.8	132.8 ± 0.4	0.156 ± 0.021	K	10	I
2007 Mar 25	54184.53	108.9 ± 0.4	132.61 ± 0.11	0.189 ± 0.008	$K_{\rm cont}$	6	I
2007 May 11	54231.47	105.80 ± 0.12	132.10 ± 0.08	0.273 ± 0.014	H	12	I*
2007 Jul 25	54306.24	97.89 ± 0.25	131.16 ± 0.13	0.236 ± 0.013	H	8	I
2007 Jul 25	54306.25	98.20 ± 0.30	131.10 ± 0.24	0.250 ± 0.030	$H_{\rm cont}$	6	I
2008 Jan 15	54480.69	71.90 ± 0.22	127.9 ± 0.4	0.150 ± 0.030	K_S	11	I
2008 Mar 29	54554.57	57.97 ± 0.16	124.9 ± 0.4	0.178 ± 0.007	K	10	I
2008 Mar 29	54554.59	57.3 ± 0.6	124.6 ± 0.6	0.13 ± 0.05	J	9	I
2008 Mar 29	54554.66	58.4 ± 2.3	124.1 ± 0.7	0.30 ± 0.30	H	8	I
2008 Apr 27	54583.61	51.7 ± 0.4	124.1 ± 0.5	0.185 ± 0.010	K_S	4	I
2009 Dec 18	55183.70	84.60 ± 0.30	318.55 ± 0.14	0.151 ± 0.011	K_S	24	I
2010 Jan 9	55205.69	88.8 ± 0.4	318.31 ± 0.25	0.226 ± 0.013	K_S	12	I
2010 Mar 22	55277.65	100.04 ± 0.15	316.95 ± 0.07	0.2010 ± 0.002	K	8	I
2011 Mar 25	55645.56	128.4 ± 0.8	313.3 ± 0.4	0.258 ± 0.009	H	8	I**
2012 Jan 14	55940.59	119.26 ± 0.08	310.42 ± 0.04	0.237 ± 0.004	H	10	I
2013 Apr 28	56410.60	63.26 ± 0.22	301.1 ± 0.4	0.355 ± 0.023	K	10	I
		Gl 569Bab ($N_{\rm ep} = 14, \Delta t = 11.07\,{\rm yr}$)					
2003 Apr 15	52744.48	60.9 ± 0.9	267.1 ± 1.1	0.50 ± 0.06	$K_{\rm cont}$	27	I**
2004 Aug 10	53227.25	101.2 ± 0.4	69.00 ± 0.30	0.559 ± 0.027	$FeII$	24	I**
2004 Dec 24	53363.68	93.8 ± 0.4	110.9 ± 0.4	0.700 ± 0.030	H	7	I
2005 Feb 25	53426.50	83.9 ± 0.7	133.6 ± 0.7	0.49 ± 0.08	$H_{\rm cont}$	18	I
2005 Feb 25	53426.50	84.0 ± 1.4	133.8 ± 2.1	0.49 ± 0.08	$K_{\rm cont}$	12	I
2008 Jan 16	54481.69	61.43 ± 0.15	272.4 ± 1.3	0.520 ± 0.030	$H_{\rm cont}$	10	I

Table 2—Continued

Observation Date (UT)	(MJD)	Separation (mas)	PA (°)	Δm (mag)	Bandpass	$N_{\rm frames}$	Notes
2009 Apr 29	54950.52	100.4 ± 0.7	66.6 ± 0.7	0.36 ± 0.04	$K_{\rm cont}$	8	I
2009 May 29	54980.46	99.7 ± 0.6	75.9 ± 0.8	0.58 ± 0.04	$K_{\rm cont}$	9	I
2010 Mar 22	55277.66	55.78 ± 0.19	207.10 ± 0.30	0.464 ± 0.009	K	8	I
2010 May 23	55339.45	58.1 ± 1.2	266.5 ± 1.4	0.81 ± 0.12	J	18	I
2010 May 23	55339.48	58.1 ± 1.3	266.7 ± 1.1	0.60 ± 0.08	L'	9	I
2010 May 23	55339.48	59.6 ± 0.9	267.5 ± 0.8	0.56 ± 0.05	H	16	I
2010 May 23	55339.49	59.6 ± 0.4	267.2 ± 0.9	0.56 ± 0.04	K	19	I
2011 Mar 25	55645.56	105.69 ± 0.15	21.05 ± 0.07	0.515 ± 0.017	H	9	I**
2012 Jan 14	55940.62	95.57 ± 0.13	103.64 ± 0.07	0.672 ± 0.013	H	10	I
2013 Apr 28	56410.43	103.5 ± 0.4	353.90 ± 0.30	0.427 ± 0.007	K	5	I
2014 Jan 22	56679.62	104.2 ± 1.9	64.5 ± 1.1	0.40 ± 0.07	K	18	I
2014 May 9	56786.55	96.5 ± 0.4	98.2 ± 0.5	0.460 ± 0.030	$K_{\rm cont}$	16	I
SDSS J1534+1615AB ($N_{\rm ep} = 4, \Delta t = 10.23\,{\rm yr}$)							
2005 May 1	53491.56	109.0 ± 3.0	289.8 ± 2.3	0.914 ± 0.015	K'	5	I
2005 May 1	53491.56	111.1 ± 2.5	288.3 ± 1.9	0.587 ± 0.017	H	5	I
2005 May 1	53491.57	113.6 ± 2.5	286.4 ± 1.9	-0.179 ± 0.005	J	3	I
2011 Apr 21	55672.58	122.6 ± 2.0	335.6 ± 0.7	1.16 ± 0.06	K	7	I
2013 Mar 20	56371.58	119.5 ± 0.5	349.21 ± 0.26	0.366 ± 0.022	CH_4s	9	I
2015 Jul 23	57226.39	119.1 ± 0.9	6.60 ± 0.30	0.29 ± 0.05	CH_4s	8	I
2MASS J1534−2952AB ($N_{\rm ep} = 13, \Delta t = 9.94\,{\rm yr}$)							
2005 May 1	53491.51	211.7 ± 1.0	14.12 ± 0.30	0.296 ± 0.009	K'	5	I
2005 May 1	53491.52	211.2 ± 0.8	14.25 ± 0.13	0.301 ± 0.004	H	5	I
2005 May 1	53491.52	210.3 ± 1.5	13.97 ± 0.30	0.151 ± 0.022	J	5	I
2006 May 5	53860.44	190.51 ± 0.20	15.83 ± 0.09	0.289 ± 0.023	K_S	3	I
2007 Mar 25	54184.59	157.4 ± 0.6	17.61 ± 0.19	0.315 ± 0.012	K	6	I
2007 Apr 22	54212.53	153.80 ± 0.30	17.99 ± 0.10	0.257 ± 0.015	K_S	7	I
2008 Jan 15	54480.66	115.2 ± 1.1	20.9 ± 0.9	0.269 ± 0.023	K_S	4	I
2008 Apr 1	54557.56	104.5 ± 1.3	22.4 ± 0.8	0.218 ± 0.018	K_S	7	I
2008 Apr 1	54557.59	103.3 ± 1.5	23.3 ± 1.5	0.122 ± 0.019	CH_4s	5	I
2008 Jun 30	54647.31	90.2 ± 0.5	22.3 ± 0.5	0.27 ± 0.05	K_S	12	I
2010 Jul 8	55385.28	45.8 ± 0.5	172.8 ± 0.8	0.24 ± 0.04	K	8	M
2011 Apr 21	55672.54	90.9 ± 1.7	185.4 ± 0.9	0.34 ± 0.10	K	9	I
2011 Apr 22	55673.51	91.9 ± 0.8	183.7 ± 0.5	0.25 ± 0.05	K	9	M
2013 Jul 1	56474.33	192.1 ± 0.4	191.60 ± 0.09	0.2860 ± 0.003	H	8	I
2014 Mar 14	56730.61	208.6 ± 0.6	192.9 ± 0.4	0.354 ± 0.023	H	7	I
2015 Apr 10	57122.56	213.30 ± 0.29	194.00 ± 0.21	0.287 ± 0.024	CH_4s	9	I

2MASS J1728+3948AB ($N_{\rm ep} = 10, \Delta t = 7.93\,{\rm yr}$)

Table 2—Continued

Observation Date (UT)	(MJD)	Separation (mas)	PA (°)	Δm (mag)	Bandpass	$N_{\rm frames}$	Notes
2006 Jun 3	53889.54	194.0 ± 0.7	89.31 ± 0.13	0.573 ± 0.008	K_S	7	I
2006 Jun 3	53889.55	194.7 ± 0.5	89.35 ± 0.19	0.418 ± 0.012	H	7	I
2006 Jun 3	53889.56	194.45 ± 0.20	89.28 ± 0.11	0.236 ± 0.021	J	7	I
2007 Mar 25	54184.61	203.50 ± 0.30	94.52 ± 0.18	0.599 ± 0.011	K_S	5	I
2007 Aug 7	54319.37	204.4 ± 1.7	96.90 ± 0.30	0.521 ± 0.026	K_S	6	I
2008 Jun 30	54647.37	213.8 ± 0.4	101.66 ± 0.030	0.618 ± 0.014	K_S	8	I
2009 May 30	54981.59	216.3 ± 1.9	106.0 ± 0.5	0.56 ± 0.08	K_S	5	I
2010 May 1	55317.59	220.4 ± 0.8	111.36 ± 0.11	0.677 ± 0.018	K	6	I
2011 Jul 1	55743.50	216.9 ± 1.0	117.18 ± 0.19	0.607 ± 0.020	K	10	I
2012 Sep 7	56177.25	210.05 ± 0.26	123.96 ± 0.05	0.636 ± 0.009	K	16	I
2013 Jul 1	56474.44	203.1 ± 0.4	128.60 ± 0.11	0.634 ± 0.007	K	4	I
2013 Jul 1	56474.45	203.0 ± 0.9	128.78 ± 0.08	0.294 ± 0.009	J	3	I
2013 Jul 1	56474.46	202.6 ± 0.5	128.90 ± 0.30	0.428 ± 0.011	H	6	I
2014 May 9	56786.57	193.55 ± 0.20	134.15 ± 0.09	0.616 ± 0.011	K	11	I
LSPM J1735+2634AB ($N_{\rm ep} = 9, \Delta t = 6.19\,{\rm yr}$)							
2007 Apr 22	54212.54	192.9 ± 0.8	197.80 ± 0.10	0.55 ± 0.05	K_S	4	I
2007 Aug 1	54313.39	171.9 ± 0.4	204.3 ± 0.7	0.491 ± 0.017	K	16	I**
2007 Aug 1	54313.41	173.7 ± 1.9	204.8 ± 1.7	0.54 ± 0.07	H	8	I**
2007 Aug 1	54313.42	171 ± 4	203.1 ± 1.3	0.60 ± 0.09	J	16	I**
2008 May 28	54614.54	107.54 ± 0.08	234.56 ± 0.26	0.573 ± 0.023	K_S	12	I
2008 Sep 8	54717.29	92.1 ± 1.2	254.00 ± 0.29	0.46 ± 0.11	K_S	12	I
2009 May 30	54981.56	101.7 ± 0.9	314.0 ± 0.4	0.463 ± 0.029	K_S	10	I
2010 May 1	55317.60	159.39 ± 0.07	352.10 ± 0.020	0.4850 ± 0.001	K	4	I
2010 May 23	55339.52	162.4 ± 0.6	353.63 ± 0.15	0.469 ± 0.014	K	12	I
2010 May 23	55339.52	163.8 ± 1.4	353.10 ± 0.30	0.52 ± 0.04	J	11	I
2010 May 23	55339.53	162.7 ± 0.5	353.65 ± 0.09	0.526 ± 0.016	H	8	I
2010 May 23	55339.53	159.5 ± 1.6	353.82 ± 0.20	0.350 ± 0.030	L'	8	I
2011 Apr 21	55672.62	193.58 ± 0.18	13.010 ± 0.030	0.491 ± 0.018	K	15	I
2013 Jun 30	56473.49	206.47 ± 0.22	49.22 ± 0.16	0.450 ± 0.030	K	6	I
2MASS J1750+4424AB ($N_{\rm ep} = 4, \Delta t = 3.86\,{\rm yr}$)							
2006 Jun 20	53906.55	163 ± 5	36.0 ± 3.0	0.69 ± 0.09	K'	9	I
2008 May 28	54614.55	185.40 ± 0.30	53.35 ± 0.06	0.637 ± 0.005	K_S	11	I
2008 May 28	54614.55	185.16 ± 0.30	53.24 ± 0.05	0.782 ± 0.019	J	6	I
2009 May 1	54952.47	202.19 ± 0.30	60.90 ± 0.05	0.663 ± 0.008	K'	8	I
2010 May 1	55317.61	221.5 ± 0.4	67.68 ± 0.05	0.605 ± 0.010	K	10	I
2MASS J1847+5522AB ($N_{\rm ep} = 8, \Delta t = 5.65\,{\rm yr}$)							
2007 Sep 6	54349.37	179.49 ± 0.15	115.39 ± 0.04	0.282 ± 0.007	K_S	9	I

Table 2—Continued

Observation Date (UT)	(MJD)	Separation (mas)	PA (°)	Δm (mag)	Bandpass	$N_{\rm frames}$	Notes
2008 May 20	54606.60	191.64 ± 0.22	117.03 ± 0.05	0.220 ± 0.025	K'	9	I*
2008 May 20	54606.62	191.67 ± 0.21	116.97 ± 0.09	0.242 ± 0.011	H	6	I*
2008 May 28	54614.56	192.21 ± 0.11	117.18 ± 0.020	0.2810 ± 0.003	K_S	12	I
2008 Sep 8	54717.30	196.85 ± 0.14	117.78 ± 0.030	0.277 ± 0.007	K_S	12	I
2009 May 4	54955.47	206.76 ± 0.10	119.15 ± 0.04	0.275 ± 0.008	K'	9	I*
2010 May 1	55317.62	219.50 ± 0.15	121.02 ± 0.020	0.2670 ± 0.003	K	17	I
2011 Jun 26	55738.48	229.81 ± 0.26	122.98 ± 0.04	0.268 ± 0.007	K	14	I
2013 Apr 29	56411.56	237.56 ± 0.07	125.78 ± 0.020	0.257 ± 0.006	K	9	I
SDSS J2052−1609AB ($N_{\rm ep} = 7, \Delta t = 8.58\,{\rm yr}$)							
2005 Oct 11	53654.30	120.4 ± 0.5	13.9 ± 0.5	0.839 ± 0.028	K	5	I
2005 Oct 11	53654.32	120.4 ± 0.4	13.2 ± 0.4	0.324 ± 0.027	H	5	I
2005 Oct 11	53654.33	119.2 ± 0.6	12.91 ± 0.25	-0.003 ± 0.019	J	8	I
2007 Apr 23	54213.63	110.4 ± 0.9	33.8 ± 0.5	0.11 ± 0.07	J	3	I
2007 Aug 7	54319.48	107.4 ± 0.6	37.39 ± 0.30	0.321 ± 0.025	H	4	I
2009 Aug 15	55058.44	106.4 ± 0.4	68.40 ± 0.30	0.37 ± 0.10	H	3	I*
2009 Aug 15	55058.45	105.2 ± 1.2	70.5 ± 1.7	0.056 ± 0.028	J	3	I*
2009 Aug 15	55058.45	105.90 ± 0.30	67.0 ± 1.0	0.80 ± 0.09	K_S	3	I*
2010 May 1	55317.63	108.3 ± 0.5	79.19 ± 0.19	0.86 ± 0.04	K	8	I
2011 Jun 26	55738.52	117.9 ± 0.7	94.6 ± 0.8	0.925 ± 0.026	K	7	I
2014 May 9	56786.63	146.1 ± 0.8	124.01 ± 0.20	0.861 ± 0.025	K	10	I
2MASS J2132+1341AB ($N_{\rm ep} = 11, \Delta t = 6.19\,{\rm yr}$)							
2008 Aug 20	54698.50	58.9 ± 0.4	351.6 ± 1.4	0.750 ± 0.030	H	13	I
2008 Aug 20	54698.50	57.9 ± 0.8	354 ± 6	0.63 ± 0.04	J	15	I
2008 Aug 20	54698.50	58.2 ± 0.9	352.4 ± 1.1	0.813 ± 0.010	K_S	13	I
2009 May 29	54980.60	72.1 ± 0.6	318.5 ± 0.8	0.820 ± 0.030	K_S	11	I
2009 Sep 28	55102.46	80.0 ± 1.0	306.4 ± 0.5	1.12 ± 0.06	K_S	11	I
2009 Dec 15	55180.21	85.6 ± 0.6	301.7 ± 0.5	0.94 ± 0.04	K_S	9	I
2010 May 22	55338.58	93.8 ± 0.6	289.8 ± 0.4	0.82 ± 0.06	K	17	I
2011 Jul 1	55743.56	108.8 ± 0.7	269.11 ± 0.20	0.85 ± 0.04	K	15	I
2013 Oct 14	56579.39	104.30 ± 0.30	233.01 ± 0.14	0.932 ± 0.023	K	14	I
2007 Aug 7	54319.56	56.8 ± 0.4	57.0 ± 0.4	0.850 ± 0.030	K_S	17	M
2007 Sep 6	54349.31	56.65 ± 0.24	51.96 ± 0.22	0.831 ± 0.015	K_S	12	M
2008 Apr 27	54583.62	54.4 ± 1.5	10.5 ± 1.6	1.19 ± 0.12	K_S	8	M
2008 Aug 20	54698.51	58.50 ± 0.30	352.8 ± 0.4	0.800 ± 0.030	K_S	15	M
2008 Sep 8	54717.31	58.9 ± 0.4	350.3 ± 0.4	0.829 ± 0.023	K_S	9	M
2MASS J2140+1625AB ($N_{\rm ep} = 12, \Delta t = 7.87\,{\rm yr}$)							
2008 Jun 30	54647.54	110.0 ± 0.9	246.41 ± 0.22	0.674 ± 0.027	K_S	8	I

Table 2—Continued

Observation Date (UT)	(MJD)	Separation (mas)	PA (°)	Δm (mag)	Bandpass	$N_{\rm frames}$	Notes
2008 Dec 1	54801.26	115.4 ± 2.6	254.0 ± 3.0	0.82 ± 0.10	K_S	5	I
2009 Dec 16	55181.22	114.8 ± 0.9	272.7 ± 0.4	0.78 ± 0.04	K_S	14	I
2010 May 23	55339.58	113.4 ± 1.7	280.1 ± 0.4	0.68 ± 0.12	K	21	I
2011 Apr 22	55673.63	113.8 ± 1.6	297.3 ± 0.5	0.64 ± 0.04	K	12	I
2012 Sep 7	56177.43	106.62 ± 0.20	323.58 ± 0.10	0.813 ± 0.022	K	10	I
2013 Jun 30	56473.50	104.10 ± 0.30	340.8 ± 0.6	0.694 ± 0.015	K	5	I
2013 Oct 14	56579.32	104.1 ± 0.4	347.39 ± 0.14	0.772 ± 0.022	K	21	I
2014 Jun 16	56824.48	105.00 ± 0.30	1.81 ± 0.23	0.769 ± 0.009	H	14	I
2014 Jun 16	56824.48	105.5 ± 0.7	2.1 ± 0.4	0.795 ± 0.018	J	16	I
2014 Jun 16	56824.49	105.1 ± 1.2	2.1 ± 0.6	0.970 ± 0.030	Y	3	I
2014 Jun 16	56824.49	105.0 ± 0.5	1.84 ± 0.16	0.712 ± 0.010	K	14	I
2014 Jun 16	56824.50	106.5 ± 0.8	1.40 ± 0.30	0.602 ± 0.016	L'	10	I
2014 Oct 17	56947.22	106.9 ± 0.4	8.82 ± 0.23	0.794 ± 0.013	K	15	I
2015 Jul 27	57230.60	112.7 ± 0.9	24.44 ± 0.18	0.60 ± 0.04	K	8	I
2016 May 13	57521.61	119.3 ± 0.5	37.40 ± 0.30	0.812 ± 0.015	K	4	I
		2MASS J2206−2047AB ($N_{\rm ep} = 6, \Delta t = 6.54$ yr)					
2007 Dec 2	54436.25	120.06 ± 0.10	159.30 ± 0.30	0.062 ± 0.016	K'	3	I*
2008 May 29	54615.62	119.10 ± 0.14	170.07 ± 0.09	0.068 ± 0.010	K_S	11	I
2008 Sep 8	54717.35	119.60 ± 0.30	176.02 ± 0.10	0.080 ± 0.019	H	6	I
2008 Sep 8	54717.35	120.1 ± 0.4	175.89 ± 0.10	0.059 ± 0.022	K_S	8	I
2008 Sep 8	54717.36	119.7 ± 0.5	175.91 ± 0.14	0.107 ± 0.017	J	15	I
2008 Sep 8	54717.37	120.9 ± 0.6	176.0 ± 0.4	0.030 ± 0.026	L'	9	I
2008 Dec 1	54801.24	120.9 ± 1.6	180.7 ± 0.7	0.09 ± 0.05	K_S	12	I
2011 Jul 1	55743.62	148.20 ± 0.15	225.79 ± 0.04	0.042 ± 0.008	K	13	I
2014 Jun 16	56824.57	167.50 ± 0.13	260.77 ± 0.030	0.051 ± 0.006	K	16	I
		DENIS J2252−1730AB ($N_{\rm ep} = 7, \Delta t = 8.03$ yr)					
2005 Oct 11	53654.42	115.0 ± 3.0	349.4 ± 2.5	1.74 ± 0.09	K_S	8	I
2005 Oct 11	53654.43	111 ± 8	347.0 ± 3.0	1.17 ± 0.23	L'	3	I
2007 Aug 7	54319.53	74.0 ± 3.0	193.4 ± 2.2	1.71 ± 0.18	K_S	12	M
2007 Sep 6	54349.39	76.2 ± 1.9	188.9 ± 1.2	1.55 ± 0.12	K_S	12	M
2010 Jul 9	55386.62	58 ± 4	51 ± 4	1.68 ± 0.27	K	10	M
2012 Sep 7	56177.43	143.8 ± 0.7	7.42 ± 0.26	0.987 ± 0.028	CH_4s	6	I
2012 Sep 7	56177.43	146 ± 4	7.6 ± 1.0	1.18 ± 0.06	H	6	I
2013 Jul 1	56474.58	148.2 ± 0.7	1.3 ± 0.8	0.95 ± 0.05	CH_4s	4	I
2013 Oct 22	56587.23	142.5 ± 1.4	357.93 ± 0.22	0.569 ± 0.021	Y	6	I
2013 Oct 22	56587.24	142.1 ± 1.4	358.20 ± 0.30	0.77 ± 0.04	J	6	I

Note. — In the notes column, "I" indicates an observation done with direct imaging and "M" indicates non-redundant aperture masking.

*This denotes a previously published data set that we obtained from the public NIRC2 archive.

**This denotes a previously unpublished data set that we obtained from the public NIRC2 archive.

Table 3. Relative astrometry from *HST* Imaging and the Literature

Date (UT)	Separation (mas)	PA (°)	Δm (mag)	Bandpass	Notes
			LP 349-25AB ($N_{\rm ep} = 2$)		
2004 Jul 3	125 ± 10	12.7 ± 2.0	0.26 ± 0.05	K'	CFHT/PUEO (Forveille et al. 2005)
2004 Sep 26	107 ± 10	7.1 ± 0.5	0.38 ± 0.05	H	VLT/NACO (Forveille et al. 2005)
			LP 415-20AB ($N_{\rm ep} = 1$)		
2002 Feb 7	119.0 ± 1.0	91.2 ± 0.7	0.66 ± 0.06	K'	Gemini/QUIRC (Siegler et al. 2003)
			SDSS J0423−0414AB ($N_{\rm ep} = 8$)		
2004 Jul 22	159.7 ± 0.6	19.73 ± 0.30	0.535 ± 0.022	$F110W$	HST/NICMOS-NIC1
2004 Jul 22	159.3 ± 1.2	19.73 ± 0.16	0.818 ± 0.012	$F170M$	HST/NICMOS-NIC1
2008 Aug 7	84.0 ± 3.0	183 ± 9	0.5 ± 0.8	$F110W$	HST/NICMOS-NIC1
2008 Aug 7	83.8 ± 2.6	183 ± 5	0.7 ± 0.6	$F170M$	HST/NICMOS-NIC1
2009 Dec 10	148.1 ± 0.6	216.4 ± 0.7	1.139 ± 0.017	$F814W$	HST/ACS-WFC
2010 Jul 29	151.2 ± 0.6	223.3 ± 0.7	1.052 ± 0.018	$F814W$	HST/ACS-WFC
2011 Feb 14	146.3 ± 0.6	232.2 ± 0.7	1.137 ± 0.010	$F814W$	HST/ACS-WFC
2011 Aug 14	134.1 ± 0.6	238.9 ± 0.7	1.18 ± 0.03	$F814W$	HST/ACS-WFC
2012 Feb 17	118.6 ± 0.6	249.9 ± 0.7	1.187 ± 0.021	$F814W$	HST/ACS-WFC
2012 Aug 30	103.8 ± 0.6	263.7 ± 0.7	1.03 ± 0.03	$F814W$	HST/ACS-WFC
			2MASS J0700+3157AB ($N_{\rm ep} = 1$)		
2004 Dec 29	180.4 ± 1.3	105.54 ± 0.27	1.60 ± 0.05	$F110W$	HST/NICMOS-NIC1
2004 Dec 29	179.7 ± 2.4	105.8 ± 0.5	1.476 ± 0.021	$F170M$	HST/NICMOS-NIC1
			LHS 1901AB ($N_{\rm ep} = 3$)		
2004 Jan 8	275 ± 5	208.0 ± 0.5	0.130 ± 0.030	K'	CFHT/PUEO (Montagnier et al. 2006)
2005 Apr 27	204 ± 5	215.0 ± 0.5	0.070 ± 0.030	K'	CFHT/PUEO (Montagnier et al. 2006)
2005 Oct 14	174 ± 5	219.6 ± 0.5	0.14 ± 0.05	H	CFHT/PUEO (Montagnier et al. 2006)
			2MASS J0746+2000AB ($N_{\rm ep} = 6$)		
2000 Apr 15	217.8 ± 2.9	168.8 ± 0.5	0.624 ± 0.022	$F814W$	HST/WFPC2-PC1
2002 Feb 7	121 ± 8	86 ± 4	0.44 ± 0.15	K'	Gemini/QUIRC (Bouy et al. 2004)
2002 Oct 21	121.78 ± 0.10	33.80 ± 0.28	0.6320 ± 0.0030	$F850LP$	HST/ACS-HRC
2003 Mar 22	123.5 ± 2.1	4.6 ± 1.0	0.46 ± 0.15	H	VLT/NACO (Bouy et al. 2004)
2003 Dec 4	126.5 ± 1.8	317.9 ± 0.7	0.520 ± 0.030	K_S	Keck I/NIRC speckle (Bouy et al. 2004)
2004 Jan 9	134.5 ± 3.0	311.1 ± 1.2	···	$F28X50LP$	HST/STIS (Bouy et al. 2004)
			2MASS J0850+1057AB ($N_{\rm ep} = 3$)		
2000 Feb 1	156 ± 4	114.2 ± 1.2	1.22 ± 0.09	$F814W$	HST/WFPC2-PC1
2002 Oct 21	143.0 ± 3.0	123.2 ± 1.1	0.98 ± 0.10	$F850LP$	HST/ACS-HRC
2003 Nov 9	132.6 ± 1.1	128.40 ± 0.30	1.19 ± 0.05	$F110W$	HST/NICMOS-NIC1
2003 Nov 9	128.0 ± 3.0	127.8 ± 0.8	0.92 ± 0.04	$F170M$	HST/NICMOS-NIC1
			2MASS J0920+3517AB ($N_{\rm ep} = 3$)		
2000 Feb 9	74.0 ± 3.0	247.2 ± 1.5	0.30 ± 0.10	$F814W$	HST/WFPC2-PC1
2002 Oct 19	27 ± 8	57 ± 7	0.3 ± 0.6	$F850LP$	HST/ACS-HRC

Table 3—Continued

Date (UT)	Separation (mas)	PA (°)	Δm (mag)	Bandpass	Notes
2006 Apr 8	51 ± 5	241 ± 9	0.52 ± 0.17	$F850LP$	HST/ACS-HRC
			SDSS J0926+5847AB ($N_{\rm ep} = 6$)		
2004 Feb 5	66.6 ± 1.9	132.9 ± 1.4	0.41 ± 0.12	$F110W$	HST/NICMOS-NIC1
2004 Feb 5	67 ± 6	133.2 ± 3.0	0.84 ± 0.11	$F170M$	HST/NICMOS-NIC1
2009 Nov 13	64 ± 4	315.50 ± 0.30	0.61 ± 0.12	$F814W$	HST/ACS-WFC
2010 Jun 17	70.6 ± 0.8	314.3 ± 0.8	0.58 ± 0.08	$F814W$	HST/ACS-WFC
2010 Nov 30	72.7 ± 0.9	313.8 ± 0.6	0.565 ± 0.018	$F814W$	HST/ACS-WFC
2012 Apr 7	63.3 ± 0.8	313.2 ± 0.9	0.585 ± 0.026	$F814W$	HST/ACS-WFC
2012 Nov 9	33 ± 5	283 ± 30	···	$F814W$	HST/ACS-WFC; $\Delta F814W$ fixed at 0.56 mag
			2MASS J1017+1308AB ($N_{\rm ep} = 1$)		
2001 Apr 16	99.7 ± 1.6	89.6 ± 1.2	0.27 ± 0.05	$F814W$	HST/WFPC2-PC1
			SDSS J1021−0304AB ($N_{\rm ep} = 1$)		
2004 May 2	172 ± 5	244.6 ± 0.8	1.030 ± 0.019	$F170M$	HST/NICMOS-NIC1 (Burgasser et al. 2006)
			2MASS J1047+4026AB (a.k.a. LP 213-68) ($N_{\rm ep} = 1$)		
2002 Apr 25	122 ± 8	328 ± 4	0.50 ± 0.15	K'	Gemini/QUIRC (Close et al. 2003)
			Gl 417BC ($N_{\rm ep} = 1$)		
2001 Feb 14	63.9 ± 2.3	76.2 ± 1.5	0.55 ± 0.07	$F814W$	HST/WFPC2-PC1 (Dupuy et al. 2014)
			LHS 2397aAB ($N_{\rm ep} = 3$)		
1997 Apr 12	274 ± 4	87.3 ± 0.8	4.18 ± 0.08	$F814W$	HST/WFPC2-PC1 (Dupuy et al. 2009c)
2003 May 31	168 ± 8	188.6 ± 1.2	···	K_S	VLT/NACO (Dupuy et al. 2009c)
2006 Jan 12	129 ± 5	276.2 ± 1.4	···	K_S	VLT/NACO (Dupuy et al. 2009c)
			DENIS J1228−1557AB ($N_{\rm ep} = 8$)		
1998 Jun 2	275.0 ± 2.0	41.00 ± 0.20	···	$F110M$	HST/NICMOS-NIC1 (Martín et al. 1999)
2001 Mar 4	246 ± 20	23.0 ± 2.0	0.44 ± 0.09	$F814W$	HST/WFPC2-PC1 (Bouy et al. 2003)
2001 Jun 16	255.4 ± 2.8	18.30 ± 0.30	0.36 ± 0.07	$F814W$	HST/WFPC2-PC1 (Bouy et al. 2003)
2002 Jan 3	252.1 ± 2.8	13.70 ± 0.30	···	$F814W$	HST/WFPC2-PC1 (Brandner et al. 2004)
2002 Apr 25	250 ± 7	11.4 ± 0.8	···	$F28X50LP$	HST/STIS (Brandner et al. 2004)
2002 Jun 9	247.6 ± 2.8	9.80 ± 0.30	···	$F814W$	HST/WFPC2-PC1 (Brandner et al. 2004)
2002 Dec 30	243.6 ± 2.8	5.70 ± 0.30	···	$F814W$	HST/WFPC2-PC1 (Brandner et al. 2004)
2003 Dec 29	239.2 ± 2.8	356.70 ± 0.30	···	$F814W$	HST/WFPC2-PC1 (Brandner et al. 2004)
			Kelu-1AB ($N_{\rm ep} = 1$)		
1998 Aug 14	42.5 ± 1.7	34 ± 5	0.58 ± 0.21	$F110M$	HST/NICMOS-NIC1
1998 Aug 14	49 ± 5	30.9 ± 2.2	1.3 ± 0.4	$F165M$	HST/NICMOS-NIC1
			HD 130948BC ($N_{\rm ep} = 2$)		
2002 Sep 6	94.6 ± 1.1	306.9 ± 1.0	0.47 ± 0.05	$FR914M$	HST/ACS-HRC coronagraph (Dupuy et al. 2009b)
2005 Feb 23	56.8 ± 0.6	146.6 ± 0.6	0.24 ± 0.05	$F850LP$	HST/ACS-HRC coronagraph (Dupuy et al. 2009b)

Table 3—Continued

Date (UT)	Separation (mas)	PA (°)	Δm (mag)	Bandpass	Notes
		Gl 569Bab ($N_{\rm ep} = 1$)			
2002 Jun 26	97.3 ± 1.3	94.0 ± 1.3	0.990 ± 0.030	$F28X50LP$	HST/STIS (Dupuy et al. 2010)
		2MASS J1534−2952AB ($N_{\rm ep} = 3$)			
2000 Aug 18	62.8 ± 1.2	357.1 ± 0.8	0.30 ± 0.05	$F814W$	HST/WFPC2-PC1 (Liu et al. 2008)
2006 Jan 19	199.0 ± 1.1	14.5 ± 0.6	0.28 ± 0.06	$F814W$	HST/ACS-HRC (Liu et al. 2008)
2006 Apr 11	191.2 ± 1.1	15.5 ± 0.4	0.30 ± 0.04	$F814W$	HST/ACS-HRC (Liu et al. 2008)
		2MASS J1728+3948AB ($N_{\rm ep} = 5$)			
2000 Aug 12	130.1 ± 2.4	27.2 ± 0.8	0.41 ± 0.07	$F814W$	HST/WFPC2-PC1
2003 Sep 7	158.0 ± 2.0	66.80 ± 0.30	0.290 ± 0.030	$F110W$	HST/NICMOS-NIC1
2003 Sep 7	158.7 ± 1.2	66.85 ± 0.22	0.465 ± 0.012	$F170M$	HST/NICMOS-NIC1
2005 Aug 14	182 ± 7	82.9 ± 0.9	0.47 ± 0.11	$F814W$	HST/ACS-HRC
2006 Jan 1	188 ± 6	86.1 ± 1.9	0.59 ± 0.12	$F814W$	HST/ACS-HRC
2006 May 18	195.2 ± 2.3	88.8 ± 2.3	0.50 ± 0.30	$F814W$	HST/ACS-HRC
		2MASS J1750+4424AB ($N_{\rm ep} = 1$)			
2002 Apr 25	158 ± 5	339.6 ± 0.7	0.64 ± 0.10	K'	Gemini/QUIRC (Siegler et al. 2003)
		2MASS J1847+5522AB ($N_{\rm ep} = 1$)			
2003 Jul 10	82 ± 5	91.1 ± 1.4	0.16 ± 0.10	K_S	Subaru/CIAO (Siegler et al. 2005)
		SDSS J2052−1609AB ($N_{\rm ep} = 1$)			
2008 Jun 24	104 ± 7	50.1 ± 1.7	0.2 ± 0.4	$F110W$	HST/NICMOS-NIC1
2008 Jun 24	101 ± 6	50.0 ± 1.8	0.42 ± 0.24	$F170M$	HST/NICMOS-NIC1
		2MASS J2140+1625AB ($N_{\rm ep} = 1$)			
2001 May 31	157.0 ± 2.8	131.5 ± 0.6	1.26 ± 0.04	$F814W$	HST/WFPC2-PC1
		2MASS J2206−2047AB ($N_{\rm ep} = 1$)			
2000 Aug 13	161.1 ± 1.8	57.5 ± 1.1	0.060 ± 0.020	$F814W$	HST/WFPC2-PC1 (Dupuy et al. 2009a)
		DENIS J2252−1730AB ($N_{\rm ep} = 2$)			
2005 Jun 21	126.4 ± 1.0	353.1 ± 0.4	0.980 ± 0.030	$F110W$	HST/NICMOS-NIC1
2005 Jun 21	127.4 ± 1.5	352.90 ± 0.30	1.300 ± 0.024	$F170M$	HST/NICMOS-NIC1
2008 May 1	87.8 ± 2.8	165.0 ± 3.0	0.7 ± 0.4	$F110W$	HST/NICMOS-NIC1
2008 May 1	88 ± 5	169 ± 4	1.07 ± 0.13	$F170M$	HST/NICMOS-NIC1

Note. — The measurements reported in this table are from our own analysis of archival data in this paper, unless another reference is given in the Notes column.

Table 4. Integrated-light astrometry from CFHT/WIRCam

Observation Date (UT)	(MJD)	R.A. (deg)	Dec. (deg)	$\sigma_{\rm R.A.} \cos\delta$ (mas)	$\sigma_{\rm Dec.}$ (mas)	Airmass	Seeing (arcsec)
LP 349-25AB ($N_{\rm ep} = 20, \Delta t = 8.26\,{\rm yr}$)							
2008 Aug 9	54687.5662	006.98451510	+22.32547171	2.4	2.6	1.001	0.61
2008 Sep 6	54715.4857	006.98451751	+22.32546921	3.0	8.6	1.001	0.48
2008 Oct 8	54747.4233	006.98451811	+22.32545820	2.8	3.3	1.008	0.53
2008 Oct 9	54748.3920	006.98451801	+22.32545770	2.7	3.5	1.002	0.75
2008 Nov 16	54786.2900	006.98451972	+22.32544801	1.9	3.2	1.002	0.90
2009 Jul 29	55041.6143	006.98463346	+22.32542572	2.6	4.0	1.006	0.84
2009 Aug 4	55047.6397	006.98463611	+22.32542544	3.1	3.6	1.063	0.56
2009 Aug 8	55051.5876	006.98463564	+22.32542301	2.0	2.3	1.006	0.68
2009 Aug 25	55068.5222	006.98463634	+22.32542258	2.8	2.1	1.001	0.68
2009 Oct 21	55125.3717	006.98463934	+22.32540909	2.8	2.5	1.001	0.71
2009 Nov 6	55141.3542	006.98463957	+22.32540230	8.4	8.7	1.016	0.79
2009 Dec 22	55187.2217	006.98464710	+22.32538996	1.6	1.8	1.010	0.58
2010 Aug 15	55423.5592	006.98475726	+22.32537588	1.4	2.4	1.002	0.58
2010 Sep 15	55454.4572	006.98476077	+22.32536973	3.1	2.8	1.003	0.47
2010 Oct 22	55491.3577	006.98475905	+22.32536073	5.2	3.8	1.002	0.63
2011 Jul 19	55761.6019	006.98487661	+22.32533064	3.3	1.5	1.012	0.53
2011 Jul 25	55767.5641	006.98487564	+22.32533050	3.1	4.2	1.039	0.69
2016 Aug 17	57617.5512	006.98549184	+22.32509917	4.6	5.2	1.002	0.46
2016 Sep 10	57641.4343	006.98549407	+22.32509416	3.6	5.6	1.038	0.57
2016 Nov 13	57705.2584	006.98549810	+22.32507409	18.4	12.0	1.040	0.51
LP 415-20AB ($N_{\rm ep} = 29, \Delta t = 8.20\,{\rm yr}$)							
2008 Sep 6	54715.6377	065.45707764	+19.48577984	2.6	4.1	1.004	0.50
2008 Oct 9	54748.5746	065.45707891	+19.48577781	2.0	2.0	1.003	0.62
2008 Nov 7	54777.4642	065.45707952	+19.48577686	3.5	3.5	1.007	0.44
2009 Jan 20	54851.2642	065.45707825	+19.48577261	2.8	2.7	1.005	0.48
2009 Aug 26	55069.6266	065.45711418	+19.48576986	2.4	2.7	1.060	0.49
2009 Oct 21	55125.5383	065.45711501	+19.48576642	2.4	2.2	1.001	0.68
2009 Dec 23	55188.3265	065.45711472	+19.48576463	2.2	2.8	1.018	0.54
2011 Feb 14	55606.2458	065.45715239	+19.48575444	4.1	5.7	1.017	0.43
2011 Feb 15	55607.2601	065.45715280	+19.48575233	1.9	2.2	1.043	0.55
2011 Feb 16	55608.2193	065.45715244	+19.48575193	3.8	6.0	1.002	0.87
2011 Feb 17	55609.2185	065.45715328	+19.48575339	2.9	3.6	1.003	0.47
2011 Feb 18	55610.2212	065.45715390	+19.48575184	3.7	5.2	1.006	0.42
2011 Sep 12	55816.6272	065.45718873	+19.48574905	4.5	6.3	1.002	0.49
2011 Oct 13	55847.5666	065.45718887	+19.48574814	1.8	4.0	1.003	0.51
2011 Dec 29	55924.3353	065.45718785	+19.48574534	5.3	4.4	1.001	0.58
2012 Mar 12	55998.2204	065.45719159	+19.48574187	1.6	4.1	1.120	0.69
2012 Mar 13	55999.2149	065.45719315	+19.48574251	2.8	4.6	1.111	0.66

Table 4—Continued

Observation Date (UT)	(MJD)	R.A. (deg)	Dec. (deg)	$\sigma_{\rm R.A.} \cos\delta$ (mas)	$\sigma_{\rm Dec.}$ (mas)	Airmass	Seeing (arcsec)
2012 Sep 2	56172.6480	065.45722338	+19.48573924	4.7	8.3	1.004	0.53
2012 Oct 4	56204.5559	065.45722569	+19.48573706	6.2	5.6	1.007	0.67
2012 Oct 26	56226.5337	065.45722586	+19.48573689	5.1	8.5	1.005	0.49
2013 Oct 20	56585.5096	065.45726237	+19.48572826	2.9	4.9	1.010	0.47
2013 Dec 11	56637.3933	065.45726175	+19.48572620	3.7	4.3	1.000	0.75
2014 Oct 4	56934.6139	065.45729950	+19.48571693	4.7	6.3	1.024	0.69
2014 Oct 15	56945.5615	065.45729939	+19.48571782	4.7	5.2	1.003	0.51
2014 Nov 28	56989.4224	065.45729962	+19.48571765	2.9	4.2	1.000	0.58
2015 Jan 31	57053.2523	065.45729715	+19.48571173	3.6	6.4	1.000	0.46
2016 Aug 19	57619.6315	065.45736797	+19.48569915	3.4	3.7	1.094	0.44
2016 Sep 10	57641.6047	065.45737049	+19.48569838	3.6	5.2	1.025	0.47
2016 Nov 19	57711.4847	065.45737296	+19.48569813	3.4	4.1	1.021	0.51
		SDSS J0423−0414AB ($N_{\rm ep} = 25, \Delta t = 9.23\,{\rm yr}$)					
2007 Aug 29	54341.6436	065.95181860	−04.23391019	2.7	2.6	1.122	0.48
2007 Sep 20	54363.6214	065.95181115	−04.23391064	1.4	2.1	1.095	0.68
2007 Oct 21	54394.5392	065.95179837	−04.23391479	3.6	3.7	1.096	0.54
2008 Sep 6	54715.6290	065.95172439	−04.23388613	2.3	3.3	1.109	0.61
2008 Oct 9	54748.5832	065.95171189	−04.23388825	2.7	2.6	1.103	0.75
2008 Nov 7	54777.4729	065.95169711	−04.23388941	2.6	3.6	1.098	0.51
2009 Jan 22	54853.2749	065.95165483	−04.23388602	2.4	3.5	1.095	0.66
2009 Aug 26	55069.6420	065.95163530	−04.23386030	2.2	1.8	1.137	0.58
2009 Oct 21	55125.5477	065.95161613	−04.23386429	3.0	2.1	1.101	1.02
2009 Oct 23	55127.5111	065.95161449	−04.23386382	1.9	3.2	1.100	0.97
2011 Feb 11	55603.2255	065.95146664	−04.23383042	2.6	3.7	1.095	0.77
2011 Feb 14	55606.2283	065.95146584	−04.23382883	2.3	2.9	1.098	0.50
2011 Sep 19	55823.6537	065.95144784	−04.23381093	3.9	4.7	1.120	0.91
2011 Sep 26	55830.6302	065.95144604	−04.23381120	2.0	2.3	1.114	0.73
2011 Oct 16	55850.5521	065.95143746	−04.23381313	2.6	1.8	1.095	0.72
2011 Dec 6	55901.4306	065.95140957	−04.23381558	2.0	2.2	1.107	0.78
2012 Sep 4	56174.6340	065.95136483	−04.23378537	3.6	3.3	1.109	0.69
2012 Oct 12	56212.5810	065.95134917	−04.23378733	5.2	6.0	1.109	1.01
2012 Oct 28	56228.5512	065.95134037	−04.23378896	3.0	3.9	1.130	0.76
2015 Feb 2	57055.2870	065.95111041	−04.23373150	4.3	4.8	1.129	0.78
2015 Aug 21	57255.6458	065.95109653	−04.23370841	3.7	3.2	1.163	0.68
2015 Oct 22	57317.5458	065.95107366	−04.23371352	2.7	2.6	1.100	0.56
2016 Aug 19	57619.6378	065.95100546	−04.23368359	3.6	2.5	1.198	0.47
2016 Sep 9	57640.6240	065.95100199	−04.23368419	2.7	2.6	1.106	0.47
2016 Nov 21	57713.4566	065.95096784	−04.23368899	2.7	3.8	1.097	0.45

Table 4—Continued

Observation Date (UT)	(MJD)	R.A. (deg)	Dec. (deg)	$\sigma_{\rm R.A.}\cos\delta$ (mas)	$\sigma_{\rm Dec.}$ (mas)	Airmass	Seeing (arcsec)
			2MASS J0700+3157AB ($N_{\rm ep}=19, \Delta t = 7.85\,{\rm yr}$)				
2008 Feb 17	54513.3004	105.15335763	+31.95614074	4.1	3.5	1.027	0.45
2008 Feb 23	54519.2949	105.15335608	+31.95613904	2.9	6.5	1.023	0.51
2008 Nov 7	54777.5824	105.15343295	+31.95602426	3.0	3.3	1.025	0.47
2009 Jan 20	54851.3886	105.15341125	+31.95599745	2.0	1.9	1.023	0.83
2009 Mar 12	54902.2632	105.15340038	+31.95597555	2.2	4.1	1.025	0.57
2009 Oct 21	55125.6123	105.15348317	+31.95587559	3.3	2.8	1.036	0.78
2009 Dec 22	55187.4874	105.15346990	+31.95585519	1.4	2.5	1.027	0.66
2010 Mar 24	55279.2824	105.15344757	+31.95581541	1.9	2.6	1.090	0.64
2010 Apr 4	55290.2176	105.15344673	+31.95581009	3.0	2.9	1.035	0.67
2011 Mar 17	55637.2585	105.15349297	+31.95566447	2.7	2.7	1.029	0.66
2011 Sep 30	55834.6489	105.15357193	+31.95557487	3.3	2.9	1.066	0.59
2011 Oct 15	55849.6443	105.15357411	+31.95557031	3.7	3.3	1.026	0.58
2011 Dec 5	55900.5321	105.15356721	+31.95555165	2.9	5.1	1.026	0.71
2012 Mar 2	55988.2727	105.15353799	+31.95551788	3.7	2.6	1.023	0.79
2012 Apr 1	56018.2275	105.15353912	+31.95550288	8.5	3.6	1.039	0.61
2012 Oct 12	56212.6295	105.15361571	+31.95541771	3.5	4.1	1.043	0.65
2012 Oct 26	56226.6404	105.15361767	+31.95541017	3.6	4.3	1.026	0.59
2015 Oct 22	57317.6369	105.15372454	+31.95495739	3.2	4.2	1.023	0.56
2015 Dec 24	57380.4323	105.15370973	+31.95493516	3.2	2.9	1.043	0.52
			LHS 1901AB ($N_{\rm ep}=15, \Delta t = 3.81\,{\rm yr}$)				
2008 Feb 17	54513.3089	107.79887618	+43.49844276	17.4	16.7	1.096	0.55
2008 Feb 23	54519.3013	107.79887797	+43.49843496	13.6	9.7	1.092	0.54
2008 Nov 7	54777.5905	107.79901700	+43.49831760	10.2	6.6	1.093	0.56
2009 Jan 20	54851.3976	107.79901056	+43.49829468	3.2	2.4	1.092	0.83
2009 Mar 12	54902.2717	107.79900991	+43.49826914	2.5	4.2	1.094	0.56
2009 Oct 21	55125.6209	107.79914462	+43.49816864	3.1	3.3	1.104	0.83
2009 Dec 23	55188.4847	107.79914914	+43.49814873	3.3	3.0	1.093	0.69
2010 Mar 25	55280.2349	107.79914829	+43.49810699	1.8	3.7	1.093	0.83
2010 Apr 5	55291.2182	107.79915157	+43.49810026	1.3	2.0	1.101	0.67
2011 Feb 10	55602.3753	107.79927998	+43.49797025	1.4	4.6	1.109	0.58
2011 Mar 17	55637.2639	107.79928238	+43.49795582	3.0	4.5	1.096	0.72
2011 Mar 20	55640.2380	107.79928508	+43.49795280	4.2	2.9	1.092	0.76
2011 Apr 16	55667.2219	107.79929395	+43.49793735	3.0	4.3	1.145	0.61
2011 Dec 5	55900.5395	107.79942454	+43.49784055	2.5	6.2	1.094	0.75
2011 Dec 9	55904.5536	107.79942433	+43.49784183	4.0	2.6	1.115	0.64
			2MASS J0746+2000AB ($N_{\rm ep}=17, \Delta t = 8.73\,{\rm yr}$)				
2008 Feb 21	54517.3357	116.67639167	+20.00895385	2.0	1.7	1.000	0.66

Table 4—Continued

Observation Date (UT)	(MJD)	R.A. (deg)	Dec. (deg)	$\sigma_{\mathrm{R.A.}} \cos\delta$ (mas)	$\sigma_{\mathrm{Dec.}}$ (mas)	Airmass	Seeing (arcsec)
2008 Feb 24	54520.3197	116.67638952	+20.00895422	1.6	1.3	1.002	0.66
2008 Nov 7	54777.6254	116.67634931	+20.00893836	3.1	3.6	1.000	0.63
2008 Nov 15	54785.6035	116.67634348	+20.00893820	2.6	3.0	1.000	0.63
2009 Jan 20	54851.4246	116.67630394	+20.00893927	1.9	1.8	1.000	0.78
2009 Mar 12	54902.3242	116.67627084	+20.00894205	1.4	2.4	1.029	0.65
2009 Oct 21	55125.6377	116.67624770	+20.00892504	2.6	2.3	1.021	0.83
2010 Apr 22	55308.2266	116.67614615	+20.00892748	1.6	1.9	1.053	0.63
2011 Oct 16	55850.6579	116.67603021	+20.00889689	2.8	2.5	1.016	0.64
2011 Dec 5	55900.5863	116.67600946	+20.00889448	4.0	3.6	1.022	0.62
2012 Jan 1	55927.4358	116.67599041	+20.00889564	3.0	3.1	1.031	0.64
2015 Feb 8	57061.3256	116.67564015	+20.00884914	2.4	2.2	1.040	0.64
2015 Oct 22	57317.6571	116.67559848	+20.00883194	3.4	3.8	1.003	0.55
2016 Mar 20	57467.2703	116.67551015	+20.00883319	3.2	4.0	1.001	0.54
2016 Apr 25	57503.2650	116.67549896	+20.00883141	2.6	6.3	1.213	0.51
2016 Sep 12	57643.6452	116.67550263	+20.00882084	6.9	5.3	1.414	0.74
2016 Nov 12	57704.6633	116.67548532	+20.00881803	4.7	4.4	1.048	0.49
2MASS J0850+1057AB ($N_{\mathrm{ep}} = 17, \Delta t = 8.97\,\mathrm{yr}$)							
2007 Nov 24	54428.6123	132.64945253	+10.95438678	3.2	3.4	1.015	0.62
2008 Feb 22	54518.3805	132.64943195	+10.95438736	3.4	2.8	1.012	0.56
2008 Apr 20	54576.2294	132.64942188	+10.95438818	2.8	3.1	1.014	0.61
2008 Apr 28	54584.2268	132.64942092	+10.95438810	2.1	2.2	1.027	0.48
2008 Nov 9	54779.6573	132.64941468	+10.95438227	1.5	1.3	1.013	0.62
2009 Jan 21	54852.4611	132.64939969	+10.95438154	1.3	1.7	1.012	0.58
2009 Oct 26	55130.6511	132.64937571	+10.95437891	2.4	2.1	1.065	1.11
2010 Mar 24	55279.2949	132.64934368	+10.95437974	1.2	2.1	1.012	0.80
2010 Apr 24	55310.2247	132.64933835	+10.95438151	2.5	2.0	1.016	0.84
2011 Dec 4	55899.6309	132.64928937	+10.95436891	2.5	2.6	1.033	0.56
2012 Jan 23	55949.4455	132.64927661	+10.95437053	2.9	2.6	1.017	0.77
2012 Mar 12	55998.3735	132.64926492	+10.95437218	1.0	1.9	1.053	0.57
2012 Apr 10	56027.2801	132.64925897	+10.95437150	2.2	1.7	1.031	0.54
2012 Oct 29	56229.6484	132.64925354	+10.95436777	2.7	2.5	1.053	0.50
2015 Feb 8	57061.4245	132.64915069	+10.95435940	1.8	2.1	1.013	0.60
2016 Nov 8	57700.6490	132.64908829	+10.95434866	2.0	3.2	1.018	0.46
2016 Nov 11	57703.6267	132.64908811	+10.95435022	2.5	2.3	1.032	0.43
2MASS J0920+3517AB ($N_{\mathrm{ep}} = 26, \Delta t = 8.96\,\mathrm{yr}$)							
2007 Nov 23	54427.6629	140.05058120	+35.29485824	8.6	7.4	1.041	0.95
2007 Nov 24	54428.6288	140.05058328	+35.29485459	3.2	2.0	1.042	0.57
2008 Feb 17	54513.4041	140.05055711	+35.29484718	3.7	2.1	1.039	0.58

Table 4—Continued

Observation Date (UT)	(MJD)	R.A. (deg)	Dec. (deg)	$\sigma_{\rm R.A.}\cos\delta$ (mas)	$\sigma_{\rm Dec.}$ (mas)	Airmass	Seeing (arcsec)
2008 Feb 23	54519.4006	140.05055489	+35.29484749	2.6	4.5	1.038	0.81
2008 Apr 20	54576.2474	140.05053741	+35.29483700	3.1	2.1	1.038	0.64
2008 Apr 28	54584.2397	140.05053460	+35.29483313	3.1	4.4	1.044	0.47
2009 Jan 19	54850.4910	140.05050054	+35.29479413	2.1	3.2	1.037	0.93
2009 Apr 7	54928.2870	140.05047564	+35.29478346	1.9	2.3	1.039	0.64
2009 Apr 8	54929.2815	140.05047440	+35.29478416	3.2	1.9	1.038	0.94
2009 Apr 13	54934.2309	140.05047435	+35.29478327	1.3	1.7	1.053	0.75
2009 Nov 6	55141.6622	140.05045709	+35.29474589	3.4	3.3	1.054	0.68
2009 Dec 24	55189.5483	140.05044400	+35.29474044	1.8	2.0	1.041	0.50
2010 Mar 24	55279.3186	140.05041319	+35.29473096	1.4	2.2	1.037	0.58
2010 Apr 4	55290.2745	140.05040964	+35.29472838	1.9	1.7	1.040	0.65
2010 Apr 21	55307.2497	140.05040606	+35.29472527	1.2	1.1	1.039	0.56
2010 May 4	55320.2328	140.05040261	+35.29472258	1.8	2.1	1.050	0.64
2011 Dec 5	55900.6128	140.05032326	+35.29463349	2.7	4.6	1.037	0.60
2012 Mar 14	56000.2716	140.05029128	+35.29462167	2.4	2.9	1.126	0.56
2012 Mar 31	56017.2790	140.05028517	+35.29462035	3.8	3.3	1.042	0.64
2012 Oct 27	56227.6377	140.05026895	+35.29458134	2.2	1.7	1.159	0.64
2015 May 3	57145.2758	140.05009674	+35.29444974	1.7	2.0	1.117	0.56
2015 Dec 24	57380.5919	140.05007370	+35.29441250	3.2	2.1	1.050	0.49
2016 Mar 21	57468.3295	140.05004438	+35.29440250	2.1	3.1	1.038	0.55
2016 Apr 24	57502.2504	140.05003447	+35.29439516	1.8	2.0	1.044	0.70
2016 May 22	57530.2493	140.05002879	+35.29438964	1.5	2.7	1.204	0.72
2016 Nov 9	57701.6522	140.05001664	+35.29435887	5.6	5.2	1.055	0.39
SDSS J0926+5847AB ($N_{\rm ep} = 14, \Delta t = 4.12\,{\rm yr}$)							
2008 Feb 17	54513.4135	141.56432724	+58.78890076	1.8	2.4	1.286	0.59
2008 Apr 20	54576.2566	141.56431001	+58.78888534	3.1	3.0	1.287	0.59
2009 Jan 19	54850.5090	141.56434228	+58.78884176	2.2	2.4	1.288	1.08
2009 Apr 5	54926.2877	141.56431765	+58.78883159	2.3	3.6	1.285	0.87
2010 Mar 24	55279.3311	141.56432615	+58.78877363	0.9	2.0	1.287	0.62
2010 Apr 4	55290.2870	141.56432437	+58.78877051	1.2	2.1	1.285	0.57
2010 Apr 21	55307.2624	141.56432132	+58.78876583	1.1	1.9	1.290	0.60
2010 May 6	55322.2278	141.56432077	+58.78876135	1.4	2.3	1.295	0.60
2011 Jan 22	55583.4874	141.56435285	+58.78872302	1.8	1.4	1.285	0.70
2011 Feb 10	55602.4389	141.56434613	+58.78871998	1.6	2.3	1.285	0.69
2011 Mar 17	55637.3323	141.56433547	+58.78871491	2.4	1.6	1.286	0.70
2011 Mar 20	55640.3260	141.56433367	+58.78871443	3.6	3.9	1.286	0.69
2011 Dec 6	55901.5962	141.56437142	+58.78866537	2.3	1.7	1.292	0.68
2012 Mar 31	56017.2886	141.56433967	+58.78865056	3.2	3.4	1.287	0.67

Table 4—Continued

Observation Date (UT)	(MJD)	R.A. (deg)	Dec. (deg)	$\sigma_{\mathrm{R.A.}} \cos\delta$ (mas)	$\sigma_{\mathrm{Dec.}}$ (mas)	Airmass	Seeing (arcsec)
2MASS J1017+1308AB ($N_{\mathrm{ep}} = 22, \Delta t = 8.73\,\mathrm{yr}$)							
2008 Feb 18	54514.4408	154.28178693	+13.14419220	2.2	1.4	1.009	0.61
2008 Feb 23	54519.4475	154.28178626	+13.14419198	2.0	1.9	1.009	0.71
2008 Apr 20	54576.2675	154.28178328	+13.14418986	2.8	3.0	1.010	0.61
2008 Apr 28	54584.2617	154.28178313	+13.14418841	3.5	2.7	1.007	0.49
2009 Jan 19	54850.5444	154.28180388	+13.14416131	2.7	3.8	1.011	0.91
2009 Apr 8	54929.3172	154.28179646	+13.14415595	2.2	4.0	1.007	0.83
2009 Apr 15	54936.2737	154.28179669	+13.14415722	1.8	2.9	1.016	0.75
2010 Mar 24	55279.3487	154.28181173	+13.14412620	1.6	3.1	1.008	0.75
2010 Apr 4	55290.3212	154.28181172	+13.14412566	2.6	2.8	1.007	0.87
2010 Apr 21	55307.2751	154.28180957	+13.14412474	1.9	2.0	1.007	0.56
2010 May 4	55320.2434	154.28180828	+13.14412410	2.0	2.3	1.007	0.49
2011 Feb 10	55602.4977	154.28182943	+13.14409501	2.4	2.5	1.020	0.64
2011 Mar 21	55641.3577	154.28182553	+13.14409305	3.0	3.6	1.008	0.67
2011 Apr 12	55663.3229	154.28182210	+13.14409101	3.2	3.8	1.013	0.63
2012 Apr 1	56018.3340	154.28183944	+13.14406108	3.0	3.8	1.007	0.63
2013 Mar 21	56372.3944	154.28185286	+13.14403045	3.1	4.2	1.025	0.68
2013 Apr 27	56409.2801	154.28185076	+13.14402706	2.8	3.8	1.013	0.53
2014 Nov 30	56991.6529	154.28188776	+13.14397029	3.1	3.2	1.011	0.54
2015 May 3	57145.2922	154.28187570	+13.14396132	2.8	3.3	1.045	0.47
2015 Dec 25	57381.5867	154.28190039	+13.14393577	2.6	2.2	1.011	0.71
2016 Apr 23	57501.2788	154.28188949	+13.14392813	5.2	3.9	1.008	0.49
2016 Nov 9	57701.6592	154.28191389	+13.14390551	4.0	4.6	1.090	0.43
SDSS J1021−0304AB ($N_{\mathrm{ep}} = 12, \Delta t = 3.80\,\mathrm{yr}$)							
2008 Feb 18	54514.4496	155.29018457	−03.07199613	2.0	2.6	1.086	0.75
2008 Apr 20	54576.2765	155.29016960	−03.07199666	2.7	1.9	1.087	0.63
2009 Jan 20	54851.5353	155.29014765	−03.07201795	2.7	2.2	1.086	0.81
2009 Apr 13	54934.3110	155.29012740	−03.07201833	2.1	2.9	1.087	0.61
2009 Apr 15	54936.2847	155.29012581	−03.07201846	1.4	1.2	1.090	0.64
2010 Mar 24	55279.3573	155.29008606	−03.07203851	1.8	1.7	1.086	0.82
2010 Apr 25	55311.2714	155.29007891	−03.07203988	2.9	3.2	1.086	0.72
2011 Jan 24	55585.5290	155.29005805	−03.07205911	2.8	1.7	1.088	0.89
2011 Feb 11	55603.4648	155.29005516	−03.07205865	10.0	15.7	1.087	1.24
2011 Feb 12	55604.4662	155.29005189	−03.07205961	1.4	2.3	1.086	0.76
2011 Mar 21	55641.3907	155.29004152	−03.07205976	2.4	2.4	1.098	0.76
2011 Dec 7	55902.6550	155.29002367	−03.07207642	2.6	2.1	1.086	0.88
2MASS J1047+4026AB (a.k.a. LP 213-68) ($N_{\mathrm{ep}} = 26, \Delta t = 8.56\,\mathrm{yr}$)							
2008 Apr 20	54576.2863	161.80657096	+40.44722711	4.8	3.3	1.072	0.59

Table 4—Continued

Observation Date (UT)	(MJD)	R.A. (deg)	Dec. (deg)	$\sigma_{\rm R.A.} \cos\delta$ (mas)	$\sigma_{\rm Dec.}$ (mas)	Airmass	Seeing (arcsec)
2009 Jan 20	54851.5487	161.80650379	+40.44721755	5.1	4.8	1.068	0.77
2009 Apr 15	54936.2968	161.80646366	+40.44721696	2.6	2.7	1.074	0.60
2009 Jun 4	54986.2354	161.80644609	+40.44721364	2.3	2.6	1.120	0.54
2010 Mar 25	55280.3839	161.80636686	+40.44721239	2.8	5.1	1.070	0.80
2010 Apr 4	55290.3324	161.80635982	+40.44720998	2.5	2.1	1.071	0.72
2010 Apr 21	55307.2859	161.80635367	+40.44720929	1.9	2.7	1.071	0.48
2010 May 4	55320.2546	161.80634806	+40.44720986	3.5	2.8	1.070	0.42
2011 Feb 11	55603.5086	161.80628118	+40.44720156	2.9	3.3	1.074	0.82
2011 Mar 20	55640.4269	161.80626511	+40.44720146	5.3	4.5	1.092	0.58
2011 Apr 15	55666.3487	161.80624726	+40.44720177	3.5	5.4	1.084	0.74
2011 May 16	55697.2344	161.80623627	+40.44719951	2.0	2.8	1.068	0.53
2011 Dec 9	55904.6586	161.80620424	+40.44718608	4.5	4.2	1.069	0.51
2013 Dec 7	56633.6598	161.80598681	+40.44716786	3.1	4.1	1.069	0.63
2013 Dec 11	56637.6453	161.80598559	+40.44717045	3.6	3.1	1.071	0.60
2014 May 20	56797.2681	161.80591623	+40.44717097	2.9	4.2	1.104	0.52
2014 Dec 2	56993.6596	161.80588114	+40.44715900	1.6	2.1	1.077	0.51
2015 Apr 30	57142.3096	161.80581589	+40.44716468	4.1	6.0	1.086	0.65
2015 May 2	57144.2980	161.80581355	+40.44716705	2.2	3.1	1.080	0.60
2015 Jun 1	57174.2330	161.80580367	+40.44716346	3.5	3.3	1.099	0.46
2015 Dec 23	57379.6546	161.80576794	+40.44715396	3.2	3.0	1.080	0.54
2016 Mar 19	57466.3811	161.80572670	+40.44715861	3.7	3.7	1.069	0.54
2016 Apr 24	57502.2785	161.80570913	+40.44715762	3.4	3.4	1.070	0.61
2016 May 23	57531.2822	161.80570001	+40.44715101	6.6	10.5	1.153	0.63
2016 May 24	57532.2317	161.80569840	+40.44715290	2.7	6.4	1.076	0.57
2016 Nov 11	57703.6355	161.80567442	+40.44713951	4.7	4.4	1.269	0.45
		SDSS J1052+4422AB ($N_{\rm ep} = 25, \Delta t = 7.85\,{\rm yr}$)					
2008 Feb 17	54513.4691	163.05663183	+44.38222483	1.7	2.1	1.100	0.55
2008 Feb 23	54519.4578	163.05663067	+44.38222560	1.8	2.9	1.099	0.58
2008 Apr 19	54575.3258	163.05662028	+44.38221962	2.0	1.6	1.104	0.60
2008 Apr 28	54584.2898	163.05661843	+44.38221752	2.6	3.3	1.100	0.53
2009 Apr 15	54936.3076	163.05662851	+44.38218386	1.2	2.0	1.101	0.59
2009 Jun 6	54988.2377	163.05662468	+44.38217404	2.9	2.7	1.160	0.62
2010 Mar 24	55279.4032	163.05663759	+44.38215056	1.8	1.5	1.107	0.90
2010 Apr 4	55290.3434	163.05663461	+44.38214921	1.9	1.8	1.100	0.70
2010 Apr 21	55307.2971	163.05663322	+44.38214642	1.4	1.6	1.100	0.62
2010 May 5	55321.2619	163.05663170	+44.38214527	1.1	1.5	1.099	0.59
2011 Feb 12	55604.5235	163.05665512	+44.38211697	1.6	2.2	1.117	0.62
2011 Mar 20	55640.4343	163.05664838	+44.38211539	3.1	2.3	1.128	0.67
2011 Apr 15	55666.3584	163.05664344	+44.38211172	2.1	3.1	1.122	0.83

Table 4—Continued

Observation Date (UT)	(MJD)	R.A. (deg)	Dec. (deg)	$\sigma_{\rm R.A.} \cos\delta$ (mas)	$\sigma_{\rm Dec.}$ (mas)	Airmass	Seeing (arcsec)
2011 May 18	55699.2707	163.05663914	+44.38210543	2.0	3.8	1.125	0.66
2011 Dec 9	55904.6656	163.05667201	+44.38208038	2.2	1.9	1.099	0.55
2012 Jan 2	55928.5799	163.05667008	+44.38207996	2.1	2.2	1.107	0.59
2012 Apr 4	56021.3795	163.05665410	+44.38207716	1.6	2.1	1.114	0.63
2013 Apr 27	56409.3155	163.05666568	+44.38203601	2.2	3.2	1.112	0.58
2013 Dec 17	56643.6628	163.05669580	+44.38200526	3.3	1.7	1.104	0.95
2014 May 10	56787.2846	163.05667558	+44.38199660	1.5	1.8	1.116	0.54
2014 Dec 2	56993.6691	163.05670678	+44.38196556	2.4	2.0	1.104	0.56
2014 Dec 3	56994.6475	163.05670632	+44.38196543	2.6	2.7	1.121	0.55
2015 Jan 21	57043.5711	163.05670325	+44.38196597	2.9	1.7	1.106	0.73
2015 Apr 30	57142.3183	163.05668496	+44.38195896	3.3	5.4	1.123	0.64
2015 Dec 23	57379.6622	163.05671538	+44.38192885	1.5	2.0	1.115	0.78
LHS 2397aAB ($N_{\rm ep} = 31, \Delta t = 7.84\,{\rm yr}$)							
2008 Feb 19	54515.4849	170.45393417	−13.21895501	2.6	2.3	1.195	0.56
2008 Feb 24	54520.4880	170.45393175	−13.21895632	3.1	3.3	1.196	0.56
2008 Apr 19	54575.3360	170.45389292	−13.21895070	2.0	3.7	1.195	0.69
2008 Apr 27	54583.3142	170.45388766	−13.21894726	2.9	7.4	1.195	0.61
2008 May 17	54603.2433	170.45387447	−13.21894658	4.9	3.6	1.196	0.80
2008 May 26	54612.2329	170.45387077	−13.21894540	7.3	4.6	1.194	0.46
2009 Jan 20	54851.5782	170.45380691	−13.21896971	6.8	8.9	1.195	0.83
2009 Apr 4	54925.3913	170.45375594	−13.21896681	4.4	4.2	1.205	0.80
2009 Apr 5	54926.3742	170.45375409	−13.21896377	8.0	15.9	1.195	0.97
2009 Apr 15	54936.3337	170.45374693	−13.21896556	2.1	3.7	1.195	0.60
2009 Jun 8	54990.2358	170.45371862	−13.21896059	2.1	2.9	1.243	0.59
2010 Mar 24	55279.4161	170.45361695	−13.21898068	2.3	5.0	1.200	0.77
2010 Apr 21	55307.3102	170.45360073	−13.21897591	4.2	4.1	1.199	0.58
2010 May 5	55321.2747	170.45359122	−13.21897521	3.1	3.9	1.197	0.57
2010 May 22	55338.2446	170.45358171	−13.21897378	3.5	3.7	1.194	0.54
2010 Jun 27	55374.2406	170.45356788	−13.21897340	4.1	4.4	1.504	0.61
2010 Jul 4	55381.2376	170.45356585	−13.21897030	2.8	3.5	1.648	0.57
2011 Feb 13	55605.5099	170.45350187	−13.21899615	2.5	4.4	1.194	0.60
2011 May 16	55697.2764	170.45344322	−13.21898750	2.7	7.1	1.204	0.79
2012 Jan 21	55947.6147	170.45337949	−13.21900456	4.9	5.9	1.244	0.54
2012 Mar 2	55988.4692	170.45334941	−13.21900578	3.0	4.8	1.196	0.63
2012 Mar 14	56000.5027	170.45334224	−13.21900599	6.8	4.5	1.360	0.78
2012 Apr 2	56019.3887	170.45332834	−13.21900195	2.3	3.1	1.199	0.54
2013 Mar 21	56372.4318	170.45319947	−13.21901320	3.0	7.8	1.208	0.66
2013 Apr 28	56410.3459	170.45317352	−13.21900925	5.1	5.2	1.240	0.63
2013 Dec 25	56651.6564	170.45311593	−13.21902717	4.6	2.5	1.198	0.57

Table 4—Continued

Observation Date (UT)	(MJD)	R.A. (deg)	Dec. (deg)	$\sigma_{\mathrm{R.A.}} \cos\delta$ (mas)	$\sigma_{\mathrm{Dec.}}$ (mas)	Airmass	Seeing (arcsec)
2014 May 10	56787.2714	170.45303497	−13.21901997	3.4	3.0	1.194	0.57
2014 Dec 3	56994.6556	170.45298859	−13.21903715	6.1	5.7	1.259	0.58
2015 Jan 21	57043.5794	170.45297058	−13.21904092	6.0	5.7	1.196	0.68
2015 May 4	57146.3111	170.45290377	−13.21903555	4.4	2.8	1.206	0.51
2015 Dec 24	57380.6417	170.45284960	−13.21905205	2.3	2.8	1.195	0.53
DENIS J1228−1557AB ($N_{\mathrm{ep}} = 13, \Delta t = 2.37\,\mathrm{yr}$)							
2008 Feb 18	54514.5363	187.06388239	−15.79320340	3.6	2.9	1.231	0.80
2008 Apr 21	54577.3497	187.06387599	−15.79321020	1.7	3.5	1.241	0.57
2008 May 19	54605.2730	187.06387490	−15.79321134	3.8	4.7	1.241	0.66
2009 Jan 20	54851.6162	187.06392184	−15.79325372	3.8	4.0	1.231	0.83
2009 Apr 15	54936.3617	187.06391610	−15.79326158	3.1	3.1	1.247	0.75
2009 Jun 6	54988.2498	187.06391202	−15.79326309	4.4	3.9	1.232	0.64
2010 Mar 24	55279.4276	187.06395723	−15.79330972	1.7	4.1	1.241	1.02
2010 Apr 5	55291.3812	187.06395553	−15.79331365	2.2	3.7	1.261	0.80
2010 Apr 21	55307.3435	187.06395448	−15.79331332	1.7	1.7	1.251	0.60
2010 May 5	55321.3208	187.06395309	−15.79331209	1.8	2.7	1.235	0.57
2010 May 22	55338.2739	187.06395360	−15.79331390	3.5	5.9	1.235	0.61
2010 Jun 26	55373.2500	187.06395113	−15.79331667	4.2	4.5	1.335	0.82
2010 Jul 4	55381.2459	187.06395478	−15.79331704	2.4	3.1	1.415	0.63
Kelu-1AB ($N_{\mathrm{ep}} = 12, \Delta t = 2.26\,\mathrm{yr}$)							
2008 Feb 18	54514.5646	196.41672713	−25.68481497	3.1	2.2	1.428	0.87
2008 Apr 22	54578.3755	196.41669962	−25.68480986	7.4	6.8	1.438	0.70
2008 May 19	54605.3169	196.41668424	−25.68480981	4.6	4.6	1.428	0.70
2009 Jan 20	54851.6352	196.41664490	−25.68481781	3.3	5.2	1.431	0.81
2009 Apr 6	54927.4596	196.41661417	−25.68481526	3.0	6.5	1.446	0.92
2009 Apr 7	54928.4233	196.41661299	−25.68481578	2.4	4.4	1.432	0.96
2009 Jun 2	54984.2875	196.41658911	−25.68481053	4.6	6.0	1.430	0.99
2010 Mar 24	55279.4542	196.41652862	−25.68481729	1.7	4.6	1.440	0.90
2010 Apr 5	55291.4235	196.41652025	−25.68481479	2.2	5.3	1.438	0.76
2010 Apr 21	55307.3845	196.41651449	−25.68481218	3.2	3.2	1.433	0.72
2010 May 5	55321.3412	196.41650781	−25.68481368	2.5	5.4	1.438	0.69
2010 May 22	55338.2950	196.41650001	−25.68481168	4.4	6.3	1.438	0.75
2MASS J1404−3159AB ($N_{\mathrm{ep}} = 24, \Delta t = 7.30\,\mathrm{yr}$)							
2008 Feb 18	54514.6004	211.20710270	−31.99247602	3.4	7.9	1.621	1.06
2008 Feb 19	54515.6050	211.20710291	−31.99247591	1.7	2.1	1.619	0.63
2008 Apr 19	54575.4435	211.20711049	−31.99247925	2.5	3.3	1.619	0.58
2008 May 16	54602.3622	211.20711579	−31.99247542	1.9	2.4	1.620	0.58

Table 4—Continued

Observation Date (UT)	(MJD)	R.A. (deg)	Dec. (deg)	$\sigma_{\mathrm{R.A.}} \cos\delta$ (mas)	$\sigma_{\mathrm{Dec.}}$ (mas)	Airmass	Seeing (arcsec)
2008 Jun 19	54636.2805	211.20711935	−31.99247560	3.0	3.6	1.620	0.63
2009 Jan 20	54851.6783	211.20721132	−31.99247962	5.1	10.8	1.621	1.13
2009 Apr 6	54927.4981	211.20722583	−31.99248221	1.8	4.0	1.637	0.86
2009 Jun 2	54984.3272	211.20723050	−31.99247792	2.8	3.2	1.620	0.69
2010 Apr 2	55288.4775	211.20733781	−31.99248293	5.0	9.4	1.625	0.54
2010 Apr 21	55307.4108	211.20733703	−31.99248156	2.7	3.8	1.649	0.65
2010 May 22	55338.3406	211.20733871	−31.99247986	3.0	5.6	1.625	0.67
2010 Jun 26	55373.2860	211.20734641	−31.99247636	6.0	12.2	1.654	0.74
2011 Jan 15	55576.6365	211.20743288	−31.99248450	3.4	3.6	1.804	0.63
2012 Mar 1	55987.5736	211.20755182	−31.99249311	3.1	6.0	1.619	0.77
2012 Mar 2	55988.5834	211.20755266	−31.99249209	3.2	3.1	1.624	0.67
2012 Apr 6	56023.4835	211.20755733	−31.99249163	1.6	6.0	1.621	0.78
2013 Mar 21	56372.5107	211.20766589	−31.99249753	2.6	5.9	1.624	0.76
2013 Apr 30	56412.4084	211.20767082	−31.99249252	3.2	6.0	1.620	0.56
2014 Mar 17	56733.5450	211.20777526	−31.99249900	6.2	8.9	1.626	0.95
2015 Jan 22	57044.6432	211.20787264	−31.99250217	3.7	3.4	1.681	0.47
2015 Jan 29	57051.6716	211.20787666	−31.99250492	2.5	4.7	1.624	0.73
2015 Feb 12	57065.6447	211.20787867	−31.99250555	2.1	4.4	1.638	1.04
2015 May 5	57147.4345	211.20788885	−31.99250223	2.8	7.1	1.671	0.68
2015 Jun 6	57179.3359	211.20789305	−31.99250336	3.5	4.5	1.643	0.53
SDSS J1534+1615AB ($N_{\mathrm{ep}} = 16, \Delta t = 8.49\,\mathrm{yr}$)							
2008 Feb 19	54515.6528	233.57107853	+16.26319385	2.8	2.1	1.006	0.63
2008 Apr 20	54576.5006	233.57107129	+16.26319499	2.3	2.4	1.002	0.69
2008 May 15	54601.4253	233.57106629	+16.26319508	2.1	4.4	1.003	0.56
2008 Jun 18	54635.3336	233.57106031	+16.26319450	2.5	3.1	1.003	0.60
2008 Jul 10	54657.2993	233.57105768	+16.26319333	5.5	2.3	1.009	0.55
2009 Mar 12	54902.6052	233.57105428	+16.26318288	1.7	1.9	1.002	0.61
2009 Apr 6	54927.5435	233.57105081	+16.26318376	1.5	1.5	1.002	0.79
2009 Jun 2	54984.3892	233.57103968	+16.26318442	2.0	2.1	1.002	0.46
2009 Aug 1	55044.2753	233.57103141	+16.26318081	2.4	2.4	1.060	0.94
2009 Aug 9	55052.2576	233.57103092	+16.26318099	2.8	2.9	1.069	1.20
2010 Apr 21	55307.4890	233.57102514	+16.26317503	1.9	2.4	1.004	0.62
2010 May 22	55338.4421	233.57101915	+16.26317365	2.0	2.6	1.016	0.55
2010 Jun 27	55374.3395	233.57101317	+16.26317319	2.5	2.5	1.012	0.51
2010 Aug 15	55423.2408	233.57100640	+16.26316884	2.7	1.4	1.066	0.46
2016 May 24	57532.4359	233.57088482	+16.26311212	1.8	2.0	1.016	0.54
2016 Aug 18	57618.2335	233.57087361	+16.26310676	1.8	2.4	1.072	0.52

2MASS J1534−2952AB ($N_{\mathrm{ep}} = 19, \Delta t = 8.26\,\mathrm{yr}$)

Table 4—Continued

Observation Date (UT)	(MJD)	R.A. (deg)	Dec. (deg)	$\sigma_{\rm R.A.}\cos\delta$ (mas)	$\sigma_{\rm Dec.}$ (mas)	Airmass	Seeing (arcsec)
2008 Feb 19	54515.6620	233.70806967	−29.87472545	1.8	3.5	1.548	0.58
2008 Feb 24	54520.6436	233.70807014	−29.87472850	2.8	6.0	1.551	0.60
2008 Apr 19	54575.5055	233.70806543	−29.87473855	3.1	5.7	1.547	0.60
2008 Apr 27	54583.4879	233.70806423	−29.87474252	5.0	4.9	1.548	0.76
2008 May 15	54601.4346	233.70805825	−29.87474356	3.4	4.0	1.547	0.60
2008 May 26	54612.3866	233.70805502	−29.87474148	5.8	6.2	1.557	0.60
2008 Jun 18	54635.3456	233.70805075	−29.87474679	4.6	9.8	1.548	0.70
2008 Jun 24	54641.3256	233.70804914	−29.87474715	3.6	6.4	1.547	0.61
2008 Jul 10	54657.2903	233.70804709	−29.87474679	4.3	4.6	1.551	0.75
2008 Jul 17	54664.2511	233.70804694	−29.87474793	3.9	9.2	1.550	0.59
2009 Apr 6	54927.5565	233.70809689	−29.87480987	1.3	4.2	1.557	0.80
2009 Jun 3	54985.3607	233.70808183	−29.87481871	3.8	5.0	1.564	0.60
2009 Aug 4	55047.2341	233.70807712	−29.87482126	5.7	6.8	1.565	0.88
2010 Mar 25	55280.5874	233.70812939	−29.87487714	1.7	4.6	1.554	0.81
2010 Apr 21	55307.4981	233.70812491	−29.87488120	2.0	2.9	1.547	0.60
2010 May 25	55341.3951	233.70811708	−29.87488902	4.5	6.7	1.552	0.84
2010 Jun 29	55376.3111	233.70810858	−29.87489187	2.7	2.6	1.547	0.44
2016 Apr 27	57505.5178	233.70830566	−29.87531397	6.7	7.0	1.598	0.46
2016 May 24	57532.4439	233.70829858	−29.87532008	3.3	4.1	1.598	0.52
		2MASS J1728+3948AB ($N_{\rm ep}=22, \Delta t=9.11\,{\rm yr}$)					
2007 Aug 2	54314.2851	262.04823420	+39.81649657	2.8	2.4	1.067	0.81
2008 Apr 20	54576.5891	262.04826236	+39.81649271	1.6	2.2	1.066	0.53
2008 May 15	54601.5019	262.04825826	+39.81649489	1.9	3.1	1.065	0.48
2008 Jun 18	54635.4153	262.04825446	+39.81649491	2.0	2.4	1.064	0.55
2008 Jul 10	54657.3542	262.04825014	+39.81649376	1.8	2.4	1.064	0.58
2008 Aug 10	54688.2645	262.04824445	+39.81648899	1.2	1.2	1.065	0.58
2009 Apr 7	54928.5898	262.04827722	+39.81648551	1.8	2.7	1.075	0.79
2009 Jun 2	54984.4598	262.04826943	+39.81648942	2.0	2.1	1.064	0.54
2009 Jul 30	55042.2988	262.04826082	+39.81648723	3.2	2.5	1.065	0.93
2009 Aug 9	55052.2945	262.04825833	+39.81648438	2.0	1.5	1.069	0.88
2009 Aug 26	55069.2643	262.04825542	+39.81648319	1.6	1.4	1.083	0.53
2010 Mar 25	55280.6480	262.04829011	+39.81647786	1.0	1.8	1.064	0.94
2010 Apr 21	55307.5419	262.04828878	+39.81648167	0.9	1.4	1.086	0.56
2010 May 22	55338.4954	262.04828466	+39.81648345	1.7	2.1	1.064	0.62
2010 Jun 27	55374.4265	262.04827659	+39.81648364	1.3	1.6	1.080	0.56
2011 Aug 11	55784.2845	262.04828439	+39.81647652	3.2	4.9	1.066	0.60
2011 Aug 14	55787.2570	262.04828345	+39.81647524	1.5	1.4	1.065	0.52
2011 Sep 17	55821.2210	262.04828376	+39.81646863	4.0	3.0	1.104	0.75
2011 Sep 26	55830.2057	262.04828449	+39.81646835	2.2	2.0	1.122	0.74

Table 4—Continued

Observation Date (UT)	(MJD)	R.A. (deg)	Dec. (deg)	$\sigma_{\mathrm{R.A.}} \cos\delta$ (mas)	$\sigma_{\mathrm{Dec.}}$ (mas)	Airmass	Seeing (arcsec)
2015 May 2	57144.5494	262.04835286	+39.81645643	2.8	2.1	1.064	0.55
2016 Aug 17	57617.2794	262.04835140	+39.81644861	2.7	2.1	1.074	0.58
2016 Sep 10	57641.2403	262.04834974	+39.81644336	2.3	1.8	1.108	0.55
			LSPM J1735+2634AB ($N_{\mathrm{ep}} = 21, \Delta t = 8.39\,\mathrm{yr}$)				
2008 Apr 20	54576.5976	263.80451966	+26.57929126	2.0	4.2	1.010	0.57
2008 May 15	54601.5103	263.80451878	+26.57928880	4.6	3.9	1.008	0.38
2008 Jun 18	54635.4388	263.80451228	+26.57928409	3.1	2.8	1.011	0.54
2008 Jul 10	54657.3627	263.80450674	+26.57927820	2.3	2.8	1.007	0.55
2008 Aug 10	54688.2761	263.80450228	+26.57926518	2.5	1.6	1.007	0.53
2009 Jul 29	55041.3018	263.80455016	+26.57917970	3.5	2.9	1.009	0.68
2009 Aug 9	55052.3071	263.80454846	+26.57917676	2.2	2.5	1.018	0.99
2009 Aug 26	55069.2764	263.80454625	+26.57916932	3.2	2.6	1.036	0.79
2010 Mar 24	55279.6567	263.80461245	+26.57911366	2.4	3.8	1.007	0.80
2010 May 22	55338.5226	263.80460872	+26.57911181	2.0	2.1	1.017	0.51
2010 Jun 27	55374.3966	263.80460073	+26.57910351	1.8	2.5	1.007	0.59
2011 Mar 23	55643.6416	263.80465530	+26.57902712	4.3	2.9	1.015	0.61
2011 May 15	55696.5405	263.80465485	+26.57902471	2.2	2.6	1.015	0.63
2011 Jul 18	55760.3676	263.80464409	+26.57900872	2.5	3.2	1.017	0.54
2015 May 1	57143.5964	263.80484196	+26.57868228	2.5	4.8	1.035	0.65
2015 Aug 21	57255.2744	263.80482604	+26.57865434	3.7	4.8	1.017	0.67
2016 Apr 23	57501.5913	263.80489153	+26.57859854	6.4	3.1	1.011	0.67
2016 May 22	57530.5285	263.80488484	+26.57859688	2.7	3.0	1.024	0.53
2016 Aug 17	57617.3141	263.80487087	+26.57856918	3.2	2.6	1.060	0.56
2016 Sep 10	57641.2567	263.80487234	+26.57855840	2.1	3.1	1.078	0.59
2016 Sep 11	57642.2614	263.80487310	+26.57855718	2.9	3.9	1.096	0.53
			2MASS J1750+4424AB ($N_{\mathrm{ep}} = 16, \Delta t = 2.18\,\mathrm{yr}$)				
2008 Apr 20	54576.6042	267.55384786	+44.40206069	2.6	3.3	1.101	0.55
2008 May 15	54601.5269	267.55384414	+44.40206597	2.4	2.4	1.100	0.48
2008 Jun 18	54635.4451	267.55383793	+44.40207047	2.5	5.7	1.102	0.50
2008 Jul 10	54657.3691	267.55383308	+44.40207311	2.0	3.4	1.100	0.57
2008 Aug 10	54688.2848	267.55382601	+44.40207377	2.4	2.3	1.100	0.58
2008 Sep 7	54716.2148	267.55382541	+44.40207652	4.6	8.4	1.100	0.59
2008 Sep 8	54717.2140	267.55382401	+44.40207239	2.6	3.6	1.100	0.58
2009 Apr 6	54927.6437	267.55384453	+44.40209646	1.9	5.4	1.101	0.82
2009 Jun 2	54984.4771	267.55383486	+44.40210746	2.3	2.7	1.100	0.44
2009 Jul 29	55041.3102	267.55382330	+44.40211281	3.1	3.8	1.102	0.71
2009 Aug 9	55052.3172	267.55381795	+44.40211504	3.3	3.7	1.110	0.93
2009 Aug 26	55069.2875	267.55381831	+44.40211241	3.0	2.8	1.128	0.64

Table 4—Continued

Observation Date (UT)	(MJD)	R.A. (deg)	Dec. (deg)	$\sigma_{\mathrm{R.A.}} \cos\delta$ (mas)	$\sigma_{\mathrm{Dec.}}$ (mas)	Airmass	Seeing (arcsec)
2010 Mar 26	55281.6385	267.55383748	+44.40213471	1.8	3.0	1.110	0.87
2010 Apr 21	55307.5742	267.55383525	+44.40213976	1.9	2.6	1.105	0.57
2010 May 22	55338.5119	267.55382910	+44.40214675	2.3	2.8	1.100	0.57
2010 Jun 27	55374.3808	267.55382362	+44.40214988	2.6	3.2	1.114	0.57
2MASS J1847+5522AB ($N_{\mathrm{ep}} = 16, \Delta t = 8.55\,\mathrm{yr}$)							
2008 Apr 21	54577.6145	281.76519366	+55.37875534	3.1	4.5	1.234	0.59
2008 May 15	54601.5517	281.76519152	+55.37875751	3.8	3.7	1.232	0.49
2008 Jun 18	54635.4626	281.76519502	+55.37875687	4.0	8.5	1.231	0.58
2008 Jul 11	54658.4055	281.76519389	+55.37875730	2.3	3.0	1.229	0.63
2008 Aug 10	54688.3202	281.76519039	+55.37875244	1.9	4.6	1.230	0.55
2008 Sep 6	54715.2754	281.76519229	+55.37874925	1.6	3.8	1.236	0.46
2009 Jun 2	54984.5202	281.76525752	+55.37873871	2.7	5.2	1.229	0.48
2009 Jul 29	55041.3493	281.76525409	+55.37873690	3.8	5.0	1.232	0.75
2009 Aug 8	55051.3467	281.76525677	+55.37873525	4.0	3.8	1.232	0.78
2009 Aug 26	55069.3142	281.76525139	+55.37873317	2.5	3.2	1.243	0.51
2010 Apr 21	55307.6245	281.76531529	+55.37872022	1.1	2.8	1.230	0.58
2010 May 22	55338.5316	281.76531828	+55.37872168	2.3	4.6	1.233	0.56
2010 Jun 26	55373.4712	281.76531425	+55.37872255	2.3	3.8	1.235	0.54
2016 Aug 17	57617.3294	281.76568542	+55.37861471	3.3	5.6	1.236	0.54
2016 Sep 9	57640.2604	281.76568528	+55.37861123	1.9	4.3	1.233	0.51
2016 Nov 9	57701.1807	281.76570012	+55.37860174	4.1	2.7	1.411	0.58
SDSS J2052−1609AB ($N_{\mathrm{ep}} = 24, \Delta t = 9.28\,\mathrm{yr}$)							
2007 Aug 2	54314.4465	313.14758622	−16.15794590	3.0	3.2	1.237	0.70
2007 Aug 4	54316.4394	313.14758653	−16.15794597	2.5	3.0	1.236	0.97
2007 Sep 20	54363.3060	313.14759510	−16.15794273	1.7	2.2	1.235	0.53
2007 Oct 22	54395.2026	313.14760151	−16.15793877	2.4	2.9	1.242	0.58
2007 Nov 23	54427.1818	313.14761317	−16.15793588	3.9	6.0	1.311	1.05
2007 Nov 25	54429.1793	313.14761089	−16.15793609	9.9	4.8	1.320	0.93
2007 Nov 26	54430.1811	313.14761301	−16.15793395	4.2	3.3	1.336	0.82
2008 Jun 18	54635.5576	313.14769390	−16.15790736	2.6	2.5	1.235	0.71
2008 Jul 10	54657.4942	313.14769754	−16.15790517	1.8	2.0	1.236	0.63
2008 Aug 9	54687.4163	313.14770227	−16.15790368	1.8	1.4	1.235	0.50
2008 Sep 6	54715.3248	313.14770774	−16.15790175	1.3	1.5	1.243	0.52
2008 Oct 13	54752.2585	313.14771580	−16.15789825	1.6	2.2	1.244	0.46
2008 Nov 8	54778.1850	313.14772482	−16.15789455	2.8	2.9	1.242	0.77
2008 Nov 9	54779.1849	313.14772378	−16.15789597	2.3	4.1	1.244	0.65
2009 Jun 3	54985.5936	313.14780584	−16.15786541	1.6	2.2	1.237	0.81
2009 Jul 29	55041.4436	313.14781657	−16.15786216	2.1	2.1	1.236	0.95

Table 4—Continued

Observation Date (UT)	(MJD)	R.A. (deg)	Dec. (deg)	$\sigma_{\mathrm{R.A.}} \cos\delta$ (mas)	$\sigma_{\mathrm{Dec.}}$ (mas)	Airmass	Seeing (arcsec)
2009 Aug 8	55051.4317	313.14781831	−16.15786048	1.5	1.9	1.238	0.54
2009 Aug 25	55068.3588	313.14782180	−16.15785952	2.3	2.1	1.242	0.74
2009 Oct 21	55125.2279	313.14783352	−16.15785427	1.8	2.2	1.237	0.80
2015 May 6	57148.6363	313.14849453	−16.15761070	2.3	7.3	1.288	0.61
2015 May 7	57149.6342	313.14849444	−16.15760828	1.9	5.1	1.286	0.71
2016 Aug 19	57619.3816	313.14863111	−16.15755745	1.5	1.8	1.237	0.55
2016 Sep 9	57640.3571	313.14863610	−16.15755652	2.2	3.6	1.250	0.49
2016 Nov 10	57702.2126	313.14865105	−16.15754985	3.3	2.5	1.302	0.54
2MASS J2132+1341AB ($N_{\mathrm{ep}} = 30, \Delta t = 9.28\,\mathrm{yr}$)							
2007 Aug 2	54314.4976	323.04801180	+13.69944204	2.8	2.9	1.024	0.51
2007 Aug 29	54341.4002	323.04800794	+13.69943942	3.8	4.4	1.007	0.38
2007 Sep 20	54363.3166	323.04800591	+13.69943337	4.0	3.6	1.010	0.45
2007 Oct 20	54393.2584	323.04800256	+13.69942937	3.2	2.0	1.007	0.49
2008 Jun 18	54635.5683	323.04802493	+13.69941046	2.4	3.0	1.012	0.69
2008 Jun 24	54641.5704	323.04802391	+13.69940985	2.0	3.0	1.006	0.50
2008 Jul 10	54657.5302	323.04802231	+13.69940959	2.0	2.7	1.006	0.53
2008 Jul 17	54664.5167	323.04802130	+13.69940902	2.2	1.8	1.007	0.57
2008 Aug 9	54687.4433	323.04801843	+13.69940646	1.9	1.5	1.006	0.50
2008 Aug 17	54695.4193	323.04801672	+13.69940444	2.1	2.4	1.006	0.53
2008 Sep 6	54715.3703	323.04801356	+13.69940101	2.3	2.6	1.006	0.47
2008 Sep 17	54726.3592	323.04801475	+13.69939932	3.1	2.4	1.013	0.47
2008 Oct 8	54747.2859	323.04801092	+13.69939588	1.5	1.5	1.006	0.71
2008 Oct 13	54752.2720	323.04800965	+13.69939424	2.2	2.0	1.006	0.46
2008 Nov 7	54777.1968	323.04800922	+13.69938957	2.8	2.7	1.006	0.47
2009 Jun 3	54985.6059	323.04803133	+13.69937846	2.4	2.6	1.016	0.75
2009 Jul 30	55042.4869	323.04802716	+13.69937359	2.5	2.8	1.009	0.86
2009 Aug 1	55044.4753	323.04802619	+13.69937269	1.9	2.0	1.007	0.88
2009 Aug 8	55051.4444	323.04802595	+13.69937269	1.5	1.8	1.006	0.67
2009 Aug 25	55068.3781	323.04802293	+13.69936999	2.2	2.2	1.017	0.75
2009 Oct 21	55125.2612	323.04801852	+13.69935981	1.5	1.9	1.010	0.73
2009 Nov 6	55141.1970	323.04801745	+13.69935747	1.9	2.0	1.006	0.67
2010 May 22	55338.5980	323.04803926	+13.69934453	1.4	2.3	1.087	0.59
2010 Jul 4	55381.5472	323.04803688	+13.69934237	1.8	1.9	1.006	0.62
2015 May 31	57173.6160	323.04806164	+13.69918282	3.1	3.2	1.015	0.48
2015 Aug 21	57255.4555	323.04805190	+13.69917464	2.4	2.8	1.037	0.81
2015 Oct 24	57319.2980	323.04804467	+13.69916215	3.1	2.9	1.071	0.51
2016 Aug 18	57618.3932	323.04805652	+13.69913915	3.5	3.9	1.020	0.42
2016 Sep 9	57640.3813	323.04805352	+13.69913616	2.5	4.4	1.013	0.46
2016 Nov 10	57702.2311	323.04804799	+13.69912297	4.3	3.1	1.035	0.44

Table 4—Continued

Observation Date (UT)	(MJD)	R.A. (deg)	Dec. (deg)	$\sigma_{\mathrm{R.A.}} \cos\delta$ (mas)	$\sigma_{\mathrm{Dec.}}$ (mas)	Airmass	Seeing (arcsec)
			2MASS J2140+1625AB ($N_{\mathrm{ep}} = 22, \Delta t = 8.40\,\mathrm{yr}$)				
2008 Jun 18	54635.5750	325.12210743	+16.42161618	4.0	5.1	1.008	0.71
2008 Jun 23	54640.5897	325.12210755	+16.42161832	3.5	5.5	1.004	0.46
2008 Jul 10	54657.5372	325.12210362	+16.42161728	3.5	4.4	1.002	0.55
2008 Jul 17	54664.5239	325.12210287	+16.42161540	3.1	3.5	1.004	0.59
2008 Aug 9	54687.4526	325.12210034	+16.42161421	1.4	2.0	1.002	0.49
2008 Sep 6	54715.3792	325.12209366	+16.42161054	2.4	3.1	1.002	0.53
2008 Oct 8	54747.2955	325.12208834	+16.42160635	2.2	2.9	1.003	0.58
2008 Nov 7	54777.2063	325.12208486	+16.42160215	3.8	3.6	1.002	0.49
2009 Jun 3	54985.6148	325.12208963	+16.42159389	2.1	3.1	1.009	0.77
2009 Jul 30	55042.4979	325.12208133	+16.42159293	3.6	2.8	1.008	0.74
2009 Aug 8	55051.4537	325.12207929	+16.42159247	2.5	2.9	1.002	0.55
2009 Aug 25	55068.3885	325.12207736	+16.42159020	3.5	3.1	1.009	0.67
2009 Oct 21	55125.2705	325.12206793	+16.42158259	1.7	2.1	1.008	0.68
2010 May 22	55338.6071	325.12207070	+16.42157341	2.1	3.4	1.072	0.59
2010 Jun 26	55373.5596	325.12206657	+16.42157355	2.3	2.5	1.005	0.77
2015 Jun 3	57176.6259	325.12196899	+16.42146838	3.7	4.7	1.004	0.57
2015 Aug 21	57255.4849	325.12195602	+16.42146209	2.8	2.6	1.081	0.85
2015 Oct 22	57317.2852	325.12194486	+16.42145476	4.2	4.0	1.023	0.67
2016 May 24	57532.6130	325.12194865	+16.42144636	3.0	2.9	1.045	0.63
2016 Aug 18	57618.3993	325.12193392	+16.42144156	3.6	3.7	1.015	0.44
2016 Sep 10	57641.3221	325.12193003	+16.42143981	3.2	4.8	1.034	0.48
2016 Nov 10	57702.2524	325.12192392	+16.42143000	5.8	5.7	1.059	0.42
			2MASS J2206−2047AB ($N_{\mathrm{ep}} = 27, \Delta t = 8.40\,\mathrm{yr}$)				
2008 Jun 18	54635.6078	331.59519991	−20.78468446	3.5	5.7	1.317	0.62
2008 Jun 23	54640.5980	331.59520105	−20.78468143	3.7	7.8	1.316	0.55
2008 Jul 11	54658.5582	331.59519793	−20.78468472	4.4	3.6	1.319	0.73
2008 Jul 17	54664.5306	331.59519835	−20.78468556	4.4	5.2	1.316	0.67
2008 Aug 9	54687.4611	331.59519384	−20.78468693	2.4	2.4	1.318	0.51
2008 Aug 17	54695.4532	331.59519236	−20.78468795	3.0	3.0	1.317	0.56
2008 Sep 6	54715.3879	331.59518962	−20.78468963	2.1	3.1	1.317	0.54
2008 Sep 17	54726.3686	331.59518895	−20.78468938	4.0	4.2	1.317	0.51
2008 Oct 8	54747.3037	331.59518665	−20.78469210	2.3	3.4	1.316	0.61
2008 Oct 13	54752.3000	331.59518489	−20.78469172	3.6	4.3	1.318	0.51
2008 Nov 7	54777.2149	331.59518217	−20.78469131	4.2	3.4	1.318	0.52
2009 Jul 29	55041.4812	331.59520174	−20.78469407	2.9	3.7	1.327	0.63
2009 Aug 1	55044.4873	331.59520143	−20.78469548	3.1	3.6	1.317	0.97
2009 Aug 9	55052.4981	331.59519932	−20.78469622	5.4	5.0	1.341	0.70

Table 4—Continued

Observation Date (UT)	(MJD)	R.A. (deg)	Dec. (deg)	$\sigma_{\mathrm{R.A.}} \cos\delta$ (mas)	$\sigma_{\mathrm{Dec.}}$ (mas)	Airmass	Seeing (arcsec)
2009 Aug 25	55068.4151	331.59519698	−20.78469690	4.2	3.6	1.320	0.66
2009 Oct 24	55128.2559	331.59518971	−20.78470009	2.2	2.2	1.317	0.57
2009 Nov 6	55141.2310	331.59519104	−20.78470310	6.8	4.9	1.317	0.74
2010 Jun 26	55373.6075	331.59520905	−20.78470214	3.4	3.8	1.325	0.56
2010 Jul 4	55381.5571	331.59520864	−20.78470131	2.4	5.5	1.320	0.65
2010 Aug 14	55422.4636	331.59520571	−20.78470557	4.2	3.9	1.317	0.63
2010 Sep 15	55454.3667	331.59519770	−20.78470666	2.8	4.2	1.316	0.54
2010 Oct 22	55491.2569	331.59519678	−20.78470781	4.1	3.8	1.320	0.73
2016 May 22	57530.6280	331.59524434	−20.78475207	3.2	3.3	1.420	0.63
2016 May 24	57532.6200	331.59524382	−20.78475094	4.1	4.4	1.430	0.67
2016 Aug 20	57620.4664	331.59523581	−20.78475808	3.6	4.7	1.338	0.59
2016 Sep 10	57641.3373	331.59523355	−20.78475693	2.8	7.0	1.378	0.63
2016 Nov 11	57703.1871	331.59522695	−20.78476002	5.0	4.7	1.335	0.53
DENIS J2252−1730AB ($N_{\mathrm{ep}} = 21, \Delta t = 9.29\,\mathrm{yr}$)							
2007 Aug 6	54318.5115	343.04574077	−17.50322778	3.6	4.9	1.257	0.40
2007 Aug 28	54340.4462	343.04574211	−17.50322770	2.4	2.9	1.257	0.66
2007 Sep 21	54364.4128	343.04574325	−17.50322727	3.3	3.8	1.278	1.26
2007 Sep 23	54366.3844	343.04574383	−17.50322511	3.5	3.3	1.257	0.52
2007 Oct 20	54393.3123	343.04574738	−17.50322509	5.1	5.7	1.258	0.61
2008 Jul 11	54658.5908	343.04585579	−17.50318624	2.1	3.1	1.260	0.67
2008 Jul 17	54664.5553	343.04585604	−17.50318713	3.7	5.8	1.259	0.67
2008 Aug 9	54687.4932	343.04585738	−17.50318582	2.5	2.0	1.258	0.57
2008 Aug 17	54695.4702	343.04585731	−17.50318599	3.6	2.9	1.259	0.53
2008 Sep 6	54715.4193	343.04585923	−17.50318808	2.0	3.0	1.257	0.49
2008 Sep 17	54726.3850	343.04585860	−17.50318656	3.8	2.3	1.259	0.52
2008 Oct 8	54747.3318	343.04586083	−17.50318619	2.1	3.2	1.257	0.58
2008 Nov 7	54777.2506	343.04586526	−17.50318569	3.4	3.4	1.257	0.55
2008 Nov 15	54785.2516	343.04586884	−17.50318397	4.9	4.0	1.266	0.72
2009 Jul 29	55041.5142	343.04597515	−17.50314849	4.4	5.7	1.265	0.82
2009 Aug 1	55044.5274	343.04597408	−17.50314746	4.0	3.7	1.257	0.97
2009 Aug 9	55052.5306	343.04597747	−17.50314634	3.9	3.7	1.281	0.52
2009 Oct 23	55127.3108	343.04597976	−17.50314745	4.2	4.0	1.262	0.70
2016 Sep 9	57640.4566	343.04680205	−17.50286927	3.0	3.9	1.303	0.52
2016 Nov 11	57703.2546	343.04681021	−17.50286503	5.0	6.3	1.259	0.49
2016 Nov 21	57713.2838	343.04681161	−17.50286463	4.3	7.6	1.393	0.46

Table 5. MCMC Posteriors for the Orbit and Parallax of LP 349-25AB

Property	Median $\pm 1\sigma$	Best fit	95.4% c.i.	Prior/Notes
		Fitted parameters		
Orbital period P (yr)	7.698 ± 0.014	7.701	7.671, 7.727	$1/P$ (log-flat)
Semimajor axis a (mas)	$145.99^{+0.17}_{-0.18}$	145.98	145.65, 146.33	$1/a$ (log-flat)
Eccentricity e	$0.0468^{+0.0019}_{-0.0018}$	0.0470	0.0431, 0.0505	uniform, $0 \leq e < 1$
Inclination i (°)	$117.36^{+0.11}_{-0.10}$	117.36	117.16, 117.57	$\sin(i)$, $0° < i < 180°$
PA of the ascending node Ω (°)	36.64 ± 0.10	36.62	36.43, 36.84	uniform
Argument of periastron ω (°)	262.2 ± 1.8	262.2	258.6, 266.0	uniform
Mean longitude at 2455197.5 JD $\lambda_{\rm ref}$ (°)	$294.44^{+0.23}_{-0.22}$	294.40	293.98, 294.89	uniform
RA $-$ RA$_{2010}$ (mas)	$-0.1^{+1.2}_{-1.3}$	0.0	-2.6, 2.4	uniform, RA$_{2010}$ = 6.9846505
Dec $-$ Dec$_{2010}$ (mas)	0.0 ± 0.9	0.0	-1.8, 1.8	uniform, Dec$_{2010}$ = +22.3253882
Relative proper motion in RA $\mu_{\rm RA,rel}$ (mas yr^{-1})	406.4 ± 0.4	406.4	405.7, 407.1	uniform
Relative proper motion in Dec $\mu_{\rm Dec,rel}$ (mas yr^{-1})	-167.1 ± 0.5	-166.8	-168.0, -166.2	uniform
Relative parallax $\pi_{\rm rel}$ (mas)	68.0 ± 0.9	68.1	66.3, 69.8	$1/\pi^2$ (uniform volume density)
Ratio of photocenter orbit to semimajor axis α/a	$0.056^{+0.007}_{-0.008}$	0.057	0.041, 0.071	uniform
		Derived properties		
Total mass at fixed distance $a^3P^{-2}(d/14.45{\rm pc})^3$ ($M_{\rm Jup}$)	165.8 ± 0.7	165.7	164.5, 167.1	···
Time of periastron T_0 (JD)	2457758^{+15}_{-14}	2457758	2457729, 2457787	···
Photocenter semimajor axis α (mas)	$8.2^{+1.1}_{-1.2}$	8.3	6.0, 10.4	···
Correction to absolute RA proper motion $\Delta\mu_{\rm RA}$ (mas yr^{-1})	1.5 ± 1.6	1.5	-1.8, 4.7	···
Correction to absolute Dec proper motion $\Delta\mu_{\rm Dec}$ (mas yr^{-1})	-3.4 ± 1.2	-3.4	-5.8, -1.0	···
Correction to absolute parallax $\Delta\pi$ (mas)	$1.21^{+0.14}_{-0.17}$	1.21	0.92, 1.55	···
Absolute proper motion in RA $\mu_{\rm RA,abs}$ (mas yr^{-1})	407.9 ± 1.7	407.9	404.5, 411.2	···
Absolute proper motion in Dec $\mu_{\rm Dec,abs}$ (mas yr^{-1})	-170.4 ± 1.3	-170.2	-173.0, -167.8	···
Absolute parallax $\pi_{\rm abs}$ (mas)	69.2 ± 0.9	69.3	67.5, 71.0	···
Distance d (pc)	$14.45^{+0.18}_{-0.19}$	14.42	14.08, 14.82	···
Semimajor axis a (AU)	2.109 ± 0.027	2.105	2.054, 2.163	···
Total mass $M_{\rm tot}$ ($M_{\rm Jup}$)	166^{+6}_{-7}	165	154, 179	···

Table 6. MCMC Posteriors for the Orbit and Parallax of LP 415-20AB

Property	Median $\pm 1\sigma$	Best fit	95.4% c.i.	Prior/Notes
		Fitted parameters		
Orbital period P (yr)	14.82 ± 0.24	14.81	14.34, 15.29	$1/P$ (log-flat)
Semimajor axis a (mas)	$96.5^{+1.1}_{-1.4}$	96.7	94.2, 99.4	$1/a$ (log-flat)
Eccentricity e	$0.706^{+0.011}_{-0.012}$	0.707	0.684, 0.731	uniform, $0 \leq e < 1$
Inclination i (°)	62.4 ± 1.6	62.4	59.2, 65.7	$\sin(i)$, $0° < i < 180°$
PA of the ascending node Ω (°)	$82.1^{+1.1}_{-0.9}$	82.3	79.9, 84.0	uniform
Argument of periastron ω (°)	168 ± 4	168	160, 176	uniform
Mean longitude at 2455197.5 JD $\lambda_{\rm ref}$ (°)	$283.6^{+1.5}_{-1.6}$	283.3	280.6, 286.8	uniform
RA − RA_{2010} (mas)	-0.1 ± 0.8	0.0	−1.7, 1.6	uniform, $\mathrm{RA}_{2010} = 65.4571148$
Dec − Dec_{2010} (mas)	0.0 ± 0.8	0.0	−1.6, 1.5	uniform, $\mathrm{Dec}_{2010} = +19.4857641$
Relative proper motion in RA $\mu_{\rm RA,rel}$ (mas yr^{-1})	124.32 ± 0.30	124.49	123.70, 124.91	uniform
Relative proper motion in Dec $\mu_{\rm Dec,rel}$ (mas yr^{-1})	$-35.7^{+0.4}_{-0.3}$	−35.8	−36.4, −35.0	uniform
Relative parallax $\pi_{\rm rel}$ (mas)	$24.8^{+0.7}_{-0.8}$	24.4	23.3, 26.3	$1/\pi^2$ (uniform volume density)
Ratio of photocenter orbit to semimajor axis α/a	0.00 ± 0.03	0.02	−0.07, 0.07	uniform
		Derived properties		
Total mass at fixed distance $a^3P^{-2}(d/38.6\mathrm{pc})^3$ ($M_{\rm Jup}$)	247^{+16}_{-18}	249	217, 285	···
Time of periastron T_0 (JD)	2458880^{+130}_{-140}	2458870	2458620, 2459140	···
Photocenter semimajor axis α (mas)	0 ± 3	2	−7, 7	···
Correction to absolute RA proper motion $\Delta\mu_{\rm RA}$ (mas yr^{-1})	1.7 ± 0.7	1.7	0.5, 3.1	···
Correction to absolute Dec proper motion $\Delta\mu_{\rm Dec}$ (mas yr^{-1})	-2.5 ± 0.7	−2.5	−4.0, −1.1	···
Correction to absolute parallax $\Delta\pi$ (mas)	$1.11^{+0.11}_{-0.12}$	1.11	0.89, 1.36	···
Absolute proper motion in RA $\mu_{\rm RA,abs}$ (mas yr^{-1})	126.1 ± 0.7	126.2	124.6, 127.6	···
Absolute proper motion in Dec $\mu_{\rm Dec,abs}$ (mas yr^{-1})	-38.2 ± 0.8	−38.3	−39.9, −36.6	···
Absolute parallax $\pi_{\rm abs}$ (mas)	$25.9^{+0.7}_{-0.8}$	25.5	24.4, 27.4	···
Distance d (pc)	38.6 ± 1.1	39.1	36.4, 40.9	···
Semimajor axis a (AU)	3.73 ± 0.12	3.78	3.50, 3.98	···
Total mass $M_{\rm tot}$ ($M_{\rm Jup}$)	248^{+26}_{-29}	259	198, 309	···

Table 7. MCMC Posteriors for the Orbit and Parallax of SDSS J0423−0414AB

Property	Median ±1σ	Best fit	95.4% c.i.	Prior/Notes
		Fitted parameters		
Orbital period P (yr)	12.30 ± 0.06	12.30	12.18, 12.41	$1/P$ (log-flat)
Semimajor axis a (mas)	162.9 ± 0.5	162.6	161.9, 163.9	$1/a$ (log-flat)
Eccentricity e	$0.272^{+0.008}_{-0.007}$	0.270	0.258, 0.287	uniform, $0 \leq e < 1$
Inclination i (°)	65.4 ± 0.3	65.2	64.7, 66.0	$\sin(i)$, $0° < i < 180°$
PA of the ascending node Ω (°)	$34.35^{+0.22}_{-0.23}$	34.33	33.89, 34.78	uniform
Argument of periastron ω (°)	97.4 ± 0.3	97.5	96.7, 98.1	uniform
Mean longitude at 2455197.5 JD $\lambda_{\rm ref}$ (°)	154.7 ± 0.3	154.8	154.0, 155.3	uniform
RA − RA$_{2010}$ (mas)	$0.2^{+1.0}_{-0.9}$	0.0	−1.7, 2.1	uniform, RA$_{2010}$ = 65.9515754
Dec − Dec$_{2010}$ (mas)	$0.2^{+0.7}_{-0.8}$	0.0	−1.2, 1.6	uniform, Dec$_{2010}$ = −4.2338632
Relative proper motion in RA $\mu_{\rm RA,rel}$ (mas yr^{-1})	-324.28 ± 0.18	−324.29	−324.65, −323.91	uniform
Relative proper motion in Dec $\mu_{\rm Dec,rel}$ (mas yr^{-1})	89.85 ± 0.25	89.90	89.34, 90.35	uniform
Relative parallax $\pi_{\rm rel}$ (mas)	69.8 ± 0.8	70.0	68.2, 71.5	$1/\pi^2$ (uniform volume density)
Ratio of photocenter orbit to semimajor axis α/a	$-0.023^{+0.007}_{-0.006}$	−0.023	−0.036, −0.010	uniform
		Derived properties		
Total mass at fixed distance $a^3P^{-2}(d/14.07\rm pc)^3$ ($M_{\rm Jup}$)	83.3 ± 0.9	82.8	81.6, 85.2	···
Time of periastron T_0 (JD)	2458975 ± 20	2458977	2458936, 2459015	···
Photocenter semimajor axis α (mas)	$-3.8^{+1.1}_{-1.0}$	−3.7	−5.9, −1.7	···
Correction to absolute RA proper motion $\Delta\mu_{\rm RA}$ (mas yr^{-1})	2.6 ± 1.0	2.6	0.7, 4.7	···
Correction to absolute Dec proper motion $\Delta\mu_{\rm Dec}$ (mas yr^{-1})	-1.8 ± 1.2	−1.8	−4.0, 0.6	···
Correction to absolute parallax $\Delta\pi$ (mas)	$1.25^{+0.15}_{-0.17}$	1.25	0.95, 1.59	···
Absolute proper motion in RA $\mu_{\rm RA,abs}$ (mas yr^{-1})	-321.6 ± 1.0	−321.7	−323.6, −319.5	···
Absolute proper motion in Dec $\mu_{\rm Dec,abs}$ (mas yr^{-1})	88.1 ± 1.2	88.1	85.7, 90.4	···
Absolute parallax $\pi_{\rm abs}$ (mas)	71.1 ± 0.8	71.2	69.4, 72.7	···
Distance d (pc)	$14.07^{+0.16}_{-0.17}$	14.04	13.74, 14.39	···
Semimajor axis a (AU)	$2.291^{+0.027}_{-0.028}$	2.282	2.237, 2.347	···
Total mass $M_{\rm tot}$ ($M_{\rm Jup}$)	83 ± 3	82	77, 90	···

Table 8. MCMC Posteriors for the Orbit and Parallax of 2MASS J0700+3157AB

Property	Median ±1σ	Best fit	95.4% c.i.	Prior/Notes
Fitted parameters				
Orbital period P (yr)	23.9 ± 0.5	23.9	22.7, 25.1	$1/P$ (log-flat)
Semimajor axis a (mas)	377^{+5}_{-6}	377	364, 389	$1/a$ (log-flat)
Eccentricity e	$0.017^{+0.005}_{-0.007}$	0.013	0.007, 0.040	uniform, $0 \leq e < 1$
Inclination i (°)	$88.143^{+0.025}_{-0.024}$	88.140	88.094, 88.193	$\sin(i)$, $0° < i < 180°$
PA of the ascending node Ω (°)	$102.666^{+0.022}_{-0.021}$	102.666	102.623, 102.708	uniform
Argument of periastron ω (°)	70^{+60}_{-40}	80	0, 140	uniform
Mean longitude at 2455197.5 JD $\lambda_{\rm ref}$ (°)	136.6 ± 0.7	136.7	135.0, 138.2	uniform
RA − RA_{2010} (mas)	$0.2^{+0.9}_{-0.8}$	0.0	−1.5, 1.8	uniform, RA_{2010} = 105.1534668
Dec − Dec_{2010} (mas)	0.3 ± 0.8	0.0	−1.3, 1.8	uniform, Dec_{2010} = +31.9558506
Relative proper motion in RA $\mu_{\rm RA,rel}$ (mas yr^{-1})	123.1 ± 0.4	123.2	122.3, 123.9	uniform
Relative proper motion in Dec $\mu_{\rm Dec,rel}$ (mas yr^{-1})	-550.4 ± 0.4	−550.3	−551.2, −549.7	uniform
Relative parallax $\pi_{\rm rel}$ (mas)	87.5 ± 0.9	87.9	85.7, 89.3	$1/\pi^2$ (uniform volume density)
Ratio of photocenter orbit to semimajor axis α/a	0.310 ± 0.011	0.308	0.288, 0.332	uniform
Derived properties				
Total mass at fixed distance $a^3P^{-2}(d/11.29{\rm pc})^3$ ($M_{\rm Jup}$)	141.4 ± 0.6	141.3	140.2, 142.5	···
Time of periastron T_0 (JD)	2462500^{+1100}_{-1700}	2462600	2460400, 2464600	···
Photocenter semimajor axis α (mas)	117 ± 5	116	108, 126	···
Correction to absolute RA proper motion $\Delta\mu_{\rm RA}$ (mas yr^{-1})	-0.4 ± 0.5	−0.4	−1.4, 0.6	···
Correction to absolute Dec proper motion $\Delta\mu_{\rm Dec}$ (mas yr^{-1})	-3.1 ± 0.7	−3.1	−4.6, −1.8	···
Correction to absolute parallax $\Delta\pi$ (mas)	$1.07^{+0.10}_{-0.12}$	1.07	0.87, 1.31	···
Absolute proper motion in RA $\mu_{\rm RA,abs}$ (mas yr^{-1})	122.7 ± 0.7	122.8	121.4, 124.1	···
Absolute proper motion in Dec $\mu_{\rm Dec,abs}$ (mas yr^{-1})	-553.6 ± 0.8	−553.4	−555.2, −552.0	···
Absolute parallax $\pi_{\rm abs}$ (mas)	88.6 ± 0.9	89.0	86.7, 90.4	···
Distance d (pc)	11.29 ± 0.12	11.24	11.06, 11.53	···
Semimajor axis a (AU)	4.25 ± 0.08	4.24	4.09, 4.42	···
Total mass $M_{\rm tot}$ ($M_{\rm Jup}$)	141^{+4}_{-5}	139	133, 150	···

Table 9. MCMC Posteriors for the Orbit and Parallax of LHS 1901AB

Property	Median $\pm 1\sigma$	Best fit	95.4% c.i.	Prior/Notes
		Fitted parameters		
Orbital period P (yr)	16.21 ± 0.08	16.19	16.05, 16.37	$1/P$ (log-flat)
Semimajor axis a (mas)	$287.7^{+0.7}_{-0.8}$	287.4	286.2, 289.2	$1/a$ (log-flat)
Eccentricity e	0.8304 ± 0.0009	0.8302	0.8287, 0.8322	uniform, $0 \leq e < 1$
Inclination i (°)	71.97 ± 0.05	71.98	71.86, 72.07	$\sin(i)$, $0° < i < 180°$
PA of the ascending node Ω (°)	2.27 ± 0.05	2.28	2.17, 2.37	uniform
Argument of periastron ω (°)	$44.49^{+0.14}_{-0.15}$	44.44	44.19, 44.78	uniform
Mean longitude at 2455197.5 JD $\lambda_{\rm ref}$ (°)	70.88 ± 0.08	70.87	70.72, 71.04	uniform
RA − $\rm RA_{2010}$ (mas)	$0.2^{+1.6}_{-1.5}$	0.0	−3.1, 3.3	uniform, $\rm RA_{2010} = 107.7991482$
Dec − $\rm Dec_{2010}$ (mas)	-0.3 ± 1.3	0.0	−2.9, 2.3	uniform, $\rm Dec_{2010} = +43.4981455$
Relative proper motion in RA $\mu_{\rm RA,rel}$ (mas yr^{-1})	$356.5^{+1.1}_{-1.2}$	356.3	354.3, 358.8	uniform
Relative proper motion in Dec $\mu_{\rm Dec,rel}$ (mas yr^{-1})	-562 ± 3	−563	−568, −556	uniform
Relative parallax $\pi_{\rm rel}$ (mas)	75.2 ± 1.1	75.2	73.0, 77.5	$1/\pi^2$ (uniform volume density)
Ratio of photocenter orbit to semimajor axis α/a	$-0.009^{+0.030}_{-0.027}$	0.002	−0.065, 0.047	uniform
		Derived properties		
Total mass at fixed distance $a^3 P^{-2} (d/13.08{\rm pc})^3$ ($M_{\rm Jup}$)	212.6 ± 0.7	212.6	211.2, 214.0	···
Time of periastron T_0 (JD)	2460684^{+30}_{-29}	2460676	2460626, 2460742	···
Photocenter semimajor axis α (mas)	-3 ± 8	1	−19, 14	···
Correction to absolute RA proper motion $\Delta\mu_{\rm RA}$ (mas yr^{-1})	-0.3 ± 0.5	−0.3	−1.4, 0.7	···
Correction to absolute Dec proper motion $\Delta\mu_{\rm Dec}$ (mas yr^{-1})	-3.8 ± 0.7	−3.8	−5.3, −2.3	···
Correction to absolute parallax $\Delta\pi$ (mas)	1.21 ± 0.11	1.21	1.01, 1.45	···
Absolute proper motion in RA $\mu_{\rm RA,abs}$ (mas yr^{-1})	356.2 ± 1.2	356.0	353.7, 358.6	···
Absolute proper motion in Dec $\mu_{\rm Dec,abs}$ (mas yr^{-1})	-566 ± 3	−567	−572, −559	···
Absolute parallax $\pi_{\rm abs}$ (mas)	76.4 ± 1.1	76.5	74.2, 78.7	···
Distance d (pc)	$13.08^{+0.20}_{-0.19}$	13.08	12.70, 13.48	···
Semimajor axis a (AU)	3.76 ± 0.06	3.76	3.65, 3.88	···
Total mass $M_{\rm tot}$ ($M_{\rm Jup}$)	213^{+9}_{-10}	212	194, 232	···

Table 10. MCMC Posteriors for the Orbit and Parallax of 2MASS J0746+2000AB

Property	Median $\pm 1\sigma$	Best fit	95.4% c.i.	Prior/Notes
		Fitted parameters		
Orbital period P (yr)	$12.736^{+0.031}_{-0.029}$	12.749	12.674, 12.796	$1/P$ (log-flat)
Semimajor axis a (mas)	237.18 ± 0.11	237.16	236.96, 237.40	$1/a$ (log-flat)
Eccentricity e	0.4854 ± 0.0003	0.4856	0.4848, 0.4861	uniform, $0 \leq e < 1$
Inclination i ($^\circ$)	$138.56^{+0.20}_{-0.21}$	138.68	138.15, 138.96	$\sin(i)$, $0^\circ < i < 180^\circ$
PA of the ascending node Ω ($^\circ$)	$29.77^{+0.30}_{-0.28}$	29.79	29.19, 30.35	uniform
Argument of periastron ω ($^\circ$)	355.6 ± 0.6	355.8	354.5, 356.8	uniform
Mean longitude at 2455197.5 JD $\lambda_{\rm ref}$ ($^\circ$)	198.70 ± 0.22	198.58	198.25, 199.14	uniform
RA − $\rm RA_{2010}$ (mas)	0.1 ± 0.8	0.0	−1.4, 1.6	uniform, $\rm RA_{2010} = 116.6762086$
Dec − $\rm Dec_{2010}$ (mas)	0.1 ± 0.8	0.0	−1.4, 1.7	uniform, $\rm Dec_{2010} = +20.0089253$
Relative proper motion in RA $\mu_{\rm RA,rel}$ (mas yr^{-1})	-363.78 ± 0.29	−363.82	−364.36, −363.20	uniform
Relative proper motion in Dec $\mu_{\rm Dec,rel}$ (mas yr^{-1})	-51.1 ± 0.4	−51.1	−51.9, −50.4	uniform
Relative parallax $\pi_{\rm rel}$ (mas)	79.9 ± 0.8	80.0	78.4, 81.5	$1/\pi^2$ (uniform volume density)
Ratio of photocenter orbit to semimajor axis α/a	0.069 ± 0.007	0.070	0.055, 0.083	uniform
		Derived properties		
Total mass at fixed distance $a^3 P^{-2} (d/12.35\rm pc)^3$ ($M_{\rm Jup}$)	162.5 ± 0.9	162.1	160.6, 164.4	···
Time of periastron T_0 (JD)	2461877^{+24}_{-22}	2461887	2461830, 2461923	···
Photocenter semimajor axis α (mas)	$16.4^{+1.5}_{-1.7}$	16.5	13.2, 19.6	···
Correction to absolute RA proper motion $\Delta\mu_{\rm RA}$ (mas yr^{-1})	-1.4 ± 0.8	−1.4	−3.0, 0.0	···
Correction to absolute Dec proper motion $\Delta\mu_{\rm Dec}$ (mas yr^{-1})	-1.9 ± 0.9	−1.9	−3.7, −0.4	···
Correction to absolute parallax $\Delta\pi$ (mas)	$1.02^{+0.10}_{-0.12}$	1.02	0.82, 1.29	···
Absolute proper motion in RA $\mu_{\rm RA,abs}$ (mas yr^{-1})	-365.1 ± 0.8	−365.2	−366.8, −363.6	···
Absolute proper motion in Dec $\mu_{\rm Dec,abs}$ (mas yr^{-1})	-53.1 ± 0.9	−53.0	−54.9, −51.2	···
Absolute parallax $\pi_{\rm abs}$ (mas)	80.9 ± 0.8	81.0	79.4, 82.6	···
Distance d (pc)	$12.35^{+0.12}_{-0.13}$	12.34	12.11, 12.60	···
Semimajor axis a (AU)	$2.930^{+0.030}_{-0.028}$	2.927	2.871, 2.987	···
Total mass $M_{\rm tot}$ ($M_{\rm Jup}$)	163 ± 5	162	153, 173	···

Table 11. MCMC Posteriors for the Orbit and Parallax of 2MASS J0850+1057AB

Property	Median $\pm 1\sigma$	Best fit	95.4% c.i.	Prior/Notes
Fitted parameters				
Orbital period P (yr)	48^{+7}_{-6}	45	34, 94	$1/P$ (log-flat)
Semimajor axis a (mas)	156^{+8}_{-9}	152	140, 212	$1/a$ (log-flat)
Eccentricity e	$0.06^{+0.05}_{-0.06}$	0.02	0.00, 0.38	uniform, $0 \leq e < 1$
Inclination i (°)	$64.9^{+1.5}_{-1.4}$	65.7	60.7, 67.9	$\sin(i)$, $0° < i < 180°$
PA of the ascending node Ω (°)	$113.3^{+1.6}_{-1.7}$	112.9	110.0, 119.0	uniform
Argument of periastron ω (°)	70^{+150}_{-40}	270	−60, 270	uniform
Mean longitude at 2455197.5 JD $\lambda_{\rm ref}$ (°)	80 ± 5	80	63, 90	uniform
RA − $\rm RA_{2010}$ (mas)	$0.0^{+0.7}_{-0.6}$	0.3	−1.3, 1.3	uniform, $\rm RA_{2010}$ = 132.6493640
Dec − $\rm Dec_{2010}$ (mas)	0.1 ± 0.6	0.1	−1.1, 1.3	uniform, $\rm Dec_{2010}$ = +10.9543778
Relative proper motion in RA $\mu_{\rm RA,rel}$ ($\rm mas\,yr^{-1}$)	-144.9 ± 2.2	−145.1	−149.3, −140.4	uniform
Relative proper motion in Dec $\mu_{\rm Dec,rel}$ ($\rm mas\,yr^{-1}$)	-14.0 ± 1.1	−13.9	−16.2, −11.8	uniform
Relative parallax $\pi_{\rm rel}$ (mas)	30.6 ± 0.6	30.7	29.3, 31.8	$1/\pi^2$ (uniform volume density)
Ratio of photocenter orbit to semimajor axis α/a	0.04 ± 0.12	0.05	−0.21, 0.29	uniform
Derived properties				
Total mass at fixed distance $a^3P^{-2}(d/31.8\rm pc)^3$ ($M_{\rm Jup}$)	54^{+6}_{-8}	59	32, 67	···
Time of periastron T_0 (JD)	2476000^{+4000}_{-5000}	2480000	2469000, 2489000	···
Photocenter semimajor axis α (mas)	6 ± 20	8	−34, 50	···
Correction to absolute RA proper motion $\Delta\mu_{\rm RA}$ ($\rm mas\,yr^{-1}$)	-2.2 ± 0.8	−2.8	−3.8, −0.7	···
Correction to absolute Dec proper motion $\Delta\mu_{\rm Dec}$ ($\rm mas\,yr^{-1}$)	-1.3 ± 0.8	−1.2	−2.9, 0.2	···
Correction to absolute parallax $\Delta\pi$ (mas)	$0.82^{+0.07}_{-0.08}$	0.84	0.68, 0.99	···
Absolute proper motion in RA $\mu_{\rm RA,abs}$ ($\rm mas\,yr^{-1}$)	-147.1 ± 2.3	−147.9	−151.9, −142.5	···
Absolute proper motion in Dec $\mu_{\rm Dec,abs}$ ($\rm mas\,yr^{-1}$)	-15.4 ± 1.3	−15.2	−18.1, −12.8	···
Absolute parallax $\pi_{\rm abs}$ (mas)	$31.4^{+0.7}_{-0.6}$	31.5	30.1, 32.7	···
Distance d (pc)	31.8 ± 0.6	31.7	30.6, 33.2	···
Semimajor axis a (AU)	$4.98^{+0.25}_{-0.33}$	4.83	4.42, 6.78	···
Total mass $M_{\rm tot}$ ($M_{\rm Jup}$)	54 ± 8	58	32, 69	···

Table 12. MCMC Posteriors for the Orbit and Parallax of 2MASS J0920+3517AB

Property	Median $\pm 1\sigma$	Best fit	95.4% c.i.	Prior/Notes
		Fitted parameters		
Orbital period P (yr)	7.258 ± 0.009	7.257	7.239, 7.277	$1/P$ (log-flat)
Semimajor axis a (mas)	68.15 ± 0.23	68.12	67.68, 68.62	$1/a$ (log-flat)
Eccentricity e	$0.180^{+0.006}_{-0.007}$	0.181	0.167, 0.193	uniform, $0 \leq e < 1$
Inclination i (°)	87.15 ± 0.17	87.18	86.81, 87.49	$\sin(i)$, $0° < i < 180°$
PA of the ascending node Ω (°)	66.73 ± 0.12	66.76	66.49, 66.97	uniform
Argument of periastron ω (°)	$317.5^{+1.4}_{-1.5}$	317.4	314.7, 320.6	uniform
Mean longitude at 2455197.5 JD $\lambda_{\rm ref}$ (°)	$305.14^{+0.18}_{-0.19}$	305.11	304.76, 305.51	uniform
RA − $\rm RA_{2010}$ (mas)	0.4 ± 1.0	0.0	−1.7, 2.4	uniform, $\rm RA_{2010} = 140.0504412$
Dec − $\rm Dec_{2010}$ (mas)	0.1 ± 0.5	0.0	−0.9, 1.2	uniform, $\rm Dec_{2010} = +35.2947397$
Relative proper motion in RA $\mu_{\rm RA,rel}$ (mas yr^{-1})	-183.88 ± 0.15	−183.91	−184.19, −183.58	uniform
Relative proper motion in Dec $\mu_{\rm Dec,rel}$ (mas yr^{-1})	-198.16 ± 0.16	−198.19	−198.49, −197.83	uniform
Relative parallax $\pi_{\rm rel}$ (mas)	31.0 ± 0.6	30.9	29.7, 32.2	$1/\pi^2$ (uniform volume density)
Ratio of photocenter orbit to semimajor axis α/a	$0.183^{+0.010}_{-0.011}$	0.184	0.162, 0.204	uniform
		Derived properties		
Total mass at fixed distance $a^3P^{-2}(d/30.9\rm pc)^3$ ($M_{\rm Jup}$)	186.7 ± 2.1	186.4	182.4, 190.9	···
Time of periastron T_0 (JD)	2457940^{+11}_{-10}	2457938	2457919, 2457962	···
Photocenter semimajor axis α (mas)	12.4 ± 0.7	12.6	11.0, 13.9	···
Correction to absolute RA proper motion $\Delta\mu_{\rm RA}$ (mas yr^{-1})	-2.5 ± 1.0	−2.5	−4.6, −0.4	···
Correction to absolute Dec proper motion $\Delta\mu_{\rm Dec}$ (mas yr^{-1})	-4.2 ± 1.0	−4.2	−6.4, −2.2	···
Correction to absolute parallax $\Delta\pi$ (mas)	$1.33^{+0.12}_{-0.13}$	1.33	1.09, 1.60	···
Absolute proper motion in RA $\mu_{\rm RA,abs}$ (mas yr^{-1})	-186.3 ± 1.1	−186.4	−188.5, −184.3	···
Absolute proper motion in Dec $\mu_{\rm Dec,abs}$ (mas yr^{-1})	-202.4 ± 1.1	−202.4	−204.6, −200.3	···
Absolute parallax $\pi_{\rm abs}$ (mas)	32.3 ± 0.6	32.3	31.1, 33.6	···
Distance d (pc)	30.9 ± 0.6	31.0	29.7, 32.1	···
Semimajor axis a (AU)	2.11 ± 0.04	2.11	2.03, 2.19	···
Total mass $M_{\rm tot}$ ($M_{\rm Jup}$)	187 ± 11	187	165, 209	···

Table 13. MCMC Posteriors for the Orbit and Parallax of SDSS J0926+5847AB

Property	Median $\pm 1\sigma$	Best fit	95.4% c.i.	Prior/Notes
Fitted parameters				
Orbital period P (yr)	$12.9^{+1.3}_{-1.9}$	11.1	10.4, 18.2	$1/P$ (log-flat)
Semimajor axis a (mas)	78^{+6}_{-8}	80	68, 105	$1/a$ (log-flat)
Eccentricity e	$0.35^{+0.22}_{-0.16}$	0.48	0.00, 0.58	uniform, $0 \leq e < 1$
Inclination i ($^\circ$)	$91.7^{+0.6}_{-0.8}$	91.3	90.5, 93.2	$\sin(i)$, $0^\circ < i < 180^\circ$
PA of the ascending node Ω ($^\circ$)	$133.6^{+0.6}_{-0.5}$	133.4	132.4, 134.6	uniform
Argument of periastron ω ($^\circ$)	275^{+11}_{-17}	277	210, 410	uniform
Mean longitude at 2455197.5 JD $\lambda_{\rm ref}$ ($^\circ$)	165^{+8}_{-9}	166	148, 182	uniform
RA $-$ RA$_{2010}$ (mas)	$-0.5^{+2.5}_{-2.7}$	-1.8	-5.8, 4.6	uniform, RA$_{2010}$ = 141.5643537
Dec $-$ Dec$_{2010}$ (mas)	0.0 ± 0.8	-0.1	-1.5, 1.6	uniform, Dec$_{2010}$ = +58.7887839
Relative proper motion in RA $\mu_{\rm RA,rel}$ (mas yr^{-1})	11.8 ± 1.0	12.1	9.9, 13.8	uniform
Relative proper motion in Dec $\mu_{\rm Dec,rel}$ (mas yr^{-1})	-216.2 ± 0.8	-216.1	-217.8, -214.6	uniform
Relative parallax $\pi_{\rm rel}$ (mas)	42.2 ± 1.0	41.7	40.2, 44.2	$1/\pi^2$ (uniform volume density)
Ratio of photocenter orbit to semimajor axis α/a	$-0.07^{+0.08}_{-0.07}$	-0.10	-0.23, 0.08	uniform
Derived properties				
Total mass at fixed distance $a^3P^{-2}(d/23.0\rm pc)^3$ ($M_{\rm Jup}$)	38^{+9}_{-18}	53	18, 70	···
Time of periastron T_0 (JD)	2461300^{+700}_{-800}	2460500	2458900, 2463600	···
Photocenter semimajor axis α (mas)	-6^{+7}_{-6}	-8	-20, 7	···
Correction to absolute RA proper motion $\Delta\mu_{\rm RA}$ (mas yr^{-1})	-1.1 ± 0.8	-1.4	-2.8, 0.4	···
Correction to absolute Dec proper motion $\Delta\mu_{\rm Dec}$ (mas yr^{-1})	-3.8 ± 0.8	-4.9	-5.5, -2.1	···
Correction to absolute parallax $\Delta\pi$ (mas)	1.20 ± 0.10	1.32	1.00, 1.41	···
Absolute proper motion in RA $\mu_{\rm RA,abs}$ (mas yr^{-1})	10.7 ± 1.3	10.8	8.2, 13.2	···
Absolute proper motion in Dec $\mu_{\rm Dec,abs}$ (mas yr^{-1})	-220.0 ± 1.2	-221.1	-222.4, -217.7	···
Absolute parallax $\pi_{\rm abs}$ (mas)	43.4 ± 1.0	43.0	41.3, 45.4	···
Distance d (pc)	$23.0^{+0.5}_{-0.6}$	23.3	22.0, 24.1	···
Semimajor axis a (AU)	$1.80^{+0.14}_{-0.21}$	1.87	1.54, 2.42	···
Total mass $M_{\rm tot}$ ($M_{\rm Jup}$)	38^{+10}_{-18}	55	17, 71	···

Table 14. MCMC Posteriors for the Orbit and Parallax of 2MASS J1017+1308AB

Property	Median $\pm 1\sigma$	Best fit	95.4% c.i.	Prior/Notes
		Fitted parameters		
Orbital period P (yr)	$18.60^{+0.22}_{-0.23}$	18.62	18.16, 19.07	$1/P$ (log-flat)
Semimajor axis a (mas)	$120.0^{+1.1}_{-1.2}$	120.0	117.7, 122.3	$1/a$ (log-flat)
Eccentricity e	0.158 ± 0.010	0.158	0.139, 0.178	uniform, $0 \leq e < 1$
Inclination i (°)	$35.4^{+1.0}_{-0.9}$	35.4	33.5, 37.2	$\sin(i)$, $0° < i < 180°$
PA of the ascending node Ω (°)	$72.7^{+1.8}_{-2.0}$	72.3	69.0, 76.7	uniform
Argument of periastron ω (°)	5 ± 5	7	−5, 16	uniform
Mean longitude at 2455197.5 JD $\lambda_{\rm ref}$ (°)	$184.9^{+1.4}_{-1.3}$	185.2	182.1, 187.6	uniform
RA − $\rm RA_{2010}$ (mas)	0.3 ± 1.6	0.0	−2.9, 3.4	uniform, $\rm RA_{2010} = 154.2818189$
Dec − $\rm Dec_{2010}$ (mas)	$0.1^{+0.7}_{-0.8}$	0.0	−1.4, 1.6	uniform, $\rm Dec_{2010} = +13.1441293$
Relative proper motion in RA $\mu_{\rm RA,rel}$ (mas yr^{-1})	$47.9^{+0.3}_{-0.4}$	48.1	47.3, 48.7	uniform
Relative proper motion in Dec $\mu_{\rm Dec,rel}$ (mas yr^{-1})	$-116.0^{+0.5}_{-0.6}$	−115.7	−117.1, −114.9	uniform
Relative parallax $\pi_{\rm rel}$ (mas)	30.9 ± 1.1	30.8	28.6, 33.0	$1/\pi^2$ (uniform volume density)
Ratio of photocenter orbit to semimajor axis α/a	0.026 ± 0.022	0.038	−0.017, 0.070	uniform
		Derived properties		
Total mass at fixed distance $a^3P^{-2}(d/31.0{\rm pc})^3$ ($M_{\rm Jup}$)	155.9 ± 2.1	155.5	151.6, 160.1	···
Time of periastron T_0 (JD)	2458650^{+90}_{-150}	2458620	2458470, 2465190	···
Photocenter semimajor axis α (mas)	$3.2^{+2.7}_{-2.6}$	4.5	−2.1, 8.4	···
Correction to absolute RA proper motion $\Delta\mu_{\rm RA}$ (mas yr^{-1})	-4.7 ± 1.9	−4.7	−8.6, −0.9	···
Correction to absolute Dec proper motion $\Delta\mu_{\rm Dec}$ (mas yr^{-1})	-3.3 ± 1.7	−3.3	−6.6, 0.2	···
Correction to absolute parallax $\Delta\pi$ (mas)	$1.38^{+0.18}_{-0.21}$	1.38	1.02, 1.81	···
Absolute proper motion in RA $\mu_{\rm RA,abs}$ (mas yr^{-1})	43.2 ± 1.9	43.4	39.2, 47.0	···
Absolute proper motion in Dec $\mu_{\rm Dec,abs}$ (mas yr^{-1})	-119.3 ± 1.8	−119.0	−123.0, −115.9	···
Absolute parallax $\pi_{\rm abs}$ (mas)	32.3 ± 1.1	32.2	30.0, 34.5	···
Distance d (pc)	$31.0^{+1.0}_{-1.1}$	31.1	28.9, 33.2	···
Semimajor axis a (AU)	3.72 ± 0.13	3.73	3.47, 4.00	···
Total mass $M_{\rm tot}$ ($M_{\rm Jup}$)	156^{+14}_{-18}	157	126, 191	···

Table 15. MCMC Posteriors for the Orbit and Parallax of SDSS J1021−0304AB

Property	Median $\pm 1\sigma$	Best fit	95.4% c.i.	Prior/Notes
Fitted parameters				
Orbital period P (yr)	86^{+13}_{-17}	75	60, 119	$1/P$ (log-flat)
Semimajor axis a (mas)	241^{+19}_{-28}	224	201, 294	$1/a$ (log-flat)
Eccentricity e	0.38 ± 0.07	0.31	0.24, 0.51	uniform, $0 \le e < 1$
Inclination i (°)	165^{+6}_{-7}	161	154, 177	$\sin(i)$, $0° < i < 180°$
PA of the ascending node Ω (°)	260^{+100}_{-90}	260	60, 400	uniform
Argument of periastron ω (°)	110^{+70}_{-120}	70	−40, 300	uniform
Mean longitude at 2455197.5 JD $\lambda_{\rm ref}$ (°)	100^{+70}_{-120}	70	−40, 290	uniform
RA − RA_{2010} (mas)	-0.3 ± 1.3	0.0	−3.0, 2.4	uniform, $RA_{2010} = 155.2901072$
Dec − Dec_{2010} (mas)	0.4 ± 1.0	0.0	−1.6, 2.3	uniform, $Dec_{2010} = -3.0720382$
Relative proper motion in RA $\mu_{\rm RA,rel}$ (mas yr^{-1})	-182 ± 8	−183	−198, −167	uniform
Relative proper motion in Dec $\mu_{\rm Dec,rel}$ (mas yr^{-1})	-69.8 ± 1.8	−69.6	−73.3, −66.1	uniform
Relative parallax $\pi_{\rm rel}$ (mas)	32.5 ± 1.2	32.8	30.1, 35.1	$1/\pi^2$ (uniform volume density)
Ratio of photocenter orbit to semimajor axis α/a	-0.9 ± 0.3	−0.9	−1.5, −0.2	uniform
Derived properties				
Total mass at fixed distance $a^3 P^{-2} (d/29.7{\rm pc})^3$ ($M_{\rm Jup}$)	52^{+3}_{-4}	56	47, 60	···
Time of periastron T_0 (JD)	2487000^{+4000}_{-6000}	2482000	2478000, 2499000	···
Photocenter semimajor axis α (mas)	-210 ± 80	−200	−380, −50	···
Correction to absolute RA proper motion $\Delta\mu_{\rm RA}$ (mas yr^{-1})	-4.9 ± 1.0	−4.9	−7.1, −3.0	···
Correction to absolute Dec proper motion $\Delta\mu_{\rm Dec}$ (mas yr^{-1})	-1.5 ± 0.9	−1.5	−3.3, 0.2	···
Correction to absolute parallax $\Delta\pi$ (mas)	$1.15^{+0.10}_{-0.11}$	1.15	0.95, 1.37	···
Absolute proper motion in RA $\mu_{\rm RA,abs}$ (mas yr^{-1})	-187 ± 8	−188	−204, −171	···
Absolute proper motion in Dec $\mu_{\rm Dec,abs}$ (mas yr^{-1})	-71.3 ± 2.0	−71.1	−75.3, −67.3	···
Absolute parallax $\pi_{\rm abs}$ (mas)	$33.7^{+1.2}_{-1.3}$	33.9	31.2, 36.1	···
Distance d (pc)	29.7 ± 1.1	29.5	27.6, 32.0	···
Semimajor axis a (AU)	$7.2^{+0.7}_{-0.8}$	6.6	5.8, 8.8	···
Total mass $M_{\rm tot}$ ($M_{\rm Jup}$)	52^{+6}_{-7}	54	40, 68	···

Table 16. MCMC Posteriors for the Orbit and Parallax of 2MASS J1047+4026AB (a.k.a. LP 213-68)

Property	Median $\pm 1\sigma$	Best fit	95.4% c.i.	Prior/Notes
Fitted parameters				
Orbital period P (yr)	$6.562^{+0.029}_{-0.026}$	6.557	6.508, 6.619	$1/P$ (log-flat)
Semimajor axis a (mas)	$75.98^{+0.21}_{-0.22}$	75.94	75.55, 76.41	$1/a$ (log-flat)
Eccentricity e	0.7485 ± 0.0013	0.7479	0.7458, 0.7511	uniform, $0 \leq e < 1$
Inclination i (°)	30.0 ± 0.5	29.9	29.0, 30.9	$\sin(i)$, $0° < i < 180°$
PA of the ascending node Ω (°)	$85.5^{+1.1}_{-1.0}$	85.6	83.4, 87.5	uniform
Argument of periastron ω (°)	63.5 ± 1.0	63.4	61.6, 65.6	uniform
Mean longitude at 2455197.5 JD $\lambda_{\rm ref}$ (°)	329.6 ± 1.2	329.5	327.2, 332.2	uniform
RA − $\rm RA_{2010}$ (mas)	-0.2 ± 1.7	0.0	−3.7, 3.1	uniform, $\rm RA_{2010} = 161.8064070$
Dec − $\rm Dec_{2010}$ (mas)	-0.3 ± 1.0	0.0	−2.2, 1.7	uniform, $\rm Dec_{2010} = +40.4472059$
Relative proper motion in RA $\mu_{\rm RA,rel}$ (mas yr^{-1})	-293.54 ± 0.24	−293.55	−294.02, −293.05	uniform
Relative proper motion in Dec $\mu_{\rm Dec,rel}$ (mas yr^{-1})	-31.19 ± 0.25	−31.18	−31.68, −30.69	uniform
Relative parallax $\pi_{\rm rel}$ (mas)	37.6 ± 0.8	37.6	36.0, 39.1	$1/\pi^2$ (uniform volume density)
Ratio of photocenter orbit to semimajor axis α/a	$0.019^{+0.016}_{-0.015}$	0.014	−0.011, 0.049	uniform
Derived properties				
Total mass at fixed distance $a^3P^{-2}(d/25.5{\rm pc})^3$ ($M_{\rm Jup}$)	177.5 ± 1.0	177.5	175.5, 179.5	···
Time of periastron T_0 (JD)	$2455822.5^{+0.5}_{-0.4}$	2455822.5	2455821.8, 2455823.2	···
Photocenter semimajor axis α (mas)	$1.4^{+1.2}_{-1.1}$	1.1	−0.9, 3.7	···
Correction to absolute RA proper motion $\Delta\mu_{\rm RA}$ (mas yr^{-1})	-3.7 ± 2.8	−3.7	−9.7, 1.4	···
Correction to absolute Dec proper motion $\Delta\mu_{\rm Dec}$ (mas yr^{-1})	-4.3 ± 2.4	−4.3	−9.4, 0.3	···
Correction to absolute parallax $\Delta\pi$ (mas)	$1.60^{+0.26}_{-0.29}$	1.60	1.09, 2.21	···
Absolute proper motion in RA $\mu_{\rm RA,abs}$ (mas yr^{-1})	-297.2 ± 2.8	−297.2	−303.3, −292.1	···
Absolute proper motion in Dec $\mu_{\rm Dec,abs}$ (mas yr^{-1})	-35.5 ± 2.4	−35.5	−40.6, −30.9	···
Absolute parallax $\pi_{\rm abs}$ (mas)	39.2 ± 0.8	39.2	37.5, 40.8	···
Distance d (pc)	25.5 ± 0.5	25.5	24.5, 26.6	···
Semimajor axis a (AU)	1.94 ± 0.04	1.94	1.86, 2.02	···
Total mass $M_{\rm tot}$ ($M_{\rm Jup}$)	178^{+11}_{-12}	177	156, 201	···

Table 17. MCMC Posteriors for the Orbit and Parallax of SDSS J1052+4422AB

Property	Median $\pm 1\sigma$	Best fit	95.4% c.i.	Prior/Notes
		Fitted parameters		
Orbital period P (yr)	$8.608^{+0.025}_{-0.024}$	8.603	8.559, 8.656	$1/P$ (log-flat)
Semimajor axis a (mas)	70.67 ± 0.24	70.61	70.19, 71.15	$1/a$ (log-flat)
Eccentricity e	$0.1399^{+0.0022}_{-0.0023}$	0.1410	0.1354, 0.1445	uniform, $0 \leq e < 1$
Inclination i (°)	62.1 ± 0.3	62.1	61.5, 62.7	$\sin(i)$, $0° < i < 180°$
PA of the ascending node Ω (°)	126.8 ± 0.3	126.8	126.2, 127.5	uniform
Argument of periastron ω (°)	187.3 ± 1.6	186.8	184.0, 190.6	uniform
Mean longitude at 2455197.5 JD $\lambda_{\rm ref}$ (°)	113.4 ± 0.4	113.6	112.5, 114.2	uniform
RA − $\rm RA_{2010}$ (mas)	$-0.4^{+1.3}_{-1.1}$	0.0	−2.8, 2.0	uniform, $\rm RA_{2010} = 163.0566530$
Dec − $\rm Dec_{2010}$ (mas)	0.3 ± 0.6	0.0	−0.8, 1.5	uniform, $\rm Dec_{2010} = +44.3821517$
Relative proper motion in RA $\mu_{\rm RA,rel}$ ($\rm mas\,yr^{-1}$)	24.06 ± 0.18	24.02	23.70, 24.41	uniform
Relative proper motion in Dec $\mu_{\rm Dec,rel}$ ($\rm mas\,yr^{-1}$)	-133.33 ± 0.19	−133.22	−133.71, −132.96	uniform
Relative parallax $\pi_{\rm rel}$ (mas)	36.8 ± 0.6	37.0	35.6, 38.0	$1/\pi^2$ (uniform volume density)
Ratio of photocenter orbit to semimajor axis α/a	-0.165 ± 0.008	−0.162	−0.181, −0.150	uniform
		Derived properties		
Total mass at fixed distance $a^3 P^{-2} (d/26.2{\rm pc})^3$ ($M_{\rm Jup}$)	90.3 ± 1.0	90.1	88.3, 92.3	···
Time of periastron T_0 (JD)	2458987 ± 14	2458980	2458960, 2459016	···
Photocenter semimajor axis α (mas)	$-11.7^{+0.6}_{-0.5}$	−11.5	−12.8, −10.6	···
Correction to absolute RA proper motion $\Delta\mu_{\rm RA}$ ($\rm mas\,yr^{-1}$)	-3.0 ± 1.4	−3.0	−5.9, −0.5	···
Correction to absolute Dec proper motion $\Delta\mu_{\rm Dec}$ ($\rm mas\,yr^{-1}$)	-4.2 ± 1.2	−4.2	−6.7, −1.9	···
Correction to absolute parallax $\Delta\pi$ (mas)	$1.33^{+0.13}_{-0.16}$	1.33	1.05, 1.64	···
Absolute proper motion in RA $\mu_{\rm RA,abs}$ ($\rm mas\,yr^{-1}$)	21.1 ± 1.4	21.0	18.2, 23.7	···
Absolute proper motion in Dec $\mu_{\rm Dec,abs}$ ($\rm mas\,yr^{-1}$)	-137.5 ± 1.2	−137.4	−140.0, −135.2	···
Absolute parallax $\pi_{\rm abs}$ (mas)	38.1 ± 0.6	38.3	36.8, 39.3	···
Distance d (pc)	26.2 ± 0.4	26.1	25.4, 27.1	···
Semimajor axis a (AU)	1.86 ± 0.03	1.84	1.79, 1.92	···
Total mass $M_{\rm tot}$ ($M_{\rm Jup}$)	90^{+4}_{-5}	89	81, 100	···

Table 18. MCMC Posteriors for the Orbit and Parallax of Gl 417BC

Property	Median $\pm 1\sigma$	Best fit	95.4% c.i.	Prior/Notes
Fitted parameters				
Orbital period P (yr)	15.65 ± 0.08	15.65	15.49, 15.81	$1/P$ (log-flat)
Semimajor axis a (mas)	130.0 ± 0.4	130.0	129.2, 130.9	$1/a$ (log-flat)
Eccentricity e	0.105 ± 0.003	0.106	0.099, 0.112	uniform, $0 \leq e < 1$
Inclination i (°)	102.9 ± 0.5	102.9	101.9, 103.9	$\sin(i)$, $0° < i < 180°$
PA of the ascending node Ω (°)	101.01 ± 0.22	101.06	100.56, 101.45	uniform
Argument of periastron ω (°)	348^{+4}_{-5}	348	339, 356	uniform
Mean longitude at 2455197.5 JD $\lambda_{\rm ref}$ (°)	255.6 ± 0.6	255.7	254.4, 256.9	uniform
Derived properties				
Total mass at fixed distance $a^3 P^{-2} (d/21.93{\rm pc})^3$ ($M_{\rm Jup}$)	99.2 ± 1.3	99.2	96.7, 101.9	···
Time of periastron T_0 (JD)	2462370 ± 50	2462370	2462270, 2462470	···
Absolute parallax $\pi_{\rm abs}$ (mas)	45.61 ± 0.44	46.02	44.73, 46.49	···
Distance d (pc)	21.93 ± 0.21	21.73	21.51, 22.35	···
Semimajor axis a (AU)	2.851 ± 0.029	2.825	2.795, 2.911	···
Total mass $M_{\rm tot}$ ($M_{\rm Jup}$)	$99.2^{+3.0}_{-3.3}$	96.5	93.0, 105.6	···

Table 19. MCMC Posteriors for the Orbit and Parallax of LHS 2397aAB

Property	Median $\pm 1\sigma$	Best fit	95.4% c.i.	Prior/Notes
Fitted parameters				
Orbital period P (yr)	14.37 ± 0.05	14.36	14.27, 14.46	$1/P$ (log-flat)
Semimajor axis a (mas)	214.8 ± 0.8	214.6	213.2, 216.4	$1/a$ (log-flat)
Eccentricity e	0.351 ± 0.003	0.353	0.345, 0.358	uniform, $0 \leq e < 1$
Inclination i (°)	$42.55^{+0.28}_{-0.29}$	42.41	41.98, 43.13	$\sin(i)$, $0° < i < 180°$
PA of the ascending node Ω (°)	74.7 ± 0.8	74.4	73.2, 76.2	uniform
Argument of periastron ω (°)	221.2 ± 1.3	221.5	218.5, 223.8	uniform
Mean longitude at 2455197.5 JD $\lambda_{\rm ref}$ (°)	314.0 ± 0.6	314.2	312.7, 315.2	uniform
RA $-$ RA_{2010} (mas)	-0.6 ± 1.6	0.0	-3.8, 2.7	uniform, $\mathrm{RA}_{2010} = 170.4536705$
Dec $-$ Dec_{2010} (mas)	0.7 ± 0.9	0.0	-1.1, 2.4	uniform, $\mathrm{Dec}_{2010} = -13.2189824$
Relative proper motion in RA $\mu_{\rm RA,rel}$ (mas yr^{-1})	$-487.67^{+0.30}_{-0.32}$	-487.76	-488.29, -487.06	uniform
Relative proper motion in Dec $\mu_{\rm Dec,rel}$ (mas yr^{-1})	-57.8 ± 0.5	-57.7	-58.7, -56.8	uniform
Relative parallax $\pi_{\rm rel}$ (mas)	$66.9^{+1.0}_{-1.1}$	67.3	64.7, 69.0	$1/\pi^2$ (uniform volume density)
Ratio of photocenter orbit to semimajor axis α/a	0.344 ± 0.009	0.344	0.326, 0.363	uniform
Derived properties				
Total mass at fixed distance $a^3P^{-2}(d/14.66\mathrm{pc})^3$ ($M_{\rm Jup}$)	$158.5^{+1.3}_{-1.4}$	158.2	155.9, 161.2	···
Time of periastron T_0 (JD)	2459093^{+23}_{-22}	2459092	2459047, 2459137	···
Photocenter semimajor axis α (mas)	74.0 ± 2.0	73.8	70.0, 77.9	···
Correction to absolute RA proper motion $\Delta\mu_{\rm RA}$ (mas yr^{-1})	-6.2 ± 1.6	-6.2	-9.4, -3.2	···
Correction to absolute Dec proper motion $\Delta\mu_{\rm Dec}$ (mas yr^{-1})	-1.1 ± 1.2	-1.1	-3.5, 1.4	···
Correction to absolute parallax $\Delta\pi$ (mas)	$1.31^{+0.14}_{-0.15}$	1.31	1.04, 1.64	···
Absolute proper motion in RA $\mu_{\rm RA,abs}$ (mas yr^{-1})	-493.9 ± 1.6	-494.0	-497.1, -490.8	···
Absolute proper motion in Dec $\mu_{\rm Dec,abs}$ (mas yr^{-1})	-58.8 ± 1.3	-58.7	-61.5, -56.3	···
Absolute parallax $\pi_{\rm abs}$ (mas)	$68.2^{+1.1}_{-1.0}$	68.6	66.1, 70.4	···
Distance d (pc)	14.66 ± 0.23	14.58	14.21, 15.13	···
Semimajor axis a (AU)	3.15 ± 0.05	3.13	3.05, 3.25	···
Total mass $M_{\rm tot}$ ($M_{\rm Jup}$)	159^{+7}_{-8}	156	144, 174	···

Table 20. MCMC Posteriors for the Orbit and Parallax of DENIS J1228−1557AB

Property	Median ±1σ	Best fit	95.4% c.i.	Prior/Notes
Fitted parameters				
Orbital period P (yr)	50^{+5}_{-7}	47	40, 65	$1/P$ (log-flat)
Semimajor axis a (mas)	303^{+8}_{-11}	297	288, 331	$1/a$ (log-flat)
Eccentricity e	$0.089^{+0.027}_{-0.035}$	0.075	0.044, 0.197	uniform, $0 \leq e < 1$
Inclination i (°)	142 ± 4	140	135, 150	$\sin(i)$, $0° < i < 180°$
PA of the ascending node Ω (°)	$60.0^{+2.5}_{-2.0}$	60.4	54.4, 64.3	uniform
Argument of periastron ω (°)	10^{+50}_{-40}	−30	−70, 60	uniform
Mean longitude at 2455197.5 JD $\lambda_{\rm ref}$ (°)	105^{+6}_{-5}	107	93, 115	uniform
RA − $\rm RA_{2010}$ (mas)	$0.5^{+2.3}_{-2.1}$	0.0	−4.0, 4.9	uniform, $\rm RA_{2010}$ = 187.0639596
Dec − $\rm Dec_{2010}$ (mas)	-0.5 ± 1.2	0.0	−2.9, 1.8	uniform, $\rm Dec_{2010}$ = −15.7933016
Relative proper motion in RA $\mu_{\rm RA,rel}$ (mas yr^{-1})	110^{+31}_{-30}	118	49, 170	uniform
Relative proper motion in Dec $\mu_{\rm Dec,rel}$ (mas yr^{-1})	-209^{+27}_{-26}	−201	−262, −156	uniform
Relative parallax $\pi_{\rm rel}$ (mas)	46.8 ± 1.7	46.4	43.5, 50.2	$1/\pi^2$ (uniform volume density)
Ratio of photocenter orbit to semimajor axis α/a	0.9 ± 1.1	0.6	−1.2, 3.1	uniform
Derived properties				
Total mass at fixed distance $a^3P^{-2}(d/20.9{\rm pc})^3$ ($M_{\rm Jup}$)	106^{+13}_{-16}	115	78, 135	···
Time of periastron T_0 (JD)	2476000^{+5000}_{-8000}	2483000	2468000, 2485000	···
Photocenter semimajor axis α (mas)	300 ± 300	200	−400, 900	···
Correction to absolute RA proper motion $\Delta\mu_{\rm RA}$ (mas yr^{-1})	-5.7 ± 1.0	−5.7	−7.6, −3.8	···
Correction to absolute Dec proper motion $\Delta\mu_{\rm Dec}$ (mas yr^{-1})	-1.4 ± 0.6	−1.4	−2.7, −0.2	···
Correction to absolute parallax $\Delta\pi$ (mas)	1.11 ± 0.09	1.11	0.93, 1.30	···
Absolute proper motion in RA $\mu_{\rm RA,abs}$ (mas yr^{-1})	100 ± 30	110	40, 170	···
Absolute proper motion in Dec $\mu_{\rm Dec,abs}$ (mas yr^{-1})	-210 ± 27	−203	−263, −157	···
Absolute parallax $\pi_{\rm abs}$ (mas)	$48.0^{+1.8}_{-1.6}$	47.5	44.6, 51.3	···
Distance d (pc)	20.9 ± 0.7	21.0	19.5, 22.4	···
Semimajor axis a (AU)	$6.36^{+0.29}_{-0.35}$	6.26	5.78, 7.09	···
Total mass $M_{\rm tot}$ ($M_{\rm Jup}$)	106^{+16}_{-19}	118	72, 145	···

Table 21. MCMC Posteriors for the Orbit and Parallax of Kelu-1AB

Property	Median $\pm 1\sigma$	Best fit	95.4% c.i.	Prior/Notes
		Fitted parameters		
Orbital period P (yr)	24.98 ± 0.19	24.97	24.60, 25.36	$1/P$ (log-flat)
Semimajor axis a (mas)	$227.9^{+0.9}_{-1.1}$	227.7	226.0, 230.0	$1/a$ (log-flat)
Eccentricity e	0.709 ± 0.005	0.709	0.699, 0.719	uniform, $0 \leq e < 1$
Inclination i (°)	82.35 ± 0.08	82.34	82.18, 82.51	$\sin(i)$, $0° < i < 180°$
PA of the ascending node Ω (°)	44.78 ± 0.20	44.80	44.39, 45.20	uniform
Argument of periastron ω (°)	3.7 ± 2.1	3.4	−0.5, 7.8	uniform
Mean longitude at 2455197.5 JD $\lambda_{\rm ref}$ (°)	158.23 ± 0.13	158.23	157.96, 158.48	uniform
RA − $\rm RA_{2010}$ (mas)	$0.4^{+2.5}_{-2.4}$	0.0	−4.4, 5.3	uniform, $\rm RA_{2010} = 196.4165748$
Dec − $\rm Dec_{2010}$ (mas)	0.3 ± 1.7	0.0	−3.1, 3.7	uniform, $\rm Dec_{2010} = -25.6847822$
Relative proper motion in RA $\mu_{\rm RA,rel}$ (mas yr^{-1})	-294 ± 8	−295	−311, −277	uniform
Relative proper motion in Dec $\mu_{\rm Dec,rel}$ (mas yr^{-1})	-1 ± 5	−2	−11, 10	uniform
Relative parallax $\pi_{\rm rel}$ (mas)	47.0 ± 2.2	46.8	42.6, 51.3	$1/\pi^2$ (uniform volume density)
Ratio of photocenter orbit to semimajor axis α/a	-0.7 ± 0.9	−0.6	−2.5, 1.0	uniform
		Derived properties		
Total mass at fixed distance $a^3 P^{-2} (d/20.8\rm pc)^3$ ($M_{\rm Jup}$)	180.1 ± 1.1	179.6	177.9, 182.4	···
Time of periastron T_0 (JD)	2460410^{+80}_{-110}	2460400	2460230, 2460650	···
Photocenter semimajor axis α (mas)	-160 ± 200	−130	−560, 240	···
Correction to absolute RA proper motion $\Delta\mu_{\rm RA}$ (mas yr^{-1})	-6.0 ± 0.7	−6.0	−7.5, −4.5	···
Correction to absolute Dec proper motion $\Delta\mu_{\rm Dec}$ (mas yr^{-1})	-1.5 ± 0.5	−1.5	−2.3, −0.5	···
Correction to absolute parallax $\Delta\pi$ (mas)	$0.96^{+0.07}_{-0.09}$	0.96	0.81, 1.12	···
Absolute proper motion in RA $\mu_{\rm RA,abs}$ (mas yr^{-1})	-300 ± 8	−301	−317, −283	···
Absolute proper motion in Dec $\mu_{\rm Dec,abs}$ (mas yr^{-1})	-2 ± 5	−3	−12, 9	···
Absolute parallax $\pi_{\rm abs}$ (mas)	48.0 ± 2.2	47.8	43.6, 52.3	···
Distance d (pc)	$20.8^{+0.9}_{-1.0}$	20.9	19.0, 22.8	···
Semimajor axis a (AU)	$4.75^{+0.21}_{-0.22}$	4.76	4.34, 5.21	···
Total mass $M_{\rm tot}$ ($M_{\rm Jup}$)	180^{+22}_{-26}	182	134, 233	···

Table 22. MCMC Posteriors for the Orbit and Parallax of 2MASS J1404−3159AB

Property	Median $\pm 1\sigma$	Best fit	95.4% c.i.	Prior/Notes
Fitted parameters				
Orbital period P (yr)	$16.52^{+0.21}_{-0.22}$	16.51	16.10, 16.97	$1/P$ (log-flat)
Semimajor axis a (mas)	$133.7^{+1.5}_{-2.3}$	135.9	131.0, 138.8	$1/a$ (log-flat)
Eccentricity e	0.825 ± 0.005	0.825	0.814, 0.836	uniform, $0 \leq e < 1$
Inclination i (°)	164^{+8}_{-7}	157	151, 177	$\sin(i)$, $0^\circ < i < 180^\circ$
PA of the ascending node Ω (°)	207^{+176}_{-13}	208	23, 376	uniform
Argument of periastron ω (°)	52^{+172}_{-17}	45	−60, 242	uniform
Mean longitude at 2455197.5 JD $\lambda_{\rm ref}$ (°)	84^{+170}_{-18}	76	−44, 272	uniform
RA − RA_{2010} (mas)	$0.3^{+1.4}_{-1.5}$	0.0	−2.6, 3.2	uniform, $RA_{2010} = 211.2073153$
Dec − Dec_{2010} (mas)	1.0 ± 1.2	0.0	−1.4, 3.3	uniform, $Dec_{2010} = -31.9924797$
Relative proper motion in RA $\mu_{\rm RA,rel}$ (mas yr^{-1})	$339.11^{+0.29}_{-0.27}$	338.93	338.55, 339.66	uniform
Relative proper motion in Dec $\mu_{\rm Dec,rel}$ (mas yr^{-1})	-20.3 ± 0.7	−19.8	−21.7, −18.9	uniform
Relative parallax $\pi_{\rm rel}$ (mas)	41.8 ± 1.1	41.5	39.6, 44.0	$1/\pi^2$ (uniform volume density)
Ratio of photocenter orbit to semimajor axis α/a	-0.165 ± 0.016	−0.153	−0.197, −0.132	uniform
Derived properties				
Total mass at fixed distance $a^3 P^{-2} (d/23.5{\rm pc})^3$ ($M_{\rm Jup}$)	119^{+5}_{-7}	125	110, 135	···
Time of periastron T_0 (JD)	2460690^{+80}_{-90}	2460710	2460510, 2460870	···
Photocenter semimajor axis α (mas)	$-22.1^{+2.1}_{-2.0}$	−20.7	−26.2, −17.8	···
Correction to absolute RA proper motion $\Delta\mu_{\rm RA}$ (mas yr^{-1})	-5.2 ± 0.4	−5.2	−6.1, −4.4	···
Correction to absolute Dec proper motion $\Delta\mu_{\rm Dec}$ (mas yr^{-1})	-1.79 ± 0.25	−1.79	−2.31, −1.33	···
Correction to absolute parallax $\Delta\pi$ (mas)	0.75 ± 0.05	0.75	0.66, 0.84	···
Absolute proper motion in RA $\mu_{\rm RA,abs}$ (mas yr^{-1})	333.9 ± 0.5	333.7	332.8, 334.9	···
Absolute proper motion in Dec $\mu_{\rm Dec,abs}$ (mas yr^{-1})	-22.1 ± 0.7	−21.6	−23.6, −20.6	···
Absolute parallax $\pi_{\rm abs}$ (mas)	42.5 ± 1.1	42.2	40.3, 44.7	···
Distance d (pc)	23.5 ± 0.6	23.7	22.3, 24.8	···
Semimajor axis a (AU)	$3.15^{+0.09}_{-0.11}$	3.22	2.96, 3.37	···
Total mass $M_{\rm tot}$ ($M_{\rm Jup}$)	120^{+11}_{-13}	128	98, 147	···

Table 23. MCMC Posteriors for the Orbit and Parallax of HD 130948BC

Property	Median $\pm 1\sigma$	Best fit	95.4% c.i.	Prior/Notes
Fitted parameters				
Orbital period P (yr)	10.009 ± 0.010	10.008	9.990, 10.029	$1/P$ (log-flat)
Semimajor axis a (mas)	122.52 ± 0.08	122.53	122.37, 122.68	$1/a$ (log-flat)
Eccentricity e	0.1627 ± 0.0017	0.1622	0.1592, 0.1660	uniform, $0 \leq e < 1$
Inclination i (°)	95.70 ± 0.05	95.71	95.60, 95.81	$\sin(i)$, $0° < i < 180°$
PA of the ascending node Ω (°)	133.56 ± 0.03	133.56	133.50, 133.63	uniform
Argument of periastron ω (°)	68.39 ± 0.24	68.35	67.93, 68.88	uniform
Mean longitude at 2455197.5 JD $\lambda_{\rm ref}$ (°)	123.11 ± 0.06	123.11	122.99, 123.23	uniform
Derived properties				
Total mass at fixed distance $a^3P^{-2}(d/18.17{\rm pc})^3$ ($M_{\rm Jup}$)	$115.45^{+0.30}_{-0.32}$	115.50	114.83, 116.05	···
Time of periastron T_0 (JD)	2458298 ± 5	2458297	2458287, 2458308	···
Absolute parallax $\pi_{\rm abs}$ (mas)	55.03 ± 0.34	54.64	54.35, 55.71	···
Distance d (pc)	18.17 ± 0.11	18.30	17.95, 18.40	···
Semimajor axis a (AU)	$2.226^{+0.014}_{-0.013}$	2.242	2.199, 2.254	···
Total mass $M_{\rm tot}$ ($M_{\rm Jup}$)	$115.4^{+2.2}_{-2.1}$	118.0	111.2, 119.8	···

Table 24. MCMC Posteriors for the Orbit and Parallax of Gl 569Bab

Property	Median $\pm 1\sigma$	Best fit	95.4% c.i.	Prior/Notes
		Fitted parameters		
Orbital period P (yr)	2.3707 ± 0.0005	2.3707	2.3696, 2.3718	$1/P$ (log-flat)
Semimajor axis a (mas)	93.64 ± 0.14	93.62	93.35, 93.93	$1/a$ (log-flat)
Eccentricity e	0.3186 ± 0.0010	0.3184	0.3166, 0.3207	uniform, $0 \leq e < 1$
Inclination i ($^\circ$)	32.70 ± 0.23	32.65	32.24, 33.15	$\sin(i)$, $0^\circ < i < 180^\circ$
PA of the ascending node Ω ($^\circ$)	142.5 ± 0.3	142.6	141.9, 143.2	uniform
Argument of periastron ω ($^\circ$)	$81.19^{+0.28}_{-0.29}$	81.18	80.63, 81.76	uniform
Mean longitude at 2455197.5 JD $\lambda_{\rm ref}$ ($^\circ$)	41.28 ± 0.30	41.24	40.69, 41.89	uniform
		Derived properties		
Total mass at fixed distance $a^3 P^{-2} (d/9.65{\rm pc})^3$ ($M_{\rm Jup}$)	137.7 ± 0.6	137.6	136.5, 139.0	···
Time of periastron T_0 (JD)	2456159.2 ± 0.4	2456159.5	2456158.5, 2456160.2	···
Absolute parallax $\pi_{\rm abs}$ (mas)	103.6 ± 1.7	104.5	100.2, 107.0	···
Distance d (pc)	9.65 ± 0.16	9.57	9.34, 9.98	···
Semimajor axis a (AU)	0.904 ± 0.015	0.896	0.874, 0.935	···
Total mass $M_{\rm tot}$ ($M_{\rm Jup}$)	138 ± 7	134	124, 152	···

Table 25. MCMC Posteriors for the Orbit and Parallax of SDSS J1534+1615AB

Property	Median $\pm 1\sigma$	Best fit	95.4% c.i.	Prior/Notes
Fitted parameters				
Orbital period P (yr)	58^{+39}_{-24}	48	30, 454	$1/P$ (log-flat)
Semimajor axis a (mas)	150^{+60}_{-40}	130	100, 590	$1/a$ (log-flat)
Eccentricity e	$0.22^{+0.21}_{-0.22}$	0.11	0.00, 0.80	uniform, $0 \leq e < 1$
Inclination i (°)	36^{+15}_{-10}	28	13, 55	$\sin(i)$, $0° < i < 180°$
PA of the ascending node Ω (°)	146^{+19}_{-18}	132	101, 189	uniform
Argument of periastron ω (°)	168^{+13}_{-42}	128	−12, 234	uniform
Mean longitude at 2455197.5 JD $\lambda_{\rm ref}$ (°)	175^{+8}_{-14}	183	135, 213	uniform
RA − $\rm RA_{2010}$ (mas)	$0.4^{+0.8}_{-0.9}$	0.5	−1.3, 2.2	uniform, $\rm RA_{2010}$ = 233.5710344
Dec − $\rm Dec_{2010}$ (mas)	-0.6 ± 1.1	−0.6	−2.8, 1.5	uniform, $\rm Dec_{2010}$ = +16.2631701
Relative proper motion in RA $\mu_{\rm RA,rel}$ (mas yr^{-1})	$-76.4^{+1.3}_{-1.4}$	−76.7	−79.2, −73.7	uniform
Relative proper motion in Dec $\mu_{\rm Dec,rel}$ (mas yr^{-1})	$-37.2^{+0.5}_{-0.4}$	−37.2	−38.1, −36.3	uniform
Relative parallax $\pi_{\rm rel}$ (mas)	26.6 ± 0.9	26.5	24.9, 28.4	$1/\pi^2$ (uniform volume density)
Ratio of photocenter orbit to semimajor axis α/a	$0.07^{+0.10}_{-0.09}$	0.06	−0.12, 0.26	uniform
Derived properties				
Total mass at fixed distance $a^3P^{-2}(d/36.2\rm pc)^3$ ($M_{\rm Jup}$)	45^{+4}_{-5}	44	37, 60	···
Time of periastron T_0 (JD)	$2477000^{+13000}_{-15000}$	2470000	2461000, 2621000	···
Photocenter semimajor axis α (mas)	12^{+16}_{-19}	7	−33, 81	···
Correction to absolute RA proper motion $\Delta\mu_{\rm RA}$ (mas yr^{-1})	-2.3 ± 0.7	−2.0	−3.6, −1.0	···
Correction to absolute Dec proper motion $\Delta\mu_{\rm Dec}$ (mas yr^{-1})	-3.2 ± 0.8	−3.0	−4.9, −1.8	···
Correction to absolute parallax $\Delta\pi$ (mas)	0.99 ± 0.09	1.00	0.81, 1.18	···
Absolute proper motion in RA $\mu_{\rm RA,abs}$ (mas yr^{-1})	-78.8 ± 1.5	−78.7	−81.8, −75.7	···
Absolute proper motion in Dec $\mu_{\rm Dec,abs}$ (mas yr^{-1})	-40.4 ± 0.9	−40.2	−42.2, −38.6	···
Absolute parallax $\pi_{\rm abs}$ (mas)	27.6 ± 0.9	27.5	25.9, 29.4	···
Distance d (pc)	$36.2^{+1.1}_{-1.2}$	36.3	34.0, 38.6	···
Semimajor axis a (AU)	$5.3^{+2.3}_{-1.6}$	4.6	3.5, 21.6	···
Total mass $M_{\rm tot}$ ($M_{\rm Jup}$)	46^{+6}_{-7}	44	34, 63	···

Table 26. MCMC Posteriors for the Orbit and Parallax of 2MASS J1534−2952AB

Property	Median $\pm 1\sigma$	Best fit	95.4% c.i.	Prior/Notes
Fitted parameters				
Orbital period P (yr)	$20.35^{+0.05}_{-0.06}$	20.38	20.26, 20.48	$1/P$ (log-flat)
Semimajor axis a (mas)	$214.07^{+0.27}_{-0.23}$	213.92	213.54, 214.55	$1/a$ (log-flat)
Eccentricity e	$0.0027^{+0.0028}_{-0.0027}$	0.0058	0.0000, 0.0139	uniform, $0 \leq e < 1$
Inclination i (°)	$85.56^{+0.08}_{-0.07}$	85.55	85.40, 85.70	$\sin(i)$, $0° < i < 180°$
PA of the ascending node Ω (°)	13.61 ± 0.05	13.61	13.51, 13.71	uniform
Argument of periastron ω (°)	80 ± 40	80	−70, 260	uniform
Mean longitude at 2455197.5 JD $\lambda_{\rm ref}$ (°)	$92.06^{+0.15}_{-0.14}$	91.97	91.73, 92.33	uniform
RA − RA$_{2010}$ (mas)	-0.2 ± 0.9	0.0	−1.9, 1.6	uniform, RA$_{2010}$ = 233.7081207
Dec − Dec$_{2010}$ (mas)	$-0.4^{+1.4}_{-1.3}$	0.0	−3.2, 2.2	uniform, Dec$_{2010}$ = −29.8748566
Relative proper motion in RA $\mu_{\rm RA,rel}$ (mas yr^{-1})	94.4 ± 0.6	94.6	93.2, 95.5	uniform
Relative proper motion in Dec $\mu_{\rm Dec,rel}$ (mas yr^{-1})	-260.0 ± 1.5	−259.5	−262.9, −257.0	uniform
Relative parallax $\pi_{\rm rel}$ (mas)	62.3 ± 1.1	62.5	60.0, 64.5	$1/\pi^2$ (uniform volume density)
Ratio of photocenter orbit to semimajor axis α/a	0.02 ± 0.04	0.02	−0.06, 0.10	uniform
Derived properties				
Total mass at fixed distance $a^3P^{-2}(d/15.88{\rm pc})^3$ ($M_{\rm Jup}$)	$99.5^{+0.8}_{-0.6}$	99.0	97.7, 100.6	···
Time of periastron T_0 (JD)	2462500^{+800}_{-900}	2462400	2460900, 2467100	···
Photocenter semimajor axis α (mas)	5^{+9}_{-8}	3	−12, 22	···
Correction to absolute RA proper motion $\Delta\mu_{\rm RA}$ (mas yr^{-1})	-3.2 ± 0.4	−3.2	−3.9, −2.3	···
Correction to absolute Dec proper motion $\Delta\mu_{\rm Dec}$ (mas yr^{-1})	-2.2 ± 0.3	−2.2	−2.8, −1.6	···
Correction to absolute parallax $\Delta\pi$ (mas)	$0.70^{+0.05}_{-0.06}$	0.70	0.59, 0.80	···
Absolute proper motion in RA $\mu_{\rm RA,abs}$ (mas yr^{-1})	91.2 ± 0.7	91.4	89.8, 92.6	···
Absolute proper motion in Dec $\mu_{\rm Dec,abs}$ (mas yr^{-1})	-262.2 ± 1.5	−261.7	−265.2, −259.1	···
Absolute parallax $\pi_{\rm abs}$ (mas)	63.0 ± 1.1	63.2	60.7, 65.2	···
Distance d (pc)	$15.88^{+0.29}_{-0.28}$	15.83	15.32, 16.46	···
Semimajor axis a (AU)	3.40 ± 0.06	3.39	3.28, 3.52	···
Total mass $M_{\rm tot}$ ($M_{\rm Jup}$)	99 ± 5	98	89, 110	···

Table 27. MCMC Posteriors for the Orbit and Parallax of 2MASS J1728+3948AB

Property	Median $\pm 1\sigma$	Best fit	95.4% c.i.	Prior/Notes
Fitted parameters				
Orbital period P (yr)	$40.8^{+1.6}_{-1.2}$	43.8	37.8, 47.9	$1/P$ (log-flat)
Semimajor axis a (mas)	221^{+6}_{-5}	232	210, 247	$1/a$ (log-flat)
Eccentricity e	$0.015^{+0.013}_{-0.015}$	0.055	0.000, 0.106	uniform, $0 \leq e < 1$
Inclination i (°)	54.4 ± 0.6	55.4	53.2, 56.8	$\sin(i)$, $0° < i < 180°$
PA of the ascending node Ω (°)	111.3 ± 0.6	110.6	109.7, 112.3	uniform
Argument of periastron ω (°)	330^{+50}_{-130}	340	100, 420	uniform
Mean longitude at 2455197.5 JD $\lambda_{\rm ref}$ (°)	356.93 ± 0.13	356.87	356.64, 357.21	uniform
$\rm RA - RA_{2010}$ (mas)	0.1 ± 0.6	0.0	−1.1, 1.3	uniform, $\rm RA_{2010} = 262.0482783$
$\rm Dec - Dec_{2010}$ (mas)	-0.1 ± 1.0	0.0	−2.1, 2.0	uniform, $\rm Dec_{2010} = +39.8164696$
Relative proper motion in RA $\mu_{\rm RA,rel}$ (mas yr^{-1})	35.7 ± 0.5	35.8	34.7, 36.7	uniform
Relative proper motion in Dec $\mu_{\rm Dec,rel}$ (mas yr^{-1})	-19.3 ± 0.4	−19.4	−20.2, −18.5	uniform
Relative parallax $\pi_{\rm rel}$ (mas)	35.7 ± 0.6	35.8	34.4, 37.0	$1/\pi^2$ (uniform volume density)
Ratio of photocenter orbit to semimajor axis α/a	$0.042^{+0.031}_{-0.030}$	0.042	−0.019, 0.101	uniform
Derived properties				
Total mass at fixed distance $a^3P^{-2}(d/27.4{\rm pc})^3$ ($M_{\rm Jup}$)	$140.0^{+1.3}_{-1.6}$	140.3	137.2, 143.4	···
Time of periastron T_0 (JD)	2466000 ± 5000	2471000	2455000, 2472000	···
Photocenter semimajor axis α (mas)	9^{+6}_{-7}	10	−4, 23	···
Correction to absolute RA proper motion $\Delta\mu_{\rm RA}$ (mas yr^{-1})	-0.9 ± 0.4	−0.9	−1.9, −0.1	···
Correction to absolute Dec proper motion $\Delta\mu_{\rm Dec}$ (mas yr^{-1})	-2.6 ± 0.7	−2.6	−4.0, −1.3	···
Correction to absolute parallax $\Delta\pi$ (mas)	$0.75^{+0.06}_{-0.07}$	0.75	0.62, 0.90	···
Absolute proper motion in RA $\mu_{\rm RA,abs}$ (mas yr^{-1})	34.8 ± 0.7	34.9	33.5, 36.1	···
Absolute proper motion in Dec $\mu_{\rm Dec,abs}$ (mas yr^{-1})	-22.0 ± 0.8	−22.0	−23.5, −20.3	···
Absolute parallax $\pi_{\rm abs}$ (mas)	36.4 ± 0.6	36.5	35.1, 37.7	···
Distance d (pc)	$27.4^{+0.4}_{-0.5}$	27.4	26.5, 28.4	···
Semimajor axis a (AU)	$6.09^{+0.17}_{-0.22}$	6.35	5.70, 6.81	···
Total mass $M_{\rm tot}$ ($M_{\rm Jup}$)	140^{+7}_{-8}	139	126, 156	···

Table 28. MCMC Posteriors for the Orbit and Parallax of LSPM J1735+2634AB

Property	Median $\pm 1\sigma$	Best fit	95.4% c.i.	Prior/Notes
Fitted parameters				
Orbital period P (yr)	$21.65^{+0.24}_{-0.23}$	21.64	21.17, 22.13	$1/P$ (log-flat)
Semimajor axis a (mas)	$283.2^{+2.2}_{-2.0}$	283.0	278.9, 287.5	$1/a$ (log-flat)
Eccentricity e	0.497 ± 0.004	0.497	0.490, 0.505	uniform, $0 \leq e < 1$
Inclination i (°)	53.89 ± 0.11	53.89	53.67, 54.11	$\sin(i)$, $0° < i < 180°$
PA of the ascending node Ω (°)	179.08 ± 0.15	179.12	178.77, 179.39	uniform
Argument of periastron ω (°)	118.3 ± 0.4	118.3	117.4, 119.1	uniform
Mean longitude at 2455197.5 JD $\lambda_{\rm ref}$ (°)	128.69 ± 0.22	128.68	128.25, 129.14	uniform
RA − $\rm RA_{2010}$ (mas)	0.0 ± 0.8	0.0	−1.6, 1.5	uniform, $\rm RA_{2010} = 263.8045883$
Dec − $\rm Dec_{2010}$ (mas)	$0.0^{+1.3}_{-1.4}$	0.0	−2.7, 2.7	uniform, $\rm Dec_{2010} = +26.5791198$
Relative proper motion in RA $\mu_{\rm RA,rel}$ (mas yr^{-1})	151.9 ± 0.3	151.8	151.2, 152.6	uniform
Relative proper motion in Dec $\mu_{\rm Dec,rel}$ (mas yr^{-1})	$-311.59^{+0.21}_{-0.20}$	−311.67	−312.00, −311.17	uniform
Relative parallax $\pi_{\rm rel}$ (mas)	63.5 ± 0.8	63.7	61.9, 65.2	$1/\pi^2$ (uniform volume density)
Ratio of photocenter orbit to semimajor axis α/a	$0.077^{+0.006}_{-0.007}$	0.075	0.064, 0.090	uniform
Derived properties				
Total mass at fixed distance $a^3P^{-2}(d/15.45\rm pc)^3$ ($M_{\rm Jup}$)	187.2 ± 0.4	187.1	186.5, 188.0	···
Time of periastron T_0 (JD)	2462870 ± 90	2462870	2462690, 2463050	···
Photocenter semimajor axis α (mas)	$21.9^{+1.9}_{-1.8}$	21.2	18.2, 25.6	···
Correction to absolute RA proper motion $\Delta\mu_{\rm RA}$ (mas yr^{-1})	-1.0 ± 0.7	−1.0	−2.5, 0.2	···
Correction to absolute Dec proper motion $\Delta\mu_{\rm Dec}$ (mas yr^{-1})	-3.6 ± 1.2	−3.6	−6.1, −1.3	···
Correction to absolute parallax $\Delta\pi$ (mas)	$1.18^{+0.12}_{-0.15}$	1.18	0.92, 1.46	···
Absolute proper motion in RA $\mu_{\rm RA,abs}$ (mas yr^{-1})	150.9 ± 0.8	150.7	149.3, 152.3	···
Absolute proper motion in Dec $\mu_{\rm Dec,abs}$ (mas yr^{-1})	-315.2 ± 1.2	−315.3	−317.7, −312.8	···
Absolute parallax $\pi_{\rm abs}$ (mas)	$64.7^{+0.8}_{-0.9}$	64.9	63.1, 66.4	···
Distance d (pc)	$15.45^{+0.19}_{-0.20}$	15.41	15.05, 15.84	···
Semimajor axis a (AU)	$4.37^{+0.07}_{-0.06}$	4.36	4.25, 4.51	···
Total mass $M_{\rm tot}$ ($M_{\rm Jup}$)	187 ± 7	186	173, 202	···

Table 29. MCMC Posteriors for the Orbit and Parallax of 2MASS J1750+4424AB

Property	Median ±1σ	Best fit	95.4% c.i.	Prior/Notes
Fitted parameters				
Orbital period P (yr)	210^{+40}_{-60}	170	140, 330	$1/P$ (log-flat)
Semimajor axis a (mas)	660^{+100}_{-150}	580	470, 940	$1/a$ (log-flat)
Eccentricity e	$0.73^{+0.09}_{-0.07}$	0.70	0.57, 0.85	uniform, $0 \leq e < 1$
Inclination i (°)	52^{+3}_{-4}	53	46, 61	$\sin(i)$, $0° < i < 180°$
PA of the ascending node Ω (°)	129^{+10}_{-6}	131	112, 142	uniform
Argument of periastron ω (°)	194^{+18}_{-26}	185	159, 234	uniform
Mean longitude at 2455197.5 JD $\lambda_{\rm ref}$ (°)	210^{+19}_{-26}	206	175, 252	uniform
RA − $\rm RA_{2010}$ (mas)	-0.1 ± 1.2	−0.2	−2.5, 2.2	uniform, $\rm RA_{2010}$ = 267.5538299
Dec − $\rm Dec_{2010}$ (mas)	$-0.1^{+1.6}_{-1.7}$	0.4	−3.5, 3.2	uniform, $\rm Dec_{2010}$ = +44.4021159
Relative proper motion in RA $\mu_{\rm RA,rel}$ (mas yr^{-1})	-40 ± 60	−50	−160, 80	uniform
Relative proper motion in Dec $\mu_{\rm Dec,rel}$ (mas yr^{-1})	154 ± 28	160	97, 212	uniform
Relative parallax $\pi_{\rm rel}$ (mas)	31.2 ± 0.9	30.9	29.4, 33.0	$1/\pi^2$ (uniform volume density)
Ratio of photocenter orbit to semimajor axis α/a	-0.8 ± 2.0	−1.2	−5.0, 3.3	uniform
Derived properties				
Total mass at fixed distance $a^3P^{-2}(d/30.9\rm pc)^3$ ($M_{\rm Jup}$)	190^{+30}_{-50}	210	130, 330	···
Time of periastron T_0 (JD)	$2530000^{+15000}_{-22000}$	2514000	2502000, 2572000	···
Photocenter semimajor axis α (mas)	-500 ± 1400	−700	−3700, 2400	···
Correction to absolute RA proper motion $\Delta\mu_{\rm RA}$ (mas yr^{-1})	-1.1 ± 0.6	−0.8	−2.2, 0.0	···
Correction to absolute Dec proper motion $\Delta\mu_{\rm Dec}$ (mas yr^{-1})	-3.4 ± 1.0	−4.4	−5.4, −1.3	···
Correction to absolute parallax $\Delta\pi$ (mas)	$1.14^{+0.10}_{-0.11}$	1.11	0.94, 1.37	···
Absolute proper motion in RA $\mu_{\rm RA,abs}$ (mas yr^{-1})	-40 ± 60	−50	−160, 80	···
Absolute proper motion in Dec $\mu_{\rm Dec,abs}$ (mas yr^{-1})	151 ± 29	155	93, 208	···
Absolute parallax $\pi_{\rm abs}$ (mas)	32.4 ± 0.9	32.0	30.6, 34.2	···
Distance d (pc)	30.9 ± 0.9	31.3	29.2, 32.7	···
Semimajor axis a (AU)	20^{+3}_{-4}	18	14, 29	···
Total mass $M_{\rm tot}$ ($M_{\rm Jup}$)	190^{+40}_{-50}	220	130, 340	···

Table 30. MCMC Posteriors for the Orbit and Parallax of 2MASS J1847+5522AB

Property	Median $\pm 1\sigma$	Best fit	95.4% c.i.	Prior/Notes
Fitted parameters				
Orbital period P (yr)	45^{+5}_{-3}	34	35, 51	$1/P$ (log-flat)
Semimajor axis a (mas)	221^{+18}_{-10}	186	188, 239	$1/a$ (log-flat)
Eccentricity e	$0.09^{+0.05}_{-0.09}$	0.31	0.00, 0.27	uniform, $0 \leq e < 1$
Inclination i (°)	$77.3^{+0.7}_{-0.4}$	75.9	75.7, 78.1	$\sin(i)$, $0° < i < 180°$
PA of the ascending node Ω (°)	126.3 ± 0.5	127.9	125.5, 127.6	uniform
Argument of periastron ω (°)	170^{+31}_{-29}	158	92, 264	uniform
Mean longitude at 2455197.5 JD $\lambda_{\rm ref}$ (°)	$331.8^{+3.1}_{-2.3}$	326.9	325.3, 335.8	uniform
RA − $\rm RA_{2010}$ (mas)	$0.0^{+1.5}_{-1.4}$	−0.5	−2.9, 2.7	uniform, $\rm RA_{2010}$ = 281.7652848
Dec − $\rm Dec_{2010}$ (mas)	$0.4^{+1.5}_{-1.6}$	−0.1	−2.7, 3.6	uniform, $\rm Dec_{2010}$ = +55.3787162
Relative proper motion in RA $\mu_{\rm RA,rel}$ (mas yr^{-1})	$126.10^{+0.24}_{-0.23}$	126.13	125.62, 126.57	uniform
Relative proper motion in Dec $\mu_{\rm Dec,rel}$ (mas yr^{-1})	-62.1 ± 0.6	−62.2	−63.2, −61.0	uniform
Relative parallax $\pi_{\rm rel}$ (mas)	26.5 ± 0.9	26.5	24.6, 28.2	$1/\pi^2$ (uniform volume density)
Ratio of photocenter orbit to semimajor axis α/a	0.05 ± 0.08	0.08	−0.12, 0.21	uniform
Derived properties				
Total mass at fixed distance $a^3P^{-2}(d/36.5\rm pc)^3$ ($M_{\rm Jup}$)	270^{+10}_{-11}	286	248, 293	···
Time of periastron T_0 (JD)	2463900^{+1700}_{-2000}	2461700	2461000, 2470000	···
Photocenter semimajor axis α (mas)	10^{+18}_{-19}	15	−26, 46	···
Correction to absolute RA proper motion $\Delta\mu_{\rm RA}$ (mas yr^{-1})	-0.8 ± 0.6	−0.8	−2.0, 0.3	···
Correction to absolute Dec proper motion $\Delta\mu_{\rm Dec}$ (mas yr^{-1})	-2.3 ± 0.9	−2.5	−4.0, −0.5	···
Correction to absolute parallax $\Delta\pi$ (mas)	$0.93^{+0.08}_{-0.11}$	1.08	0.75, 1.13	···
Absolute proper motion in RA $\mu_{\rm RA,abs}$ (mas yr^{-1})	125.3 ± 0.6	125.3	124.1, 126.5	···
Absolute proper motion in Dec $\mu_{\rm Dec,abs}$ (mas yr^{-1})	-64.4 ± 1.1	−64.7	−66.5, −62.3	···
Absolute parallax $\pi_{\rm abs}$ (mas)	27.4 ± 0.9	27.6	25.6, 29.2	···
Distance d (pc)	36.5 ± 1.2	36.3	34.2, 39.0	···
Semimajor axis a (AU)	$8.0^{+0.7}_{-0.6}$	6.7	6.7, 9.0	···
Total mass $M_{\rm tot}$ ($M_{\rm Jup}$)	270^{+26}_{-31}	280	216, 331	···

Table 31. MCMC Posteriors for the Orbit and Parallax of SDSS J2052−1609AB

Property	Median $\pm 1\sigma$	Best fit	95.4% c.i.	Prior/Notes
		Fitted parameters		
Orbital period P (yr)	44^{+10}_{-14}	37	27, 88	$1/P$ (log-flat)
Semimajor axis a (mas)	169^{+15}_{-20}	158	146, 235	$1/a$ (log-flat)
Eccentricity e	$0.20^{+0.09}_{-0.11}$	0.13	0.08, 0.50	uniform, $0 \leq e < 1$
Inclination i (°)	42^{+7}_{-5}	45	29, 51	$\sin(i)$, $0° < i < 180°$
PA of the ascending node Ω (°)	157 ± 3	157	149, 164	uniform
Argument of periastron ω (°)	229^{+34}_{-27}	199	138, 268	uniform
Mean longitude at 2455197.5 JD $\lambda_{\rm ref}$ (°)	261 ± 6	261	249, 274	uniform
RA − $\rm RA_{2010}$ (mas)	-0.1 ± 0.9	0.2	−1.9, 1.7	uniform, $\rm RA_{2010}$ = 313.1478608
Dec − $\rm Dec_{2010}$ (mas)	-0.3 ± 0.5	−0.4	−1.3, 0.7	uniform, $\rm Dec_{2010}$ = −16.1578445
Relative proper motion in RA $\mu_{\rm RA,rel}$ (mas yr^{-1})	$400.96^{+0.23}_{-0.25}$	400.99	400.48, 401.45	uniform
Relative proper motion in Dec $\mu_{\rm Dec,rel}$ (mas yr^{-1})	153.8 ± 1.3	153.9	151.2, 156.4	uniform
Relative parallax $\pi_{\rm rel}$ (mas)	32.9 ± 0.7	32.8	31.5, 34.3	$1/\pi^2$ (uniform volume density)
Ratio of photocenter orbit to semimajor axis α/a	0.06 ± 0.05	0.05	−0.05, 0.17	uniform
		Derived properties		
Total mass at fixed distance $a^3P^{-2}(d/29.6{\rm pc})^3$ ($M_{\rm Jup}$)	69^{+13}_{-20}	80	42, 100	···
Time of periastron T_0 (JD)	2470000^{+4000}_{-8000}	2466000	2461000, 2487000	···
Photocenter semimajor axis α (mas)	10^{+9}_{-10}	8	−10, 31	···
Correction to absolute RA proper motion $\Delta\mu_{\rm RA}$ (mas yr^{-1})	-0.5 ± 0.4	0.3	−1.4, 0.3	···
Correction to absolute Dec proper motion $\Delta\mu_{\rm Dec}$ (mas yr^{-1})	-4.0 ± 0.4	−3.9	−4.9, −3.2	···
Correction to absolute parallax $\Delta\pi$ (mas)	$0.81^{+0.05}_{-0.06}$	0.85	0.70, 0.92	···
Absolute proper motion in RA $\mu_{\rm RA,abs}$ (mas yr^{-1})	400.4 ± 0.5	401.3	399.4, 401.4	···
Absolute proper motion in Dec $\mu_{\rm Dec,abs}$ (mas yr^{-1})	149.8 ± 1.4	149.9	147.1, 152.6	···
Absolute parallax $\pi_{\rm abs}$ (mas)	33.7 ± 0.7	33.6	32.3, 35.1	···
Distance d (pc)	29.6 ± 0.6	29.8	28.4, 30.9	···
Semimajor axis a (AU)	$5.0^{+0.5}_{-0.6}$	4.7	4.3, 7.0	···
Total mass $M_{\rm tot}$ ($M_{\rm Jup}$)	69^{+14}_{-20}	81	41, 103	···

Table 32. MCMC Posteriors for the Orbit and Parallax of 2MASS J2132+1341AB

Property	Median $\pm 1\sigma$	Best fit	95.4% c.i.	Prior/Notes
Fitted parameters				
Orbital period P (yr)	$10.74^{+0.16}_{-0.17}$	10.72	10.42, 11.08	$1/P$ (log-flat)
Semimajor axis a (mas)	86.1 ± 0.4	86.1	85.4, 87.0	$1/a$ (log-flat)
Eccentricity e	$0.315^{+0.004}_{-0.005}$	0.315	0.306, 0.324	uniform, $0 \le e < 1$
Inclination i (°)	$144.8^{+0.6}_{-0.5}$	144.7	143.7, 145.8	$\sin(i)$, $0° < i < 180°$
PA of the ascending node Ω (°)	82.0 ± 2.2	81.8	77.8, 86.4	uniform
Argument of periastron ω (°)	15^{+4}_{-5}	14	6, 24	uniform
Mean longitude at 2455197.5 JD $\lambda_{\rm ref}$ (°)	$102.8^{+2.3}_{-2.4}$	102.5	98.2, 107.5	uniform
RA − RA_{2010} (mas)	0.2 ± 0.7	0.0	−1.2, 1.7	uniform, $\mathrm{RA}_{2010} = 323.0480216$
Dec − Dec_{2010} (mas)	$0.4^{+0.7}_{-0.6}$	0.0	−0.9, 1.7	uniform, $\mathrm{Dec}_{2010} = +13.6993492$
Relative proper motion in RA $\mu_{\rm RA,rel}$ (mas yr^{-1})	17.83 ± 0.18	17.92	17.47, 18.19	uniform
Relative proper motion in Dec $\mu_{\rm Dec,rel}$ (mas yr^{-1})	$-121.57^{+0.26}_{-0.25}$	−121.49	−122.08, −121.06	uniform
Relative parallax $\pi_{\rm rel}$ (mas)	34.8 ± 0.6	35.0	33.6, 36.0	$1/\pi^2$ (uniform volume density)
Ratio of photocenter orbit to semimajor axis α/a	0.155 ± 0.010	0.153	0.135, 0.174	uniform
Derived properties				
Total mass at fixed distance $a^3P^{-2}(d/28.1\mathrm{pc})^3$ ($M_{\rm Jup}$)	$128.2^{+2.8}_{-2.9}$	128.7	122.7, 134.0	···
Time of periastron T_0 (JD)	2458160 ± 70	2458150	2458020, 2458300	···
Photocenter semimajor axis α (mas)	13.3 ± 0.9	13.2	11.6, 15.0	···
Correction to absolute RA proper motion $\Delta\mu_{\rm RA}$ (mas yr^{-1})	-1.3 ± 0.4	−1.3	−2.1, −0.6	···
Correction to absolute Dec proper motion $\Delta\mu_{\rm Dec}$ (mas yr^{-1})	-4.2 ± 0.4	−4.2	−5.0, −3.4	···
Correction to absolute parallax $\Delta\pi$ (mas)	0.84 ± 0.05	0.84	0.75, 0.94	···
Absolute proper motion in RA $\mu_{\rm RA,abs}$ (mas yr^{-1})	16.5 ± 0.4	16.6	15.7, 17.4	···
Absolute proper motion in Dec $\mu_{\rm Dec,abs}$ (mas yr^{-1})	-125.8 ± 0.5	−125.7	−126.7, −124.8	···
Absolute parallax $\pi_{\rm abs}$ (mas)	35.6 ± 0.6	35.9	34.5, 36.8	···
Distance d (pc)	28.1 ± 0.5	27.9	27.1, 29.0	···
Semimajor axis a (AU)	2.42 ± 0.04	2.40	2.34, 2.50	···
Total mass $M_{\rm tot}$ ($M_{\rm Jup}$)	128^{+7}_{-8}	126	115, 143	···

Table 33. MCMC Posteriors for the Orbit and Parallax of 2MASS J2140+1625AB

Property	Median $\pm 1\sigma$	Best fit	95.4% c.i.	Prior/Notes
		Fitted parameters		
Orbital period P (yr)	24.45 ± 0.25	24.34	23.95, 24.96	$1/P$ (log-flat)
Semimajor axis a (mas)	143.0 ± 1.4	142.5	140.2, 145.8	$1/a$ (log-flat)
Eccentricity e	0.196 ± 0.007	0.193	0.181, 0.211	uniform, $0 \leq e < 1$
Inclination i (°)	37.3 ± 0.6	37.2	36.0, 38.6	$\sin(i)$, $0° < i < 180°$
PA of the ascending node Ω (°)	100.5 ± 0.6	100.3	99.3, 101.8	uniform
Argument of periastron ω (°)	$186.6^{+1.1}_{-1.2}$	186.7	184.4, 189.0	uniform
Mean longitude at 2455197.5 JD $\lambda_{\rm ref}$ (°)	$176.4^{+0.6}_{-0.7}$	176.5	175.2, 177.7	uniform
RA − $\rm RA_{2010}$ (mas)	0.2 ± 1.1	0.0	−2.1, 2.5	uniform, $\rm RA_{2010}$ = 325.1220654
Dec − $\rm Dec_{2010}$ (mas)	0.1 ± 1.1	0.0	−2.1, 2.2	uniform, $\rm Dec_{2010}$ = +16.4215747
Relative proper motion in RA $\mu_{\rm RA,rel}$ (mas yr^{-1})	$-69.2^{+0.6}_{-0.7}$	−69.1	−70.4, −67.9	uniform
Relative proper motion in Dec $\mu_{\rm Dec,rel}$ (mas yr^{-1})	-76.3 ± 0.5	−76.3	−77.3, −75.3	uniform
Relative parallax $\pi_{\rm rel}$ (mas)	$29.2^{+0.9}_{-0.8}$	29.0	27.5, 30.9	$1/\pi^2$ (uniform volume density)
Ratio of photocenter orbit to semimajor axis α/a	$0.042^{+0.026}_{-0.025}$	0.042	−0.009, 0.093	uniform
		Derived properties		
Total mass at fixed distance $a^3P^{-2}(d/32.9\rm pc)^3$ ($M_{\rm Jup}$)	$183.3^{+2.1}_{-2.2}$	183.1	179.0, 187.5	···
Time of periastron T_0 (JD)	2464380 ± 90	2464340	2464210, 2464560	···
Photocenter semimajor axis α (mas)	6 ± 4	6	−1, 13	···
Correction to absolute RA proper motion $\Delta\mu_{\rm RA}$ (mas yr^{-1})	-0.4 ± 1.5	−0.4	−3.1, 2.9	···
Correction to absolute Dec proper motion $\Delta\mu_{\rm Dec}$ (mas yr^{-1})	-3.9 ± 1.4	−3.9	−6.9, −1.3	···
Correction to absolute parallax $\Delta\pi$ (mas)	$1.16^{+0.15}_{-0.18}$	1.16	0.87, 1.54	···
Absolute proper motion in RA $\mu_{\rm RA,abs}$ (mas yr^{-1})	-69.5 ± 1.6	−69.5	−72.7, −66.2	···
Absolute proper motion in Dec $\mu_{\rm Dec,abs}$ (mas yr^{-1})	-80.2 ± 1.5	−80.2	−83.2, −77.2	···
Absolute parallax $\pi_{\rm abs}$ (mas)	$30.4^{+0.9}_{-0.8}$	30.2	28.6, 32.1	···
Distance d (pc)	$32.9^{+0.9}_{-1.0}$	33.1	31.1, 34.8	···
Semimajor axis a (AU)	4.71 ± 0.14	4.72	4.43, 5.00	···
Total mass $M_{\rm tot}$ ($M_{\rm Jup}$)	183^{+14}_{-17}	186	153, 216	···

Table 34. MCMC Posteriors for the Orbit and Parallax of 2MASS J2206−2047AB

Property	Median $\pm 1\sigma$	Best fit	95.4% c.i.	Prior/Notes
Fitted parameters				
Orbital period P (yr)	$23.96^{+0.23}_{-0.21}$	23.98	23.55, 24.35	$1/P$ (log-flat)
Semimajor axis a (mas)	167.7 ± 0.5	167.9	166.8, 168.7	$1/a$ (log-flat)
Eccentricity e	0.015 ± 0.008	0.015	0.000, 0.027	uniform, $0 \leq e < 1$
Inclination i (°)	43.8 ± 0.5	43.8	42.9, 44.7	$\sin(i)$, $0° < i < 180°$
PA of the ascending node Ω (°)	77.6 ± 0.4	77.5	76.9, 78.4	uniform
Argument of periastron ω (°)	96 ± 13	98	42, 168	uniform
Mean longitude at 2455197.5 JD $\lambda_{\rm ref}$ (°)	115.7 ± 0.4	115.9	115.0, 116.5	uniform
RA − RA$_{2010}$ (mas)	$0.3^{+1.1}_{-1.2}$	0.3	−2.0, 2.5	uniform, RA$_{2010}$ = 331.5951921
Dec − Dec$_{2010}$ (mas)	$-0.4^{+0.9}_{-0.8}$	−0.7	−2.1, 1.4	uniform, Dec$_{2010}$ = −20.7847000
Relative proper motion in RA $\mu_{\rm RA,rel}$ (mas yr^{-1})	19.0 ± 0.6	19.1	17.8, 20.2	uniform
Relative proper motion in Dec $\mu_{\rm Dec,rel}$ (mas yr^{-1})	$-32.0^{+0.7}_{-0.6}$	−31.9	−33.3, −30.7	uniform
Relative parallax $\pi_{\rm rel}$ (mas)	34.5 ± 1.0	34.4	32.5, 36.6	$1/\pi^2$ (uniform volume density)
Ratio of photocenter orbit to semimajor axis α/a	$-0.033^{+0.029}_{-0.027}$	−0.035	−0.091, 0.023	uniform
Derived properties				
Total mass at fixed distance $a^3P^{-2}(d/28.0\rm pc)^3$ ($M_{\rm Jup}$)	$188.3^{+2.9}_{-3.1}$	188.3	183.0, 194.0	···
Time of periastron T_0 (JD)	2463500^{+300}_{-400}	2463500	2462000, 2465100	···
Photocenter semimajor axis α (mas)	-5 ± 5	−6	−15, 4	···
Correction to absolute RA proper motion $\Delta\mu_{\rm RA}$ (mas yr^{-1})	1.7 ± 1.6	0.0	−1.3, 4.8	···
Correction to absolute Dec proper motion $\Delta\mu_{\rm Dec}$ (mas yr^{-1})	-3.7 ± 1.2	−2.1	−6.3, −1.3	···
Correction to absolute parallax $\Delta\pi$ (mas)	$1.28^{+0.15}_{-0.16}$	1.55	0.99, 1.62	···
Absolute proper motion in RA $\mu_{\rm RA,abs}$ (mas yr^{-1})	20.7 ± 1.7	19.1	17.5, 24.1	···
Absolute proper motion in Dec $\mu_{\rm Dec,abs}$ (mas yr^{-1})	-35.7 ± 1.4	−34.0	−38.6, −32.9	···
Absolute parallax $\pi_{\rm abs}$ (mas)	35.8 ± 1.0	35.9	33.7, 37.8	···
Distance d (pc)	$28.0^{+0.7}_{-0.9}$	27.9	26.4, 29.6	···
Semimajor axis a (AU)	$4.69^{+0.13}_{-0.14}$	4.68	4.43, 4.97	···
Total mass $M_{\rm tot}$ ($M_{\rm Jup}$)	188^{+16}_{-17}	186	158, 223	···

Table 35. MCMC Posteriors for the Orbit and Parallax of DENIS J2252−1730AB

Property	Median $\pm 1\sigma$	Best fit	95.4% c.i.	Prior/Notes
		Fitted parameters		
Orbital period P (yr)	$8.822^{+0.026}_{-0.027}$	8.832	8.771, 8.876	$1/P$ (log-flat)
Semimajor axis a (mas)	$123.3^{+0.8}_{-0.7}$	123.2	121.8, 124.8	$1/a$ (log-flat)
Eccentricity e	0.334 ± 0.009	0.335	0.316, 0.352	uniform, $0 \leq e < 1$
Inclination i (°)	108.6 ± 0.5	108.8	107.6, 109.6	$\sin(i)$, $0° < i < 180°$
PA of the ascending node Ω (°)	178.0 ± 0.3	178.0	177.4, 178.7	uniform
Argument of periastron ω (°)	314.6 ± 1.2	314.6	312.3, 317.0	uniform
Mean longitude at 2455197.5 JD $\lambda_{\rm ref}$ (°)	57.6 ± 0.6	57.6	56.4, 58.9	uniform
RA − $\rm RA_{2010}$ (mas)	$-0.6^{+1.5}_{-1.6}$	0.0	−3.7, 2.6	uniform, $\rm RA_{2010} = 343.0460008$
Dec − $\rm Dec_{2010}$ (mas)	$0.2^{+2.2}_{-2.1}$	0.0	−4.1, 4.5	uniform, $\rm Dec_{2010} = -17.5031371$
Relative proper motion in RA $\mu_{\rm RA,rel}$ (mas yr^{-1})	$404.42^{+0.29}_{-0.28}$	404.36	403.85, 404.99	uniform
Relative proper motion in Dec $\mu_{\rm Dec,rel}$ (mas yr^{-1})	143.0 ± 0.4	143.0	142.3, 143.8	uniform
Relative parallax $\pi_{\rm rel}$ (mas)	$61.9^{+1.3}_{-1.4}$	61.2	59.2, 64.6	$1/\pi^2$ (uniform volume density)
Ratio of photocenter orbit to semimajor axis α/a	$0.081^{+0.027}_{-0.028}$	0.086	0.026, 0.136	uniform
		Derived properties		
Total mass at fixed distance $a^3P^{-2}(d/15.9{\rm pc})^3$ ($M_{\rm Jup}$)	$100.5^{+2.1}_{-2.0}$	100.2	96.4, 104.6	···
Time of periastron T_0 (JD)	2460720 ± 23	2460727	2460676, 2460767	···
Photocenter semimajor axis α (mas)	10 ± 3	11	3, 17	···
Correction to absolute RA proper motion $\Delta\mu_{\rm RA}$ (mas yr^{-1})	2.0 ± 1.3	2.0	−0.4, 4.7	···
Correction to absolute Dec proper motion $\Delta\mu_{\rm Dec}$ (mas yr^{-1})	-4.5 ± 1.1	−4.5	−6.9, −2.4	···
Correction to absolute parallax $\Delta\pi$ (mas)	$1.19^{+0.12}_{-0.14}$	1.19	0.93, 1.47	···
Absolute proper motion in RA $\mu_{\rm RA,abs}$ (mas yr^{-1})	406.5 ± 1.3	406.4	404.0, 409.2	···
Absolute proper motion in Dec $\mu_{\rm Dec,abs}$ (mas yr^{-1})	138.5 ± 1.2	138.5	136.0, 140.8	···
Absolute parallax $\pi_{\rm abs}$ (mas)	$63.1^{+1.4}_{-1.3}$	62.4	60.4, 65.8	···
Distance d (pc)	15.9 ± 0.3	16.0	15.2, 16.6	···
Semimajor axis a (AU)	1.95 ± 0.04	1.97	1.87, 2.04	···
Total mass $M_{\rm tot}$ ($M_{\rm Jup}$)	101 ± 7	103	88, 115	···

Table 36. Summary of MCMC Results

Name	13-parameter fit		Relative orbit		Acceptance fraction
	χ^2	d.o.f.	χ^2	d.o.f.	
LP 349-25AB	45.1	51	12.6	17	0.369
LP 415-20AB	50.9	69	20.2	17	0.292
SDSS J0423−0414AB	53.5	59	12.1	15	0.369
2MASS J0700+3157AB	70.1	65	35.6	33	0.132
LHS 1901AB	48.5	47	24.8	23	0.369
2MASS J0746+2000AB	42.2	41	8.9	13	0.369
2MASS J0850+1057AB	51.0	43	16.7	15	0.068
2MASS J0920+3517AB	90.2	89	42.1	43	0.368
SDSS J0926+5847AB	29.9	29	7.7	7	0.170
2MASS J1017+1308AB	50.4	49	11.5	11	0.355
SDSS J1021−0304AB	27.9	25	9.1	7	0.056
2MASS J1047+4026AB	74.8	61	17.4	15	0.369
SDSS J1052+4422AB	66.2	67	17.0	23	0.369
Gl 417BC	⋯	⋯	21.6	17	0.485
LHS 2397aAB	74.6	79	25.4	23	0.369
DENIS J1228−1557AB	38.6	47	14.8	27	0.093
Kelu-1AB	39.1	43	13.9	25	0.321
2MASS J1404−3159AB	67.0	55	13.5	13	0.090
HD 130948BC	⋯	⋯	36.9	31	0.486
Gl 569Bab	⋯	⋯	37.1	31	0.486
SDSS J1534+1615AB	30.3	31	5.0	5	0.072
2MASS J1534−2952AB	66.6	63	34.6	31	0.170
2MASS J1728+3948AB	50.0	63	16.8	33	0.068
LSPM J1735+2634AB	62.7	57	18.4	21	0.367
2MASS J1750+4424AB	31.1	31	6.0	5	0.053
2MASS J1847+5522AB	45.4	39	15.6	13	0.056
SDSS J2052−1609AB	59.3	61	19.9	19	0.087
2MASS J2132+1341AB	75.9	75	18.4	21	0.364
2MASS J2140+1625AB	63.5	65	33.4	27	0.368
2MASS J2206−2047AB	51.8	61	14.1	13	0.230
DENIS J2252−1730AB	51.4	57	18.4	21	0.369

Note. — The minimum χ^2 and degrees of freedom (d.o.f.) for the full 13-parameter MCMC fits are given for all objects with absolute astrometry from CFHT/WIRCam. We also report the χ^2 of the best-fit solution computed using only the relative orbit data (Keck, *HST*, etc.). The last column gives the mean final acceptance fraction for the MCMC analysis as reported by `emcee`, averaging over all parameters and walkers.

Table 37. Summary of Orbit Quality Metrics

Name	SpT (A+B)	Orbit Quality Metrics: $\Delta \log M_{\rm tot}$ (dex)	Δe	$\Delta t_{\rm obs}/P$	P (yr)	$M_{\rm tot}$ ($M_{\rm Jup}$)
Orbit Determinations Used in Our Analysis						
LP 349-25AB	M7+M8	0.0035	0.0037	0.978	7.698 ± 0.014	166^{+6}_{-7}
LP 415-20AB	M6+M8	0.0586	0.0233	0.673	14.82 ± 0.24	248^{+26}_{-29}
SDSS J0423−0414AB	L6.5+T2	0.0093	0.0147	0.659	12.30 ± 0.06	83 ± 3
2MASS J0700+3157AB	L3+L6.5	0.0035	0.0128	0.431	23.9 ± 0.5	141^{+4}_{-5}
LHS 1901AB	M7+M7	0.0029	0.0017	0.497	16.21 ± 0.08	213^{+9}_{-10}
2MASS J0746+2000AB	L0+L1.5	0.0050	0.0007	0.760	$12.736^{+0.031}_{-0.029}$	163 ± 5
2MASS J0920+3517AB	L5.5+L9	0.0098	0.0130	1.822	7.258 ± 0.009	187 ± 11
2MASS J1017+1308AB	L1.5+L3	0.0119	0.0196	0.647	$18.60^{+0.22}_{-0.23}$	156^{+14}_{-18}
2MASS J1047+4026AB	M8+L0	0.0048	0.0027	2.136	$6.562^{+0.029}_{-0.026}$	178^{+11}_{-12}
SDSS J1052+4422AB	L6.5+T1.5	0.0096	0.0046	1.048	$8.608^{+0.025}_{-0.024}$	90^{+4}_{-5}
Gl 417BC	L4.5+L6	0.0114	0.0064	0.846	15.65 ± 0.08	$99.2^{+3.0}_{-3.3}$
LHS 2397aAB	M8+null	0.0072	0.0063	1.178	14.37 ± 0.05	159^{+7}_{-8}
Kelu-1AB	L2+L4	0.0053	0.0098	0.667	24.98 ± 0.19	180^{+22}_{-26}
2MASS J1404−3159AB	L9+T5	0.0445	0.0106	0.536	$16.52^{+0.21}_{-0.22}$	120^{+11}_{-13}
HD 130948BC	L4+L4	0.0023	0.0034	1.063	10.009 ± 0.010	$115.4^{+2.2}_{-2.1}$
Gl 569Bab	M8.5+M9	0.0040	0.0020	5.006	2.3707 ± 0.0005	138 ± 7
2MASS J1534−2952AB	T4.5+T5	0.0060	0.0055	0.719	$20.35^{+0.05}_{-0.06}$	99 ± 5
2MASS J1728+3948AB	L5+L7	0.0089	0.0277	0.337	$40.8^{+1.6}_{-1.2}$	140^{+7}_{-8}
LSPM J1735+2634AB	M7.5+L0	0.0017	0.0075	0.286	$21.65^{+0.24}_{-0.23}$	187 ± 7
2MASS J2132+1341AB	L4.5+L8.5	0.0192	0.0094	0.576	$10.74^{+0.16}_{-0.17}$	128^{+7}_{-8}
2MASS J2140+1625AB	M8+L0.5	0.0101	0.0146	0.612	24.45 ± 0.25	183^{+14}_{-17}
2MASS J2206−2047AB	M8+M8	0.0140	0.0160	0.578	$23.96^{+0.23}_{-0.21}$	188^{+16}_{-17}
DENIS J2252−1730AB	L4+T3.5	0.0176	0.0182	0.945	$8.822^{+0.026}_{-0.027}$	101 ± 7
Marginal Orbit Determinations						
DENIS J1228−1557AB	L5.5+L5.5	0.1201	0.0623	0.292	50^{+5}_{-7}	106^{+16}_{-19}
2MASS J1847+5522AB	M6+M7	0.0346	0.1363	0.216	45^{+5}_{-3}	270^{+26}_{-31}
Poorly Constrained Orbits						
2MASS J0850+1057AB	L6.5+L8.5	0.1167	0.1118	0.310	48^{+7}_{-6}	54 ± 8
SDSS J0926+5847AB	T3.5+T5	0.3815	0.3761	0.682	$12.9^{+1.3}_{-1.9}$	38^{+10}_{-18}
SDSS J1021−0304AB	T0+T5	0.0600	0.1435	0.101	86^{+13}_{-17}	52^{+6}_{-7}
SDSS J1534+1615AB	T0+T5.5	0.0881	0.4296	0.175	58^{+39}_{-24}	46^{+6}_{-7}
2MASS J1750+4424AB	M6.5+M8.5	0.1963	0.1523	0.038	210^{+40}_{-60}	190^{+40}_{-50}
SDSS J2052−1609AB	L8.5+T1.5	0.2291	0.2069	0.195	44^{+10}_{-14}	69^{+14}_{-20}

Table 37—Continued

Name	SpT (A+B)	Orbit Quality Metrics $\Delta \log M_{\rm tot}$ (dex)	Δe	$\Delta t_{\rm obs}/P$	P (yr)	$M_{\rm tot}$ ($M_{\rm Jup}$)

Note. — $\Delta \log M_{\rm tot}$ is defined as the difference between the maximum and minimum values of the 68.3% (1σ) credible interval of the total mass posterior distribution *without* including the uncertainty in the distance. Likewise, Δe is the difference between the maximum and minimum values of the 1σ credible interval of the eccentricity posterior distribution. $\Delta t_{\rm obs}/P$ is the time baseline of the resolved astrometry used in the orbit fit divided by the median of the orbital period psoterior distribution. For convenience, we also list here the median and 1σ credible intervals of the orbital period and the total mass *including* the uncertainty on the distance.

Table 38. Comparison of Parallaxes and Proper Motions to Literature Values

Object	Absolute Parallax (mas)				ΔProper Motion (mas/yr)[a]		Ref.
	Here	Lit.	Difference		RA	Dec.	
LP 349-25AB	69.2 ± 0.9	75.8 ± 1.6	1.9σ	10%	7	18	Gate09
SDSS J0423−0414AB	71.1 ± 0.8	65.9 ± 1.7	-1.5σ	−7%	-1.3 ± 2.9	-6.2 ± 1.9	Vrba04
SDSS J0423−0414AB	71.1 ± 0.8	67.5 ± 2.3	-0.6σ	−5%	0.6 ± 1.4	-6.0 ± 1.3	Wein16
2MASS J0700+3157AB	88.6 ± 0.9	82.0 ± 2.0	-1.4σ	−7%	7.1 ± 1.0	7.2 ± 1.1	Thor03
LHS 1901AB	76.4 ± 1.1	78 ± 3	0.1σ	2%	2	−8	Lepi09
2MASS J0746+2000AB	80.9 ± 0.8	86 ± 5	0.2σ	6%	9 ± 5	-11 ± 5	Fahe12
2MASS J0746+2000AB	80.9 ± 0.8	81.9 ± 0.3	1.3σ	1%	-8.9 ± 0.9	-4.8 ± 1.2	Dahn02
2MASS J0850+1057AB	31.4 ± 0.6	39 ± 4	0.6σ	24%	3 ± 3	7.8 ± 2.7	Dahn02
2MASS J0850+1057AB	31.4 ± 0.6	26 ± 4	-0.3σ	−17%	1 ± 7	-5 ± 3	Vrba04
2MASS J0850+1057AB	31.4 ± 0.6	35 ± 8	0.1σ	11%	3 ± 6	-23 ± 6	Fahe11
SDSS J1021−0304AB	33.7 ± 1.2	41 ± 11	0.1σ	21%	23 ± 16	-1 ± 9	Vrba04
SDSS J1021−0304AB	33.7 ± 1.2	34 ± 5	0.0σ	2%	16 ± 9	5 ± 4	Tinn03
LHS 2397aAB	68.2 ± 1.1	65.8 ± 2.0	-0.5σ	−4%	-10.8 ± 1.7	12.0 ± 1.6	Diet14
LHS 2397aAB	68.2 ± 1.1	70.0 ± 2.1	0.3σ	3%	28.9 ± 1.8	8.5 ± 1.5	Mone92
DENIS J1228−1557AB	48.0 ± 1.7	49.4 ± 1.9	0.2σ	3%	30 ± 30	31 ± 27	Dahn02
Kelu-1AB	48.0 ± 2.2	53.6 ± 2.0	0.6σ	12%	15 ± 8	13 ± 5	Dahn02
Kelu-1AB	48.0 ± 2.2	51.8 ± 1.2	0.6σ	8%	1 ± 8	-7 ± 5	Wein16
2MASS J1404−3159AB	42.5 ± 1.1	49 ± 3	0.5σ	16%	3.7 ± 2.0	5.8 ± 2.5	Maro13
2MASS J1404−3159AB	42.5 ± 1.1	40 ± 6	-0.1σ	−6%	1 ± 5	7 ± 5	Fahe12
2MASS J1534−2952AB	63.0 ± 1.1	73.6 ± 1.2	3.9σ	17%	4.7 ± 1.1	11.1 ± 2.4	Tinn03
2MASS J1728+3948AB	36.4 ± 0.6	42 ± 3	0.4σ	14%	2 ± 6	-4 ± 5	Vrba04
SDSS J2052−1609AB	33.7 ± 0.7	27 ± 9	-0.1σ	−21%	10 ± 11	21 ± 10	Fahe12
2MASS J2132+1341AB	35.6 ± 0.6	30 ± 8	-0.1σ	−16%	0 ± 12	-15 ± 11	Fahe12
2MASS J2206−2047AB	35.8 ± 1.0	38 ± 3	0.1σ	5%	-2 ± 7	5 ± 5	Cost06
Previously Published CFHT Parallaxes							
LP 349-25AB	69.2 ± 0.9	69.6 ± 0.9	0.2σ	1%	-3.9 ± 2.0	5.0 ± 2.0	Dupu12
SDSS J0423−0414AB	71.1 ± 0.8	72.1 ± 1.1	0.5σ	1%	-6.0 ± 1.1	3.1 ± 1.3	Dupu12
2MASS J0700+3157AB	88.6 ± 0.9	86.7 ± 1.2	-0.8σ	−2%	20.0 ± 1.0	-1.6 ± 1.1	Dupu12
LHS 1901AB	76.4 ± 1.1	74.2 ± 1.0	-1.0σ	−3%	-1.8 ± 1.5	0 ± 3	Dupu12
2MASS J0746+2000AB	80.9 ± 0.8	81.1 ± 0.9	0.1σ	0%	-0.8 ± 1.1	0.4 ± 1.1	Dupu12
2MASS J0850+1057AB	31.4 ± 0.6	30.1 ± 0.8	-1.2σ	−4%	2.9 ± 2.4	2.8 ± 1.5	Dupu12
2MASS J0920+3517AB	32.3 ± 0.6	34.4 ± 0.8	2.0σ	6%	-2.3 ± 1.5	2.6 ± 1.3	Dupu12
SDSS J0926+5847AB	43.4 ± 1.0	43.7 ± 1.1	0.1σ	1%	-1.9 ± 1.4	3.3 ± 1.3	Dupu12
2MASS J1017+1308AB	32.3 ± 1.1	30.2 ± 1.4	-0.6σ	−6%	0.9 ± 2.0	5.0 ± 1.9	Dupu12
SDSS J1021−0304AB	33.7 ± 1.2	29.9 ± 1.3	-1.2σ	−11%	24 ± 8	-3.2 ± 2.1	Dupu12
SDSS J1052+4422AB	38.1 ± 0.6	38.4 ± 0.7	0.3σ	1%	-2 ± 3	-2 ± 3	Dupu15
LHS 2397aAB	68.2 ± 1.1	73.0 ± 2.1	0.9σ	7%	7.0 ± 3.0	-2.6 ± 2.1	Dupu12
DENIS J1228−1557AB	48.0 ± 1.7	44.8 ± 1.8	-0.5σ	−7%	30 ± 30	25 ± 27	Dupu12
Kelu-1AB	48.0 ± 2.2	49.7 ± 2.4	0.2σ	4%	1 ± 9	-2 ± 5	Dupu12
2MASS J1404−3159AB	42.5 ± 1.1	42.1 ± 1.1	-0.2σ	−1%	10.9 ± 1.1	11.4 ± 1.6	Dupu12
SDSS J1534+1615AB	27.6 ± 0.9	24.9 ± 1.1	-1.4σ	−10%	-1.1 ± 1.7	4.2 ± 1.2	Dupu12
2MASS J1534−2952AB	63.0 ± 1.1	62.4 ± 1.3	-0.2σ	−1%	2.2 ± 1.2	2.2 ± 2.0	Dupu12
2MASS J1728+3948AB	36.4 ± 0.6	38.7 ± 0.7	2.5σ	6%	1.0 ± 0.8	3.6 ± 1.0	Dupu12
LSPM J1735+2634AB	64.7 ± 0.8	66.7 ± 1.4	0.7σ	3%	-1.3 ± 1.1	-3.9 ± 1.5	Dupu12
2MASS J1750+4424AB	32.4 ± 0.9	30.3 ± 1.0	-1.1σ	−6%	30 ± 60	-7 ± 29	Dupu12
2MASS J1847+5522AB	27.4 ± 0.9	29.8 ± 1.1	1.2σ	9%	-0.9 ± 1.1	2.3 ± 1.6	Dupu12
SDSS J2052−1609AB	33.7 ± 0.7	33.9 ± 0.8	0.1σ	1%	-0.7 ± 0.8	2.9 ± 1.5	Dupu12
2MASS J2132+1341AB	35.6 ± 0.6	36.0 ± 0.7	0.4σ	1%	3.0 ± 1.4	3.3 ± 0.9	Dupu12
2MASS J2140+1625AB	30.4 ± 0.9	32.5 ± 1.1	1.1σ	7%	0.9 ± 1.8	-2.5 ± 1.7	Dupu12
2MASS J2206−2047AB	35.8 ± 1.0	35.7 ± 1.2	-0.0σ	0%	-7.7 ± 1.9	3.9 ± 1.8	Dupu12
DENIS J2252−1730AB	63.1 ± 1.4	63.2 ± 1.6	0.0σ	0%	-9.2 ± 2.0	6 ± 4	Dupu12

References. — Cost06 = Costa et al. (2006); Dahn02 = Dahn et al. (2002); Diet14 = Dieterich et al. (2014); Dupu12 = Dupuy & Liu (2012); Dupu15 = Dupuy et al. (2015b); Fahe11 = Faherty et al. (2011); Fahe12 = Faherty et al. (2012); Gate09 = Gatewood & Coban (2009); Lepi09 = Lépine et al. (2009); Maro13 = Marocco et al. (2013); Mone92 = Monet et al. (1992); Thor03 = Thorstensen & Kirkpatrick (2003); Tinn03 = Tinney et al. (2003); Vrba04 = Vrba et al. (2004); Wein16 = Weinberger et al. (2016).

[a]The difference between our absolute proper motions and literature values that are typically reported as relative.

Table 39. Apparent Magnitudes for the Sample

Filter	Integrated	$\Delta m = m_{\rm B} - m_{\rm A}$	$m_{\rm A}$	$m_{\rm B}$	References
			LP 349-25AB		
MKO J	10.563 ± 0.022	0.350 ± 0.030	11.155 ± 0.025	11.505 ± 0.028	Cutr03, Dupu10, Dupu12
MKO H	10.005 ± 0.023	0.326 ± 0.011	10.607 ± 0.023	10.933 ± 0.024	Cutr03, Dupu10, Dupu12
MKO K	9.540 ± 0.017	0.307 ± 0.008	10.150 ± 0.017	10.457 ± 0.018	Cutr03, Dupu10, Dupu12
2MASS J	10.615 ± 0.025	0.346 ± 0.037	11.208 ± 0.029	11.555 ± 0.032	Cutr03, Dupu10, Dupu12, Dupu16
2MASS H	9.976 ± 0.023	0.320 ± 0.012	10.580 ± 0.024	10.900 ± 0.024	Cutr03, Dupu10, Dupu12, Dupu16
2MASS K_S	9.569 ± 0.017	0.318 ± 0.007	10.174 ± 0.017	10.492 ± 0.017	Cutr03, Dupu10
			LP 415-20AB		
MKO J	12.661 ± 0.021	0.715 ± 0.024	13.114 ± 0.023	13.829 ± 0.026	Dupu16
MKO H	12.100 ± 0.022	0.652 ± 0.011	12.575 ± 0.022	13.227 ± 0.023	Dupu16
MKO K	11.641 ± 0.021	0.567 ± 0.030	12.146 ± 0.024	12.714 ± 0.028	Cutr03, Dupu16
2MASS J	12.715 ± 0.024	0.708 ± 0.032	13.170 ± 0.027	13.878 ± 0.030	Dupu16
2MASS H	12.072 ± 0.022	0.641 ± 0.012	12.551 ± 0.023	13.192 ± 0.023	Dupu16
2MASS K_S	11.668 ± 0.020	0.566 ± 0.029	12.174 ± 0.023	12.740 ± 0.027	Cutr03, Dupu16
			SDSS J0423−0414AB		
MKO J	14.300 ± 0.030	0.420 ± 0.060	14.863 ± 0.039	15.283 ± 0.047	Dupu12, Legg02a
MKO H	13.510 ± 0.030	0.720 ± 0.050	13.961 ± 0.034	14.681 ± 0.045	Dupu12, Legg02a
MKO K	12.960 ± 0.030	1.180 ± 0.080	13.276 ± 0.036	14.456 ± 0.067	Dupu12, Legg02a
2MASS J	14.432 ± 0.032	0.473 ± 0.064	14.974 ± 0.041	15.448 ± 0.049	Dupu12, Dupu16, Legg02a
2MASS H	13.452 ± 0.030	0.720 ± 0.050	13.903 ± 0.035	14.623 ± 0.045	Dupu12, Dupu16, Legg02a
2MASS K_S	12.929 ± 0.034	1.110 ± 0.080	13.263 ± 0.040	14.373 ± 0.068	Cutr03, Dupu12
$F110W$	15.280 ± 0.050	0.535 ± 0.022	15.798 ± 0.051	16.333 ± 0.052	Burg06b, Dupu16
$F170M$	13.620 ± 0.050	0.818 ± 0.012	14.039 ± 0.050	14.857 ± 0.051	Burg06b, Dupu16
			2MASS J0700+3157AB		
MKO J	12.843 ± 0.023	1.487 ± 0.021	13.089 ± 0.023	14.576 ± 0.028	Cutr03, Dupu12, Dupu16
MKO H	11.997 ± 0.016	1.403 ± 0.017	12.260 ± 0.016	13.664 ± 0.021	Cutr03, Dupu12, Dupu16

Table 39—Continued

Filter	Integrated	$\Delta m = m_B - m_A$	m_A	m_B	References
MKO K	11.294 ± 0.023	1.393 ± 0.017	11.560 ± 0.023	12.953 ± 0.027	Cutr03, Dupu12, Dupu16
2MASS J	12.921 ± 0.026	1.537 ± 0.030	13.157 ± 0.028	14.694 ± 0.032	Cutr03, Dupu12, Dupu16
2MASS H	11.943 ± 0.016	1.397 ± 0.018	12.207 ± 0.017	13.605 ± 0.021	Cutr03, Dupu12, Dupu16
2MASS K_S	11.316 ± 0.023	1.390 ± 0.019	11.583 ± 0.024	12.973 ± 0.027	Cutr03, Dupu12, Dupu16
$F110W$	13.170 ± 0.050	1.600 ± 0.050	13.394 ± 0.051	14.994 ± 0.064	Dupu16, Reid06a
$F170M$	11.270 ± 0.050	1.476 ± 0.021	11.518 ± 0.050	12.994 ± 0.053	Dupu16, Reid06a
			LHS 1901AB		
MKO J	9.933 ± 0.018	0.111 ± 0.016	10.632 ± 0.020	10.743 ± 0.020	Cutr03, Dupu10, Dupu12
MKO H	9.500 ± 0.016	0.115 ± 0.009	10.197 ± 0.017	10.312 ± 0.017	Cutr03, Dupu10, Dupu12
MKO K	9.095 ± 0.018	0.107 ± 0.007	9.795 ± 0.018	9.902 ± 0.018	Cutr03, Dupu10, Dupu12
2MASS J	9.988 ± 0.021	0.109 ± 0.027	10.688 ± 0.025	10.797 ± 0.025	Cutr03, Dupu10, Dupu12, Dupu16
2MASS H	9.475 ± 0.016	0.113 ± 0.011	10.173 ± 0.017	10.285 ± 0.017	Cutr03, Dupu10, Dupu12, Dupu16
2MASS K_S	9.126 ± 0.018	0.094 ± 0.003	9.833 ± 0.018	9.927 ± 0.018	Cutr03, Dupu10
			2MASS J0746+2000AB		
MKO J	11.640 ± 0.030	0.526 ± 0.010	12.161 ± 0.030	12.687 ± 0.031	Dupu16, Legg02a
MKO H	11.010 ± 0.030	0.440 ± 0.030	11.565 ± 0.032	12.005 ± 0.035	Kono10, Legg02a
MKO K	10.430 ± 0.030	0.347 ± 0.008	11.023 ± 0.030	11.370 ± 0.030	Dupu16, Legg02a
2MASS J	11.695 ± 0.032	0.532 ± 0.023	12.214 ± 0.034	12.746 ± 0.034	Dupu16, Legg02a
2MASS H	10.962 ± 0.030	0.436 ± 0.031	11.518 ± 0.033	11.955 ± 0.035	Dupu16, Kono10, Legg02a
2MASS K_S	10.468 ± 0.022	0.357 ± 0.025	11.057 ± 0.024	11.414 ± 0.026	Cutr03, Kono10
			2MASS J0850+1057AB		
MKO J	16.200 ± 0.030	1.340 ± 0.130	16.479 ± 0.042	17.819 ± 0.105	Dupu16, Legg02a
MKO H	15.210 ± 0.030	1.060 ± 0.090	15.558 ± 0.039	16.618 ± 0.072	Dupu16, Legg02a
MKO K	14.350 ± 0.030	0.869 ± 0.104	14.754 ± 0.044	15.623 ± 0.078	Dupu16, Legg02a
2MASS J	16.307 ± 0.032	1.377 ± 0.132	16.578 ± 0.045	17.955 ± 0.106	Dupu16, Legg02a
2MASS H	15.152 ± 0.030	1.059 ± 0.090	15.500 ± 0.039	16.559 ± 0.072	Dupu16, Legg02a

Table 39—Continued

Filter	Integrated	$\Delta m = m_\mathrm{B} - m_\mathrm{A}$	m_A	m_B	References
2MASS K_S	14.473 ± 0.066	0.840 ± 0.100	14.886 ± 0.073	15.726 ± 0.095	Cutr03, Dupu16
$F110W$	17.380 ± 0.070	1.190 ± 0.050	17.693 ± 0.071	18.883 ± 0.079	Burg11, Dupu16
$F170M$	15.360 ± 0.050	0.920 ± 0.040	15.747 ± 0.051	16.667 ± 0.057	Burg11, Dupu16
			2MASS J0920+3517AB		
MKO J	15.521 ± 0.063	0.275 ± 0.026	16.145 ± 0.064	16.420 ± 0.065	Cutr03, Dupu12, Dupu16
MKO H	14.730 ± 0.057	0.224 ± 0.034	15.376 ± 0.059	15.600 ± 0.060	Cutr03, Dupu12, Dupu16
MKO K	13.970 ± 0.061	0.426 ± 0.061	14.531 ± 0.066	14.957 ± 0.071	Cutr03, Dupu12, Dupu16
2MASS J	15.621 ± 0.064	0.292 ± 0.034	16.238 ± 0.066	16.530 ± 0.066	Cutr03, Dupu12, Dupu16
2MASS H	14.672 ± 0.057	0.223 ± 0.034	15.319 ± 0.059	15.542 ± 0.060	Cutr03, Dupu12, Dupu16
2MASS K_S	13.979 ± 0.061	0.336 ± 0.113	14.578 ± 0.078	14.914 ± 0.089	Cutr03, Dupu16
			SDSS J0926+5847AB		
MKO J	15.701 ± 0.065	0.210 ± 0.130	16.356 ± 0.088	16.566 ± 0.097	Cutr03, Dupu12
$F110W$	16.570 ± 0.050	0.410 ± 0.120	17.138 ± 0.070	17.548 ± 0.087	Burg06b, Dupu16
$F170M$	15.640 ± 0.050	0.840 ± 0.110	16.053 ± 0.061	16.893 ± 0.091	Burg06b, Dupu16
			2MASS J1017+1308AB		
MKO J	14.026 ± 0.024	0.201 ± 0.018	14.683 ± 0.025	14.884 ± 0.026	Cutr03, Dupu12, Dupu16
MKO H	13.331 ± 0.027	0.150 ± 0.040	14.011 ± 0.033	14.161 ± 0.034	Cutr03, Dupu12, Dupu16
MKO K	12.687 ± 0.023	0.124 ± 0.080	13.380 ± 0.044	13.504 ± 0.048	Cutr03, Dupu12, Dupu16
2MASS J	14.086 ± 0.026	0.204 ± 0.028	14.742 ± 0.030	14.945 ± 0.030	Cutr03, Dupu12, Dupu16
2MASS H	13.280 ± 0.027	0.149 ± 0.040	13.961 ± 0.033	14.110 ± 0.035	Cutr03, Dupu12, Dupu16
2MASS K_S	12.710 ± 0.023	0.113 ± 0.024	13.408 ± 0.026	13.521 ± 0.026	Cutr03, Dupu16
$F814W$	17.410 ± 0.050	0.270 ± 0.050	18.036 ± 0.055	18.306 ± 0.057	Dupu16, Gizi03
			SDSS J1021−0304AB		
MKO J	15.880 ± 0.030	-0.104 ± 0.012	16.686 ± 0.031	16.582 ± 0.031	Dupu16, Legg00
MKO H	15.410 ± 0.030	0.745 ± 0.023	15.853 ± 0.031	16.598 ± 0.034	Dupu16, Legg00

Table 39—Continued

Filter	Integrated	$\Delta m = m_{\rm B} - m_{\rm A}$	$m_{\rm A}$	$m_{\rm B}$	References
MKO $CH4_S$	15.222 ± 0.030	0.518 ± 0.030	15.746 ± 0.032	16.264 ± 0.035	Dupu12, Dupu16
MKO K	15.260 ± 0.030	1.134 ± 0.022	15.587 ± 0.031	16.721 ± 0.034	Dupu16, Legg00
2MASS J	16.049 ± 0.032	-0.051 ± 0.024	16.827 ± 0.034	16.777 ± 0.034	Dupu16, Legg00
2MASS H	15.351 ± 0.030	0.746 ± 0.024	15.794 ± 0.031	16.540 ± 0.034	Dupu16, Legg00
2MASS K_S	15.223 ± 0.029	1.023 ± 0.025	15.580 ± 0.029	16.603 ± 0.035	Dupu16, Legg00
$F170M$	15.830 ± 0.050	1.030 ± 0.019	16.185 ± 0.050	17.215 ± 0.052	Burg06b
		2MASS J1047+4026AB (a.k.a. LP 213-68)			
MKO J	12.386 ± 0.022	0.850 ± 0.250	12.801 ± 0.082	13.651 ± 0.173	Clos03, Dupu16
MKO H	11.736 ± 0.019	0.315 ± 0.179	12.346 ± 0.079	12.661 ± 0.104	Dupu16
MKO K	11.224 ± 0.018	0.289 ± 0.049	11.842 ± 0.028	12.131 ± 0.033	Dupu16
2MASS J	12.435 ± 0.025	0.850 ± 0.251	12.850 ± 0.084	13.700 ± 0.173	Clos03, Dupu16
2MASS H	11.699 ± 0.019	0.310 ± 0.179	12.311 ± 0.079	12.621 ± 0.104	Dupu16
2MASS K_S	11.254 ± 0.018	0.289 ± 0.049	11.872 ± 0.028	12.161 ± 0.033	Cutr03, Dupu16
		SDSS J1052+4422AB			
MKO J	15.890 ± 0.030	-0.450 ± 0.090	16.892 ± 0.062	16.442 ± 0.047	Chiu06, Dupu15
MKO H	15.090 ± 0.030	0.060 ± 0.070	15.814 ± 0.045	15.874 ± 0.047	Chiu06, Dupu15
MKO K	14.460 ± 0.030	0.520 ± 0.050	14.984 ± 0.036	15.504 ± 0.043	Chiu06, Dupu15
2MASS J	16.031 ± 0.032	-0.426 ± 0.092	17.018 ± 0.064	16.592 ± 0.049	Chiu06, Dupu15, Dupu16
2MASS H	15.031 ± 0.030	0.060 ± 0.070	15.755 ± 0.046	15.814 ± 0.047	Chiu06, Dupu15, Dupu16
2MASS K_S	14.461 ± 0.029	0.472 ± 0.048	15.003 ± 0.036	15.475 ± 0.039	Chiu06, Dupu15, Dupu16
		Gl 417BC			
MKO Y	15.802 ± 0.033	0.400 ± 0.040	16.373 ± 0.037	16.773 ± 0.041	Dupu12, Dupu14
MKO J	14.493 ± 0.033	0.440 ± 0.040	15.048 ± 0.037	15.488 ± 0.041	Cutr03, Dupu12, Dupu14
MKO H	13.560 ± 0.032	0.260 ± 0.090	14.191 ± 0.051	14.451 ± 0.060	Cutr03, Dupu12, Dupu14
MKO K	12.692 ± 0.028	0.347 ± 0.025	13.285 ± 0.030	13.632 ± 0.032	Cutr03, Dupu12
2MASS J	14.573 ± 0.035	0.452 ± 0.045	15.124 ± 0.040	15.575 ± 0.043	Cutr03, Dupu12, Dupu14, Dupu16

Table 39—Continued

Filter	Integrated	$\Delta m = m_{\rm B} - m_{\rm A}$	$m_{\rm A}$	$m_{\rm B}$	References
2MASS H	13.504 ± 0.032	0.258 ± 0.090	14.137 ± 0.051	14.395 ± 0.060	Cutr03, Dupu12, Dupu14, Dupu16
2MASS K_S	12.721 ± 0.028	0.412 ± 0.050	13.287 ± 0.035	13.699 ± 0.041	Cutr03, Dupu16
$F814W$	18.140 ± 0.050	0.550 ± 0.070	18.653 ± 0.057	19.203 ± 0.066	Dupu14, Gizi03
			LHS 2397aAB		
MKO J	11.830 ± 0.030	3.120 ± 0.080	11.890 ± 0.030	15.010 ± 0.081	Dupu09c, Legg02a
MKO H	11.260 ± 0.030	2.960 ± 0.050	11.329 ± 0.030	14.289 ± 0.056	Dupu09c, Legg02a
MKO $CH4_S$	11.281 ± 0.030	3.370 ± 0.240	11.330 ± 0.032	14.700 ± 0.231	Dupu09c, Dupu12
MKO K	10.690 ± 0.030	2.728 ± 0.033	10.775 ± 0.030	13.503 ± 0.043	Dupu16, Legg02a
2MASS J	11.882 ± 0.033	3.188 ± 0.083	11.938 ± 0.034	15.127 ± 0.083	Dupu09c, Dupu16, Legg02a
2MASS H	11.221 ± 0.030	2.939 ± 0.050	11.291 ± 0.030	14.230 ± 0.056	Dupu09c, Dupu16, Legg02a
2MASS K_S	10.735 ± 0.023	2.800 ± 0.030	10.814 ± 0.023	13.614 ± 0.036	Cutr03, Dupu09c
			DENIS J1228−1557AB		
MKO Y	15.526 ± 0.030	0.010 ± 0.030	16.274 ± 0.033	16.284 ± 0.034	Dupu12, Dupu16
MKO J	14.280 ± 0.050	0.105 ± 0.035	14.982 ± 0.053	15.086 ± 0.053	Dupu16, Legg02a
MKO H	13.400 ± 0.050	0.113 ± 0.011	14.098 ± 0.050	14.211 ± 0.050	Dupu16, Legg02a
MKO K	12.710 ± 0.050	0.122 ± 0.023	13.403 ± 0.051	13.525 ± 0.051	Dupu16, Legg02a
2MASS J	14.365 ± 0.051	0.109 ± 0.041	15.065 ± 0.055	15.174 ± 0.055	Dupu16, Legg02a
2MASS H	13.343 ± 0.050	0.112 ± 0.012	14.041 ± 0.050	14.154 ± 0.051	Dupu16, Legg02a
2MASS K_S	12.767 ± 0.030	0.126 ± 0.013	13.458 ± 0.031	13.584 ± 0.031	Cutr03, Dupu16
			Kelu-1AB		
MKO J	13.230 ± 0.050	0.700 ± 0.050	13.688 ± 0.053	14.388 ± 0.060	Dupu16, Legg02a
MKO H	12.450 ± 0.050	0.525 ± 0.030	12.972 ± 0.051	13.497 ± 0.053	Dupu16, Legg02a
MKO K	11.723 ± 0.023	0.408 ± 0.014	12.291 ± 0.024	12.698 ± 0.025	Cutr03, Dupu16
2MASS J	13.287 ± 0.051	0.708 ± 0.054	13.743 ± 0.055	14.451 ± 0.062	Dupu16, Legg02a
2MASS H	12.401 ± 0.050	0.521 ± 0.031	12.924 ± 0.051	13.445 ± 0.054	Dupu16, Legg02a
2MASS K_S	11.747 ± 0.023	0.407 ± 0.011	12.315 ± 0.023	12.722 ± 0.024	Cutr03, Dupu16

Table 39—Continued

Filter	Integrated	$\Delta m = m_B - m_A$	m_A	m_B	References
		2MASS J1404−3159AB			
MKO J	15.409 ± 0.063	-0.540 ± 0.030	16.465 ± 0.066	15.925 ± 0.064	Cutr03, Dupu12, Dupu16
MKO H	15.012 ± 0.067	0.544 ± 0.046	15.527 ± 0.069	16.071 ± 0.073	Cutr03, Dupu12, Dupu16
MKO $CH4_S$	14.854 ± 0.063	0.310 ± 0.017	15.463 ± 0.063	15.773 ± 0.064	Dupu12, Dupu16
MKO K	14.552 ± 0.095	1.402 ± 0.027	14.816 ± 0.095	16.218 ± 0.097	Cutr03, Dupu12, Dupu16
2MASS J	15.579 ± 0.064	-0.474 ± 0.037	16.594 ± 0.068	16.120 ± 0.066	Cutr03, Dupu12, Dupu16
2MASS H	14.953 ± 0.067	0.545 ± 0.046	15.468 ± 0.069	16.013 ± 0.073	Cutr03, Dupu12, Dupu16
2MASS K_S	14.538 ± 0.095	1.206 ± 0.010	14.847 ± 0.095	16.053 ± 0.095	Cutr03, Dupu16
		HD 130948BC			
MKO J	13.200 ± 0.080	0.305 ± 0.014	13.811 ± 0.080	14.116 ± 0.080	Dupu09b, Dupu09c
MKO H	12.420 ± 0.150	0.290 ± 0.020	13.037 ± 0.150	13.327 ± 0.150	Dupu09b, Dupu09c
MKO K	11.690 ± 0.040	0.197 ± 0.003	12.349 ± 0.040	12.545 ± 0.040	Dupu09b, Dupu09c
2MASS J	13.263 ± 0.081	0.310 ± 0.025	13.872 ± 0.082	14.182 ± 0.082	Dupu09b, Dupu09c, Dupu16
2MASS H	12.368 ± 0.150	0.288 ± 0.021	12.986 ± 0.150	13.275 ± 0.150	Dupu09b, Dupu09c, Dupu16
2MASS K_S	11.713 ± 0.040	0.197 ± 0.009	12.372 ± 0.040	12.569 ± 0.040	Dupu09b, Dupu09c, Dupu16
		Gl 569Bab			
MKO J	10.750 ± 0.060	0.510 ± 0.020	11.277 ± 0.060	11.787 ± 0.061	Dupu10, Lane01
MKO H	10.150 ± 0.040	0.540 ± 0.020	10.666 ± 0.041	11.206 ± 0.042	Dupu10
MKO K	9.620 ± 0.030	0.473 ± 0.010	10.162 ± 0.030	10.635 ± 0.031	Dupu10
2MASS J	10.802 ± 0.061	0.515 ± 0.029	11.327 ± 0.062	11.842 ± 0.063	Dupu10, Dupu16, Lane01
2MASS H	10.106 ± 0.040	0.534 ± 0.021	10.624 ± 0.041	11.158 ± 0.042	Dupu10, Dupu16
2MASS K_S	9.650 ± 0.030	0.470 ± 0.020	10.193 ± 0.031	10.663 ± 0.032	Dupu10, Dupu12
		SDSS J1534+1615AB			
MKO J	16.620 ± 0.030	-0.179 ± 0.005	17.466 ± 0.030	17.287 ± 0.030	Chiu06, Dupu16
MKO H	16.370 ± 0.030	0.587 ± 0.017	16.868 ± 0.031	17.455 ± 0.032	Chiu06, Dupu16

Table 39—Continued

Filter	Integrated	$\Delta m = m_B - m_A$	m_A	m_B	References
MKO $CH4_S$	16.190 ± 0.030	0.333 ± 0.064	16.789 ± 0.040	17.122 ± 0.047	Chiu06, Dupu16
MKO K	16.060 ± 0.030	1.160 ± 0.060	16.381 ± 0.034	17.541 ± 0.054	Chiu06, Dupu16
2MASS J	16.808 ± 0.032	-0.125 ± 0.022	17.624 ± 0.034	17.500 ± 0.034	Chiu06, Dupu16
2MASS H	16.312 ± 0.030	0.589 ± 0.018	16.810 ± 0.031	17.398 ± 0.032	Chiu06, Dupu16
2MASS K_S	15.992 ± 0.029	1.089 ± 0.059	16.332 ± 0.032	17.421 ± 0.054	Chiu06, Dupu16
			2MASS J1534−2952AB		
MKO J	14.600 ± 0.030	0.163 ± 0.014	15.274 ± 0.031	15.437 ± 0.031	Knap04, Liu08
MKO H	14.740 ± 0.030	0.286 ± 0.011	15.359 ± 0.030	15.645 ± 0.031	Knap04, Liu08
MKO $CH4_S$	14.418 ± 0.030	0.210 ± 0.040	15.071 ± 0.035	15.281 ± 0.037	Knap04, Liu08
MKO K	14.910 ± 0.030	0.287 ± 0.012	15.529 ± 0.030	15.816 ± 0.031	Knap04, Liu08
2MASS J	14.809 ± 0.032	0.176 ± 0.025	15.477 ± 0.034	15.653 ± 0.034	Dupu16, Knap04, Liu08
2MASS H	14.683 ± 0.030	0.287 ± 0.012	15.301 ± 0.031	15.588 ± 0.031	Dupu16, Knap04, Liu08
2MASS K_S	14.791 ± 0.030	0.286 ± 0.016	15.410 ± 0.031	15.695 ± 0.031	Dupu16, Knap04, Liu08
$F814W$	19.620 ± 0.020	0.296 ± 0.031	20.235 ± 0.024	20.531 ± 0.027	Burg03b, Dupu16
			2MASS J1728+3948AB		
MKO J	15.889 ± 0.076	0.266 ± 0.051	16.517 ± 0.079	16.783 ± 0.081	Cutr03, Dupu12, Dupu16
MKO H	14.815 ± 0.066	0.423 ± 0.008	15.377 ± 0.066	15.800 ± 0.066	Cutr03, Dupu12, Dupu16
MKO K	13.893 ± 0.048	0.634 ± 0.027	14.374 ± 0.049	15.008 ± 0.051	Cutr03, Dupu12, Dupu16
2MASS J	15.997 ± 0.077	0.292 ± 0.055	16.614 ± 0.081	16.906 ± 0.082	Cutr03, Dupu12, Dupu16
2MASS H	14.757 ± 0.066	0.422 ± 0.010	15.319 ± 0.066	15.741 ± 0.066	Cutr03, Dupu12, Dupu16
2MASS K_S	13.909 ± 0.048	0.581 ± 0.037	14.410 ± 0.050	14.991 ± 0.053	Cutr03, Dupu16
$F814W$	19.680 ± 0.050	0.460 ± 0.075	20.227 ± 0.058	20.687 ± 0.067	Dupu16, Gizi03
$F110W$	16.760 ± 0.050	0.290 ± 0.030	17.377 ± 0.052	17.667 ± 0.053	Burg11, Dupu16
$F170M$	14.770 ± 0.050	0.465 ± 0.012	15.315 ± 0.050	15.780 ± 0.051	Burg11, Dupu16
			LSPM J1735+2634AB		
MKO J	11.198 ± 0.026	0.570 ± 0.030	11.703 ± 0.028	12.273 ± 0.032	Cutr03, Dupu12

Table 39—Continued

Filter	Integrated	$\Delta m = m_{\rm B} - m_{\rm A}$	$m_{\rm A}$	$m_{\rm B}$	References
MKO H	10.628 ± 0.031	0.557 ± 0.005	11.137 ± 0.031	11.694 ± 0.031	Cutr03, Dupu12
MKO K	10.131 ± 0.020	0.488 ± 0.011	10.667 ± 0.020	11.155 ± 0.021	Cutr03, Dupu12
2MASS J	11.247 ± 0.028	0.570 ± 0.037	11.752 ± 0.032	12.322 ± 0.035	Cutr03, Dupu12, Dupu16
2MASS H	10.591 ± 0.031	0.549 ± 0.008	11.103 ± 0.031	11.653 ± 0.031	Cutr03, Dupu12, Dupu16
2MASS K_S	10.157 ± 0.020	0.490 ± 0.020	10.692 ± 0.021	11.182 ± 0.023	Cutr03, Dupu12
			2MASS J1750+4424AB		
MKO J	12.749 ± 0.023	0.782 ± 0.019	13.180 ± 0.024	13.962 ± 0.026	Cutr03, Dupu12, Dupu16
MKO H	12.198 ± 0.021	0.770 ± 0.120	12.634 ± 0.045	13.404 ± 0.083	Cutr03, Dupu12, Kono10
MKO K	11.741 ± 0.017	0.637 ± 0.036	12.221 ± 0.021	12.858 ± 0.029	Cutr03, Dupu12, Dupu16
2MASS J	12.799 ± 0.026	0.784 ± 0.029	13.229 ± 0.028	14.012 ± 0.030	Cutr03, Dupu12, Dupu16
2MASS H	12.160 ± 0.021	0.761 ± 0.120	12.599 ± 0.045	13.359 ± 0.083	Cutr03, Dupu12, Dupu16, Kono10
2MASS K_S	11.768 ± 0.017	0.637 ± 0.005	12.248 ± 0.017	12.885 ± 0.017	Cutr03, Dupu16
			2MASS J1847+5522AB		
MKO J	11.874 ± 0.021	0.240 ± 0.090	12.514 ± 0.045	12.754 ± 0.054	Cutr03, Dupu12, Kono10
MKO H	11.305 ± 0.019	0.242 ± 0.011	11.943 ± 0.020	12.185 ± 0.020	Cutr03, Dupu12, Dupu16
MKO K	10.877 ± 0.020	0.264 ± 0.022	11.506 ± 0.022	11.770 ± 0.023	Cutr03, Dupu12, Dupu16
2MASS J	11.941 ± 0.024	0.232 ± 0.092	12.585 ± 0.048	12.816 ± 0.056	Cutr03, Dupu12, Dupu16, Kono10
2MASS H	11.290 ± 0.019	0.236 ± 0.012	11.931 ± 0.020	12.167 ± 0.020	Cutr03, Dupu12, Dupu16
2MASS K_S	10.901 ± 0.020	0.281 ± 0.060	11.523 ± 0.033	11.804 ± 0.039	Cutr03, Dupu16
			SDSS J2052−1609AB		
MKO J	16.040 ± 0.030	0.042 ± 0.057	16.772 ± 0.041	16.814 ± 0.042	Chiu06, Dupu16
MKO H	15.450 ± 0.030	0.324 ± 0.027	16.053 ± 0.032	16.377 ± 0.034	Chiu06, Dupu16
MKO K	15.000 ± 0.030	0.873 ± 0.037	15.402 ± 0.032	16.275 ± 0.039	Chiu06, Dupu16
2MASS J	16.193 ± 0.032	0.083 ± 0.061	16.905 ± 0.044	16.988 ± 0.044	Chiu06, Dupu16
2MASS H	15.391 ± 0.030	0.324 ± 0.028	15.994 ± 0.032	16.318 ± 0.034	Chiu06, Dupu16
2MASS K_S	14.981 ± 0.028	0.773 ± 0.034	15.415 ± 0.030	16.187 ± 0.036	Chiu06, Dupu16

Table 39—Continued

Filter	Integrated	$\Delta m = m_{\rm B} - m_{\rm A}$	$m_{\rm A}$	$m_{\rm B}$	References
$F110W$	17.140 ± 0.020	0.200 ± 0.400	17.815 ± 0.185	18.015 ± 0.220	Dupu16, Stum11
$F170M$	15.370 ± 0.020	0.420 ± 0.240	15.939 ± 0.100	16.359 ± 0.144	Dupu16, Stum11
			2MASS J2132+1341AB		
MKO J	15.708 ± 0.062	0.850 ± 0.040	16.117 ± 0.063	16.967 ± 0.068	Cutr03, Dupu12
MKO H	14.659 ± 0.055	0.910 ± 0.050	15.049 ± 0.057	15.960 ± 0.065	Cutr03, Dupu12
MKO K	13.824 ± 0.058	0.860 ± 0.050	14.230 ± 0.060	15.090 ± 0.067	Cutr03, Dupu12
2MASS J	15.809 ± 0.063	0.885 ± 0.045	16.207 ± 0.065	17.092 ± 0.070	Cutr03, Dupu12, Dupu16
2MASS H	14.602 ± 0.055	0.908 ± 0.050	14.993 ± 0.057	15.901 ± 0.065	Cutr03, Dupu12, Dupu16
2MASS K_S	13.839 ± 0.058	0.819 ± 0.023	14.258 ± 0.058	15.077 ± 0.060	Cutr03, Dupu12
			2MASS J2140+1625AB		
MKO Y	13.726 ± 0.033	0.970 ± 0.030	14.099 ± 0.034	15.069 ± 0.039	Dupu12, Dupu16
MKO J	12.885 ± 0.033	0.795 ± 0.018	13.311 ± 0.034	14.106 ± 0.035	Cutr03, Dupu12, Dupu16
MKO H	12.303 ± 0.040	0.769 ± 0.009	12.738 ± 0.040	13.507 ± 0.040	Cutr03, Dupu12, Dupu16
MKO K	11.797 ± 0.031	0.732 ± 0.078	12.245 ± 0.041	12.977 ± 0.060	Cutr03, Dupu12, Dupu16
2MASS J	12.935 ± 0.035	0.796 ± 0.028	13.361 ± 0.037	14.157 ± 0.038	Cutr03, Dupu12, Dupu16
2MASS H	12.267 ± 0.040	0.758 ± 0.011	12.705 ± 0.040	13.463 ± 0.041	Cutr03, Dupu12, Dupu16
2MASS K_S	11.826 ± 0.031	0.743 ± 0.075	12.270 ± 0.040	13.013 ± 0.059	Cutr03, Dupu16
$F814W$	15.720 ± 0.050	1.260 ± 0.040	16.016 ± 0.051	17.276 ± 0.059	Dupu16, Gizi03
			2MASS J2206−2047AB		
MKO J	12.321 ± 0.022	0.107 ± 0.017	13.021 ± 0.023	13.128 ± 0.024	Cutr03, Dupu09a, Dupu12
MKO H	11.720 ± 0.022	0.080 ± 0.019	12.433 ± 0.024	12.513 ± 0.024	Cutr03, Dupu09a, Dupu12
MKO K	11.289 ± 0.027	0.049 ± 0.010	12.017 ± 0.027	12.066 ± 0.027	Cutr03, Dupu12, Dupu16
2MASS J	12.370 ± 0.024	0.107 ± 0.027	13.070 ± 0.028	13.177 ± 0.028	Cutr03, Dupu09a, Dupu12, Dupu16
2MASS H	11.685 ± 0.022	0.079 ± 0.020	12.398 ± 0.024	12.478 ± 0.024	Cutr03, Dupu09a, Dupu12, Dupu16
2MASS K_S	11.315 ± 0.027	0.067 ± 0.016	12.035 ± 0.028	12.102 ± 0.028	Cutr03, Dupu16
$F814W$	15.010 ± 0.050	0.060 ± 0.020	15.733 ± 0.051	15.793 ± 0.051	Dupu09a, Gizi03

Table 39—Continued

Filter	Integrated	$\Delta m = m_{\rm B} - m_{\rm A}$	$m_{\rm A}$	$m_{\rm B}$	References
		DENIS J2252−1730AB			
MKO Y	15.257 ± 0.029	0.569 ± 0.021	15.762 ± 0.030	16.331 ± 0.032	Dupu12, Dupu16
MKO J	14.200 ± 0.029	0.770 ± 0.040	14.635 ± 0.032	15.405 ± 0.040	Cutr03, Dupu12, Dupu16
MKO H	13.413 ± 0.030	1.180 ± 0.060	13.729 ± 0.034	14.909 ± 0.054	Cutr03, Dupu12, Dupu16
MKO $CH4_S$	13.363 ± 0.029	0.978 ± 0.026	13.733 ± 0.030	14.711 ± 0.034	Dupu12, Dupu16
MKO K	12.896 ± 0.025	1.775 ± 0.114	13.090 ± 0.031	14.865 ± 0.100	Cutr03, Dupu16
2MASS J	14.319 ± 0.031	0.848 ± 0.046	14.728 ± 0.035	15.576 ± 0.043	Cutr03, Dupu12, Dupu16
2MASS H	13.355 ± 0.030	1.178 ± 0.060	13.672 ± 0.034	14.850 ± 0.054	Cutr03, Dupu12, Dupu16
2MASS K_S	12.901 ± 0.024	1.677 ± 0.102	13.112 ± 0.030	14.789 ± 0.087	Cutr03, Dupu16
$F110W$	15.100 ± 0.050	0.978 ± 0.030	15.470 ± 0.051	16.448 ± 0.054	Dupu16, Reid06a
$F170M$	13.460 ± 0.050	1.292 ± 0.024	13.748 ± 0.050	15.040 ± 0.053	Dupu16, Reid06a

References. — Burg03b = Burgasser et al. (2003b); Burg06b = Burgasser et al. (2006b); Burg11 = Burgasser et al. (2011); Chiu06 = Chiu et al. (2006); Clos03 = Close et al. (2003); Cutr03 = Cutri et al. (2003); Dupu09a = Dupuy et al. (2009a); Dupu09b = Dupuy et al. (2009b); Dupu09c = Dupuy et al. (2009c); Dupu10 = Dupuy et al. (2010); Dupu12 = Dupuy & Liu (2012); Dupu14 = Dupuy et al. (2014); Dupu15 = Dupuy et al. (2015b); Dupu16 = this work; Gizi03 = Gizis et al. (2003); Knap04 = Knapp et al. (2004); Kono10 = Konopacky et al. (2010); Lane01 = Lane et al. (2001); Legg00 = Leggett et al. (2000); Legg02a = Leggett et al. (2002); Liu08 = Liu et al. (2008); Reid06a = Reid et al. (2006a); Stum11 = Stumpf et al. (2011).

Table 40. Summary of Key Parameters from Orbit Analysis

System	$M_{\rm tot}$ ($M_{\rm Jup}$)	q $\equiv M_2/M_1$	e	P (days)	a (AU)	$a_{\rm phot}/a$	β $\equiv F_2/(F_1+F_2)^*$
LP 349-25AB	166^{+6}_{-7}	$0.941^{+0.029}_{-0.030}$	$0.0468^{+0.0019}_{-0.0018}$	2812 ± 5	2.109 ± 0.027	0.056 ± 0.008	0.4286 ± 0.0018
LP 415-20AB	248^{+26}_{-29}	$0.59^{+0.10}_{-0.12}$	$0.706^{+0.011}_{-0.012}$	5410 ± 90	3.73 ± 0.12	0.00 ± 0.03	0.370 ± 0.028
SDSS J0423−0414AB	83 ± 3	0.62 ± 0.04	$0.272^{+0.008}_{-0.007}$	4491^{+21}_{-22}	$2.291^{+0.027}_{-0.028}$	-0.023 ± 0.006	0.404 ± 0.013
2MASS J0700+3157AB	141^{+4}_{-5}	1.08 ± 0.05	$0.017^{+0.005}_{-0.007}$	8720 ± 190	4.25 ± 0.08	0.310 ± 0.011	0.208 ± 0.005
LHS 1901AB	213^{+9}_{-10}	$0.87^{+0.09}_{-0.11}$	0.8304 ± 0.0009	5921 ± 29	3.76 ± 0.06	-0.009 ± 0.028	0.4750 ± 0.0016
2MASS J0746+2000AB	$160.8^{+1.8}_{-1.7}$	$0.952^{+0.026}_{-0.027}$	0.4854 ± 0.0003	4652 ± 11	2.919 ± 0.009	0.069 ± 0.007	0.4186 ± 0.0018
2MASS J0850+1057AB	$54 \pm 8^{\dagger}$	···	$0.06^{+0.05\dagger}_{-0.06}$	$17600^{+2700\dagger}_{-2300}$	$4.98^{+0.25\dagger}_{-0.33}$	0.04 ± 0.12	0.225 ± 0.021
2MASS J0920+3517AB	187 ± 11	$1.63^{+0.08}_{-0.09}$	$0.180^{+0.006}_{-0.007}$	2651 ± 3	2.11 ± 0.04	0.183 ± 0.010	0.437 ± 0.006
SDSS J0926+5847AB	$38^{+10\dagger}_{-18}$	···	$0.35^{+0.22\dagger}_{-0.16}$	$4700^{+500\dagger}_{-700}$	$1.80^{+0.14\dagger}_{-0.21}$	-0.07 ± 0.08	0.452 ± 0.030
2MASS J1017+1308AB	156^{+14}_{-18}	0.92 ± 0.08	0.158 ± 0.010	6790 ± 80	3.72 ± 0.13	0.026 ± 0.022	0.454 ± 0.004
SDSS J1021−0304AB	$52^{+6\dagger}_{-7}$	···	$0.38 \pm 0.07^{\dagger}$	$31000^{+5000\dagger}_{-6000}$	$7.2^{+0.7\dagger}_{-0.8}$	-0.9 ± 0.3	0.5239 ± 0.0028
2MASS J1047+4026AB	178^{+11}_{-12}	0.82 ± 0.06	0.7485 ± 0.0013	2397^{+11}_{-10}	1.94 ± 0.04	0.019 ± 0.015	0.432 ± 0.011
SDSS J1052+4422AB	90^{+4}_{-5}	0.78 ± 0.07	$0.1399^{+0.0022}_{-0.0023}$	3144 ± 9	1.86 ± 0.03	-0.165 ± 0.008	0.602 ± 0.020
Gl 417BC	$99.2^{+3.0}_{-3.3}$	···	0.105 ± 0.003	5714^{+29}_{-30}	2.851 ± 0.029	···	···
LHS 2397aAB	159^{+7}_{-8}	$0.706^{+0.027}_{-0.028}$	0.351 ± 0.003	5248^{+18}_{-17}	3.15 ± 0.05	0.344 ± 0.009	0.0693 ± 0.0025
DENIS J1228−1557AB	$106^{+16\dagger}_{-19}$	···	$0.089^{+0.027\dagger}_{-0.035}$	$18300^{+1900\dagger}_{-2400}$	$6.36^{+0.29\dagger}_{-0.35}$	0.9 ± 1.1	0.476 ± 0.008
Kelu-1AB	$180^{+22\ddagger}_{-26}$	···	0.709 ± 0.005	9120 ± 70	$4.75^{+0.21}_{-0.22}$	-0.7 ± 0.9	0.344 ± 0.010
2MASS J1404−3159AB	120^{+11}_{-13}	0.84 ± 0.06	0.825 ± 0.005	6030 ± 80	$3.15^{+0.09}_{-0.11}$	-0.165 ± 0.016	0.622 ± 0.006
HD 130948BC	$115.4^{+2.2}_{-2.1}$	···	0.1627 ± 0.0017	3656 ± 4	$2.226^{+0.014}_{-0.013}$	···	···
Gl 569Bab	138 ± 7	···	0.3186 ± 0.0010	865.89 ± 0.20	0.904 ± 0.015	···	···
SDSS J1534+1615AB	$46^{+6\dagger}_{-7}$	···	$0.22^{+0.21\dagger}_{-0.22}$	$21000^{+14000\dagger}_{-9000}$	$5.3^{+2.3\dagger}_{-1.6}$	0.07 ± 0.10	0.5411 ± 0.0011
2MASS J1534−2952AB	99 ± 5	$0.95^{+0.13}_{-0.16}$	$0.0027^{+0.0028}_{-0.0027}$	7434^{+18}_{-21}	3.40 ± 0.06	0.02 ± 0.04	0.463 ± 0.003
2MASS J1728+3948AB	140^{+7}_{-8}	$0.93^{+0.11}_{-0.13}$	$0.015^{+0.013}_{-0.015}$	14900^{+600}_{-400}	$6.09^{+0.17}_{-0.22}$	0.04 ± 0.03	0.439 ± 0.012
LSPM J1735+2634AB	187 ± 7	$0.868^{+0.023}_{-0.025}$	0.497 ± 0.004	7910 ± 90	$4.37^{+0.07}_{-0.06}$	0.077 ± 0.007	0.3872 ± 0.0025
2MASS J1750+4424AB	$190^{+40\dagger}_{-50}$	···	$0.73^{+0.09\dagger}_{-0.07}$	$78000^{+15000\dagger}_{-22000}$	$20^{+3\dagger}_{-4}$	-0.8 ± 2.1	0.354 ± 0.008
2MASS J1847+5522AB	$270^{+26\dagger}_{-31}$	···	$0.09^{+0.05\dagger}_{-0.09}$	$16500^{+2000\dagger}_{-1200}$	$8.0^{+0.7\dagger}_{-0.6}$	0.05 ± 0.08	0.439 ± 0.005
SDSS J2052−1609AB	$69^{+14\dagger}_{-20}$	···	$0.20^{+0.09\dagger}_{-0.11}$	$16000^{+4000\dagger}_{-5000}$	$5.0^{+0.5\dagger}_{-0.6}$	0.06 ± 0.05	0.490 ± 0.013
2MASS J2132+1341AB	128^{+7}_{-8}	$0.88^{+0.04}_{-0.05}$	$0.315^{+0.004}_{-0.005}$	3920 ± 60	2.42 ± 0.04	0.155 ± 0.010	0.314 ± 0.008
2MASS J2140+1625AB	183^{+14}_{-17}	$0.60^{+0.07}_{-0.08}$	0.196 ± 0.007	8930 ± 90	4.71 ± 0.14	0.042 ± 0.025	0.334 ± 0.016
2MASS J2206−2047AB	188^{+16}_{-17}	$0.84^{+0.09}_{-0.10}$	0.015 ± 0.008	8750 ± 80	$4.69^{+0.13}_{-0.14}$	-0.033 ± 0.028	0.4885 ± 0.0023

Table 40—Continued

System	$M_{\rm tot}$ ($M_{\rm Jup}$)	q $\equiv M_2/M_1$	e	P (days)	a (AU)	$a_{\rm phot}/a$	β $\equiv F_2/(F_1+F_2)^*$
DENIS J2252−1730AB	101 ± 7	$0.70^{+0.08}_{-0.09}$	0.334 ± 0.009	3222^{+9}_{-10}	1.95 ± 0.04	0.081 ± 0.027	0.330 ± 0.008

*This is the ratio of the secondary's flux to the total flux in the bandpass used for our CFHT/WIRCam absolute astrometry observations, which was either broadband J (MKO) or a narrowband filter in K band centered at $2.122\,\mu$m.

†We do not use these orbit determinations in our analysis given their questionable quality (see Section 4.1).

‡This is the total mass of Kelu-1AB using our CFHT parallax, but we do not use it in our analysis given that parallaxes from the literature differ from ours at a level sufficient to result in significantly different physical properties.

Table 41. Summary of Properties for Dynamical Mass Sample

System	Primary component: M ($M_{\rm Jup}$)	$\log(L_{\rm bol}/L_\odot)$	SpT	$T_{\rm eff}$ (K)	Secondary component: M ($M_{\rm Jup}$)	$\log(L_{\rm bol}/L_\odot)$	SpT	$T_{\rm eff}$ (K)	Age (Gyr)
LP 349-25AB	85 ± 4	$-3.075^{+0.027}_{-0.026}$	M7±1.0	2729^{+26}_{-27}	80 ± 3	-3.198 ± 0.027	M8±1.0	2629^{+29}_{-27}	$0.271^{+0.022}_{-0.029}$
LP 415-20AB	156^{+17}_{-18}	-3.010 ± 0.030	M6±1.0	···	92^{+16}_{-18}	$-3.260^{+0.030}_{-0.040}$	M8±0.5	2640^{+40}_{-30}	···
SDSS J0423−0414AB	$51.6^{+2.3}_{-2.5}$	-4.41 ± 0.04	L6.5±1.5	1430^{+30}_{-40}	$31.8^{+1.5}_{-1.6}$	-4.72 ± 0.07	T2±0.5	1200 ± 40	$0.81^{+0.07}_{-0.09}$
2MASS J0700+3157AB	68.0 ± 2.6	-3.95 ± 0.04	L3±1.0	1860 ± 40	$73.3^{+2.9}_{-3.0}$	-4.45 ± 0.04	L6.5±1.5	···	$0.76^{+0.09}_{-0.14}$
LHS 1901AB	113 ± 8	$-3.005^{+0.026}_{-0.027}$	M7±1.0	2844 ± 16	99 ± 7	$-3.046^{+0.026}_{-0.027}$	M7±1.0	2820^{+20}_{-10}	···
2MASS J0746+2000AB	$82.4^{+1.4}_{-1.5}$	$-3.596^{+0.028}_{-0.025}$	L0±0.5	2318^{+24}_{-23}	78.4 ± 1.4	$-3.777^{+0.028}_{-0.027}$	L1.5±0.5	2134^{+26}_{-25}	···
2MASS J0920+3517AB	71 ± 5	-4.270 ± 0.030	L5.5±1.0	1621^{+32}_{-30}	116^{+7}_{-8}	-4.340 ± 0.030	L9±1.5	···	···
2MASS J1017+1308AB	81^{+10}_{-11}	-3.78 ± 0.04	L1.5±1.0	2090 ± 50	75 ± 7	-3.84 ± 0.04	L3±1.0	2040^{+60}_{-50}	···
2MASS J1047+4026AB	97^{+6}_{-7}	-3.27 ± 0.04	M8±0.5	2640^{+50}_{-40}	80 ± 6	-3.39 ± 0.05	L0±1.0	2510^{+60}_{-50}	···
SDSS J1052+4422AB	51 ± 3	-4.51 ± 0.04	L6.5±1.5	1366^{+25}_{-29}	$39.4^{+2.6}_{-2.7}$	-4.64 ± 0.07	T1.5±1.0	1270 ± 40	$1.04^{+0.14}_{-0.15}$
Gl 417BC†	$51.5^{+1.7}_{-1.8}$	-4.132 ± 0.030	L4.5±1.0	1639^{+29}_{-31}	47.7 ± 1.9	-4.220 ± 0.030	L6±1.0	1560^{+29}_{-26}	$0.49^{+0.03}_{-0.04}$
LHS 2397aAB	93 ± 4	-3.34 ± 0.04	M8±0.5	2560 ± 50	66 ± 4	-4.48 ± 0.04	···	1440 ± 40	$2.8^{+2.1}_{-1.5}$
2MASS J1404−3159AB	65 ± 6	$-4.52^{+0.06}_{-0.05}$	L9±1.0	1400^{+40}_{-50}	55^{+6}_{-7}	$-4.87^{+0.08}_{-0.07}$	T5±0.5	1190 ± 50	$3.0^{+0.8}_{-1.3}$
HD 130948BC†	$59.8^{+2.0}_{-2.1}$	-3.85 ± 0.06	L4±1.0	1920^{+70}_{-60}	$55.6^{+2.0}_{-1.9}$	-3.96 ± 0.06	L4±1.0	1800^{+50}_{-70}	0.44 ± 0.04
Gl 569Bab‡	80^{+9}_{-8}	-3.440 ± 0.030	M8.5±0.5	2420 ± 40	58^{+7}_{-9}	-3.670 ± 0.030	M9±0.5	2170 ± 50	$0.44^{+0.05}_{-0.06}$
2MASS J1534−2952AB	51 ± 5	-4.91 ± 0.07	T4.5±0.5	1150^{+40}_{-50}	48 ± 5	-4.99 ± 0.07	T5±0.5	1100^{+40}_{-50}	$3.0^{+0.4}_{-0.5}$
2MASS J1728+3948AB	73 ± 7	$-4.29^{+0.04}_{-0.05}$	L5±1.0	1600 ± 40	67 ± 5	-4.49 ± 0.04	L7±1.0	1440 ± 40	$3.4^{+2.8}_{-2.1}$
LSPM J1735+2634AB	100 ± 4	-3.221 ± 0.028	M7.5±0.5	2677^{+28}_{-26}	87 ± 3	$-3.445^{+0.029}_{-0.028}$	L0±1.0	2462 ± 30	···
2MASS J2132+1341AB	68 ± 4	-4.22 ± 0.05	L4.5±1.5	1660^{+50}_{-40}	60 ± 4	$-4.50^{+0.05}_{-0.04}$	L8.5±1.5	1400^{+30}_{-40}	$1.44^{+0.26}_{-0.37}$
2MASS J2140+1625AB	114^{+10}_{-12}	-3.20 ± 0.04	M8±0.5	2680 ± 40	69^{+8}_{-9}	-3.51 ± 0.04	L0.5±1.0	2410^{+60}_{-50}	···
2MASS J2206−2047AB	102^{+10}_{-11}	$-3.220^{+0.030}_{-0.040}$	M8±0.5	2670 ± 40	86^{+8}_{-10}	$-3.260^{+0.040}_{-0.030}$	M8±0.5	2650^{+40}_{-30}	···
DENIS J2252−1730AB	59 ± 5	$-4.26^{+0.05}_{-0.04}$	L4±1.0	1590 ± 50	41 ± 4	$-4.76^{+0.08}_{-0.07}$	T3.5±0.5	1210^{+50}_{-40}	$1.11^{+0.19}_{-0.22}$

Note. — The effective temperatures quoted here are derived from SM08 models for objects cooler than 2100 K and from BHAC models for objects hotter than 2100 K. System ages are only reported in cases where the observations provide a meaningful constraint, and most of the quoted values are from our total-mass analysis using SM08 models. The exceptions are LP 349-25AB and Gl 569Bab (total-mass analysis using BHAC models), 2MASS J0700+3157AB (individual-mass analysis of the primary using SM08 models), and LHS 2397aAB (individual-mass analysis of the secondary using SM08 models). The individual masses given here are directly measured in this work unless otherwise noted.

†The individual masses quoted for Gl 417BC and HD 130948BC are not measured directly but rather are inferred from evolutionary models in our total-mass analysis. The component effective temperatures are also from our total-mass analysis.

‡The individual masses quoted for Gl 569Bab are computed from our total mass and the mass ratio from Konopacky et al. (2010). The component effective temperatures are from our total-mass analysis.

Table 42. Average Mass Per Spectral Type Bin

Spectral Type	Mass ($M_{\rm Jup}$) mean	rms	Number in bin
M7–M7.5	102	8	3
M8–M8.5	94	11	7
M9–L0.5	81	10	7
L1–L3.5	76	6	4
L4–L7.5	58	9	7
L8–T1.5	48	14	3
T2–T5.5	36	9	5

Note. — The mean is computed as the weighted average among the individual mass measurements in each spectral type bin. Bin sizes vary in order to include a reasonable number of objects per bin, and the bins are larger at later types. From our own 38 individual masses we exclude the pre–main-sequence binary LP 349-25AB; objects that are possible unresolved binaries (LP 415-20A, 2MASS J0700+3157B, and 2MASS J0920+3517B); and LHS 2397aB ($66 \pm 4\,M_{\rm Jup}$) because it has no directly measured spectral type. Individual masses from the literature that we include here are LHS 1070BC (M9.5+L0; Köhler et al. 2012) and Gl 569Bab (M8.5+M9; total mass from this work and mass ratio from Konopacky et al. 2010).

Table 43. Properties of LP 349-25AB

Property	Using Total Mass			Using Individual Masses		
	Primary	Secondary	$\Delta = \mathrm{B} - \mathrm{A}$	Primary	Secondary	$\Delta = \mathrm{B} - \mathrm{A}$
Input Observed Properties						
Mass M (M_{Jup})	166^{+6}_{-7}		···	85 ± 4	80 ± 3	$-5.0^{+2.6}_{-2.7}$
Mass ratio q	···	···	···	$0.941^{+0.029}_{-0.030}$		···
$\log(L_{\mathrm{bol}})$ [$L_\odot$]	-3.075 ± 0.026	-3.198 ± 0.027	$-0.12^{+0.03}_{-0.04}$	···	···	···
Derived from Baraffe et al. (2015) Evolutionary Models						
Mass M (M_{Jup})	89 ± 4	78^{+3}_{-4}	-10 ± 3	86 ± 4	81 ± 3	-5 ± 5
$\log(L_{\mathrm{bol}})$ [$L_\odot$]	$-3.074^{+0.029}_{-0.032}$	-3.20 ± 0.03	-0.12 ± 0.04	$-3.076^{+0.031}_{-0.029}$	$-3.199^{+0.029}_{-0.031}$	-0.12 ± 0.04
Mass ratio q	$0.88^{+0.03}_{-0.04}$		···	$0.94^{+0.05}_{-0.06}$		···
Age t (Gyr)	$0.271^{+0.022}_{-0.029}$		···	$0.251^{+0.026}_{-0.033}$	$0.30^{+0.03}_{-0.04}$	0.05 ± 0.05
$\log(t)$ [yr]	8.43 ± 0.04		···	8.40 ± 0.05	8.47 ± 0.05	0.07 ± 0.07
T_{eff} (K)	2740^{+32}_{-29}	2620 ± 30	-120 ± 40	2729^{+26}_{-27}	2629^{+29}_{-27}	-100 ± 40
Radius (R_{Jup})	$1.255^{+0.019}_{-0.024}$	$1.193^{+0.020}_{-0.017}$	-0.061 ± 0.021	$1.262^{+0.025}_{-0.026}$	$1.181^{+0.021}_{-0.023}$	-0.08 ± 0.03
$\log(g)$ [cm s^{-2}]	$5.143^{+0.024}_{-0.020}$	5.133 ± 0.024	$-0.010^{+0.005}_{-0.004}$	$5.125^{+0.027}_{-0.029}$	5.156 ± 0.027	0.03 ± 0.04
$\log(\mathrm{Li}/\mathrm{Li}_{\mathrm{init}})$	< -4.0	< -4.0	···	< -4.0	< -4.0	···
MKO($J - K$) (mag)	0.808 ± 0.002	$0.810^{+0.005}_{-0.003}$	$0.003^{+0.003}_{-0.002}$	$0.809^{+0.004}_{-0.003}$	$0.806^{+0.003}_{-0.004}$	-0.003 ± 0.005
MKO($J - H$) (mag)	0.492 ± 0.004	$0.486^{+0.001}_{-0.002}$	-0.006 ± 0.004	$0.491^{+0.004}_{-0.003}$	0.487 ± 0.002	-0.005 ± 0.004

Table 44. Properties of LP 415-20AB

Property	Using Total Mass Primary	Using Total Mass Secondary	Using Total Mass $\Delta = \mathrm{B} - \mathrm{A}$	Using Individual Masses Primary	Using Individual Masses Secondary	Using Individual Masses $\Delta = \mathrm{B} - \mathrm{A}$
Input Observed Properties						
Mass M (M_{Jup})	248^{+26}_{-29}		$\cdots$	156^{+17}_{-18}	92^{+16}_{-18}	-64^{+20}_{-22}
Mass ratio q	$\cdots$	$\cdots$	$\cdots$	$0.59^{+0.10}_{-0.12}$		$\cdots$
$\log(L_{\mathrm{bol}})$ [$L_{\odot}$]	-3.01 ± 0.03	$-3.26^{+0.03}_{-0.04}$	$-0.25^{+0.04}_{-0.03}$	$\cdots$	$\cdots$	$\cdots$
Derived from Baraffe et al. (2015) Evolutionary Models						
Mass M (M_{Jup})	$107.9^{+2.8}_{-3.9}$	$93.3^{+1.9}_{-1.7}$	-14 ± 4	$109.8^{+3.1}_{-2.9}$	$94.4^{+2.0}_{-1.9}$	-16 ± 4
$\log(L_{\mathrm{bol}})$ [$L_{\odot}$]	$-3.03^{+0.04}_{-0.03}$	$-3.28^{+0.04}_{-0.05}$	-0.25 ± 0.05	$-3.011^{+0.029}_{-0.030}$	-3.25 ± 0.04	-0.24 ± 0.05
Mass ratio q	0.87 ± 0.03		$\cdots$	0.86 ± 0.03		$\cdots$
Age t (Gyr)	$5.0^{+1.8}_{-4.4}$		$\cdots$	$5.4^{+2.0}_{-4.4}$	$5.0^{+1.9}_{-4.7}$	0^{+5}_{-4}
$\log(t)$ [yr]	$9.70^{+0.30}_{-0.16}$		$\cdots$	$9.73^{+0.27}_{-0.21}$	$9.70^{+0.30}_{-0.20}$	$0.0^{+0.6}_{-0.3}$
T_{eff} (K)	2829^{+23}_{-17}	2620^{+50}_{-40}	-210^{+40}_{-50}	2839 ± 17	2640^{+40}_{-30}	-200 ± 40
Radius (R_{Jup})	$1.236^{+0.025}_{-0.038}$	$1.087^{+0.022}_{-0.021}$	$-0.15^{+0.04}_{-0.03}$	$1.253^{+0.027}_{-0.029}$	$1.102^{+0.019}_{-0.021}$	$-0.15^{+0.03}_{-0.04}$
$\log(g)$ [$\mathrm{cm\,s^{-2}}$]	$5.240^{+0.008}_{-0.009}$	$5.294^{+0.009}_{-0.010}$	$0.053^{+0.013}_{-0.011}$	$5.235^{+0.008}_{-0.007}$	$5.287^{+0.010}_{-0.008}$	$0.052^{+0.013}_{-0.012}$
$\log(\mathrm{Li}/\mathrm{Li_{init}})$	< -4.0	< -4.0	$\cdots$	< -4.0	< -4.0	$\cdots$
MKO($J-K$) (mag)	0.819 ± 0.001	$0.792^{+0.011}_{-0.007}$	$-0.026^{+0.012}_{-0.007}$	0.818 ± 0.001	$0.798^{+0.008}_{-0.005}$	$-0.020^{+0.008}_{-0.006}$
MKO($J-H$) (mag)	$0.516^{+0.005}_{-0.004}$	$0.486^{+0.007}_{-0.006}$	-0.030 ± 0.008	$0.517^{+0.005}_{-0.004}$	$0.490^{+0.006}_{-0.005}$	$-0.027^{+0.008}_{-0.006}$

Note. — In BHAC total mass analysis, the median mass after rejection sampling was $201^{+4}_{-3}\,M_{\mathrm{Jup}}$, 1.7σ lower than the input measurement. In BHAC individual mass analysis of the primary, the median mass after rejection sampling was 2.6σ lower than the input measurement.

Table 45. Properties of LP 415-20AB (Unresolved Triple Hypothesis)

Property	Using Total Mass			Using Individual Masses		
	Primary	Secondary	$\Delta = \mathrm{B} - \mathrm{A}$	Primary	Secondary	$\Delta = \mathrm{B} - \mathrm{A}$
Input Observed Properties						
Mass M ($M_{\rm Jup}$)	170^{+20}_{-22}		$\cdots$	78^{+8}_{-9}	92^{+16}_{-18}	14 ± 17
Mass ratio q	$\cdots$	$\cdots$	$\cdots$	$1.18^{+0.21}_{-0.24}$		$\cdots$
$\log(L_{\rm bol})$ [$L_\odot$]	-3.32 ± 0.03	$-3.26^{+0.03}_{-0.04}$	$0.06^{+0.03}_{-0.04}$	$\cdots$	$\cdots$	$\cdots$
Derived from Baraffe et al. (2015) Evolutionary Models						
Mass M ($M_{\rm Jup}$)	$92.3^{+2.1}_{-1.5}$	$94.7^{+2.7}_{-1.9}$	$2.5^{+2.4}_{-2.3}$	$92.3^{+2.2}_{-1.6}$	94.4 ± 1.9	$2.4^{+2.8}_{-3.8}$
$\log(L_{\rm bol})$ [$L_\odot$]	-3.30 ± 0.04	$-3.24^{+0.05}_{-0.04}$	$0.06^{+0.05}_{-0.06}$	-3.30 ± 0.04	-3.25 ± 0.04	$0.05^{+0.05}_{-0.06}$
Mass ratio q	$1.027^{+0.024}_{-0.029}$		$\cdots$	$1.03^{+0.03}_{-0.04}$		$\cdots$
Age t (Gyr)	$4.2^{+2.1}_{-3.9}$		$\cdots$	$4.1^{+2.2}_{-3.9}$	$5.0^{+1.9}_{-4.7}$	1^{+5}_{-4}
$\log(t)$ [yr]	$9.62^{+0.38}_{-0.28}$		$\cdots$	$9.6^{+0.4}_{-0.3}$	$9.70^{+0.30}_{-0.20}$	0.1 ± 0.6
$T_{\rm eff}$ (K)	2590^{+50}_{-30}	2650^{+50}_{-40}	50 ± 50	2590 ± 40	2640^{+40}_{-30}	50^{+50}_{-60}
Radius ($R_{\rm Jup}$)	1.081 ± 0.019	$1.109^{+0.022}_{-0.021}$	$0.027^{+0.023}_{-0.027}$	$1.082^{+0.017}_{-0.022}$	$1.102^{+0.019}_{-0.021}$	$0.020^{+0.031}_{-0.027}$
$\log(g)$ [cm s^{-2}]	$5.295^{+0.012}_{-0.007}$	$5.283^{+0.013}_{-0.008}$	-0.009 ± 0.011	$5.295^{+0.012}_{-0.008}$	$5.287^{+0.009}_{-0.008}$	$-0.007^{+0.015}_{-0.019}$
$\log(\mathrm{Li}/\mathrm{Li}_{\rm init})$	< -4.0	< -4.0	$\cdots$	< -4.0	< -4.0	$\cdots$
MKO($J-K$) (mag)	$0.790^{+0.009}_{-0.012}$	$0.800^{+0.007}_{-0.006}$	$0.008^{+0.011}_{-0.010}$	$0.791^{+0.009}_{-0.013}$	$0.798^{+0.008}_{-0.005}$	$0.007^{+0.014}_{-0.012}$
MKO($J-H$) (mag)	0.484 ± 0.006	0.491 ± 0.006	$0.007^{+0.007}_{-0.009}$	0.484 ± 0.006	$0.490^{+0.006}_{-0.005}$	$0.006^{+0.008}_{-0.009}$

Note. — For this analysis, the input mass and luminosity of LP 415-20A were both divided by two in order to simulate a hypothetical scenario where it is an unresolved equal-mass, equal-flux binary. In BHAC total mass analysis, the median mass after rejection sampling was $187.3^{+4.0}_{-2.6}\,M_{\rm Jup}$, 0.8σ higher than the input measurement. In BHAC individual mass analysis of the primary, the median mass after rejection sampling was 1.6σ higher than the input measurement.

Table 46. Properties of SDSS J0423−0414AB

Property	Using Total Mass			Using Individual Masses		
	Primary	Secondary	$\Delta = \mathrm{B} - \mathrm{A}$	Primary	Secondary	$\Delta = \mathrm{B} - \mathrm{A}$
Input Observed Properties						
Mass M (M_{Jup})	83 ± 3		$\cdots$	$51.6^{+2.3}_{-2.5}$	$31.8^{+1.5}_{-1.6}$	$-19.8^{+2.7}_{-2.6}$
Mass ratio q	$\cdots$	$\cdots$	$\cdots$	0.62 ± 0.04		$\cdots$
$\log(L_{\mathrm{bol}})$ [$L_{\odot}$]	-4.41 ± 0.04	-4.72 ± 0.07	$-0.31^{+0.09}_{-0.08}$	$\cdots$	$\cdots$	$\cdots$
Derived from Saumon & Marley (2008) Hybrid Evolutionary Models						
Mass M (M_{Jup})	$50.6^{+2.7}_{-2.5}$	$32.9^{+1.8}_{-2.4}$	-18^{+3}_{-4}	$51.7^{+2.4}_{-2.3}$	$32.0^{+1.7}_{-1.6}$	$-19.8^{+2.9}_{-2.8}$
$\log(L_{\mathrm{bol}})$ [$L_{\odot}$]	-4.42 ± 0.05	-4.69 ± 0.08	-0.28 ± 0.09	-4.42 ± 0.05	$-4.71^{+0.07}_{-0.08}$	$-0.29^{+0.09}_{-0.08}$
Mass ratio q	$0.65^{+0.05}_{-0.06}$		$\cdots$	0.62 ± 0.04		$\cdots$
Age t (Gyr)	$0.81^{+0.07}_{-0.09}$		$\cdots$	$0.85^{+0.09}_{-0.12}$	$0.78^{+0.12}_{-0.13}$	$-0.07^{+0.17}_{-0.16}$
$\log(t)$ [yr]	$8.91^{+0.04}_{-0.05}$		$\cdots$	$8.93^{+0.05}_{-0.06}$	8.89 ± 0.07	$-0.04^{+0.09}_{-0.08}$
T_{eff} (K)	1430 ± 40	1210 ± 50	-220^{+70}_{-60}	1430^{+30}_{-40}	1200 ± 40	-230 ± 50
Radius (R_{Jup})	$0.982^{+0.012}_{-0.011}$	$0.995^{+0.012}_{-0.011}$	$0.0122^{+0.0039}_{-0.0029}$	$0.976^{+0.015}_{-0.012}$	$0.998^{+0.019}_{-0.017}$	$0.022^{+0.022}_{-0.024}$
$\log(g)$ [cm s^{-2}]	$5.113^{+0.034}_{-0.026}$	4.92 ± 0.03	-0.20 ± 0.04	$5.128^{+0.028}_{-0.031}$	4.90 ± 0.03	$-0.23^{+0.05}_{-0.04}$
MKO($J - K$) (mag)	$2.060^{+0.087}_{-0.066}$	$0.484^{+0.256}_{-0.410}$	$-1.558^{+0.265}_{-0.434}$	$2.061^{+0.075}_{-0.072}$	$0.399^{+0.219}_{-0.304}$	$-1.647^{+0.234}_{-0.319}$
MKO($J - H$) (mag)	$1.134^{+0.060}_{-0.034}$	$0.464^{+0.151}_{-0.204}$	$-0.660^{+0.149}_{-0.219}$	$1.132^{+0.057}_{-0.038}$	$0.420^{+0.125}_{-0.155}$	$-0.702^{+0.135}_{-0.165}$
Derived from Baraffe et al. (2003) Cond Evolutionary Models						
Mass M (M_{Jup})	$46.5^{+2.2}_{-2.0}$	$37.1^{+1.6}_{-2.2}$	$-9.3^{+2.6}_{-2.3}$	$51.8^{+2.4}_{-2.5}$	32.0 ± 1.6	$-19.8^{+3.0}_{-2.8}$
$\log(L_{\mathrm{bol}})$ [$L_{\odot}$]	-4.41 ± 0.04	-4.72 ± 0.07	$-0.31^{+0.08}_{-0.09}$	-4.41 ± 0.04	-4.73 ± 0.07	$-0.32^{+0.09}_{-0.08}$
Mass ratio q	0.80 ± 0.05		$\cdots$	0.62 ± 0.04		$\cdots$
Age t (Gyr)	$0.80^{+0.07}_{-0.08}$		$\cdots$	$1.03^{+0.12}_{-0.13}$	$0.59^{+0.08}_{-0.09}$	-0.44 ± 0.15
$\log(t)$ [yr]	$8.90^{+0.05}_{-0.04}$		$\cdots$	9.01 ± 0.05	$8.77^{+0.06}_{-0.07}$	-0.24 ± 0.08
T_{eff} (K)	1490 ± 40	1240 ± 50	-250^{+60}_{-70}	1510 ± 40	1210 ± 50	-300 ± 60
Radius (R_{Jup})	0.924 ± 0.011	$0.935^{+0.014}_{-0.012}$	0.012 ± 0.005	$0.894^{+0.013}_{-0.012}$	$0.967^{+0.011}_{-0.009}$	$0.074^{+0.016}_{-0.018}$
$\log(g)$ [cm s^{-2}]	$5.130^{+0.029}_{-0.030}$	$5.020^{+0.028}_{-0.029}$	-0.110 ± 0.030	5.21 ± 0.03	4.93 ± 0.03	$-0.28^{+0.05}_{-0.04}$
$\log(\mathrm{Li}/\mathrm{Li}_{\mathrm{init}})$	-0.011 ± 0.005	0.0 ± 0.0	0.011 ± 0.005	$-0.04^{+0.04}_{-0.20}$	0.0 ± 0.0	$0.04^{+0.20}_{-0.04}$
MKO($J - K$) (mag)	$0.086^{+0.015}_{-0.016}$	$0.000^{+0.028}_{-0.027}$	$-0.089^{+0.032}_{-0.025}$	$0.065^{+0.018}_{-0.020}$	$0.045^{+0.034}_{-0.027}$	$-0.022^{+0.040}_{-0.033}$
MKO($J - H$) (mag)	$-0.118^{+0.020}_{-0.024}$	$-0.249^{+0.024}_{-0.026}$	$-0.131^{+0.032}_{-0.035}$	$-0.117^{+0.020}_{-0.021}$	$-0.246^{+0.026}_{-0.027}$	-0.129 ± 0.034

Table 47. Properties of 2MASS J0700+3157AB

Property	Using Total Mass: Primary	Using Total Mass: Secondary	Using Total Mass: $\Delta = \mathrm{B} - \mathrm{A}$	Using Individual Masses: Primary	Using Individual Masses: Secondary	Using Individual Masses: $\Delta = \mathrm{B} - \mathrm{A}$
Input Observed Properties						
Mass M (M_{Jup})	141^{+4}_{-5}		$\cdots$	68.0 ± 2.6	$73.3^{+2.9}_{-3.0}$	5 ± 3
Mass ratio q	$\cdots$	$\cdots$	$\cdots$	1.08 ± 0.05		$\cdots$
$\log(L_{\mathrm{bol}})$ [$L_{\odot}$]	-3.95 ± 0.04	-4.45 ± 0.04	-0.50 ± 0.06	$\cdots$	$\cdots$	$\cdots$
Derived from Saumon & Marley (2008) Hybrid Evolutionary Models						
Mass M (M_{Jup})	$77.8^{+1.4}_{-1.2}$	$66.1^{+6.7}_{-2.6}$	$-11.3^{+5.3}_{-2.5}$	$68.5^{+2.9}_{-2.6}$	$72.2^{+0.8}_{-0.6}$	$3.5^{+2.9}_{-3.0}$
$\log(L_{\mathrm{bol}})$ [$L_{\odot}$]	$-3.95^{+0.04}_{-0.05}$	$-4.46^{+0.05}_{-0.04}$	$-0.51^{+0.05}_{-0.07}$	-3.96 ± 0.04	-4.45 ± 0.04	-0.49 ± 0.06
Mass ratio q	$0.85^{+0.07}_{-0.03}$		$\cdots$	$1.05^{+0.05}_{-0.04}$		$\cdots$
Age t (Gyr)	$1.9^{+0.6}_{-0.7}$		$\cdots$	$0.76^{+0.09}_{-0.14}$	$7.8^{+2.8}_{-5.2}$	7^{+3}_{-5}
$\log(t)$ [yr]	$9.27^{+0.15}_{-0.17}$		$\cdots$	$8.88^{+0.06}_{-0.08}$	$9.89^{+0.28}_{-0.14}$	$1.00^{+0.29}_{-0.20}$
T_{eff} (K)	1910^{+40}_{-50}	1450 ± 40	-450^{+60}_{-50}	1860 ± 40	1480 ± 30	-390 ± 50
Radius (R_{Jup})	0.942 ± 0.006	$0.905^{+0.012}_{-0.022}$	$-0.037^{+0.018}_{-0.012}$	$0.977^{+0.016}_{-0.013}$	0.886 ± 0.005	-0.093 ± 0.016
$\log(g)$ [cm s^{-2}]	$5.336^{+0.010}_{-0.005}$	$5.300^{+0.063}_{-0.025}$	$-0.036^{+0.056}_{-0.019}$	$5.249^{+0.028}_{-0.029}$	$5.359^{+0.005}_{-0.004}$	$0.108^{+0.032}_{-0.028}$
MKO($J-K$) (mag)	$1.082^{+0.053}_{-0.063}$	$2.002^{+0.082}_{-0.078}$	$0.913^{+0.094}_{-0.101}$	$1.139^{+0.059}_{-0.065}$	$1.937^{+0.047}_{-0.056}$	$0.801^{+0.080}_{-0.087}$
MKO($J-H$) (mag)	$0.591^{+0.021}_{-0.031}$	$1.089^{+0.056}_{-0.050}$	$0.491^{+0.062}_{-0.053}$	$0.616^{+0.025}_{-0.035}$	$1.045^{+0.030}_{-0.036}$	$0.430^{+0.040}_{-0.050}$
Derived from Baraffe et al. (2003) Cond Evolutionary Models						
Mass M (M_{Jup})	$76.8^{+1.5}_{-1.3}$	66^{+4}_{-3}	$-11.0^{+2.7}_{-2.5}$	$68.7^{+2.7}_{-2.8}$	$73.6^{+2.1}_{-1.3}$	5 ± 3
$\log(L_{\mathrm{bol}})$ [$L_{\odot}$]	$-3.95^{+0.04}_{-0.05}$	-4.45 ± 0.04	-0.50 ± 0.06	-3.95 ± 0.04	-4.45 ± 0.04	-0.50 ± 0.06
Mass ratio q	$0.86^{+0.04}_{-0.03}$		$\cdots$	1.07 ± 0.05		$\cdots$
Age t (Gyr)	$2.1^{+0.4}_{-0.6}$		$\cdots$	$1.01^{+0.13}_{-0.19}$	$5.0^{+1.6}_{-2.1}$	$3.9^{+1.6}_{-2.2}$
$\log(t)$ [yr]	$9.33^{+0.09}_{-0.13}$		$\cdots$	$9.00^{+0.06}_{-0.08}$	$9.70^{+0.16}_{-0.18}$	$0.69^{+0.18}_{-0.19}$
T_{eff} (K)	1990 ± 40	1530^{+30}_{-40}	-450^{+50}_{-60}	1950 ± 40	1560 ± 30	-390 ± 50
Radius (R_{Jup})	$0.876^{+0.010}_{-0.008}$	$0.828^{+0.014}_{-0.013}$	$-0.047^{+0.013}_{-0.012}$	$0.910^{+0.015}_{-0.012}$	$0.794^{+0.006}_{-0.008}$	$-0.115^{+0.015}_{-0.018}$
$\log(g)$ [cm s^{-2}]	$5.395^{+0.013}_{-0.009}$	5.38 ± 0.04	$-0.021^{+0.029}_{-0.027}$	$5.314^{+0.028}_{-0.027}$	5.462 ± 0.015	0.14 ± 0.03
$\log(\mathrm{Li}/\mathrm{Li}_{\mathrm{init}})$	$\cdots$	-1.9 ± 0.5	$\cdots$	$-2.75^{+0.16}_{-0.34}$	$\cdots$	$\cdots$
MKO($J-K$) (mag)	$0.368^{+0.036}_{-0.041}$	$0.037^{+0.024}_{-0.020}$	$-0.331^{+0.042}_{-0.049}$	$0.366^{+0.036}_{-0.035}$	$0.010^{+0.022}_{-0.023}$	$-0.357^{+0.041}_{-0.043}$
MKO($J-H$) (mag)	$0.147^{+0.022}_{-0.023}$	$-0.129^{+0.021}_{-0.022}$	$-0.274^{+0.033}_{-0.030}$	0.132 ± 0.022	$-0.130^{+0.021}_{-0.022}$	$-0.263^{+0.031}_{-0.030}$

Note. — Despite the fact that this is a likely triple system with 2MASS J0700+3157B as an unresolved binary, the total mass and individual luminosities are consistent with models. In the SM08 total mass analysis, the median mass after rejection sampling was $144^{+8}_{-4}\,M_{\mathrm{Jup}}$, only 0.5σ higher than the input measurement. In the Cond total mass analysis, the median mass after rejection sampling was $142 \pm 5\,M_{\mathrm{Jup}}$, only 0.2σ higher than the input measurement.

Table 48. Properties of 2MASS J0700+3157AB (Unresolved Triple Hypothesis)

Property	Using Total Mass			Using Individual Masses		
	Primary	Secondary	$\Delta = \mathrm{B} - \mathrm{A}$	Primary	Secondary	$\Delta = \mathrm{B} - \mathrm{A}$
Input Observed Properties						
Mass M ($M_{\rm Jup}$)	105 ± 3		$\cdots$	68.0 ± 2.6	36.7 ± 1.5	$-31.4^{+2.6}_{-2.7}$
Mass ratio q	$\cdots$	$\cdots$	$\cdots$	$0.539^{+0.024}_{-0.027}$		$\cdots$
$\log(L_{\rm bol})$ [$L_{\odot}$]	-3.95 ± 0.04	-4.75 ± 0.04	-0.80 ± 0.06	$\cdots$	$\cdots$	$\cdots$
Derived from Saumon & Marley (2008) Hybrid Evolutionary Models						
Mass M ($M_{\rm Jup}$)	$71.8^{+2.1}_{-1.9}$	$33.2^{+1.6}_{-2.0}$	$-38.7^{+1.9}_{-1.8}$	$68.5^{+2.7}_{-2.8}$	36.9 ± 1.5	-32 ± 3
$\log(L_{\rm bol})$ [$L_{\odot}$]	-3.96 ± 0.04	$-4.75^{+0.05}_{-0.04}$	-0.79 ± 0.06	-3.96 ± 0.04	-4.75 ± 0.04	-0.79 ± 0.06
Mass ratio q	$0.461^{+0.020}_{-0.023}$		$\cdots$	0.54 ± 0.03		$\cdots$
Age t (Gyr)	$0.89^{+0.09}_{-0.11}$		$\cdots$	$0.76^{+0.09}_{-0.14}$	$1.15^{+0.11}_{-0.12}$	$0.39^{+0.20}_{-0.15}$
$\log(t)$ [yr]	$8.95^{+0.04}_{-0.05}$		$\cdots$	$8.88^{+0.06}_{-0.08}$	9.06 ± 0.04	$0.18^{+0.09}_{-0.07}$
$T_{\rm eff}$ (K)	1870 ± 40	1180^{+29}_{-30}	-700 ± 50	1870 ± 40	1194^{+27}_{-26}	-670 ± 50
Radius ($R_{\rm Jup}$)	$0.964^{+0.007}_{-0.009}$	$0.983^{+0.011}_{-0.014}$	0.019 ± 0.004	$0.977^{+0.015}_{-0.014}$	0.958 ± 0.010	-0.020 ± 0.018
$\log(g)$ [cm s^{-2}]	$5.281^{+0.017}_{-0.015}$	4.93 ± 0.03	$-0.351^{+0.022}_{-0.023}$	5.250 ± 0.029	$4.999^{+0.025}_{-0.026}$	-0.25 ± 0.04
MKO($J-K$) (mag)	$1.120^{+0.055}_{-0.065}$	$0.318^{+0.149}_{-0.195}$	$-0.808^{+0.166}_{-0.195}$	$1.138^{+0.060}_{-0.066}$	$0.424^{+0.142}_{-0.167}$	$-0.718^{+0.163}_{-0.170}$
MKO($J-H$) (mag)	$0.607^{+0.025}_{-0.032}$	$0.374^{+0.086}_{-0.098}$	$-0.237^{+0.091}_{-0.097}$	$0.616^{+0.026}_{-0.034}$	$0.432^{+0.078}_{-0.087}$	$-0.186^{+0.082}_{-0.094}$
Derived from Baraffe et al. (2003) Cond Evolutionary Models						
Mass M ($M_{\rm Jup}$)	$66.6^{+1.9}_{-2.2}$	$38.5^{+1.7}_{-1.8}$	$-28.1^{+2.2}_{-1.9}$	$68.7^{+2.5}_{-2.9}$	36.8 ± 1.5	-32 ± 3
$\log(L_{\rm bol})$ [$L_{\odot}$]	$-3.95^{+0.05}_{-0.04}$	-4.75 ± 0.04	-0.80 ± 0.06	-3.95 ± 0.04	-4.76 ± 0.04	-0.80 ± 0.06
Mass ratio q	$0.578^{+0.024}_{-0.026}$		$\cdots$	0.54 ± 0.03		$\cdots$
Age t (Gyr)	$0.90^{+0.08}_{-0.09}$		$\cdots$	$1.01^{+0.14}_{-0.19}$	$0.83^{+0.08}_{-0.09}$	$-0.18^{+0.20}_{-0.17}$
$\log(t)$ [yr]	8.96 ± 0.04		$\cdots$	$9.00^{+0.06}_{-0.08}$	8.92 ± 0.04	$-0.09^{+0.09}_{-0.08}$
$T_{\rm eff}$ (K)	1940^{+50}_{-40}	1221^{+26}_{-35}	-720^{+50}_{-60}	1950 ± 40	1212^{+27}_{-28}	-740 ± 50
Radius ($R_{\rm Jup}$)	$0.918^{+0.008}_{-0.010}$	$0.919^{+0.008}_{-0.009}$	0.003 ± 0.006	$0.910^{+0.015}_{-0.012}$	$0.932^{+0.010}_{-0.015}$	$0.022^{+0.018}_{-0.020}$
$\log(g)$ [cm s^{-2}]	$5.294^{+0.018}_{-0.019}$	$5.047^{+0.029}_{-0.030}$	$-0.246^{+0.018}_{-0.021}$	$5.314^{+0.029}_{-0.025}$	$5.018^{+0.025}_{-0.027}$	-0.30 ± 0.04
$\log(\mathrm{Li}/\mathrm{Li}_{\rm init})$	$-2.95^{+0.20}_{-0.31}$	0.0 ± 0.0	$2.96^{+0.30}_{-0.21}$	$-2.72^{+0.20}_{-0.32}$	0.0 ± 0.0	$2.72^{+0.31}_{-0.21}$
MKO($J-K$) (mag)	$0.364^{+0.038}_{-0.036}$	$-0.019^{+0.021}_{-0.018}$	$-0.386^{+0.043}_{-0.039}$	$0.366^{+0.034}_{-0.036}$	-0.016 ± 0.022	$-0.382^{+0.041}_{-0.042}$
MKO($J-H$) (mag)	$0.130^{+0.023}_{-0.022}$	$-0.263^{+0.013}_{-0.014}$	$-0.392^{+0.026}_{-0.025}$	$0.132^{+0.023}_{-0.020}$	-0.262 ± 0.015	$-0.393^{+0.026}_{-0.027}$

Note. — For this analysis, the input mass and luminosity of 2MASS J0700+3157B were both divided by two in order to simulate a hypothetical scenario where it is an unresolved equal-mass, equal-flux binary.

Table 49. Properties of LHS 1901AB

Property	Using Total Mass			Using Individual Masses		
	Primary	Secondary	$\Delta = \mathrm{B} - \mathrm{A}$	Primary	Secondary	$\Delta = \mathrm{B} - \mathrm{A}$
Input Observed Properties						
Mass M ($M_{\rm Jup}$)	213^{+9}_{-10}		$\cdots$	113 ± 8	99 ± 7	-14 ± 12
Mass ratio q	$\cdots$	$\cdots$	$\cdots$	$0.87^{+0.09}_{-0.11}$		$\cdots$
$\log(L_{\rm bol})$ [$L_\odot$]	$-3.005^{+0.026}_{-0.027}$	$-3.046^{+0.026}_{-0.027}$	-0.04 ± 0.03	$\cdots$	$\cdots$	$\cdots$
Derived from Baraffe et al. (2015) Evolutionary Models						
Mass M ($M_{\rm Jup}$)	110 ± 3	$106.8^{+2.3}_{-3.0}$	-3 ± 4	$110.5^{+3.0}_{-2.9}$	$106.3^{+2.3}_{-2.4}$	-4 ± 4
$\log(L_{\rm bol})$ [$L_\odot$]	$-3.005^{+0.030}_{-0.029}$	$-3.040^{+0.031}_{-0.024}$	-0.04 ± 0.04	-3.003 ± 0.028	$-3.044^{+0.028}_{-0.021}$	-0.04 ± 0.04
Mass ratio q	$0.97^{+0.03}_{-0.04}$		$\cdots$	0.96 ± 0.03		$\cdots$
Age t (Gyr)	$5.2^{+1.9}_{-4.7}$		$\cdots$	$5.2^{+2.1}_{-4.4}$	$5.1^{+1.8}_{-4.8}$	0^{+5}_{-4}
$\log(t)$ [yr]	$9.71^{+0.29}_{-0.19}$		$\cdots$	$9.71^{+0.29}_{-0.18}$	$9.70^{+0.30}_{-0.20}$	$0.0^{+0.5}_{-0.4}$
$T_{\rm eff}$ (K)	2843 ± 17	2823^{+19}_{-13}	-20^{+24}_{-23}	2844 ± 16	2820^{+20}_{-10}	-24^{+24}_{-22}
Radius ($R_{\rm Jup}$)	$1.259^{+0.029}_{-0.028}$	$1.227^{+0.023}_{-0.026}$	-0.03 ± 0.04	$1.261^{+0.026}_{-0.027}$	$1.223^{+0.019}_{-0.024}$	$-0.04^{+0.03}_{-0.04}$
$\log(g)$ [cm s^{-2}]	5.234 ± 0.008	5.242 ± 0.007	0.009 ± 0.009	5.233 ± 0.007	$5.243^{+0.006}_{-0.007}$	0.010 ± 0.010
$\log(\mathrm{Li}/\mathrm{Li}_{\rm init})$	< -4.0	< -4.0	$\cdots$	< -4.0	< -4.0	$\cdots$
MKO($J-K$) (mag)	0.818 ± 0.001	0.819 ± 0.001	0.001 ± 0.001	0.818 ± 0.001	0.819 ± 0.001	$0.001^{+0.002}_{-0.003}$
MKO($J-H$) (mag)	$0.517^{+0.005}_{-0.004}$	$0.515^{+0.006}_{-0.004}$	$-0.001^{+0.002}_{-0.001}$	$0.517^{+0.005}_{-0.004}$	$0.515^{+0.006}_{-0.004}$	$-0.002^{+0.005}_{-0.009}$

Table 50. Properties of 2MASS J0746+2000AB

Property	Using Total Mass			Using Individual Masses		
	Primary	Secondary	$\Delta = \mathrm{B} - \mathrm{A}$	Primary	Secondary	$\Delta = \mathrm{B} - \mathrm{A}$
Input Observed Properties						
Mass M (M_{Jup})	$160.8^{+1.8}_{-1.7}$		$\cdots$	$82.4^{+1.4}_{-1.5}$	78.4 ± 1.4	$-4.0^{+2.3}_{-2.2}$
Mass ratio q	$\cdots$	$\cdots$	$\cdots$	$0.952^{+0.026}_{-0.027}$		$\cdots$
$\log(L_{\mathrm{bol}})$ [$L_{\odot}$]	$-3.596^{+0.028}_{-0.026}$	-3.777 ± 0.027	-0.18 ± 0.04	$\cdots$	$\cdots$	$\cdots$
Derived from Baraffe et al. (2015) Evolutionary Models						
Mass M (M_{Jup})	83.2 ± 0.7	$79.9^{+1.1}_{-0.7}$	$-3.6^{+1.2}_{-0.7}$	$83.4^{+0.7}_{-0.6}$	$80.0^{+0.8}_{-0.5}$	$-3.4^{+1.1}_{-1.0}$
$\log(L_{\mathrm{bol}})$ [$L_{\odot}$]	$-3.599^{+0.023}_{-0.027}$	$-3.782^{+0.027}_{-0.025}$	$-0.18^{+0.03}_{-0.04}$	$-3.599^{+0.026}_{-0.023}$	$-3.783^{+0.026}_{-0.027}$	$-0.18^{+0.03}_{-0.04}$
Mass ratio q	$0.957^{+0.012}_{-0.010}$		$\cdots$	$0.959^{+0.013}_{-0.011}$		$\cdots$
Age t (Gyr)	$3.2^{+2.4}_{-2.2}$		$\cdots$	$5.1^{+1.9}_{-4.2}$	$4.4^{+2.1}_{-3.4}$	0^{+4}_{-5}
$\log(t)$ [yr]	$9.51^{+0.27}_{-0.45}$		$\cdots$	$9.71^{+0.29}_{-0.18}$	$9.64^{+0.36}_{-0.22}$	$0.0^{+0.4}_{-0.5}$
T_{eff} (K)	2317^{+24}_{-25}	2134^{+23}_{-28}	-180^{+30}_{-40}	2318^{+24}_{-23}	2134^{+26}_{-25}	-180^{+30}_{-40}
Radius (R_{Jup})	$0.959^{+0.007}_{-0.008}$	$0.914^{+0.008}_{-0.006}$	$-0.044^{+0.009}_{-0.010}$	$0.959^{+0.007}_{-0.008}$	$0.914^{+0.007}_{-0.008}$	$-0.045^{+0.011}_{-0.010}$
$\log(g)$ [$\mathrm{cm\,s^{-2}}$]	$5.351^{+0.006}_{-0.005}$	$5.374^{+0.009}_{-0.007}$	0.021 ± 0.006	$5.352^{+0.005}_{-0.004}$	$5.375^{+0.007}_{-0.004}$	$0.023^{+0.009}_{-0.007}$
$\log(\mathrm{Li}/\mathrm{Li}_{\mathrm{init}})$	< -4.0	< -4.0	$\cdots$	< -4.0	< -4.0	$\cdots$
MKO($J-K$) (mag)	$0.738^{+0.012}_{-0.011}$	$0.830^{+0.027}_{-0.023}$	$0.086^{+0.027}_{-0.030}$	$0.735^{+0.005}_{-0.009}$	$0.829^{+0.026}_{-0.020}$	$0.090^{+0.030}_{-0.024}$
MKO($J-H$) (mag)	0.453 ± 0.011	$0.519^{+0.014}_{-0.015}$	$0.062^{+0.018}_{-0.019}$	$0.450^{+0.004}_{-0.009}$	$0.518^{+0.013}_{-0.014}$	$0.066^{+0.018}_{-0.016}$

Table 51. Properties of 2MASS J0920+3517AB

Property	Using Total Mass			Using Individual Masses		
	Primary	Secondary	$\Delta = \mathrm{B} - \mathrm{A}$	Primary	Secondary	$\Delta = \mathrm{B} - \mathrm{A}$
Input Observed Properties						
Mass M (M_{Jup})	187 ± 11		···	71 ± 5	116^{+7}_{-8}	45 ± 5
Mass ratio q	···	···	···	$1.63^{+0.08}_{-0.09}$		···
$\log(L_{\mathrm{bol}})$ [$L_{\odot}$]	-4.27 ± 0.03	-4.34 ± 0.03	-0.06 ± 0.04	···	···	···
Derived from Saumon & Marley (2008) Hybrid Evolutionary Models						
Mass M (M_{Jup})	···	···	···	$74.2^{+0.9}_{-0.6}$	···	···
$\log(L_{\mathrm{bol}})$ [$L_{\odot}$]	···	···	···	-4.27 ± 0.03	···	···
Mass ratio q	···		···	···		···
Age t (Gyr)	···		···	7^{+3}_{-5}	···	···
$\log(t)$ [yr]	···		···	$9.82^{+0.35}_{-0.24}$	···	···
T_{eff} (K)	···	···	···	1621^{+33}_{-30}	···	···
Radius (R_{Jup})	···	···	···	$0.902^{+0.004}_{-0.005}$	···	···
$\log(g)$ [cm s^{-2}]	···	···	···	$5.3560^{+0.0020}_{-0.0032}$	···	···
MKO($J - K$) (mag)	···	···	···	$1.691^{+0.077}_{-0.066}$	···	···
MKO($J - H$) (mag)	···	···	···	$0.912^{+0.043}_{-0.034}$	···	···
Derived from Baraffe et al. (2003) Cond Evolutionary Models						
Mass M (M_{Jup})	···	···	···	$73.4^{+3.5}_{-2.3}$	···	···
$\log(L_{\mathrm{bol}})$ [$L_{\odot}$]	···	···	···	-4.27 ± 0.03	···	···
Mass ratio q	···		···	···		···
Age t (Gyr)	···		···	$3.1^{+1.5}_{-1.7}$	···	···
$\log(t)$ [yr]	···		···	$9.49^{+0.22}_{-0.28}$	···	···
T_{eff} (K)	···	···	···	1700 ± 30	···	···
Radius (R_{Jup})	···	···	···	$0.826^{+0.012}_{-0.016}$	···	···
$\log(g)$ [cm s^{-2}]	···	···	···	$5.430^{+0.029}_{-0.025}$	···	···
$\log(\mathrm{Li}/\mathrm{Li}_{\mathrm{init}})$	···	···	···	$-3.16^{+0.20}_{-0.43}$	···	···
MKO($J - K$) (mag)	···	···	···	$0.119^{+0.026}_{-0.025}$	···	···
MKO($J - H$) (mag)	···	···	···	-0.032 ± 0.020	···	···

Note. — The total mass analysis failed due to the anomalously high mass of this system given our measured luminosities and under the assumption that it is a binary and not higher order multiple. The individual mass analysis of the secondary likewise failed.

Table 52. Properties of 2MASS J0920+3517AB (Unresolved Triple Hypothesis)

Property	Using Total Mass			Using Individual Masses		
	Primary	Secondary	$\Delta = \mathrm{B} - \mathrm{A}$	Primary	Secondary	$\Delta = \mathrm{B} - \mathrm{A}$
Input Observed Properties						
Mass M (M_{Jup})	129^{+7}_{-8}		$\cdots$	71 ± 5	58^{+3}_{-4}	-13 ± 3
Mass ratio q	$\cdots$	$\cdots$	$\cdots$	0.81 ± 0.04		$\cdots$
$\log(L_{\mathrm{bol}})$ [$L_{\odot}$]	-4.27 ± 0.03	$-4.639^{+0.029}_{-0.031}$	-0.37 ± 0.04	$\cdots$	$\cdots$	$\cdots$
Derived from Saumon & Marley (2008) Hybrid Evolutionary Models						
Mass M (M_{Jup})	$72.3^{+2.2}_{-1.3}$	58^{+5}_{-9}	-14^{+4}_{-6}	$74.2^{+0.9}_{-0.6}$	59 ± 4	-15^{+4}_{-5}
$\log(L_{\mathrm{bol}})$ [$L_{\odot}$]	-4.27 ± 0.04	$-4.64^{+0.03}_{-0.04}$	$-0.36^{+0.04}_{-0.05}$	-4.27 ± 0.03	-4.64 ± 0.03	-0.37 ± 0.05
Mass ratio q	$0.81^{+0.07}_{-0.08}$		$\cdots$	$0.80^{+0.05}_{-0.06}$		$\cdots$
Age t (Gyr)	$2.2^{+0.4}_{-0.7}$		$\cdots$	7^{+3}_{-5}	$2.3^{+0.3}_{-0.4}$	-4^{+5}_{-3}
$\log(t)$ [yr]	$9.34^{+0.10}_{-0.14}$		$\cdots$	$9.82^{+0.35}_{-0.24}$	$9.36^{+0.07}_{-0.08}$	$-0.44^{+0.29}_{-0.40}$
T_{eff} (K)	1610 ± 30	1322^{+34}_{-24}	-290^{+30}_{-40}	1621^{+33}_{-30}	1322 ± 23	-300 ± 40
Radius (R_{Jup})	$0.908^{+0.004}_{-0.006}$	$0.890^{+0.019}_{-0.023}$	$-0.017^{+0.017}_{-0.015}$	$0.902^{+0.004}_{-0.005}$	0.888 ± 0.014	$-0.016^{+0.017}_{-0.014}$
$\log(g)$ [cm s^{-2}]	$5.336^{+0.021}_{-0.007}$	$5.26^{+0.06}_{-0.07}$	$-0.07^{+0.05}_{-0.06}$	$5.3560^{+0.0020}_{-0.0032}$	5.27 ± 0.04	$-0.08^{+0.04}_{-0.05}$
MKO($J - K$) (mag)	$1.695^{+0.078}_{-0.069}$	$1.578^{+0.291}_{-0.218}$	$-0.108^{+0.333}_{-0.255}$	$1.691^{+0.077}_{-0.066}$	$1.575^{+0.216}_{-0.213}$	$-0.110^{+0.235}_{-0.217}$
MKO($J - H$) (mag)	$0.912^{+0.042}_{-0.037}$	$0.973^{+0.111}_{-0.088}$	$0.062^{+0.130}_{-0.111}$	$0.912^{+0.043}_{-0.034}$	$0.971^{+0.089}_{-0.081}$	$0.062^{+0.094}_{-0.093}$
Derived from Baraffe et al. (2003) Cond Evolutionary Models						
Mass M (M_{Jup})	$69.9^{+2.8}_{-2.7}$	60^{+4}_{-5}	$-9.6^{+2.4}_{-2.0}$	$73.4^{+3.5}_{-2.3}$	59 ± 4	-14^{+5}_{-6}
$\log(L_{\mathrm{bol}})$ [$L_{\odot}$]	$-4.27^{+0.03}_{-0.04}$	$-4.640^{+0.041}_{-0.027}$	$-0.37^{+0.04}_{-0.06}$	$-4.27^{+0.03}_{-0.04}$	-4.64 ± 0.03	-0.37 ± 0.05
Mass ratio q	$0.863^{+0.042}_{-0.030}$		$\cdots$	$0.81^{+0.06}_{-0.07}$		$\cdots$
Age t (Gyr)	$2.2^{+0.4}_{-0.5}$		$\cdots$	$3.1^{+1.4}_{-1.7}$	$1.99^{+0.25}_{-0.37}$	$-1.0^{+1.9}_{-1.6}$
$\log(t)$ [yr]	$9.33^{+0.08}_{-0.10}$		$\cdots$	$9.49^{+0.22}_{-0.28}$	$9.30^{+0.06}_{-0.08}$	-0.19 ± 0.26
T_{eff} (K)	1690^{+30}_{-40}	1380 ± 30	-310^{+30}_{-50}	1700^{+40}_{-30}	1370 ± 30	-330 ± 50
Radius (R_{Jup})	0.839 ± 0.009	$0.823^{+0.017}_{-0.018}$	$-0.016^{+0.009}_{-0.008}$	$0.826^{+0.012}_{-0.016}$	$0.831^{+0.016}_{-0.017}$	$0.004^{+0.023}_{-0.021}$
$\log(g)$ [cm s^{-2}]	$5.393^{+0.026}_{-0.027}$	$5.34^{+0.05}_{-0.06}$	$-0.051^{+0.026}_{-0.024}$	$5.430^{+0.030}_{-0.025}$	5.32 ± 0.05	$-0.10^{+0.05}_{-0.06}$
$\log(\mathrm{Li}/\mathrm{Li}_{\mathrm{init}})$	$-3.10^{+-0.21}_{-0.22}$	$-0.0202^{+0.0020}_{-0.0027}$	$3.3^{+0.0}_{-0.2}$	$-3.26^{+0.20}_{-0.32}$	$-0.0215^{+0.0019}_{-0.0018}$	$3.5^{+0.0}_{-0.6}$
MKO($J - K$) (mag)	0.127 ± 0.021	$-0.034^{+0.017}_{-0.013}$	$-0.163^{+0.024}_{-0.028}$	$0.119^{+0.026}_{-0.025}$	$-0.032^{+0.015}_{-0.014}$	$-0.151^{+0.029}_{-0.030}$
MKO($J - H$) (mag)	-0.033 ± 0.021	$-0.219^{+0.016}_{-0.013}$	$-0.186^{+0.022}_{-0.030}$	$-0.032^{+0.020}_{-0.019}$	$-0.219^{+0.014}_{-0.015}$	$-0.187^{+0.025}_{-0.024}$

Note. — For this analysis, the input mass and luminosity of 2MASS J0920+3517B were both divided by two in order to simulate a hypothetical scenario where it is an unresolved equal-mass, equal-flux binary.

Table 53. Properties of 2MASS J1017+1308AB

Property	Using Total Mass			Using Individual Masses		
	Primary	Secondary	$\Delta = \mathrm{B} - \mathrm{A}$	Primary	Secondary	$\Delta = \mathrm{B} - \mathrm{A}$
Input Observed Properties						
Mass M ($M_{\rm Jup}$)	156^{+14}_{-18}		$\cdots$	81^{+10}_{-11}	75 ± 7	-6 ± 7
Mass ratio q	$\cdots$	$\cdots$	$\cdots$	0.92 ± 0.08		$\cdots$
$\log(L_{\rm bol})$ [$L_\odot$]	-3.78 ± 0.04	-3.84 ± 0.04	-0.06 ± 0.04	$\cdots$	$\cdots$	$\cdots$
Derived from Saumon & Marley (2008) Hybrid Evolutionary Models						
Mass M ($M_{\rm Jup}$)	$81.4^{+1.5}_{-0.7}$	$80.4^{+1.3}_{-1.1}$	$-1.0^{+1.4}_{-1.2}$	$81.4^{+1.1}_{-0.9}$	$80.6^{+1.2}_{-0.9}$	$-0.8^{+1.8}_{-1.6}$
$\log(L_{\rm bol})$ [$L_\odot$]	$-3.77^{+0.06}_{-0.04}$	-3.83 ± 0.05	$-0.06^{+0.07}_{-0.06}$	-3.78 ± 0.05	-3.82 ± 0.05	-0.04 ± 0.07
Mass ratio q	$0.987^{+0.017}_{-0.015}$		$\cdots$	$0.990^{+0.023}_{-0.019}$		$\cdots$
Age t (Gyr)	6^{+3}_{-6}		$\cdots$	$7.3^{+2.8}_{-6.8}$	$7.0^{+2.9}_{-6.4}$	0^{+6}_{-7}
$\log(t)$ [yr]	$9.80^{+0.37}_{-0.24}$		$\cdots$	$9.86^{+0.31}_{-0.20}$	$9.84^{+0.33}_{-0.23}$	0.0 ± 0.5
$T_{\rm eff}$ (K)	2090^{+60}_{-40}	2030 ± 60	-60 ± 70	2090 ± 50	2040^{+60}_{-50}	-50^{+80}_{-70}
Radius ($R_{\rm Jup}$)	$0.963^{+0.008}_{-0.010}$	0.955 ± 0.008	-0.007 ± 0.009	$0.961^{+0.007}_{-0.009}$	$0.955^{+0.007}_{-0.008}$	$-0.005^{+0.012}_{-0.013}$
$\log(g)$ [cm s^{-2}]	$5.3387^{+0.0040}_{-0.0025}$	$5.3416^{+0.0015}_{-0.0033}$	$0.0009^{+0.0041}_{-0.0018}$	$5.3396^{+0.0029}_{-0.0023}$	$5.3416^{+0.0013}_{-0.0026}$	$0.001^{+0.006}_{-0.004}$
MKO($J-K$) (mag)	$0.940^{+0.020}_{-0.027}$	$0.973^{+0.026}_{-0.038}$	$0.030^{+0.035}_{-0.042}$	$0.943^{+0.022}_{-0.027}$	$0.968^{+0.025}_{-0.035}$	0.023 ± 0.040
MKO($J-H$) (mag)	$0.540^{+0.007}_{-0.008}$	0.550 ± 0.009	$0.009^{+0.010}_{-0.013}$	$0.541^{+0.007}_{-0.008}$	$0.549^{+0.007}_{-0.010}$	0.007 ± 0.012
Derived from Baraffe et al. (2015) Evolutionary Models						
Mass M ($M_{\rm Jup}$)	$80.2^{+1.5}_{-1.0}$	$79.2^{+1.4}_{-1.1}$	$-1.0^{+1.1}_{-1.4}$	$80.2^{+1.2}_{-1.0}$	$79.4^{+1.3}_{-1.0}$	$-0.8^{+2.1}_{-1.9}$
$\log(L_{\rm bol})$ [$L_\odot$]	-3.77 ± 0.05	-3.83 ± 0.05	$-0.06^{+0.07}_{-0.06}$	-3.78 ± 0.05	-3.82 ± 0.05	-0.04 ± 0.07
Mass ratio q	$0.987^{+0.017}_{-0.015}$		$\cdots$	$0.990^{+0.026}_{-0.023}$		$\cdots$
Age t (Gyr)	$4.4^{+2.3}_{-3.7}$		$\cdots$	$5.0^{+1.9}_{-4.3}$	$4.8^{+1.9}_{-4.2}$	0 ± 4
$\log(t)$ [yr]	$9.64^{+0.35}_{-0.22}$		$\cdots$	$9.70^{+0.30}_{-0.19}$	$9.68^{+0.32}_{-0.21}$	0.0 ± 0.5
$T_{\rm eff}$ (K)	2140^{+60}_{-50}	2090 ± 50	-60 ± 70	2140 ± 50	2100 ± 50	-40^{+70}_{-80}
Radius ($R_{\rm Jup}$)	$0.918^{+0.012}_{-0.014}$	$0.906^{+0.010}_{-0.013}$	$-0.010^{+0.012}_{-0.014}$	0.916 ± 0.013	$0.907^{+0.009}_{-0.013}$	$-0.008^{+0.017}_{-0.018}$
$\log(g)$ [cm s^{-2}]	$5.372^{+0.013}_{-0.006}$	$5.379^{+0.008}_{-0.006}$	$0.004^{+0.008}_{-0.006}$	$5.374^{+0.011}_{-0.005}$	$5.378^{+0.008}_{-0.005}$	$0.004^{+0.014}_{-0.013}$
$\log(\mathrm{Li}/\mathrm{Li}_{\rm init})$	< -4.0	< -4.0	$\cdots$	< -4.0	< -4.0	$\cdots$
MKO($J-K$) (mag)	$0.822^{+0.035}_{-0.037}$	$0.860^{+0.055}_{-0.058}$	$0.039^{+0.068}_{-0.056}$	$0.826^{+0.033}_{-0.039}$	$0.855^{+0.049}_{-0.053}$	$0.033^{+0.066}_{-0.071}$
MKO($J-H$) (mag)	$0.515^{+0.020}_{-0.027}$	$0.540^{+0.028}_{-0.036}$	$0.026^{+0.037}_{-0.036}$	$0.517^{+0.020}_{-0.026}$	$0.536^{+0.028}_{-0.031}$	$0.022^{+0.038}_{-0.042}$

Table 54. Properties of 2MASS J1047+4026AB (a.k.a. LP 213-68)

Property	Using Total Mass: Primary	Using Total Mass: Secondary	Using Total Mass: $\Delta = \mathrm{B} - \mathrm{A}$	Using Individual Masses: Primary	Using Individual Masses: Secondary	Using Individual Masses: $\Delta = \mathrm{B} - \mathrm{A}$
Input Observed Properties						
Mass M ($M_{\rm Jup}$)	178^{+11}_{-12}		$\cdots$	97^{+6}_{-7}	80 ± 6	-17 ± 7
Mass ratio q	$\cdots$	$\cdots$	$\cdots$	0.82 ± 0.06		$\cdots$
$\log(L_{\rm bol})$ [$L_\odot$]	-3.27 ± 0.04	-3.39 ± 0.05	-0.13 ± 0.06	$\cdots$	$\cdots$	$\cdots$
Derived from Baraffe et al. (2015) Evolutionary Models						
Mass M ($M_{\rm Jup}$)	$94.2^{+2.4}_{-2.2}$	$89.5^{+2.4}_{-2.0}$	$-5.0^{+3.0}_{-2.7}$	94.2 ± 2.1	$89.1^{+2.8}_{-2.2}$	-5^{+4}_{-3}
$\log(L_{\rm bol})$ [$L_\odot$]	-3.26 ± 0.05	$-3.39^{+0.05}_{-0.07}$	-0.13 ± 0.07	-3.26 ± 0.05	$-3.39^{+0.05}_{-0.06}$	$-0.13^{+0.08}_{-0.07}$
Mass ratio q	0.947 ± 0.029		$\cdots$	$0.94^{+0.04}_{-0.03}$		$\cdots$
Age t (Gyr)	$4.7^{+2.0}_{-4.3}$		$\cdots$	$5.2^{+2.0}_{-4.5}$	$4.3^{+2.1}_{-4.0}$	-1^{+4}_{-5}
$\log(t)$ [yr]	$9.67^{+0.33}_{-0.22}$		$\cdots$	$9.72^{+0.28}_{-0.18}$	$9.63^{+0.37}_{-0.29}$	-0.1 ± 0.5
$T_{\rm eff}$ (K)	2640 ± 50	2510^{+50}_{-60}	-130 ± 70	2640^{+50}_{-40}	2510^{+60}_{-50}	-130 ± 70
Radius ($R_{\rm Jup}$)	$1.099^{+0.024}_{-0.023}$	$1.042^{+0.021}_{-0.029}$	-0.06 ± 0.03	$1.097^{+0.023}_{-0.024}$	$1.042^{+0.025}_{-0.026}$	$-0.06^{+0.03}_{-0.04}$
$\log(g)$ [$\mathrm{cm\,s^{-2}}$]	5.288 ± 0.011	$5.312^{+0.014}_{-0.012}$	$0.023^{+0.016}_{-0.014}$	5.289 ± 0.010	$5.312^{+0.016}_{-0.012}$	$0.022^{+0.021}_{-0.017}$
$\log(\mathrm{Li}/\mathrm{Li}_{\rm init})$	< -4.0	< -4.0	$\cdots$	< -4.0	< -4.0	$\cdots$
MKO($J-K$) (mag)	$0.797^{+0.009}_{-0.006}$	$0.769^{+0.019}_{-0.017}$	$-0.027^{+0.021}_{-0.018}$	$0.796^{+0.010}_{-0.007}$	$0.769^{+0.019}_{-0.021}$	$-0.025^{+0.021}_{-0.022}$
MKO($J-H$) (mag)	$0.489^{+0.007}_{-0.006}$	$0.471^{+0.012}_{-0.013}$	$-0.018^{+0.018}_{-0.009}$	$0.489^{+0.007}_{-0.006}$	$0.471^{+0.019}_{-0.006}$	$-0.017^{+0.015}_{-0.014}$

Table 55. Properties of SDSS J1052+4422AB

Property	Using Total Mass: Primary	Using Total Mass: Secondary	Using Total Mass: $\Delta = \mathrm{B} - \mathrm{A}$	Using Individual Masses: Primary	Using Individual Masses: Secondary	Using Individual Masses: $\Delta = \mathrm{B} - \mathrm{A}$
Input Observed Properties						
Mass M ($M_{\rm Jup}$)	90^{+4}_{-5}		$\cdots$	51 ± 3	$39.4^{+2.6}_{-2.7}$	-11 ± 4
Mass ratio q	$\cdots$	$\cdots$	$\cdots$	0.78 ± 0.07		$\cdots$
$\log(L_{\rm bol})$ [$L_\odot$]	-4.51 ± 0.04	-4.64 ± 0.07	-0.13 ± 0.08	$\cdots$	$\cdots$	$\cdots$
Derived from Saumon & Marley (2008) Hybrid Evolutionary Models						
Mass M ($M_{\rm Jup}$)	50 ± 4	41^{+3}_{-4}	-9^{+5}_{-6}	51 ± 3	$39.9^{+2.6}_{-2.8}$	-11 ± 4
$\log(L_{\rm bol})$ [$L_\odot$]	-4.52 ± 0.04	$-4.62^{+0.07}_{-0.06}$	-0.10 ± 0.08	-4.52 ± 0.04	-4.64 ± 0.07	-0.12 ± 0.08
Mass ratio q	$0.82^{+0.09}_{-0.11}$		$\cdots$	0.78 ± 0.07		$\cdots$
Age t (Gyr)	$1.04^{+0.14}_{-0.15}$		$\cdots$	$1.10^{+0.17}_{-0.21}$	$1.05^{+0.21}_{-0.24}$	-0.1 ± 0.3
$\log(t)$ [yr]	9.02 ± 0.06		$\cdots$	9.04 ± 0.08	$9.02^{+0.10}_{-0.09}$	-0.02 ± 0.12
$T_{\rm eff}$ (K)	1361^{+30}_{-33}	1280^{+50}_{-40}	-80 ± 60	1366^{+25}_{-29}	1270 ± 40	-100 ± 50
Radius ($R_{\rm Jup}$)	$0.960^{+0.015}_{-0.016}$	0.966 ± 0.014	$0.006^{+0.004}_{-0.005}$	$0.954^{+0.018}_{-0.019}$	$0.967^{+0.022}_{-0.024}$	0.013 ± 0.029
$\log(g)$ [cm s^{-2}]	5.12 ± 0.04	5.04 ± 0.04	$-0.09^{+0.05}_{-0.07}$	5.14 ± 0.04	$5.02^{+0.05}_{-0.04}$	-0.12 ± 0.06
MKO($J-K$) (mag)	$1.927^{+0.205}_{-0.150}$	$1.143^{+0.432}_{-0.491}$	$-0.759^{+0.499}_{-0.548}$	$1.948^{+0.179}_{-0.116}$	$1.021^{+0.386}_{-0.405}$	$-0.898^{+0.411}_{-0.439}$
MKO($J-H$) (mag)	$1.104^{+0.083}_{-0.049}$	$0.783^{+0.219}_{-0.193}$	$-0.314^{+0.222}_{-0.233}$	$1.110^{+0.071}_{-0.039}$	$0.727^{+0.184}_{-0.174}$	$-0.375^{+0.193}_{-0.185}$
Derived from Baraffe et al. (2003) Cond Evolutionary Models						
Mass M ($M_{\rm Jup}$)	$47.4^{+2.5}_{-2.7}$	$43.3^{+2.7}_{-2.4}$	$-4.3^{+2.6}_{-2.7}$	51 ± 3	$39.8^{+2.7}_{-2.8}$	-11^{+5}_{-4}
$\log(L_{\rm bol})$ [$L_\odot$]	-4.51 ± 0.04	$-4.65^{+0.08}_{-0.07}$	$-0.14^{+0.09}_{-0.08}$	-4.51 ± 0.04	-4.65 ± 0.07	$-0.14^{+0.08}_{-0.09}$
Mass ratio q	0.91 ± 0.05		$\cdots$	$0.78^{+0.07}_{-0.08}$		$\cdots$
Age t (Gyr)	0.99 ± 0.12		$\cdots$	$1.18^{+0.16}_{-0.20}$	$0.83^{+0.13}_{-0.16}$	$-0.35^{+0.25}_{-0.22}$
$\log(t)$ [yr]	8.99 ± 0.05		$\cdots$	$9.07^{+0.07}_{-0.06}$	$8.92^{+0.08}_{-0.07}$	-0.15 ± 0.10
$T_{\rm eff}$ (K)	1420 ± 40	1310^{+60}_{-50}	-110^{+60}_{-70}	1430 ± 40	1290 ± 50	-140^{+60}_{-70}
Radius ($R_{\rm Jup}$)	$0.902^{+0.010}_{-0.013}$	$0.908^{+0.007}_{-0.011}$	$0.0048^{+0.0029}_{-0.0048}$	0.883 ± 0.016	$0.924^{+0.019}_{-0.018}$	0.042 ± 0.025
$\log(g)$ [cm s^{-2}]	5.16 ± 0.04	$5.11^{+0.03}_{-0.04}$	$-0.047^{+0.031}_{-0.027}$	5.21 ± 0.04	$5.06^{+0.04}_{-0.05}$	$-0.15^{+0.07}_{-0.06}$
$\log(\mathrm{Li}/\mathrm{Li}_{\rm init})$	$-0.014^{+0.007}_{-0.006}$	-0.003 ± 0.003	$0.009^{+0.006}_{-0.007}$	$-0.022^{+0.017}_{-0.039}$	0.0 ± 0.0	$0.021^{+0.039}_{-0.019}$
MKO($J-K$) (mag)	$0.045^{+0.016}_{-0.019}$	$0.015^{+0.029}_{-0.024}$	$-0.030^{+0.025}_{-0.020}$	0.030 ± 0.019	$0.021^{+0.027}_{-0.025}$	$-0.010^{+0.036}_{-0.031}$
MKO($J-H$) (mag)	$-0.165^{+0.021}_{-0.019}$	-0.225 ± 0.029	$-0.061^{+0.033}_{-0.038}$	$-0.162^{+0.020}_{-0.019}$	$-0.227^{+0.026}_{-0.030}$	$-0.064^{+0.035}_{-0.033}$

Table 56. Properties of Gl 417BC

Property	Primary	Secondary	$\Delta = \mathrm{B} - \mathrm{A}$
Input Observed Properties			
Mass M (M_{Jup})	$99.2^{+3.0}_{-3.3}$		···
$\log(L_{\mathrm{bol}})$ [$L_{\odot}$]	$-4.132^{+0.031}_{-0.029}$	$-4.219^{+0.030}_{-0.032}$	-0.09 ± 0.04
Derived from Saumon & Marley (2008) Hybrid Evolutionary Models			
Mass M (M_{Jup})	$51.5^{+1.7}_{-1.8}$	$47.7^{+1.9}_{-1.8}$	-3.9 ± 1.9
$\log(L_{\mathrm{bol}})$ [$L_{\odot}$]	$-4.136^{+0.032}_{-0.030}$	$-4.217^{+0.032}_{-0.029}$	$-0.08^{+0.05}_{-0.04}$
Mass ratio q	$0.92^{+0.03}_{-0.04}$		···
Age t (Gyr)	$0.49^{+0.03}_{-0.04}$		···
$\log(t)$ [yr]	$8.69^{+0.03}_{-0.04}$		···
T_{eff} (K)	1639^{+29}_{-31}	1560^{+29}_{-26}	-80 ± 40
Radius (R_{Jup})	$1.032^{+0.010}_{-0.009}$	$1.036^{+0.010}_{-0.009}$	$0.0043^{+0.0022}_{-0.0020}$
$\log(g)$ [$\mathrm{cm\,s^{-2}}$]	$5.078^{+0.021}_{-0.022}$	$5.041^{+0.025}_{-0.021}$	$-0.037^{+0.018}_{-0.019}$
MKO($J-K$) (mag)	$1.530^{+0.054}_{-0.058}$	$1.697^{+0.064}_{-0.070}$	$0.167^{+0.088}_{-0.090}$
MKO($J-H$) (mag)	$0.810^{+0.026}_{-0.032}$	$0.899^{+0.037}_{-0.038}$	$0.089^{+0.046}_{-0.050}$
Derived from Baraffe et al. (2015) Evolutionary Models			
Mass M (M_{Jup})	$51.1^{+1.8}_{-1.7}$	$48.3^{+1.6}_{-1.5}$	$-2.8^{+1.4}_{-1.5}$
$\log(L_{\mathrm{bol}})$ [$L_{\odot}$]	-4.13 ± 0.03	-4.22 ± 0.03	-0.09 ± 0.04
Mass ratio q	$0.945^{+0.027}_{-0.026}$		···
Age t (Gyr)	$0.49^{+0.03}_{-0.04}$		···
$\log(t)$ [yr]	$8.692^{+0.030}_{-0.033}$		···
T_{eff} (K)	1677^{+28}_{-35}	1592^{+28}_{-32}	-90 ± 40
Radius (R_{Jup})	$0.993^{+0.006}_{-0.010}$	$0.995^{+0.007}_{-0.009}$	$0.0034^{+0.0018}_{-0.0023}$
$\log(g)$ [$\mathrm{cm\,s^{-2}}$]	$5.109^{+0.025}_{-0.021}$	$5.081^{+0.023}_{-0.019}$	-0.028 ± 0.014
$\log(\mathrm{Li}/\mathrm{Li}_{\mathrm{init}})$	$-0.020^{+0.006}_{-0.005}$	-0.014 ± 0.004	$0.006^{+0.003}_{-0.005}$
MKO($J-K$) (mag)	$2.050^{+0.018}_{-0.016}$	$2.076^{+0.014}_{-0.016}$	0.000 ± 0.000
MKO($J-H$) (mag)	$1.140^{+0.017}_{-0.016}$	$1.166^{+0.014}_{-0.016}$	0.000 ± 0.000

Table 57. Properties of LHS 2397aAB

Property	Using Total Mass			Using Individual Masses		
	Primary	Secondary	$\Delta = \mathrm{B} - \mathrm{A}$	Primary	Secondary	$\Delta = \mathrm{B} - \mathrm{A}$
Input Observed Properties						
Mass M (M_{Jup})	159^{+7}_{-8}		$\cdots$	93 ± 4	66 ± 4	$-27.3^{+3.0}_{-2.9}$
Mass ratio q	$\cdots$	$\cdots$	$\cdots$	$0.706^{+0.027}_{-0.028}$		$\cdots$
$\log(L_{\mathrm{bol}})$ [$L_{\odot}$]	$-3.34^{+0.04}_{-0.05}$	-4.48 ± 0.04	-1.14 ± 0.06	$\cdots$	$\cdots$	$\cdots$
Derived from Baraffe et al. (2015) Evolutionary Models						
Mass M (M_{Jup})	$\cdots$	$\cdots$	$\cdots$	$91.5^{+1.7}_{-1.8}$	$\cdots$	$\cdots$
$\log(L_{\mathrm{bol}})$ [$L_{\odot}$]	$\cdots$	$\cdots$	$\cdots$	-3.34 ± 0.05	$\cdots$	$\cdots$
Mass ratio q	$\cdots$		$\cdots$	$\cdots$		$\cdots$
Age t (Gyr)	$\cdots$		$\cdots$	$5.3^{+1.9}_{-4.5}$	$\cdots$	$\cdots$
$\log(t)$ [yr]	$\cdots$		$\cdots$	$9.72^{+0.28}_{-0.17}$	$\cdots$	$\cdots$
T_{eff} (K)	$\cdots$	$\cdots$	$\cdots$	2560^{+40}_{-50}	$\cdots$	$\cdots$
Radius (R_{Jup})	$\cdots$	$\cdots$	$\cdots$	$1.063^{+0.020}_{-0.023}$	$\cdots$	$\cdots$
$\log(g)$ [$\mathrm{cm\,s^{-2}}$]	$\cdots$	$\cdots$	$\cdots$	$5.304^{+0.011}_{-0.009}$	$\cdots$	$\cdots$
$\log(\mathrm{Li}/\mathrm{Li}_{\mathrm{init}})$	$\cdots$	$\cdots$	$\cdots$	< -4.0	$\cdots$	$\cdots$
MKO($J - K$) (mag)	$\cdots$	$\cdots$	$\cdots$	$0.779^{+0.016}_{-0.010}$	$\cdots$	$\cdots$
MKO($J - H$) (mag)	$\cdots$	$\cdots$	$\cdots$	$0.478^{+0.012}_{-0.006}$	$\cdots$	$\cdots$
Derived from Saumon & Marley (2008) Hybrid Evolutionary Models						
Mass M (M_{Jup})	$\cdots$	$\cdots$	$\cdots$	$\cdots$	$69.3^{+3.7}_{-2.9}$	$\cdots$
$\log(L_{\mathrm{bol}})$ [$L_{\odot}$]	$\cdots$	$\cdots$	$\cdots$	$\cdots$	$-4.48^{+0.05}_{-0.04}$	$\cdots$
Mass ratio q	$\cdots$		$\cdots$	$\cdots$		$\cdots$
Age t (Gyr)	$\cdots$		$\cdots$	$\cdots$	$2.8^{+2.1}_{-1.5}$	$\cdots$
$\log(t)$ [yr]	$\cdots$		$\cdots$	$\cdots$	$9.45^{+0.26}_{-0.31}$	$\cdots$
T_{eff} (K)	$\cdots$	$\cdots$	$\cdots$	$\cdots$	1440 ± 40	$\cdots$
Radius (R_{Jup})	$\cdots$	$\cdots$	$\cdots$	$\cdots$	0.890 ± 0.013	$\cdots$
$\log(g)$ [$\mathrm{cm\,s^{-2}}$]	$\cdots$	$\cdots$	$\cdots$	$\cdots$	$5.335^{+0.033}_{-0.029}$	$\cdots$
MKO($J - K$) (mag)	$\cdots$	$\cdots$	$\cdots$	$\cdots$	$2.013^{+0.077}_{-0.089}$	$\cdots$
MKO($J - H$) (mag)	$\cdots$	$\cdots$	$\cdots$	$\cdots$	$1.100^{+0.043}_{-0.060}$	$\cdots$
Derived from Baraffe et al. (2003) Cond Evolutionary Models						
Mass M (M_{Jup})	92.3 ± 1.8	69^{+6}_{-3}	-23^{+7}_{-4}	92.2 ± 1.8	67 ± 4	-25^{+4}_{-5}
$\log(L_{\mathrm{bol}})$ [$L_{\odot}$]	-3.33 ± 0.05	$-4.48^{+0.05}_{-0.04}$	$-1.15^{+0.06}_{-0.07}$	-3.33 ± 0.05	$-4.48^{+0.05}_{-0.04}$	-1.15 ± 0.07
Mass ratio q	$0.75^{+0.07}_{-0.04}$		$\cdots$	0.73 ± 0.05		$\cdots$
Age t (Gyr)	$3.2^{+1.1}_{-1.8}$		$\cdots$	$5.1^{+1.9}_{-4.4}$	$2.6^{+0.6}_{-1.0}$	-2^{+4}_{-3}
$\log(t)$ [yr]	$9.50^{+0.17}_{-0.29}$		$\cdots$	$9.71^{+0.29}_{-0.18}$	$9.42^{+0.11}_{-0.17}$	$-0.25^{+0.28}_{-0.37}$
T_{eff} (K)	2570 ± 50	1520 ± 40	-1040 ± 60	2560 ± 50	1520 ± 40	-1050 ± 60
Radius (R_{Jup})	$1.068^{+0.020}_{-0.023}$	$0.810^{+0.014}_{-0.026}$	$-0.258^{+0.029}_{-0.032}$	$1.068^{+0.020}_{-0.023}$	$0.819^{+0.016}_{-0.017}$	$-0.251^{+0.028}_{-0.026}$
$\log(g)$ [$\mathrm{cm\,s^{-2}}$]	$5.300^{+0.010}_{-0.009}$	$5.42^{+0.06}_{-0.03}$	$0.12^{+0.06}_{-0.04}$	5.300 ± 0.010	5.40 ± 0.04	0.10 ± 0.04

Table 57—Continued

Property	Using Total Mass			Using Individual Masses		
	Primary	Secondary	$\Delta = \mathrm{B} - \mathrm{A}$	Primary	Secondary	$\Delta = \mathrm{B} - \mathrm{A}$
$\log(\mathrm{Li}/\mathrm{Li}_{\mathrm{init}})$	$\cdots$	$-0.8^{+0.8}_{-0.5}$	$\cdots$	$\cdots$	$-1.8^{+0.4}_{-0.7}$	$\cdots$
MKO$(J-K)$ (mag)	$0.703^{+0.017}_{-0.012}$	$0.013^{+0.028}_{-0.025}$	$-0.689^{+0.028}_{-0.031}$	$0.702^{+0.016}_{-0.013}$	$0.019^{+0.027}_{-0.023}$	-0.683 ± 0.029
MKO$(J-H)$ (mag)	0.362 ± 0.013	$-0.143^{+0.023}_{-0.022}$	$-0.505^{+0.026}_{-0.024}$	$0.361^{+0.014}_{-0.012}$	$-0.142^{+0.022}_{-0.024}$	$-0.503^{+0.025}_{-0.027}$

Note. — The BHAC models do not extend to the luminosity of the secondary, so for the BHAC individual mass analysis only the results for LHS 2397aA are given. The SM08 models do not extend to the luminosity of the primary, so for the SM08 individual mass analysis only the results for LHS 2397aB are given.

Table 58. Properties of 2MASS J1404−3159AB

Property	Using Total Mass			Using Individual Masses		
	Primary	Secondary	$\Delta = \mathrm{B} - \mathrm{A}$	Primary	Secondary	$\Delta = \mathrm{B} - \mathrm{A}$
Input Observed Properties						
Mass M ($M_{\rm Jup}$)	120^{+11}_{-13}		···	65 ± 6	55^{+6}_{-7}	-10 ± 4
Mass ratio q	···	···	···	0.84 ± 0.06		···
$\log(L_{\rm bol})$ [$L_\odot$]	$-4.52^{+0.06}_{-0.05}$	$-4.87^{+0.08}_{-0.07}$	$-0.35^{+0.09}_{-0.10}$	···	···	···
Derived from Saumon & Marley (2008) Hybrid Evolutionary Models						
Mass M ($M_{\rm Jup}$)	$67.9^{+4.4}_{-2.3}$	53^{+7}_{-9}	-14^{+5}_{-6}	69 ± 4	57 ± 7	-10 ± 8
$\log(L_{\rm bol})$ [$L_\odot$]	-4.55 ± 0.06	-4.86 ± 0.08	-0.32 ± 0.10	-4.54 ± 0.06	-4.86 ± 0.08	-0.33 ± 0.10
Mass ratio q	$0.79^{+0.08}_{-0.11}$		···	$0.86^{+0.11}_{-0.12}$		···
Age t (Gyr)	$3.0^{+0.8}_{-1.3}$		···	$3.5^{+2.4}_{-2.2}$	$3.9^{+1.0}_{-1.7}$	0^{+3}_{-4}
$\log(t)$ [yr]	$9.48^{+0.14}_{-0.19}$		···	$9.54^{+0.28}_{-0.36}$	$9.59^{+0.13}_{-0.21}$	0.1 ± 0.4
$T_{\rm eff}$ (K)	1400^{+40}_{-50}	1180 ± 60	-220^{+70}_{-60}	1400^{+40}_{-50}	1190 ± 50	-210^{+80}_{-60}
Radius ($R_{\rm Jup}$)	$0.884^{+0.010}_{-0.012}$	$0.862^{+0.034}_{-0.029}$	$-0.018^{+0.023}_{-0.018}$	$0.883^{+0.014}_{-0.018}$	$0.841^{+0.023}_{-0.030}$	-0.04 ± 0.03
$\log(g)$ [cm s^{-2}]	$5.335^{+0.028}_{-0.025}$	$5.24^{+0.08}_{-0.12}$	$-0.09^{+0.05}_{-0.09}$	$5.34^{+0.03}_{-0.04}$	5.30 ± 0.08	-0.03 ± 0.09
MKO($J-K$) (mag)	$2.012^{+0.118}_{-0.082}$	$0.313^{+0.271}_{-0.396}$	$-1.645^{+0.305}_{-0.446}$	$1.984^{+0.136}_{-0.074}$	$0.382^{+0.300}_{-0.397}$	$-1.577^{+0.331}_{-0.424}$
MKO($J-H$) (mag)	$1.118^{+0.054}_{-0.034}$	$0.393^{+0.162}_{-0.210}$	$-0.706^{+0.177}_{-0.219}$	$1.104^{+0.047}_{-0.056}$	$0.432^{+0.163}_{-0.207}$	$-0.663^{+0.169}_{-0.217}$
Derived from Baraffe et al. (2003) Cond Evolutionary Models						
Mass M ($M_{\rm Jup}$)	66^{+4}_{-5}	55^{+7}_{-8}	-10^{+4}_{-3}	68^{+7}_{-3}	57^{+7}_{-8}	-10^{+9}_{-10}
$\log(L_{\rm bol})$ [$L_\odot$]	$-4.53^{+0.07}_{-0.06}$	$-4.88^{+0.08}_{-0.07}$	-0.34 ± 0.10	-4.53 ± 0.06	-4.88 ± 0.08	-0.35 ± 0.10
Mass ratio q	$0.85^{+0.07}_{-0.06}$		···	$0.86^{+0.12}_{-0.14}$		···
Age t (Gyr)	$2.5^{+0.6}_{-0.9}$		···	$3.0^{+1.1}_{-1.5}$	$2.9^{+0.8}_{-1.2}$	$-0.1^{+2.0}_{-2.4}$
$\log(t)$ [yr]	$9.40^{+0.12}_{-0.17}$		···	$9.48^{+0.17}_{-0.25}$	$9.46^{+0.14}_{-0.20}$	$-0.01^{+0.29}_{-0.28}$
$T_{\rm eff}$ (K)	1470^{+50}_{-60}	1200 ± 60	-270^{+70}_{-80}	1480 ± 50	1210^{+50}_{-60}	-270 ± 80
Radius ($R_{\rm Jup}$)	$0.818^{+0.018}_{-0.019}$	0.82 ± 0.03	$0.003^{+0.013}_{-0.015}$	$0.810^{+0.013}_{-0.028}$	$0.808^{+0.027}_{-0.035}$	0.00 ± 0.04
$\log(g)$ [cm s^{-2}]	5.39 ± 0.05	$5.30^{+0.08}_{-0.10}$	$-0.08^{+0.06}_{-0.03}$	$5.41^{+0.07}_{-0.03}$	$5.34^{+0.10}_{-0.09}$	$-0.07^{+0.10}_{-0.11}$
$\log(\mathrm{Li}/\mathrm{Li}_{\rm init})$	$-0.6^{+0.5}_{-0.7}$	$-0.017^{+0.003}_{-0.007}$	$0.6^{+0.5}_{-0.6}$	$-1.0^{+1.0}_{-0.4}$	$-0.018^{+0.003}_{-0.006}$	$1.0^{+0.5}_{-1.0}$
MKO($J-K$) (mag)	-0.002 ± 0.029	$-0.149^{+0.056}_{-0.045}$	$-0.149^{+0.063}_{-0.047}$	$-0.007^{+0.033}_{-0.031}$	$-0.159^{+0.062}_{-0.051}$	$-0.153^{+0.067}_{-0.064}$
MKO($J-H$) (mag)	$-0.168^{+0.029}_{-0.034}$	$-0.307^{+0.026}_{-0.024}$	$-0.138^{+0.039}_{-0.041}$	$-0.166^{+0.029}_{-0.031}$	$-0.307^{+0.024}_{-0.027}$	$-0.141^{+0.040}_{-0.039}$

Table 59. Properties of HD 130948BC

Property	Primary	Secondary	$\Delta = \mathrm{B} - \mathrm{A}$
Input Observed Properties			
Mass M (M_{Jup})	$115.4^{+2.2}_{-2.1}$		$\cdots$
$\log(L_{\mathrm{bol}})$ $[L_{\odot}]$	-3.85 ± 0.06	-3.96 ± 0.06	-0.11 ± 0.09
Derived from Saumon & Marley (2008) Hybrid Evolutionary Models			
Mass M (M_{Jup})	59.9 ± 2.0	$55.6^{+1.9}_{-2.0}$	-4 ± 3
$\log(L_{\mathrm{bol}})$ $[L_{\odot}]$	$-3.86^{+0.07}_{-0.06}$	$-3.97^{+0.06}_{-0.07}$	$-0.11^{+0.09}_{-0.08}$
Mass ratio q	0.93 ± 0.05		$\cdots$
Age t (Gyr)	0.44 ± 0.04		$\cdots$
$\log(t)$ [yr]	8.64 ± 0.04		$\cdots$
T_{eff} (K)	1920^{+70}_{-60}	1800^{+50}_{-70}	-120^{+100}_{-90}
Radius (R_{Jup})	$1.040^{+0.011}_{-0.010}$	1.041 ± 0.010	$0.0011^{+0.0014}_{-0.0011}$
$\log(g)$ $[\mathrm{cm\,s^{-2}}]$	$5.136^{+0.020}_{-0.018}$	5.103 ± 0.019	$-0.033^{+0.026}_{-0.024}$
MKO($J-K$) (mag)	$1.081^{+0.059}_{-0.090}$	$1.242^{+0.100}_{-0.112}$	$0.161^{+0.121}_{-0.132}$
MKO($J-H$) (mag)	$0.588^{+0.027}_{-0.043}$	$0.663^{+0.050}_{-0.057}$	$0.075^{+0.056}_{-0.065}$
Derived from Baraffe et al. (2015) Evolutionary Models			
Mass M (M_{Jup})	$59.6^{+1.6}_{-1.8}$	$56.0^{+1.8}_{-1.6}$	$-3.5^{+2.8}_{-2.3}$
$\log(L_{\mathrm{bol}})$ $[L_{\odot}]$	$-3.83^{+0.07}_{-0.06}$	$-3.98^{+0.06}_{-0.07}$	$-0.15^{+0.09}_{-0.10}$
Mass ratio q	$0.94^{+0.05}_{-0.04}$		$\cdots$
Age t (Gyr)	0.49 ± 0.03		$\cdots$
$\log(t)$ [yr]	$8.689^{+0.030}_{-0.026}$		$\cdots$
T_{eff} (K)	2000^{+70}_{-60}	1830^{+60}_{-70}	-160^{+90}_{-110}
Radius (R_{Jup})	$0.989^{+0.008}_{-0.009}$	$0.987^{+0.006}_{-0.005}$	$-0.0002^{+0.0016}_{-0.0023}$
$\log(g)$ $[\mathrm{cm\,s^{-2}}]$	$5.178^{+0.015}_{-0.017}$	$5.152^{+0.020}_{-0.016}$	$-0.025^{+0.020}_{-0.017}$
$\log(\mathrm{Li}/\mathrm{Li}_{\mathrm{init}})$	$-0.7^{+0.5}_{-0.3}$	$-0.14^{+0.12}_{-0.06}$	$0.5^{+0.4}_{-0.6}$
MKO($J-K$) (mag)	$0.904^{+0.023}_{-0.021}$	$1.787^{+0.287}_{-0.278}$	$0.847^{+0.297}_{-0.387}$
MKO($J-H$) (mag)	$0.560^{+0.013}_{-0.010}$	$1.008^{+0.146}_{-0.149}$	$0.434^{+0.133}_{-0.203}$

Table 60. Properties of Gl 569Bab

Property	Primary	Secondary	$\Delta = \mathrm{B} - \mathrm{A}$
Input Observed Properties			
Mass M (M_{Jup})	138 ± 7		$\cdots$
$\log(L_{\mathrm{bol}})$ [$L_\odot$]	-3.44 ± 0.03	-3.67 ± 0.03	-0.22 ± 0.04
Derived from Baraffe et al. (2015) Evolutionary Models			
Mass M (M_{Jup})	75 ± 4	64 ± 4	$-11.4^{+2.4}_{-2.6}$
$\log(L_{\mathrm{bol}})$ [$L_\odot$]	-3.44 ± 0.04	-3.66 ± 0.04	-0.22 ± 0.05
Mass ratio q	0.85 ± 0.03		$\cdots$
Age t (Gyr)	$0.44^{+0.05}_{-0.06}$		$\cdots$
$\log(t)$ [yr]	$8.64^{+0.05}_{-0.06}$		$\cdots$
T_{eff} (K)	2420 ± 40	2170 ± 50	-250^{+50}_{-60}
Radius (R_{Jup})	$1.057^{+0.017}_{-0.015}$	$1.014^{+0.018}_{-0.013}$	$-0.042^{+0.013}_{-0.010}$
$\log(g)$ [$\mathrm{cm\,s^{-2}}$]	$5.222^{+0.026}_{-0.031}$	$5.18^{+0.03}_{-0.04}$	$-0.036^{+0.013}_{-0.011}$
$\log(\mathrm{Li}/\mathrm{Li}_{\mathrm{init}})$	< -4.0	$-3.1^{+3.1}_{-1.7}$	$5.5^{+1.8}_{-1.5}$
MKO($J - K$) (mag)	$0.793^{+0.010}_{-0.008}$	$0.894^{+0.014}_{-0.019}$	$0.103^{+0.018}_{-0.027}$
MKO($J - H$) (mag)	$0.481^{+0.009}_{-0.006}$	$0.550^{+0.001}_{-0.021}$	$0.066^{+0.021}_{-0.023}$

Table 61. Properties of 2MASS J1534−2952AB

Property	Using Total Mass: Primary	Using Total Mass: Secondary	Using Total Mass: $\Delta = \mathrm{B} - \mathrm{A}$	Using Individual Masses: Primary	Using Individual Masses: Secondary	Using Individual Masses: $\Delta = \mathrm{B} - \mathrm{A}$
Input Observed Properties						
Mass M (M_{Jup})	99 ± 5		$\cdots$	51 ± 5	48 ± 5	-3 ± 8
Mass ratio q	$\cdots$	$\cdots$	$\cdots$	$0.95^{+0.13}_{-0.16}$		$\cdots$
$\log(L_{\mathrm{bol}})$ [$L_\odot$]	-4.91 ± 0.07	-4.99 ± 0.07	$-0.07^{+0.09}_{-0.10}$	$\cdots$	$\cdots$	$\cdots$
Derived from Saumon & Marley (2008) Hybrid Evolutionary Models						
Mass M (M_{Jup})	51 ± 3	49 ± 3	-2.1 ± 3.0	52 ± 5	49 ± 5	-3 ± 7
$\log(L_{\mathrm{bol}})$ [$L_\odot$]	$-4.91^{+0.07}_{-0.08}$	-4.98 ± 0.07	$-0.07^{+0.10}_{-0.11}$	$-4.91^{+0.08}_{-0.07}$	-4.99 ± 0.07	$-0.08^{+0.10}_{-0.11}$
Mass ratio q	0.96 ± 0.06		$\cdots$	$0.94^{+0.12}_{-0.13}$		$\cdots$
Age t (Gyr)	$3.0^{+0.4}_{-0.5}$		$\cdots$	$3.2^{+0.6}_{-1.0}$	$3.1^{+0.6}_{-0.9}$	$-0.1^{+1.1}_{-1.2}$
$\log(t)$ [yr]	$9.48^{+0.06}_{-0.07}$		$\cdots$	$9.51^{+0.11}_{-0.12}$	$9.50^{+0.10}_{-0.12}$	$-0.01^{+0.16}_{-0.15}$
T_{eff} (K)	1150 ± 50	1100 ± 50	-50 ± 70	1150^{+40}_{-50}	1100^{+40}_{-50}	-50^{+60}_{-70}
Radius (R_{Jup})	$0.862^{+0.015}_{-0.011}$	$0.863^{+0.016}_{-0.012}$	$0.0012^{+0.0022}_{-0.0019}$	$0.856^{+0.020}_{-0.026}$	$0.860^{+0.021}_{-0.026}$	0.00 ± 0.03
$\log(g)$ [$\mathrm{cm\,s^{-2}}$]	5.23 ± 0.04	5.21 ± 0.04	$-0.019^{+0.029}_{-0.027}$	5.25 ± 0.06	$5.22^{+0.07}_{-0.06}$	-0.03 ± 0.09
MKO($J-K$) (mag)	$0.123^{+0.196}_{-0.278}$	$-0.092^{+0.172}_{-0.184}$	$-0.202^{+0.287}_{-0.338}$	$0.130^{+0.205}_{-0.266}$	$-0.096^{+0.148}_{-0.192}$	$-0.223^{+0.309}_{-0.292}$
MKO($J-H$) (mag)	$0.286^{+0.132}_{-0.148}$	$0.155^{+0.114}_{-0.117}$	$-0.129^{+0.186}_{-0.194}$	$0.294^{+0.122}_{-0.150}$	$0.153^{+0.105}_{-0.117}$	$-0.140^{+0.181}_{-0.174}$
Derived from Baraffe et al. (2003) Cond Evolutionary Models						
Mass M (M_{Jup})	51 ± 3	49 ± 3	-3 ± 4	52 ± 5	49 ± 5	-3 ± 7
$\log(L_{\mathrm{bol}})$ [$L_\odot$]	-4.92 ± 0.07	$-4.99^{+0.08}_{-0.07}$	-0.07 ± 0.10	-4.92 ± 0.07	-5.00 ± 0.07	-0.07 ± 0.10
Mass ratio q	0.95 ± 0.07		$\cdots$	$0.95^{+0.12}_{-0.14}$		$\cdots$
Age t (Gyr)	$2.25^{+0.29}_{-0.32}$		$\cdots$	$2.4^{+0.5}_{-0.6}$	$2.4^{+0.5}_{-0.6}$	$0.0^{+0.9}_{-0.8}$
$\log(t)$ [yr]	9.35 ± 0.06		$\cdots$	$9.37^{+0.10}_{-0.11}$	9.37 ± 0.11	$0.00^{+0.16}_{-0.15}$
T_{eff} (K)	1160 ± 50	1110 ± 50	-50 ± 70	1170 ± 50	1110^{+40}_{-50}	-50 ± 70
Radius (R_{Jup})	0.835 ± 0.015	$0.842^{+0.016}_{-0.015}$	0.006 ± 0.009	$0.829^{+0.024}_{-0.028}$	$0.837^{+0.025}_{-0.030}$	0.01 ± 0.04
$\log(g)$ [$\mathrm{cm\,s^{-2}}$]	5.26 ± 0.04	$5.23^{+0.04}_{-0.05}$	-0.03 ± 0.04	5.27 ± 0.07	5.24 ± 0.07	$-0.03^{+0.10}_{-0.09}$
$\log(\mathrm{Li/Li_{init}})$	$-0.0184^{+0.0025}_{-0.0052}$	$-0.015^{+0.004}_{-0.008}$	$0.004^{+0.008}_{-0.006}$	$-0.017^{+0.003}_{-0.007}$	$-0.014^{+0.004}_{-0.010}$	$0.002^{+0.010}_{-0.009}$
MKO($J-K$) (mag)	$-0.165^{+0.058}_{-0.044}$	$-0.220^{+0.065}_{-0.057}$	$-0.056^{+0.080}_{-0.073}$	$-0.171^{+0.059}_{-0.047}$	$-0.227^{+0.066}_{-0.058}$	$-0.055^{+0.084}_{-0.082}$
MKO($J-H$) (mag)	$-0.322^{+0.017}_{-0.022}$	$-0.339^{+0.014}_{-0.018}$	$-0.016^{+0.023}_{-0.025}$	$-0.322^{+0.019}_{-0.023}$	$-0.340^{+0.016}_{-0.019}$	$-0.019^{+0.030}_{-0.026}$

Table 62. Properties of 2MASS J1728+3948AB

Property	Using Total Mass: Primary	Using Total Mass: Secondary	Using Total Mass: $\Delta = \mathrm{B} - \mathrm{A}$	Using Individual Masses: Primary	Using Individual Masses: Secondary	Using Individual Masses: $\Delta = \mathrm{B} - \mathrm{A}$
Input Observed Properties						
Mass M (M_{Jup})	140^{+7}_{-8}		$\cdots$	73 ± 7	67 ± 5	-5 ± 9
Mass ratio q	$\cdots$	$\cdots$	$\cdots$	$0.93^{+0.11}_{-0.13}$		$\cdots$
$\log(L_{\mathrm{bol}})$ [$L_{\odot}$]	$-4.29^{+0.05}_{-0.04}$	-4.49 ± 0.04	-0.19 ± 0.06	$\cdots$	$\cdots$	$\cdots$
Derived from Saumon & Marley (2008) Hybrid Evolutionary Models						
Mass M (M_{Jup})	$73.4^{+1.5}_{-1.6}$	70.3 ± 2.8	$-3.2^{+2.0}_{-1.7}$	$73.9^{+1.0}_{-0.7}$	$71.0^{+1.8}_{-2.1}$	$-2.8^{+2.5}_{-3.8}$
$\log(L_{\mathrm{bol}})$ [$L_{\odot}$]	-4.29 ± 0.05	-4.50 ± 0.05	$-0.20^{+0.06}_{-0.07}$	-4.29 ± 0.05	-4.49 ± 0.05	$-0.20^{+0.07}_{-0.06}$
Mass ratio q	$0.956^{+0.030}_{-0.022}$		$\cdots$	$0.96^{+0.03}_{-0.05}$		$\cdots$
Age t (Gyr)	$3.4^{+2.8}_{-2.1}$		$\cdots$	$6.9^{+3.0}_{-5.9}$	$4.5^{+3.0}_{-3.2}$	-1^{+5}_{-7}
$\log(t)$ [yr]	$9.53^{+0.27}_{-0.38}$		$\cdots$	$9.84^{+0.33}_{-0.22}$	$9.65^{+0.30}_{-0.41}$	$-0.1^{+0.4}_{-0.5}$
T_{eff} (K)	1600 ± 40	1440 ± 40	-160 ± 50	1600 ± 40	1440 ± 40	-160 ± 50
Radius (R_{Jup})	$0.902^{+0.006}_{-0.007}$	$0.887^{+0.013}_{-0.012}$	$-0.013^{+0.010}_{-0.007}$	$0.900^{+0.004}_{-0.006}$	$0.885^{+0.008}_{-0.013}$	$-0.016^{+0.013}_{-0.014}$
$\log(g)$ [$\mathrm{cm\,s^{-2}}$]	$5.351^{+0.007}_{-0.013}$	$5.346^{+0.023}_{-0.030}$	$-0.004^{+0.016}_{-0.014}$	5.3563 ± 0.0021	$5.354^{+0.018}_{-0.020}$	$0.001^{+0.019}_{-0.039}$
MKO($J-K$) (mag)	$1.740^{+0.087}_{-0.085}$	$2.008^{+0.079}_{-0.094}$	$0.275^{+0.133}_{-0.104}$	$1.738^{+0.081}_{-0.084}$	$2.000^{+0.087}_{-0.082}$	$0.275^{+0.111}_{-0.121}$
MKO($J-H$) (mag)	$0.937^{+0.047}_{-0.043}$	$1.101^{+0.043}_{-0.061}$	$0.167^{+0.060}_{-0.073}$	$0.937^{+0.045}_{-0.042}$	$1.094^{+0.046}_{-0.053}$	$0.163^{+0.057}_{-0.074}$
Derived from Baraffe et al. (2003) Cond Evolutionary Models						
Mass M (M_{Jup})	$72.3^{+3.6}_{-2.2}$	68 ± 4	$-3.8^{+2.1}_{-1.3}$	$74.0^{+2.8}_{-2.4}$	$69.6^{+5.7}_{-2.5}$	-4^{+5}_{-6}
$\log(L_{\mathrm{bol}})$ [$L_{\odot}$]	$-4.30^{+0.04}_{-0.06}$	$-4.49^{+0.04}_{-0.05}$	-0.19 ± 0.06	-4.29 ± 0.05	$-4.49^{+0.04}_{-0.05}$	-0.20 ± 0.06
Mass ratio q	$0.947^{+0.032}_{-0.017}$		$\cdots$	$0.95^{+0.07}_{-0.08}$		$\cdots$
Age t (Gyr)	$2.9^{+0.7}_{-1.1}$		$\cdots$	$3.6^{+1.8}_{-2.4}$	$3.3^{+1.0}_{-1.7}$	$-0.3^{+2.9}_{-3.0}$
$\log(t)$ [yr]	$9.46^{+0.12}_{-0.17}$		$\cdots$	$9.56^{+0.30}_{-0.25}$	$9.52^{+0.16}_{-0.24}$	0.0 ± 0.3
T_{eff} (K)	1680^{+40}_{-50}	1520 ± 40	-170 ± 50	1690^{+50}_{-40}	1520 ± 40	-170 ± 60
Radius (R_{Jup})	$0.827^{+0.012}_{-0.013}$	$0.815^{+0.015}_{-0.018}$	$-0.013^{+0.006}_{-0.005}$	$0.820^{+0.013}_{-0.017}$	$0.808^{+0.013}_{-0.022}$	$-0.015^{+0.027}_{-0.022}$
$\log(g)$ [$\mathrm{cm\,s^{-2}}$]	$5.422^{+0.028}_{-0.025}$	5.41 ± 0.04	$-0.013^{+0.010}_{-0.013}$	$5.439^{+0.026}_{-0.025}$	$5.423^{+0.055}_{-0.027}$	$0.00^{+0.05}_{-0.06}$
$\log(\mathrm{Li}/\mathrm{Li}_{\mathrm{init}})$	$\cdots$	-0.1 ± 0.0	$\cdots$	$-2.9^{+0.4}_{-0.7}$	$-1.5^{+0.7}_{-0.6}$	0.9 ± 0.0
MKO($J-K$) (mag)	$0.103^{+0.029}_{-0.030}$	$0.013^{+0.022}_{-0.025}$	$-0.089^{+0.032}_{-0.037}$	$0.103^{+0.031}_{-0.034}$	$0.007^{+0.027}_{-0.028}$	$-0.097^{+0.043}_{-0.042}$
MKO($J-H$) (mag)	$-0.046^{+0.025}_{-0.027}$	-0.145 ± 0.023	$-0.100^{+0.032}_{-0.035}$	$-0.045^{+0.027}_{-0.025}$	-0.146 ± 0.022	$-0.101^{+0.034}_{-0.035}$

Table 63. Properties of LSPM J1735+2634AB

Property	Using Total Mass: Primary	Using Total Mass: Secondary	Using Total Mass: $\Delta = \mathrm{B} - \mathrm{A}$	Using Individual Masses: Primary	Using Individual Masses: Secondary	Using Individual Masses: $\Delta = \mathrm{B} - \mathrm{A}$
Input Observed Properties						
Mass M (M_{Jup})	187 ± 7		···	100 ± 4	87 ± 3	$-13.2^{+2.8}_{-2.6}$
Mass ratio q	···	···	···	$0.868^{+0.023}_{-0.025}$		···
$\log(L_{\mathrm{bol}})$ [$L_{\odot}$]	-3.221 ± 0.028	$-3.445^{+0.028}_{-0.029}$	-0.22 ± 0.04	···	···	···
Derived from Baraffe et al. (2015) Evolutionary Models						
Mass M (M_{Jup})	$96.1^{+1.4}_{-1.7}$	87.8 ± 1.1	$-8.4^{+1.9}_{-1.7}$	$96.3^{+1.5}_{-1.6}$	$87.8^{+1.2}_{-1.1}$	$-8.5^{+2.0}_{-1.9}$
$\log(L_{\mathrm{bol}})$ [$L_{\odot}$]	-3.22 ± 0.03	-3.45 ± 0.03	$-0.23^{+0.04}_{-0.05}$	-3.22 ± 0.03	-3.44 ± 0.03	$-0.23^{+0.05}_{-0.04}$
Mass ratio q	$0.913^{+0.019}_{-0.017}$		···	$0.912^{+0.020}_{-0.019}$		···
Age t (Gyr)	$5.3^{+2.1}_{-4.2}$		···	$5.3^{+2.0}_{-4.3}$	$5.2^{+1.9}_{-4.5}$	0 ± 4
$\log(t)$ [yr]	$9.73^{+0.27}_{-0.17}$		···	$9.72^{+0.28}_{-0.17}$	$9.72^{+0.28}_{-0.18}$	0.0 ± 0.4
T_{eff} (K)	2674 ± 27	2458^{+28}_{-31}	-210 ± 40	2677^{+28}_{-26}	2462 ± 30	-210 ± 40
Radius (R_{Jup})	$1.118^{+0.016}_{-0.017}$	$1.015^{+0.012}_{-0.014}$	$-0.103^{+0.019}_{-0.021}$	$1.120^{+0.016}_{-0.017}$	$1.017^{+0.014}_{-0.013}$	-0.103 ± 0.021
$\log(g)$ [$\mathrm{cm\,s^{-2}}$]	$5.281^{+0.007}_{-0.006}$	$5.325^{+0.007}_{-0.006}$	$0.043^{+0.009}_{-0.008}$	$5.281^{+0.007}_{-0.006}$	5.324 ± 0.007	0.044 ± 0.010
$\log(\mathrm{Li}/\mathrm{Li}_{\mathrm{init}})$	< -4.0	< -4.0	···	< -4.0	< -4.0	···
MKO($J-K$) (mag)	0.803 ± 0.004	$0.750^{+0.008}_{-0.012}$	$-0.051^{+0.010}_{-0.012}$	0.803 ± 0.004	$0.751^{+0.010}_{-0.011}$	$-0.051^{+0.010}_{-0.013}$
MKO($J-H$) (mag)	$0.494^{+0.005}_{-0.004}$	$0.459^{+0.006}_{-0.008}$	$-0.036^{+0.007}_{-0.010}$	$0.495^{+0.005}_{-0.004}$	$0.459^{+0.007}_{-0.008}$	$-0.035^{+0.008}_{-0.010}$

Table 64. Properties of 2MASS J2132+1341AB

Property	Using Total Mass: Primary	Using Total Mass: Secondary	Using Total Mass: $\Delta = \mathrm{B} - \mathrm{A}$	Using Individual Masses: Primary	Using Individual Masses: Secondary	Using Individual Masses: $\Delta = \mathrm{B} - \mathrm{A}$
Input Observed Properties						
Mass M (M_{Jup})	128^{+7}_{-8}		···	68 ± 4	60 ± 4	-8 ± 3
Mass ratio q	···	···	···	$0.88^{+0.04}_{-0.05}$		···
$\log(L_{\mathrm{bol}})$ [$L_{\odot}$]	-4.22 ± 0.05	-4.50 ± 0.05	-0.28 ± 0.06	···	···	···
Derived from Saumon & Marley (2008) Hybrid Evolutionary Models						
Mass M (M_{Jup})	$69.9^{+3.2}_{-2.9}$	59^{+5}_{-6}	-10 ± 4	$74.3^{+2.0}_{-2.8}$	61^{+4}_{-5}	-12^{+5}_{-7}
$\log(L_{\mathrm{bol}})$ [$L_{\odot}$]	-4.22 ± 0.05	$-4.51^{+0.04}_{-0.05}$	-0.28 ± 0.07	-4.22 ± 0.05	-4.51 ± 0.05	-0.29 ± 0.07
Mass ratio q	0.85 ± 0.06		···	$0.84^{+0.06}_{-0.09}$		···
Age t (Gyr)	$1.44^{+0.26}_{-0.37}$		···	$3.6^{+3.9}_{-2.8}$	$1.6^{+0.3}_{-0.4}$	$-1.7^{+2.9}_{-5.0}$
$\log(t)$ [yr]	$9.16^{+0.09}_{-0.10}$		···	$9.6^{+0.4}_{-0.6}$	$9.21^{+0.09}_{-0.11}$	-0.3 ± 0.5
T_{eff} (K)	1650^{+40}_{-50}	1400^{+30}_{-40}	-250 ± 60	1660^{+50}_{-40}	1400^{+30}_{-40}	-260^{+50}_{-70}
Radius (R_{Jup})	$0.925^{+0.010}_{-0.012}$	$0.925^{+0.019}_{-0.021}$	$0.000^{+0.009}_{-0.008}$	$0.909^{+0.010}_{-0.012}$	$0.915^{+0.020}_{-0.017}$	$0.001^{+0.024}_{-0.023}$
$\log(g)$ [$\mathrm{cm\,s^{-2}}$]	5.306 ± 0.028	$5.23^{+0.05}_{-0.06}$	-0.07 ± 0.04	$5.352^{+0.006}_{-0.029}$	$5.26^{+0.04}_{-0.06}$	-0.08 ± 0.06
MKO($J - K$) (mag)	$1.607^{+0.113}_{-0.103}$	$2.004^{+0.109}_{-0.074}$	$0.389^{+0.154}_{-0.144}$	$1.579^{+0.121}_{-0.111}$	$2.023^{+0.078}_{-0.091}$	$0.438^{+0.157}_{-0.134}$
MKO($J - H$) (mag)	$0.863^{+0.060}_{-0.057}$	$1.116^{+0.046}_{-0.033}$	$0.249^{+0.083}_{-0.056}$	$0.849^{+0.066}_{-0.060}$	$1.124^{+0.042}_{-0.032}$	$0.272^{+0.075}_{-0.073}$
Derived from Baraffe et al. (2003) Cond Evolutionary Models						
Mass M (M_{Jup})	$68.6^{+3.0}_{-2.9}$	60^{+5}_{-4}	$-7.9^{+2.3}_{-2.5}$	$70.5^{+6.5}_{-2.4}$	61^{+4}_{-5}	-9^{+5}_{-6}
$\log(L_{\mathrm{bol}})$ [$L_{\odot}$]	-4.22 ± 0.05	$-4.50^{+0.06}_{-0.04}$	$-0.27^{+0.07}_{-0.06}$	-4.22 ± 0.05	-4.50 ± 0.05	-0.28 ± 0.07
Mass ratio q	$0.884^{+0.046}_{-0.027}$		···	$0.87^{+0.07}_{-0.08}$		···
Age t (Gyr)	$1.71^{+0.28}_{-0.36}$		···	$2.0^{+0.6}_{-0.9}$	$1.77^{+0.29}_{-0.40}$	$-0.2^{+1.0}_{-0.9}$
$\log(t)$ [yr]	$9.23^{+0.08}_{-0.09}$		···	$9.30^{+0.13}_{-0.21}$	$9.25^{+0.08}_{-0.10}$	$-0.05^{+0.23}_{-0.18}$
T_{eff} (K)	1730 ± 50	1480^{+40}_{-50}	-240 ± 60	1740 ± 50	1480 ± 40	-250 ± 60
Radius (R_{Jup})	$0.856^{+0.012}_{-0.011}$	$0.844^{+0.016}_{-0.020}$	$-0.012^{+0.007}_{-0.008}$	0.846 ± 0.019	0.840 ± 0.018	$-0.007^{+0.027}_{-0.025}$
$\log(g)$ [$\mathrm{cm\,s^{-2}}$]	$5.366^{+0.030}_{-0.029}$	$5.32^{+0.06}_{-0.04}$	$-0.043^{+0.026}_{-0.016}$	$5.390^{+0.057}_{-0.029}$	5.33 ± 0.05	$-0.06^{+0.06}_{-0.07}$
$\log(\mathrm{Li}/\mathrm{Li}_{\mathrm{init}})$	$-3.01^{+0.14}_{-0.45}$	$-0.7^{+0.7}_{-0.5}$	$2.8^{+0.6}_{-0.4}$	$-3.24^{+0.22}_{-0.35}$	$-1.1^{+1.1}_{-0.4}$	$2.2^{+0.7}_{-0.6}$
MKO($J - K$) (mag)	$0.167^{+0.033}_{-0.031}$	0.025 ± 0.022	$-0.143^{+0.044}_{-0.029}$	0.161 ± 0.035	$0.023^{+0.022}_{-0.023}$	$-0.139^{+0.043}_{-0.041}$
MKO($J - H$) (mag)	$-0.007^{+0.029}_{-0.025}$	$-0.153^{+0.022}_{-0.026}$	$-0.145^{+0.040}_{-0.030}$	$-0.005^{+0.027}_{-0.028}$	-0.154 ± 0.024	$-0.149^{+0.037}_{-0.035}$

Table 65. Properties of 2MASS J2140+1625AB

Property	Using Total Mass: Primary	Using Total Mass: Secondary	Using Total Mass: $\Delta = \mathrm{B} - \mathrm{A}$	Using Individual Masses: Primary	Using Individual Masses: Secondary	Using Individual Masses: $\Delta = \mathrm{B} - \mathrm{A}$
Input Observed Properties						
Mass M ($M_{\rm Jup}$)	183^{+14}_{-17}		$\cdots$	114^{+10}_{-12}	69^{+8}_{-9}	-45^{+12}_{-11}
Mass ratio q	$\cdots$	$\cdots$	$\cdots$	$0.60^{+0.07}_{-0.08}$		$\cdots$
$\log(L_{\rm bol})$ $[L_\odot]$	-3.20 ± 0.04	-3.51 ± 0.04	-0.31 ± 0.04	$\cdots$	$\cdots$	$\cdots$
Derived from Baraffe et al. (2015) Evolutionary Models						
Mass M ($M_{\rm Jup}$)	$96.9^{+2.2}_{-2.6}$	$85.6^{+1.7}_{-1.5}$	$-11.5^{+2.9}_{-2.6}$	$96.2^{+2.2}_{-2.3}$	$85.6^{+4.2}_{-2.7}$	-11^{+6}_{-4}
$\log(L_{\rm bol})$ $[L_\odot]$	$-3.20^{+0.05}_{-0.04}$	-3.51 ± 0.05	-0.31 ± 0.06	$-3.22^{+0.05}_{-0.04}$	$-3.50^{+0.05}_{-0.04}$	$-0.28^{+0.07}_{-0.06}$
Mass ratio q	$0.882^{+0.028}_{-0.024}$		$\cdots$	$0.88^{+0.06}_{-0.04}$		$\cdots$
Age t (Gyr)	$5.0^{+1.9}_{-4.6}$		$\cdots$	$5.2^{+2.6}_{-3.8}$	$3.0^{+2.6}_{-2.8}$	-2^{+4}_{-5}
$\log(t)$ [yr]	$9.70^{+0.30}_{-0.20}$		$\cdots$	$9.72^{+0.28}_{-0.17}$	9.5 ± 0.5	$-0.2^{+0.5}_{-0.8}$
$T_{\rm eff}$ (K)	2690^{+50}_{-30}	2400 ± 40	-290^{+60}_{-50}	2680 ± 40	2410^{+60}_{-50}	-270^{+80}_{-60}
Radius ($R_{\rm Jup}$)	$1.128^{+0.021}_{-0.028}$	0.990 ± 0.018	$-0.137^{+0.027}_{-0.030}$	$1.120^{+0.026}_{-0.021}$	$1.006^{+0.021}_{-0.027}$	$-0.11^{+0.03}_{-0.04}$
$\log(g)$ [cm s^{-2}]	5.277 ± 0.010	$5.336^{+0.010}_{-0.009}$	$0.058^{+0.015}_{-0.011}$	$5.281^{+0.009}_{-0.010}$	$5.327^{+0.022}_{-0.018}$	$0.044^{+0.033}_{-0.022}$
$\log(\mathrm{Li}/\mathrm{Li}_{\rm init})$	< -4.0	< -4.0	$\cdots$	< -4.0	< -4.0	$\cdots$
MKO($J-K$) (mag)	$0.804^{+0.007}_{-0.005}$	$0.736^{+0.007}_{-0.014}$	$-0.066^{+0.011}_{-0.015}$	0.803 ± 0.006	$0.748^{+0.016}_{-0.026}$	$-0.053^{+0.019}_{-0.027}$
MKO($J-H$) (mag)	$0.496^{+0.007}_{-0.006}$	$0.450^{+0.005}_{-0.011}$	$-0.046^{+0.009}_{-0.013}$	$0.495^{+0.007}_{-0.005}$	$0.456^{+0.009}_{-0.017}$	$-0.038^{+0.013}_{-0.019}$

Note. — In the total-mass analysis, the median mass after rejection sampling was $183 \pm 3\,M_{\rm Jup}$, 0.05σ lower than the input measurement. In the individual-mass analysis of the primary, the median mass after rejection sampling was 1.7σ lower than the input measurement, and for the secondary the median mass after rejection sampling was 2.0σ higher than the input measurement.

Table 66. Properties of 2MASS J2206−2047AB

Property	Using Total Mass: Primary	Using Total Mass: Secondary	Using Total Mass: $\Delta = \mathrm{B} - \mathrm{A}$	Using Individual Masses: Primary	Using Individual Masses: Secondary	Using Individual Masses: $\Delta = \mathrm{B} - \mathrm{A}$
Input Observed Properties						
Mass M (M_{Jup})	188^{+16}_{-17}		···	102^{+10}_{-11}	86^{+8}_{-10}	-17 ± 11
Mass ratio q	···	···	···	$0.84^{+0.09}_{-0.10}$		···
$\log(L_{\mathrm{bol}})$ [$L_\odot$]	$-3.22^{+0.04}_{-0.03}$	$-3.26^{+0.03}_{-0.04}$	$-0.03^{+0.04}_{-0.03}$	···	···	···
Derived from Baraffe et al. (2015) Evolutionary Models						
Mass M (M_{Jup})	$96.1^{+2.4}_{-2.2}$	$94.8^{+2.0}_{-2.2}$	$-1.4^{+2.7}_{-2.8}$	$95.7^{+2.0}_{-2.3}$	$95.0^{+2.3}_{-2.0}$	-1 ± 3
$\log(L_{\mathrm{bol}})$ [$L_\odot$]	$-3.22^{+0.05}_{-0.04}$	$-3.25^{+0.05}_{-0.04}$	-0.03 ± 0.06	-3.23 ± 0.04	-3.24 ± 0.04	-0.01 ± 0.06
Mass ratio q	$0.986^{+0.028}_{-0.029}$		···	$0.99^{+0.04}_{-0.03}$		···
Age t (Gyr)	$5.0^{+1.9}_{-4.6}$		···	$5.2^{+2.0}_{-4.5}$	$4.8^{+1.9}_{-4.5}$	0 ± 4
$\log(t)$ [yr]	$9.70^{+0.30}_{-0.20}$		···	$9.71^{+0.29}_{-0.18}$	$9.68^{+0.32}_{-0.22}$	0.0 ± 0.5
T_{eff} (K)	2680^{+40}_{-30}	2650^{+50}_{-30}	-30 ± 50	2670 ± 40	2650^{+40}_{-30}	-10 ± 60
Radius (R_{Jup})	$1.120^{+0.023}_{-0.022}$	$1.105^{+0.025}_{-0.019}$	$-0.015^{+0.031}_{-0.027}$	$1.114^{+0.023}_{-0.022}$	1.110 ± 0.022	0.00 ± 0.03
$\log(g)$ [cm s^{-2}]	$5.280^{+0.010}_{-0.009}$	5.286 ± 0.010	$0.005^{+0.011}_{-0.012}$	$5.282^{+0.010}_{-0.009}$	$5.284^{+0.011}_{-0.009}$	$0.001^{+0.016}_{-0.013}$
$\log(\mathrm{Li}/\mathrm{Li}_{\mathrm{init}})$	< -4.0	< -4.0	···	< -4.0	< -4.0	···
MKO($J - K$) (mag)	$0.803^{+0.006}_{-0.005}$	$0.799^{+0.007}_{-0.006}$	-0.003 ± 0.008	0.802 ± 0.006	0.800 ± 0.006	-0.001 ± 0.009
MKO($J - H$) (mag)	$0.494^{+0.007}_{-0.005}$	0.491 ± 0.006	$-0.003^{+0.007}_{-0.008}$	0.493 ± 0.006	0.491 ± 0.006	-0.002 ± 0.009

Note. — In the total-mass analysis, the median mass after rejection sampling was $191^{+4}_{-3}\,M_{\mathrm{Jup}}$, 0.2σ higher than the input measurement. In the individual-mass analysis, the median mass of the primary after rejection sampling was 0.6σ lower than the input measurement, and the median mass of the secondary after rejection sampling was 1.0σ higher than the input measurement.

Table 67. Properties of DENIS J2252−1730AB

Property	Using Total Mass: Primary	Using Total Mass: Secondary	Using Total Mass: $\Delta = $ B − A	Using Individual Masses: Primary	Using Individual Masses: Secondary	Using Individual Masses: $\Delta = $ B − A
Input Observed Properties						
Mass M ($M_{\rm Jup}$)	101 ± 7		$\cdots$	59 ± 5	41 ± 4	-18 ± 6
Mass ratio q	$\cdots$	$\cdots$	$\cdots$	$0.70^{+0.08}_{-0.09}$		$\cdots$
$\log(L_{\rm bol})$ [$L_\odot$]	-4.26 ± 0.04	-4.76 ± 0.07	-0.50 ± 0.08	$\cdots$	$\cdots$	$\cdots$
Derived from Saumon & Marley (2008) Hybrid Evolutionary Models						
Mass M ($M_{\rm Jup}$)	65 ± 4	$37.1^{+3.0}_{-4.4}$	$-27.6^{+2.8}_{-3.4}$	61^{+5}_{-8}	42 ± 4	-19^{+9}_{-7}
$\log(L_{\rm bol})$ [$L_\odot$]	-4.26 ± 0.05	-4.74 ± 0.08	-0.48 ± 0.09	-4.25 ± 0.05	-4.75 ± 0.08	-0.50 ± 0.09
Mass ratio q	$0.57^{+0.03}_{-0.05}$		$\cdots$	$0.69^{+0.09}_{-0.10}$		$\cdots$
Age t (Gyr)	$1.11^{+0.19}_{-0.22}$		$\cdots$	$0.94^{+0.20}_{-0.31}$	$1.5^{+0.3}_{-0.4}$	$0.5^{+0.6}_{-0.5}$
$\log(t)$ [yr]	9.04 ± 0.08		$\cdots$	$8.97^{+0.10}_{-0.15}$	$9.18^{+0.11}_{-0.10}$	$0.20^{+0.20}_{-0.16}$
$T_{\rm eff}$ (K)	1600 ± 50	1200^{+60}_{-50}	-400 ± 70	1590 ± 50	1210^{+50}_{-40}	-380 ± 70
Radius ($R_{\rm Jup}$)	$0.941^{+0.011}_{-0.018}$	$0.961^{+0.018}_{-0.020}$	$0.0193^{+0.0037}_{-0.0029}$	$0.956^{+0.032}_{-0.027}$	$0.929^{+0.024}_{-0.027}$	-0.03 ± 0.04
$\log(g)$ [cm s^{-2}]	5.26 ± 0.04	$5.00^{+0.05}_{-0.06}$	$-0.257^{+0.028}_{-0.043}$	$5.22^{+0.06}_{-0.08}$	5.08 ± 0.06	$-0.14^{+0.10}_{-0.09}$
MKO($J-K$) (mag)	$1.691^{+0.119}_{-0.094}$	$0.459^{+0.281}_{-0.393}$	$-1.221^{+0.309}_{-0.416}$	$1.703^{+0.115}_{-0.093}$	$0.520^{+0.284}_{-0.415}$	$-1.176^{+0.314}_{-0.416}$
MKO($J-H$) (mag)	$0.905^{+0.060}_{-0.055}$	$0.453^{+0.175}_{-0.191}$	$-0.447^{+0.176}_{-0.216}$	$0.911^{+0.056}_{-0.055}$	$0.493^{+0.160}_{-0.199}$	$-0.416^{+0.169}_{-0.206}$
Derived from Baraffe et al. (2003) Cond Evolutionary Models						
Mass M ($M_{\rm Jup}$)	59^{+5}_{-4}	42 ± 3	-17 ± 3	61 ± 6	42 ± 4	-19 ± 7
$\log(L_{\rm bol})$ [$L_\odot$]	-4.26 ± 0.05	$-4.76^{+0.08}_{-0.07}$	-0.50 ± 0.09	-4.25 ± 0.05	$-4.77^{+0.07}_{-0.08}$	-0.52 ± 0.09
Mass ratio q	$0.71^{+0.05}_{-0.04}$		$\cdots$	$0.69^{+0.09}_{-0.10}$		$\cdots$
Age t (Gyr)	$1.10^{+0.15}_{-0.18}$		$\cdots$	$1.17^{+0.24}_{-0.32}$	$1.13^{+0.23}_{-0.29}$	$-0.1^{+0.5}_{-0.4}$
$\log(t)$ [yr]	$9.04^{+0.06}_{-0.07}$		$\cdots$	$9.07^{+0.09}_{-0.13}$	9.05 ± 0.10	$-0.02^{+0.16}_{-0.15}$
$T_{\rm eff}$ (K)	1660^{+50}_{-60}	1230^{+50}_{-60}	-430 ± 70	1670 ± 50	1230^{+50}_{-60}	-440 ± 70
Radius ($R_{\rm Jup}$)	$0.886^{+0.012}_{-0.017}$	$0.904^{+0.014}_{-0.013}$	$0.016^{+0.007}_{-0.006}$	$0.880^{+0.021}_{-0.024}$	$0.902^{+0.020}_{-0.022}$	0.02 ± 0.03
$\log(g)$ [cm s^{-2}]	$5.27^{+0.05}_{-0.04}$	5.10 ± 0.05	$-0.167^{+0.030}_{-0.031}$	5.29 ± 0.06	5.11 ± 0.06	-0.18 ± 0.09
$\log(\mathrm{Li}/\mathrm{Li}_{\rm init})$	$-2.1^{+0.7}_{-1.5}$	$-0.00019^{+0.00019}_{-0.00356}$	$2.1^{+1.5}_{-0.7}$	$-2.1^{+0.7}_{-1.5}$	$-0.0005^{+0.0005}_{-0.0046}$	$2.1^{+1.5}_{-0.7}$
MKO($J-K$) (mag)	$0.143^{+0.029}_{-0.033}$	$-0.043^{+0.045}_{-0.040}$	$-0.188^{+0.058}_{-0.052}$	$0.144^{+0.027}_{-0.032}$	$-0.049^{+0.056}_{-0.045}$	$-0.195^{+0.063}_{-0.053}$
MKO($J-H$) (mag)	$-0.033^{+0.028}_{-0.030}$	$-0.265^{+0.022}_{-0.027}$	$-0.231^{+0.040}_{-0.035}$	$-0.031^{+0.026}_{-0.029}$	$-0.267^{+0.024}_{-0.025}$	$-0.236^{+0.035}_{-0.039}$

Table 68. Coefficients of Polynomial Fits

y	x	c_0	c_1	c_2	c_3	c_4	c_5	rms	valid x range
$T_{\rm eff}$ (Lyon)	SpT	4251.0	−238.03	4.582	···	···	···	90 K	M7–T5
$T_{\rm eff}$ (SM08)	SpT	4544.3	−284.52	6.001	···	···	···	80 K	L1.5–T5
MKO Photometric System									
$\log(L_{\rm bol}/L_\odot)$	M_K	−172.188	68.11147	−10.671188	0.8162709	−0.03068824	0.000454547	0.05 dex*	9.1–17.8 mag
$\log(L_{\rm bol}/L_\odot)$	M_H	−13.282	3.46876	−0.351721	0.0106200	···	···	0.023 dex	9.6–13.3 mag
$J_{\rm MKO} - J_{\rm 2MASS}$	M_K	−2.284	0.55165	−0.043190	0.0010379	···	···	0.015 mag	9.1–17.0 mag
$H_{\rm MKO} - H_{\rm 2MASS}$	M_H	−0.051	0.00850	···	···	···	···	0.003 mag	9.6–13.4 mag
$H_{\rm MKO} - H_{\rm 2MASS}$	M_K	−0.702	0.15644	−0.010605	0.0002365	···	···	0.004 mag	9.1–17.0 mag
$K_{\rm MKO} - K_{S,\rm 2MASS}$	M_K	−0.048	0.00221	···	···	···	···	0.006 mag	9.1–13.0 mag
$K_{\rm MKO} - K_{S,\rm 2MASS}$	M_K	−1.526	0.11594	···	···	···	···	0.007 mag	13.0–14.2 mag
$K_{\rm MKO} - K_{S,\rm 2MASS}$	M_K	0.054	0.00447	···	···	···	···	0.007 mag	14.2–17.0 mag
$K_{\rm H2} - K$	M_K	−0.207	0.07241	−0.004693	···	···	···	0.025 mag	9.1–13.1 mag
2MASS Photometric System									
$\log(L_{\rm bol}/L_\odot)$	M_{K_S}	−59.877	22.58776	−3.364101	0.2357643	−0.00785837	0.000098821	0.05 dex*	8.8–16.6 mag
$\log(L_{\rm bol}/L_\odot)$	M_H	−10.426	2.74259	−0.290797	0.0089222	···	···	0.023 dex	9.2–13.3 mag
$J_{\rm MKO} - J_{\rm 2MASS}$	M_{K_S}	−2.747	0.66217	−0.051739	0.0012518	···	···	0.017 mag	9.1–16.6 mag
$H_{\rm MKO} - H_{\rm 2MASS}$	M_{K_S}	−0.754	0.16903	−0.011606	0.0002626	···	···	0.004 mag	9.1–16.6 mag
$H_{\rm MKO} - H_{\rm 2MASS}$	M_H	−0.050	0.00845	···	···	···	···	0.003 mag	9.6–13.4 mag
$K_{\rm MKO} - K_{S,\rm 2MASS}$	M_{K_S}	−0.048	0.00219	···	···	···	···	0.006 mag	9.1–12.9 mag
$K_{\rm MKO} - K_{S,\rm 2MASS}$	M_{K_S}	−1.413	0.10801	···	···	···	···	0.026 mag	12.9–14.2 mag
$K_{\rm MKO} - K_{S,\rm 2MASS}$	M_{K_S}	0.088	0.00240	···	···	···	···	0.007 mag	14.2–17.0 mag
$K_{\rm H2} - K_S$	M_{K_S}	−0.036	0.03407	−0.002824	···	···	···	0.021 mag	9.1–13.1 mag

Note. — The coefficients are defined as:

$$y = \sum_{i=0} c_i x^i$$

where y and x are the quantities listed in the first two columns. For spectral types, M7 corresponds to 7.0 and T5 corresponds to 25.0.

*The luminosity relations have significantly different scatter at bright and faint magnitudes. For both, the scatter is 0.04 dex at $\leq$13.0 mag and 0.07 dex at $>$13.0 mag.